UNIVERSITE DE LILLE, DEPARTEMENT DES SCIENCES DE LA TERRE
LABORATOIRE D'OCEANOLOGIE ET GEOSCIENCES

THÈSE DE DOCTORAT

Ecole doctorale : Science de la matière, du Rayonnement et de l'Environnement
Spécialité : Géosciences, Ecologie, Paléontologie et Océanographie

par :
Alexandre FADEL

Micro et nanoanalyses des microfossiles du Protérozoïque et de tapis microbiens fossiles

Soutenue publiquement le 29 juin 2018
Devant le jury composé de :

Karim BENZERARA	Directeur de recherche CNRS (IMPMC, Paris)	Rapporteur
Volker THIEL	Professeur (Université de Göttingen)	Rapporteur
Emmanuelle JAVAUX	Professeur (Université de Liège)	Examinatrice
Frances WESTALL	Directrice de recherche CNRS (CBM, Orléans)	Examinatrice
Armelle RIBOULLEAU	Maitre de Conférences, HDR (Université de Lille)	Directrice
Kevin LEPOT	Maitre de Conférences (Université de Lille)	Encadrant

Laboratoire d’Océanologie et de Géosciences
UMR 8187 LOG - CNRS
Université de Lille
Cité Scientifique – Bâtiment SN5
59655 VILLENEUVE D’ASCQ
France

A mes grands-parents,
A mes parents et ma sœur.

« La nature ne peut pas être dupe » (R. P. Feynman)

« La forêt précède les peuples ; le désert les suit. »
(F. R. de Chateaubriand)

Remerciements

Un travail de thèse n'étant pas le fruit que d'une seule personne, je souhaite remercier toutes les personnes qui ont contribué à la réalisation de ce projet.

Je tiens tout d'abord à remercier mes deux encadrants de thèse qui m'ont guidé, aidé et soutenu tout au long de ce travail de thèse. Je remercie ma directrice de thèse, Armelle Riboulleau pour sa disponibilité et les conseils avisés qu'elle m'a apporté tout au long de ce projet. Je remercie tout particulièrement et chaleureusement mon co-encadrant de thèse, Kevin Lepot qui m'a fait entrer dans le monde de la paléontologie précambrienne. Depuis 2012, Kevin m'a formé et a toujours été disponible pour moi afin de répondre à mes interrogations, me conseiller et me motiver. Ce travail n'aurait pu aboutir sans son soutien et sa confiance. Ces quelques lignes ne sauraient exprimer toute la gratitude que j'ai envers lui.

Mes remerciements vont également aux membres du jury, aux rapporteurs Karim Benzerara, Volker Thiel et aux examinatrices Emmanuelle Javaux, Frances Westall qui ont accepté de juger mon travail de thèse.

Je remercie Sylvain Bernard pour l'aide qu'il m'a apporté au synchrotron et pour ses conseils sur mon travail et mon avenir professionnel. Je remercie également Vincent Busigny pour ses conseils et sa précieuse aide lors de la rédaction de mon premier article. Merci à Cristian Focsa et Yvain Carpentier pour les échanges que nous avons eus sur la ToF-SIMS.

Merci également à Nicolas Nuns qui a toujours été présent lors des analyses à la ToF SIMS. Son aide a été aussi indispensable lors du traitement des données et les interprétations de ces dernières. Je remercie Ahmed Addad qui m'a aidé à plusieurs reprises pour les analyses TEM, leurs interprétations et les divers problèmes techniques que j'ai eu à résoudre. Merci à David Troadec pour la réalisation des nombreuses lames FIB.

Merci aux personnes avec qui j'ai travaillé au sein du bâtiment SN5 au cours de ces dernières années : Nicolas Tribovillard, Franck Bourdelle, Béatrice Beauvière, Philippe Recourt, Sandra Ventalon, Monique Gentric, David Decroocq et Déborah Ponlevé. Je remercie tout particulièrement Sylvie Regnier pour son aide lors de la réalisation de mes tranches épaisses et pour les discussions enrichissantes au sein de l'atelier de lames minces.

Je tiens à remercier également Jean Jacques Raux, Franck Bizet et Alain Deparcy pour leur assistance technique.

Merci également à mes deux collègues de bureau, Arnaud Sanchez-Hachair et Stellina Lekele Baghekema avec qui j'ai passé d'excellents moments au bureau 127. Nos diverses discussions m'auront permis de passer les moments difficiles de cette thèse.

Je remercie Maxence Delaine que je connais depuis mes années de master et avec qui j'ai partagé des discussions intéressantes et motivantes. Merci aux collègues doctorants/post doctorants que j'ai rencontré au cours de ces dernières années : François Beny, Tom Caquineau, Marie Catherine Genge, Noémie Sévêque, Léa Devaere, Melesio Quijada, Alexis Caillaud, Marie Fabio Francescangeli et Sandra Borderie et tous ceux que je n'ai pas cité.

Enfin, merci à toute ma famille qui m'a soutenu et aidé au cours de ces dernières années.

Résumé

L’étude de la matière organique formant les microfossiles et tapis microbiens préservés dans les roches précambriennes est cruciale pour comprendre comment la vie à évolué au cours du Précambrien. Plusieurs techniques de spectroscopie in situ ont été utilisées pour contraindre la nature biologique de ces microstructures organiques. Cependant ces diverses techniques n’offrent pas la possibilité d’accéder aux informations moléculaires complexes préservées dans ces structures organiques. La spectroscopie de masse à temps de vol (ToF SIMS), permet d’accéder à ce type d’information, cependant, du fait de sa forte sensibilité aux contaminations, elle n’a encore jamais été appliquée avec succès sur des (micro)fossiles précambriens.

Un premier aspect de ce travail a été la mise au point d’un protocole de préparation de tranches épaisses de roches sans résine et exempte de toute contamination organique. Ce type de préparation permet d’effectuer des observations optiques classiques de microstructures organiques, des nettoyages avec des solvants organiques, mais surtout des analyses à la ToF SIMS.

Les structures moléculaires des matières organiques préservés dans des tapis microbiens fossiles d’âge kimméridgien (Orbagnoux, France) et archéen (formation de Strelley Pool, Australie occidentale, 3,4 milliards d’années) ont ensuite été caractérisées à l’échelle micrométrique. L’examen des données obtenues à la ToF SIMS a permis de mettre en évidence la présence de micro-hétérogénéités moléculaires et de renseigner les caractères aliphatiques et aromatiques des matières organiques préservées, confirmant l’intérêt de la ToF SIMS pour l’étude moléculaire des microfossiles.

Un second aspect de ce travail était la caractérisation à micro- et nanoéchelle de deux assemblages de microfossiles du Précambrien. L’étude de l’assemblage de microfossiles de la formation de Draken (700-800 millions d’années) a permis de documenter des structures organiques encore jamais rapportées et provenant de cyanobactéries filamenteuses, coccoïdes (chroococcales, pleurocapsales), et d’eucaryotes (amibes fossiles). L’étude des roches de Turee Creek group (2,3 milliards d’années, Australie occidentale) a permis de caractériser différentes morpho-espèces de microfossiles. Cet assemblage de microfossiles porte une signature en isotopie du fer d’une oxydation microbienne du fer.

Abstract

The study of organic matter forming microfossils and microbial mats preserved in Precambrian rocks is important to understand the evolution of early life during the Precambrian. Several *in situ* spectroscopy techniques have been used to infer the biological nature of these organic microstructures. However, these various techniques did not offer the possibility to constrain the complex molecular information preserved in these organic structures. This type of information is accessible with Time-of-Flight Secondary Ion Mass Spectroscopy (ToF SIMS), nevertheless the technique has not been appled to Precambrian fossils with success so far, because of its high sensitivity to contamination.

A first aim of this research was to develop a preparation method for resin-free semi-thin sections, devoid of organic contaminants. This semi-thin section preparation makes it possible to perform classical optical observations of organic microstructures, cleaning processes with organic solvents and, above all, ToF SIMS analyzes.

The molecular structures of organic matter of fossil microbial mats preserved in Kimmeridgian (Orbagnoux, France) and Archean (Strelley Pool formation, 3.4 billion years ago) rocks were characterized at the micrometric scale. Examination of the data obtained with ToF SIMS shows the presence of molecular micro-heterogeneities and permits to constrain the aliphatic and aromatic characters of the preserved organic materials, confirming the interest of ToF SIMS for the molecular study of microfossils.

A second aim of this research was the micro- and nanoscale caracterisation of two microfossil assemblages of Precambrian age. The study of microfossils from the Draken Formation (700–800 million years ago) allowed to document new organic ultrastructure, which come from filamentous, coccoid (chroococcal, pleurocapsal) cyanobacteria and eukaryotes (amoebae). The study of the rocks from the Turee Creek group (~2.3 billion years old, Western Australia) allowed characterize different microfossil morphospecies. This microfossil assemblage bears the Fe-isotope signature of microbial iron oxidation.

Sommaire

INTRODUCTION ET GENERALITES 12

I/ Introduction générale 13

II/ Généralités sur le précambrien : évolution des environnements et de la biosphère 17

1 L'Hadéen 17
2 L'Archéen: une atmosphère anoxique 17
3 Le Grand Evènement d'Oxydation 19
4 Le Protérozoïque 20
  4.1 Un océan stratifié 20
  4.2 L'émergence des eucaryotes et la domination des cyanobactéries 22
5 L'Evènement d'Oxygénation du Néoprotérozoïque (NOE). 23
Références 25

CHAPITRE I METHODE DE PREPARATION DE LAMES SEMI-EPAISSES POUR LA CARACTERISATION MOLECULAIRE DE MICRO- ET NANO-STRUCTURE ORGANIQUE 34

Préambule sur la spectrométrie ToF-SIMS. 35

Références 38

A semi-thin section preparation method for *in situ* molecular characterization of organic micro- and nano-structures 40

Abstract 41
1 Introduction 41
2 Samples 43
3 Semi-thin section preparations 44
  3.1 Equipment 44
  3.2 Protocol 45
    3.2.1 Coarse slide preparation 45
    3.2.2 Fine grinding process 49
    3.2.3 Polishing. 51
4 Characterization techniques. 53
5 Results and discussion 53
  5.1 Conventional thin section procedures 53
  5.2 Physical properties of resin-free semi-thin sections 55
  5.3 ToF-SIMS of semi-thin sections. 56
Conclusions 61

Acknowledgements 62
References 62
Supplementary figure 68

CHAPITRE II CARACTERISATION MOLECULAIRE A LA TOF SIMS D'ANCIENS TAPIS MICROBIENS A LA MICRO ECHELLE 69

ToF-SIMS molecular characterization of ancient microbial mats at the microscale 70

Abstract 71
1 Introduction 71
2 Geological setting 74
  2.1 Orbagnoux deposit 74
  2.2 Strelley Pool Chert 75
3 Methods 75
  3.1 Sample preparation 75
  3.2 Optical microscopy 76
  3.3 Scanning electron microscopy 77
  3.4 ToF-SIMS 77
4 Results 78
  4.1 Pure molecule standards 78
    4.1.1 Sputtering effect. 78
    4.1.2 2-nonadecanone 82
    4.1.3 Phenanthrene and anthracene-D_{10} 89
    4.1.4 Semi-quantitative ratio 94
  4.2 Rock samples 97
    4.2.1 Orbagnoux stromatolite 97
    1.1.1 Strelley Pool OM 106
5 Discussion 110
  5.1 Standard fractionation 110
    5.1.1 The impact of low dose sputtering. 110
    5.1.2 The 2-nonadecanone standard 111
    5.1.3 PAH standards 112
  5.2 Orbagnoux heterogeneity 113
  5.3 Strelley Pool OM 116
  5.4 Semi-quantification between different kerogen 118
Conclusion and perspectives 119
Acknowledgment 120
Appendix 120
References 121

CHAPITRE III ANALYSE A NANO-ECHELLE DE MICROFOSSILES DE DRAKEN , SPITSBERGEN. 130

Nanoscale analysis of preservation of 700–800 My-old Draken microfossils, Spitsbergen 131

Abstract 132
1 Introduction 133
2 Geological setting 135
3 Methods 138
  3.1 Semi-thin sections 138
  3.2 Optical microscopy 138
  3.3 Raman spectroscopy 139
  3.4 Scanning electron microscopy and focused ion beam 139
  3.5 Scanning transmitted electron microscopy 139
  3.6 XANES –STXM 140
4 Results 141
  4.1 Microfossil assemblage 141
    4.1.1 Microfossils assemblage 141
    4.1.2 Geothermometry of the carbonaceous material 144
    4.1.3 Filamentous microfossils 146
      4.1.3.1 Siphonophycus 146
      4.1.3.2 Salome Svalbardensis 148
    4.1.4 Coccoidal microfossils 150
      4.1.4.1 Gloeodiniopsis mikros 150
      4.1.4.2 Sphaerophycus 152
      4.1.4.3 Synodophycus 153
      4.1.4.4 Polybessurus 155
      4.1.4.5 Myxococcoides 156
    4.1.5 Vase-shaped microfossils 158
5 Discussion 160
  5.1 Organic matter maturity 160
  5.2 Taphonomy and taxonomy of the microfossils 161
    5.2.1 Filamentous microfossils 161
      5.2.1.1 Siphonophycus 161
      5.2.1.2 Salome Svalbardendis 163
    5.2.2 Benthic coccoidal microfossils 164
      5.2.2.1 Gloeodiniopsis 164
      5.2.2.2 Sphaerophycus 164
      5.2.2.3 Synodophycus 167
      5.2.2.4 Polybessurus 167
    5.2.3 Myxococcoides spheroids 168
    5.2.4 The organic envelopes of vase-shaped microfossils 168
Conclusions 172

Acknowledgments 174
References 174
Supplementary figures 174

CHAPITRE IV MINERALISATION DE FER ET TAPHONOMIE DES MICROFOSSILES DE 2,45-2,21 MILLIARD D'ANNEE DU TUREE CREEK GROUP, AUSTRALIE OCCIDENTALE 186
Présentation 187

Iron mineralization and taphonomy of microfossils of the 2.45–2.21 Ga Turee creek group, Western Australia 190

Abstract 190
1 Introduction 190
2 Geological setting 191
3 Methods 193
4 Results 194
  4.1 Mineralogy of the chert nodules and surrounding carbonates 194
  4.2 Microfossil assemblage 194
5 Discussion 201
  5.1 Development of chert fabrics 201
  5.2 Taphonomy and taxonomy of the microfossils 203
  5.3 Origin of Fe minerals associated with microfossils 205
  5.4 Summary 208
Acknowledgment 209
Referencres 209

CONCLUSION GENERALE ET PERSPECTIVES 212

ANNEXES 216
Nanonascale analysis of preservation of ca. 2.1 Ga old Francevillian microfossils, Gabon 217
ToF-SIMS Tables 235

Introduction et généralités

I/ Introduction générale

Le Précambrien [4,5-0,5 milliards d'années (Ga)] est la période la plus longue de l'histoire de la Terre. Cette période est divisée en trois éons : l'Hadéen (4,5-4,0 Ga), l'Archéen (4,0-2,4 Ga) et le Protérozoïque (2,4-0,5Ga). Les transitions entre ces différents éons sont marquées par d'importants changements environnementaux et biologiques. En comparaison avec le Phanérozoïque (0,54Ga-aujourd'hui), les informations disponibles via l'enregistrement géologique sur l'évolution de la géosphère, l'hydrosphère, l'atmosphère et la biosphère précambrienne sont très parcellaires. Cependant, les études sur le précambrien sont d'une importance primordiale pour comprendre comment la Terre primitive a évolué jusqu'à aujourd'hui pour donner les systèmes écologiques et biologiques complexes et fragiles dans lesquelles nous évoluons. La biosphère précambrienne est dominée par les procaryotes (archées et bactéries), des organismes microscopiques (microorganismes) pour la plupart unicellulaires aux structures cellulaires simples (ex : absence de noyau cellulaire) (Knoll, 2012). L'étudier offre l'opportunité de répondre à une des questions primordiales de la science : comment les premières formes de vies sont-elles apparues et comment ont-elles évolué sur notre planète ?

Le Protérozoïque (2,4-0,5 Ga) est un éon important et un des plus long de l'histoire de notre planète, marqué par l'augmentation de la diversité et la complexité des communautés microbiennes (Knoll et al., 2016), l'apparition de microorganismes eucaryotes (aux structures complexes, dont un noyau cellulaire) et l'apparition des premiers organismes macroscopiques (Gaidos et al., 2007). Le début et la fin de cet éon sont aussi caractérisés par des augmentations de la teneur en dioxygène dans l'atmosphère qui ont eu d'importantes conséquences sur l'évolution de la biosphère. La transition entre l'Archéen et le Protérozoïque est marquée par le passage d'un monde anoxique à une atmosphère légèrement oxygénée (~1-10% du taux actuel d'oxygène) lors du Grand Bond d'Oxygénation (ou « Great Oxidation Event », GOE (Holland, 2009, 2002)). L'atmosphère à la fin du Protérozoïque voit quant-à elle son taux d'oxygène augmenter jusqu'à une teneur proche de l'actuelle lors de l'Evènement d'Oxygénation du Néoprotérozoïque (« Neoproterozoïc oxygenation event », NOE; Och and Shields-Zhou, 2012). Le Protérozoïque fut aussi qualifié « d'Age des cyanobactéries » par Schopf et Walter (1982) à cause des premières découvertes de nombreux microfossiles ayant des morphologies similaires à des cyanobactéries et préservés dans des roches sédimentaires composées à plus de 90% de quartz, appelées « cherts ». Les découvertes de nombreux autres assemblages fossilifères issus de formations protérozoïques (revues dans Sergeev, 2009) confirmèrent l'importance des cyanobactéries dans le registre fossile du Protérozoïque (Knoll, 2007). Les cyanobactéries sont des microorganismes importants pour l'évolution de la biosphère, puisque ce sont des bactéries capables d'effectuer la photosynthèse oxygénique, Elles ont donc été responsables des premières étapes d'oxygénation de la Terre (Schirrmeister et al., 2013). L'interprétation de certains microfossiles comme étant des cyanobactéries fut basée essentiellement sur la morphologie. Cependant, dans le cas de microfossiles ayant des formes simples (sphères et filaments simples de quelques micromètres de diamètre), la morphologie n'est pas suffisante pour déterminer la phylogénie ou le métabolisme des microfossiles. Par exemple, certaines bactéries oxydant le soufre ont une morphologie qui peut être confondue avec celle des cyanobactéries les plus complexes (multicellulaires) (Knoll et al., 1988). De plus, les bactéries peuvent utiliser plusieurs métabolismes : les cyanobactéries peuvent par exemple oxyder du soufre par photosynthèse anoxygénique plutôt que de produire de l'oxygène (Klatt et al., 2015).

Pour déterminer les métabolismes des microfossiles préservés dans les cherts, les paléontologues ont traditionnellement essayé de connaitre l'environnement sédimentaire de dépôt afin de mieux contraindre les écosystèmes microbiens. De plus, de nouvelles techniques incluant des analyses géochimiques et texturales aux échelles nanométriques (nano-échelle) et micrométriques (micro-échelle) de la matière organique composant les microfossiles et des minéraux associés, ont apporté des informations phylogénétiques/physiologiques et de taphonomie (i.e. processus de fossilisation et état de préservation des microorganismes) supplémentaires. Ces diverses techniques utilisées pour caractériser les microfossiles protérozoïques ont aussi offert de nombreux critères de biogénicité (origine biologique) pour des microstructures plus anciennes (archéennes notamment) dont l'origine biologique n'est pas établie. Les microfossiles paléoprotérozoïques de la formation de Gunflint (1,9 Ga, Barghoorn et Tyler, 1965) et des assemblages similaires (composés principalement de filaments et sphères) furent parmi les premiers étudiés avec ces nouvelles techniques pour caractériser leurs ultrastructures (structure à nano-échelle résultant de leur structure interne/externe d'origine et de leur taphonomie) et leurs chimies (Moreau and Sharp, 2004; Wacey et al., 2012). De manières similaires, les microfossiles néoprotérozoïques préservés dans des cherts de la formation de Bitter Springs (0.8Ga, Schopf, 1968) et des assemblages apparentés ont offert la possibilité de définir des critères taxonomiques et de biogénicité. Elles ont aussi permis de comprendre comment sont préservés les procaryotes et de tester ces techniques innovantes de caractérisation (Foucher and Westall, 2013; Oehler, 1976; Oehler et al., 2006). Cependant, les microfossiles procaryotes ne sont pas les seuls organismes présents dans le registre fossilifère protérozoïque. Plusieurs fossiles interprétés comme des eucaryotes ont aussi été découverts et caractérisés (Javaux, 2011; Knoll, 2012). Les études de l'ultrastructure et de la chimie de ces eucaryotes fossiles ont apporté des critères permettant de déterminer les affinités taxonomiques de nombreux autre microfossiles (Javaux and Marshal, 2006). Ces études sont essentielles pour déterminer quand sont apparus les premiers eucaryotes au cours du Précambrien. Cependant la structure ultrafine des microfossiles et leur morphologie ne sont pas les seules traces de l'activité des microorganismes précambriens présents dans l'enregistrement géologique et permettant de dater les innovations/évolutions de la biosphère précambrienne. Ainsi, on peut aussi prendre en compte : les signatures isotopiques de l'activité microbienne (isotopie du carbone ou des éléments – soufre, fer- dans les minéralisations associées aux microfossiles) ; les molécules organiques préservés (les « biomarqueurs »), et les minéralisations induites par les microorganismes.

Les roches formées par des interactions entre des microorganismes et des sédiments sont des cibles importantes pour étudier la vie au Précambrien. Le meilleur exemple en est les stromatolites. Ces roches stratifiées dont l'accrétion (par précipitation et piégeage de sédiments) est liée à l'activité de communautés microbiennes, représentent aussi une part importante de l'enregistrement fossile précambrien et font partie des premières traces de vie découvertes datant de l'Archéen (Riding, 2000). Dans certains cas, les tapis bactériens peuvent être préservés sous forme de matière carbonée (dont la fraction insoluble s'appelle le kérogène) et même contenir des microfossiles. De manière similaire aux microfossiles, la matière organique préservée dans ces stromatolites peut être caractérisée géo-chimiquement et l'ultrastructure peut être documentée à l'aide des techniques spectroscopiques à micro et nano-échelle (Benzerara et al., 2006). Cependant, les résultats obtenus par ces techniques de caractérisation in situ ne donnent pas accès à la composition moléculaire complexe de la matière organique préservée. D'un autre côté, l'obtention d'informations moléculaires plus complexes (généralement par spectrométrie de masse) nécessite dans la plupart des cas d'avoir une certaine quantité de matière organique et de détruire l'échantillon. La spectroscopie de masse à temps de vol (Time of Flight Secondary Ion Mass Spectrometry- ToF SIMS), technique d'analyse d'ultra-surface (premières couches moléculaires de surface d'un échantillon) offre la possibilité d'obtenir des informations moléculaires à l'échelle micrométrique avec de faibles quantités de matière organique et sans détruire les microstructures organiques préservés dans la roche. Elle est de plus en plus utilisée en géologie (Thiel and Sjövall, 2014), mais du fait de sa très grande sensibilité, ne peut pas s'appliquer à des objets indurés par une résine ou une colle, technique de préparation utilisée dans la majorité des études ultrafines d'objets précambriens (Ivarsson, 2006).

Objectifs

Le premier objectif de cette thèse fut de mettre au point une préparation d'échantillons pour étudier des microstructures organiques (microfossiles, tapis bactériens fossiles) sensibles aux contaminations. Dans un deuxième temps, nous avons étudié la possibilité d'obtenir des informations moléculaires in-situ provenant de microstructures organiques, ici des tapis microbiens fossiles. Le troisième objectif fut de renseigner la taphonomie, l'affinité biologique et la biogénicité de microfossiles préservés dans des cherts paléo et néo-protérozoïques en combinant différentes techniques de caractérisation.

Structure de la thèse

Une présentation de l'évolution générale des environnements et de la biosphère au cours du Précambrien fait suite à cette introduction générale. La présentation des résultats de ce travail de thèse est ensuite divisée en quatre chapitres rédigés sous forme d'articles en anglais (acceptés, en cours de préparation ou restant à peaufiner). Nous avons pris le parti de présenter cette thèse sous ce format car il présente l'avantage de pouvoir être accessible au plus grand nombre au sein de la communauté concernée. Le **premier chapitre** comprend un préambule présentant la ToF SIMS qui est la technique d'analyse principale introduite dans cette thèse. Ce chapitre expose ensuite la nouvelle méthode de préparation de tranches épaisses mise au point pour effectuer des micro-et nano-analyses de la matière organique. Les données sur l'état d'ultra-surface de ces tranches épaisses obtenues à la ToF-SIMS y sont également présentées. Le **second chapitre** traite de la caractérisation moléculaire à micro-échelle de la matière organique issue d'anciens tapis microbiens (d'âges phanérozoïque et archéen) avec la ToF-SIMS. Le **troisième chapitre** présente l'étude à nano-échelle d'un assemblage de microfossiles Néoprotérozoïque très diversifié de type Bitter Springs. Enfin, le **quatrième chapitre** présente une étude combinant des techniques de caractérisation à micro et nano-échelle avec des analyses isotopiques sur un assemblage de microfossiles de type Gunflint daté du GOE et associé avec des minéralisations de fer. Pour terminer, l'**annexe** comprend un article dont je ne suis pas le premier auteur. Cet article paru dans *Precambrian Research* présente des microfossiles de type Gunflint âgés de 2.1Ga et provenant du Gabon. J'ai participé activement à ces travaux en aidant à la préparation d'échantillons, à l'acquisition de certaines données de même qu'à la présentation et l'interprétation des résultats.

II/ Généralités sur le précambrien : évolution des environnements et de la biosphère

Cette thèse traitant principalement de l'étude de microfossiles et de tapis microbiens précambriens, il apparait important de rappeler comment à évoluer la vie au cours des différents éons précambriens et dans quels environnements les microorganismes précambriens ont pu se développer.

1 L'Hadéen

L'Hadéen (4.5–4 Ga) une des périodes les plus mal connues de l'histoire de la Terre. En effet, les roches datant de cette époque ont toutes été recyclées par des processus magmatiques (Cavosie et al., 2005). Seuls des zircons déterminés comme étant détritiques inclus dans ces roches métamorphiques sont préservés (Black et al., 1986; Cavosie et al., 2004; Froude et al., 1983; Liu et al., 1992; Mueller et al., 1992). Les rapports isotopiques d'oxygène obtenus sur ces zircons indiquent que de l'eau liquide était déjà présente à l'Hadéen (Kasting and Ono, 2006; Valley et al., 2002; Wilde et al., 2001). Cependant si des océans étaient présents au cours de cet éon, ils ont probablement été vaporisés et condensés à plusieurs reprises durant la phase d'accrétion de la Terre et lors des derniers bombardements datés de 3,9 Ga (« Late heavy Bombardment ») (Claeys and Morbidelli, 2011).

2 L'Archéen: une atmosphère anoxique

L'Archéen (4–2.5 Ga) est une période mieux connue que l'Hadéen, avec un registre géologique plus important. Il est communément admis que l'atmosphère archéenne ne contenait que très peu d'oxygène (<10-5 fois la concentration actuelle ou present atmospheric level « PAL ») (Lyons et al., 2014). Cette affirmation se base sur plusieurs indices dont la présence de dépôts détritiques de minéraux sensibles à l'oxygène comme l'uraninite et la pyrite dans les roches archéennes (Rasmussen and Buick, 1999), ainsi que la présence de fractionnements isotopiques du soufre indépendants de la masse (ou Mass Independent Fractionation of Sulfur, « MIF-S ») (Farquhar and Wing, 2003). Le processus exact à l'origine de ces fractionnements isotopiques est inconnu mais des expériences de photolyse de SO2 sous condition anoxique ont produit de tels fractionnements isotopiques (Farquhar James et al., 2001). Ceci confirme donc que l'atmosphère archéenne était anoxique (Anbar et al., 2007; Arnold et al., 2004; Farquhar et al., 2000; Holland, 2006). En plus de cette absence d'oxygène, l'atmosphère contenait certainement plus de gaz à effet de serre qu'aujourd'hui. L'absence de glaciation majeure dans le registre géologique archéen (Eriksson et al., 1998) malgré une activité solaire plus faible de 70% par rapport à l'actuelle (Kasting, 2001; Kasting and Ono, 2006; Sagan and Mullen, 1972) semblent indiquer que l'atmosphère contenait une forte concentration de gaz à effet de serre. Les simulations montrent que des taux de dioxyde de carbone (CO2) et/ou de méthane (CH4) très élevés ont été nécessaires pour expliquer l'absence de glaciation majeure au cours de l'Archéen (Pavlov et al., 2003; Tajika, 2003). La grande quantité de CH4 atmosphérique au cours de l'Archéen pourrait être liée à une activité importante des bactéries méthanogènes dans une atmosphère riche en dihydrogène et CO2 (Kasting and Ono, 2006) L'importance des méthanogènes dans les écosystèmes archéens et la production de CH4 semblent être cohérents avec les valeurs isotopiques de carbone 13 (δ13C) négatives obtenues dans des roches archéennes (Hayes, 1994; Hinrichs, 2002; Knoll et al., 2016; Ueno et al., 2006).

La vie à l'Archéen était microbienne : outre les bactéries méthanogènes documentées par les valeurs isotopiques du carbone (c.f. Isua supracrustal belt, Rosing, 1999), les études isotopiques effectuées sur le soufre des pyrites semblent aussi indiquer que des communautés bactériennes diverses métabolisant le soufre étaient présentes dans l'océan au début de l'archéen (Johnston, 2011; Philippot et al., 2007; Shen et al., 2009). La présence de vie microbienne au début de l'archéen est aussi corroborée par la présence de stromatolite de 3,7Ga provenant de l'Isua supracrustal belt (Groenland) (Nutman et al., 2016), des cherts d'Afrique du Sud présentant des structures sédimentaires influencées par des tapis bactériens datés de 3,5 Ga (Tice and Lowe, 2004). Les structures provenant de stromatolites préservés dans les carbonates de la formation de Strelley Pool (Australie, 3,45 Ga) sont aussi une preuve de la présence de vie microbienne dans les océans au début de l'Archéen (Allwood et al., 2009). Les roches archéennes contiennent aussi des microfossiles. Javaux et al., (2010) rapportent les plus vieux microfossiles extraits et incontestables provenant de roches âgées de 3,2 Ga. Des microfossiles dont l'origine biologique n'a pas encore remise en question ont aussi été étudiés dans des cherts de la formation de Strelley Pool (3,43 Ga) par Sugitani et al., (2015), Wacey et al., (2011), Sugitani et al., (2010), . Enfin, les célèbres microfossiles de l'Apex Chert provenant du Warrawoona Group (3,46 Ga, Australie) sont l'un des meilleurs exemples de la difficulté de contraindre la biogénicité d'une microstructure organique. Avec des analyses Raman, des observations optiques et morphologiques, Schopf et al., (2002) concluent que ces microstructures sont composées de kérogène d'origine biologique, soutenant l'hypothèse de la biogenicité de l'assemblage présent dans les cherts de l'Apex. Cependant, Brasier et al. (2002)

en reprenant les mêmes échantillons arrivèrent à la conclusion que le carbone a été déplacé et déposé par des fluides hydrothermaux en formant des microstructures similaires à des cellules. La morphologie de ces microstructures aurait ensuite été préservée par le quartz formant le chert au cours de la diagénèse.

3 Le Grand Evènement d’Oxydation

La fin de l’Archéen est marquée par la production d’oxygène par des organismes photosynthétiques (cyanobactéries). La présence de cyanobactéries dans les eaux peu profondes archéennes est suggérée par la présence de stromatolites et de fractionnements des isotopes du carbone organique dans les roches (Knoll, 2012). Des biomarqueurs provenant de roche âgée de 2,7Ga (Australie) ont aussi été invoqués pour confirmer la présence d’une activité des cyanobactéries au cours de la fin du Précambrien (Summons et al., 1999). Cependant, il a été par la suite montré que ces biomarqueurs résultaient d’une contamination (Brocks et al., 2008; French et al., 2015; Rasmussen et al., 2008). Malgré cela, la présence d’oxygène, probablement d’origine biologique dans l’atmosphère archéenne (vers ~2,8Ga) fut confirmée par les fractionnements isotopiques du chrome (Frei et al., 2009) et du molybdène (Planavsky et al., 2014; Wille et al., 2007) et par les abondances en rhénium et molybdène (Anbar et al., 2007). Le passage d’une atmosphère sans oxygène vers une atmosphère contenant de l’oxygène semble avoir été progressif (Fig.1) (Holland, 2006; Knoll et al., 2016; Lyons et al., 2014). Ceci peut s’expliquer par la présence dans l’océan archéen de fer ferreux qui dans un premier temps joua le rôle de puits à oxygène. En présence d’oxygène, le fer océanique fut oxydé et les oxydes produits (hématite, magnétite…) précipitèrent au fond de l’océan. Les formations de fer rubanées (ou « Banded Iron Formation » BIF) caractéristiques de la fin de l’Archéen témoignent de cette transition (Konhauser et al., 2017). L’oxygénation de l’océan puis de l’atmosphère n’a été possible que lorsque tout (ou du moins la plus grande partie) le fer ferreux océanique fut oxydé.

A partir d’environ 2,4 Ga, diverses preuves montrent que l’oxygène était présent à la surface de l’hydrosphère et l’atmosphère de la Terre (Fig.1) : la présence de dépôt fluviaux appelée « Red Beds » (Cloud, 1968; Roscoe, 1968), des dépôts de manganèse (Johnson et al., 2016), la fin des dépôts détritiques d’uraninite et de pyrite (Johnson et al., 2014; Rasmussen and Buick, 1999), la fin des BIFs (Bekker et al., 2010) et surtout la fin des MIF-S (Bekker et al., 2004; Bekker and Holland, 2012; Condie et al., 2009; Farquhar and Wing, 2003). C’est le Grand Evènement d’Oxydation (ou “Great Oxidation Event”, GOE) qui se déroula entre 2,4 et

2,3 Ga. Cette augmentation du taux d'oxygène fut aussi accompagnée par des glaciations paléoprotérozoïques (Kasting and Ono, 2006; Roscoe, 1973, 1968; Young et al., 2001).

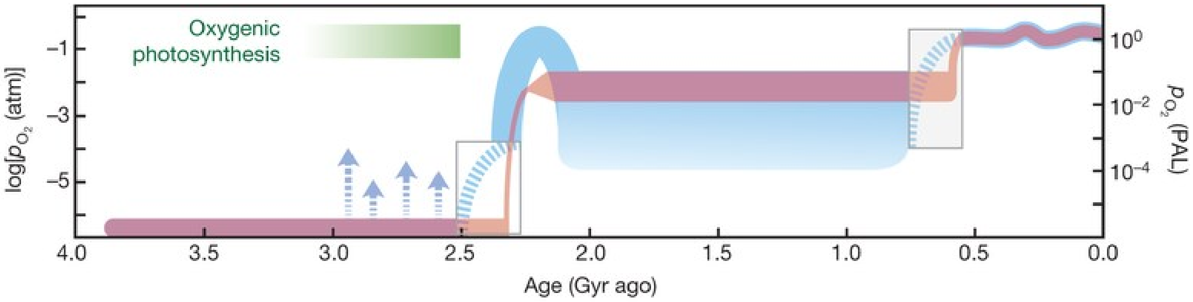

Fig. 1. Graphique montrant l'évolution de la teneur en oxygène atmosphérique de la Terre à partir de l'Archéen jusqu'à aujourd'hui. *La courbe rose correspond à l'évolution de la teneur en oxygène atmosphérique « classique ». La courbe bleue correspond au « nouveau » modèle d'évolution de la teneur en* O_2 *atmosphérique issue des travaux récents cités ci-dessus.* PO_2 *est la pression partielle atmosphérique de* O_2*. Axes des ordonnées de droite :* PO_2 *par rapport au niveau atmosphérique actuel (PAL). Axe de gauche :* $\log p_{O2}$*. Les flèches bleues correspondent aux «bouffées» d'*O_2 *ayant eu lieu à la fin de l'Archéen. Les boîtes bleues correspondent aux périodes où l'évolution du taux d'oxygène atmosphérique est importante (le GOE et NOE) mais reste encore mal comprise (Lyons et al., 2014).*

4 Le Protérozoïque

4.1 Un océan stratifié

Après le GOE, les roches paléoprotérozoïques sont caractérisées par des valeurs positives et importantes du rapport des isotopes du carbone (δ13C) des carbonates avec des valeurs comprises entre +6-8‰ pouvant atteindre jusque +28‰ entre 2,22 et 2,06 Ga. Ceci caractérise l'évènement Lomagundi (Bekker et al., 2006; Buick et al., 1998; Melezhik et al., 2007; Melezhik and Fallick, 1996; Schidlowski et al., 1975). Cette période est aussi caractérisée par une fragmentation des continents avec une reprise importante de l'activité magmatique (Bekker and Holland, 2012; Condie et al., 2009). Une des interprétations communément admises est que cet enrichissement en carbone 13 des carbonates reflète une augmentation de l'enfouissement de matière organique, appauvrie en carbone 13, enrichissant les différents réservoirs de la surface terrestre (océan, atmosphère) en isotope lourd du carbone (Kump and Arthur, 1999, Karhu and Holland, 1996). Cette augmentation de l'enfouissement de matière organique dans les océans fut interprétée comme une conséquence de l'augmentation de l'activité photosynthétique à la surface de la Terre. Ces conditions exceptionnelles semblent aussi être liées à l'apport de nutriments aux océans lors du passage à des conditions oxiques. L'effet de cette activité photosynthétique accrue est de générer plus de dioxygène, mais aussi d'enfouir plus de matière organique dans les sédiments. Cet enfouissement permet de réduire la consommation en dioxygène par respiration microbienne aérobie de la matière organique, et de permettre in fine l'augmentation du taux d'oxygène, avec des taux d'oxygène particulièrement élevés entre 2,2 et 2,0 Ga (Fig.1). La présence d'importants gisements de gypse ($CaSO4.2H2O$) datant de cette époque indique que les concentrations en sulfate dans l'océan étaient élevées au cours de l'évènement Lomagundi (Melezhik et al., 2005; Schröder et al., 2008). L'origine de ces fortes teneurs en sulfate dans l'océan semble liée à l'altération de minéraux sulfurés (ex : pyrite) sur les continents en présence d'oxygène. L'altération continentale de minéraux phosphatés a aussi augmenté le flux de phosphate vers les océans favorisant l'activité photosynthétique et entraina la précipitation des premiers gisements important de phosphorites (Bekker and Holland, 2012).

Ces conditions particulières de l'évènement Lomagundi se terminèrent vers 2,00 Ga, comme l'indique la réapparition de dépôts de fer rubané (BIF) et l'apparition des dépôts de fer granulaires (GIF) (Konhauser et al., 2017). Ce retour des BIF est contemporain d'une activité volcanique accrue accompagnant la dislocation des cratons précambriens avec la formation de croute océanique (des roches mafiques/ultramafiques) accompagnée de dépôts massifs de sulfures (Rasmussen et al., 2012). La réapparition de formation de fer rubanée peut aussi s'expliquer par une diminution du taux d'oxygène atmosphérique entrainant une réduction du réservoir de sulfate dans l'océan (Canfield, 2005; Frei et al., 2009). La présence de sulfate dans l'océan permet l'activité des bactéries sulfato-réductrices produisant du sulfure d'hydrogène ($H2S$), qui réagit rapidement avec le fer réduit pour former des sulfures de fer (FeS, $FeS2$, …) (Berner, 1984). Ainsi, grâce à un apport important de fer réduit dans l'océan et une réduction du réservoir de sulfate, les eaux profondes ont pu s'enrichir en fer ferreux (Scott et al., 2008). La mise en contact de ces eaux profondes riches en fer réduit avec les eaux oxygénées de surface aurait provoqué la formation des BIF (Lyons et al., 2012). Cette période de précipitation des BIF se termina vers ~1,80 Ga, avec la diminution du flux de fer lié à l'activité hydrothermale (Rasmussen et al., 2012).

Après ce dernier dépôt de BIF, la Terre entre dans la période dite du « boring billion » (ou « milliard barbant ») qui est caractérisée par de faibles variations du δ13C des carbonates (Lyons et al., 2012). Durant cette longue période, les teneurs de O2 atmosphériques auraient été stables mais relativement faibles (entre 1-10% PAL, Fig.1) (Lyons et al., 2014; Rasmussen et al., 2012). Au niveau des océans, Canfield (1998) fut le premier à proposer que l'océan protérozoïque fut stratifié avec des eaux de surface oxygénées et des eaux profondes euxiniques (sans oxygène et riches en H2S) ou anoxiques (sans oxygène, probablement ferrugineuses). Ainsi à partir de 1,8 Ga, le flux de sulfate dans l'océan était suffisant pour maintenir l'activité des bactéries sulfato-réductrices permettant le développement une tranche d'eau anoxique contenant du H2S libre (euxinisme) entre les eaux de surface oxygénée et les eaux profondes anoxiques riches en éléments réduits (dont le fer ferreux) (Canfield, 2005, 1998; Kendall et al., 2011; Lyons et al., 2014, 2012; Poulton and Canfield, 2011; Rasmussen et al., 2012)..

4.2 L'émergence des eucaryotes et la domination des cyanobactéries

Cette longue période de stabilité du « boring billion » avec un océan stratifié a eu des répercussions sur le développement de la vie au cours du Protérozoïque. En effet, un euxinisme répandu aurait pu permettre aux bactéries phototrophes sulfo-oxydantes de se développer en utilisant les sulfures comme donneurs d'électrons, et cela au dépend des bactéries phototrophes oxygénétiques (Johnston et al., 2009). La présence de ces bactéries phototrophes sulfo-oxydantes fut confirmée par des biomarqueurs trouvés dans des roches de 1,64 Ga par Brocks et al., (2005). Cependant, le développement de zones euxiniques étendues ou restreintes au niveau des marges océaniques (Lyons et al., 2014, 2012), a modulé la disponibilité d'éléments essentiels au développement des eucaryotes, comme le fer et le molybdène, entrainant une stagnation de leur évolution au cours du « boring billion » (Anbar, 2008; Anbar and Knoll, 2002). Ainsi, les eaux peu profondes et oxygénées ont été dominées par les cyanobactéries jusque ~750 Ma (millions d'années) comme l'indiquent les biomarqueurs (Brocks et al., 2017). En plus d'être limité en éléments essentiels à leurs processus enzymatiques (Mo, Fe, S), les concentrations en phosphate et nitrate semblaient être faibles dans les eaux de surface du Mésoprotérozoïque, ce qui limita l'émergence des algues au profit des cyanobactéries dans les environnements côtiers à forte productivité primaire (i.e. près de l'apport continental en nutriments). Cette faible concentration de nutriments a aussi eu un effet de rétroaction négatif sur la production de O2 car l'activité photosynthétique était réduite et sur l'apport de phosphate issu de l'altération continentale (Brocks et al., 2017; Butterfield, 2015; Derry, 2015; Irwin et al., 2006; Laakso and Schrag, 2014; Reinhard et al., 2016; Zerkle and Mikhail, 2017).

Bien que les conditions environnementales soient défavorables aux eucaryotes, des microfossiles interprétés comme des eucaryotes ont été trouvés dans les roches mésoprotérozoïques (Javaux, 2007; Javaux et al., 2004; Xiao et al., 1997). Les plus anciens eucaryotes datent de 1,8 Ga (Lamb et al., 2009). La biodiversité de ces assemblages reste cependant faible et seuls quelques fossiles d'eucaryote ont une affinité taxonomique connue avec par exemple les *Bangiomorpha pubescens* âgés de 1,05 Ga et considérés comme une algue rouge (Butterfield, 2000; Gibson et al., 2018). Entre 0,85 et 0,75 Ga, la biodiversité augmenta mais resta faible (Knoll et al., 2006) avec la présence dans de fossiles d'algues vertes (Butterfield et al., 1994), de xanthophycées (Butterfield, 2004), des amibes (taxons des Amoebozoa et Rhizaria) (Porter and Knoll, 2000) et potentiellement des mycètes (fungi) (Butterfield, 2005). A ces microfossiles qui se limitent aux environnements côtiers, s'ajoutent des assemblages contenant des microorganismes bactériens (cyanobactéries) préservés dans des cherts (Butterfield, 2003). Ces assemblages de type « Bitter Springs » sont les derniers écosystèmes microbiens précambriens préservés par des silicifications précoces (Green et al., 1988; Knoll et al., 1991; Schopf, 1968). Ces assemblages offrent un aperçu des écosystèmes présents sur les plate-formes carbonatées ou marges côtières lors de la fragmentation du supercontinent Rodinia et avant les glaciations majeures du Néoprotérozoïque.

5 L'Evènement d'Oxygénation du Néoprotérozoïque (NOE).

La fin du Néoprotérozoïque est marquée par de grands changements de l'hydrosphère et de l'atmosphère qui eurent d'importantes conséquences sur la biosphère. Le supercontinent Rodinia, formé au début du Néoprotérozoïque (~1,0 Ga), commença à se disloquer à partir de ~0,75 Ga (Li et al., 2008). Cette dislocation serait en grande partie à l'origine de deux glaciations de grande ampleur au cours du Cryogénien (0,85 à 0,63 Ga) : la glaciation du Sturtien (~0,75–0,68 Ga) et la glaciation du Marinoen (~0,63 Ga) (Condon et al., 2005; Hoffman et al., 1998; Macdonald et al., 2010). Ces glaciations considérées comme globales (Kirschvink, 1992) sont suivies du dépôt de formations carbonatées (« Cap carbonates ») qui sont caractérisées par des valeurs négatives de δ13Ccarb proches des valeurs du carbone mantellique (Hoffman et al., 1998, 2017; Hoffman and Schrag, 2002; Kaufman et al., 1997; Zhou and Xiao, 2007). Le dépôt de ces carbonates et les excursions négatives de δ13C associées ont été interprétés comme reflétant l'interruption des cycles biogéochimiques et l'accumulation de carbone mantellique dans l'atmosphère pendant chaque glaciation, puis une précipitation massive de carbonate lors de la phase de déglaciation (Hoffman et al., 1998).

Bien que ces périodes soient activement étudiées, beaucoup de choses restent inconnues sur l'état et l'évolution de l'atmosphère et de l'océan au cours du Néoprotérozoïque (Lyons et al., 2014, 2012). Il apparait que la fin du Néoprotérozoïque fut marquée par une augmentation de l'oxygène dans l'atmosphère, correspondant au « Neoproterozoic Oxygenation Event » (ou

NOE, Fig 1) (Campbell and Allen, 2008; Canfield, 2005; Des Marais, 2001; Lyons et al., 2012; Shields-Zhou and Och, 2011). Cependant il est difficile de comprendre précisément comment, quand cette oxygénation a eu lieu et quel est le lien entre le NOE et les épisodes de Snowball (Hoffman et al., 2017; Lyons et al., 2014).

Les glaciations du Cryogénien et/ou l'augmentation de la teneur en oxygène ont eu d'importantes conséquences pour la biosphère. La plupart des clades d'eucaryotes, apparues avant le Cryogénien, semble avoir survécu à ces glaciations (Corsetti et al., 2003; Moczydlowska, 2008a, 2008b; Xiao Shuhai, 2013). Cependant, l'abondance des eucaryotes, notamment des algues, semblent avoir augmenté après ces glaciations globales, comme l'indiquent les biomarqueurs (Brocks et al., 2017). Le développement et la diversification des algues après les épisodes de glaciation peut s'expliquer par un apport supplémentaire de nutriments dans les océans, ainsi que des éléments essentiels pour le métabolisme des eucaryotes (Brocks et al., 2017; Lyons et al., 2012). Ces conditions ont conduit à une augmentation de la production primaire et ont permis aux algues de dominer les écosystèmes marins. Les valeurs positives du δ13C des carbonates enregistrées au cours du Néoprotérozoïque (Halverson et al., 2005) témoignent d'une augmentation de l'enfouissement de matière organique dans les sédiments, associée à l'augmentation de la productivité primaire (Holland, 2006). Tout comme au GOE, l'enfouissement de matière organique aurait conduit à l'augmentation du niveau d'oxygène, pour atteindre une concentration similaire à la concentration atmosphérique actuelle (Holland, 2006; Lyons et al., 2014, 2012). Il est généralement considéré que cette augmentation du taux d'oxygène rendit la vie multicellulaire animale possible (notamment pour la synthèse du collagène (Towe, 1970) et de nombreux métabolites (Raymond and Segrè, 2006)). Les premières formes de vie multicellulaire qui se sont développées dans les océans néoprotérozoïques semblent être les éponges (Butterfield, 2009; Erwin et al., 2011; Love et al., 2009). La présence d'éponges filtrant d'importantes quantités d'eau eut un effet de rétroaction positif sur l'oxygénation des océans (Lenton et al., 2014). Ces divers exemples montrent les nombreux effets de rétroactions induits entre l'évolution des environnements et les innovations du vivant (Knoll et al., 2006; Lenton et al., 2014). Ceci rend difficile la compréhension précise des phénomènes ayant lieu durant l'un des tournants majeurs de l'histoire de notre planète qu'est le NOE.

Références

Allwood, A.C., Grotzinger, J.P., Knoll, A.H., Burch, I.W., Anderson, M.S., Coleman, M.L., Kanik, I., 2009. Controls on development and diversity of Early Archean stromatolites. Proc. Natl. Acad. Sci. 106, 9548–9555.

Anbar, A.D., 2008. Elements and Evolution. Science 322, 1481–1483. https://doi.org/10.1126/science.1163100

Anbar, A.D., Duan, Y., Lyons, T.W., Arnold, G.L., Kendall, B., Creaser, R.A., Kaufman, A.J., Gordon, G.W., Scott, C., Garvin, J., Buick, R., 2007. A Whiff of Oxygen Before the Great Oxidation Event? Science 317, 1903–1906. https://doi.org/10.1126/science.1140325

Anbar, A.D., Knoll, A.H., 2002. Proterozoic ocean chemistry and evolution: a bioinorganic bridge? Science 297, 1137–1142. https://doi.org/10.1126/science.1069651

Arnold, G.L., Anbar, A.D., Barling, J., Lyons, T.W., 2004. Molybdenum Isotope Evidence for Widespread Anoxia in Mid-Proterozoic Oceans. Science 304, 87–90. https://doi.org/10.1126/science.1091785

Barghoorn, E.S., Tyler, S.A., 1965. Microorganisms from the Gunflint chert. Science 147, 563–577. https://doi.org/10.1126/science.147.3658.563

Bekker, A., Holland, H.D., 2012. Oxygen overshoot and recovery during the early Paleoproterozoic. Earth Planet. Sci. Lett. 317, 295–304. https://doi.org/10.1016/j.epsl.2011.12.012

Bekker, A., Holland, H.D., Wang, P.-L., Iii, D.R., Stein, H.J., Hannah, J.L., Coetzee, L.L., Beukes, N.J., 2004. Dating the rise of atmospheric oxygen. Nature 427, 117–120. https://doi.org/10.1038/nature02260

Bekker, A., Karhu, J.A., Kaufman, A.J., 2006. Carbon isotope record for the onset of the Lomagundi carbon isotope excursion in the Great Lakes area, North America. Precambrian Res. 148, 145–180. https://doi.org/10.1016/j.precamres.2006.03.008

Bekker, A., Slack, J.F., Planavsky, N., Krapez, B., Hofmann, A., Konhauser, K.O., Rouxel, O.J., 2010. Iron Formation: The Sedimentary Product of a Complex Interplay among Mantle, Tectonic, Oceanic, and Biospheric Processes. Econ. Geol. 105, 467–508. https://doi.org/10.2113/gsecongeo.105.3.467

Benzerara, K., Menguy, N., Lopez-Garcia, P., Yoon, T.-H., Kazmierczak, J., Tyliszczak, T., Guyot, F., Brown, G.E., 2006. Nanoscale detection of organic signatures in carbonate microbialites. Proc. Natl. Acad. Sci. U. S. A. 103, 9440–9445. https://doi.org/10.1073/pnas.0603255103

Berner, R.A., 1984. Sedimentary pyrite formation: An update. Geochim. Cosmochim. Acta 48, 605–615. https://doi.org/10.1016/0016-7037(84)90089-9

Black, L.P., Williams, I.S., Compston, W., 1986. Four zircon ages from one rock: the history of a 3930 Ma-old granulite from Mount Sones, Enderby Land, Antarctica. Contrib. Mineral. Petrol. 94, 427–437. https://doi.org/10.1007/BF00376336

Brasier, M.D., Green, O.R., Jephcoat, A.P., Kleppe, A.K., Van Kranendonk, M.J., Lindsay, J.F., Steele, A., Grassineau, N.V., 2002. Questioning the evidence for Earth's oldest fossils. Nature 416, 76–81. https://doi.org/10.1038/416076a

Brocks, J.J., Grosjean, E., Logan, G.A., 2008. Assessing biomarker syngeneity using branched alkanes with quaternary carbon (BAQCs) and other plastic contaminants. Geochim. Cosmochim. Acta 72, 871–888. https://doi.org/10.1016/j.gca.2007.11.028

Brocks, J.J., Jarrett, A.J.M., Sirantoine, E., Hallmann, C., Hoshino, Y., Liyanage, T., 2017. The rise of algae in Cryogenian oceans and the emergence of animals. Nature 548, 578–581. https://doi.org/10.1038/nature23457

Brocks, J.J., Love, G.D., Summons, R.E., Knoll, A.H., Logan, G.A., Bowden, S.A., 2005. Biomarker evidence for green and purple sulphur bacteria in a stratified Palaeoproterozoic sea. Nature 437, 866–870. https://doi.org/10.1038/nature04068

Buick, I.S., Uken, R., Gibson, R.L., Wallmach, T., 1998. High-δ13C Paleoproterozoic carbonates from the Transvaal Supergroup, South Africa. Geology 26, 875–878. https://doi.org/10.1130/0091-7613(1998)026<0875:HCPCFT>2.3.CO;2

Butterfield, N.J., 2015. Early evolution of the Eukaryota. Palaeontology 58, 5–17. https://doi.org/10.1111/pala.12139

Butterfield, N.J., 2009. Oxygen, animals and oceanic ventilation: an alternative view. Geobiology 7, 1–7. https://doi.org/10.1111/j.1472-4669.2009.00188.x

Butterfield, N.J., 2005. Probable Proterozoic fungi. Paleobiology 31, 165–182. https://doi.org/10.1666/0094-8373(2005)031<0165:PPF>2.0.CO;2

Butterfield, N.J., 2004. A vaucheriacean alga from the middle Neoproterozoic of Spitsbergen: implications for the evolution of Proterozoic eukaryotes and the Cambrian explosion. Paleobiology 30, 231–252. https://doi.org/10.1666/0094-8373(2004)030<0231:AVAFTM>2.0.CO;2

Butterfield, N.J., 2003. Exceptional Fossil Preservation and the Cambrian Explosion. Integr. Comp. Biol. 43, 166–177. https://doi.org/10.1093/icb/43.1.166

Butterfield, N.J., 2000. Bangiomorpha pubescens n. gen., n. sp.: implications for the evolution of sex, multicellularity, and the Mesoproterozoic/Neoproterozoic radiation of eukaryotes. Paleobiology 26, 386–404. https://doi.org/10.1666/0094-8373(2000)026<0386:BPNGNS>2.0.CO;2

Butterfield, N.J., Knoll, A.H., Swett, K., 1994. Paleobiology of the Neoproterozoic Svanbergfjellet Formation, Spitsbergen. Lethaia 27, 76–76. https://doi.org/10.1111/j.1502-3931.1994.tb01558.x

Campbell, I.H., Allen, C.M., 2008. Formation of supercontinents linked to increases in atmospheric oxygen. Nat. Geosci. 1, 554–558. https://doi.org/10.1038/ngeo259

Canfield, D.E., 2005. The Early History of Atmospheric Oxygen: Homage to Robert M. Garrels. Annu. Rev. Earth Planet. Sci. 33, 1–36. https://doi.org/10.1146/annurev.earth.33.092203.122711

Canfield, D.E., 1998. A new model for Proterozoic ocean chemistry. Nature 396, 450–453. https://doi.org/10.1038/24839

Cavosie, A.J., Valley, J.W., Wilde, S.A., E.I.M.F., 2005. Magmatic δ18O in 4400–3900 Ma detrital zircons: A record of the alteration and recycling of crust in the Early Archean. Earth Planet. Sci. Lett. 235, 663–681. https://doi.org/10.1016/j.epsl.2005.04.028

Cavosie, A.J., Wilde, S.A., Liu, D., Weiblen, P.W., Valley, J.W., 2004. Internal zoning and U–Th–Pb chemistry of Jack Hills detrital zircons: a mineral record of early Archean to Mesoproterozoic (4348–1576 Ma) magmatism. Precambrian Res., The First Billion Years - Selected Papers Presented at the 13th V.M. Goldschmidt Conference, Kurashiki, Japan 135, 251–279. https://doi.org/10.1016/j.precamres.2004.09.001

Claeys, P., Morbidelli, A., 2011. Late Heavy Bombardment, in: Encyclopedia of Astrobiology. Springer, Berlin, Heidelberg, pp. 909–912. https://doi.org/10.1007/978-3-642-11274-4_869

Cloud, P.E., 1968. Atmospheric and Hydrospheric Evolution on the Primitive Earth: Both secular accretion and biological and geochemical processes have affected earth's volatile envelope. Science 160, 729–736. https://doi.org/10.1126/science.160.3829.729

Condie, K.C., O'Neill, C., Aster, R.C., 2009. Evidence and implications for a widespread magmatic shutdown for 250 My on Earth. Earth Planet. Sci. Lett. 282, 294–298. https://doi.org/10.1016/j.epsl.2009.03.033

Condon, D., Zhu, M., Bowring, S., Wang, W., Yang, A., Jin, Y., 2005. U-Pb Ages from the Neoproterozoic Doushantuo Formation, China. Science 308, 95–98. https://doi.org/10.1126/science.1107765

Corsetti, F.A., Awramik, S.M., Pierce, D., 2003. A complex microbiota from snowball Earth times: microfossils from the Neoproterozoic Kingston Peak Formation, Death Valley, USA. Proc. Natl. Acad. Sci. U. S. A. 100, 4399–4404. https://doi.org/10.1073/pnas.0730560100

Derry, L.A., 2015. Causes and consequences of mid-Proterozoic anoxia: Causes Of Mid-Proterozoic Anoxia. Geophys. Res. Lett. 42, 8538–8546. https://doi.org/10.1002/2015GL065333

Des Marais, D.J., 2001. Isotopic evolution of the biogeochemical carbon cycle during the Precambrian, in: Valley, J.W., Cole, D.R. (Eds.), Stable Isotope Geochemistry. Mineralogical Soc Amer, Chantilly, pp. 555–578.

Eriksson, P.G., Condie, K.C., Tirsgaard, H., Mueller, W.U., Altermann, W., Miall, A.D., Aspler, L.B., Catuneanu, O., Chiarenzelli, J.R., 1998. Precambrian clastic sedimentation systems. Sediment. Geol. 120, 5–53. https://doi.org/10.1016/S0037-0738(98)00026-8

Erwin, D.H., Laflamme, M., Tweedt, S.M., Sperling, E.A., Pisani, D., Peterson, K.J., 2011. The Cambrian Conundrum: Early Divergence and Later Ecological Success in the Early History of Animals. Science 334, 1091–1097. https://doi.org/10.1126/science.1206375

Farquhar J, Bao H, Thiemens M, 2000. Atmospheric influence of Earth's earliest sulfur cycle. Science 289, 756–759.

Farquhar, J., Wing, B.A., 2003. Multiple sulfur isotopes and the evolution of the atmosphere. Earth Planet. Sci. Lett. 213, 1–13. https://doi.org/10.1016/S0012-821X(03)00296-6

Farquhar James, Savarino Joel, Airieau Sabine, Thiemens Mark H., 2001. Observation of wavelength-sensitive mass-independent sulfur isotope effects during SO2 photolysis: Implications for the early atmosphere. J. Geophys. Res. Planets 106, 32829–32839. https://doi.org/10.1029/2000JE001437

Foucher, F., Westall, F., 2013. Raman Imaging of Metastable Opal in Carbonaceous Microfossils of the 700-800Ma Old Draken Formation. Astrobiology 13, 57–67. https://doi.org/10.1089/ast.2012.0889

Frei, R., Gaucher, C., Poulton, S.W., Canfield, D.E., 2009. Fluctuations in Precambrian atmospheric oxygenation recorded by chromium isotopes. Nature 461, 250-U125. https://doi.org/10.1038/nature08266

French, K.L., Hallmann, C., Hope, J.M., Schoon, P.L., Zumberge, J.A., Hoshino, Y., Peters, C.A., George, S.C., Love, G.D., Brocks, J.J., 2015. Reappraisal of hydrocarbon biomarkers in Archean rocks. Proc. Natl. Acad. Sci. 112, 5915–5920.

Froude, D.O., Ireland, T.R., Kinny, P.D., Williams, I.S., Compston, W., Williams, I.R., Myers, J.S., 1983. Ion microprobe identification of 4,100–4,200 Myr-old terrestrial zircons. Nature 304, 616–618. https://doi.org/10.1038/304616a0

Gaidos, E., Dubuc, T., Dunford, M., Mcandrew, P., Padilla-Gamiño, J., Studer, B., Weersing, K., Stanley, S., 2007. The Precambrian emergence of animal life: a geobiological perspective. Geobiology 5, 351–373. https://doi.org/10.1111/j.1472-4669.2007.00125.x

Gibson, T.M., Shih, P.M., Cumming, V.M., Fischer, W.W., Crockford, P.W., Hodgskiss, M.S.W., Wörndle, S., Creaser, R.A., Rainbird, R.H., Skulski, T.M., Halverson, G.P., 2018. Precise age of Bangiomorpha pubescens dates the origin of eukaryotic photosynthesis. Geology 46, 135–138. https://doi.org/10.1130/G39829.1

Green, J.W., Knoll, A.H., Swett, K., 1988. Microfossils from Oolites and Pisolites of the Upper Proterozoic Eleonore Bay Group, Central East Greenland. J. Paleontol. 62, 835–852.

Halverson, G.P., Hoffman, P.F., Schrag, D.P., Maloof, A.C., Rice, A.H.N., 2005. Toward a Neoproterozoic composite carbon-isotope record. GSA Bull. 117, 1181–1207. https://doi.org/10.1130/B25630.1

Hayes, J.M., 1994. Global methanotrophy at Archean-Proterozoic transition, in: Early Life on Earth. Columbia University Press, New York, new york, pp. 220–236.

Hinrichs, K.U., 2002. Microbial fixation of methane carbon at 2.7 Ga: Was an anaerobic mechanism possible? Geochem. Geophys. Geosystems 3, 1042. https://doi.org/10.1029/2001GC000286

Hoffman, P.F., Abbot, D.S., Ashkenazy, Y., Benn, D.I., Brocks, J.J., Cohen, P.A., Cox, G.M., Creveling, J.R., Donnadieu, Y., Erwin, D.H., Fairchild, I.J., Ferreira, D., Goodman, J.C., Halverson, G.P., Jansen, M.F., Hir, G.L., Love, G.D., Macdonald, F.A., Maloof, A.C., Partin, C.A., Ramstein, G., Rose, B.E.J., Rose, C.V., Sadler, P.M., Tziperman, E., Voigt, A., Warren, S.G., 2017. Snowball Earth climate dynamics and Cryogenian geology-geobiology. Sci. Adv. 3, e1600983. https://doi.org/10.1126/sciadv.1600983

Hoffman, P.F., Kaufman, A.J., Halverson, G.P., Schrag, D.P., 1998. A Neoproterozoic Snowball Earth. Science 281, 1342–1346. https://doi.org/10.1126/science.281.5381.1342

Hoffman, P.F., Schrag, D.P., 2002. The snowball Earth hypothesis: testing the limits of global change. Terra Nova 14, 129–155. https://doi.org/10.1046/j.1365-3121.2002.00408.x

Holland, H.D., 2009. Why the atmosphere became oxygenated: A proposal. Geochim. Cosmochim. Acta 73, 5241–5255. https://doi.org/10.1016/j.gca.2009.05.070

Holland, H.D., 2006. The oxygenation of the atmosphere and oceans. Philos. Trans. R. Soc. Lond. B. Biol. Sci. 361, 903–915. https://doi.org/10.1098/rstb.2006.1838

Holland, H.D., 2002. Volcanic gases, black smokers, and the great oxidation event. Geochim. Cosmochim. Acta 66, 3811–3826. https://doi.org/10.1016/S0016-7037(02)00950-X

Irwin, A.J., Finkel, Z.V., Schofield, O.M.E., Falkowski, P.G., 2006. Scaling-up from nutrient physiology to the size-structure of phytoplankton communities. J. Plankton Res. 28, 459–471. https://doi.org/10.1093/plankt/fbi148

Ivarsson, M., 2006. Advantages of doubly polished thin sections for the study of microfossils in volcanic rock. Geochem. Trans. 7, 5.

Javaux, E., 2011. Early eukaryotes in Precambrian oceans, in: Martin, H., Gargaud, M., López-Garcìa, P. (Eds.), Origins and Evolution of Life: An Astrobiological Perspective, Cambridge Astrobiology. Cambridge University Press, Cambridge, pp. 414–449. https://doi.org/10.1017/CBO9780511933875.028

Javaux, E.J., 2007. The Early Eukaryotic Fossil Record, in: Eukaryotic Membranes and Cytoskeleton, Advances in Experimental Medicine and Biology. Springer, New York, NY, pp. 1–19. https://doi.org/10.1007/978-0-387-74021-8_1

Javaux, E.J., Knoll, A.H., Walter, M.R., 2004. TEM evidence for eukaryotic diversity in mid-Proterozoic oceans. Geobiology 2, 121–132. https://doi.org/10.1111/j.1472-4677.2004.00027.x

Javaux, E.J., Marshal, C.P., 2006. A new approach in deciphering early protist paleobiology and evolution: Combined microscopy and microchemistry of single Proterozoic acritarchs. Rev. Palaeobot. Palynol. 139, 1–15. https://doi.org/10.1016/j.revpalbo.2006.01.005

Javaux, E.J., Marshall, C.P., Bekker, A., 2010. Organic-walled microfossils in 3.2-billion-year-old shallow-marine siliciclastic deposits. Nature 463, 934–938. https://doi.org/10.1038/nature08793

Johnson, J.E., Gerpheide, A., Lamb, M.P., Fischer, W.W., 2014. O2 constraints from Paleoproterozoic detrital pyrite and uraninite. Geol. Soc. Am. Bull. 126, 813–830. https://doi.org/10.1130/B30949.1

Johnson, J.E., Webb, S.M., Ma, C., Fischer, W.W., 2016. Manganese mineralogy and diagenesis in the sedimentary rock record. Geochim. Cosmochim. Acta 173, 210–231. https://doi.org/10.1016/j.gca.2015.10.027

Johnston, D.T., 2011. Multiple sulfur isotopes and the evolution of Earth's surface sulfur cycle. Earth Sci. Rev. 106, 161–183. https://doi.org/10.1016/j.earscirev.2011.02.003

Johnston, D.T., Wolfe-Simon, F., Pearson, A., Knoll, A.H., 2009. Anoxygenic photosynthesis modulated Proterozoic oxygen and sustained Earth's middle age. Proc. Natl. Acad. Sci. 106, 16925–16929. https://doi.org/10.1073/pnas.0909248106

Karhu, J.A., Holland, H.D., 1996. Carbon isotopes and the rise of atmospheric oxygen. Geology 24, 867. https://doi.org/10.1130/0091-7613(1996)024<0867:CIATRO>2.3.CO;2

Kasting, J.F., 2001. Earth history. The rise of atmospheric oxygen. Science 293, 819–820. https://doi.org/10.1126/science.1063811

Kasting, J.F., Ono, S., 2006. Palaeoclimates: the first two billion years. Philos. Trans. R. Soc. B-Biol. Sci. 361, 917–929. https://doi.org/10.1098/rstb.2006.1839

Kaufman, A.J., Knoll, A.H., Narbonne, G.M., 1997. Isotopes, ice ages, and terminal Proterozoic earth history. Proc. Natl. Acad. Sci. U. S. A. 94, 6600–6605.

Kendall, B., Gordon, G.W., Poulton, S.W., Anbar, A.D., 2011. Molybdenum isotope constraints on the extent of late Paleoproterozoic ocean euxinia. Earth Planet. Sci. Lett. 307, 450–460. https://doi.org/10.1016/j.epsl.2011.05.019

Kirschvink, J.L., 1992. Late Proterozoic Low-Latitude Global Glaciation: the Snowball Earth, in: Schopf, J.W., Klein, C. (Eds.), The Proterozoic Biosphere : A Multidisciplinary Study. Cambridge University Press, New York, pp. 51–52.

Klatt, J.M., Al-Najjar, M.A.A., Yilmaz, P., Lavik, G., Beer, D. de, Polerecky, L., 2015. Anoxygenic Photosynthesis Controls Oxygenic Photosynthesis in a Cyanobacterium from a Sulfidic Spring. Appl. Environ. Microbiol. 81, 2025–2031. https://doi.org/10.1128/AEM.03579-14

Knoll, A.., Javaux, E.., Hewitt, D., Cohen, P., 2006. Eukaryotic organisms in Proterozoic oceans. Philos. Trans. R. Soc. B Biol. Sci. 361, 1023–1038. https://doi.org/10.1098/rstb.2006.1843

Knoll, A.H., 2012. The Fossil Record of Microbial Life, in: Fundamentals of Geobiology. Wiley-Blackwell.

Knoll, A.H., 2007. Cyanobacteria and Earth History, in: Cyanobacteria: Molecular Biology, Genomics and Evolution. Horizon Scientific Press, Heatherset UK, pp. 1–19.

Knoll, A.H., Bergmann, K.D., Strauss, J.V., 2016. Life: the first two billion years. Philos. Trans. R. Soc. B Biol. Sci. 371, 20150493. https://doi.org/10.1098/rstb.2015.0493

Knoll, A.H., Strother, P., Rossi, S., 1988. Distribution and diagenesis of microfossils from the lower Proterozoic Duck Creek Dolomite, Western Australia. Precambrian Res. 38, 257–279. https://doi.org/10.1016/0301-9268(88)90005-8

Knoll, A.H., Sweet, K., Mark, J., 1991. Paleobiology of a Neoproterozoic tidal flat/lagoonal complex: the Draken Conglomerate Formation, Spitsbergen. J. Paleontol. 65, 531–570.

Konhauser, K.O., Planavsky, N.J., Hardisty, D.S., Robbins, L.J., Warchola, T.J., Haugaard, R., Lalonde, S.V., Partin, C.A., Oonk, P.B.H., Tsikos, H., Lyons, T.W., Bekker, A., Johnson, C.M., 2017. Iron formations: A global record of Neoarchaean to Palaeoproterozoic environmental history. Earth-Sci. Rev. 172, 140–177. https://doi.org/10.1016/j.earscirev.2017.06.012

Kump, L.R., Arthur, M.A., 1999. Interpreting carbon-isotope excursions: carbonates and organic matter. Chem. Geol. 161, 181–198. https://doi.org/10.1016/S0009-2541(99)00086-8

Laakso, T.A., Schrag, D.P., 2014. Regulation of atmospheric oxygen during the Proterozoic. Earth Planet. Sci. Lett. 388, 81–91. https://doi.org/10.1016/j.epsl.2013.11.049

Lamb, D.M., Awramik, S.M., Chapman, D.J., Zhu, S., 2009. Evidence for eukaryotic diversification in the ∼1800 million-year-old Changzhougou Formation, North China. Precambrian Res., World Summit on Ancient Microscopic Fossils 173, 93–104. https://doi.org/10.1016/j.precamres.2009.05.005

Lenton, T.M., Boyle, R.A., Poulton, S.W., Shields-Zhou, G.A., Butterfield, N.J., 2014. Co-evolution of eukaryotes and ocean oxygenation in the Neoproterozoic era. Nat. Geosci. 7, 257–265. https://doi.org/10.1038/ngeo2108

Li, Z.X., Bogdanova, S.V., Collins, A.S., Davidson, A., De Waele, B., Ernst, R.E., Fitzsimons, I.C.W., Fuck, R.A., Gladkochub, D.P., Jacobs, J., Karlstrom, K.E., Lu, S., Natapov, L.M., Pease, V., Pisarevsky, S.A., Thrane, K., Vernikovsky, V., 2008. Assembly, configuration, and break-up history of Rodinia: A synthesis. Precambrian Res., Testing the Rodinia Hypothesis: Records in its Building Blocks 160, 179–210. https://doi.org/10.1016/j.precamres.2007.04.021

Liu, D.Y., Nutman, A.P., Compston, W., Wu, J.S., Shen, Q.H., 1992. Remnants of ≥3800 Ma crust in the Chinese part of the Sino-Korean craton. Geology 20, 339–342. https://doi.org/10.1130/0091-7613(1992)020<0339:ROMCIT>2.3.CO;2

Love, G.D., Grosjean, E., Stalvies, C., Fike, D.A., Grotzinger, J.P., Bradley, A.S., Kelly, A.E., Bhatia, M., Meredith, W., Snape, C.E., Bowring, S.A., Condon, D.J., Summons, R.E., 2009. Fossil steroids record the appearance of Demospongiae during the Cryogenian period. Nature 457, 718–721. https://doi.org/10.1038/nature07673

Lyons, T.W., Reinhard, C.T., Love, G.D., Xiao, S., 2012. Geobiology of the Proterozoic Eon, in: Fundamentals of Geobiology. Wiley-Blackwell, pp. 371–402. https://doi.org/10.1002/9781118280874.ch20

Lyons, T.W., Reinhard, C.T., Planavsky, N.J., 2014. The rise of oxygen in Earth's early ocean and atmosphere. Nature 506, 307–315. https://doi.org/10.1038/nature13068

Macdonald, F.A., Schmitz, M.D., Crowley, J.L., Roots, C.F., Jones, D.S., Maloof, A.C., Strauss, J.V., Cohen, P.A., Johnston, D.T., Schrag, D.P., 2010. Calibrating the Cryogenian. Science 327, 1241–1243. https://doi.org/10.1126/science.1183325

Melezhik, V.A., Fallick, A.E., 1996. A widespread positive δ13Ccarb anomaly at around 2.33–2.06 Ga on the Fennoscandian Shield: a paradox? Terra Nova 8, 141–157. https://doi.org/10.1111/j.1365-3121.1996.tb00738.x

Melezhik, V.A., Fallick, A.E., Rychanchik, D.V., Kuznetsov, A.B., 2005. Palaeoproterozoic evaporites in Fennoscandia: implications for seawater sulphate, the rise of atmospheric oxygen and local amplification of the δ13C excursion. Terra Nova 17, 141–148. https://doi.org/10.1111/j.1365-3121.2005.00600.x

Melezhik, V.A., Huhma, H., Condon, D.J., Fallick, A.E., Whitehouse, M.J., 2007. Temporal constraints on the Paleoproterozoic Lomagundi-Jatuli carbon isotopic event. Geology 35, 655–658. https://doi.org/10.1130/G23764A.1

Moczydlowska, M., 2008a. The Ediacaran microbiota and the survival of Snowball Earth conditions. Precambrian Res. 167, 1–15. https://doi.org/10.1016/j.precamres.2008.06.008

Moczydlowska, M., 2008b. New records of late Ediacaran microbiota from Poland. Precambrian Res. 167, 71–92. https://doi.org/10.1016/j.precamres.2008.07.007

Moreau, J.W., Sharp, T.G., 2004. A transmission electron microscopy study of silica and kerogen biosignatures in-1.9 Ga gunflint microfossils. Astrobiology 4, 196–210. https://doi.org/10.1089/153110704323175142

Mueller, P.A., Wooden, J.L., Nutman, A.P., 1992. 3.96 Ga zircons from an Archean quartzite, Beartooth Mountains, Montana. Geology 20, 327–330. https://doi.org/10.1130/0091-7613(1992)020<0327:GZFAAQ>2.3.CO;2

Nutman, A.P., Bennett, V.C., Friend, C.R.L., Van Kranendonk, M.J., Chivas, A.R., 2016. Rapid emergence of life shown by discovery of 3,700-million-year-old microbial structures. Nature 537, 535–538. https://doi.org/10.1038/nature19355

Och, L.M., Shields-Zhou, G.A., 2012. The Neoproterozoic oxygenation event: Environmental perturbations and biogeochemical cycling. Earth-Sci. Rev. 110, 26–57. https://doi.org/10.1016/j.earscirev.2011.09.004

Oehler, D.Z., 1976. Transmission Electron Microscopy of Organic Microfossils from the Late Precambrian Bitter Springs Formation of Australia: Techniques and Survey of Preserved Ultrastructure. J. Paleontol. 50, 90–106.

Oehler, D.Z., Robert, F., Mostefaoui, S., Meibom, A., Selo, M., McKay, D.S., 2006. Chemical mapping of Proterozoic organic matter at submicron spatial resolution. Astrobiology 6, 838–850.

Pavlov, A.A., Hurtgen, M.T., Kasting, J.F., Arthur, M.A., 2003. Methane-rich Proterozoic atmosphere? Geology 31, 87–90. https://doi.org/10.1130/0091-7613(2003)031<0087:MRPA>2.0.CO;2

Philippot, P., Van Zuilen, M., Lepot, K., Thomazo, C., Farquhar, J., Van Kranendonk, M.J., 2007. Early Archaean microorganisms preferred elemental sulfur, not sulfate. Science 317, 1534–1537. https://doi.org/10.1126/science.1145861

Planavsky, N.J., Asael, D., Hofmann, A., Reinhard, C.T., Lalonde, S.V., Knudsen, A., Wang, X., Ossa Ossa, F., Pecoits, E., Smith, A.J.B., Beukes, N.J., Bekker, A., Johnson, T.M., Konhauser, K.O., Lyons, T.W., Rouxel, O.J., 2014. Evidence for oxygenic photosynthesis half a billion years before the Great Oxidation Event. Nat. Geosci. 7, 283–286. https://doi.org/10.1038/ngeo2122

Porter, S.M., Knoll, A.H., 2000. Testate amoebae in the Neoproterozoic Era: evidence from vase-shaped microfossils in the Chuar Group, Grand Canyon. Paleobiology 26, 360–385. https://doi.org/10.1666/0094-8373(2000)026<0360:TAITNE>2.0.CO;2

Poulton, S.W., Canfield, D.E., 2011. Ferruginous Conditions: A Dominant Feature of the Ocean through Earth's History. Elements 7, 107–112. https://doi.org/10.2113/gselements.7.2.107

Rasmussen, B., Buick, R., 1999. Redox state of the Archean atmosphere: Evidence from detrital heavy minerals in ca. 3250–2750 Ma sandstones from the Pilbara Craton, Australia. Geology 27, 115–118. https://doi.org/10.1130/0091-7613(1999)027<0115:RSOTAA>2.3.CO;2

Rasmussen, B., Fletcher, I.R., Bekker, A., Muhling, J.R., Gregory, C.J., Thorne, A.M., 2012. Deposition of 1.88-billion-year-old iron formations as a consequence of rapid crustal growth. Nature 484, 498–501. https://doi.org/10.1038/nature11021

Rasmussen, B., Fletcher, I.R., Brocks, J.J., Kilburn, M.R., 2008. Reassessing the first appearance of eukaryotes and cyanobacteria. Nature 455, 1101-U9. https://doi.org/10.1038/nature07381

Raymond, J., Segrè, D., 2006. The effect of oxygen on biochemical networks and the evolution of complex life. Science 311, 1764–1767. https://doi.org/10.1126/science.1118439

Reinhard, C.T., Planavsky, N.J., Gill, B.C., Ozaki, K., Robbins, L.J., Lyons, T.W., Fischer, W.W., Wang, C., Cole, D.B., Konhauser, K.O., 2016. Evolution of the global phosphorus cycle. Nature 541, 386–389. https://doi.org/10.1038/nature20772

Riding, R., 2000. Microbial carbonates: the geological record of calcifed bacterial-algal mats and biofilms. Sedimentology 47, 174–214.

Roscoe, S.M., 1973. The Huronian Supergroup: a Paleophebian succession showing evidence of atmospheric evolution. Geol. Surv. Can. Spec. Pap. 12, 31–48.

Roscoe, S.M., 1968. Huronian rocks and uraniferous conglomerates in the Canadian Shield. Geol. Surv. Can. Pap. 68-40 1–205.

Rosing, null, 1999. 13C-Depleted carbon microparticles in >3700-Ma sea-floor sedimentary rocks from west greenland. Science 283, 674–676.

Rosing, M.T., Bird, D.K., Sleep, N.H., Bjerrum, C.J., 2010. No climate paradox under the faint early Sun. Nature 464, 744–747. https://doi.org/10.1038/nature08955

Sagan, C., Mullen, G., 1972. Earth and Mars: evolution of atmospheres and surface temperatures. Science 177, 52–56. https://doi.org/10.1126/science.177.4043.52

Schidlowski, M., Eichmann, R., Junge, C.E., 1975. Precambrian sedimentary carbonates: carbon and oxygen isotope geochemistry and implications for the terrestrial oxygen budget. Precambrian Res. 2, 1–69. https://doi.org/10.1016/0301-9268(75)90018-2

Schirrmeister, B.E., Vos, J.M. de, Antonelli, A., Bagheri, H.C., 2013. Evolution of multicellularity coincided with increased diversification of cyanobacteria and the Great Oxidation Event. Proc. Natl. Acad. Sci. 110, 1791–1796. https://doi.org/10.1073/pnas.1209927110

Schopf, J.W., 1968. Microflora of the Bitter Springs Formation, Late Precambrian, Central Australia. J. Paleontol. 42, 651–688.

Schopf, J.W., Kudryavtsev, A.B., Agresti, D.G., Wdowiak, T.J., Czaja, A.D., 2002. Laser-Raman imagery of Earth's earliest fossils. Nature 416, 73–76. https://doi.org/10.1038/416073a

Schopf, J.W., Walter, M.R., 1982. Origin and early evolution of cyanobacteria: The geological evidence., in: The Biology of Cyanobacteria. University of California Press, pp. 543–564.

Schröder, S., Bekker, A., Beukes, N.J., Strauss, H., van Niekerk, H.S., 2008. Rise in seawater sulphate concentration associated with the Paleoproterozoic positive carbon isotope excursion: evidence from sulphate evaporites in the ∼2.2–2.1 Gyr shallow-marine Lucknow Formation, South Africa. Terra Nova 20, 108–117. https://doi.org/10.1111/j.1365-3121.2008.00795.x

Scott, C., Lyons, T.W., Bekker, A., Shen, Y., Poulton, S.W., Chu, X., Anbar, A.D., 2008. Tracing the stepwise oxygenation of the Proterozoic ocean. Nature 452, 456–459. https://doi.org/10.1038/nature06811

Sergeev, V.N., 2009. The distribution of microfossil assemblages in Proterozoic rocks. Precambrian Res. 173, 212–222. https://doi.org/10.1016/j.precamres.2009.04.002

Shen, Y., Farquhar, J., Masterson, A., Kaufman, A.J., Buick, R., 2009. Evaluating the role of microbial sulfate reduction in the early Archean using quadruple isotope systematics. Earth Planet. Sci. Lett. 279, 383–391. https://doi.org/10.1016/j.epsl.2009.01.018

Shields-Zhou, G., Och, L., 2011. The case for a Neoproterozoic Oxygenation Event: Geochemical evidence and biological consequences. GSA Today 21, 4–11. https://doi.org/10.1130/GSATG102A.1

Sugitani, K., Lepot, K., Nagaoka, T., Mimura, K., Van Kranendonk, M., Oehler, D.Z., Walter, M.R., 2010. Biogenicity of Morphologically Diverse Carbonaceous Microstructures from the ca. 3400 Ma Strelley Pool Formation, in the Pilbara Craton, Western Australia. Astrobiology 10, 899–920. https://doi.org/10.1089/ast.2010.0513

Sugitani, K., Mimura, K., Takeuchi, M., Lepot, K., Ito, S., Javaux, E.J., 2015. Early evolution of large micro-organisms with cytological complexity revealed by microanalyses of 3.4 Ga organic-walled microfossils. Geobiology 13, 507–521. https://doi.org/10.1111/gbi.12148

Summons, R.E., Jahnke, L.L., Hope, J.M., Logan, G.A., 1999. 2-Methylhopanoids as biomarkers for cyanobacterial oxygenic photosynthesis. Nature 400, 554–557. https://doi.org/10.1038/23005

Tajika, E., 2003. Faint young Sun and the carbon cycle: implication for the Proterozoic global glaciations. Earth Planet. Sci. Lett. 214, 443–453. https://doi.org/10.1016/S0012-821X(03)00396-0

Thiel, V., Sjövall, P., 2014. CHAPTER 5:Time-of-Flight Secondary Ion Mass Spectrometry (TOF-SIMS): Principles and Practice in the Biogeosciences, in: Principles and Practice of Analytical Techniques in Geosciences. pp. 122–170. https://doi.org/10.1039/9781782625025-00122

Tice, M.M., Lowe, D.R., 2004. Photosynthetic microbial mats in the 3,416-Myr-old ocean. Nature 431, 549–552. https://doi.org/10.1038/nature02888

Towe, K.M., 1970. Oxygen-collagen priority and the early metazoan fossil record. Proc. Natl. Acad. Sci. U. S. A. 65, 781–788.

Ueno, Y., Yamada, K., Yoshida, N., Maruyama, S., Isozaki, Y., 2006. Evidence from fluid inclusions for microbial methanogenesis in the early Archaean era. Nature 440, 516–519. https://doi.org/10.1038/nature04584

Valley, J.W., Peck, W.H., King, E.M., Wilde, S.A., 2002. A cool early Earth. Geology 30, 351–354. https://doi.org/10.1130/0091-7613(2002)030<0351:ACEE>2.0.CO;2

Wacey, D., Kilburn, M.R., Saunders, M., Cliff, J., Brasier, M.D., 2011. Microfossils of sulphur-metabolizing cells in 3.4-billion-year-old rocks of Western Australia. Nat. Geosci. 4, 698–702. https://doi.org/10.1038/ngeo1238

Wacey, D., Menon, S., Green, L., Gerstmann, D., Kong, C., Mcloughlin, N., Saunders, M., Brasier, M., 2012. Taphonomy of very ancient microfossils from the similar to 3400 Ma Strelley Pool Formation and similar to 1900 Ma Gunflint Formation: New insights using a focused ion beam. Precambrian Res. 220, 234–250. https://doi.org/10.1016/j.precamres.2012.08.005

Wilde, S.A., Valley, J.W., Peck, W.H., Graham, C.M., 2001. Evidence from detrital zircons for the existence of continental crust and oceans on the Earth 4.4 Gyr ago. Nature 409, 175–178. https://doi.org/10.1038/35051550

Wille, M., Kramers, J.D., Nägler, T.F., Beukes, N.J., Schröder, S., Meisel, T., Lacassie, J.P., Voegelin, A.R., 2007. Evidence for a gradual rise of oxygen between 2.6 and 2.5Ga from Mo isotopes and Re-PGE signatures in shales. Geochim. Cosmochim. Acta 71, 2417–2435. https://doi.org/10.1016/j.gca.2007.02.019

Xiao, S., Knoll, A.H., Kaufman, A.J., Yin, L., Zhang, Y., 1997. Neoproterozoic fossils in Mesoproterozoic rocks? Chemostratigraphic resolution of a biostratigraphic conundrum from the North China Platform. Precambrian Res. 84, 197–220. https://doi.org/10.1016/S0301-9268(97)00029-6

Xiao Shuhai, 2013. Neoproterozoic Glaciations and the Fossil Record. Extreme Proterozoic Geol. Geochem. Clim., Geophysical Monograph Series. https://doi.org/10.1029/146GM16

Young, G.M., Long, D.G.F., Fedo, C.M., Nesbitt, H.W., 2001. Paleoproterozoic Huronian basin: product of a Wilson cycle punctuated by glaciations and a meteorite impact. Sediment. Geol. 141–142, 233–254. https://doi.org/10.1016/S0037-0738(01)00076-8

Zerkle, A.L., Mikhail, S., 2017. The geobiological nitrogen cycle: From microbes to the mantle. Geobiology 15, 343–352. https://doi.org/10.1111/gbi.12228

Zhou, C., Xiao, S., 2007. Ediacaran δ13C chemostratigraphy of South China. Chem. Geol., Precambrian Chemostratigraphy 237, 89–108. https://doi.org/10.1016/j.chemgeo.2006.06.021

Chapitre I

Méthode de préparation de lames semi-épaisses pour la caractérisation moléculaire de micro- et nano-structure organique

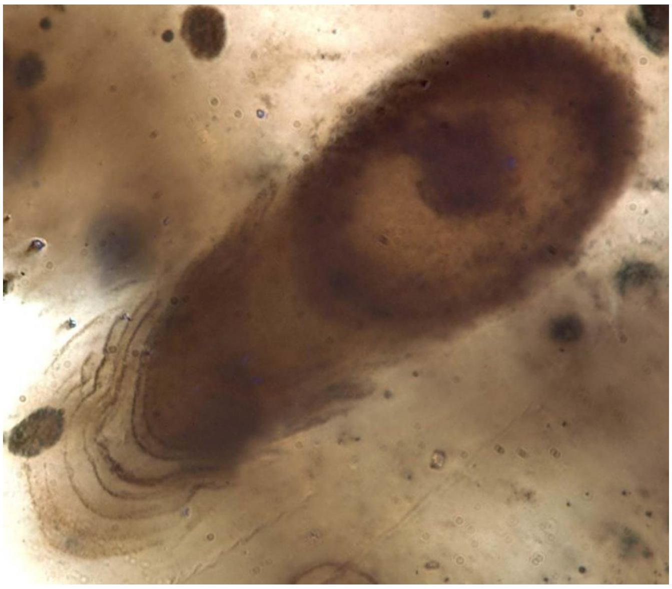

Préambule sur la spectrométrie ToF-SIMS.

La Spectroscopie de masse des ions secondaire à temps de vol (« Time of Flight Secondary Ion Mass Sprectroscopy » ou ToF-SIMS) est une technique permettant de caractériser la composition moléculaire et élémentaire de l'extrême surface des matériaux. Le principe de la spectroscopie à ions secondaires est de bombarder la surface de l'échantillon avec un faisceau d'ions incidents (source pulsée), appelés ions primaires (primary ion source, Fig.P.1) porteurs d'une énergie de quelques keV. Sous l'effet du bombardement, les premières couches atomiques de surface de l'échantillon émettent des particules, dites secondaires, dont des ions chargés positivement ou négativement (Fig. P.1). Dans le cas des analyses ToF-SIMS, la dose d'ions primaires est généralement faible ($<10^{13}$ ions/cm^2) afin d'éviter que la surface de l'échantillon ne soit détériorée au cours de l'analyse, on parle alors d'analyse en mode statique (« SIMS static »). Les ions secondaires sont focalisés et accélérés avec la même énergie cinétique dans le tube d'analyse (secondary ion flight path, Fig. P.1). L'ensemble des ions émis passe ensuite au niveau du reflectron (ayant le rôle d'un « miroir ») qui les renvoie vers le détecteur (Fig. P.1). Le temps de parcours des ions secondaires dans l'analyseur est proportionnel à la racine carrée de leur masse. Les ions légers arrivent donc les plus rapidement sur le détecteur. Les spectres de masse obtenus représentent l'intensité des ions secondaires en fonction de leur masse indiquée par le rapport masse sur charge (m/z). Grâce à un dispositif de balayage du faisceau d'ions primaires, on peut obtenir une cartographie des différents éléments et espèces moléculaires présents à la surface. L'acquisition de ces cartographies peut s'effectuer à partir de deux modes : -« bunch » mode où la machine est paramétrée afin d'obtenir une bonne résolution spectrale permettant de bien différencier les espèces sur les spectres (exemple : différencier l'isotope 13 du carbone de l'ion $CH^{+/-}$), alors que la résolution latérale (résolution de l'image) sera de l'ordre de quelques micromètres.

-« burst » mode où la résolution latérale est optimisée, avec une résolution d'image pouvant aller jusqu'à 100nm selon la source primaire utilisée, au détriment de la résolution spectrale. (Sodhi, 2004)

Une deuxième source d'ions (« sputter ion source ») permet d'effectuer des abrasions de la surface de l'échantillon avec des ions monoatomique (Ar^+, Cs^+, Ga^+,…) ou multi-atomiques (C_{60}^+, Ar_n^+,…). L'utilisation de cette deuxième source permet de nettoyer la surface de l'échantillon et/ou de tracer des profils de composition en profondeur en alternant les phases d'acquisition et d'abrasion.

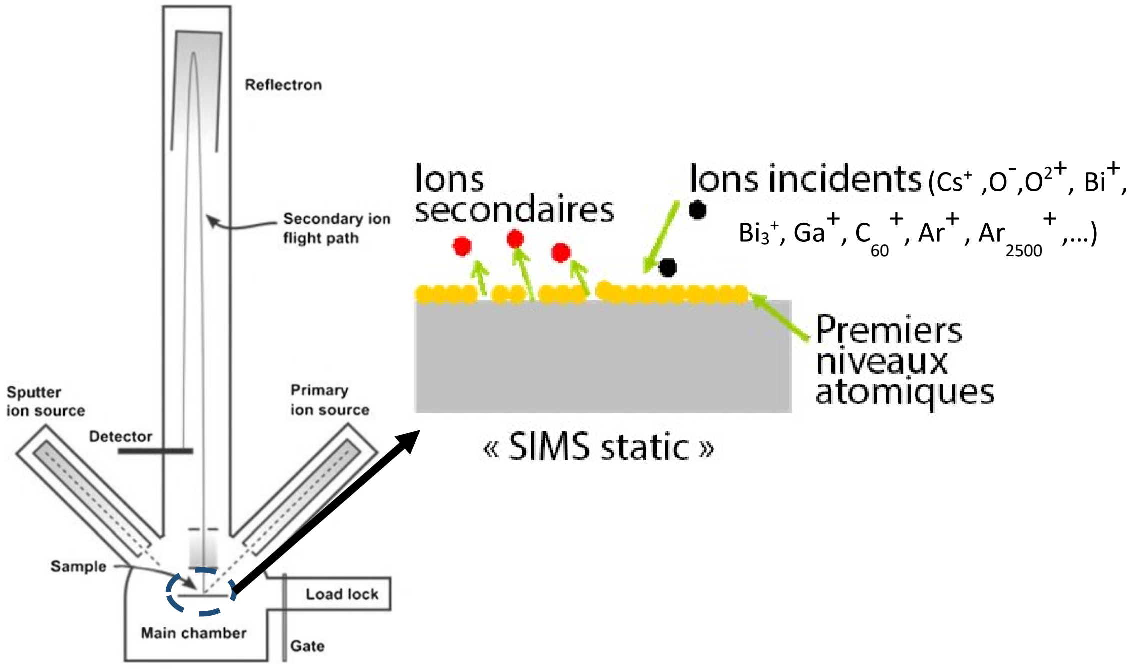

Fig. P.1. Schéma explicatif du principe de la ToF SIMS. *A gauche : schéma simplifié du spectromètre ToF-SIMS présentant la géométrie de la machine. Celle-ci se compose d'une chambre associée à deux canon d'ions (ions primaires et ions pour l'abrasion), un sas et d'une porte ('gate' et 'load lock') permettant de charger les echantillons et d'un tube d'analyse composé d'un reflectron et du dectecteur. A droite : schéma montrant l'interaction des ions primaires avec la surface d'un échantillon. Les ions secondaires sont générés et ejectés par le bombardement d'ions primaires au niveau de l'extrême surface de l'échantillon en mode statique (SIMS stactic).*

La spectrométrie ToF-SIMS est un outil puissant pour analyser l'extrême surface des échantillons. Elle a donc de nombreuses applications dans le domaine des sciences des matériaux, des polymères, de la biologie et la géologie. En géosciences, la caractérisation de matériaux organiques fossiles insoluble (kérogène) est difficile à cause de la complexité des données obtenues avec la ToF SIMS (Thiel and Sjovall, 2011; Thiel and Sjövall, 2014). Les résultats les plus notables sont concentrés sur la détection de molécules organiques spécifiques de masse connue : par exemple des hopanes et stéranes détectés dans des inclusions fluides par Siljestrom et al., (2010). Néanmoins, les résultats les plus spectaculaires ont été obtenus dans le cadre de recherches de pigments ou de molécules typiques de structures organiques (mélanine, hémoglobine …) pouvant être préservées dans les fossiles (Fig. P.2) (Greenwalt et al., 2013; Lindgren et al., 2012). La mélanine est un polymère issu d'une petite molécule simple et est identifiée par comparaison de son spectre de fragmentation sur des masses faibles (<200 u) en ToF-SIMS (Lindgren et al., 2012). L'hémoglobine est de son côté une grosse molécule qui est directement identifiée par l'analyse des pics ToF-SIMS à des masses élevées (>400 u, molécule complète ou peu fragmentée, Greenwalt et al., 2013). Peu d'études ont eu pour but de regarder la composition de macromolécules complexes comme le kérogene (Vandenbroucke and Largeau, 2007) et de comprendre leur fragmentation en ToF-SIMS (Toporski et al., 2002) (Fig. P.4).

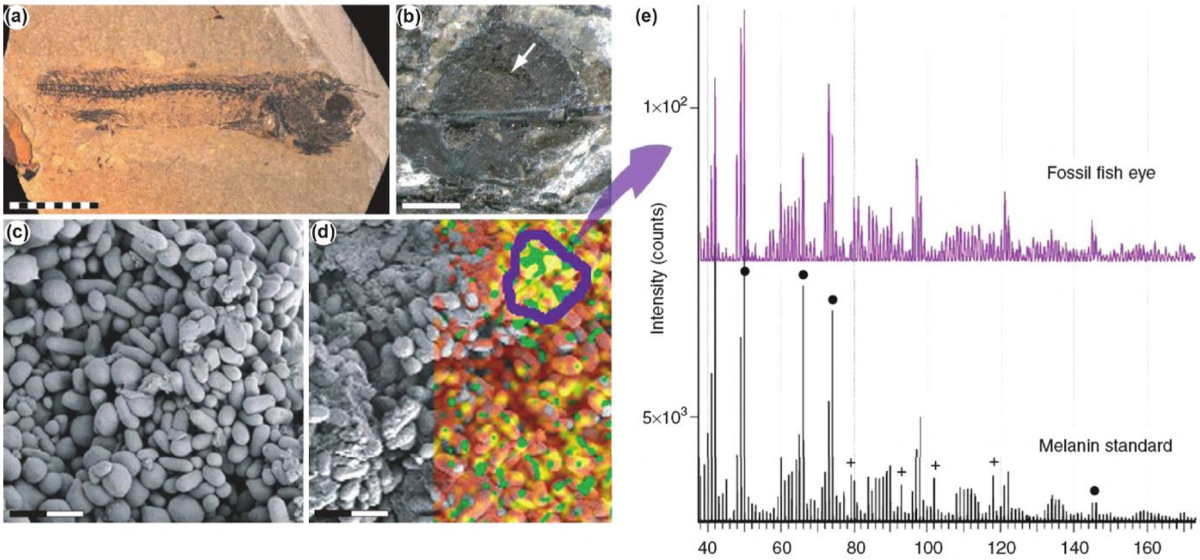

Fig. P.2. Analyse de mélanine préservé dans un œil de poisson de l'Eocène. *A. Vue générale du fossile. Barre d'échelle : 10mm B. Zoom sur la structure analysée (flèche blanche : zone analysée en ToF SIMS). Barre d'échelle : 1mm. C. Vue de la zone analysée au Microscope électronique à balayage. Barre d'échelle : 2µm. D. Image montrant la distribution de plusieurs fragment générés par la mélanine (identifié avec le standard de mélanine) en ToF SIMS superposée à l'imagerie MEB. E. Comparaison entre les spectres négatifs du fossile (en haut et violet) obtenues à partir de la zone entourée en violet sur l'image d et du standard e mélanine analysée (noire). Les deux spectres sont similaires indiquant que la mélanine contenu dans les yeux du yeux du poissons a été préservé au cours de la fossilisation. Image reprise de Thiel and Sjövall, 2014 et issue Lindgren et al., 2012.*

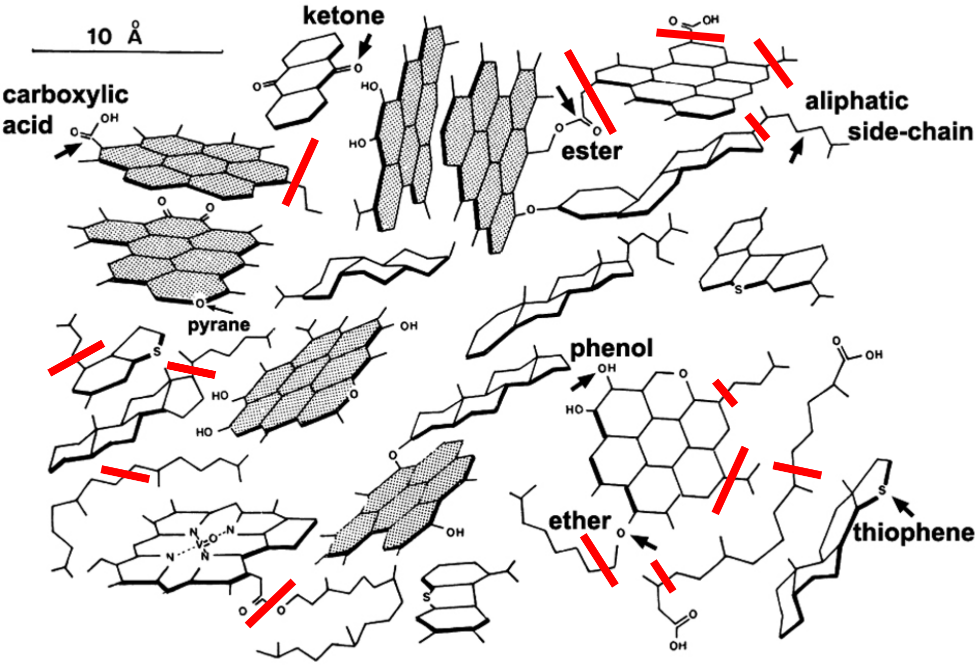

Fig.P.3. Schéma strutural d'un kérogène au stade de maturation avant d'entrée en catagénèse *(Oberlin et al., 1980). Les traits rouges montrent des exemples de ruptures de liaisons chimiques pouvant être induites lors d'analyse ToF SIMS avec la prodution de fragments de faibles et hautes masses issues de la macromolécule.*

Références

Greenwalt, D.E., Goreva, Y.S., Siljestroem, S.M., Rose, T., Harbach, R.E., 2013. Hemoglobin-derived porphyrins preserved in a Middle Eocene blood-engorged mosquito. Proc. Natl. Acad. Sci. U. S. A. 110, 18496–18500. https://doi.org/10.1073/pnas.1310885110

Lindgren, J., Uvdal, P., Sjovall, P., Nilsson, D.E., Engdahl, A., Schultz, B.P., Thiel, V., 2012. Molecular preservation of the pigment melanin in fossil melanosomes. Nat. Commun. 3, 824. https://doi.org/10.1038/ncomms1819

Oberlin, A., Boulmier, J.L., Villey, M., 1980. Electron microscopic study of kerogen microtexture. Selectred criteria for determining the evolution path and evolution stage of kerogen., in: Kerogen : Insoluble Organic Matter from Sedimentary Rocks. Durand, B.

Siljestrom, S., Lausmaa, J., Sjovall, P., Broman, C., Thiel, V., Hode, T., 2010. Analysis of hopanes and steranes in single oil-bearing fluid inclusions using time-of-flight secondary ion mass spectrometry (ToF-SIMS). Geobiology 8, 37–44. https://doi.org/10.1111/j.1472-4669.2009.00223.x

Sodhi, R.N.S., 2004. Time-of-flight secondary ion mass spectrometry (TOF-SIMS):—versatility in chemical and imaging surface analysis. The Analyst 129, 483–487. https://doi.org/10.1039/B402607C

Thiel, V., Sjövall, P., 2014. CHAPTER 5:Time-of-Flight Secondary Ion Mass Spectrometry (TOF-SIMS): Principles and Practice in the Biogeosciences, in: Principles and Practice of Analytical Techniques in Geosciences. pp. 122–170. https://doi.org/10.1039/9781782625025-00122

Thiel, V., Sjovall, P., 2011. Using Time-of-Flight Secondary Ion Mass Spectrometry to Study Biomarkers, in: Jeanloz, R., Freeman, K.H. (Eds.), Annual Review of Earth and Planetary Sciences, Vol 39. Annual Reviews, Palo Alto, pp. 125–156.

Toporski, J.K.W., Steele, A., Westall, F., Avci, R., Martill, D.M., McKay, D.S., 2002. Morphologic and spectral investigation of exceptionally well-preserved bacterial biofilms from the Oligocene Enspel formation, Germany. Geochim. Cosmochim. Acta 66, 1773–1791. https://doi.org/10.1016/S0016-7037(01)00870-5

Vandenbroucke, M., Largeau, C., 2007. Kerogen origin, evolution and structure. Org. Geochem. 38, 719–833. https://doi.org/10.1016/j.orggeochem.2007.01.001

A semi-thin section preparation method for *in situ* molecular characterization of organic micro- and nano-structures

Alexandre Fadel[1], Kevin Lepot[1], Nicolas Nuns[2], Armelle Riboulleau[1]

[1] Laboratoire d'Océanologie et de Géosciences, Université de Lille, CNRS, Université Littoral Côté d'Opale, UMR8187, Cité Scientifique SN5, 59655 Villeneuve d'Ascq, France.

[2] Univ. Lille, CNRS, INRA, Centrale Lille, ENSCL, Univ. Artois, FR 2638 - IMEC - Institut Michel-Eugène Chevreul, F-59000 Lille, France

Abstract

Organic microfossils preserved in three dimensions in transparent mineral matrices such as cherts/quartzites, phosphates or carbonates are dominant in the Precambrian fossil record. These are best studied in petrographic thin sections. However, contamination by epoxy resin in traditional petrographic sections is problematic for the geochemical study of the kerogen in these microfossils and more generally for the in situ analysis of fossil organic matter. Here, we show that epoxy contamination may be pervasive down to the nanoscale porosity of quartzites. To solve this problem, we present a new semi-thin section preparation without resin medium for micro- to nanoscale in situ investigation of insoluble organic matter. We show that these sections are suited for microscopic observation of Proterozoic microfossils in cherts. Using Time-of-Flight Secondary Ion Mass Spectrometry (ToF-SIMS), we show that these sections are ultra-clean after final removal of a <10 nm layer of contamination using low dose ion sputtering. ToF-SIMS maps of fragments of aliphatic and aromatic molecules correlated with organic micro-laminae in a Jurassic stromatolithe. These developments in analytical procedures should help future investigations of organic matter and in particular, microfossils, by allowing the spatial correlation of microscopy, spectroscopy, precise isotopic microanalyses, and novel molecular microanalyses such as ToF-SIMS.

1 Introduction

Unlike the fossil record of the Phanerozoic, the earlier and much longer Precambrian time is characterized by a comparatively scarce fossil record dominated by microscopic prokaryotes and eukaryotes (Javaux and Lepot, 2018; Knoll, 2003; Knoll et al., 2016). Precambrian carbonaceous microfossils hosted in various matrices including cherts, shales and phosphates represent important targets to understand the evolution of early life (Butterfield, 2015a, 2015b; Javaux, 2011; Knoll et al., 2006; Sergeev, 2009) When they are preserved by impregnation by e.g. chert or phosphates, microfossils display three dimensional morphological preservation. However, morphology has proven insufficient to identify the taxonomy, and even to determine the biogenicity of a large fraction of Precambrian microfossils (Brasier et al., 2005; Javaux and Lepot, 2018; Wacey et al., 2016). Micro- to nano-scale characterization of organic structures and the associated minerals are important to demonstrate that a cell-like structure is endogenous, syngenetic and of biogenic morphology (Buick, 1990; Fadel et al., 2017; Lekele Baghekema et al., 2017; Lepot et al., 2017; Wacey et al., 2016, 2012). Microscopy combined with microanalyses can help demonstrate true microfossils and decipher their taxonomy. These analytical techniques include multiplane optical microscopy and Confocal Laser Scanning Microscopy (CLSM) that help reconstruct the 3D microstructure (Schopf et al., 2006; Sutton et al., 2014). Raman microspectrometry and imagery help determine organic-matter maturity (Beyssac et al., 2002; Kouketsu et al., 2014; Schopf et al., 2005). Transmitted Electron Microscopy (TEM) performed on Focused Ion Beam (FIB) foils (Kempe et al., 2005; Lepot et al., 2017; Moreau and Sharp, 2004; Wacey et al., 2012) and FIB-Scanning Electron Microscopy (SEM) nano-tomography (Schiffbauer and Xiao, 2009; Wacey et al., 2016) inform on ultrastructures at the nanoscale. Microfossil ultrastructure can be used for example to demonstrate the eukaryotic affinities (Javaux et al., 2004; Moczydłowska and Willman, 2009) and can help constrain the affinities of simple shaped (e.g. sphere, filaments), likely prokaryotic microfossils (Brasier et al., 2015; Lekele Baghekema et al., 2017; Lepot et al., 2017).

Nondestructive microanalyses of the organic structures such as micro Fourier Transform InfraRed spectroscopy (FTIR) combined with Raman micro spectrometry permit to constrain the nature of single microfossils based on functional groups attached to carbon chains (such as CH_2, CH_3, C-N, C-C, C=C, C=O and others) at the ca. 10 µm scale (Arouri et al., 1999; Igisu et al., 2009; Marshall et al., 2005). Scanning (Transmission) X-ray Microscopy (S(T)XM) permits to distinguish functional groups at the nanoscale, e.g. revealing intra-cellular molecular heterogeneities in Phanerozoic fossil spores (Bernard et al. 2007), preservation of organic N in Paleoproterozoic microfossils (Alleon et al., 2016) and organic sulfur in ~750 Ma microfossils (Lemelle et al., 2008).

Secondary Ion Mass Spectrometry (SIMS) comprise surface ablation techniques that measure elemental, molecular and isotopic compositions. For example, NanoSIMS revealed N/C heterogeneities among Neoproterozoic microfossils (Oehler et al., 2006), the presence nitrogen and sulfur from cell wall structure of Proterozoic microfossil and also revealed the nature of non-carbonaceous material (e.g. iron oxides) associated with microfossils (Wacey et al., 2016). SIMS of carbon isotope ratio constrained the metabolisms of Proterozoic microfossils (House et al., 2000; Williford et al., 2013) and argued for Archean microfossils (Lepot et al., 2013). Time-of-Flight SIMS (ToF-SIMS) can be used to image molecular ions at the microscale (Abbott et al., 2018; Lindgren et al., 2017, 2012).

All these techniques can be performed in polished petrographic thin sections, which allows correlation of 3D morphology and micro-/nano-analayses. This preparation also offers flat surface that is crucial for surface microanalysis and allows the precise localization of microfossil with transmitted light microscopy, which is commonly required for micro and nanoscale analyses (Miyagi, 2017). Microfossils extracted by acid maceration can be analyzed by a number of the above techniques. Organic microfossils that have been compressed in clastic sediments usually are flat enough for FIB-based ultrastructural studies (Schiffbauer and Xiao, 2009), for SIMS analyses (Kaufman and Xiao, 2003), and for FTIR (Javaux and Marshal, 2006). Microfossils that were preserved in 3D (e.g. in cherts) retain their volume after acid maceration (e.g. Lekele Baghekema et al., 2017), making them difficult to analyze with FIB-based techniques (Sugitani et al., 2015). For such "3D" microfossils, SIMS and ToF-SIMS analyses are best performed in polished sections as analytical bias appear when topography is higher than micrometric (Belu et al., 2003; Kita et al., 2009; Thiel and Sjovall, 2011; Vandenbroucke et al., 2015). Moreover, some drastic acid maceration protocols such as those required to dissolve quartz (Grey, 1999) may alter the molecular structure of organic matter (e.g. Shi et al., 2012). In contrast, the main disadvantage of petrographic thin sections is that they use soluble or insoluble (e.g. epoxy) resins. Epoxy resins have been shown to contaminate micrometric pores in petrographic sections (Bernard, 2008, Wacey et al. in press), and we show below that this contamination can sometimes reach the sub-micrometric porosity associated with microfossils in cherts. Insoluble resins are thus a problematic contamination for the *in situ* investigations of organic matter in microfossils. Soluble resins may be compatible with molecular analyses of relatively low sensitivity such as FTIR (Igisu et al., 2009), but their impact on high sensitivity analyses such as ToF-SIMS is difficult to address. Here we present a new procedure for the preparation of resin-free semi thin section (300 - 500 µm thick). We show that these sections can be used for transmitted light microscope observation of organic microstructures in chert, and that they are compatible with SIMS isotope microanalyses, FIB-based ultrastructurales techniques and ToF-SIMS molecular microanalyses.

2 Samples

The studied samples correspond to four cherts and one bituminous limestone. The first chert sample originates from the ca. 3.4 Ga Strelley Pool Formation (Western Australia); it was prepared in conventional petrographic thin section as detailed in Lepot et al. (2013; Fig. 4) that includes organic microstructures interpreted as organic microfossils (Lepot et al., 2013; Sugitani et al., 2015, 2010). This sample comes from the zone in Fig. 4 of Lepot et al. (2013). The second chert comes the member 1 of ca. 3.4Ga Strelley Pool Formation, which contains organic clasts (Allwood et al., 2006). The third chert sample comes from the ca. 2.1 Ga FC formation of the Francevillian Supergroup (Gabon) sampled at the Bambaye locality (Gauthier-

Lafaye and Weber, 2003; Lekele Baghekema, 2017). The fourth chert sample comes from the 700-800 Ma microfossiliferous Draken Formation (sample P4353, Knoll et al., 1991). The bituminous limestone corresponds to lagoonal microbial mats displaying alternating carbonate and organic matter laminae, from the Kimmeridgian deposits of Orbagnoux (French Southern Jura Mountains) (Tribovillard et al., 2000).

3 Semi-thin section preparations

3.1 Equipment

Hardware equipment required include, (1) for large pieces of rock, workbench drilling machine with a 1" diamond drill bit and adapted sample holders. Here we used a Cincinnati PE 15 model. (2) A rock-cutting saw with a blade at least 200 mm diameter, 1 mm in thickness, and a core-holder to facilitate the sawing. (3) A grinding unit equipped with a sample-holder cavity 2.54 mm in diameter and 1 mm deep, holding samples with a water suction piston, and a micrometric gauge with 0.1 mm graduations. (4) A thickness measuring set with a gauge resolution of <10 µm. (5) A glass plate (minimal dimension: 200 mm x 200 mm x 13 mm). (6) A semi-automatic polishing machine allowing to polish 3 sample simultaneously, here we used a customized BROT model 1.03.17 with stainless steel structure. (7) Custom-made sample holders for the polishing machine with 3 cavity depths: 1, 0.5 and 0.3 mm. (8) An ultrasonic cleaning tank. (9) A microscope with reflecting and transmitted light for the control of the thick section during the procedure (here an Olympus BX60 with X5 to X100 objectives). (10) a dry (i.e. without oil) vacuum pump.

The required consumption supplies include: (1) metallic grinding discs that can be fixed and exchanged magnetically onto the polishing stage, impregnated with diamonds of grain sizes ranging between 76 and 36µm). (2) A cast iron polishing disk 250 mm in diameter machined with a perfectly flat surface. Surface damage produced by polishing should be frequently corrected by polishing in contact with 5-10 cm large, flat stainless steel disks and silicon carbide (1000 FEPA). (3) Polishing clothes (woven and felt cloths) to support water-based diamond and corundum (Al_2O_3) suspensions. (4) Abrasives including silicon carbide (SiC 500, 600 and 1000 FEPA), water-based diamond suspension (6, 3 ,1 µm grain size) and corundum (4, 2, 1 µm grain size). (5) Vessels: glass jars and high-vacuum mini-desiccators (40 cm^3 Vacu-Storr^{TM} from Ted Pella). (6) Tweezers: coarse, straight, fine with flat (and 25° angle) tips for the manipulation of delicate sample. (7) Solvents: deionized water, ethanol (95%), acetone (99,5%)

for cleaning during the sample preparation process and HPLC-grade ultrapure dichloromethane and methanol for final cleaning under fume hood. (8) For sample storage and transport: aluminum foil, glass micro beads (1-2 mm diameter), stainless steel cleaning basket (40 mm diameter), glass slides for the microscopic control during the procedure. (9) Compressed (>150 bar) pure N_2 supply for sample drying. (10) Safety accessories: nitrile and latex (powder-free) gloves, goggles, and ear protection.

3.2 Protocol

3.2.1 Coarse slide preparation

The first step is to drill the sample with the workbench drilling machine to get a sample core 2.54 cm in diameter (Fig. 1.1 A, B). The machine and the sample holder are thoroughly cleaned with ethanol. The drill bit and the sample are rinsed three times with ethanol and acetone. The sample should contain a minimum of fissures, cracks, pores and should be oriented to reduce the risk of splitting and cracking during the drilling, cutting and grinding processes. The resulting sample core is rinsed 3 times with ethanol and acetone and stored in rinsed glass jar sealed with aluminum foil.

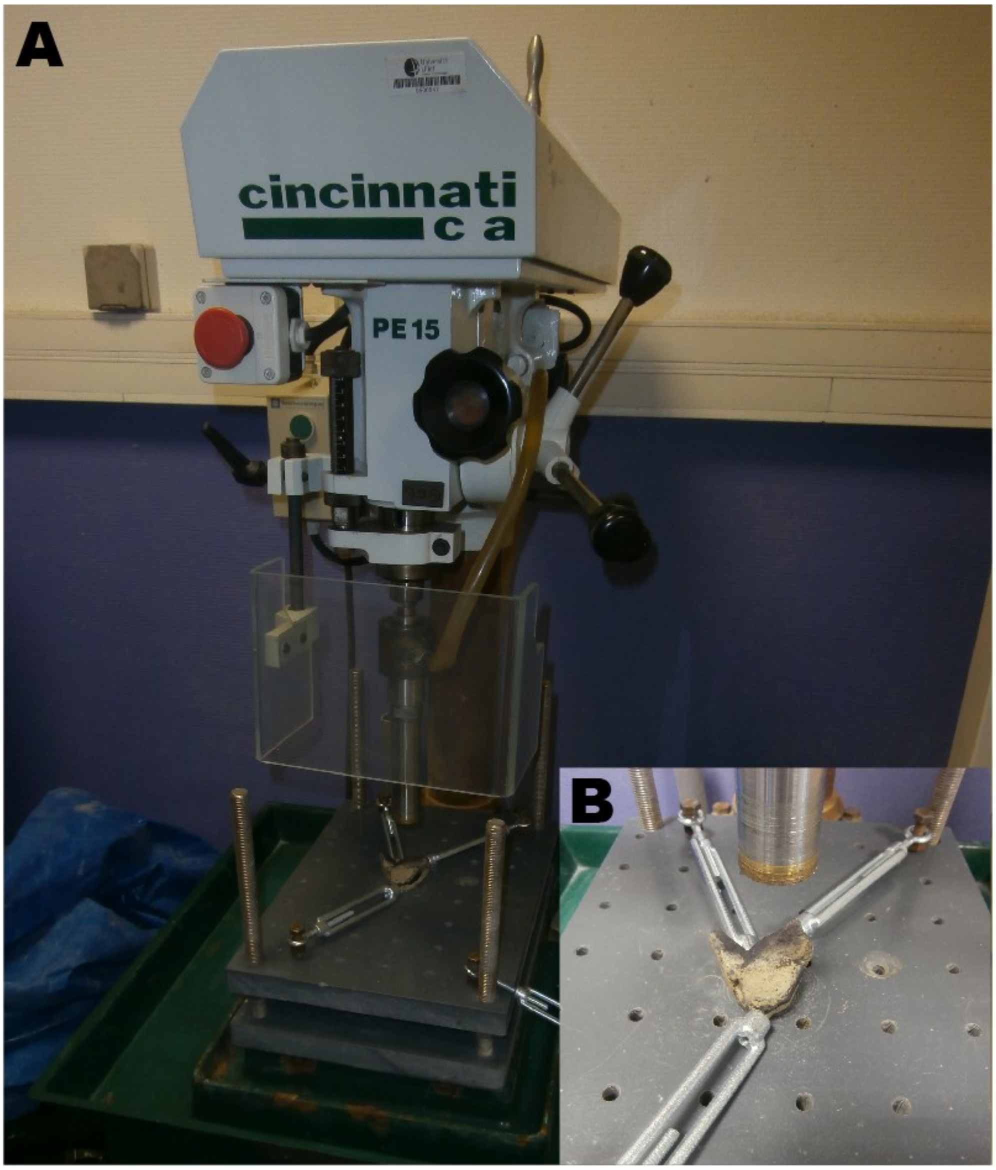

Fig 1.1. Workbench drilling machine. *(A) Machine setting during drilling process. (B) View of sample holder and 1" diamond drill bit.*

The core is sawn to a 3-4 mm thick slide with the diamond blade using the sample core holders (Fig 1.2 A,B). All the instruments in contact with the sample core or slice are cleaned three times with ethanol and acetone before and after the sawing. The saw is cleaned with ethanol.

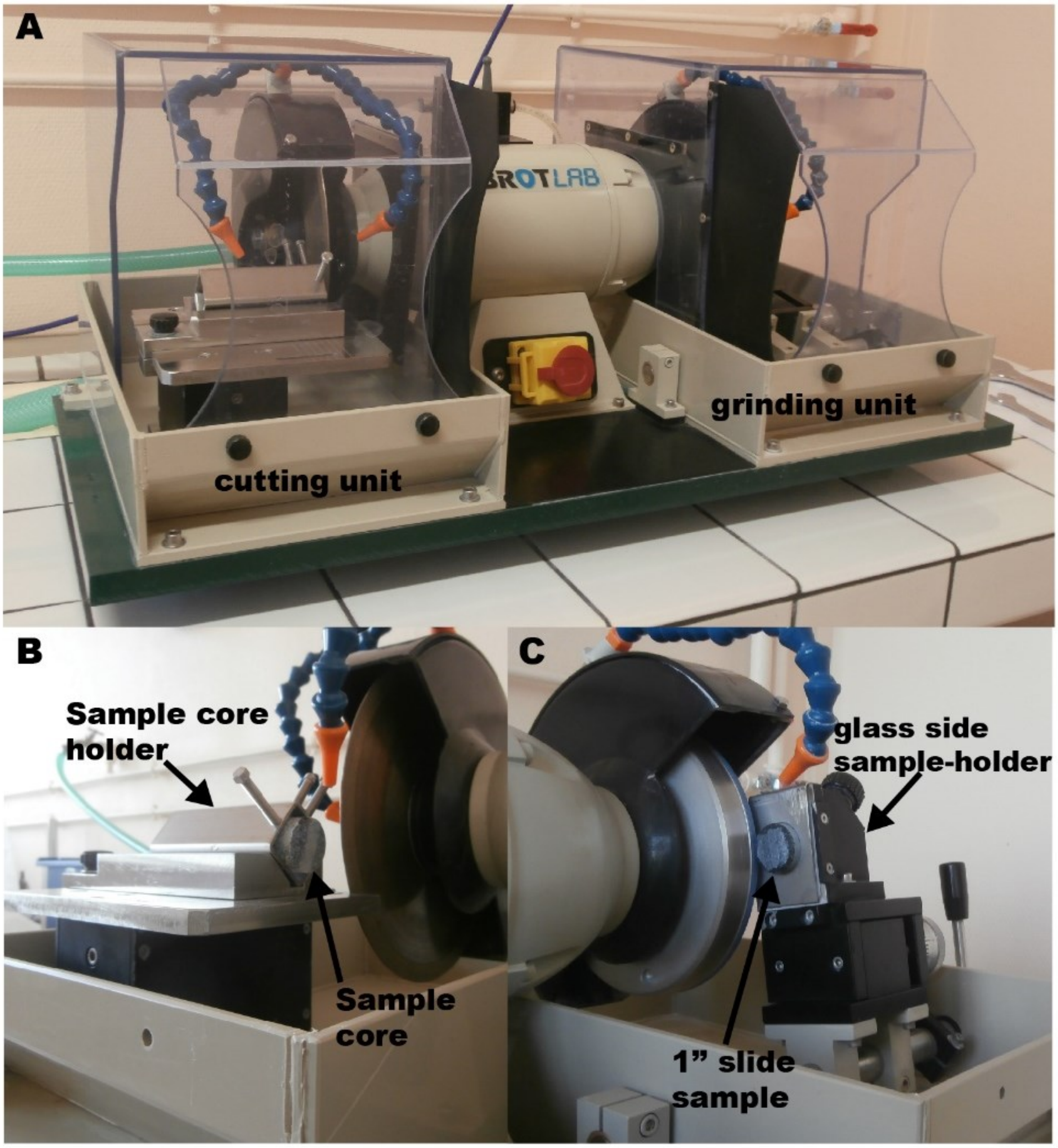

Fig 1.2. *(A) rock-cutting and grinding machine. (B) Cutting unit and sample core set with sample core holder before the sawing step. (C) Grinding unit during the coarse grinding. The sample is maintain by water suction onto a vertical sample-holder mounted on an horizontal micrometric translation.*

Particles are removed from the freshly sawn slide by ultrasonic cleaning in deionized water on glass beads within a glass jar (Fig. 1.3A). The slide is rinsed 3 times with acetone, ethanol and dried with N_2 before storage. The slide is stored in glass jar sealed with aluminum foil (Fig 1.3A) on clean glass beads that facilitate sample handling with flat tips tweezers (Fig 1.3A). The glass jar and micro beads are cleaned following a sequential process: rinsed with deionized water, dried with N_2, rinsed 3 timed with ethanol and acetone.

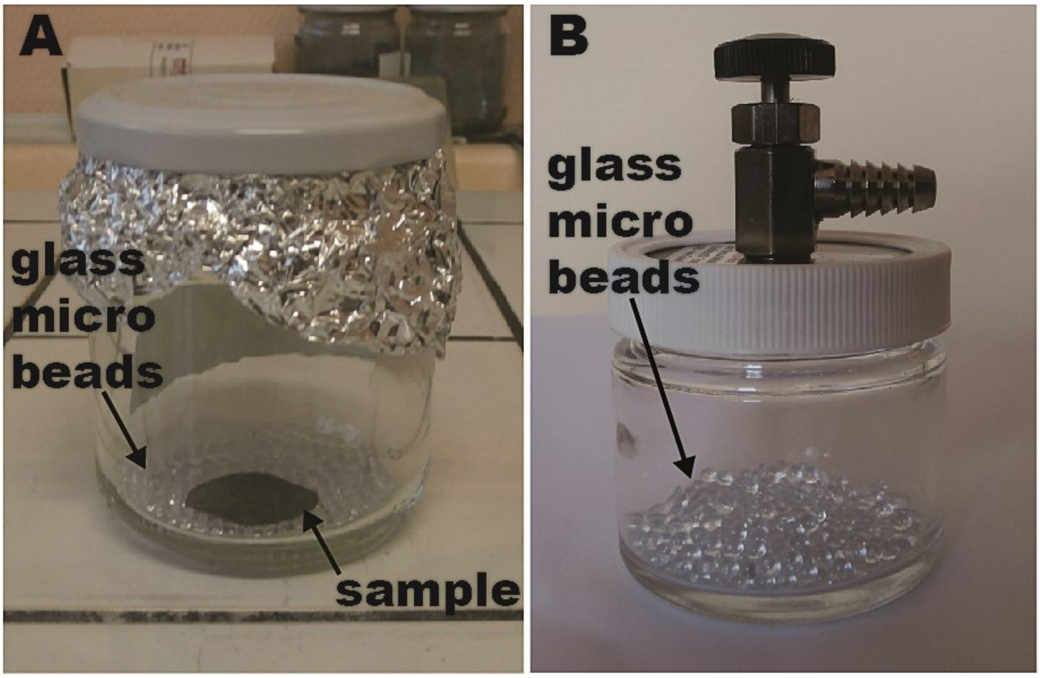

Fig 1.3. Sample storage. *(A) Samples stored in clean glass jar sealed with aluminum and clean glass beads at the bottom. (B) High-vacuum mini-desiccator with glass beads at the bottom.*

Next, the slide is ground to a thickness ranging between 2 and 1.75 mm using a coarse grinding unit (Fig 1.2 A,C). The surface of the slide to be placed opposite to the grinding disk is first manually lapped on one surface with SiC (500 or 600 mesh) on a glass plate, so that the slide is smooth enough to adhere on the suction sample holder (Fig 1.2C). The sample must be cleaned immediately with ultrasounds in deionized water to remove material dirt and SiC from sample pores or fractures. The sample is then gently ground by applying a low pressure on the sample holder, which is especially important with brittle samples. The surfaces must be kept parallel and the thickness of the slide controlled at each step with measuring set to prevent slopes. Flat edges are then made on the slide so that it fits in the special sample holder of the polishing machine (Fig. 1.4). Depending on the material, the grinding or the sawing unit can be used. The sawing unit is more precise, but generates vibrations that may break fragile samples.

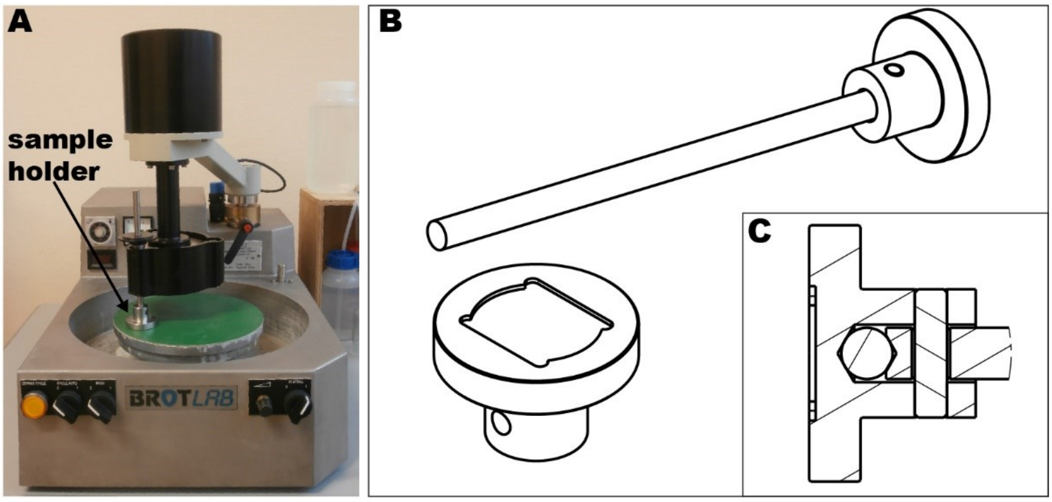

Fig 1.4. (A) Polishing machine with special sample holder. (B) Illustrative drawing of the special stainless steel sample holder designed for the preparation of a semi-thin section. The sample holder is composed of a stainless steel rod mounted on the holder with a mounting ball to reduce slope effect. Bottom left of (B): view of the sample holder. (C) Technical drawing of the sample holder showing the central mounting ball.

3.2.2 Fine grinding process

The fine grinding can be processed using a machine or manually. Fine grinding process is the most time-consuming and delicate step of the semi-thin section preparation because of the absence of embedding resin, which consolidates fragile samples during traditional thin section preparation.

Automated grinding is performed on a grinding/polishing machine using special sample holders (Figs. 1.4). The thickness of the slide is first reduced with diamond-impregnated grinding discs of 76-µm grain size and a 1 mm-deep sample holder (Figs 1.4C 1.5A,B). The slide is then ground with a 0.5 mm deep sample holder and a diamond-impregnated grinding disc of 36 µm grain size. The last grinding step is processed with a 0.3 mm deep sample holder with SiC powder (1000 mesh, i.e. 5 µm grain size) in distilled water continuously dripping (Fig. 1.5B) on a cast iron disc. During the automatic grinding process with the polishing machine, the sample must describe the trajectory drawn in Figure 1.5C. This unusual geometry is required to reduce thickness heterogeneities. Moreover, to obtain constant thickness, the diamond-impregnated discs (or the cast iron disc) must rotate at high speed (100, 200 rpm for chert sample). The maximal rotating speed (200 rpm) yielded less than 30 µm of thickness difference on a fractured Phanerozoic chert. The additional weight applied on the sample (Fig. 1.5B) during automatic grinding must also be reduced (0 - 250 g per sample) or removed to prevent thickness heterogeneities. At 200 rpm, without additional weight, 14 hours of grinding were required to remove 200 µm from a Phanerozoic chert.

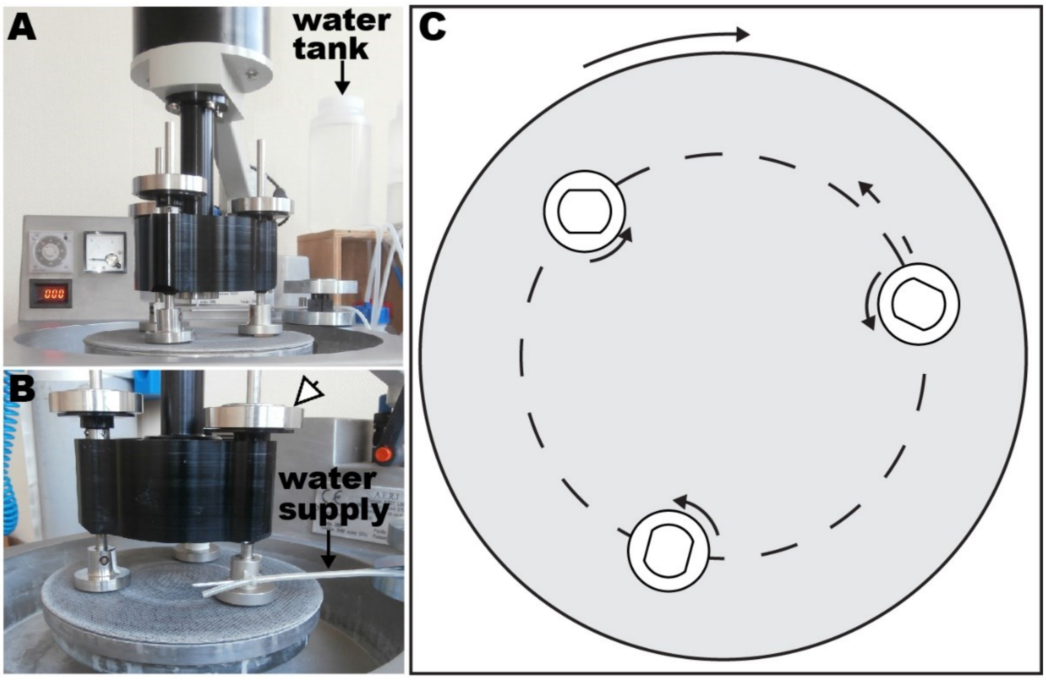

Fig 1.5. Fine grinding process. *(A) Polishing machine set for fine grinding. (B) Zoom on the polishing machine with diamond grinding disc, water supply and slides set in special sample holders. Additional weights (here 250 g, arrow) can be put above the sample holders. (C) Geometry of the polishing machine double rotation during the fine grinding process. In grey: the ginding (cast iron or diamond) disc plate, in white: sample holders and rock slides. The arrows indicate the rotation directions of the plate and sample holder. Dashed lines and arrows: rotation direction of the sample holders on the plate.*

Alternatively, the fine grinding steps can be performed manually. First, the slide is ground on the machine by holding the sample manually in contact with diamond discs rotating at 100-150 rpm. The 76-µm grain size diamond disc is first used to reach a thickness of 1.3–1 mm, then the 36-µm grain size diamond disc to reach a thickness of 1–0.7 mm. The final fine grinding down to a thickness of 0.5–0.3 mm is performed by manually rotating the slide along a “8” shape on a glass plate with 600 and 1000 mesh SiC. This alternative manual grinding has the disadvantage of increasing the risk of sample breaking up. However, it is faster than automated grinding, i.e. grinding a Precambrian chert with the machine can take more than 24 hours, while manual grinding may take less than 2 hours. In addition, manual grinding is the only option for slides that do not fit the special sample holder, e.g. when they broke along micro-fractures during sawing or initial grinding. A combination of automated and manual grinding can be used to accelerate the process. Automated grinding steps usually have the advantage of applying a homogenous load onto the sample, which is difficult to control with hands, thus preventing and removing thickness heterogeneities. Some samples with irregular dimensions and irregular hardness distributions can nevertheless form thickness heterogeneities during automated grinding. During each step of grinding, the thickness has thus to be controlled and thickness heterogeneities must be corrected by manually applying heterogeneous load onto the sample rotated with SiC (600 mesh) on glass plate. The sample is finally cleaned ultrasonically in deionised water, dried with N2, and rinsed 3 times with ethanol and acetone.

3.2.3 Polishing.

The polishing step is crucial for the quality of optical images and for surface microanalyses. Indeed, the thickness of sections is not the only parameter limiting the observations of microfossils. Surface imperfections disperse light and degrade the quality of images, which is important to fully describe microstructures (i.e. microfossils) in three dimensions. The absence of epoxy resin, which might turn yellow or become cloudy, also improves imaging (Ivarsson, 2006). However, the production of flat surfaces without scratches or furrows is difficult, especially with hard materials such as chert, because of the preservation of residual deep cutting scratches and surface damages created by hard waste particles from the surface (here micro or cryptocrystalline quartz) during the use of abrasive powders with “coarse” grain sizes (4 to 1µm) (Guenter and Scholz, 2015; Miyagi, 2017). The nature of the polishing clothes (felt cloth, woven cloth) influences the polishing results. For example, the felt cloth increases the polishing relief between hard and soft materials. On the opposite, woven clothes reduce relief but can increase surface furrows and deterioration of the edges of softer crystals (Guenter and Scholz, 2015). Thus, we combine woven and felt clothes with diamond and corundum water-based suspensions to reduce scratches and tears on rock surfaces. After the pre-polishing steps (final grinding steps with 1000 mesh SiC), the surface is polished with water-based corundum (4 µm) suspension on felt clothes for 1 to 2 hours. The semi-automatic polishing machine parameters are: 10 rpm rotation speed and 0 or 250 g additional loading on the sample holder(s). This polishing step removes the roughness produced by the final grinding (pre-polishing) from the surface (Fig 1.6B) and the flexibility of the felt cloth combined with corundum reduce the occurrence of furrows. Next, the surface is polished with diamond suspension (3 µm) on woven cloth for 30 min to 1 hour. At this step, the flatness is enhanced with the polishing of the surface with corundum suspension (2µm) on felt cloth. Finally, the small craters and scratches can be reduced with sequential polishing steps (10–15 minutes) with abrasion using 1 µm diamond suspension (1µm) on woven cloth alternated several times with 1 µm corundum on felt cloth. Between each polishing steps, semi-thin sections (and the special sample holders) are cleaned ultrasonically in deionized water and rinsed three times with ethanol and acetone.

This polishing procedure combining different polishing agents and cloths is unusual. The advantages are to reduce scratches and pits and to smooth contacts between materials of different roughness. Our tests on a ~2.1 Ga chert (Fig. 1.6A), which is representative of the samples that are most difficult to polish, show that the density of scratches and craters remaining after polishing using only diamond suspensions on woven clothes (Fig. 1.6C) is higher than the procedure presented above (Fig. 1.6D).

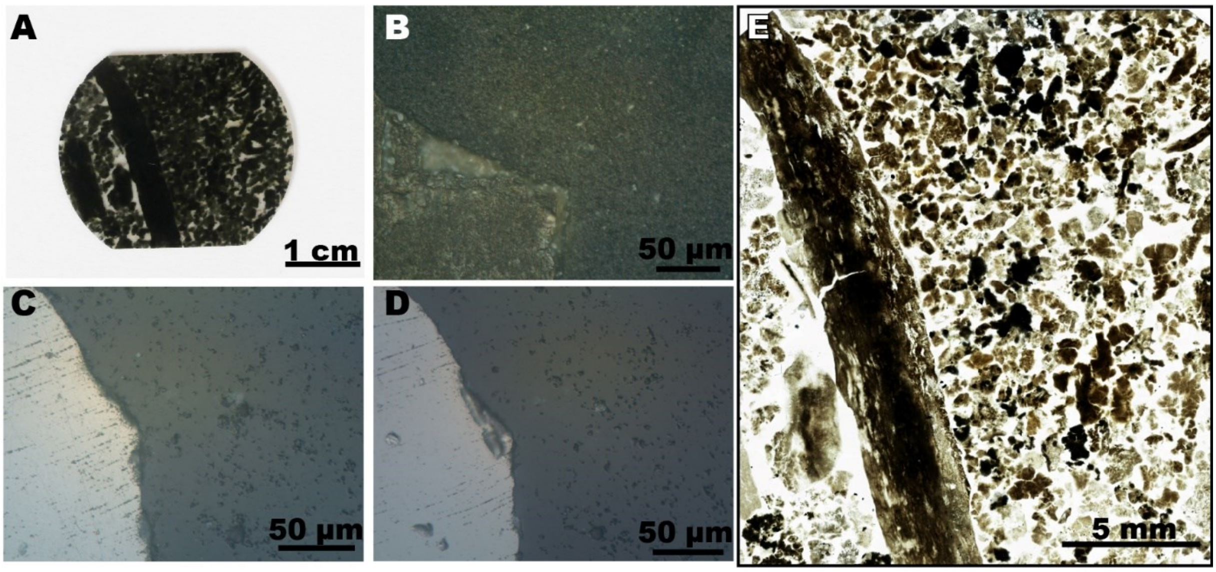

Fig. 1.6. Semi thin section of chert from the FC formation of the ca. 2.1 Ga Francevillian basin. *(A) General view of the semi-thin section. (B) Surface at the end of fine grinding and before polishing procedure. (reflected light). (C). Surface after diamond-only abrasion. The left part of the field of view shows a pyrite crystal (light grey) while the quartz appears as dark grey (reflected light). (D) Same surface abraded with diamond and corundum polishing agent displaying less/smaller scratches and craters. Note that no better surface state could be achieved with traditional petrographic thin section preparation. (E). General view of the semi-thin in transmitted light.*

Polished semi-thin sections are stored in cleaned jars sealed with aluminum. Before surface analysis (e.g. SIMS, ToF-SIMS), the sample can be rinsed 3 times in organic solvent (e.g. dichloromethane/methanol solution) to remove superficial soluble molecules. Finally, the semi-thin section is stored in a high vacuum mini-desiccator to drastically reduce the contamination of polished surfaces by dust particles or airborne molecules (Fig. 1.3B).

4 Characterization techniques.

Optical observations of semi-thin sections were carried out using Olympus BX60 and automated Nikon Ni-E microscopes (LOG, Université de Lille) under bright field transmitted and reflected lights. Mosaic images (image produced by the assemblage of hundreds of photomicrographs) were acquired using the automated Nikon Ni-E microscope. Scanning Transmitted Electron Microscopy (STEM) analyses were performed on FIB foils (prepared as detailed in Lepot et al., 2017) on a Philips CM30 (CCM, Université de Lille) operated at 300 kV. Bright and dark-field images were acquired in Scanning Transmitted Electron Microscopy (STEM) mode using axial annular detectors. Elemental distributions were mapped using Energy Dispersive X-ray Spectrometry (EDXS).

ToF SIMS analyses were performed on TOF.SIMS 5 instrument by ION-TOF GmbH, Germany (UCCS, Université de Lille) equipped with a Bi liquid metal ion gun (LMIG). The surface analyses were performed in bunched mode with Bi_3^+ beam operating at 25 keV and a low energy electron flood source (20 eV) for charge compensation. For the Orbagnoux sample, the sputtering was performed using low dose ion beams of either 0.25 keV Ar^+ beam on a 700 × 700 µm² area or 1 keV Cs^+ beam on a 800 × 800 µm² areas during respectively 21 and 10 minutes. For the Strelley Pool chert the sputtering was performed using low dose 0.25 keV Cs^+ beam on a 800 × 800 µm² area during 5 minutes. With the low dose Ar^+ beam, the sputtering profile was performed on a gold coated surface (~20 Å thick deposit), in non-interlaced mode (two Bi_3^+ raster analyses are follow by 1 second of sputtering and 1 second of waiting time to evacuate charge). Data were analyzed using SurfaceLab 6.2.

5 Results and discussion

5.1 Conventional thin section procedures

Conventional polished thin sections require samples to be embedded or impregnated with polymer resin. Dyes such as methylene blue can be used to track the penetration of the resin within samples at the microsale by optical microscopy (Oehler et al., 2009), but do not help locate nanoscale resin contaminations. Moreover, resins used to glue or embed sample have a low coefficient of viscosity and a long curation time (Guenter and Scholz, 2015) that make the penetration of resin in nano-porosity possible. Figure 1.7 illustrates such possible nano-contaminations within an organic microstructure in cherts of the ~3.4 Ga Strelley Pool

Formation (Lepot et al., 2013; Sugitani et al., 2010, 2013). Here, organic matter is embedded in microcrystalline quartz (Fig. 1.7 B-I). Two different types of organic matter could be distinguished based on texture and heterogenous chlorine concentrations (Fig 1.7D-F, G-I). The organic matter in direct contact with the micro-quartz crystals is generally chlorine-poor whereas the central parts of two organic zones are enriched in chlorine and display a central pore. The contacts between these two organic matter types display nanoscale porosity (white in bright field in Fig 1.7D and G). The presence of chlorine in epoxy resin is a common feature that affect its characteristics, including color, reactivity, and resistance to heat and moisture (Hamerton, 1996). Thus, the presence of chlorinated organic matter associated with nano-porosity within sub-micrometric organic microstructure demonstrates the nano-contamination of sample by resin within the organic microstructure. This contamination can occur below the surface of a thin section. Due to its small size and embedding within opaque Archean organic matter, this resin contamination is likely not detectable with Raman spectroscopy and imagery as in other samples (Wacey et al in press).

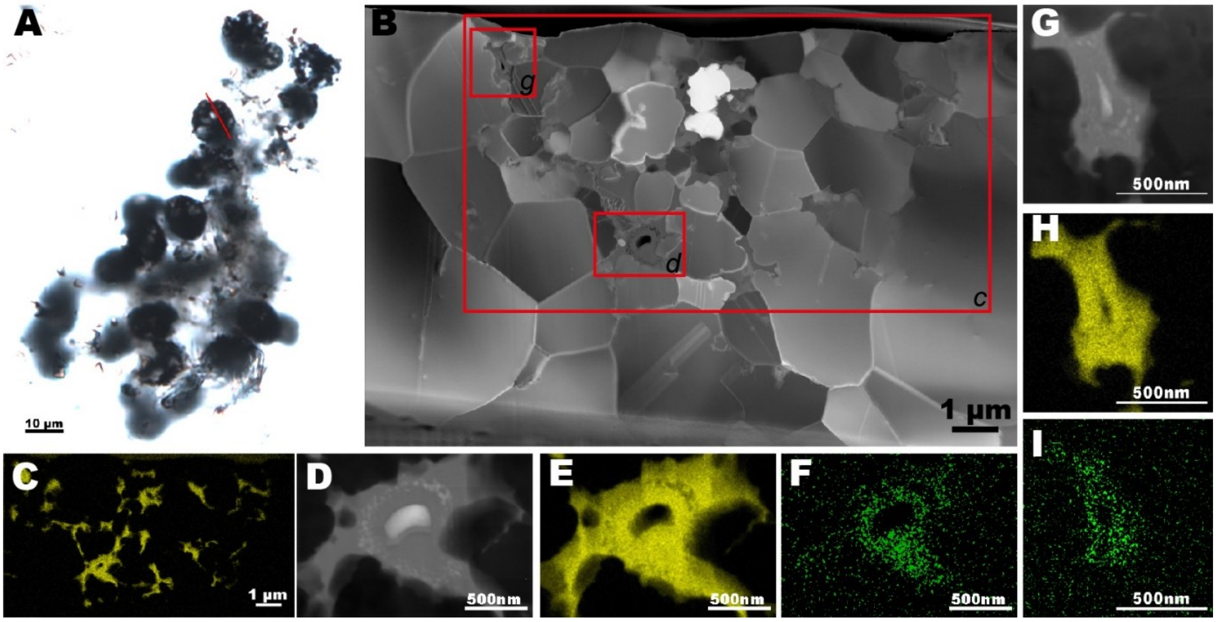

Fig 1.7. Clusters of spherical microstructures in a chert of the Strelley Pool Formation. *(A) Photomicrograph of the microstructures in transmitted light (red line: FIB foil position). (B) STEM dark field image of the FIB foil. (C) EDXS map of the carbon from the larger red box in (B). (D)-(F) STEM bright field image and EDXS maps of the lower box in (B) displaying organic matter (carbon, map in E) with heterogenous chlorine content (map in F). (G) STEM bright field image of the top boxed in (B) displaying similarly heterogenous organic matter as indicated by EDX maps of carbon (H) and chlorine (I).*

This example of organic contamination by epoxy resin is also problematic for the carbon isotope microanalyses with SIMS, elemental (N, C, O) analyses with NanoSIMS and molecular microanalyses with ToF-SIMS. Studied samples usually comprise polished thin sections or pieces of thin sections (or doubly polished section) mounted in epoxy. Thorough cleaning procedure (multiple sequential ultrasonication in deionized water, alcohol and various detergent) can remove most of surface contamination such as abraded and smeared epoxy particles (Lepot et al., 2013; Williford et al., 2013). However, possible epoxy contamination within nano- (Fig. 1.7) or micro-porosity (Wavey et al in press) may remain. We note that this example of resin contamination (Fig. 1.7) represented only ~10% of the organic matter in the FIB section (image analysis of EDXS maps) on was only observed in one out of more than 50 FIB sections we similarly analyzed with STEM (Fadel et al., 2017; Lekele Baghekema et al., 2017; Lepot et al., 2017, 2009, unpublished data). Therefore, we believe that the presence of nano-contaminations by epoxy have likely not affected published SIMS C-isotope data, but they may have decreased the spot-to-spot reproducibility, hence increasing the error bars. Such nano-contaminations are, however, much more problematic for techniques used to detect and quantify organic molecules with ppm-range sensitivity such as ToF-SIMS (Kollmer, 2004; Thiel and Sjovall, 2011).

5.2 Physical properties of resin-free semi-thin sections

Our semi-thin section preparation offers the possibility to observe and analyze carbonaceous microfossils hosted in minerals without the doubt of resin contamination. Micro-paleontological thin sections are usually ~30 to 200 µm thick. Thicker thin sections (150 - 200 µm) are commonly more suitable to locate abundant as wells as larger microfossil (Ivarsson, 2006). The thickness of this semi-thin sections can reduce the light in transmission and limit observation of fine microstructure. Microscopic images of a 330 µm thick semi-thin section of a black chert show the possibility to observe relatively opaque material in chert with our preparation (Fig 1.6A, E). Small mineral grain size is also another factor, which may limit the visibility of fine microstructures (i.e. microfossil). However, Figure 1.8 illustrates the possibility to observe microfossils in cryptocrystalline quartz from the ca. ~750 Ma Draken formation (Foucher and Westall, 2013; Knoll, 1982; Knoll et al., 1991) with a 500 µm thick semi-thin section. Optical microscopy is, however, best performed in the upper ~40 µm (depending on the mineral matrix), and blurred and darkened in the deeper parts of the section (e.g. Fig. 1.8C).

Our protocol yielded an excellent surface state for cryptocrystalline quartz with only sub-micrometric furrows, scratches or pits (Fig. 8B,D) similar to the best of standard petrographic sections. Semi-thin sections can also be polished on both side by hand to view more microfossil like standard (unglued) doubly-polished thin sections. Moreover, doubly-polished semi-thin section prepared with our protocol are less fragile than <200 µm-thick doubly-polished unglued sections (Ivarsson, 2006).

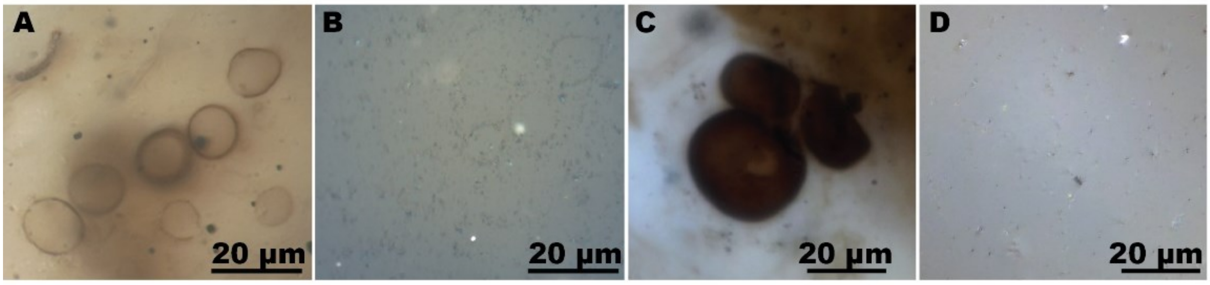

Fig 1.8. Microfossils in a semi-thin section of the ~750 Ma Draken Formation chert. *(A) Transmited light photomicrograph of Myxococcoide sp. at/near the surface of the semi thin section. (B) Photomicrograph of the surface of (A) in reflected light. (C) Transmited light photomicrograph of Myxococcoide sp. 50 µm below the surface of the sample. (D) Photomicrograph of the surface of (C) in reflected light.*

For SIMS analyses, the advantage of using semi-thin section is the absence of supplementary sample preparation. Thus, embedding sample with resin, supplementary localization and polishing of the sample mount are unnecessary. Semi-thin sections can be rinsed or ultrasonic cleaned with various organic solvents without the risk to break-up sample and altering the epoxy mount. The absence of resin is also an advantage for surface analysis in ultra-high vacuum instruments (i.e. SIMS). Upon introduction from the high-vacuum loadlack into the analytical chamber of the IMS1280 SIMS (at CRPG Nancy), without the use of N_2 cooling, our semi-thin section prepared with the above protocol reached a vacuum 10^{-9} torr range within minutes without the need of degassing the sample in high vacuum for long hours as usually done with epoxy-containing mounts (e.g. Lepot et al., 2013). A better vacuum limits the in-vacuum adsorption of volatile contaminants that could be detected with highly sensitive, extreme-surface techniques such as ToF-SIMS.

5.3 ToF-SIMS of semi-thin sections.

We studied semi-thin section prepared in a Kimmeridgian stromatolite and an Archean chert from the Strelley Pool Formation. The first sample is composed predominately of light-colored carbonate and dark laminae that comprise mostly highly immature organic matter with a high organic sulfur content (Mongenot et al., 1999, 1997). The second sample is a silicified conglomerate of the member 1, of the Strelley Pool formation, which contains some clasts composed of highly mature organic materiel (Allwood et al., 2007, 2006). For the Kimmeridgian stromatolite, we investigated the distribution of organic molecules at the surface of this semi-thin section with ToF-SIMS depth profiles during sputtering with low dose Ar^+ and Cs^+ beam. For Ar^+ sputtering the sample was gold coated (~20 Å thick deposit) to increase the signal of organics and reduced charge effect (Delcorte et al., 2003; Heile et al., 2008; Keune and Boon, 2004). We also investigated the surface state of the organic clast contained the Archean chert during sputtering with low dose (0.25 keV) Cs^+ beam. Due to the high content of organic matter on the Orbagnoux samples and the polishing steps, the surface is expected to present a surface layer of smeared organic matter as well as possible airborne contaminants, which can be detected with molecular imaging as permitted by ToF SIMS (Heim et al., 2012; Palmquist et al., 2012; Thiel and Sjovall, 2015, 2011). Compared to the Orbagnoux sample, the Strelley Pool Formation chert contains low organic matter. Thus, the surface layer of smeared organic matter is thinner on the Archean chert than the Kimmeridgian sample. Moreover, this "smearing effect" of the organic matter by the polishing process was reduced by the ultrasonication and the final cleaning processes with dichloromethane/methanol solutions. The presence of airborne contamination is also reduced by the storage of sample in high-vacuum mini-desiccators (Illing et al., 2014). Poly(dimethylsiloxane) (PDMS), a common surface contamination molecule in ToF-SIMS analyses (Beynon et al., 1959; Fletcher and Vickerman, 2013; Fray et al., 2016; Oran et al., 2004; Toporski and Steele, 2004; Viornery et al., 2002; Yang et al., 2009), is absent from our surface analyses.

Here, the depth profiles and positive ion images of inorganic ions (Ca^+, Al^+, Si^+ and Au^+) display a dramatic increase during the first 200 seconds and reach a steady state signal after ~400 seconds of sputtering, for the Orbagnoux sample (Fig 1.9A). The distribution of these ions is consistent with SEM-EDXS analyses (not shown). Moreover, SEM images performed after the surface analyses with ToF-SIMS reveal that gold coating was removed during to the Ar^+ sputtering. We note that the total ion signal was nearly homogenously spread over the surface of the sample (Fig. 1.9B) and that it reached a distribution similar to metallic ions such as Ca^+ during longer sputtering. Similarly, the distribution of organic ions at the beginning of sputtering was much more homogenous (Fig. 1.10C) than toward then end of sputtering, when the laminated distribution of organic matter appeared with high contrast (Fig. 1.10D). The same observation is made with Cs^+ beam sputtering and negative ion imaging. The Figure 1.11 shows the distribution of small hydrocarbon fragment: C_2^-, C_2H^- before and after

Cs^+ sputtering. Here again, before the Cs^+ sputtering, the signal of both molecules was relatively uniform. After the Cs^+ sputtering, the distribution of the hydrocarbon fragment is correlated with the spatial distribution of the organic matter of the ancient microbial mats. We used a relative high energy 1keV Cs^+ ion beam during the sputtering because of the difficulties to remove the surface layer, which is composed mostly of smeared organic material and airborne contamination. The negative images obtained from the Archean chert before and after sputtering also show the remove of this surface layer with low energy and low dose Cs^+ beam. The Figure 1.12 shows the uniform distribution of small hydrocarbon fragments C_4^- and C_4H^- before the sputtering and the correlation of the negative ion distribution and the spatial distribution of the organic matter, after the Cs^+ sputtering. As mentioned above, the quantity of smearing organic material produced during the polishing of this chert was lower than the Orbagnoux sample due to the high maturity of the organic clasts and the relative low concentration of organic matter of this sample. Thus, the surface layer sputtered by the low dose Cs^+ ion beam must be mostly surface airborne contamination. Moreover, this explanation is coherent with the required use of high energy ion Cs^+ beam to sputter this surface layer from the Orbagnoux sample, while low energy Cs^+ beam was sufficient for the Archean chert.

During the Ar^+ sputtering, the signal of saturated fragments, $C_2H_5^+$ and $C_4H_7^+$ ions (characteristic of aliphatic hydrocarbons) decrease rapidly during the first 20 seconds of sputtering. In contrast, fragments with low H/C such as $C_7H_7^+$ and $C_{14}H_{10}^+$ (produced mostly by aromatic hydrocarbons: (Toporski and Steele, 2004) display a small signal increase during the first 20 s of sputtering that is likely due to the stability of the aromatic structure and the inherent difficulty to cleave aromatic (Toporski and Steele, 2004). Then, the signal of the aromatic ions decreases rapidly until it reaches a steady state after 800 s of sputtering (Fig 1.10B), that is when the positive ion images of the organic material became spatially coherent with the optical distribution of organic laminae from the ancient bacterial mat (Fig 1.10D).

From these analyses, we conclude that before sputtering, the distribution of the organics ions formed a homogenous layer on the surface that may have come from airborne contamination (Saga and Hattori, 1996) and/or smearing of material during polishing and/or cleaning. Estimation based on sputtering duration and sputter setting (ion energy, intensity, angle of incidence) indicates that the maximal thickness of this contamination layer was ~6 nm in the case of the Orbagnoux sample. Moreover, caution must be taken during analysis with the redeposition of hydrocarbon fragment onto a clean surface after sputtering within the chamber (Mogk and Mathez, 2000). We observed such phenomenon during the analyzes of quartz from a Draken chert, after the analyses of a deuterated anthracene standard (Anthracene D10, 188.14amu, deposited on a clean silica wafer). The spectra obtained after 5 min of Ar^+ sputtering (0.25keV, 800x800µm²) indicates that Anthracene D10 was present onto surface of the Draken chert (Supplementary Fig.1.1). This case illustrates the caution to take concerning the state of the chamber prior sputtering/analysis and the redeposition of organic materiel sputtered on clean surface. However, we removed the surface contamination with a second ion source dedicated to sputtering (Kurczy et al., 2010; Thiel and Sjovall, 2015). Thus, these ToF-SIMS analyses demonstrate the possibility to perform surface analyses with our semi-thin sections, free of preparation contaminants such as resin, after removing the nanometric surface layer of airborne contamination and/or smeared sample organics with low dose ion beam.

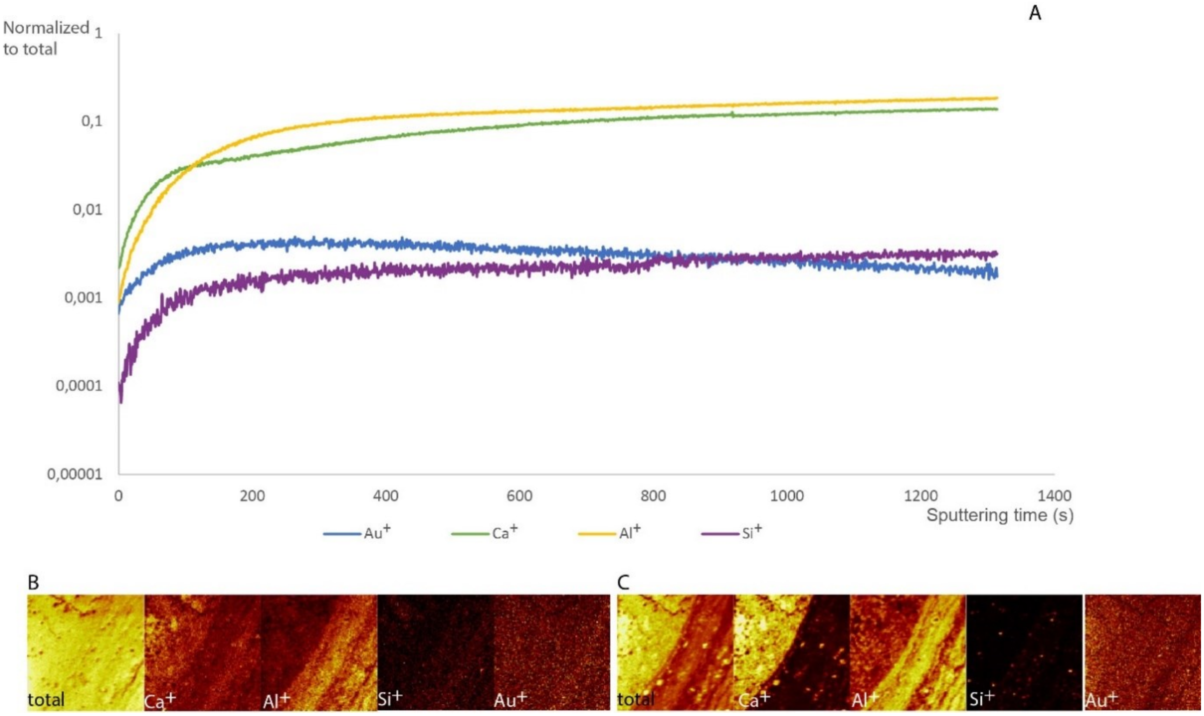

Fig. 1.9. *ToF-SIMS depth profiles (A) and maps (B) of inorganic ions (Ca^+, Al^+, Si^+ and Au^+) from the area sputtered by low dose Ar^+ beam. (A) Depths profiles showing that metallic ions increase dramatically during the initial ~200 seconds of sputtering before entering a quasi-steady state near ~400 seconds. (B) Positive ion images of total ion signal and inorganic ions from the area (500 × 500 µm²) at the beginning of the sputtering (between 0-200s). (C) Same area (500 × 500 µm²) at the end of the sputtering (between 800-1300 s).*

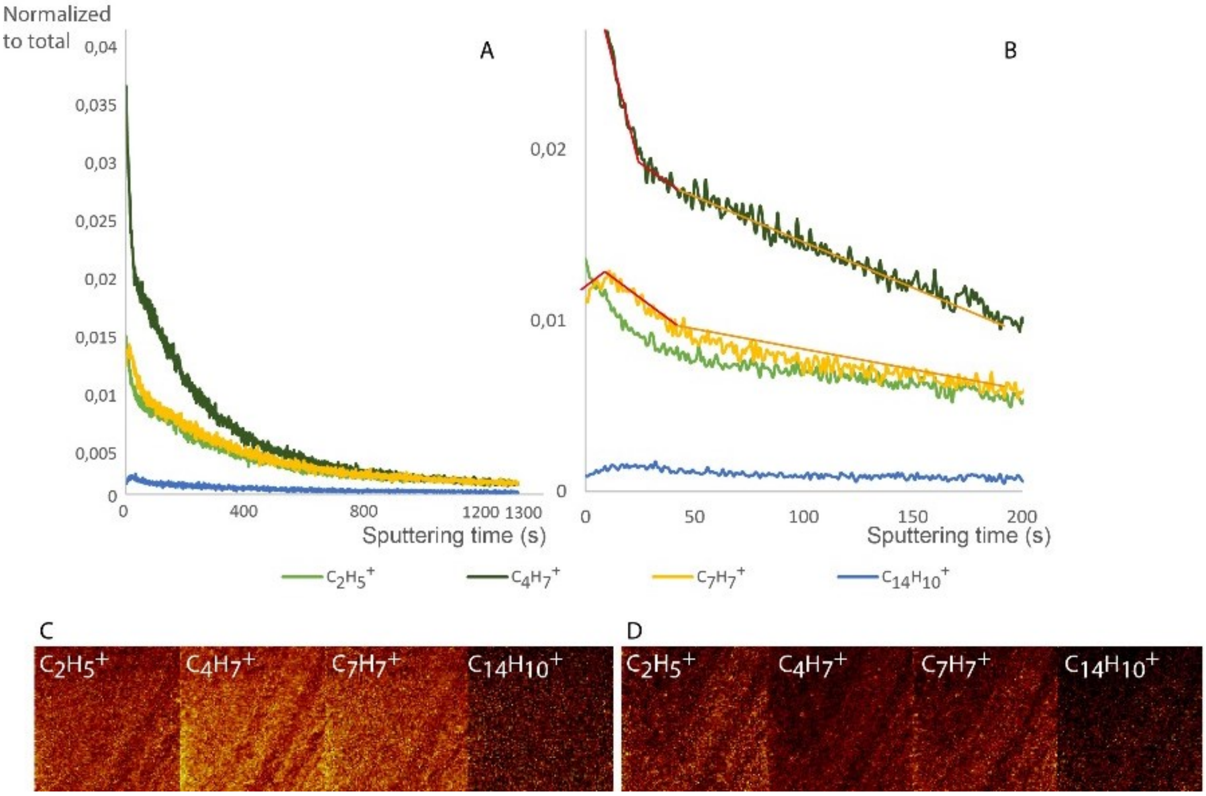

Fig. 1.10. *(A). ToF-SIMS depth profiles of organic ions ($C_2H_5^+$, $C_4H_7^+$, $C_7H_7^+$ and $C_{14}H_{10}^+$) from the area sputtered by low dose Ar^+ beam. (B) Zoom on the depth profiles showing the rapid signal decrease of the saturated ions ($C_2H_5^+$ and $C_4H_7^+$ions) at the beginning of the sputtering (0 to 50s). The signal of unsaturated fragments($C_7H_7^+$ and $C_{14}H_{10}^+$ ions), most likely produced by aromatics, show a small increase during the first cycles of sputtering (0 to10 s of sputter). The signals for aromatics decrease rapidly between 20-50 s. (C) Positive ion images of various hydrocarbon ions from the area (500 × 500 µm²) at the beginning of the sputtering (between 0-200 s). (D) Positive ion images of the same hydrocarbon fragments from the same aera (500 × 500 µm²) at the end of the sputtering (800-1300 s).*

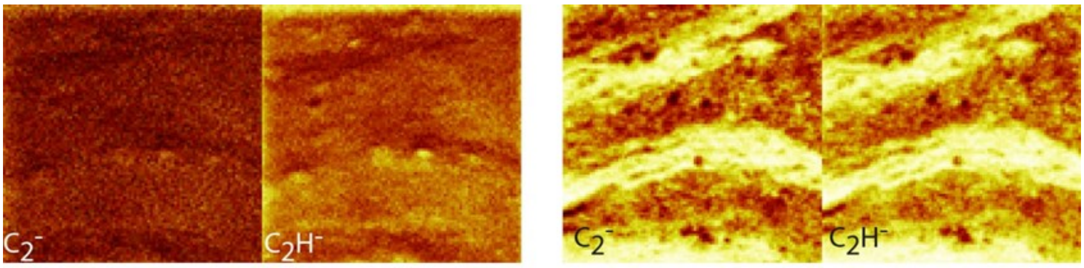

Fig. 1.11. *Bunched negatives ions images of C_2^- and C_2H^- ions from the same area (500 × 500 µm²) before (left) and after (right) Cs^+ sputtering (800 × 800 µm², 1 keV, 5 minutes).*

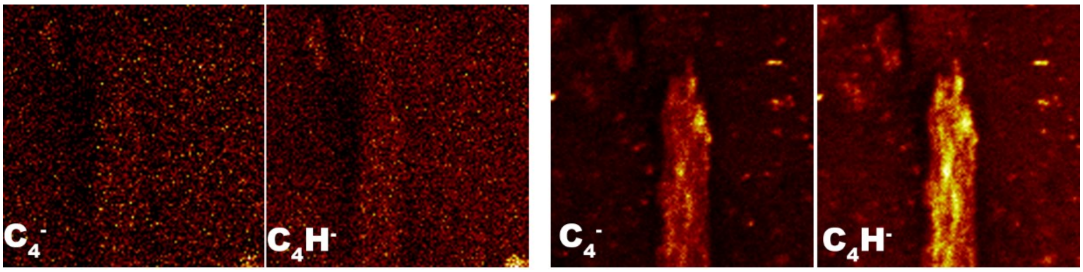

Fig. 1.12. *Bunched negatives ions images of* C_4^- *and* C_4H^- *ions from the same area (500 × 500* μm^2*) before (left) and after (right)* Cs^+ *sputtering (700 × 700* μm^2*, 0.25 keV, 5 minutes).*

Conclusions

Here, we show that epoxy resin can penetrate even nano-porosity in traditional petrographic thin sections. Distinguishing epoxy contamination from indigenous organic matter with techniques such as STEM, XANES, ToF-SIMS, Raman, FTIR, SIMS is difficult and time-consuming. We developed a novel protocol to prepare semi-thin sections of rock samples containing organic matter without resin. Semi-thin sections display enough mechanical strength to withstand multiple cleaning procedures, including the use of solvents such as dichloromethane/methanol solutions that extract soluble contaminants from laboratory, groundwater, or drilling fluids. However, these solvents also extract indigenous labile molecules such as biomarkers, hence this preparation procedure limits subsequent molecular (micro)analyses to the insoluble fraction of the organic matter (kerogen). With the exception of a nanometric surface contamination that can be removed with a low dose ion beam sputtering in ToF-SIMS, the surface of the semi-thin sections we produced appeared ultra clean. This new sample preparation offers the possibility to characterize organic matter at the top surface layer with highly sensible surface techniques such as ToF SIMS (Thiel and Sjovall, 2011). Using this technique, we were able to map the distribution of fragments of aliphatic and aromatic molecules in the kerogen at the micrometric scale in a Jurassic stromatolite. Semi-quantification and complete analysis of the ToF-SIMS mass spectra will be reported elsewhere. The semi-thin sections can be observed in transmitted white light provided the mineral matrix is relatively transparent, which is often the case for mono-mineral matrices such as cherts/quartzites. Altogether, this new sample preparation protocol opens avenues for *in situ* characterization of organic matter with high spatial resolution techniques. It should enable to correlate multiple characterization (e.g. ultrastructural, isotopic, spectroscopic, molecular) with optical microscopy on the same microfossil. This approach could help distinguish the taxonomy of problematic morphospecies. In particular, it may help unravelling the possible molecular preservation bias imparted to isotopic compositions (Williford et al. 2013; Lepot et al. 2013).

Acknowledgements

Abderrazak El Albani (U. Poitiers), Andrew H. Knoll (Harvard U.), Nicolas Tribovillard (U. Lille), and Kenichiro Sugitani (Nagoya U.) are thanked for providing the samples studied here. Sylvie Regnier (U. Lille) is thanked for help in developing the protocol. Jean-Jacques Raux and the company Brot Lab are thanked for making customized sample preparation machines. Alain Deparcy and Christophe Vermander (Ecole Centrale Lille) are thanked for making the sample holders. Funding was provided by ANR M6fossils ANR-15-CE31-0003-01, CNRS INSU-INTERRVIE program, and University of Lille (BQR program).

References

Abbott, G.D., Fletcher, I.W., Tardio, S., Hack, E., 2018. Exploring the geochemical distribution of organic carbon in early land plants: a novel approach. Philos. Trans. R. Soc. B Biol. Sci. 373, 20160499. https://doi.org/10.1098/rstb.2016.0499

Alleon, J., Bernard, S., Le Guillou, C., Marin-Carbonne, J., Pont, S., Beyssac, O., McKeegan, K.D., Robert, F., 2016. Molecular preservation of 1.88 Ga Gunflint organic microfossils as a function of temperature and mineralogy. Nat. Commun. 7, 11977. https://doi.org/10.1038/ncomms11977

Allwood, A.C., Walter, M.R., Burch, I.W., Kamber, B.S., 2007. 3.43 billion-year-old stromatolite reef from the Pilbara Craton of Western Australia: Ecosystem-scale insights to early life on Earth. Precambrian Res. 158, 198–227. https://doi.org/10.1016/j.precamres.2007.04.013

Allwood, A.C., Walter, M.R., Marshall, C.P., 2006. Raman spectroscopy reveals thermal palaeoenvironments of c.3.5 billion-year-old organic matter. Vib. Spectrosc. 41, 190–197. https://doi.org/10.1016/j.vibspec.2006.02.006

Arouri, K., Greenwood, P.F., Walter, M.R., 1999. A possible chlorophycean affinity of some Neoproterozoic acritarchs. Org. Geochem. 30, 1323–1337.

Barghoorn, E.S., Tyler, S.A., 1965. Microorganisms from the Gunflint chert. Science 147, 563–577. https://doi.org/10.1126/science.147.3658.563

Belu, A.M., Graham, D.J., Castner, D.G., 2003. Time-of-flight secondary ion mass spectrometry: techniques and applications for the characterization of biomaterial surfaces. Biomaterials 24, 3635–3653. https://doi.org/10.1016/S0142-9612(03)00159-5

Bernard, S., 2008. Préservation de fossiles organiques au cours de la diagenèse et du métamorphisme : études d'échantillons naturels et approche expérimentale. Paris 7.

Bernard, S., Benzerara, K., Beyssac, O., Menguy, N., Guyot, F., Brown, G.E., Goffe, B., 2007. Exceptional preservation of fossil plant spores in high-pressure metamorphic rocks. Earth Planet. Sci. Lett. 262, 257–272. https://doi.org/10.1016/j.epsl.2007.07.041

Beynon, J.H., Lester, G.R., Williams, A.E., 1959. Some Specific Molecular Rearrangements in the Mass Spectra of Organic Compounds. J. Phys. Chem. 63, 1861–1868. https://doi.org/10.1021/j150581a018

Beyssac, O., Goffe, B., Chopin, C., Rouzaud, J.N., 2002. Raman spectra of carbonaceous material in metasediments: a new geothermometer. J. Metamorph. Geol. 20, 859–871. https://doi.org/10.1046/j.1525-1314.2002.00408.x

Brasier, M., Green, O., Lindsay, J., Mcloughlin, N., Steele, A., Stoakes, C., 2005. Critical testing of Earth's oldest putative fossil assemblage from the ~3.5Ga Apex chert, Chinaman Creek, Western Australia. Precambrian Res. 140, 55–102. https://doi.org/10.1016/j.precamres.2005.06.008

Brasier, M.D., Antcliffe, J., Saunders, M., Wacey, D., 2015. Changing the picture of Earth's earliest fossils (3.5–1.9 Ga) with new approaches and new discoveries. Proc. Natl. Acad. Sci. 112, 4859–4864.

Buick, R., 1990. Microfossil Recognition in Archean Rocks: An Appraisal of Spheroids and Filaments from a 3500 M.Y. Old Chert-Barite Unit at North Pole, Western Australia. PALAIOS 5, 441–459. https://doi.org/10.2307/3514837

Butterfield, N.J., 2015a. Proterozoic photosynthesis - a critical review. Palaeontology 58, 953–972. https://doi.org/10.1111/pala.12211

Butterfield, N.J., 2015b. Early evolution of the Eukaryota. Palaeontology 58, 5–17. https://doi.org/10.1111/pala.12139

Delcorte, A., Bour, J., Aubriet, F., Muller, J.-F., Bertrand, P., 2003. Sample Metallization for Performance Improvement in Desorption/Ionization of Kilodalton Molecules: Quantitative Evaluation, Imaging Secondary Ion MS, and Laser Ablation. Anal. Chem. 75, 6875–6885. https://doi.org/10.1021/ac0302105

Fadel, A., Lepot, K., Busigny, V., Addad, A., Troadec, D., 2017. Iron mineralization and taphonomy of microfossils of the 2.45–2.21 Ga Turee Creek Group, Western Australia. Precambrian Res. 298, 530–551. https://doi.org/10.1016/j.precamres.2017.07.003

Fletcher, J.S., Vickerman, J.C., 2013. Secondary Ion Mass Spectrometry: Characterizing Complex Samples in Two and Three Dimensions. Anal. Chem. 85, 610–639. https://doi.org/10.1021/ac303088m

Foucher, F., Westall, F., 2013. Raman Imaging of Metastable Opal in Carbonaceous Microfossils of the 700-800Ma Old Draken Formation. Astrobiology 13, 57–67. https://doi.org/10.1089/ast.2012.0889

Fray, N., Bardyn, A., Cottin, H., Altwegg, K., Baklouti, D., Briois, C., Colangeli, L., Engrand, C., Fischer, H., Glasmachers, A., Grün, E., Haerendel, G., Henkel, H., Höfner, H., Hornung, K., Jessberger, E.K., Koch, A., Krüger, H., Langevin, Y., Lehto, H., Lehto, K., Le Roy, L., Merouane, S., Modica, P., Orthous-Daunay, F.-R., Paquette, J., Raulin, F., Rynö, J., Schulz, R., Silén, J., Siljeström, S., Steiger, W., Stenzel, O., Stephan, T., Thirkell, L., Thomas, R., Torkar, K., Varmuza, K., Wanczek, K.-P., Zaprudin, B., Kissel, J., Hilchenbach, M., 2016. High-molecular-weight organic matter in the particles of comet 67P/Churyumov–Gerasimenko. Nature 538, 72–74. https://doi.org/10.1038/nature19320

Gauthier-Lafaye, F., Weber, F., 2003. Natural nuclear fission reactors: time constraints for occurrence, and their relation to uranium and manganese deposits and to the evolution of the atmosphere. Precambrian Res. 120, 81–100.

Grey, K., 1999. A modified palynological preparation technique for the extraction of large Neoproterozoic acanthomorph acritarchs and other acid-soluble microfossils,Geological Survey of Western Australia. Dept. of Minerals and Energy, East Perth, W.A.

Guenter, G., Scholz, H., 2015. Preparation methods in Mineralogy & Geology: The Preparation of thin sections, polished sections, acetate foil prints, preparation for elutriation analysis, and staining tests for the optical and electron microscopy. https://doi.org/10.13140/rg.2.1.2593.9360

Hamerton, I., 1996. Recent Developments in Epoxy Resins. iSmithers Rapra Publishing.

Heile, A., Lipinsky, D., Wehbe, N., Delcorte, A., Bertrand, P., Felten, A., Houssiau, L., Pireaux, J.-J., De Mondt, R., Van Royen, P., Van Vaeck, L., Arlinghaus, H.F., 2008. Investigation of methods to enhance the secondary ion yields in TOF-SIMS of organic samples. Surf. Interface Anal. 40, 538–542. https://doi.org/10.1002/sia.2810

Heim, C., Lausmaa, J., Sjovall, P., Toporski, J., Dieing, T., Simon, K., Hansen, B.T., Kronz, A., Arp, G., Reitner, J., Thiel, V., 2012. Ancient microbial activity recorded in fracture fillings from granitic rocks (Aspo Hard Rock Laboratory, Sweden). Geobiology 10, 280–297. https://doi.org/10.1111/j.1472-4669.2012.00328.x

House, C.H., Schopf, J.W., McKeegan, K.D., Coath, C.D., Harrison, T.M., Stetter, K.O., 2000. Carbon isotopic composition of individual Precambrian microfossils. Geology 28, 707–710.

Igisu, M., Ueno, Y., Shimojima, M., Nakashima, S., Awramik, S.M., Ohta, H., Maruyama, S., 2009. Micro-FTIR spectroscopic signatures of Bacterial lipids in Proterozoic microfossils. Precambrian Res. 173, 19–26. https://doi.org/10.1016/j.precamres.2009.03.006

Illing, C.J., Hallmann, C., Miller, K.E., Summons, R.E., Strauss, H., 2014. Airborne hydrocarbon contamination from laboratory atmospheres. Org. Geochem. 76, 26–38. https://doi.org/10.1016/j.orggeochem.2014.07.006

Ivarsson, M., 2006. Advantages of doubly polished thin sections for the study of microfossils in volcanic rock. Geochem. Trans. 7, 5.

Javaux, E., 2011. Early eukaryotes in Precambrian oceans, in: Martin, H., Gargaud, M., López-Garcìa, P. (Eds.), Origins and Evolution of Life: An Astrobiological Perspective, Cambridge Astrobiology. Cambridge University Press, Cambridge, pp. 414–449. https://doi.org/10.1017/CBO9780511933875.028

Javaux, E.J., Knoll, A.H., Walter, M.R., 2004. TEM evidence for eukaryotic diversity in mid-Proterozoic oceans. Geobiology 2, 121–132. https://doi.org/10.1111/j.1472-4677.2004.00027.x

Javaux, E.J., Lepot, K., 2018. The Paleoproterozoic fossil record: Implications for the evolution of the biosphere during Earth’s middle-age. Earth-Sci. Rev. 176, 68–86. https://doi.org/10.1016/j.earscirev.2017.10.001

Javaux, E.J., Marshal, C.P., 2006. A new approach in deciphering early protist paleobiology and evolution: Combined microscopy and microchemistry of single Proterozoic acritarchs. Rev. Palaeobot. Palynol. 139, 1–15. https://doi.org/10.1016/j.revpalbo.2006.01.005

Kaufman, A.J., Xiao, S., 2003. High CO2 levels in the Proterozoic atmosphere estimated from analyses of individual microfossils. Nature 425, 279–282. https://doi.org/10.1038/nature01902

Kempe, A., Wirth, R., Altermann, W., Stark, R.W., Schopf, J.W., Heckl, W.A., 2005. Focussed ion beam preparation and in situ nanoscopic study of Precambrian acritarchs. Precambrian Res. 140, 36–54. https://doi.org/10.1016/j.precamres.2005.07.002

Keune, K., Boon, J.J., 2004. Enhancement of the static SIMS secondary ion yields of lipid moieties by ultrathin gold coating of aged oil paint surfaces. Surf. Interface Anal. 36, 1620–1628. https://doi.org/10.1002/sia.1996

Kita, N.T., Ushikubo, T., Fu, B., Valley, J.W., 2009. High precision SIMS oxygen isotope analysis and the effect of sample topography. Chem. Geol. 264, 43–57. https://doi.org/10.1016/j.chemgeo.2009.02.012

Knoll, A.., Javaux, E.., Hewitt, D., Cohen, P., 2006. Eukaryotic organisms in Proterozoic oceans. Philos. Trans. R. Soc. B Biol. Sci. 361, 1023–1038. https://doi.org/10.1098/rstb.2006.1843

Knoll, A.H., 2003. The geological consequences of evolution. Geobiology 1, 3–14. https://doi.org/10.1046/j.1472-4669.2003.00002.x

Knoll, A.H., 1982. Microorganisms from the late Precambrian Draken Conglomerate, Ny Friesland, Spitsbergen. J. Paleontol. 56, 755–790.

Knoll, A.H., Bergmann, K.D., Strauss, J.V., 2016. Life: the first two billion years. Philos. Trans. R. Soc. B Biol. Sci. 371, 20150493. https://doi.org/10.1098/rstb.2015.0493

Knoll, A.H., Sweet, K., Mark, J., 1991. Paleobiology of a Neoproterozoic tidal flat/lagoonal complex: the Draken Conglomerate Formation, Spitsbergen. J. Paleontol. 65, 531–570.

Kollmer, F., 2004. Cluster primary ion bombardment of organic materials. Appl. Surf. Sci. 231–232, 153–158. https://doi.org/10.1016/j.apsusc.2004.03.101

Kouketsu, Y., Mizukami, T., Mori, H., Endo, S., Aoya, M., Hara, H., Nakamura, D., Wallis, S., 2014. A new approach to develop the Raman carbonaceous material geothermometer for low-grade metamorphism using peak width. Isl. Arc 23, 33–50.

Kurczy, M.E., Piehowsky, P.D., Willingham, D., Molyneaux, K.A., Heien, M.L., Winograd, N., Ewing, A.G., 2010. Nanotome Cluster Bombardment to Recover Spatial Chemistry After Preparation of Biological Samples for SIMS Imaging. J. Am. Soc. Mass Spectrom. 21, 833–836. https://doi.org/10.1016/j.jasms.2010.01.014

Lekele Baghekema, S.G., 2017. Etudes multi-proxies et multi-scalaires des roches siliceuses (cherts) du bassin de franceville (2,1ga): origine et processus de formation (PhD Thesis). Université de Poitiers.

Lekele Baghekema, S.G., Lepot, K., Riboulleau, A., Fadel, A., Trentesaux, A., El Albani, A., 2017. Nanoscale analysis of preservation of ca. 2.1 Ga old Francevillian microfossils, Gabon. Precambrian Res. 301, 1–18. https://doi.org/10.1016/j.precamres.2017.08.024

Lemelle, L., Labrot, P., Salome, M., Simionovici, A., Viso, M., Westall, F., 2008. In situ imaging of organic sulfur in 700-800 My-old Neoproterozoic microfossils using X-ray spectromicroscopy at the SK-edge. Org. Geochem. 39, 188–202. https://doi.org/10.1016/j.orggeochem.2007.10.008

Lepot, K., Addad, A., Knoll, A.H., Wang, J., Troadec, D., Beche, A., Javaux, E.J., 2017. Iron minerals within specific microfossil morphospecies of the 1.88 Ga Gunflint Formation. Nat. Commun. 8, 14890. https://doi.org/10.1038/ncomms14890

Lepot, K., Benzerara, K., Rividi, N., Cotte, M., Brown, G.E., Philippot, P., 2009. Organic matter heterogeneities in 2.72 Ga stromatolites: Alteration versus preservation by sulfur incorporation. Geochim. Cosmochim. Acta 73, 6579–6599. https://doi.org/10.1016/j.gca.2009.08.014

Lepot, K., Williford, K.H., Ushikubo, T., Sugitani, K., Mimura, K., Spicuzza, M.J., Valley, J.W., 2013. Texture-specific isotopic compositions in 3.4 Gyr old organic matter support selective preservation in cell-like structures. Geochim. Cosmochim. Acta 112, 66–86. https://doi.org/10.1016/j.gca.2013.03.004

Lindgren, J., Kuriyama, T., Madsen, H., Sjövall, P., Zheng, W., Uvdal, P., Engdahl, A., Moyer, A.E., Gren, J.A., Kamezaki, N., Ueno, S., Schweitzer, M.H., 2017. Biochemistry and adaptive colouration of an exceptionally preserved juvenile fossil sea turtle. Sci. Rep. 7. https://doi.org/10.1038/s41598-017-13187-5

Lindgren, J., Uvdal, P., Sjovall, P., Nilsson, D.E., Engdahl, A., Schultz, B.P., Thiel, V., 2012. Molecular preservation of the pigment melanin in fossil melanosomes. Nat. Commun. 3, 824. https://doi.org/10.1038/ncomms1819

Marshall, C., Javaux, E., Knoll, A., Walter, M., 2005. Combined micro-Fourier transform infrared (FTIR) spectroscopy and micro-Raman spectroscopy of Proterozoic acritarchs: A new approach to Palaeobiology. Precambrian Res. 138, 208–224. https://doi.org/10.1016/j.precamres.2005.05.006

Miyagi, I., 2017. A grooved glass surface-plate for making a flat polished surface. Earth Planets Space 69. https://doi.org/10.1186/s40623-016-0587-x

Moczydłowska, M., Willman, S., 2009. Ultrastructure of cell walls in ancient microfossils as a proxy to their biological affinities. Precambrian Res. 173, 27–38. https://doi.org/10.1016/j.precamres.2009.02.006

Mogk, D.W., Mathez, E.A., 2000. Carbonaceous films in midcrustal rocks from the KTB borehole, Germany, as characterized by time-of-flight secondary ion mass spectrometry. Geochem. Geophys. Geosystems 1.

Mongenot, T., Boussafir, M., Derenne, S., Lallier-Verges, E., Largeau, C., Tribovillard, N., 1997. Sulphur-rich organic matter from bituminous laminites of Orbagnoux (France, Upper Kimmeridgian). The role of early vulcanization. Bull. Soc. Geol. Fr. 168, 331–341.

Mongenot, T., Derenne, S., Largeau, C., Tribovillard, N., Lallier-Vergès, E., Dessort, D., Connan, J., 1999. Spectroscopic, kinetic and pyrolytic studies of kerogen from the dark parallel laminae facies of the sulphur-rich Orbagnoux deposit (Upper Kimmeridgian, Jura). Org. Geochem. 30, 39–56.

Moreau, J.W., Sharp, T.G., 2004. A transmission electron microscopy study of silica and kerogen biosignatures in-1.9 Ga gunflint microfossils. Astrobiology 4, 196–210. https://doi.org/10.1089/153110704323175142

Oehler, D.Z., Robert, F., Mostefaoui, S., Meibom, A., Selo, M., McKay, D.S., 2006. Chemical mapping of Proterozoic organic matter at submicron spatial resolution. Astrobiology 6, 838–850.

Oehler, D.Z., Robert, F., Walter, M.R., Sugitani, K., Allwood, A., Meibom, A., Mostefaoui, S., Selo, M., Thomen, A., Gibson, E.K., 2009. NanoSIMS: Insights to biogenicity and syngeneity of Archaean carbonaceous structures. Precambrian Res. 173, 70–78. https://doi.org/10.1016/j.precamres.2009.01.001

Oran, U., Ünveren, E., Wirth, T., Unger, W.E.., 2004. Poly-dimethyl-siloxane (PDMS) contamination of polystyrene (PS) oligomers samples: a comparison of time-of-flight static secondary ion mass spectrometry (TOF-SSIMS) and X-ray photoelectron spectroscopy (XPS) results. Appl. Surf. Sci. 227, 318–324. https://doi.org/10.1016/j.apsusc.2003.12.008

Palmquist, A., Emanuelsson, L., Sjovall, P., 2012. Chemical and structural analysis of the bone-implant interface by TOF-SIMS, SEM, FIB and TEM: Experimental study in animal. Appl. Surf. Sci. 258, 6485–6494. https://doi.org/10.1016/j.apsusc.2012.03.065

Saga, K., Hattori, T., 1996. Identification and removal of trace organic contamination on silicon wafers stared in plastic boxes. J. Electrochem. Soc. 143, 3279–3284.

Schiffbauer, J.D., Xiao, S., 2009. Novel application of focused ion beam electron microscopy (FIB-EM) in preparation and analysis of microfossil ultrastructures: A new view of complexity in early Eukaryotic organisms. PALAIOS 24, 616–626. https://doi.org/10.2110/palo.2009.p09-003r

Schopf, J.W., Kudryavtsev, A.B., Agresti, D.G., Czaja, A.D., Wdowiak, T.J., 2005. Raman imagery: A new approach to assess the geochemical maturity and biogenicity of permineralized Precambrian fossils. Astrobiology 5, 333–371. https://doi.org/10.1089/ast.2005.5.333

Schopf, J.W., Tripathi, A.B., Kudryavtsev, A.B., 2006. Three-dimensional confocal optical imagery of Precambrian microscopic organisms. Astrobiology 6, 1–16.

Sergeev, V.N., 2009. The distribution of microfossil assemblages in Proterozoic rocks. Precambrian Res. 173, 212–222. https://doi.org/10.1016/j.precamres.2009.04.002

Shi, K., Tao, X., Hong, F., He, H., Ji, Y., Li, J., 2012. Mechanism of oxidation of low rank coal by nitric acid. J. Coal Sci. Eng. China 18, 396–399. https://doi.org/10.1007/s12404-012-0411-6

Strother, P.K., Battison, L., Brasier, M.D., Wellman, C.H., 2011. Earth's earliest non-marine eukaryotes. Nature 473, 505–509. https://doi.org/10.1038/nature09943

Sugitani, K., Lepot, K., Nagaoka, T., Mimura, K., Van Kranendonk, M., Oehler, D.Z., Walter, M.R., 2010. Biogenicity of Morphologically Diverse Carbonaceous Microstructures from the *ca.* 3400 Ma Strelley Pool Formation, in the Pilbara Craton, Western Australia. Astrobiology 10, 899–920. https://doi.org/10.1089/ast.2010.0513

Sugitani, K., Mimura, K., Nagaoka, T., Lepot, K., Takeuchi, M., 2013. Microfossil assemblage from the 3400 Ma Strelley Pool Formation in the Pilbara Craton, Western Australia: Results form a new locality. Precambrian Res. 226, 59–74. https://doi.org/10.1016/j.precamres.2012.11.005

Sugitani, K., Mimura, K., Takeuchi, M., Lepot, K., Ito, S., Javaux, E.J., 2015. Early evolution of large micro-organisms with cytological complexity revealed by microanalyses of 3.4 Ga organic-walled microfossils. Geobiology 13, 507–521. http://dx. doi.org/10.1111/gbi.12148

Sutton, M.D., Rahman, I.A., Garwood, R.J., 2014. Techniques for virtual palaeontology, New analytical methods in earth and environmental science. Wiley Blackwell, Hoboken, NJ ; Chichester, West Sussex.

Thiel, V., Sjovall, P., 2015. Time-of-Flight Secondary Ion Mass Spectrometry (TOF-SIMS): Principles and Practice in the Biogeosciences, in: Principles and Practice of Analytical Techniques in Geosciences. The Royal Society of Chemistry, pp. 122–170. https://doi.org/10.1039/9781782625025-00122

Thiel, V., Sjovall, P., 2011. Using Time-of-Flight Secondary Ion Mass Spectrometry to Study Biomarkers, in: Jeanloz, R., Freeman, K.H. (Eds.), Annual Review of Earth and Planetary Sciences, Vol 39. Annual Reviews, Palo Alto, pp. 125–156.

Toporski, J., Steele, A., 2004. Characterization of purified biomarker compounds using time of flight-secondary ion mass spectrometry (ToF-SIMS). Org. Geochem. 35, 793–811. https://doi.org/10.1016/j.orggeochem.2004.03.006

Tribovillard, N., Trentesaux, A., Trichet, J., Défarge, C., 2000. A Jurassic counterpart for modern kopara of the Pacific atolls:: lagoonal, organic matter-rich, laminated carbonate of Orbagnoux (Jura Mountains, France). Palaeogeogr. Palaeoclimatol. Palaeoecol. 156, 277–288.

Vandenbroucke, T.R.A., Emsbo, P., Munnecke, A., Nuns, N., Duponchel, L., Lepot, K., Quijada, M., Paris, F., Servais, T., Kiessling, W., 2015. Metal-induced malformations in early Palaeozoic plankton are harbingers of mass extinction. Nat. Commun. 6, 7966. https://doi.org/10.1038/ncomms8966

Viornery, C., Chevolot, Y., Léonard, D., Aronsson, B.-O., Péchy, P., Mathieu, H.J., Descouts, P., Grätzel, M., 2002. Surface Modification of Titanium with Phosphonic Acid To Improve Bone Bonding: Characterization by XPS and ToF-SIMS. Langmuir 18, 2582–2589. https://doi.org/10.1021/la010908i

Wacey, D., Battison, L., Garwood, R.J., Hickman-Lewis, K., Brasier, M.D., 2016. Advanced analytical techniques for studying the morphology and chemistry of Proterozoic microfossils. Geol. Soc. Lond. Spec. Publ. 448, 81–104. https://doi.org/10.1144/SP448.4

Wacey, D., Menon, S., Green, L., Gerstmann, D., Kong, C., Mcloughlin, N., Saunders, M., Brasier, M., 2012. Taphonomy of very ancient microfossils from the similar to 3400 Ma Strelley Pool Formation and similar to 1900 Ma Gunflint Formation: New insights using a focused ion beam. Precambrian Res. 220, 234–250. https://doi.org/10.1016/j.precamres.2012.08.005

Williford, K.H., Ushikubo, T., Schopf, J.W., Lepot, K., Kitajima, K., Valley, J.W., 2013. Preservation and detection of microstructural and taxonomic correlations in the carbon isotopic compositions of individual Precambrian microfossils. Geochim. Cosmochim. Acta 104, 165–182. https://doi.org/10.1016/j.gca.2012.11.005

Yang, L., Shirahata, N., Saini, G., Zhang, F., Pei, L., Asplund, M.C., Kurth, D.G., Ariga, K., Sautter, K., Nakanishi, T., Smentkowski, V., Linford, M.R., 2009. Effect of Surface Free Energy on PDMS Transfer in Microcontact Printing and Its Application to ToF-SIMS to Probe Surface Energies. Langmuir 25, 5674–5683. https://doi.org/10.1021/la804272n

Supplementary figure

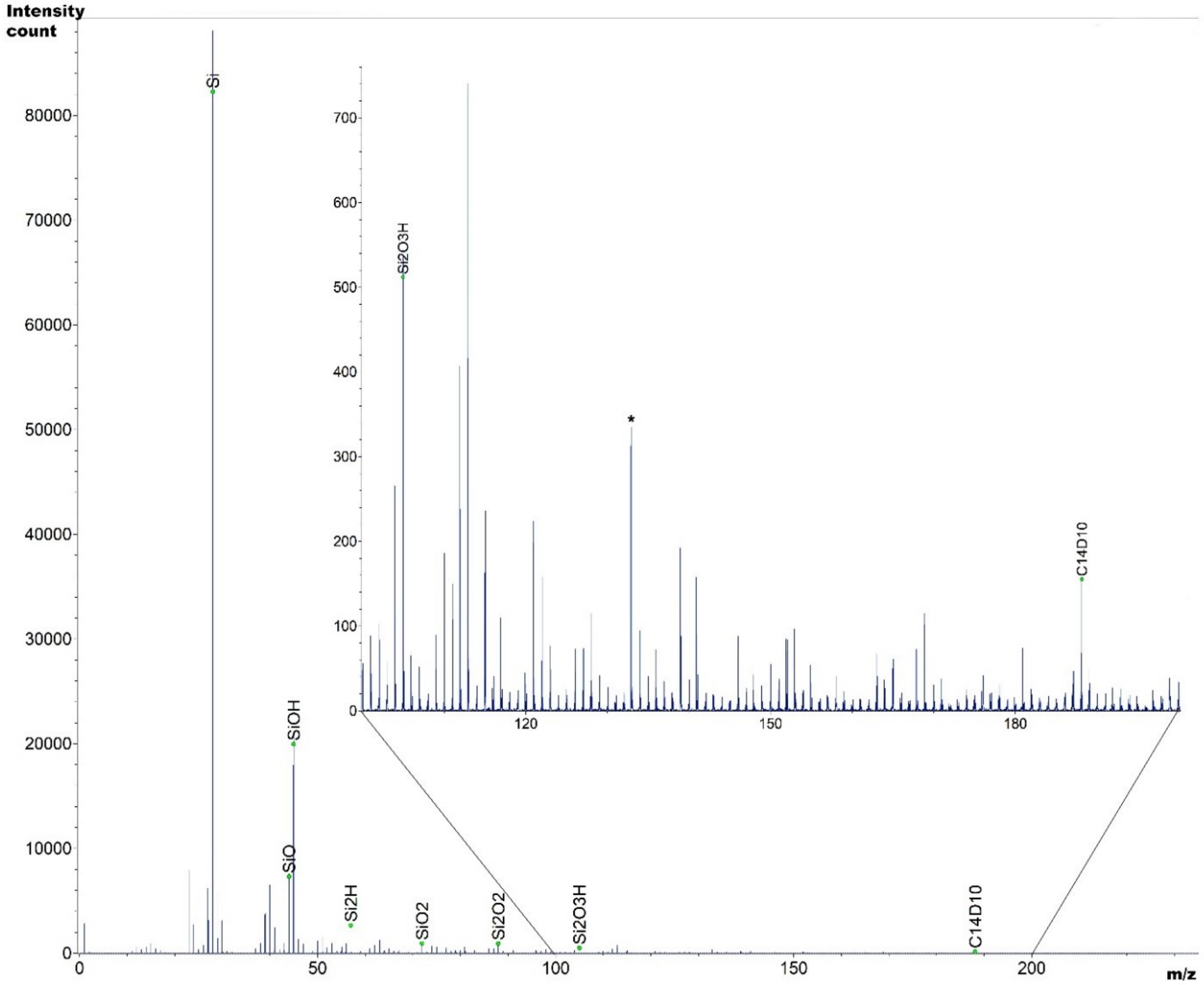

Supplementary Fig. 1.1. *Positive ToF SIMS spectra of Draken chert in bunched mode, after Ar^+ sputtering (5 minutes, 0.25keV, 800x800µm²). The spectra is dominated by Si^+ peak generated by the quartz. The other majoritary peaks correspond to ions generated by the quartz (e.g. SiO^+, SiH^+, SiO_2^+, $Si_2O_2^+$,…). At high mass, the spectra show a peak of high intensity at 188.13 amu corresponding to the molecule $C_{14}D_{10}$. (*: Cs+ peaks due to the presence of Cesium in the chamber).*

Chapitre II

Caractérisation moléculaire à la ToF SIMS d'anciens tapis microbiens à la micro échelle

ToF-SIMS molecular characterization of ancient microbial mats at the microscale

Alexandre Fadel[1], Kevin Lepot[1], Nicolas Nuns[2], Nicolas Tribovillard[1], Pascal Philippot[3], Yvain Carpentier[4], Cristian Focsa[4], Armelle Riboulleau[1]

[1] Laboratoire d'Océanologie et de Géosciences, Université de Lille, CNRS, Université Littoral Côté d'Opale, UMR8187, Cité Scientifique SN5, 59655 Villeneuve d'Ascq, France.

[2] Univ. Lille, CNRS, INRA, Centrale Lille, ENSCL, Univ. Artois, FR 2638 - IMEC - Institut Michel-Eugène Chevreul, F-59000 Lille, France

[3] Institut Physique du Globe, CNRS UMR7154, Sorbonne Paris Cité, Université Paris Diderot, 75238 Paris, France.

[4] Laboratoire de Physique des Lasers, Atomes et Molécules (UMR CNRS 8523), Université de Lille 1 Sciences et Technologies, 59655, Villeneuve d'Ascq, France

Abstract

Microscale molecular heterogeneities are important for deciphering the biogenic or abiogenic origin of ancient and/or mature organic matter. Kerogen (insoluble macromolecular organic matter, assumed to be syngenetic with the host rock) is generally analyzed with bulk rock techniques that cannot elucidate these heterogeneities. Here, we present mass spectra and molecular imaging of semi-thin sections of rocks using Time-of-Flight Secondary Ion Mass Spectroscopy (ToF-SIMS). First, we documented low-mass fragmentation patterns of a saturated molecule (2-nonadecanone) and a Polycyclic Aromatic Hydrocarbon (PAH, phenanthrene) in positive and negative ion modes, after low energy monoatomic Ar^+ sputtering. Those patterns are used to propose a suite of semi-quantitative indexes that could help decipher the macromolecular structure of unknown kerogen. Second, using the same machine settings, we analyzed thermally immature OM-rich laminae of Kimmeridgian stromatolites (French Jura Mountains, Orbagnoux village) and laminated OM-rich grains of the 3.4 Ga Strelley Pool Formation (Western Australia). Molecular imaging and mass spectra indicated a sulfurized kerogen rich in aliphatic carbon associated with PAH and possibly small single-aromatic groups in the Orbagnoux laminae. Veins cutting across carbonates are relatively enriched in aliphatic carbon and likely represent indigenous bitumen. Based on various ratio of low mass positive and negative fragments, we show a relatively higher content in aromatic structures in the Strelley Pool OM compared to Orbagnoux OM, and shorter alkyl chains in the former compared to the latter. Moreover, aromatic isomers of relatively high mass (up to m/z=202) were detected and imaged in the Strelley Pool OM laminae. Altogether, these results show that ToF-SIMS is greatly promising for the microscale study of the composition of insoluble fossil organic matter in addition to the soluble molecules traditionally analyzed in biological fresh and fossil materials using this technique.

1 Introduction

The molecular composition of living and fossil organic matter is heterogeneous down to the nanometer scale. Diverse (micro)organisms / (micro)fossils can have drastically different molecular compositions (Marshall et al., 2005; Steemans et al., 2010). Molecular heterogeneities can be preserved even in metamorphic rocks (Bernard et al., 2007; Lepot et al., 2009). Investigating the molecular signature of organic matter with spatially-resolved techniques can help address the origin of fossil OM at the scale of its individual components.

Early life investigations include the characterization of OM in microfossils, soluble biomarkers and fossil microbial mats forming stromatolites. Precambrian microfossils are scarce compared to the Phanerozoic fossil record and are dominated by microscopic prokaryotes and eukaryotes. Due to their simple cellular shape, their nature has often been difficult to address (see for review: Javaux and Lepot, 2018; Knoll, 2003; Knoll et al., 2016; Wacey et al., 2016) and the microfossil nature of the earliest (Archean) putative occurrences remains uncertain (example of Brasier et al., 2005; Schopf, 2006). Biomarker hydrocarbons in Precambrian rocks have been used to constrain the presence and metabolism (cyanobacteria/eukaryote) of Archean organisms (Brocks et al., 1999, 2003; Eigenbrode et al., 2008). However, the syngenicity of these molecules remains controversial and studies suggest that biomarkers previously detected in Precambrian rocks can be contaminants (Brocks et al., 2008, 2017; French et al., 2015; Rasmussen et al., 2008). Stromatolites (laminated sedimentary structure of probable microbial origin) have been cited as providing some of the earliest evidence for life on Earth track back to almost 3.5 Ga. (Allwood et al., 2006a; Noffke et al., 2013; Riding, 2000; Walter et al., 1980), and possibly as far back as 3.7 Ga (Nutman et al., 2016). Morphological studies were extensively used to constrain the biogenicity of these stromatolites (Allwood et al., 2009; Batchelor et al., 2004; Bosak et al., 2009; Buick et al., 1981; Grotzinger and Rothman, 1996; Lowe, 1994; Noffke et al., 2006). While the laminated rock macrostructure of stromatolites has been debated as an indicator of biological origin (Grotzinger and Knoll, 1999; Jettestuen et al., 2006), the correlation of organic laminae / microstructures with laminated mineral structures has been used to infer fossil microbial mats and argue for the biogenicity of the oldest stromatolites (Allwood et al., 2009; Lepot et al., 2008; Wacey et al., 2010). Similarly, modern stromatolites were also extensively studied with multiple analytical methods to identify the bacterial species present and propose models of stromatolite formation that help interpret Precambrian stromatolites (Awramik and Riding, 1988; Bontognali et al., 2008; Decho et al., 2005; Paerl et al., 2001; Papineau et al., 2005; Vasconcelos et al., 2006).

Fossil organic matter comprise soluble organic molecules (bitumen) that can be extracted using solvents, and insoluble macromolecular OM (kerogen) that form during diagenesis from the condensation and polymerization of biopolymers and/or labile organic molecules (Vandenbroucke and Largeau, 2007). Resolving the macromolecular structure of kerogen is often based on chemical or thermal degradations (Vandenbroucke and Largeau, 2007). These approaches, however, do not allow identify a potential heterogeneity of compounds within the kerogen. Functional groups present within the kerogen can be constrained at the microscale by Fourier Transform InfraRed Spectroscopy (FTIR), at the nanoscale using X-ray Absorption Near Edge Structure (XANES) (Bernard et al., 2010;

Bernard and Horsfield, 2014) and elemental analysis of the kerogen can also be performed with Nanoscale Secondary Ion Mass spectrometry (Oehler et al., 2009; Wacey et al., 2010) to constrain the nature and the distribution of kerogen within sample. Time of Flight Secondary Ion Mass Spectroscopy (ToF-SIMS) offers the possibility to perform mass spectrometric detection at micrometric spatial resolution (Benninghoven, 1994) with only minimal destruction (nanometer-depth sputtering: Brison et al., 2010; Mine et al., 2007). This method has been used for chemical surface analysis especially for semiconductor and polymer characterization (Belu et al., 2003; Vickerman and Briggs, 2013). The recent developments of the method for organic analysis of modern biological materials have been intense and challenging (Heim et al., 2012; Kollmer, 2004; Palmquist et al., 2012; Passarelli and Winograd, 2011; Siljeström et al., 2017; Sjövall et al., 2006; Thiel et al., 2014, 2007b; Thompson et al., 2006; Touboul et al., 2005; Tuccitto et al., 2011). Similar developments were made in cosmochemistry (Fray et al., 2016; Stephan, 2001; Stephan et al., 2003), combustion processes (Irimiea et al., 2015; Popovicheva et al., 2017) culture heritage (Keune et al., 2005; Keune and Boon, 2004; Mazel and Richardin, 2009) and forensic science (Brewer et al., 2008; Mahoney et al., 2006; Szynkowska et al., 2009). ToF-SIMS was also used in geo(bio)logical studies, on minerals (Mathez and Mogk, 1998; Mogk and Mathez, 2000), organic matter in various macrofossils (Greenwalt et al., 2013; Lindgren et al., 2012, 2014, 2017; Thiel and Sjovall, 2011), biofilms in coprolites (Toporski et al., 2002), and recent microbial mats (Thiel et al., 2007b, 2007a), microbial streamers (Siljeström et al., 2017) and oil-bearing fluid inclusions (Siljestrom et al., 2009, 2010, 2013).

Here, we characterized kerogen in ancient fossil microbial mats at the microscale from semi-thin section of sedimentary rocks with ToF-SIMS using Bi_3^+ for analysis and monoatomic Ar^+ for sputtering. Two rocks were analyzed: thermally immature, OM-rich laminae in Kimmeridgian stromatolites (French Jura Mountains, Orbagnoux village) and laminated OM-rich grains in cherts of the 3.4 Ga Strelley Pool Formation (Pilbara, Western Australia). To constrain molecular information obtained in positive and negative ion modes from the rocks with ToF-SIMS, standards (phenanthrene, anthracene-D_{10} and 2-nonadecanone) were also analyzed with the same setting. Here, we document the fragmentation pattern of the standards, constrain and image the OM in rocks, find micro-heterogeneities in OM and semi-quantify the aliphatic and aromatic character in the different kerogen.

2 Geological setting

2.1 Orbagnoux deposit

The Orbagnoux sample comes from the “Calcaires en plaquettes” Formation of Orbagnoux, Platy Limestone Formation, (French Jura Mountains, Kimmerdgian, Jurassic) (Bernier, 1984; Mongenot et al., 1997, 1999; Sarret et al., 2002; Tribovillard et al., 1999, 2000, 2004, 1992). This Platy Limestone Formation overlies the “Calcaires de Tablacon” Formation (Early Kimmeridgian), characterized by a relative drop in sea-level. Hence, massive limestone beds forming the base of the “Calcaires de Tablacon” Formation contain planktonic organisms (globigerinid foraminifera and radiolaria). These pelagic organisms are progressively replaced by neritic organisms (gastropods, bivalves, sponges and rare calcareous algae). During the Upper Kimmerdgian, the regressive sequence that affected the carbonate platform of the southern Jura led to the development of a reef barrier with a shallow lagoon in which bituminous laminites, corresponding to the lower part of Platy Limestone Formation, were deposited. The bituminous laminites from the Orbagnoux Jurassic carbonate platform were studied extensively (Mongenot et al., 1999, 1997; Tribovillard et al., 2000; Van Kaam-Peters et al., 1998; Van Kaam-Peters and Sinninghe Damsté, 1997). This laminated member mainly comprises Ca-carbonate and OM. The carbonate content varies between 75% and 96% wt%. The organic content varies between dark laminae (Total Organic Content, TOC = 4.47%–8.55 wt%) and light ones (TOC= 0.65–8.03 wt%; Mongenot et al., 2000). The kerogen is highly immature with bulk (unheated) kerogen H/C atomic ratio of 1.30 to 1.46 (Mongenot et al., 2000; Tribovillard et al., 2000). Moreover, the organic sulfur of the kerogen is abundant (representing 12-18% of the kerogen; Mongenot et al 2000). This member is divided into two subfacies: parallel laminated beds and undulating lamina beds. These laminated beds were interpreted as accumulation of coccolithophorids (lighter lamina) alternating with the accumulation of planktonic algae (darker lamina) in the presence of cyanobacterial biofilm(Pacton et al., 2006; Tribovillard et al., 1992). The sample studied here comes from the second subfacies. These are also composed of light and dark laminae, which are grossly parallel to the bedding. The light-colored laminae contain peloids, which are interpreted as being cyanobacterial in origin and indicate that the undulating lamina were the results of self-burial processes. Based on the presence of planktonic and benthonic organisms, these subfacies were the result of interaction between coccolithophorids and cyanobacteria biofilms. Cyanobacteria formed biofilms in the two subfacies and acted as barrier between the oxic water column and the underlying sediment characterized by anoxic pore water (Tribovillard et al., 2000, 1992). Due to the abundant organic content, the reducing conditions and the absence of iron, sulphate reduction was favored and sulphide reacted with OM. This early natural vulcanization of the organic matter played a major role in OM preservation (Mongenot et al., 1997).

2.2 Strelley Pool Chert

The Archean sample comes from the ca. 3.43 Ga Strelley Pool Formation localized in the Panorama Greenstone Belt (Trendall Locality, Western Australia). The age of Strelley Pool chert is constrained by zircons from felsic rocks from the underlying Panorama formation (3.456-3.426Ga) and the overlying Euro basalt (3.346-–3.426Ga) (DiMarco and Lowe, 1989; Van Kranendonk et al., 2002). The Strelley Pool Formation includes laminated dolomitic stromatolites at the studied locality (member 2 of Allwood et al., 2007, 2006a, 2006b) as well as silicified stromatolites with finely laminated OM at other localities (Sugitani et al., 2015b, 2010). This member 2 was intensively studied as a putative trace of early Archean life thriving in an isolated, partially restricted, peritidal marine carbonate platform. The studied sample comes from post-platform facies (member 4 of Allwood et al., 2007) overlying the member containing stromatolites, and includes siliciclastic and volcanoclastic material of silt/sand size that have been silicified and cemented by chert. This member 4 was marked by the end of peritidal isolated carbonate platform and the development of a subsiding basin with siliciclastic sediment influx and deposition of hydrothermal/marine cherts (Allwood et al., 2007). Though stromatolites are absent in this facies, this member contains allochthonous material including organic matter clasts, which are possible remains of microbial mats of films formed in the water column or in other environments nearby (Allwood et al., 2006b, 2007). Atomic H/C ratio of 0.02–0.46 were recorded in cherts of members 3-4 at the studied locality (Marshall et al., 2007). OM in stromatolites of member 2 (Bontognali et al., 2012) and in microfossiliferous cherts from another locality (Sugitani et al., 2015a) displays organic sulfur with atomic S/C of up to ~1% (as roughly estimated with EDXS: Sugitani et al., 2015a).

3 Methods

3.1 Sample preparation

The geological sample were prepared following the semi-thin section procedure detailed in (Fadel et al., in prep – chapter 2 of this thesis). In brief, pieces of rocks were drilled with a 1” core bit, sawed, ground and polished to semi-thin sections 400 to 500 µm in thickness. This protocol does not require the use of resin to glue the sample onto a glass slide at any step of the preparation process. Sawing, grinding and polishing were done on ethanol-cleaned instruments without use of lubricant and that have never been contaminated by epoxy-bearing samples.

Several times during the preparation procedure and after preparation, the semi thin sections were cleaned ultrasonically in ethanol during 2 minutes, rinsed three times sequentially with ethanol/acetone and stored in similarly-cleaned glass jars sealed with aluminum foil. Before ToF-SIMS analyses the samples were cleaned in a dichloromethane/methanol solution (2/1 volume and HPLC grade solvents). Due to the fragility and the high content of immature organic matter of the Orbagnoux semi-thin section, this sample was cleaned one time in the dichloromethane/methanol solution for 2 hours and the surface was cleaned three times with dichloromethane. The SPF semi-thin section was cleaned sequentially three times during 24 hours in dichloromethane/methanol solution. After cleaning, the samples were stored in a glass vacuum desiccator capped with Teflon. The SPF semi-thin section and part of the Orbagnoux semi-thin section were gold coated (~20 Å thick deposit). The gold-coated samples were immediately stored in the vacuum desiccator.

The standards [phenanthrene $C_{14}H_{10}$, anthracene-D_{10} $C_{14}D_{10}$ (98.0%, Dr Ehrenstorfer GmbH), and 2-nonadecanone $CH_3(CH_2)_{16}COCH_3$ (≥97.0%, Aldrich) see appendix to see the structure of the molecule] were prepared under laminar flow hood. The standard powders were first dissolved in dichloromethane (HPLC grade) and the obtained solutions were stored in clean glass vials with Teflon septa. A single drop of each substance was pipetted on to a cleaned silicon wafer using a cleaned glass pipette. The standard samples were then stored in clean glass jar sealed with aluminum before surface analyses.

All the instrument or substrates in contact with the samples (standards, semi-thin sections) were cleaned 3 times sequentially with ethanol, acetone and HPLC grade dichloromethane.

3.2 Optical microscopy

Optical petrography and localization of the region of interest on the semi-thin sections were carried out using an Olympus BX60 microscope (LOG, Université de Lille) under bright-field transmitted light and reflected light. Coordinates of organic microstructures located at the surface of the semi-thin sections were referenced to carry out Scanning Electron Microscopy (SEM) and Time of Flight Secondary Ion Mass Spectrometry (ToF-SIMS) observations on the same structures.

3.3 Scanning electron microscopy

SEM images were recorded after ToF-SIMS on gold coated (~20 Å thick deposit) semi-thin sections using a Quanta 200 SEM (LOG, Université de Lille) operated at 15-20 kV and at a working distance of 10 mm. Images were recorded in back-scattered electron (BSE) mode and Energy Dispersive X-ray Spectroscopy (EDXS) maps were acquired using a QuanTax QX2 (ROENTEC) detector.

3.4 ToF-SIMS

The surface analyses were carried out using a TOF.SIMS 5 instrument (ION-TOF GmbH, Germany) at surface analysis platform, Université de Lille. This instrument is equipped with a Bi liquid metal ion gun (LMIG). Pulsed (≈ 1ns) Bi_3^+ primary ions were used for analyses (25 keV) and low energy Ar^+ ions (0.25keV) for sputtering with an incidence angle of 45° for both beams. The primary currents measured in the Faraday cup were 0.3 pA for Bi_3^+ ions and 14 nA for Ar^+ ions beam. Raster for sputtering was 700 × 700 µm² during 5 minutes for standards and geological samples. The primary ion dose density (PIDD) calculated with the software showed that the static limit was reached after 1 minutes of sputtering (PIDD of 10^{13} ions/mm²) while the ion dose with the Bi_3^+ ions was below the static limit ($<10^{13}$ ions/mm²). Calculations from this experimental condition give an estimated sputter rate of $0.01 nm.s^{-1}$ for Au with monoatomic Ar^+ ions beam. Secondary ions spectra for the standard molecules were acquired in bunched mode for both polarities from an area of 500 × 500 µm² centered in the argon crater, in a raster pattern of 128 × 128 pixels. Acquisition on the geological samples were conducted with the same sputtering settings but analyzed area, centered in the argon crater, were acquired in various size areas (from 130×130µm² to 500×500µm² with raster patterns from 128×128 pixels to 256×256 pixels), in positive and negative bunched mode. To reduce charge effect build up on the sample surface, a pulsed electron flood gun was used for all analyses. In some cases, to reduce re-deposition of organic contamination from the ToF-SIMS chamber, non-interlaced mode was used with 1 second of sputtering after 10 scans of Bi_3^+ scan and 3s of pause time after each Ar^+ bombardment for charge compensation.

Mass spectra and intensity images were extracted using the SurfaceLab 6.2 software. Calculation on spectra extracted from reconstructed Region of interest (ROI) were performed with mMass 5.5.0 software (Open Source Mass Spectrometry Tool). Mass calibration was achieved using the system reference masses at m/z 12 C^+, 14.01 CH_2^+, 15.02 CH_3^+, 27.02 $C_2H_3^+$, 29.04 $C_2H_5^+$, 41.04 $C_3H_5^+$ in positive mode and 12 C^-, 13.01 CH^-, 14.01 CH_2^-, 15.02 CH_3^-, 15.99 O^-, 17.00 OH^-, 24 C_2^- in negative mode. The mass resolution m/Δm at m/z 40 is ranging from 4500 to 6000 in positive and negative mode.

4 Results

4.1 Pure molecule standards

A 2-Nonadecanone standard (a ketone organic molecule with a long aliphatic chain of carbon: $CH_3(CH_2)_{16}COCH_3$, calculated mass= 282.29u) was analyzed to understand the pattern of fragmentation of aliphatic/saturated molecules, after Ar^+ sputtering. Phenanthrene ($C_{14}H_{10}$, calculated mass = 178.08u) and anthracene-D10 ($C_{14}D_{10}$, calculated mass= 188,14) were analyzed to derive fragmentation patterns of PAH using the same setup.

4.1.1 Sputtering effect.

Ratio based on ion intensity permits to characterize the chemistry of sample with ToF-SIMS. Such ratio were used by Petrat et al., (1994) to investigate the surface chemistry of polystyrene modified by plasma treatment. They found that the integrity of the aromatic/aliphatic system could be monitored by using the intensity ratio of the hydrocarbon fragments at m/z 91 ($C_7H_7^+$) and m/z 55 ($C_4H_7^+$). They consider that the $C_7H_7^+$ and $C_4H_7^+$ fragments can be taken as key fragments for the aromatic and aliphatic systems, respectively. The decrease of the $C_4H_7^+/C_7H_7^+$ ratio values correlate with the time duration of plasma treatment indicates that the surface of the polystyrene and the carbon chain of the polymer were degraded by plasma treatment. Similarly, we use ratio to investigate the impact of the Ar^+ sputtering on the molecule standards (2-nonadecanone and Phenanthrene). The $C_4H_7^+/C_6H_5^+$ ratio is introduced instead of the $C_4H_7^+/C_7H_7^+$ ratio because the tropylium ion ($C_7H_7^+$) is generated by methylbenzene, while the $C_6H_5^+$ fragment, with H/C<1, a simple cyclic hydrocarbon (benzene) is representative of aromatics (McLafferty et al., 1993).

Figure 2.1 shows the evolution of the $C_4H_7^+/C_{14}H_{10}^+$ and $C_4H_7^+/C_6H_5^+$ ratios before and after sputtering for two standard compounds. The $C_{14}H_{10}^+$ ion corresponds to the parent ion for phenanthrene. With a H/C>1, $C_4H_7^+$ ion is considered a saturated fragment while $C_6H_5^+$ fragment with H/C<1 is supposed to have an aromatic structure. For phenanthrene the evolution of $C_4H_7^+/C_{14}H_{10}^+$ reveals that the Ar^+ sputtering induced an important decrease of the $C_4H_7^+$

signal and/or the increase of parent ions signal (Fig. 2.1A). This removal of saturated fragment by the Ar^+ beam is also supported by the decrease of the $C_4H_7^+/C_6H_5^+$ ratio (Fig. 2.1B). The presence of highly saturated fragments such as $C_4H_7^+$ in the mass spectrum of the PAH can be interpreted as either a saturated molecular ion produced by fragmentation and hydrogenation recombination or a contamination (Toporski and Steele, 2004). Evolution of the ratio of the contaminant over the PAH parent ion ($C_4H_7^+/C_{14}H_{10}^+$) indicates that >99% of the contaminant is removed after sputtering (Fig. 2.1). For nonadecanone, the $C_4H_7^+/C_6H_5^+$ ratio increases after sputtering (Fig. 2.1B), indicating increase of $C_4H_7^+$ fragment and/or decrease of $C_6H_5^+$ fragment. The $C_4H_7^+$ and $C_6H_5^+$ fragments are present in low amount on the silicon wafer devoid of molecule standard. The presence of $C_6H_5^+$ fragment on the silicon wafer suggests that the $C_6H_5^+$ detected on the nonadecanone is a surface airborne contamination removed by the sputtering. Importantly, Ar^+ does not appear to decrease the signal of aliphatic fragments from nonadecanone, (Fig. 2.1, $C_4H_7^+$) suggesting that fragmentation by Ar^+ is not dramatic, at least for the small mass fragments.

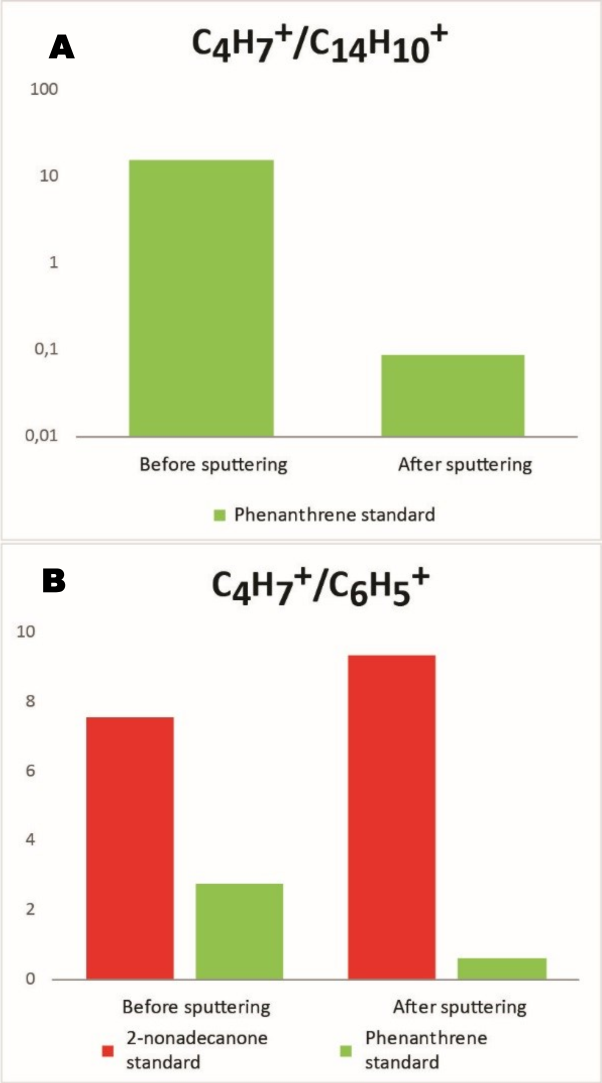

Fig. 2.1. *(A) $C_4H_7+/C_{14}H_{10}^+$ and (B) $C_4H_7^+/C_6H_5^+$ ratios in the spectra of standard compounds before and after Ar+ sputtering.*

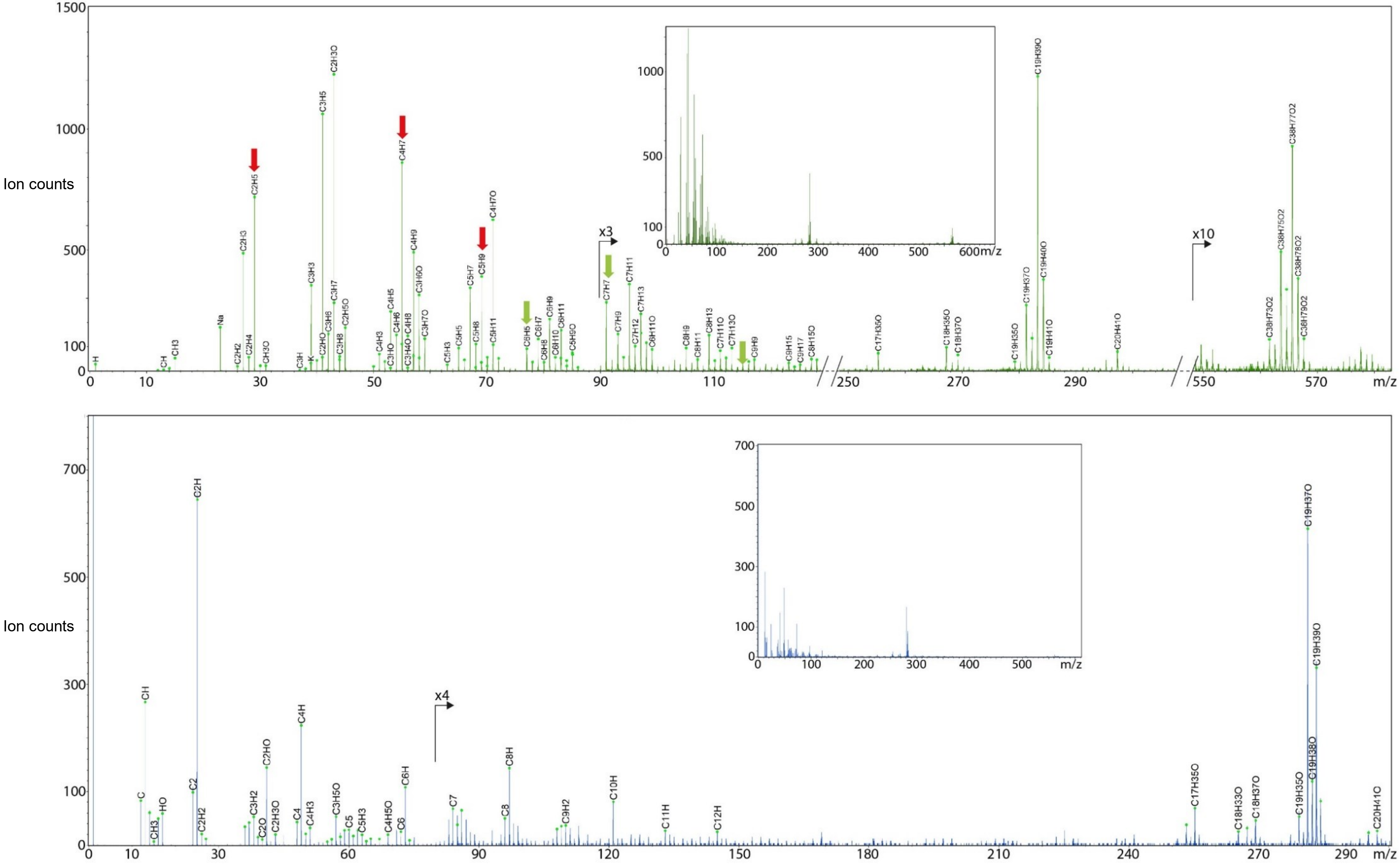

Fig. 2.2. ToF SIMS spectra of the 2-nonadecanone in bunched mode after sputtering..*Upper spectrum: positive mode. Red arrows indicated the presence of saturated ions fragments (typical of* n*-alkanes chain). Green arrows point the presence of unsaturated fragments. Lower spectrum: negative mode dominated by* C_n^- *and* C_nH^- *cluster ions.*

4.1.2 2-nonadecanone

In positive mode between 280-290 u. the parent M^+ ion ($C_{19}H_{38}O^+$, calculated m/z= 282.29 u.) is detected (Fig 2.2). The $(M+H)^+$ ion (attributed using mass calculation), which is generated by the addition of a proton to the parent ion, is the strongest peak. Less intense peaks are detected at m/z 284.29 and 285.30 which can be attributed to the contribution of (M+H)+ ion containing one or two ^{13}C atom and the addition of two or three protons to the parent M^+ ion. Similarly less intense peaks present at m/z 281.28 and 279.26 are attributed to the $(M-H)^+$ and $(M-3H)^+$ ions. A similar pattern is also observed between 500–600 u. with a dominant peak at mass 565.59 corresponding to the $(2M+H)^+$ ion. A less intense peak corresponding to clusters of two parent molecules ($C_{38}H_{76}O_2^+$) ion is present together with $(2M-H)^+$,$(2M-3H)^+$, $(2M+2H)^+$ and $(2M+3H)^+$ ions at m/z 563.60, 561.55, 566.61 and 567.62 respectively (Fig. 2.2).

At low mass (between 0–200 u) the dominant peak is at m/z 43.02, assigned to $C_2H_3O^+$ ions, which correspond to the carbonyl fragment from the ketone head group (Fig. 2.2). In our attempt to understand the fragmentation pattern of aliphatic/saturated hydrocarbons, we focused on the distribution of C_nH_y fragments produced by the long chain present in the 2-nonadecanone molecule (Table 1). First, the $C_2H_y^+$ fragments with a H/C (i.e. y/n) >1 dominate. For $C_2H_y^+$ fragments, $C_2H_5^+$ ion, at m/z 29.04 and $C_2H_3^+$ ion, at m/z 27.02 represent respectively 55.1% and 37.2% of the $C_2H_y^+$ fragments from the 2-nonadecanone. For the $C_3H_y^+$ fragments, the $C_3H_5^+$ ion represents 54.1% of the $C_3H_y^+$ signal from the molecule, while the $C_3H_3^+$, $C_3H_7^+$ represent less than 20% of the $C_3H_y^+$ ions intensity. With the $C_4H_y^+$ ions, fragments with H/C>1 dominate and fragment with H/C≤1 represent only ~6.3% of the $C_4H_y^+$ fragments. Hence, the dominant n=4 fragment is $C_4H_7^+$ (42.7% of $C_4H_n^+$) and the $C_4H_9^+$, $C_4H_5^+$ are the second and third intense ions representing respectively 24.3% and 12.2% of $C_4H_y^+$ fragments. This fragmentation pattern with the dominance of fragments with H/C>1 is also seen with the $C_5H_y^+$ fragments (Fig. 2.3A). The $C_5H_9^+$ and $C_5H_7^+$ ions respectively account for 36.2% and 31.6% of the $C_5H_y^+$ fragments. Moreover, the sum of the intensities of the $C_5H_y^+$ ions with a H/C<1 ($C_5H_2^+$, $C_5H_3^+$ and $C_5H_4^+$ ions) accounts for less than 4% of the $C_5H_y^+$ fragments. In contrast, highly saturated fragment such as $C_5H_{10}^+$ are relatively abundant (5.4%, Table 1).

Table 1. *Values of intensity from $C_nH_y^+$ ions from the 2-nonadecanone and phenanthrene standards.*

	2-nonadecanone standard	Relative percentage of $C_nH_i^+$ (1)		Phenanthrene standard	Relative percentage of $C_nH_i^+$ (1)
C_2H^+	2	0,2%		74	5,5%
$C_2H_2^+$	19	1,5%		407	30,2%
$C_2H_3^+$	486	37,2%		633	47,0%
$C_2H_4^+$	57	4,4%		35	2,6%
$C_2H_5^+$	719	55,1%		193	14,3%
$C_2H_6^+$	22	1,7%		5	0,4%
$C_3H_2^+$	9	0,5%		319	29,0%
$C_3H_3^+$	354	18,0%		276	25,1%
$C_3H_4^+$	44	2,2%		52	4,7%
$C_3H_5^+$	1062	54,1%		309	28,1%
$C_3H_6^+$	153	7,8%		28	2,5%
$C_3H_7^+$	280	14,3%		108	9,8%
$C_3H_8^+$	61	3,1%		9	0,8%
$C_4H_2^+$	18	0,9%		509	31,7%
$C_4H_3^+$	70	3,5%		700	43,5%
$C_4H_4^+$	39	1,9%		128	8,0%
$C_4H_5^+$	246	12,2%		118	7,3%
$C_4H_6^+$	149	7,4%		16	1,0%
$C_4H_7^+$	861	42,7%		99	6,2%
$C_4H_8^+$	145	7,2%		8	0,5%
$C_4H_9^+$	490	24,3%		30	1,9%
$C_5H_2^+$	3	0,3%		376	29,1%
$C_5H_3^+$	26	2,4%		667	51,6%
$C_5H_4^+$	9	0,8%		78	6,0%
$C_5H_5^+$	95	8,8%		92	7,1%
$C_5H_6^+$	46	4,2%		15	1,2%
$C_5H_7^+$	343	31,6%		33	2,6%
$C_5H_8^+$	112	10,3%		8	0,6%
$C_5H_9^+$	392	36,2%		19	1,5%
$C_5H_{10}^+$	58	5,4%		4	0,3%
$C_6H_2^+$	3	0,4%		378	30,2%
$C_6H_3^+$	10	1,3%		373	29,8%
$C_6H_4^+$	3	0,4%		110	8,8%
$C_6H_5^+$	92	11,9%		169	13,5%
$C_6H_6^+$	37	4,8%		168	13,4%
$C_6H_7^+$	132	17,1%		21	1,7%
$C_6H_8^+$	36	4,7%		6	0,5%
$C_6H_9^+$	214	27,7%		13	1,0%
$C_6H_{10}^+$	56	7,3%		2	0,2%
$C_6H_{11}^+$	168	21,8%		10	0,8%
$C_6H_{12}^+$	21	2,7%		3	0,2%
$C_7H_2^+$	2	0,5%		188	27,0%
$C_7H_3^+$	5	1,1%		279	40,0%
$C_7H_4^+$	8	1,8%		54	7,7%
$C_7H_5^+$	9	2,0%		95	13,6%
$C_7H_6^+$	7	1,6%		12	1,7%
$C_7H_7^+$	94	21,3%		42	6,0%

$C_7H_8^+$	14	3,2%		7	1,0%
$C_7H_9^+$	51	11,5%		5	0,7%
$C_7H_{10}^+$	19	4,3%		2	0,3%
$C_7H_{11}^+$	120	27,1%		7	1,0%
$C_7H_{12}^+$	34	7,7%		3	0,4%
$C_7H_{13}^+$	79	17,9%		3	0,4%
$C_8H_2^+$	2	1,1%		144	32,1%
$C_8H_3^+$	6	3,3%		106	23,7%
$C_8H_4^+$	3	1,6%		26	5,8%
$C_8H_5^+$	6	3,3%		44	9,8%
$C_8H_6^+$	6	3,3%		83	18,5%
$C_8H_7^+$	12	6,5%		24	5,4%
$C_8H_8^+$	7	3,8%		4	0,9%
$C_8H_9^+$	32	17,4%		7	1,6%
$C_8H_{10}^+$	9	4,9%		2	0,4%
$C_8H_{11}^+$	16	8,7%		2	0,4%
$C_8H_{12}^+$	7	3,8%		2	0,4%
$C_8H_{13}^+$	49	26,6%		2	0,4%
$C_8H_{14}^+$	14	7,6%		2	0,4%
$C_8H_{15}^+$	15	8,2%		0	0,0%
$C_9H_2^+$	2	1,7%		62	16,4%
$C_9H_3^+$	4	3,3%		55	14,5%
$C_9H_4^+$	4	3,3%		14	3,7%
$C_9H_5^+$	3	2,5%		58	15,3%
$C_9H_6^+$	5	4,2%		26	6,9%
$C_9H_7^+$	16	13,3%		140	36,9%
$C_9H_8^+$	13	10,8%		16	4,2%
$C_9H_9^+$	16	13,3%		4	1,1%
$C_9H_{10}^+$	3	2,5%		1	0,3%
$C_9H_{11}^+$	10	8,3%		2	0,5%
$C_9H_{12}^+$	5	4,2%		0	0,0%
$C_9H_{13}^+$	7	5,8%		1	0,3%
$C_9H_{14}^+$	6	5,0%		0	0,0%
$C_9H_{15}^+$	11	9,2%		0	0,0%
$C_9H_{16}^+$	6	5,0%		0	0,0%
$C_9H_{17}^+$	9	7,5%		0	0,0%

(1) *Intensity of each ion normalized to the total intensity of the* C_nH_y *series calculated using equation: (relative percentage)*$_{n,y}$ = $C_nH_y^+ \div \sum_i C_nH_i^+$ *for all (i) values where* $C_nH_i^+$ *is detected above background.*

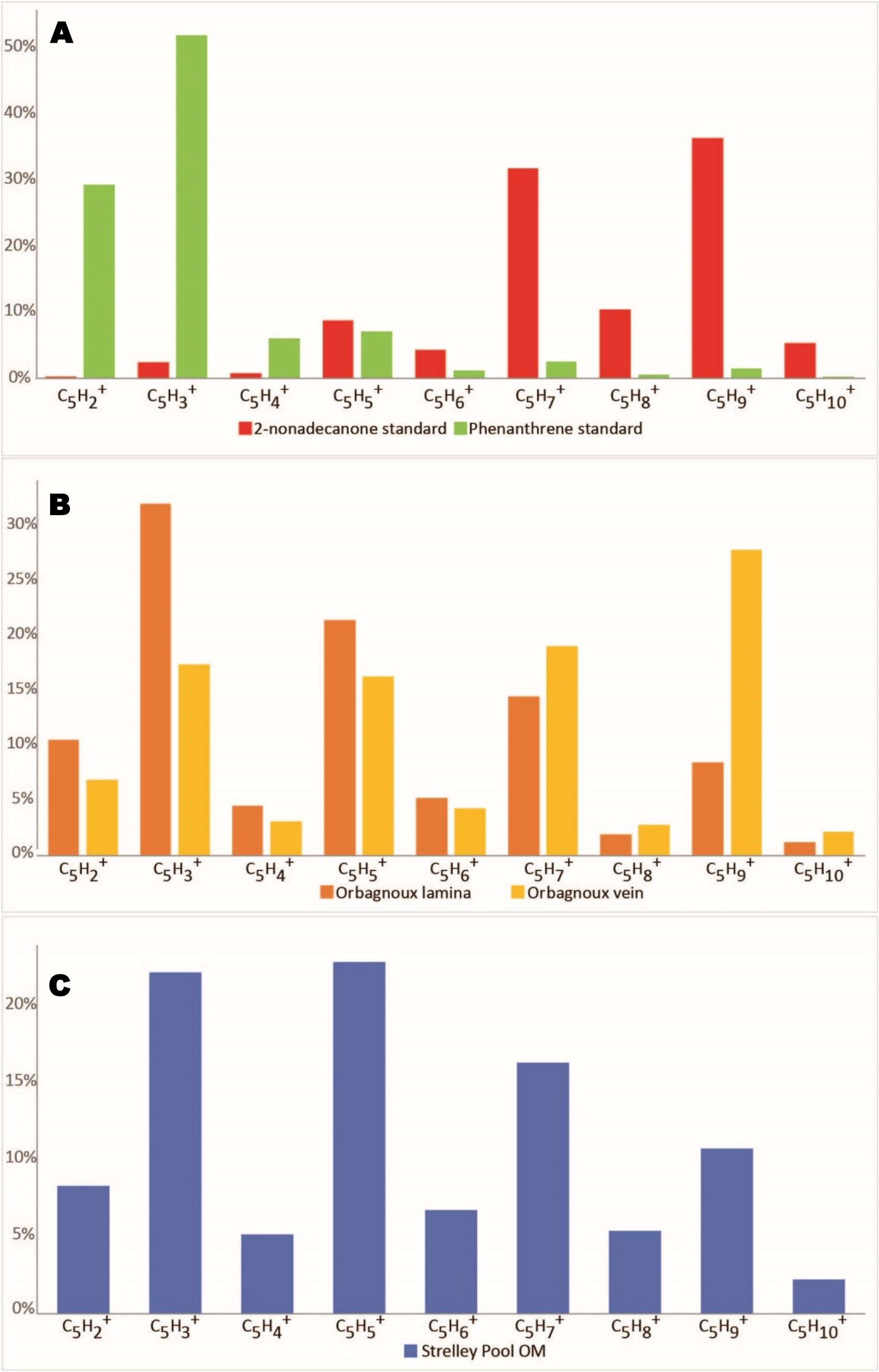

Fig. 2.3. Distribution of the $C_5H_y^+$ ion series normalized using equation (1), *for:(A) the 2-nonadecanone and phenanthrene standards, (B) the Orbagnoux lamina and veins. (C) The Strelley Pool organic matter (OM).*

The distribution of $C_6H_y^+$ ions is dominated by relatively saturated fragments with y>6 (>70% of the total intensity from $C_6H_y^+$ fragments) with maximum intensity for the $C_6H_9^+$

(27%) and $C_6H_{11}^+$ (21%) fragments. Interestingly, the $C_6H_5^+$ ions is detected with a significant intensity (11% of C_6 fragment) (Table 1). The positive $C_7H_y^+$ fragment distribution is similar to that of $C_6H_y^+$ ions (Table 1). Here, saturated fragments with H/C>1 ($C_7H_{11}^+$, $C_7H_{13}^+$ and $C_7H_9^+$) dominate whereas respective intensities of fragments with H/C<1 are below 2% (Fig. 2.4A). Moreover, the $C_7H_7^+$ ion (tropylium ion), is detected with a relative high intensity (21% of $C_7H_n^+$ ions) (Fig. 2.4A and Table 1).

At higher mass, the signal decreases strongly but fragments typical of saturated long chains are still detected. For the $C_8H_y^+$ fragment distribution, the ions with H/C>1 ($C_8H_9^+$, $C_8H_{13}^+$, $C_8H_{14}^+$ and $C_8H_{15}^+$) are still relatively significant (Table 1). In contrast, $C_9H_y^+$ fragments lack a distinct distribution. For these fragments, peaks corresponding to $C_9H_7^+$, $C_9H_8^+$ and $C_9H_9^+$ ions (fragment H/C<1) are important, while the intensity of saturated (H/C>1) ions ($C_9H_{11}^+$, $C_9H_{15}^+$and $C_9H_{17}^+$) remains significant but not predominant (respectively 8%, 9% and 7%) (Table 1). Finally, a predominance of odd over even values of y is observed in $C_nH_y^-$ series (Figs. 2.3A, 2.4A, Table 1).

In negative mode, the parent M^- is present at mass 282.29 but the spectrum at high mass (between 200-300u) is dominated by the $(M-H)^-$ ion, generated by the loss of a H^-. The second peak in height occurs at mass 284.28, which corresponds to the $(M+H)^-$ ion (Fig. 2.2) or at low mass the dominant peak is the ion C_2H^- at m/z 25.01 (Fig. 2.2). The spectrum shows the predominance of fragments with an even carbon number (Fig. 2.2), also shown by the calculation of the C_nH^-/C_n^- ratio (Fig. 2.5B). The hydrogenated fragment (C_nH^-) is more intense than the non-hydrogenated fragment of similar carbon number (C_n^-, Fig. 2.2, 2.5B). Moreover, the high values for the C_n^-/C_2^- ratio recorded for n ranging between 3-8 indicate that the fragmentation of 2-nonadecanone leads to the production of long C_n^- cluster ions.

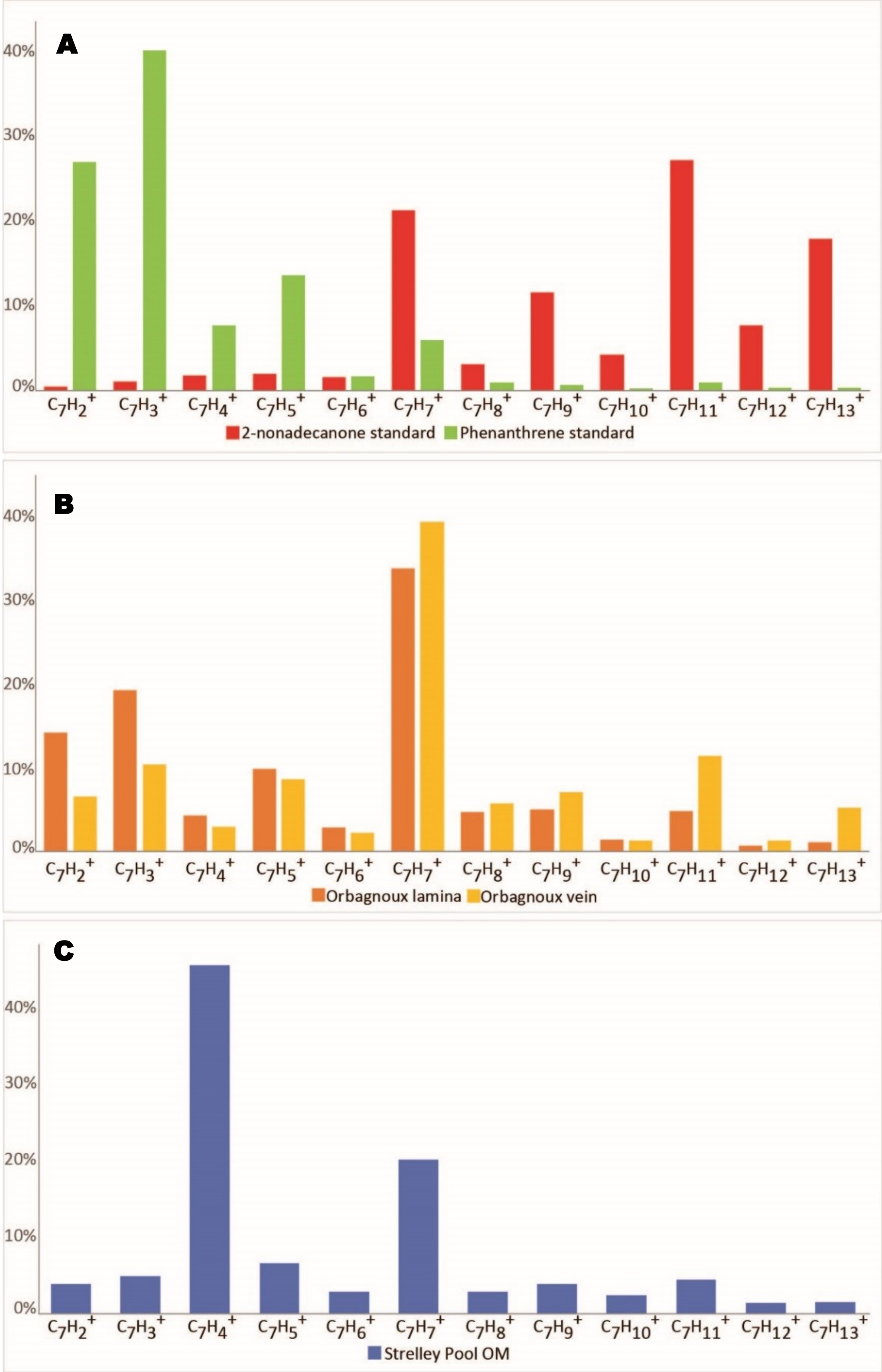

Fig. 2.4. Distribution of the $C_7H_y^+$ ion series normalized using equation (1), *for:(A) the 2-nonadecanone and phenanthrene standards, (B) the Orbagnoux lamina and veins. (C) The Strelley Pool organic matter (OM).*

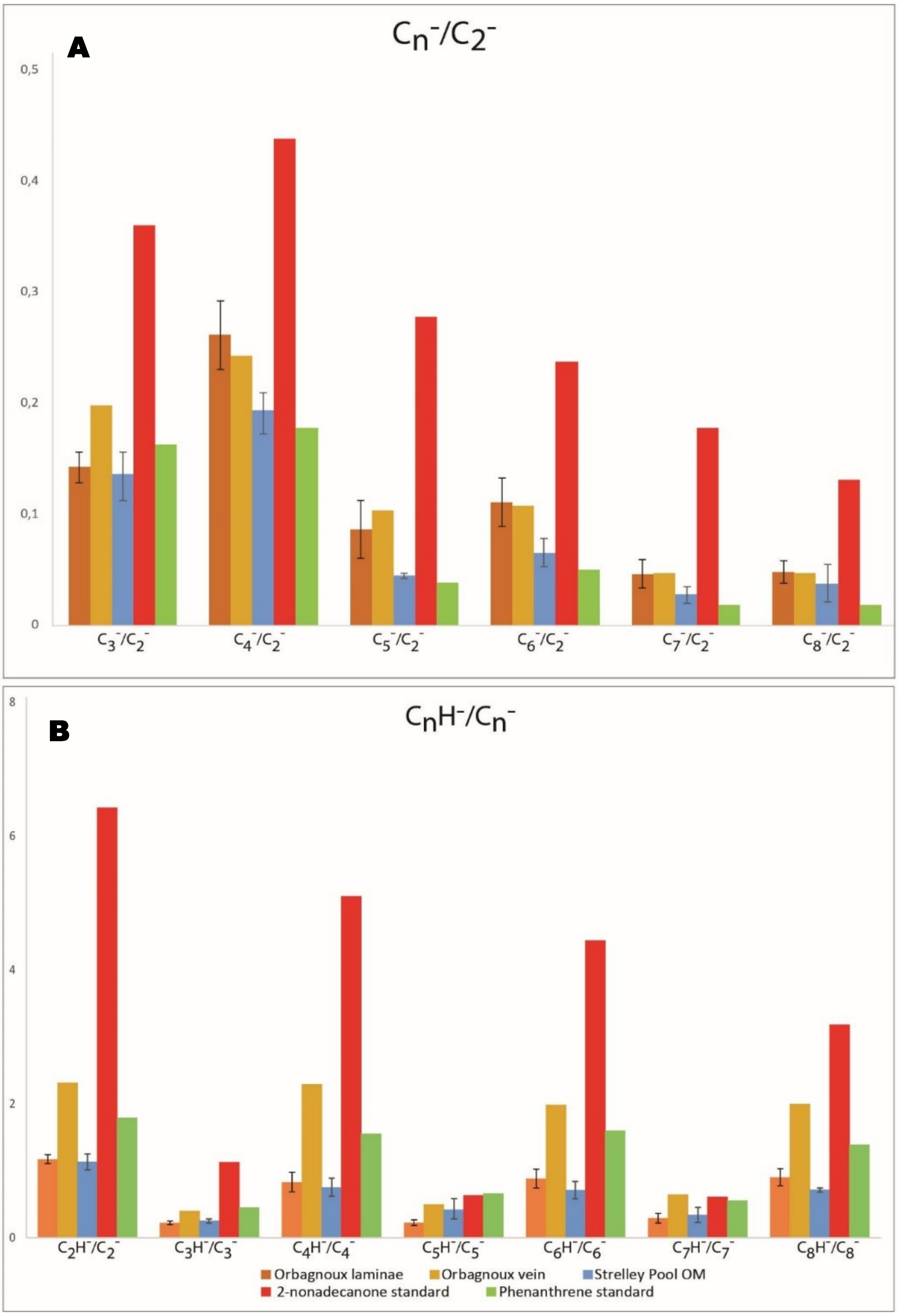

Fig. 2.5. *Negative polarity fragment intensity ratio graphs from the Orbagnoux laminae (orange) and veins (yellow), the Strelley Pool OM (blue), as well as the nonadecanone (red) and phenanthrene (green) standards. (A)* C_n^-/C_2^- *ratios. (B)* C_nH^-/C_n^- *ratios. Note that the ratios presented in these graphs for the Orbagnoux laminae and Strelley Pool OM are means from the respectively four and two ROI areas analysed in ToF SIMS*

4.1.3 Phenanthrene and anthracene-D_{10}

For the phenanthrene standard molecule, the M^+ ions (parent ions $C_{14}H_{10}^+$, calculated m/z= 178,08u) are present at m/z 178.08 and dominate the signal between 100 and 250 u. (Fig. 2.6). These parent M^+ ions are associated with $(M-2H)^+$, $(M-H)^+$, $(M+H)^+$, $(M+2H)^+$ ions that display a lower intensity. We can note that the peak attributed to the $(M+H)^+$, $(M+2H)^+$ have probably a contribution of the parent ions with one or two ^{13}C. Furthermore, numerous significant ion peaks are produced by the loss or capture of CH^+ fragments: $C_{16}H_{10}^+$ (m/z 202.07), $C_{15}H_9^+$ (m/z 189.07), $C_{13}H_9^+$ (m/z 165.07), $C_{12}H_8^+$(m/z 152.06) and $C_{11}H_7^+$ (m/z 139.05). Each of these ions is also affected by proton loss or capture as shown in the spectra. This phenomenon gives the spectra of PAH a pattern characterized by series of fragments corresponding to the ions $(M \pm aCH^+ \pm bH^+)$ as shown by the green brackets in Fig. 2.6.

At low mass, the spectrum is dominated by ions from the silicon wafer substrate (Si^+, SiH^+, $SiOH^+$ and $SiOH^+$ ions at m/z= 28.97; 28.98; 44.97 and 45.98, Fig. 2.6) due to the evaporation of the PAH in the ToF-SIMS chamber that only leaves a thin, porous layer of phenanthrene crystallites. Considering the $C_nH_y^+$ series, the low mass peaks are mainly dominated by fragment with H/C<1 (Table 1). First, the $C_2H_n^+$ fragments are dominated by $C_2H_3^+$ and $C_2H_2^+$ that represent 47% and 30% (respectively) of the total C_2Hy^+ ion intensity. Interestingly, the saturated $C_2H_5^+$ ions represent 14% of the $C_2H_y^+$ series (Table 1). The $C_3H_y^+$ fragments are also dominated by ions with low H/C: $C_3H_2^+$ and $C_3H_3^+$ represent 29% and 25% of the series total intensity, respectively. As seen with $C_2H_5^+$, $C_3H_5^+$ represents a significant part of the $C_3H_n^+$ intensity (28%) (Table 1). The presence of these saturated fragments with a H/C>1 indicates that hydrogenation of low mass-fragments is important. The $C_4H_y^+$ fragments are dominated by the $C_4H_2^+$ and $C_4H_3^+$ ions representing 32% and 43% of the series. The saturated fragment, such as $C_4H_7^+$ and $C_4H_9^+$ represent less than 8% of the $C_4H_y^+$ series. (Table 1). This pattern of dominance of fragments with H/C<1 is amplified in the $C_5H_y^+$ fragment series (Fig. 2.3A). Again, $C_5H_2^+$ and $C_5H_3^+$ ions represent 80% of the series, while the saturated fragments ($C_5H_7^+$ and $C_5H_9^+$) represent less than 4% of the series intensity (Fig. 2.3A and Table 1). For the $C_6H_y^+$ fragments, the $C_6H_2^+$ and $C_6H_3^+$ ions are also significant (with respectively 30% and 29% of the series intensity). However, the fragments $C_6H_5^+$ and $C_6H_6^+$, ions likely corresponding to benzenoid structures (Spool, 2004; Thiel and Sjövall, 2014; Toporski and Steele, 2004), represent a notable part of the $C_6H_y^+$ signal (~13% each) (Table 1). The C_7 series also displays the dominance of fragment characterized by very low H/C: $C_7H_2^+$, $C_7H_3^+$ and $C_7H_5^+$ altogether represent 80% of the $C_7H_y^+$ series intensity. Interestingly, the tropylium ion ($C_7H_7^+$) represents only 6% of the $C_7H_y^+$ series intensity (Fig. 2.4A and Table 1). For the $C_8H_y^+$

series, 55% of the signal correspond to the fragments $C_8H_2^+$, $C_8H_3^+$ and 18% for $C_8H_6^+$ ions (Table 1). This trend is also seen seen with the C_9Hy^+series where the $C_9H_7^+$ ion is the main peak with 37% of the intensity and $C_9H_2^+$, $C_9H_3^+$ and $C_9H_5^+$ ions each represent ~15% of the total intensity (Table 1).

In negative mode, the parent ion M^- of phenanthrene is absent. Moreover, the main peaks of the spectrum come from the silicon wafer substrate at m/z: 15.99 (O^-), 17.00 (OH^-), 59.96 (SiO_2^-), 60.97 (SiO_2H^-) (Fig. 2.6). The main carbonaceous signal from the PAH standard comes from the fragments C_2^- and C_2H^-. The intensities of C_n^- and C_nH^- peaks are very low (Fig. 2.5). Moreover, if present the $C_nH_2^-$ fragments have very low intensities while the $C_nH_3^-$ fragments are absent. The C_nH^-/C_n^- ratios (Fig. 2.5) show that the C_nH^- intensity for odd carbon numbered fragments represent 45–60% of the C_n^- intensity while the C_nH^- intensity for even carbon numbered fragments are 50-70% higher than the C_n^- fragments (Fig. 2.5).

For the anthracene-D_{10} ($C_{14}D_{10}$), the positive spectrum is not presented due to the difficulties to make difference between molecule having deuterium/dihydrogen ion (D^+, m/z= 2.014/ H_2^+, m/z= 2.015) and deuterium with hydrogen/tri-hydrogen (DH^+, m/z= 3.021/H_3^+, m/z= 3.023). However, this molecule standard ($C_{14}D_{10}^+$, calculated m/z=188.14) was detected and offered the opportunity to constrain the formation of $C_nH_y^-$ ions in negative mode (because of the very low quantity of $C_nH_2^-$ ions produced by the previous PAH).

In the negative mode spectrum of anthracene-D_{10} ($C_{14}D_{10}$), the parent ion is also absent (Fig. 2.7). As observed for phenanthrene, the fragmentation of the deuterated PAH predominantly generates C_n^-/C_nD^- clusters with low C number (Fig. 2.7). Besides, C_nH^- clusters are produced, the intensities of which are similar to the intensities of their respective following C_nD^- peaks (for each n>2) (Fig. 2.7 and Table 2). Thus, C_nD^- and C_nH^- clusters likely form through recombination of C_n^- with D and or H ions/radicals. Our recent GC-MS performed on this standard shows the absence of hydrogen exchange with deuterium and indicates that isotopic exchange was absent within the clean glass vial. Thus, D ions/radicals present within the ToF SIMS spectrum derive from the PAH itself, whereas H ions/radicals likely derived from contamination during the sample deposition on clean silicon wafer and/or storage and/or within the ToF-SIMS chamber.

***Table 2**. Negative ion ratio for anthracene-D_{10} ($C_{14}D_{10}$)*

	anthracene D_{10} standard		anthracene D_{10} standard
C_2D^-/C_2^-	0,57	C_2H^-/C_2^-	0,92
C_3D^-/C_3^-	0,16	C_3H^-/C_3^-	0,14
C_4D^-/C_4^-	0,50	C_4H^-/C_4^-	0,40
C_5D^-/C_5^-	0,13	C_5H^-/C_5^-	0,12
C_6D^-/C_6^-	0,37	C_6H^-/C_6^-	0,44
C_7D^-/C_7^-	0,14	C_7H^-/C_7^-	0,08
C_8D^-/C_8^-	0,43	C_8H^-/C_8^-	0,46
C_9D^-/C_9^-	0,24	C_9H^-/C_9^-	0,41
$C_{10}D^-/C_{10}^-$	0,52	$C_{10}H^-/C_{10}^-$	0,60

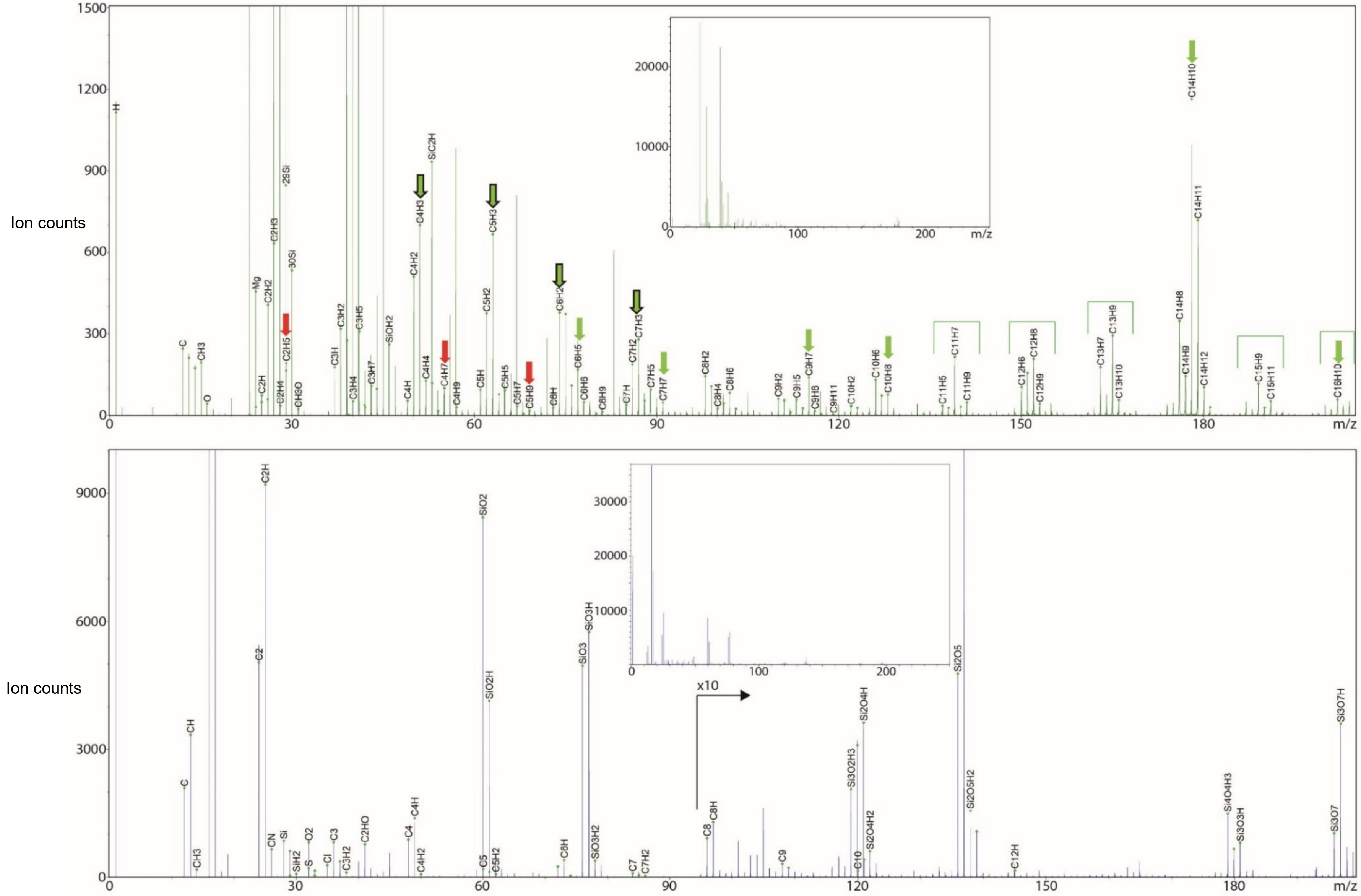

Fig. 2.6. ToF SIMS spectra of the phenanthrene standard in bunched mode, after sputtering. *Upper spectrum: positive mode. Red arrows: saturated fragments. Green arrows: unsaturated fragments (likely generated by aromatic). Green brackets: PAH fragments series. Green arrows with bold contour: Fragment ions with the lowest H/C ratio. Lower spectrum: negative mode.*

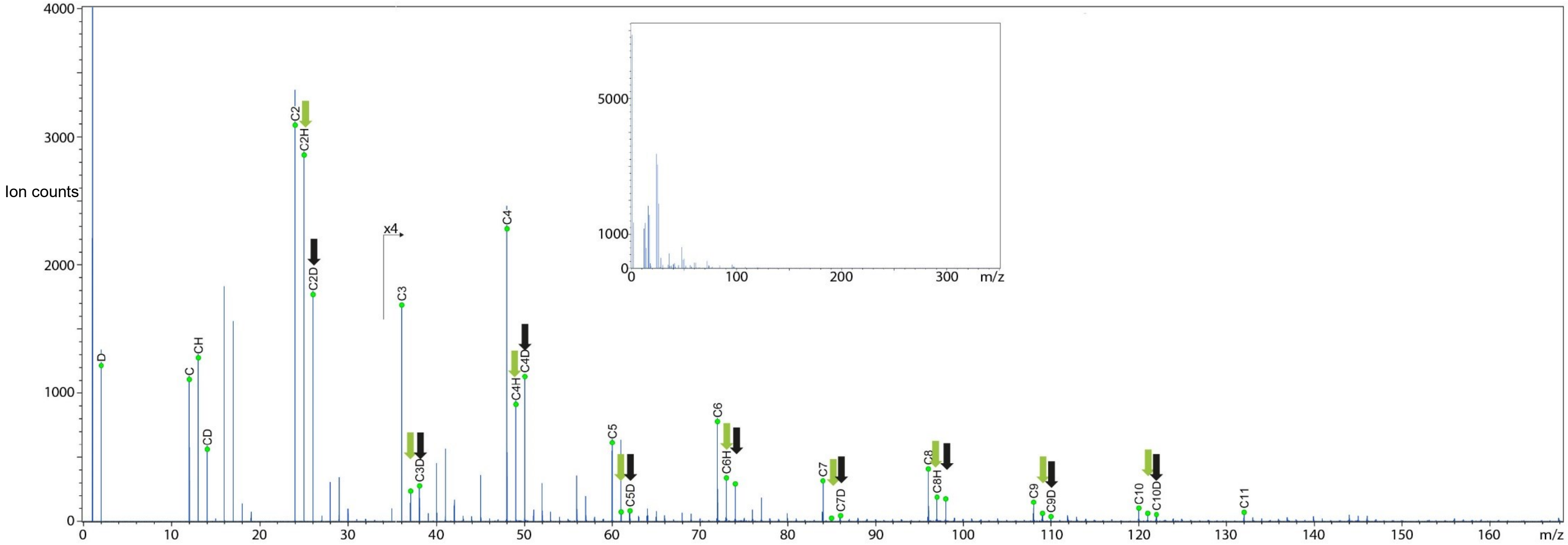

Fig. 2.7. Negative ToF SIMS spectrum of the anthracene D-10 standard in bunched mode, after sputtering. *Green arrows: C_nH^- ions. Black arrows: C_nD^- fragments, which are assumed to be generated by the deuterated standard. Here the spectrum show the equivalent intensities of C_nH^- and C_nD^- ions for the different C_n^- series.*

4.1.4 *Semi-quantitative ratio*

The analysis of the global positive ion spectra and of $C_nH_y^+$ series allows us to highlight the main mass spectral features that distinguish an aliphatic hydrocarbon chain (nonadecanone) from that of a PAH (phenanthrene). From these observations, we propose a series of semi-quantitative ratios that can be used to address the molecular structure of unknown kerogen. First, as expected from the general formula of the studied standards, $C_nH_y^+$ with H/C>1 dominate for an aliphatic compound, whereas fragments with H/C<1 dominate in the PAH; this is exemplified in Fig. 2.3A. Second, with increasing carbon number in $C_nH_y^+$ series, fragments with H/C close to unity (e.g. -1<(n-y)<1 increase in abundance relative to those with H/C<1 (dominating in phenanthrene) and/or H/C>1 (dominating in nonadecanone). The most prominent example of this effect is illustrated with the abundance of $C_7H_7^+$ in the spectrum of nonadecanone (Fig. 2.4A). This unsaturated fragment that is commonly formed in aromatic compounds (Sakamoto et al., 2004; Spool, 2004; Toporski and Steele, 2004) is also observed in our analysis of nonadecanone. Similarly, the relative intensity of $C_5H_5^+$ in the $C_5H_y^+$ series is quite similar in nonadecanone and phenanthrene (Table 1). Therefore, we defined the ratios Rn (R4 to R9) using equations (2-7) of the sum of $C_nH_y^+$ species with H/C>1 to sum of the $C_nH_y^+$ species with H/C<1; these sums exclude the $C_nH_y^+$ fragments where a similar intensity was observed in the nonadecanone and the phenanthrene, with values usually of H/C~1 (such as $C_7H_7^+$). The Rn ratio are thus used as indicators of the saturation of fragments with n carbons. For nonadecanone, Table 3 and Fig. 2.8C show that saturation is high for all carbon numbers and increases with increasing carbon number until n = 6, then decreases sharply for larger fragments. Thus, it appears that with our analytical setup large fragments from saturated aliphatic chains suffer more from hydrogen-stripping than shorter fragments. In contrast, the fragments from phenanthrene display low saturation and display a pattern where saturation of $C_nH_y^+$ fragments decreases sharply with increasing carbon number for n≥4.

Based on these observations, study of fragment ions with small carbon number is probably best suited to compare OM containing long aliphatic chains with aromatic-rich OM. Among the ratios defined below ($C_2H_5^+/C_2H_3^+$, $C_3H_5^+/C_3H_3^+$, $C_4H_7^+/C_6H_5^+$, $C_4H_7^+/C_7H_7^+$, $C_5H_9^+/C_7H_7^+$), the ratio $C_4H_7^+/C_6H_5^+$ best discriminates the long chain aliphatic against the PAH. We also introduce the aliphatic/aromatic ratio $R_{ali/aro}$ using equation (8) based on the fragments listed in a ToF-SIMS study of fossil plants in Abbott et al. (2018), which also strongly discriminates nonadecanone and phenanthrene (Table 3).

Table 3. *Various ratio values for the standards, the Orabgnoux lamina, veins and the Strelley Pool OM based on the intensities of the measured hydrocarbon ions, in positive mode. See equations (2-9) for definition of R4 to R9 and* $R_{ali/aro}$.

Fragment ratios	**Nona-decanone**	**Phen-anthrene**		**Orbagnoux lamina**	**Orbagnoux veins**	**Strelley Pool OM**
$C_2H_5^+/C_2H_3^+$	1.48	0.30		0.96	1.27	0.77
$C_3H_5^+/C_3H_3^+$	3.00	1.12		1.46	2.30	1.24
$C_4H_7^+/C_6H_5^+$	9.36	0.59		1.26	3.28	1.24
$C_4H_7^+/C_7H_7^+$	9.16	2.36		2.18	4.64	2.03
$C_5H_9^+/C_7H_7^+$	4.17	0.45		0.47	1.41	0.40
R4 (eq. 2)	18.69	0.13		1.20	3.15	2.19
R5 (eq. 3)	32.79	0.08		0.73	2.31	1.36
R6 (eq. 4)	39.19	0.06		0.75	1.82	1.60
R7 (eq. 5)	13.21	0.04		0.37	1.12	0.27
R8 (eq. 6)	5.52	0.04		0.39	1.16	1.48
R9 (eq. 7)	2.28	0.01		0.16	0.41	0.38
$R_{ali/aro}$ (eq. 8)	11.11	0.28		2.37	3.41	1.87
RC_n^- (eq. 9)	0.36	0.08		0.23	0.17	0.07
C_2H^-/C_2^-	6.52	1.79		1.24	2.31	1.07

(2) $R4 = \sum_{y=6}^{9} C_4H_y^+ \div \sum_{y=2}^{3} C_4H_y^+$

(3) $R5 = \sum_{y=6}^{11} C_5H_y^+ \div \sum_{y=2}^{3} C_5H_y^+$

(4) $R6 = \sum_{y=7}^{11} C_6H_y^+ \div \sum_{y=2}^{4} C_6H_y^+$

(5) $R7 = \sum_{y=8}^{12} C_7H_y^+ \div \sum_{y=2}^{5} C_7H_y^+$

(6) $R8 = \sum_{y=9}^{15} C_8H_y^+ \div \sum_{y=2}^{6} C_8H_y^+$

(7) $R9 = \sum_{y=10}^{17} C_9H_y^+ \div \sum_{y=2,3,5,7} C_9H_y^+$

(8) $R_{ali/aro} = (C_2H_5^+ + C_3H_5^+ + C_4H_9^+ + C_5H_9^+ + C_6H_{11}^+ + C_7H_{13}^+ + C_8H_{15}^+ + C_9H_{17}^+) / (C_6H_5^+ + C_7H_7^+ + C_8H_9^+ + C_9H_7^+ + C_{10}H_8^+ + C_{13}H_9^+ + C_{14}H_{10}^+ + C_{15}H_{11}^+ + C_{16}H_{10}^+)$

(9) $RC_n^- = \sum_{n=5}^{X} C_n^- \div \sum_{n=1}^{4} C_n^-$

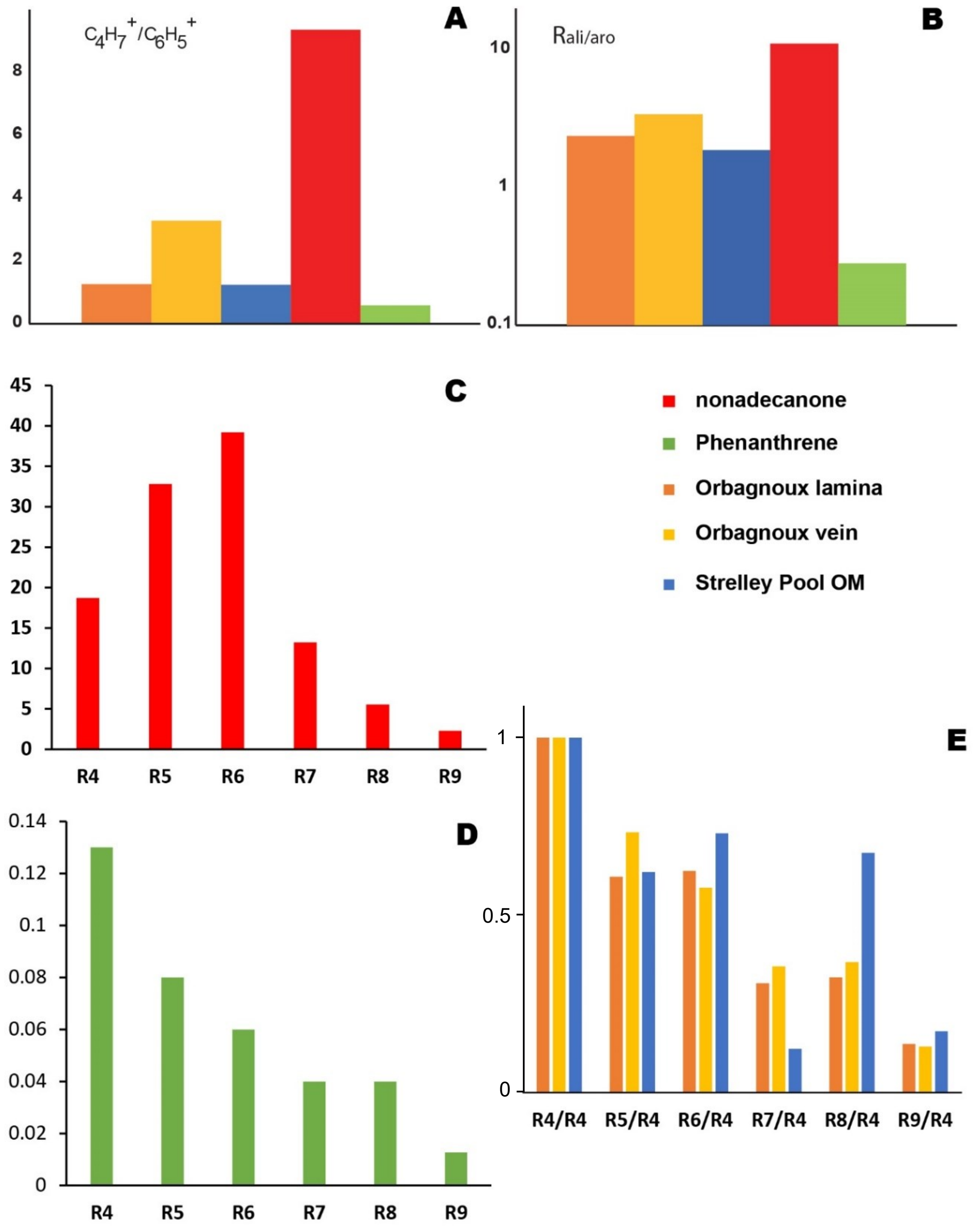

Fig. 2.8. *Plots of ion ratios defined in Table 3 from standards and the different sample areas. (A) $C_4H_7^+/C_6H_5^+$. These ratios were calculated for four and two analyzed area from the respective orbagnoux laminae and Strelley Pool OM. B) Aliphatic ions/aromatic ions (equation 8) ratios. (C-D) R4 to R9 ratios (equations 2-7) in nonadecanone (C) and phenanthrene (D). (E) Ratios R4 to R9 normalized to R4 in Orbagnoux and Strelley Pool OM. The color legend is the same for (A-E).*

4.2 Rock samples

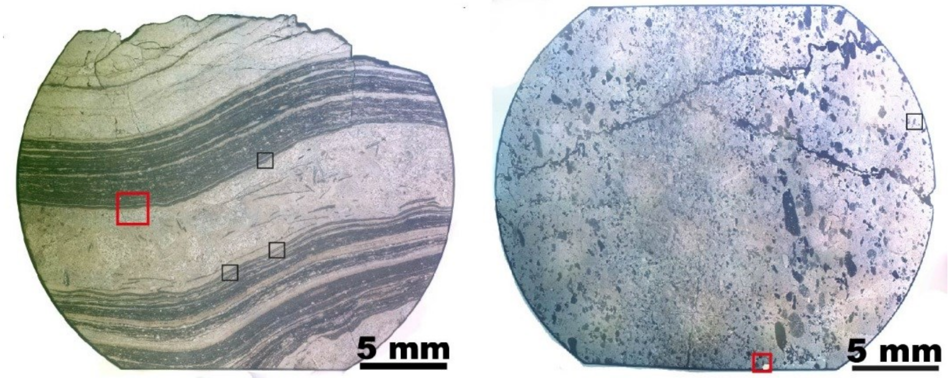

***Fig. 2.9. General reflected light images of the semi-thin sections prepared for ToF SIMS analyses**. Left: Orbagnoux sample. Right: Strelley Pool Formation sample. The red squares correspond to the analyzed areas presented here (Figs. 2.10 and 2.13). The black squares correspond to other areas analysed but not presented.*

4.2.1 Orbagnoux stromatolite

The Orbagnoux stromatolite is characterized by dark laminae, which are interpreted as fossil stromatolitic microbial mats, and light laminae composed of carbonate (Tribovillard et al., 2004). The organic-rich laminae can be easily recognized at the macroscale (Fig. 2.9) and with SEM-BSE images (Fig. 2.10A). Moreover, SEM EDXS map of sulfur performed on an area analyzed with ToF-SIMS, permit to constrain the distribution of the organic-rich laminae (Fig. 2.10D). Some of these organic rich laminae also appear enriched in microscopic Si±Al-rich minerals that likely are quartz and/or clay minerals (Fig. 2.10C-E). Importantly, some organic-rich laminae are devoid of Al-Si minerals, indicating that those were not introduced in OM during the preparation process (e.g. smearing of indigenous minerals or corundum abrasive).

In positive mode, the ToF SIMS analyses performed after Ar^+ sputtering on gold-coated sample reveal the same distribution of the calcium (Ca^+), aluminum (Al^+) and silicon (Si^+) ion as observed with EDXS map (Fig. 2.10F). Sputtering depth profiles performed with Ar^+ on this area demonstrated the necessity of removing a nanoscale layer of air-deposited (or smeared), homogeneous contamination in order to analyze the underlying OM and minerals (Fadel et al, in prep, chapter X of this thesis). After sputtering of the homogenous contaminant layer, the positive ions images of several hydrocarbon fragments correlated with the organic-rich laminae observed in SEM. However, the intensities of the positive organic fragments is higher in the aluminum-rich laminae (blue arrows in Fig. 2.10) than in the laminae that appear devoid of aluminum (green arrows in Fig. 2.10). These intensities contrast strongly with those observed in negative ion mode (Fig. 2.10G), where organic fragments are more intense in the OM-rich, Al-poor laminae. The positive ion ratios calculated on these two types of organic matter are equivalent. The $C_4H_7^+/C_7H_7^+$ ratios are 2.40 for the OM rich lamina (green arrow in Fig. 2.10), 2.46 for the OM-Al rich lamina (blue arrow). Ratios of organic ion intensities over inorganic ions are also equivalent: $C_4H_7^+/Al^+$ of 0.018 for OM-rich laminae, 0.017 for OM-Al rich laminae; $C_7H_7^+/Al^+$ of 0.007 for OM-rich laminae, 0.007 for OM-Al rich laminae; $C_4H_7^+/Ca^+$ of 0.094 for OM-rich laminae, 0.093 for OM-Al-rich; and $C_7H_7^+/Ca^+$ of 0.039 for OM rich and 0.038 for OM-Al-rich laminae. Based on these ratios of ions intensities from these apparently two different types of organic matter, we show that this heterogeneity is only due to a lower total ion intensity in the OM-rich laminae relative to the OM-Al-rich laminae during ToF-SIMS analyses. This suggests that a matrix effect, possibly linked with the presence of clay minerals, enhances the signal of OM in the OM-Al-rich laminae. In order to obtain significant signal for identification and semi-quantification, we decided to group these two types of organic matter and refer them as Orbagnoux lamina OM in tables and spectra. The spectrum (Fig. 2.11) used for the calculation of the diverse ratios was reconstructed from an area of interest (ROI) of 200 x 200 µm² within the organic lamina.

The Orbagnoux lamina spectrum is displayed in Fig. 2.11. At high mass the spectrum reveals a fragment series of unsaturated ions. Moreover, unsaturated ions peaks are present: $C_6H_5^+$, $C_7H_7^+$, $C_9H_7^+$, $C_{10}H_8^+$, $C_{14}H_{10}^+$ and $C_{16}H_{10}^+$ ions (green arrows in Fig. 2.11). Ions attributed to saturated fragments, $C_2H_5^+$, $C_4H_7^+$ and $C_5H_9^+$ ions, are relatively abundant (red arrows in Fig. 2.11).

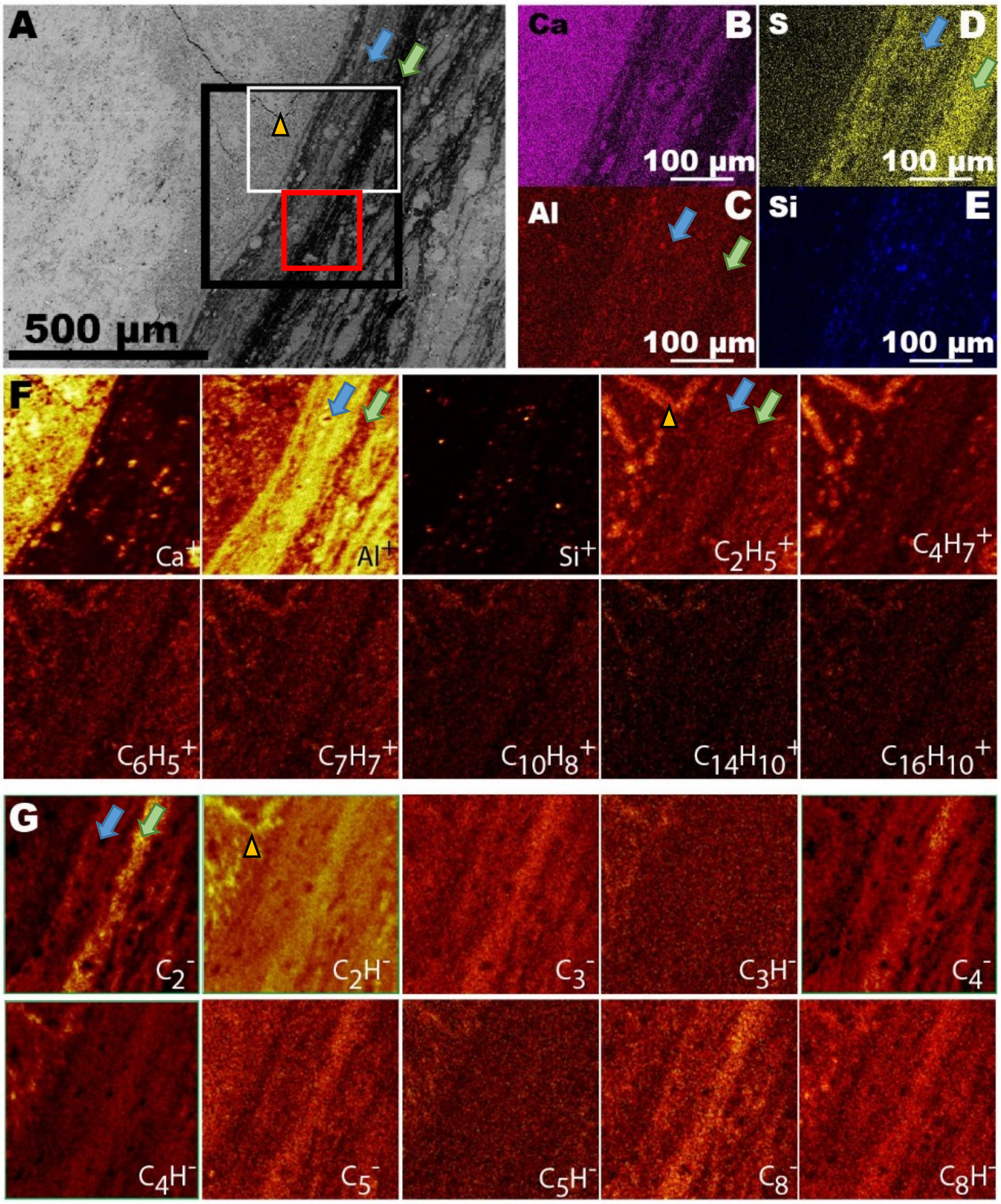

Fig. 2.10. Orbagnoux sample surface analyses. *(A) BSE image. Black square: ToF SIMS aera analysed; red square: Region of interest used to reconstruct spectrum; white square: Position of EDXS maps. OM appears in black, Ca-carbonate in light grey. (B-E) Elemental EDXS maps of calcium (B), aluminum (C), sulfur (D) and silicon (E). (F) Positive ion images of various inorganic (Ca+, Al+, Si+) and organic ($C_2H_5^+$, $C_4H_7^+$, $C_6H_5^+$, $C_7H_7^+$, $C_{10}H_8^+$, $C_{14}H_{10}^+$, $C_{16}H_{10}^+$) ions. (G) Negative ion images of various organic ions (C_n^- and C_nH^- ions). The blue arrows indicate the position of the aluminum/OM rich lamina; the green arrows, the OM-rich lamina and orange arrows, the veins.*

At low mass, between 0–200 u., the Orbagnoux laminae spectrum shows the following fragmentation pattern for hydrocarbon ions. First, the $C_2H_3^+$ ions dominated the $C_2H_y^+$

fragments representing (40% of the series intensity), while the saturated $C_2H_5^+$ ions accounted for 38% of the series intensity (Table 4). For the $C_3H_y^+$ fragments, 49% of the series intensity is generated by the saturated $C_3H_5^+$ and 34% by the unsaturated $C_3H_3^+$ (Table 4). For the $C_4H_n^+$, the intensity of $C_4H_3^+$, $C_4H_5^+$ and $C_4H_7^+$ ions represent equally ~23% of the signal, showing no clear dominance of fragment with a low or high H/C ratio (Table 4). In contrast, the $C_5H_y^+$ fragments show a dominance of ions characterized by a H/C<1 (Fig. 2.3B, Table 4). The same trend is observed for $C_6H_y^+$ fragment with the $C_6H_2^+$, $C_6H_3^+$ ions representing 11% and 14% of the series intensity (Table 4) whereas $C_6H_5^+$ ion accounted for 36%. Alike, the $C_7H_y^+$ series is dominated by the $C_7H_7^+$ ion (tropylium) while $C_7H_2^+$, $C_7H_3^+$ and $C_7H_5^+$ fragments with a low H/C represent a significant part (42% of the series intensity) (Fig. 2.4B and Table 4). The same fragmentation pattern is observed for the $C_8H_y^+$ fragments showing the domination of unsaturated ions ($C_8H_6^+$ and $C_8H_7^+$). The $C_8H_2^+$, $C_8H_3^+$ also represent a significant part of the $C_8H_y^+$ signal (19% and 15% respectively) (Table 4). Again, an unsaturated ion ($C_9H_7^+$) represent the main intensity of the $C_9H_y^+$ series signal and fragment with a low H/C ($C_3H_2^+$, $C_9H_3^+$) represent an important part (24%) of the $C_9H_y^+$ fragment series (Table 4).

All the ratios showing the relative importance of saturated over unsaturated $C_nH_y^+$ fragments $C_3H_5^+$/ $C_3H_3^+$, $C_4H_7^+/C_6H_5^+$, $C_4H_7^+/C_7H_7^+$, $C_5H_9^+/C_7H_7^+$, R4 to R9 and $R_{ali/aro}$ compare better the ratios measured in the PAH standard than in the aliphatic standard (Table 3, Fig. 2.8). Only the $C_2H_5^+$/ $C_2H_3^+$ ratio displays a value of 0.96 that is intermediate between phenanthrene (0.3) and nonadecanone (1.48). This suggests that OM in this lamina is highly unsaturated compared to a purely aliphatic molecule. Only the fragments with a small carbon number are highly saturated, as indicated by the high $C_2H_5^+$/ $C_2H_3^+$. This suggests that the Orbagnoux laminae OM is enriched in short aliphatic chains compared to long aliphatic chains. Moreover, a strong decrease of saturation indexes is observed from R4 to R9 with a pattern that is very similar to that observed in the PAH (Figs. 2.8E *versus* 2.8C and 2.8D). Nevertheless, the saturation indicators R4-R9 and the ratio $R_{ali/aro}$ are still an order of magnitude higher in the Orbagnoux laminae than in the PAH reference (phenanthrene). Altogether, these indicators point to a macromolecular structure where aliphatic side-chains are present, but in a relatively low abundance compared to unsaturated, likely aromatic structures.

In negative mode, the ions images of the hydrocarbon fragments (C_n^-, C_nH^-) are different from those obtained in positive mode (Figs. 2.10F *versus* 2.10G). Here, the negative ions images indicate that the organic fragment signal is higher in the OM-rich lamina than in the OM-Al laminae. The negative ions images are consistent with the SEM observations (Fig. 2.10D and G). The C_n^-/C_2^- ratios on the different OM laminae from the different areas are relatively low (Fig. 2.5A). Moreover, the C_nH^-/C_n^- ratios obtained in the four analysed areas of the sample (Fig. 2.9) are close to unity for the even carbon fragments and 0.3 for the odd carbon fragments (Fig. 2.5B). The laminae also contains C_2S^- and C_2SH^- (Fig. 2.11 and Supplementary Tables in Annexe). The C_2S^-/ C_2^- ratio is 0.07 for the Orbagnoux lamina shown in Figure 2.10G.

Table 4. *Values of intensity from CnHy*$^+$ *ions from the Orbagnoux lamina, Orbagnoux veins and Strelley Pool OM. Relative percentage of* $C_nH_i^+$ *calculated as in table 1*

	Orbagnoux lamina	Relative percentage of $C_nH_i^+$		Orbagnoux veins	Relative percentage of $C_nH_i^+$		Strelley Pool OM	Relative percentage of $C_nH_i^+$
C_2H^+	787	2,1%		85	0,8%		4	0,5%
$C_2H_2^+$	3475	9,3%		559	5,0%		48	5,6%
$C_2H_3^+$	15150	40,4%		4235	38,2%		372	43,4%
$C_2H_4^+$	2646	7,1%		640	5,8%		49	5,7%
$C_2H_5^+$	14471	38,6%		5391	48,6%		288	33,6%
$C_2H_6^+$	977	2,6%		172	1,6%		97	11,3%
$C_3H_2^+$	4110	6,3%		534	2,2%		53	3,1%
$C_3H_3^+$	22061	34,0%		4563	19,2%		448	26,4%
$C_3H_4^+$	2808	4,3%		366	1,5%		47	2,8%
$C_3H_5^+$	32205	49,7%		10511	44,3%		557	32,8%
$C_3H_6^+$	2506	3,9%		812	3,4%		228	13,4%
$C_3H_7^+$	772	1,2%		6704	28,2%		159	9,4%
$C_3H_8^+$	387	0,6%		246	1,0%		208	12,2%
$C_4H_2^+$	3581	8,4%		673	4,9%		41	4,7%
$C_4H_3^+$	9642	22,6%		1921	14,0%		148	17,1%
$C_4H_4^+$	3025	7,1%		621	4,5%		50	5,8%
$C_4H_5^+$	10507	24,6%		2350	17,1%		211	24,4%
$C_4H_6^+$	1520	3,6%		447	3,3%		36	4,2%
$C_4H_7^+$	10100	23,7%		5935	43,2%		244	28,2%
$C_4H_8^+$	951	2,2%		468	3,4%		91	10,5%
$C_4H_9^+$	3340	7,8%		1334	9,7%		43	5,0%
$C_5H_2^+$	2717	10,5%		446	6,9%		37	8,3%
$C_5H_3^+$	8280	32,0%		1131	17,4%		99	22,2%
$C_5H_4^+$	1180	4,6%		203	3,1%		23	5,2%
$C_5H_5^+$	5546	21,5%		1057	16,3%		102	22,9%
$C_5H_6^+$	1354	5,2%		279	4,3%		30	6,7%
$C_5H_7^+$	3752	14,5%		1239	19,1%		73	16,4%
$C_5H_8^+$	503	1,9%		180	2,8%		24	5,4%
$C_5H_9^+$	2197	8,5%		1808	27,9%		48	10,8%
$C_5H_{10}^+$	308	1,2%		143	2,2%		10	2,2%
$C_6H_2^+$	2567	11,5%		389	7,3%		38	7,9%
$C_6H_3^+$	3165	14,2%		505	9,4%		45	9,3%
$C_6H_4^+$	1134	5,1%		211	3,9%		13	2,7%
$C_6H_5^+$	8007	36,0%		1810	33,8%		197	40,8%
$C_6H_6^+$	2169	9,8%		430	8,0%		36	7,5%
$C_6H_7^+$	2337	10,5%		614	11,5%		51	10,6%
$C_6H_8^+$	461	2,1%		138	2,6%		18	3,7%
$C_6H_9^+$	1560	7,0%		766	14,3%		51	10,6%
$C_6H_{10}^+$	183	0,8%		89	1,7%		14	2,9%

$C_6H_{11}^+$	574	2,6%		361	6,7%		14	2,9%
$C_6H_{12}^+$	80	0,4%		47	0,9%		6	1,2%
$C_7H_2^+$	1946	14,0%		212	6,4%		23	3,9%
$C_7H_3^+$	2640	19,0%		334	10,1%		29	4,9%
$C_7H_4^+$	576	4,1%		94	2,9%		271	45,5%
$C_7H_5^+$	1347	9,7%		279	8,5%		39	6,5%
$C_7H_6^+$	390	2,8%		70	2,1%		17	2,9%
$C_7H_7^+$	4630	33,3%		1278	38,8%		120	20,1%
$C_7H_8^+$	638	4,6%		184	5,6%		17	2,9%
$C_7H_9^+$	684	4,9%		228	6,9%		23	3,9%
$C_7H_{10}^+$	192	1,4%		42	1,3%		14	2,3%
$C_7H_{11}^+$	653	4,7%		368	11,2%		26	4,4%
$C_7H_{12}^+$	83	0,6%		39	1,2%		8	1,3%
$C_7H_{13}^+$	144	1,0%		169	5,1%		9	1,5%
$C_8H_2^+$	1580	19,2%		187	10,7%		8	4,3%
$C_8H_3^+$	1299	15,8%		159	9,1%		14	7,6%
$C_8H_4^+$	270	3,3%		35	2,0%		8	4,3%
$C_8H_5^+$	533	6,5%		73	4,2%		9	4,9%
$C_8H_6^+$	1123	13,7%		193	11,0%		19	10,3%
$C_8H_7^+$	1095	13,3%		214	12,2%		25	13,6%
$C_8H_8^+$	390	4,7%		102	5,8%		13	7,1%
$C_8H_9^+$	1151	14,0%		447	25,5%		30	16,3%
$C_8H_{10}^+$	199	2,4%		70	4,0%		11	6,0%
$C_8H_{11}^+$	232	2,8%		77	4,4%		16	8,7%
$C_8H_{12}^+$	90	1,1%		22	1,3%		11	6,0%
$C_8H_{13}^+$	169	2,1%		120	6,9%		12	6,5%
$C_8H_{14}^+$	35	0,4%		17	1,0%		6	3,3%
$C_8H_{15}^+$	47	0,6%		35	2,0%		2	1,1%
$C_9H_2^+$	1018	11,7%		143	7,5%		8	4,0%
$C_9H_3^+$	1109	12,8%		146	7,6%		17	8,6%
$C_9H_4^+$	185	2,1%		34	1,8%		4	2,0%
$C_9H_5^+$	518	6,0%		64	3,3%		12	6,1%
$C_9H_6^+$	323	3,7%		53	2,8%		11	5,6%
$C_9H_7^+$	3312	38,1%		729	38,0%		66	33,3%
$C_9H_8^+$	672	7,7%		134	7,0%		19	9,6%
$C_9H_9^+$	566	6,5%		172	9,0%		20	10,1%
$C_9H_{10}^+$	195	2,2%		56	2,9%		10	5,1%
$C_9H_{11}^+$	412	4,7%		240	12,5%		9	4,5%
$C_9H_{12}^+$	115	1,3%		48	2,5%		3	1,5%
$C_9H_{13}^+$	107	1,2%		34	1,8%		8	4,0%
$C_9H_{14}^+$	72	0,8%		5	0,3%		5	2,5%
$C_9H_{15}^+$	67	0,8%		45	2,3%		4	2,0%
$C_9H_{16}^+$	3	0,0%		9	0,5%		1	0,5%
$C_9H_{17}^+$	9	0,1%		6	0,3%		1	0,5%

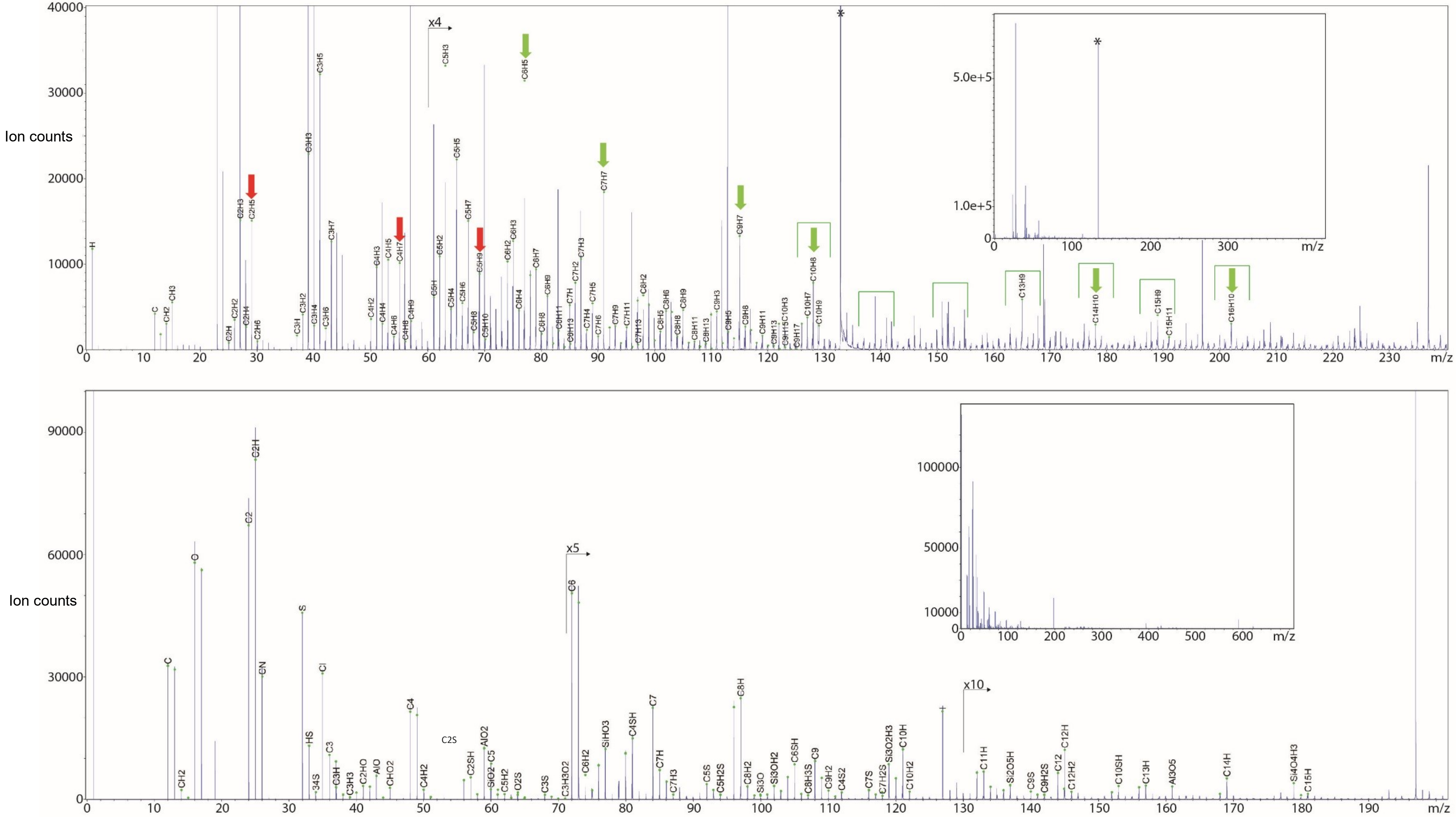

Fig. 2.11. ToF SIMS spectra of the Orbagnoux lamina OM in bunched mode after sputtering. *Upper spectrum: positive mode. Red arrows indicat the presence of saturated ions fragments (typical of* n*-alkanes chains). Green arrows point the presence of unsaturated fragments (likely generated by aromatics) Green brackets: PAH fragment series. Lower spectrum: negative mode. *: Cs+ peaks due to the presence of Cesium in the chamber.*

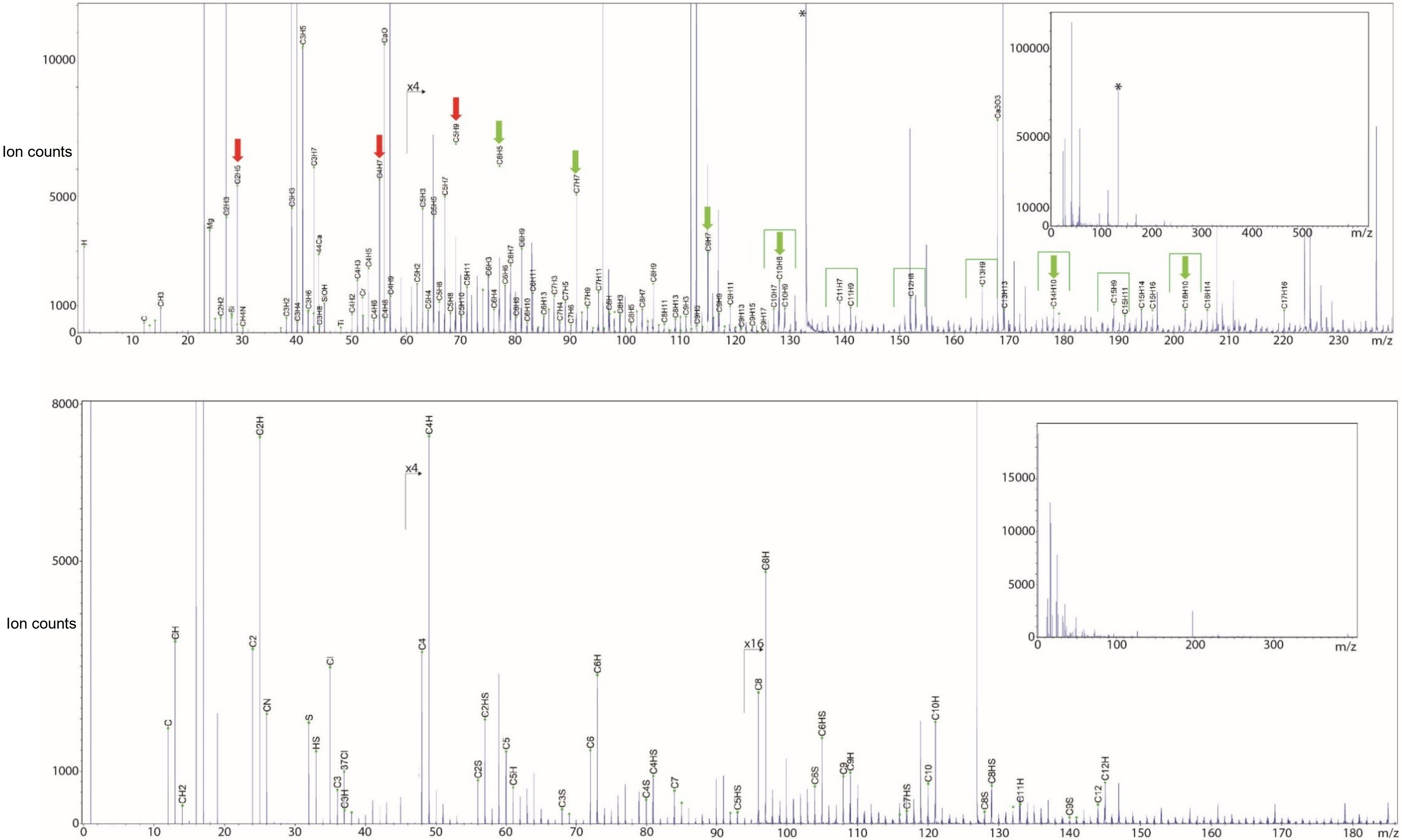

Fig. 2.12. ToF SIMS spectra of the Orbagnoux veins in bunched mode after sputtering. *Upper: spectrum: positive mode. Red arrows indicate the presence of saturated ions fragments (typical of n-alkanes chain). Green arrows point the presence of unsaturated fragments (likely generetad by aromatics). Green brackets: PAH fragment series. Lower spectrum: negative mode. *: Cs+ peaks due to the presence of Cesium in the chamber.*

The positive and negative images show also some correlated heterogeneities. In the positive mode, veins (orange arrow in Fig. 2.10) appears enriched in saturated hydrocarbon fragments ($C_2H_5^+$ and $C_4H_7^-$). The Orbagnoux veins spectrum displays the same fragments at high mass as previously observed for the laminae ($C_6H_5^+$, $C_7H_7^+$, $C_9H_7^+$, $C_{10}H_8^+$, $C_{14}H_{10}^+$ and $C_{16}H_{10}^+$ ions) together with the PAH fragments series (Fig. 2.12). Saturated fragments are more abundant in the veins than in the laminae, as indicated by all the positive ion ratio ($C_2H_5^+/C_2H_3^+$, $C_3H_5^+/C_3H_3^+$, $C_4H_7^+/C_6H_5^+$, $C_4H_7^+/C_7H_7^+$, $C_5H_9^+/C_7H_7^+$, R1-R9 and $R_{ali/aro}$) shown in Table 3 and Fig. 2.8. This higher content of saturated hydrocarbon fragments is also supported by the patterns of fragmentation. For the $C_2H_y^+$ series, the dominant peak is $C_2H_5^+$ (48% of the series intensity), followed by $C_2H_3^+$ (38%) (Table 4). Similarly, the $C_3H_y^+$ fragments are dominated by $C_3H_5^+$ (44%) and $C_3H_7^+$ (28%) ions (Table 4). In the veins, the distribution of the $C_4H_n^+$ and $C_5H_n^+$ fragments also indicate the domination of fragment with a H/C>1: $C_4H_7^+ + C_4H_9^+$ ions representing 52% of the $C_4H_y^+$ signal and $C_5H_7^+ + C_5H_9^+$ ions, 46% of the $C_5H_n^+$ total intensity (Table 4). The higher abundance of saturated ions with H/C>1 (relative to those with H/C≤1) in the veins compared to the laminae is best seen with the C_5Hy^+ (Fig. 2.3B) and $C_7H_y^+$ (Fig. 2.4B) series. For all $C_nH_y^+$ with n=6-9, the predominant ions in the veins are the same as those in the laminae ($C_6H_5^+$, $C_7H_7^+$, $C_8H_9^+$ and $C_9H_7^+$) (Table 4). However, fragments of these series with H/C>1 such as $C_6H_9^+$, $C_7H_{11}^+$, $C_8H_{13}^+$, and $C_9H_{11}^+$ are much more abundant in the veins.

In negative mode, the C_n^-/C_2^- ratios in the Orbagnoux veins are low and close to the values from the adjacent laminae, with the exception of C_3^-/C_2^- that is higher in the veins (Fig. 2.5A). In the veins, the C_nH^-/C_n^- ratio values for even carbon ions are close to 2 and for odd carbon number close to 0.5 (Fig. 2.5B). In contrast, C_nH^-/C_n^- in the laminae are all inferior to 1.24 (though with a similar even/odd distribution). C_2S^- ion is also detected within the veins, with a C_2S^-/C_2^- ratio of 0.06 that is similar to that in the adjacent laminae (0.07).

1.1.1 Strelley Pool OM

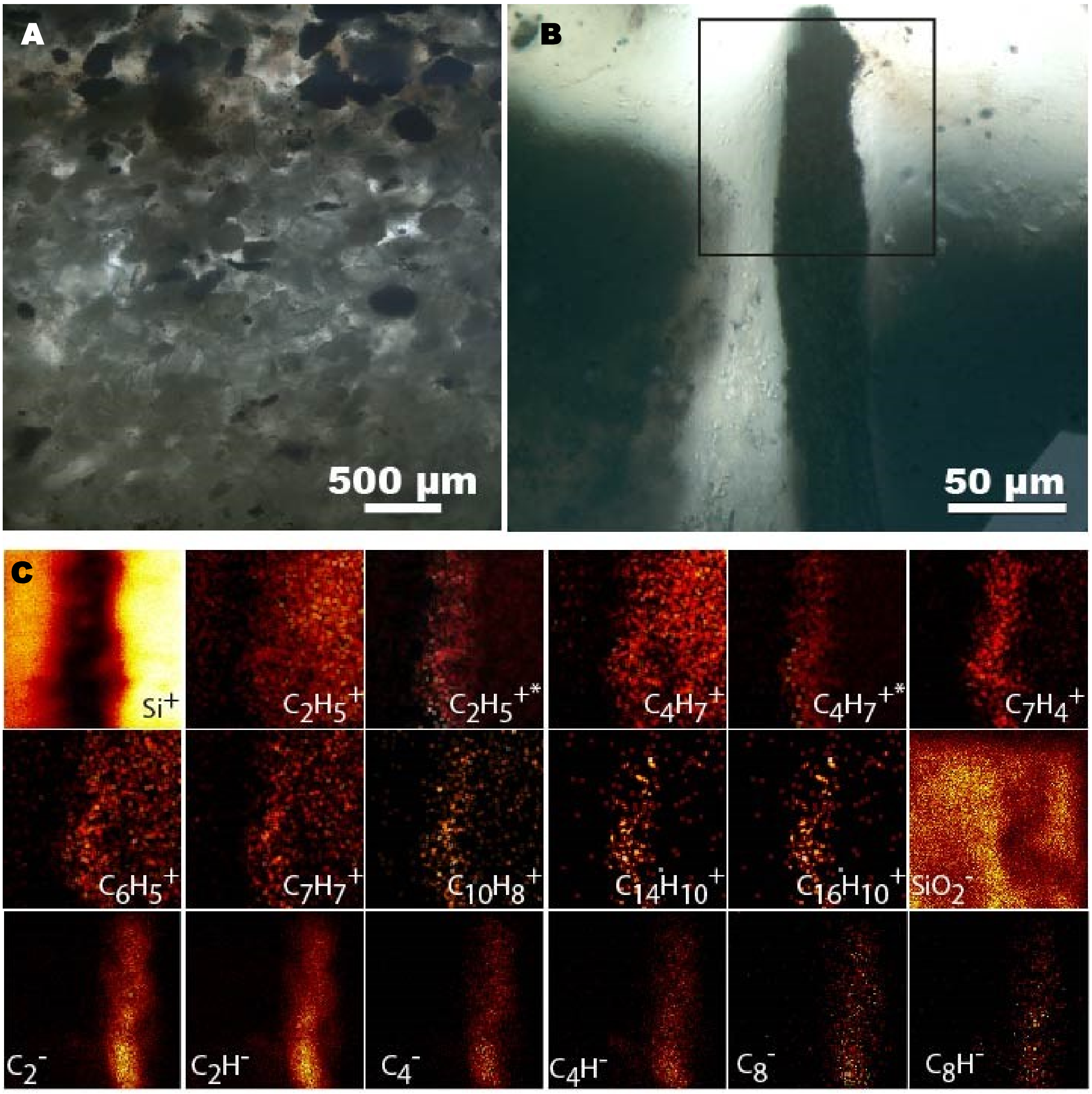

Fig. 2.13. Optical (A-B) and ToF-SIMS (C) images of the Strelley Pool Formation chert sample. *(A) Photomicrograph showing a general view of the clastic grains in transmitted light. (B) Phomicrograph of the OM clasts analyzed with ToF-SIMS. (C) Various ToF-SIMS ion images from the area boxed in (B). Starting from the top left image: positive ion signal images of* Si^+, $C_2H_5^+$, $C_2H_5^{+}$ **= normalized to the total signal,* $C_4H_7^+$, $C_4H_7^+$ **=normalized to the total signal,* $C_7H_4^+$, $C_6H_5^+$, $C_7H_7^+$, $C_{10}H_8^+$, $C_{14}H_{10}^+$, $C_{16}H_{10}^+$, *and negative ion images of* SiO_2^-, C_2^-, C_2H^-, C_4^-, C_4H^-, C_8^-, *and* C_8H^-.

The Strelley Pool Formation chert is characterized by the accumulation of siliciclastic and volcanoclastic sediment (Fig. 2.13A) interspersed with elongated OM grains. These grains are probably parts of microbial mats formed in the ocean column or in nearby environment that accumulated with the sediment and silicified (Allwood et al., 2006a, 2007). The OM analyzed in ToF-SIMS is shown in Figure 2.13B. The Si^+ ion image shows that the OM grain is embedded within the chert matrix. Moreover, the Si^+ ion image shows a higher intensity on the right than on the left of the OM. Such variation of the intensity shows the charge effect build-up during the analysis of an isolating material (here quartz). The TOF-SIMS images of small hydrocarbon fragments ($C_2H_5^+$, $C_4H_7^+$) were normalized by the total ion image (pixel-by-pixel division) to remove this secondary ion yield effect.

In positive mode, the spectrum of Strelley Pool OM shows the presence of relatively high peaks of unsaturated fragments ($C_6H_5^+$, $C_7H_7^+$, $C_9H_7^+$, $C_{10}H_8^+$, $C_{14}H_{10}^+$ and $C_{16}H_{10}^+$ ions) as well as fragment series of unsaturated ions (Fig. 2.14). The spectrum also contains peaks generated by saturated molecules (red arrows in Fig. 2.14): $C_2H_5^+$, $C_4H_7^+$ and $C_5H_9^+$. The saturation indexes $C_2H_5^+/C_2H_3^+$ (0.77), $C_3H_5^+/C_3H_3^+$ (1.23), $C_4H_7^+/C_7H_7^+$ (2.03), $C_5H_9^+/C_7H_7^+$ (0.40), $C_4H_7^+/C_6H_5^+$ (1.24) and the $R_{ali/aro}$ of 1.87 (Table 3), are all smaller than those recorded in the Orbagnoux laminae.

The strongest peak of the $C_2H_y^+$ series is $C_2H_3^+$ (43% of series) intensity, followed by $C_2H_5^+$ (33%) (Table 4). Interestingly, the highly hydrogenated $C_2H_6^+$ fragments represent a significant part of the $C_2H_y^+$signal (11%), whereas much lower proportions were measured in the Orbagnoux laminae (2.6%) and in the nonadecanone (1.69% of the series). A possible interpretation is the abundance of short aliphatic side chains with one or two carbons in the kerogen. Breaking of these short chains yields $CH_3\cdot$ and $C_2H_5\cdot$ radicals, which will abundantly generate $C_2H_6^+$ fragments by hydrogenation and/or recombination. Conversely, in the long aliphatic chains of Orbagnoux and of the nonadecanone, the abundance of -CH_2- groups relative to terminal -CH_3 groups would likely generate abundant $CH_2\cdot$ and $C_2H_4\cdot$ radicals, which after hydrogenation and/or recombination mainly yield $C_2H_5^+$ fragments. The $C_3H_y^+$ series is dominated by $C_3H_5^+$, like in Orbagnoux. However, the highly hydrogenated fragment $C_3H_8^+$ is relatively abundant in this series (12.2%) compared to its abundance in the Orbagnoux laminae (0.6%) and in the nonadecanone (3.1%) (Table 4), similarly pointing to a higher relative abundance of propyl- or isopropyl- chains in the kerogen. The $C_4H_y^+$ fragments are dominated by $C_4H_7^+$and $C_4H_5^+$. The highly hydrogenated fragment $C_4H_9^+$ is relatively less abundant in the $C_4H_y^+$ series (4.98%) compared to the Orbagnoux laminae (7.8%) and nonadecanone (24.3%). Similarly, the highly saturated fragment $C_5H_{10}^+$ (2.24%) is close to that in Orbagnoux laminae (1.19%) and lower than in nonadecanone (5.4%). The same trend can be observed for $C_6H_{11}^+$ and $C_7H_y^+$ with $y \geq 11$. In contrast, $C_8H_y^+$ with $y \geq 11$, and $C_9H_y^+$ with $y \geq 11$ commonly are a few times higher than in Orbagnoux but all intensities for the $C_8H_y^+$ and $C_9H_y^+$ series are very low, close to the detection limit. Fragmentation patterns for these series as well as the R8 and R9 ratio in the Strelley Pool OM (Table 3 and Fig. 2.8E) should be considered with care, as counting errors and extremely faint chamber contamination can become significant at such low count rates. The C_7H_y+ series show a distinctive distribution (Fig. 2.4C), strongly dominated by $C_7H_4^+$ (45% of the series) and $C_7H_7^+$ (Fig. 2.4C, Table 4). Consequently, while R4-R6 are higher in the Strelley Pool OM than in the Orbagnoux laminae, the R7 ratio is lower in the former (Table 3, Fig. 2.8E). Interestingly, $C_7H_4^+$ and $C_7H_7^+$ are relatively in low abundance relative to $C_7H_3^+$ in phenanthrene. The two former ions were likely generated by aromatic structures with short, aliphatic side chains, which are absent in phananthrene. The lower R7 ratio in the Strelley Pool OM compared to Orbagnoux's laminae is consistent with the presence of shorter aliphatic side chains grafted onto aromatics.

In negative mode, the spectrum shows the presence of silicon fragments ($Si_xO_y^-$ ions) from the chert matrix embedding the OM. The intensity of the negative ion image of SiO_2^- ions is more homogeneous than the Si^+ ion image, although increased intensity is observed in the vicinity of organic matter (Fig. 2.13C), similar to dynamic NanoSIMS images of $^{12}C^-$ and $^{28}Si^-$ (Oehler et al., 2009). The C_n^-/C_2^- ratio values are low, close to the values obtained for the phenanthrene standard (Fig. 2.5A), and systematically lower than those recorded in Orbagnoux, again pointing to a more aromatic structure with shorter aliphatic chains in Strelley Pool OM compared to the latter. The C_nH^-/C_n^- ratio values are also low and range between 0.23 and 1.07 (Fig. 2.5B). Finally, sulfur is detected in the Strelley Pool OM with a C_2S^-/C_2^- of 0.011.

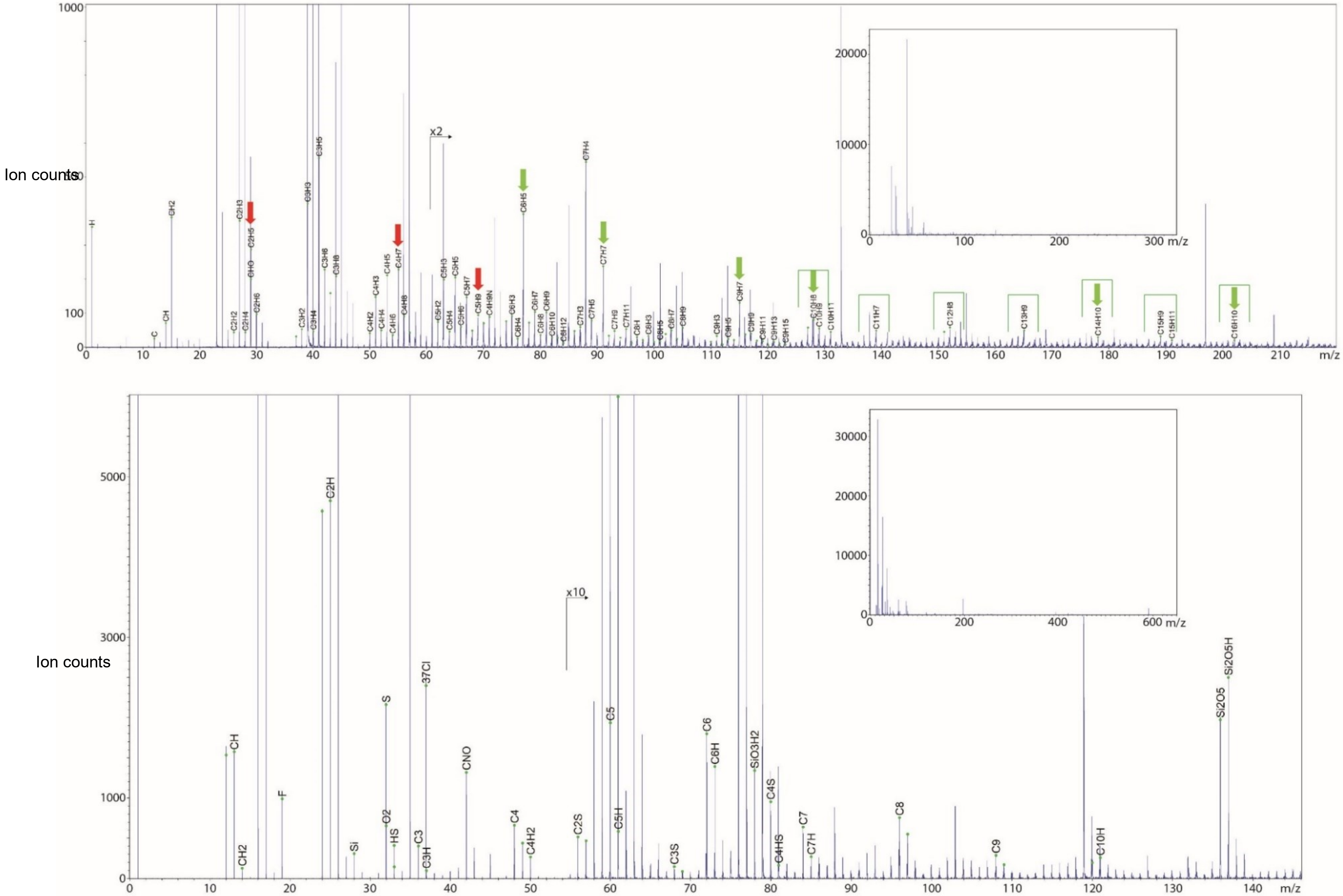

Fig. 2.14. ToF SIMS spectra of the Strelley Pool Chert OM in bunched mode, after sputtering. *Upper spectrum: positive mode. Red arrows indicate the presence of saturated ions fragments (typical of n-alkanes chains). Green arrows point the presence of unsaturated fragments (typical of aromatics). Green brackets: PAH fragment series. Lower spectrum: negative mode.*

5 Discussion

5.1 Standard fractionation

5.1.1 The impact of low dose sputtering.

The calculation of ion dose indicates that the static limit is reached rapidly by the Ar^+ sputtering. Keeping the PIDD below the static limit appears important for reducing the molecular damage on the surface and obtaining detailed information on molecular structures during ToF-SIMS analysis. Although the sputtering causes damages and takes away the possibilities to performed static SIMS especially with monoatomic ions, but its offers the possibilities to perform depth profiles, 3D imaging and remove surface contamination to make analysis on "clean" surface (Thiel and Sjövall, 2014). However, our observations on standards and previous studies using low energy monoatomic ion beam show the possibility to perform molecular analyses with sputtering or depth profiling with monoatomic ion beam (i.e. with Cs^+ : Cramer et al., (2008); Mine et al., (2007) and with Ar^+: Fadel et al, in prep, see chapter 2). Moreover, the low energy of the ion beam (250 eV) used during sputtering is expected to cause minimal molecular damage to the sub-surface as the low energy is deposited close to the surface and minimal molecular damages deep into the material. The relatively low damage caused by low energy ions at the sub surface has been modeled and studied by comparison of damage generated by impact of 15keV Au_3^+ and cluster C_{60}^+ ions (Russo et al., 2007; Vickerman and Gilmore, 2011). These studies indicate that the low energy of each carbon atom in C_{60}^+ (~250eV, i.e. 15keV/60) induced less damage to the surface compared to the high energy of each gold atom in Au_3^+ (5keV, i.e. 15keV/3) (Russo et al., 2007; Vickerman and Gilmore, 2011). Moreover, the different ratios ($C_4H_7^+/C_{14}H_{10}^+$ and $C_4H_7^+/C_6H_5^+$ in Fig. 2.1) indicate clearly that the signal of unexpected saturated ion from the phenanthrene is reduced significantly by the sputtering. On the opposite, the 2-nonadecanone show that ions generated before and after sputtering were characterized by an increase of saturated ion signals. These differences on calculated ratios from these two different standards indicate that surface contamination was removed by the low energy Ar^+ sputtering with relatively low damages on the sub surface of analyzed material. However, the used of monoatomic ion for sputtering have induced a decrease of ion yield especially for high mass molecule (i.e. the parent ion M^+ and associated ions) (Belu et al., 2003; Thiel and Sjovall, 2011; Vickerman and Gilmore, 2011). In particular, we observed that $C_nH_y^+$ fragments with n>7 are relatively depleted in H (Fig. 2.8C and Table 1) compared to smaller fragments in 2-nonadecanone, a molecule that comprises a chain of sixteen CH_2 groups. This indicates that our analytical conditions strip a larger proportion of H atoms from larger fragments compared to smaller ones.

5.1.2 The 2-nonadecanone standard

The 2-nonadecanone standard was analyzed to understand the fragmentation pattern of long aliphatic chains after Ar^+ sputtering and under Bi_3^+ analysis beam. In positive mode at low mass, the pattern of $C_2H_y^+$, $C_3H_y^+$, $C_4H_y^+$and $C_5H_y^+$ ion series with the dominance of ions with a H/C>1 (Fig. 2.2 and Table 1), is similar to the peak distribution of aliphatic standards reported in the previous studies using 11 keV Cs^+, 15 keV In^+, and 15 keV Ga^+ ions (Spool, 2004; Toporski and Steele, 2004). Moreover, the different ratios introduced here clearly indicate the predominance of saturated fragments over unsaturated fragment (Table 3, Figs. 2.3A, 2.4A, and 2.8A-B). For fragments with n<6, $C_nH_{2n+1}^+$ and/or $C_nH_{2n-1}^+$ fragments dominate (Table 1). In contrast, the predominance of ions with H/C>1 for the $C_nH_y^+$ fragments with $6 \leq n \leq 9$ is notable, with a dominance of $C_nH_{2n-3}^+$ ions, but some ions with H/C~1 are relatively significant (Table 1, Figs. 2.3A *versus* 4A). The distribution pattern of the $C_7H_y^+$ ions illustrates this generation of unsaturated ions, in particular with the tropylium ion ($C_7H_7^+$), from a saturated molecule (Fig. 2.3A). Dehydrogenation and rearrangement of fragments under the ion beam bombardment are proposed to explain the presence of such medium to low H/C fragments (Delcorte et al., 1995). Although these phenomena are observed under our experimental condition in particular for carbon numbers ≥6, we only have a relatively low abundance of unsaturated fragments with carbon numbers <6 generated by long chain aliphatic molecules (Table 1). As reported by Spool (2004); Toporski and Steele (2004), parent ions with long carbon chains typical of *n*-alkanes appear difficult due to the low count at high mass. Thus the presence of *n*-alkanes is best seen with saturated fragments with carbon numbers <6 in our condition but the detection of long carbon chains appears difficult due to the difficulty to ionize long-chain aliphatic hydrocarbons (Spool, 2004; Thiel and Sjövall, 2014).

In negative mode and at low mass, the nonadecanone standard spectrum shows the presence of C_n^- and C_nH^- at low mass. The presence of these types of ions can be explained the production of fragments with a very low H/C from the molecule under the ToF-SIMS. Moreover, the spectrum shows the significant presence of $C_nH_y^-$ fragments with a number of hydrogen (y) that is comprised between 1 and 3 (Fig 2.2). The graph of the C_n^-/C_2^- indicates that aliphatic molecule generates a significant amount of C_n^- fragments with high carbon numbers (Fig. 2.5A). Moreover, semi-quantification with negative ion ratio (based C_2H^-/C_2^-) have already been used to quantify the aliphatic or aromatic character of asphaltenes, graphite and carbon blacks (Larachi et al., 2004). Hence, the high C_nH^-/C_n^- values obtained from the 2-nonadecanone is due to its high H/C value and the presence of a long aliphatic chain (Fig. 2.5B).

5.1.3 PAH standards

In positive mode, the spectrum of phenanthrene standard shows the presence of the parent ions with a series of peaks due to the loss or capture of protons (Fig. 2.6). This association of several peaks with the parent ion is typical of PAHs (Delcorte et al., 1 997; Sakamoto et al., 2004; Toporski and Steele, 2004). Moreover, the presence of PAH fragments series produced by CH fragment loss is also well established in PAH (Sakamoto et al., 2004).

At low mass, the strongest peaks are not the same as those observed by Toporski and Steele (2004) using Ga^+ for analysis. In our case, the $C_2H_5^+$, $C_3H_5^+$, $C_4H_7^+$and $C_5H_9^+$ ions are not predominant (Fig. 2.7). The presence of these peaks has been attributed to the possibility to produce high H/C fragments from aromatic species during ToF SIMS analysis or to contaminations such as solvent residues and/or absorbed alkanes (Sakamoto et al., 2004; Steele et al., 2001; Toporski and Steele, 2004). These saturated compounds are removed after Ar^+ sputtering (Fig. 2.1), and not just fragmented away (as they are well preserved in the nonadecanone after sputtering). Hence, high abundance of such saturated fragments can be attributed to airborne contamination and the adsorption of saturated molecules (possibly *n*-alkanes). Moreover, the fragments with very low H/C ratios are predominant: $C_4H_3^+$, $C_5H_3^+$, $C_6H_2^+$, $C_7H_3^+$ and $C_8H_2^+$ with clear patterns of rapid signal decrease with increasing carbon number in the different $C_nH_y^+$ series. (Fig. 2.3A, 2.4A and Table 1) This predominance of the unsaturated fragments is also supported by the very low values obtained from all saturation indexes of Table 3. Thus, fragments listed above are indicative of PAHs and aromatics species. Interestingly, peaks attributed to the ions $C_6H_5^+$ and $C_7H_7^+$ which are usually attributed to aromatic species (Spool, 2004; Thiel and Sjövall, 2014; Toporski and Steele, 2004) are not predominant. A possible reason for this might be that these fragments originate mainly from mono-aromatic groups, and those fragments are less expressed in PAH and/or alkylated PAH. The ratios ($C_4H_7^+/C_6H_5^+$, $C_4H_7^+/C_7H_7^+$, $C_5H_9^+/C_7H_7^+$ in Table 3) based on these aromatic ions and saturated fragments have been introduced to address the aromaticity or aliphaticity of polymers (Petrat et al., 1994). Although such ratios based on two ions can appear useful to determine the aromatic content of organic matter, the production of low H/C fragments (i.e; $C_7H_7^+$) by alkanes due to dehydrogenation as seen above in the 2-nonadecanone standard, and the relative low presence of these ions in the phenanthrene standard show the limitation of the use of these simple ratios. Ratio based on the lowest mass hydrocarbon fragments ($C_2H_5^+/C_2H_3^+$

and $C_3H_5^+/C_3H_3^+$), and the ratio $C_4H_7^+/C_6H_5^+$ (see section 4.14.) also appear useful to investigate the relative aromaticity and aliphaticity of an unknown (macro)molecule (Table 3). Ratio based on the sum of aliphatic-derived ions and aromatic-derived ions can also be used with more confidence ($R_{ali/aro}$, Fig. 2.8B, which is 40 times higher in the 2-nonadecanone than in the phenanthrene). Moreover, constraining the presence of saturated or unsaturated molecules from a sample with low mass fragments can be based on the patterns of the different $C_nH_y^+$ series (Figs. 2.3 and 2.4) and/or the ratios based on these series (R4 to R9, Table 3). Here, we show the possibility to determine the presence of aromatics with ToF-SIMS analysis using low mass fragments. Moreover, due to the relative stability of aromatics, the parent PAHs ions can be detected and identified in positive mode (Spool, 2004; Thiel and Sjövall, 2014; Toporski and Steele, 2004).

In negative mode, the parent ion of phenanthrene is absent. Moreover, C_n^- fragments show a predominance of C_2^- ions and low C_n^-/C_2^- for n>2 (Fig. 2.5). Conversely to the long chain hydrocarbons, the PAH standard produces C_n^- chains with a low number of carbon (maximum for 2 carbons). In the C_nH^- series, the phenanthrene standard displays low C_nH^-/C_n^- compared to the 2-nonadecanone as expected due to its lower H/C ratio (Larachi et al., 2004). Moreover, $C_nH_2^-$ fragments have very low intensities or are absent; and the $C_nH_y^-$ fragments with higher number of hydrogen (y>3) are also absent. Interestingly, the data obtained from the deuterated anthracene (Fig. 2.8 and Table 2) and the absence of isotopic exchange with the GC-MS analysis indicates that the production of these C_nH^- ions can be due to the capture of hydrogen by C_n^- ions rather than the preservation of original C–H bonds.

5.2 Orbagnoux heterogeneity

The Orbagnoux rocks from the bituminous laminites present the accumulation of highly aliphatic OM in dark lamina. This OM is characterized by a high atomic H/C ratio of 1.44 (Mongenot et al., 1997, 1999). FTIR spectra reported from previous studies and measured in our sample using reflectance FTIR (not shown) show the presence of aliphatic moieties (Mongenot et al., 1997). The aliphatic character is also confirmed by the high values of the hydrogen index (Espitalie et al., 1985) (780 to 960 mg hydrocarbons per g) from the different subfacies of the bituminous laminites (Mongenot et al., 1999; Tribovillard et al., 2000). The study of isolated OM have also indicated that this OM is composed of gel-like nanometric amorphous sulfur rich organic particles (Mongenot et al., 1997). The homogenous high sulfur content within the different subfacies has played a major role in the preservation of the organic matter present in the laminae. Moreover the analyses of the bitumen and of pyrolysis products also indicated that most of the aliphatic OM derived from the sulfurization of cyanobacterial and algal lipids that are labile molecules (Mongenot et al., 1997; Van Kaam-Peters and Sinninghe Damsté, 1997).

In positive mode, the images show higher signal of hydrocarbons in the Al-rich laminae (blue arrow in Fig. 2.10) while the signal from the organic rich lamina is substantially lower (green arrow in Fig 2.10). However, several ratios (based on organic and inorganic ions, not shown) indicated that the organic matter present in these two types of lamina has the same composition. This observation indicates a strong and variable interference of the matrix with the total organic signal (as reported by Lindgren et al. (2014, 2012)) and the difficulty to ionize and extract ions from the kerogen (after Ar^+ sputtering). The $C_2H_5^+$ and $C_4H_7^+$ ion images confirmed the homogenous distribution of aliphatic compounds in the laminae (Fig 2.10 F), and their relative importance in the spectrum reconstructed from the Orbagnoux laminae (Fig. 2.11). The pattern of $C_nH_y^-$ series from the Orbagnoux laminae also confirmed the importance of unsaturated fragment (Figs. 2.3A, 2.4A; Table 4). These unsaturated fragments (Figs. 2.3B, 2.4B), the presence of the series of unsaturated fragments and the attribution of several peaks to PAHs ($C_{10}H_8^+$, $C_{14}H_{10}^+$ and $C_{16}H_{10}^+$) with their associated peaks (due to the loss or capture of proton) (Fig. 2.11) indicate that the OM surface of the Orbagnoux laminae contains aromatic molecules. Accordingly, previous studies have shown the presence of aromatic moieties with solid-state ^{13}C-nuclear magnetic resonance from Orbagnoux kerogen (Mongenot et al., 1997, 1999). Among these aromatic-derived fragments $C_7H_7^+$ dominate strongly (Fig. 2.11). The strong dominance of the $C_7H_7^+$ signal in the $C_7H_y^+$ series and the weak signal of $C_7H_y^+$ with $y>7$ (Fig. 2.4B) supports that $C_7H_7^+$ ions come from single aromatic rings (Hook and Scurr, 2016), possibly alkylated, rather than stripping of H from long aliphatic chains (c.f. Fig. 2.4A).

A second type of organic matter is easily recognized in positive ion image of $C_2H_5^+$ and $C_4H_7^+$ fragments (orange arrow in Fig. 2.10F) in veins cutting across the carbonate of the Orbagnoux stromatolite and possibly also present patches. However, organic matter in these veins was not visible in SEM EDX-S map (Fig. 2.10D), indicating that it can be only detected with sensitive techniques such as ToF-SIMS. Similar to the adjacent laminae, the veins also contain aliphatic and aromatic molecules (red and green arrows on the spectrum reconstructed from this area in Fig. 2.12). However, compared to the laminae, these veins are enriched in highly saturated hydrocarbons. All the different saturation indexes and the ratio of aliphatic ions/ aromatics ions show the predominance of saturated fragments in positive mode (Fig. 2.8A-B, Table 3). This higher abundance of saturated fragments within the veins is also confirmed by the distribution of the different $C_nH_y^+$ series (Figs. 2.3, 2.4 and Table 4). Importantly, from both Orbagnoux veins and laminae, the $C_nH_y^+$ series with $6 \leq n \leq 9$ show the predominance of the $C_6H_5^+$, $C_7H_7^+$, $C_8H_9^+$ and $C_9H_7^+$ ions (respectively) that are generated by aromatics species (Toporski and Steele, 2004) but also by the dehydrogenation of saturated molecules (Delcorte et al., 1995). Hence, for these latter series, making semi-quantification based only on the distribution of the ions requires to ignore ions that can be produced by either aromatics or dehydrogenation of aliphatics, that is $C_9H_7^+$ with H/C~1. Altogether, the positive ion ToF-SIMS data indicate that the aliphaticity of the veins OM is superior to the lamina OM. However, the origin of this OM present within the veins is unknow. This highly aliphatic OM in veins and in patches in the carbonates may represent parts of the bitumen fraction of the Orbagnoux sample (19% of the TOC reported by Van Kaam-Peters and Sinninghe Damsté (1997)). They may be in their original place in these veins and patches. Alternatively, such bitumen could have been dissolved from the kerogen-rich laminae in the dichloromethane/methanol (DCM/MeOH) solution during the first cleaning procedure and migrated and/or remained in the small open veins and porosities of the carbonate layers. After 2 hours of cleaning in DCM/MeOH, the solvent solution displayed a yellow-brownish color due to the dissolution of the bitumen composed mainly of polar compounds comprising sulfur-bound alkanes and hopanoids (Van Kaam-Peters and Sinninghe Damsté, 1997). These observations show the possibility to find micro-scale molecular heterogeneities within a sample and to semi-quantify the aliphaticity/aromaticity of different organic matter with low mass fragments present in a sample at the micro-scale, in positive mode.

In negative mode, the C_n^- and C_nH^- ion images indicate that the production of negative hydrocarbon fragments from the kerogen is relatively unaffected by matrix effects (Fig. 2.10G) compared to the positive ions. Similar to the positive ion, the negative ions images display more hydrogenated fragments in the veins compared to the laminae. The higher abundance of hydrogenated fragments in veins is also confirmed by the C_nH^-/C_n^- ratio graph (Fig. 2.5B). Such negative ion ratios have been used to constrain the aromaticity of OM (Larachi et al., 2004) and indicates that the OM present in the lamina is less aliphatic than that in the veins. However, the C_n^-/C_2^- ratios in veins are very similar to those in laminae, suggesting a similar origin (Fig. 2.5A). If the aliphatic molecules are indeed more readily ionized than the aromatic structures, leading to negative ion signal that is dominated by fragments of the latter (Fig. 2.5A, phenanthrene *versus* nonadecanone), then the veins may contain an increased abundance of aliphatic molecular structures of the same composition as those detected in the laminae. Moreover, the spectra from lamina and vein show the presence of sulfur bound to OM (C_2S^- ion), which come from organic sulfur compounds described previously (Mongenot et al., 1997, 1999; Van Kaam-Peters and Sinninghe Damsté, 1997). The similar C_2S^-/C_2^- ratios in the veins and in the laminae (0.06 and 0.07, respectively) suggest that OM in veins and lamina probably have the same concentration of S. Such concentration of sulfur indicates that OM in veins is not an exogenous contaminant. Moreover, the ratio of 2-methylthiophene over toluene ratios reported by Van Kaam-Peters and Sinninghe Damsté, (1997) indicates that the asphaltene and kerogen have quite similar S-organic content suggesting that the bitumen part of the kerogen may have similar C/S_{orga} ratio. Therefore, these different negative ratios appear to confirm that the OM in the veins (and also possibly in porous patches) of the carbonates probably represents an indigenous bitumen fraction.

5.3 Strelley Pool OM

The laminated kerogen grains present here comes from member 4 of the Strelley Pool Formation. This member is composed of quartzites formed by the silicification of siliciclastic and/or volcanoclastic sediments. These quartzites contain OM grains, which have been interpreted as the remains of allochthonous microbial mats formed in the ocean or in a nearby platform?? environment (Allwood et al., 2006a, 2007). The organic matter present within members 3 and 4 has been studied in depth by Marshall et al. (2007) using Raman and FTIR spectroscopies, solid-state ^{13}C nuclear magnetic resonance spectroscopy and hydropyrolysis (HyPy) followed by GC-MS. Bulk analyses indicated that the total organic carbon content is low (0.08 to 0.022 wt%) and the OM has low atomic H/C ratios (ranging from the 0.02 to 0.46). These elemental values and investigations of the OM thermal maturity based on Raman Spectroscopy (Allwood et al., 2006b) indicate that the OM is highly mature.

The positive ion images and the spectrum obtained from this highly mature kerogen indicate the difficulty to obtain ToF-SIMS signal with our experimental conditions. The low signal intensity shown in the spectrum (Fig. 2.14) may be due to matrix and charging effects caused by the surrounding material (here quartz). Such matrix/charging effects are well illustrated by the heterogeneity of the Si^+ ion image (Fig. 2.13C). We also observed distortion of ion images around coarse pyrite crystals in the quartz matrix (not shown). These matrix effects have also required to normalize some positive ion image (i.e. $C_2H_5^+$ and $C_4H_7^+$) to total ion counts to visualize realistic distributions of hydrocarbon fragments (Fig. 2.13C). Nevertheless, molecular information has been obtained from these OM clasts. In positive mode, $C_{10}H_8^+$, $C_{14}H_{10}^+$ and $C_{16}H_{10}^+$ ions are detected from the kerogen that can be attributed to PAHs (respectively possible naphthalene, anthracene/phenanthrene and pyrene molecules). Moreover, the presence of series of unsaturated fragments (green bracket in Fig. 2.14) supports the presence of PAHs. This observation is in agreement with the HyPy GC-MS data reported by Marshall et al. (2007) that indicated that 90% of the carbons are aromatic, with phenanthrene and pyrene as major components. However, positive ion images and the spectrum also show the presence of saturated fragments ($C_2H_5^+$, $C_4H_7^+$ and $C_5H_9^+$), which indicate that short aliphatic structures are likely present in the Strelley Pool kerogen (Figs. 2.13C, 14). The relative high abundance of such small aliphatic structures in the Strelley Pool OM is also confirmed by the different indexes of saturation and the aliphatic ions/ aromatics ions ratios (Table 3), which are generally higher than in the phenanthrene standard (with the exception of $C_4H_7^+/C_7H_7^+$ and $C_5H_9^+/C_7H_7^+$, which are smaller). The presence of abundant aliphatic molecules has been reported from organic matter hosted in older cherts from the Pilbara (Apex Chert and Dresser Fm in the Warrawoona group) by Derenne et al. (2008) and Skrzypczak et al. (2005). Based on Raman spectroscopy of OM, it has been proposed that the Apex Chert OM may possibly contain some late exogenous organic matter (Marshall et al., 2012; Sforna et al., 2014). The Dresser Formation OM is, however, less mature than the Strelley Pool OM, as indicated by Raman spectra (Lepot et al. personal communication, Delarue et al., 2016), and unexpectedly low aromatic content detected with ^{13}C NMR (Delarue et al., 2016). In contrast, the presence of abundant long chain of aliphatic molecules in kerogen in members 3-4 of the Strelley Pool Formation is unexpected as discussed by Marshall et al. (2007). Hydropyrolysates of Strelley Pool OM displayed 1-7 rings PAHs with side-chains dominated by one and two carbon alkyl groups and small amounts of 3+ carbon alkyl side-chains (Marshall et al., 2007). The presence PAHs with short alkyl side-chains in the Strelley Pool kerogen likely explains the relative abundances of $C_2H_6^+$ and $C_3H_8^+$ fragments and the relative high R4 to R6 ratio values (Table 3) obtained from the $C_nH_y^+$ series. Interestingly, the $C_7H_y^+$ series is dominated by $C_7H_4^+$ ions (Fig. 2.4C), which lowers the value of the R7 ratio (Table 3). In contrast, the non-alkylated phenanthrene pattern is dominated by $C_7H_y^+$ ions with $y<4$, suggesting that the $C_7H_4^+$-dominated pattern results of additional alkyl side chains. The high intensity of this unsaturated fragment remains peculiar and the nature of the molecule leading to the production of this ion remain unknown to our knowledge for our ToF-SIMS setting. We only investigated the fragmentation patterns of non-alkylated PAH and long chain aliphatic standards and the low mass fragmentation patterns of alkylated-PAHs and small aliphatics remain unknown under our ToF-SIMS conditions and should be investigated in future studies.

The saturation indexes R4-R6, R8 and R9 are higher in the Strelley Pool kerogen than in Orbagnoux kerogen laminae, but lower than the Orbagnoux veins bitumen (Table 3). These ratio globally suggest that a higher level of saturation is observed in the Strelley Pool $C_nH_y^+$ fragments. Interestingly, hydropyrolysis also liberated n-C_{14} to n-C_{20} alkanes in concentrations of 0.3 wt% of the Strelley Pool kerogen matrix, which have been interpreted as bitumen trapped in micropores of the kerogen that could not be accessed by organic solvents (Marshall et al., 2007). In contrast, the kerogen from the Orbagnoux laminae may have lost most of alkanes at/near its surface, as indicated by the important extraction in the solvents and de-lamination of kerogen layers when the solvent extraction was too long. However, the very low ToF-SIMS total signal on the Strelley Pool OM, conjugated with the very low counts used to calculate R8 and R9 suggest that care should be taken with using these ToF-SIMS data to infer preservation of long chain alkanes. At such low count rates, faint possible traces of preparation contaminants and re-deposition of volatile contaminants (Fadel et al., in prep, chapter 2 of this thesis) during ToF-SIMS may be difficult to rule out.

The production of negative ions from the Strelley Pool OM is more effective than that of positive ions. This observation confirmed the problem of the positive ion production due to sediment interference (charge/matrix effect, low rate of ionization), while the negative ion production appears less affected by such problems. Thus, the facility to produce negative ions compared to the positive ions from kerogen with ToF SIMS is confirmed for both Orbagnoux and Strelley Pool OM.

Here, the C_n^-/C_2^- ratio values of the Strelley Pool OM are slightly higher than those reported from the phenanthrene standard (Fig. 2.5A). This suggests that the kerogen from the SPF sample is mainly composed of small PAHs, which appears coherent with the hydropyrolysis-GC-MS data of Marshall et al. (2007). In particular, C_n^-/C_2^- are systematically lower than in Orbagnoux, consistent with less alkylated and/or more condensed aromatic structures. In addition, the C_nH^-/C_n^- ratio values, and in particular the C_6H^-/C_6^- and C_8H^-/C_8^- values are lower than those in the phenanthrene standard (Fig. 2.5B).

5.4 Semi-quantification between different kerogen

Our observations on Orbagnoux sample show the possibility to derive information on the structure of kerogen and bitumen using semi-quantifications. Such semi-quantification have been reported possible for ToF-SIMS analyses of fossil plants (Abbott et al., 2018), asphaltenes (Larachi et al., 2004), exhaust particles (Popovicheva et al., 2017). These difficulties are also enhanced by the presence of PAHs with small alkyl chains in the Strelley Pool OM, which might produce saturated ions. Despite these difficulties, some ratios indicate that the aromaticity of the Strelley Pool OM is higher than the Orbagnoux lamina. Indeed, $R_{ali/aro}$ and the low-mass ratios ($C_2H_5^+/C_2H_3^+$, $C_3H_5^+/C_3H_3^+$, $C_4H_7^+/C_6H_5^+$, $C_4H_7^+/C_7H_7^+$) indicate that the Strelley Pool OM is more aromatic than the Orbagnoux laminae (Fig. 2.8A-B and Table 3). Interestingly, all the ratio values indicate that the putative Orbagnoux bitumen present in the veins is highly aliphatic compared to the two-kerogen analyzed.

Semi-quantification is also informative in negative mode using the C_n^-/C_2^- and C_nH^-/C_n^- ratios (Fig. 2.5) as well as the RC_n^- ratio. Analysis of a deuterated PAH indicated that C–H^- are largely produced through recombination with hydrogen. The C_nH^- fragments from polyaromatic macromolecules are thus likely proportional to the H/C ratio, which in turn is indicative of the maturity of the kerogen. The most pronounced difference in C_nH^- ratios between nonadecanone (at H/C=2) and phenanthrene (H/C=0.71) is seen for C_2H^-/C_2^-. This ratio is lower in the Strelley Pool OM than in the Orbagnoux laminae, consistent with a lower H/C. Similarly, the C_n^-/C_2^- ratios show most pronounced differences for n>5. All the C_n^-/C_2^- with n>5 that we measured are smaller in the Strelley Pool OM than in Orbagnoux (Fig. 2.5), again consistent with a more aromatic nature and/or smaller aliphatic chains. The close similarity of the C_n^-/C_2^- pattern in the Strelley Pool OM and phenanthrene standard argues for a similar PAH-dominated composition. We introduce the RC_n^- ratio (equation 8). This ratio is lower in the Strelley Pool OM (0.07) than in Orbagnoux laminae (0.23). Surprisingly, this ratio is intermediate (0.17) in the Orbagnoux veins, when all other indexes indicate a higher aliphatic content in these veins.

Finally, C_2S^-/ C_2^- ratios obtained from the Orbagnoux sample (0.07 for the lamina, 0.06 for the vein), and the Strelley Pool OM (0.01) indicate that the sulfur bound to the organic matter is much higher in the Orbagnoux sample than in the SPF sample consistent with the important sulfurization of the OM in Orbagnoux (Mongenot et al., 2000; Sugitani et al., 2015a).

Conclusion and perspectives

ToF SIMS investigations show the possibility to perform molecular analysis on kerogen, after low energy Ar^+ sputtering, which is necessary to remove surface contamination. The low mass fragment distribution of a PAH and a highly saturated molecule show the possibility to constrain the aromatic and aliphatic character of unknown OM using a combination of positive and negative ion modes. Importantly, the aliphatic standard shows the possibility to produce low-mass unsaturated molecules, which are usually used to constrain the presence of aromatics molecule. This observation indicates the importance to investigate the distribution of hydrogen in hydrocarbon series at various, constant carbon numbers. Such semi-quantifications performed on the Orbagnoux sample distinguished the aliphatic/aromatic contents from the laminae and veins, which contain respectively the kerogen and possible bitumen part of the Orbagnoux OM. Similarly, our positive ion analyses indicate that the mature Strelley Pool OM grains are composed of PAHs with a relative important alkylation of these aromatic molecules, in positive mode. With the negative ions, semi-quantifications support the highly aromatic character of the Strelley Pool OM. Semi-quantification based on different negative and positive ions show that the higher aromaticity and lower hydrogenation and sulfuration of the Strelley Pool OM compared to the Orbagnoux lamina. This work shows the possibility to constrain the nature of fossil organic matter at the scale of microbial laminae. In a perspective work, future investigations are required to know the precise fragmentation patterns of other organic compound such as alkylate-PAHs, short alkanes, branched alkanes, and alkenes using our analytical setup. Further ToF-SIMS analysis using cluster ions (Ar_n, C_{60}, CH_{4n}) for sputtering, may permit to increase the ion yield and perform molecular investigations limiting fragmentation at higher mass.

Acknowledgment

Philippe Recourt (LOG) is thanked for help with SEM. Sylvie Regnier (U. Lille) is thanked for semi-thin section preparation. Sarah Fearn (Imperial College London) is thanked for discussion on the ToF SIMS setting and a test analysis at ICL Department of Materials. Thank Julien Foriel and Nicolas Thebaud for the Pilbara field session in 2003. Funding was provided by ANR M6fossils ANR-15-CE31-0003-01, CNRS INSU-INTERRVIE program, and University of Lille (BQR program).

Appendix

2-nonadecanone

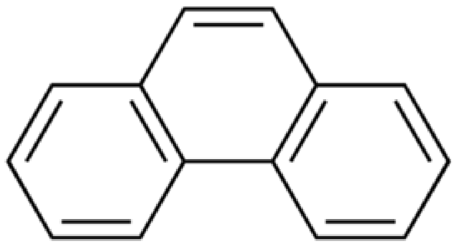

Phenanthrene

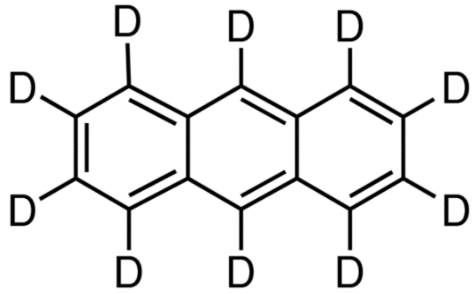

Anthracene D10.

References

Abbott, G.D., Fletcher, I.W., Tardio, S., Hack, E., 2018. Exploring the geochemical distribution of organic carbon in early land plants: a novel approach. Philos. Trans. R. Soc. B Biol. Sci. 373, 20160499. https://doi.org/10.1098/rstb.2016.0499

Allwood, A.C., Grotzinger, J.P., Knoll, A.H., Burch, I.W., Anderson, M.S., Coleman, M.L., Kanik, I., 2009. Controls on development and diversity of Early Archean stromatolites. Proc. Natl. Acad. Sci. 106, 9548–9555.

Allwood, A.C., Walter, M.R., Burch, I.W., Kamber, B.S., 2007. 3.43 billion-year-old stromatolite reef from the Pilbara Craton of Western Australia: Ecosystem-scale insights to early life on Earth. Precambrian Res. 158, 198–227. https://doi.org/10.1016/j.precamres.2007.04.013

Allwood, A.C., Walter, M.R., Kamber, B.S., Marshall, C.P., Burch, I.W., 2006a. Stromatolite reef from the Early Archaean era of Australia. Nature 441, 714–718. https://doi.org/10.1038/nature04764

Allwood, A.C., Walter, M.R., Marshall, C.P., 2006b. Raman spectroscopy reveals thermal palaeoenvironments of c.3.5 billion-year-old organic matter. Vib. Spectrosc., 6th Australian Conference on Vibrational Spectroscopy 41, 190–197. https://doi.org/10.1016/j.vibspec.2006.02.006

Awramik, S.M., Riding, R., 1988. Role of algal eukaryotes in subtidal columnar stromatolite formation. Proc. Natl. Acad. Sci. 85, 1327–1329. https://doi.org/10.1073/pnas.85.5.1327

Batchelor, M.T., Burne, R.V., Henry, B.I., Jackson, M.J., 2004. A case for biotic morphogenesis of coniform stromatolites. Phys. Stat. Mech. Its Appl. 337, 319–326. https://doi.org/10.1016/j.physa.2004.01.065

Belu, A.M., Graham, D.J., Castner, D.G., 2003. Time-of-flight secondary ion mass spectrometry: techniques and applications for the characterization of biomaterial surfaces. Biomaterials 24, 3635–3653. https://doi.org/10.1016/S0142-9612(03)00159-5

Benninghoven, A., 1994. Chemical analysis of inorganic and organic surfaces and thin films by static time-of-flight secondary ion mass spectrometry (TOF-SIMS). Angew. Chem. Int. Ed. 33, 1023–1043.

Bernard, S., Benzerara, K., Beyssac, O., Menguy, N., Guyot, F., Brown, G.E., Goffe, B., 2007. Exceptional preservation of fossil plant spores in high-pressure metamorphic rocks. Earth Planet. Sci. Lett. 262, 257–272. https://doi.org/10.1016/j.epsl.2007.07.041

Bernard, S., Horsfield, B., 2014. Thermal Maturation of Gas Shale Systems. Annu. Rev. Earth Planet. Sci. 42, 635–651. https://doi.org/10.1146/annurev-earth-060313-054850

Bernard, S., Horsfield, B., Schulz, H.-M., Schreiber, A., Wirth, R., Anh Vu, T.T., Perssen, F., Könitzer, S., Volk, H., Sherwood, N., Fuentes, D., 2010. Multi-scale detection of organic and inorganic signatures provides insights into gas shale properties and evolution. Chem. Erde - Geochem. 70, 119–133. https://doi.org/10.1016/j.chemer.2010.05.005

Bernier, P., 1984. Les formations carbonatées du Kimméridgien et du Portlandien dans le Jura méridional: stratigraphie, micropaléontologie, sédimentologie. Université Claude-Bernard, Département des Sciences de la Terre, Villeurbane, France.

Bontognali, T.R., Vasconcelos, C., Warthmann, R.J., Dupraz, C., Bernasconi, S.M., McKenzie, J.A., 2008. Microbes produce nanobacteria-like structures, avoiding cell entombment. Geology 36, 663–666.

Bontognali, T.R.R., Sessions, A.L., Allwood, A.C., Fischer, W.W., Grotzinger, J.P., Summons, R.E., Eiler, J.M., 2012. Sulfur isotopes of organic matter preserved in 3.45-billion-year-old stromatolites reveal microbial metabolism. Proc. Natl. Acad. Sci. 109, 15146–15151. https://doi.org/10.1073/pnas.1207491109

Bosak, T., Liang, B., Sim, M.S., Petroff, A.P., 2009. Morphological record of oxygenic photosynthesis in conical stromatolites. Proc. Natl. Acad. Sci. 106, 10939–10943. https://doi.org/10.1073/pnas.0900885106

Brasier, M., Green, O., Lindsay, J., Mcloughlin, N., Steele, A., Stoakes, C., 2005. Critical testing of Earth's oldest putative fossil assemblage from the ~3.5Ga Apex chert, Chinaman Creek, Western Australia. Precambrian Res. 140, 55–102. https://doi.org/10.1016/j.precamres.2005.06.008

Brewer, L.N., Ohlhausen, J.A., Kotula, P.G., Michael, J.R., 2008. Forensic analysis of bioagents by X-ray and TOF-SIMS hyperspectral imaging. Forensic Sci. Int. 179, 98–106. https://doi.org/10.1016/j.forsciint.2008.04.020

Brison, J., Muramoto, S., Castner, D.G., 2010. ToF-SIMS Depth Profiling of Organic Films: A Comparison between Single Beam and Dual-beam Analysis. J. Phys. Chem. C Nanomater. Interfaces 114, 5565–5573. https://doi.org/10.1021/jp9066179

Brocks, J.J., Buick, R., Summons, R.E., Logan, G.A., 2003. A reconstruction of Archean biological diversity based on molecular fossils from the 2.78 to 2.45 billion-year-old Mount Bruce Supergroup, Hamersley Basin, Western Australia. Geochim. Cosmochim. Acta 67, 4321–4335. https://doi.org/10.1016/S0016-7037(03)00209-6

Brocks, J.J., Grosjean, E., Logan, G.A., 2008. Assessing biomarker syngeneity using branched alkanes with quaternary carbon (BAQCs) and other plastic contaminants. Geochim. Cosmochim. Acta 72, 871–888. https://doi.org/10.1016/j.gca.2007.11.028

Brocks, J.J., Jarrett, A.J.M., Sirantoine, E., Hallmann, C., Hoshino, Y., Liyanage, T., 2017. The rise of algae in Cryogenian oceans and the emergence of animals. Nature 548, 578–581. https://doi.org/10.1038/nature23457

Brocks, J.J., Logan, G.A., Buick, R., Summons, R.E., 1999. Archean molecular fossils and the early rise of eukaryotes. Science 285, 1033–1036. https://doi.org/10.1126/science.285.5430.1033

Buick, R., Dunlop, J.S.R., Groves, D.I., 1981. Stromatolite recognition in ancient rocks: an appraisal of irregularly laminated structures in an Early Archaean chert-barite unit from North Pole, Western Australia. Alcheringa 5, 161–181.

Cramer, H.-G., Grehl, T., Kollmer, F., Moellers, R., Niehuis, E., Rading, D., 2008. Depth profiling of organic materials using improved ion beam conditions. Appl. Surf. Sci. 255, 966–969. https://doi.org/10.1016/j.apsusc.2008.05.028

Decho, A.W., Visscher, P.T., Reid, R.P., 2005. Production and cycling of natural microbial exopolymers (EPS) within a marine stromatolite. Palaeogeogr. Palaeoclimatol. Palaeoecol. 219, 71–86. https://doi.org/10.1016/j.palaeo.2004.10.015

Delarue, F., Rouzaud, J.-N., Derenne, S., Bourbin, M., Westall, F., Kremer, B., Sugitani, K., Deldicque, D., Robert, F., 2016. The Raman-Derived Carbonization Continuum: A Tool to Select the Best Preserved Molecular Structures in Archean Kerogens. Astrobiology 16, 407–417. https://doi.org/10.1089/ast.2015.1392

Delcorte, A., Segda, B.G., Bertrand, P., 1997. ToF-SIMS analyses of polystyrene and dibenzanthracene: evidence for fragmentation and metastable decay processes in molecular secondary ion emission. Surf. Sci. 381, 18–32.

Delcorte, A., Weng, L.T., Bertrand, P., 1995. Secondary molecular ion emission from aliphatic polymers bombarded with low energy ions: Effects of the molecular structure and the ion beam induced surface degradation. Nucl. Instrum. Methods Phys. Res. Sect. B Beam Interact. Mater. At. 100, 213–216.

Derenne, S., Robert, F., Skrzypczak-Bonduelle, A., Gourier, D., Binet, L., Rouzaud, J.-N., 2008. Molecular evidence for life in the 3.5 billion year old Warrawoona chert. Earth Planet. Sci. Lett. 272, 476–480. https://doi.org/10.1016/j.epsl.2008.05.014

DiMarco, M.J., Lowe, D.R., 1989. Shallow-water volcaniclastic deposition in the Early Archean Panorama Formation, Warrawoona Group, eastern Pilbara Block, Western Australia. Sediment. Geol. 64, 43–63. https://doi.org/10.1016/0037-0738(89)90083-3

Eigenbrode, J.L., Freeman, K.H., Summons, R.E., 2008. Methylhopane biomarker hydrocarbons in Hamersley Province sediments provide evidence for Neoarchean aerobiosis. Earth Planet. Sci. Lett. 273, 323–331. https://doi.org/10.1016/j.epsl.2008.06.037

Espitalie, J., Deroo, G., Marquis, F., 1985. La pyrolyse Rock-Eval et ses applications. Première partie. Rev. Inst. Fr. Pétrole 40, 563–579. https://doi.org/10.2516/ogst:1985035

Fray, N., Bardyn, A., Cottin, H., Altwegg, K., Baklouti, D., Briois, C., Colangeli, L., Engrand, C., Fischer, H., Glasmachers, A., Grün, E., Haerendel, G., Henkel, H., Höfner, H., Hornung, K., Jessberger, E.K., Koch, A., Krüger, H., Langevin, Y., Lehto, H., Lehto, K., Le Roy, L., Merouane, S., Modica, P., Orthous-Daunay, F.-R., Paquette, J., Raulin, F., Rynö, J., Schulz, R., Silén, J., Siljeström, S., Steiger, W., Stenzel, O., Stephan, T., Thirkell, L., Thomas, R., Torkar, K., Varmuza, K., Wanczek, K.-P., Zaprudin, B., Kissel, J., Hilchenbach, M., 2016. High-molecular-weight organic matter in the particles of comet 67P/Churyumov–Gerasimenko. Nature 538, 72–74. https://doi.org/10.1038/nature19320

French, K.L., Hallmann, C., Hope, J.M., Schoon, P.L., Zumberge, J.A., Hoshino, Y., Peters, C.A., George, S.C., Love, G.D., Brocks, J.J., 2015. Reappraisal of hydrocarbon biomarkers in Archean rocks. Proc. Natl. Acad. Sci. 112, 5915–5920.

Greenwalt, D.E., Goreva, Y.S., Siljestroem, S.M., Rose, T., Harbach, R.E., 2013. Hemoglobin-derived porphyrins preserved in a Middle Eocene blood-engorged mosquito. Proc. Natl. Acad. Sci. U. S. A. 110, 18496–18500. https://doi.org/10.1073/pnas.1310885110

Grotzinger, J.P., Knoll, A.H., 1999. Stromatolites in Precambrian carbonates: evolutionary mileposts or environmental dipsticks? Annu. Rev. Earth Planet. Sci. 27, 313–358.

Grotzinger, J.P., Rothman, D.H., 1996. An abiotic model for stromatolite morphogenesis. Nature 383, 423.

Heim, C., Lausmaa, J., Sjovall, P., Toporski, J., Dieing, T., Simon, K., Hansen, B.T., Kronz, A., Arp, G., Reitner, J., Thiel, V., 2012. Ancient microbial activity recorded in fracture fillings from granitic rocks (Aspo Hard Rock Laboratory, Sweden). Geobiology 10, 280–297. https://doi.org/10.1111/j.1472-4669.2012.00328.x

Hook, A.L., Scurr, D.J., 2016. ToF-SIMS analysis of a polymer microarray composed of poly(meth)acrylates with C6 derivative pendant groups. Surf. Interface Anal. 48, 226–236. https://doi.org/10.1002/sia.5959

Irimiea, B., Carpentier, Y., Ortega, I.K., Ziskind, M., Faccinetto, A., Ouf, F.X., Salm, F., Delhaye, D., Gaffié, D., Bescond, A., Yon, J., Therssen, E., Focsa, C., 2015. Chemical Characterization of Airplane Soot Particles and Surrogates Using Laser Desorption Ionization and Secondary Ion Mass Spectrometry.

Javaux, E.J., Lepot, K., 2018. The Paleoproterozoic fossil record: Implications for the evolution of the biosphere during Earth's middle-age. Earth-Sci. Rev. 176, 68–86. https://doi.org/10.1016/j.earscirev.2017.10.001

Jettestuen, E., Jamtveit, B., Podladchikov, Y., Devilliers, S., Amundsen, H., Meakin, P., 2006. Growth and characterization of complex mineral surfaces. Earth Planet. Sci. Lett. 249, 108–118. https://doi.org/10.1016/j.epsl.2006.06.045

Keune, K., Boon, J.J., 2004. Imaging Secondary Ion Mass Spectrometry of a Paint Cross Section Taken from an Early Netherlandish Painting by Rogier van der Weyden. Anal. Chem. 76, 1374–1385. https://doi.org/10.1021/ac035201a

Keune, K., Ferreira, E.S., Boon, J.J., 2005. Characterization and localization of the oil-binding medium in paint cross-sections using imaging secondary ion mass spectrometry. ICOM Comm. Conserv. Prepr. 2, 796–802.

Knoll, A.H., 2003. The geological consequences of evolution. Geobiology 1, 3–14. https://doi.org/10.1046/j.1472-4669.2003.00002.x

Knoll, A.H., Bergmann, K.D., Strauss, J.V., 2016. Life: the first two billion years. Philos. Trans. R. Soc. B Biol. Sci. 371, 20150493. https://doi.org/10.1098/rstb.2015.0493

Kollmer, F., 2004. Cluster primary ion bombardment of organic materials. Appl. Surf. Sci. 231–232, 153–158. https://doi.org/10.1016/j.apsusc.2004.03.101

Larachi, F., Dehkissia, S., Adnot, A., Chornet, E., 2004. X-ray Photoelectron Spectroscopy, Photoelectron Energy Loss Spectroscopy, X-ray Excited Auger Electron Spectroscopy, and Time-of-Flight−Secondary Ion Mass Spectroscopy Studies of Asphaltenes from Doba−Chad Heavy Crude Hydrovisbreaking. Energy Fuels 18, 1744–1756. https://doi.org/10.1021/ef049951e

Lepot, K., Benzerara, K., Brown, G.E., Philippot, P., 2008. Microbially influenced formation of 2,724-million-year-old stromatolites. Nat. Geosci. 1, 118–121. https://doi.org/10.1038/ngeo107

Lepot, K., Benzerara, K., Rividi, N., Cotte, M., Brown, G.E., Jr., Philippot, P., 2009. Organic matter heterogeneities in 2.72 Ga stromatolites: Alteration versus preservation by sulfur incorporation. Geochim. Cosmochim. Acta 73, 6579–6599. https://doi.org/10.1016/j.gca.2009.08.014

Lindgren, J., Kuriyama, T., Madsen, H., Sjövall, P., Zheng, W., Uvdal, P., Engdahl, A., Moyer, A.E., Gren, J.A., Kamezaki, N., Ueno, S., Schweitzer, M.H., 2017. Biochemistry and adaptive colouration of an exceptionally preserved juvenile fossil sea turtle. Sci. Rep. 7. https://doi.org/10.1038/s41598-017-13187-5

Lindgren, J., Sjovall, P., Carney, R.M., Uvdal, P., Gren, J.A., Dyke, G., Schultz, B.P., Shawkey, M.D., Barnes, K.R., Polcyn, M.J., 2014. Skin pigmentation provides evidence of convergent melanism in extinct marine reptiles. Nature 506, 484-+. https://doi.org/10.1038/nature12899

Lindgren, J., Uvdal, P., Sjovall, P., Nilsson, D.E., Engdahl, A., Schultz, B.P., Thiel, V., 2012. Molecular preservation of the pigment melanin in fossil melanosomes. Nat. Commun. 3, 824. https://doi.org/10.1038/ncomms1819

Lowe, D.R., 1994. Abiological origin of described stromatolites older than 3.2 Ga. Geology 22, 387–390.

Mahoney, C.M., Gillen, G., Fahey, A.J., 2006. Characterization of gunpowder samples using time-of-flight secondary ion mass spectrometry (TOF-SIMS). Forensic Sci. Int. 158, 39–51. https://doi.org/10.1016/j.forsciint.2005.02.036

Marshall, A.O., Emry, J.R., Marshall, C.P., 2012. Multiple Generations of Carbon in the Apex Chert and Implications for Preservation of Microfossils. Astrobiology 12, 160–166. https://doi.org/10.1089/ast.2011.0729

Marshall, C., Javaux, E., Knoll, A., Walter, M., 2005. Combined micro-Fourier transform infrared (FTIR) spectroscopy and micro-Raman spectroscopy of Proterozoic acritarchs: A new approach to Palaeobiology. Precambrian Res. 138, 208–224. https://doi.org/10.1016/j.precamres.2005.05.006

Marshall, C.P., Love, G.D., Snape, C.E., Hill, A.C., Allwood, A.C., Walter, M.R., Van Kranendonk, M.J., Bowden, S.A., Sylva, S.P., Summons, R.E., 2007. Structural characterization of kerogen in 3.4Ga Archaean cherts from the Pilbara Craton, Western Australia. Precambrian Res. 155, 1–23. https://doi.org/10.1016/j.precamres.2006.12.014

Mathez, E.A., Mogk, D.M., 1998. Characterization of carbon compounds on a pyroxene surface from a gabbro xenolith in basalt by time-of-flight secondary ion mass spectrometry. Am. Mineral. 83, 918–924.

Mazel, V., Richardin, P., 2009. ToF-SIMS study of organic materials in Cultural Heritage: identification and chemical imaging. Wiley.

McLafferty, F.W., Turecek, F., Choi, J., 1993. Interpretation Of Mass Spectra. University Science Books.

Mine, N., Douhard, B., Brison, J., Houssiau, L., 2007. Molecular depth-profiling of polycarbonate with low-energy Cs+ ions. Rapid Commun. Mass Spectrom. 21, 2680–2684. https://doi.org/10.1002/rcm.3135

Mogk, D.W., Mathez, E.A., 2000. Carbonaceous films in midcrustal rocks from the KTB borehole, Germany, as characterized by time-of-flight secondary ion mass spectrometry. Geochem. Geophys. Geosystems 1.

Mongenot, T., Boussafir, M., Derenne, S., Lallier-Verges, E., Largeau, C., Tribovillard, N., 1997. Sulphur-rich organic matter from bituminous laminites of Orbagnoux (France, Upper Kimmeridgian). The role of early vulcanization. Bull. Soc. Geol. Fr. 168, 331–341.

Mongenot, T., Derenne, S., Largeau, C., Tribovillard, N., Lallier-Vergès, E., Dessort, D., Connan, J., 1999. Spectroscopic, kinetic and pyrolytic studies of kerogen from the dark parallel laminae facies of the sulphur-rich Orbagnoux deposit (Upper Kimmeridgian, Jura). Org. Geochem. 30, 39–56.

Mongenot, T., Tribovillard, N.-P., Arbey, F., Lallier-Verges, E., Derenne, S., Largeau, C., Pichon, R., Dessort, D., Connan, J., 2000. Comparative studies of a high resolution sampling of the different facies of the organic-rich Orbagnoux Deposit (upper Kimmeridgian, Jura); petrographic and bulk geochemical approach; extent and origin of interfacies and intrafacies variations. Bull. Société Géologique Fr. 171, 23–36.

Noffke, N., Christian, D., Wacey, D., Hazen, R.M., 2013. Microbially Induced Sedimentary Structures Recording an Ancient Ecosystem in the *ca.* 3.48 Billion-Year-Old Dresser Formation, Pilbara, Western Australia. Astrobiology 13, 1103–1124. https://doi.org/10.1089/ast.2013.1030

Noffke, N., Eriksson, K.A., Hazen, R.M., Simpson, E.L., 2006. A new window into Early Archean life: Microbial mats in Earth's oldest siliciclastic tidal deposits (3.2 Ga Moodies Group, South Africa). Geology 34, 253–256.

Nutman, A.P., Bennett, V.C., Friend, C.R.L., Kranendonk, M.J.V., Chivas, A.R., 2016. Rapid emergence of life shown by discovery of 3,700-million-year-old microbial structures. Nature 537, 535–538. https://doi.org/10.1038/nature19355

Oehler, D.Z., Robert, F., Walter, M.R., Sugitani, K., Allwood, A., Meibom, A., Mostefaoui, S., Selo, M., Thomen, A., Gibson, E.K., 2009. NanoSIMS: Insights to biogenicity and syngeneity of Archaean carbonaceous structures. Precambrian Res. 173, 70–78. https://doi.org/10.1016/j.precamres.2009.01.001

Pacton, M., Fiet, N., Gorin, G., 2006. Revisiting amorphous organic matter in Kimmeridgian laminites: what is the role of the vulcanization process in the amorphization of organic matter? Terra Nova 18, 380–387. https://doi.org/10.1111/j.1365-3121.2006.00702.x

Paerl, H.W., Steppe, T.F., Reid, R.P., 2001. Bacterially mediated precipitation in marine stromatolites. Environ. Microbiol. 3, 123–130.

Palmquist, A., Emanuelsson, L., Sjovall, P., 2012. Chemical and structural analysis of the bone-implant interface by TOF-SIMS, SEM, FIB and TEM: Experimental study in animal. Appl. Surf. Sci. 258, 6485–6494. https://doi.org/10.1016/j.apsusc.2012.03.065

Papineau, D., Walker, J.J., Mojzsis, S.J., Pace, N.R., 2005. Composition and Structure of Microbial Communities from Stromatolites of Hamelin Pool in Shark Bay, Western Australia. Appl. Environ. Microbiol. 71, 4822–4832. https://doi.org/10.1128/AEM.71.8.4822-4832.2005

Passarelli, M.K., Winograd, N., 2011. Lipid imaging with time-of-flight secondary ion mass spectrometry (ToF-SIMS). Biochim. Biophys. Acta-Mol. Cell Biol. Lipids 1811, 976–990. https://doi.org/10.1016/j.bbalip.2011.05.007

Petrat, F.M., Wolany, D., Schwede, B.C., Wiedmann, L., Benninghoven, A., 1994. Comparative in situ ToF-SIMS/XPS study of polystyrene modified by argon, oxygen and nitrogen plasmas. Surf. Interface Anal. 21, 402–406.

Popovicheva, O.B., Shonija, N.K., Schwarz, J., Vojtíšek-Lom, M., Focsa, C., Irimiea, C., Carpentier, Y., Ortega, I.K., Kireeva, E.D., 2017. Chemical Composition of Diesel/Biodiesel Particulate Exhaust by FTIR Spectroscopy and Mass Spectrometry: Impact of Fuel and Driving Cycle. Aerosol Air Qual. Res. 17, 1717–1734. https://doi.org/10.4209/aaqr.2017.04.0127

Rasmussen, B., Fletcher, I.R., Brocks, J.J., Kilburn, M.R., 2008. Reassessing the first appearance of eukaryotes and cyanobacteria. Nature 455, 1101-U9. https://doi.org/10.1038/nature07381

Riding, R., 2000. Microbial carbonates: the geological record of calcifed bacterial-algal mats and biofilms. Sedimentology 47, 174–214.

Russo, M.F., Szakal, C., Kozole, J., Winograd, N., Garrison, B.J., 2007. Sputtering Yields for C60 and Au3 Bombardment of Water Ice as a Function of Incident Kinetic Energy. Anal. Chem. 79, 4493–4498. https://doi.org/10.1021/ac070105l

Sakamoto, T., Yamamoto, A., Owari, M., Nihei, Y., 2004. Supercritical fluid clean-up of environmental samples for the analysis of polycyclic aromatic hydrocarbons using time-of-flight secondary ion mass spectrometry. Anal. Sci. Int. J. Jpn. Soc. Anal. Chem. 20, 1379–1382.

Sarret, G., Mongenot, T., Connan, J., Derenne, S., Kasrai, M., Bancroft, G.M., Largeau, C., 2002. Sulfur speciation in kerogens of the Orbagnoux deposit (Upper Kimmeridgian, Jura) by XANES spectroscopy and pyrolysis. Org. Geochem. 33, 877–895.

Schopf, J.W., 2006. Fossil evidence of Archaean life. Philos. Trans. R. Soc. B Biol. Sci. 361, 869–885. https://doi.org/10.1098/rstb.2006.1834

Sforna, M.C., van Zuilen, M.A., Philippot, P., 2014. Structural characterization by Raman hyperspectral mapping of organic carbon in the 3.46 billion-year-old Apex chert, Western Australia. Geochim. Cosmochim. Acta 124, 18–33. https://doi.org/10.1016/j.gca.2013.09.031

Siljestrom, S., Hode, T., Lausmaa, J., Sjovall, P., Toporski, J., Thiel, V., 2009. Detection of organic biomarkers in crude oils using ToF-SIMS. Org. Geochem. 40, 135–143. https://doi.org/10.1016/j.orggeochem.2008.08.010

Siljestrom, S., Lausmaa, J., Sjovall, P., Broman, C., Thiel, V., Hode, T., 2010. Analysis of hopanes and steranes in single oil-bearing fluid inclusions using time-of-flight secondary ion mass spectrometry (ToF-SIMS). Geobiology 8, 37–44. https://doi.org/10.1111/j.1472-4669.2009.00223.x

Siljeström, S., Parenteau, M.N., Jahnke, L.L., Cady, S.L., 2017. A comparative ToF-SIMS and GC–MS analysis of phototrophic communities collected from an alkaline silica-depositing hot spring. Org. Geochem. 109, 14–30. https://doi.org/10.1016/j.orggeochem.2017.03.009

Siljestrom, S., Volk, H., George, S.C., Lausmaa, J., Sjovall, P., Dutkiewicz, A., Hode, T., 2013. Analysis of single oil-bearing fluid inclusions in mid-Proterozoic sandstones (Roper Group, Australia). Geochim. Cosmochim. Acta 122, 448–463. https://doi.org/10.1016/j.gca.2013.08.010

Sjövall, P., Johansson, B., Lausmaa, J., 2006. Localization of lipids in freeze-dried mouse brain sections by imaging TOF-SIMS. Appl. Surf. Sci. 252, 6966–6974. https://doi.org/10.1016/j.apsusc.2006.02.126

Skrzypczak, A., Derenne, S., Binet, L., Gourier, D., Robert, F., 2005. Characterization of a 3.5 Billion year old organic matter: Electron paramagnetic resonance and pyrolysis GC–MS, tools to assess syngeneity and biogenicity, in: Lunar and Planetary Science XXXVI, Abstract.

Spool, A.M., 2004. Interpretation of static secondary ion spectra. Surf. Interface Anal. 36, 264–274. https://doi.org/10.1002/sia.1685

Steele, A., Toporski, J.K.W., Avci, R., Guidry, S., McKay, D.S., 2001. Time of flight secondary ion mass spectrometry (ToFSIMS) of a number of hopanoids. Org. Geochem. 32, 905–911. https://doi.org/10.1016/S0146-6380(01)00048-1

Steemans, P., Lepot, K., Marshall, C.P., Le Hérissé, A., Javaux, E.J., 2010. FTIR characterisation of the chemical composition of Silurian miospores (cryptospores and trilete spores) from Gotland, Sweden. Rev. Palaeobot. Palynol. 162, 577–590. https://doi.org/10.1016/j.revpalbo.2010.07.006

Stephan, T., 2001. TOF-SIMS in cosmochemistry. Planet. Space Sci. 49, 859–906. https://doi.org/10.1016/S0032-0633(01)00037-X

Stephan, T., Jessberger, E.K., Heiss, C.H., Rost, D., 2003. TOF-SIMS analysis of polycyclic aromatic hydrocarbons in Allan Hills 84001. Meteorit. Planet. Sci. 38, 109–116.

Sugitani, K., Lepot, K., Nagaoka, T., Mimura, K., Van Kranendonk, M., Oehler, D.Z., Walter, M.R., 2010. Biogenicity of Morphologically Diverse Carbonaceous Microstructures from the *ca.* 3400 Ma Strelley Pool Formation, in the Pilbara Craton, Western Australia. Astrobiology 10, 899–920. https://doi.org/10.1089/ast.2010.0513

Sugitani, K., Mimura, K., Takeuchi, M., Lepot, K., Ito, S., Javaux, E.J., 2015a. Early evolution of large micro-organisms with cytological complexity revealed by microanalyses of 3.4

Ga organic-walled microfossils. Geobiology 13, 507–521. http://dx.doi.org/10.1111/gbi.12148

Sugitani, K., Mimura, K., Takeuchi, M., Yamaguchi, T., Suzuki, K., Senda, R., Asahara, Y., Wallis, S., Van Kranendonk, M., 2015b. A Paleoarchean coastal hydrothermal field inhabited by diverse microbial communities: the Strelley Pool Formation, Pilbara Craton, Western Australia. Geobiology 1–24. https://doi.org/10.1111/gbi.12150

Szynkowska, M.I., Czerski, K., Rogowski, J., Paryjczak, T., Parczewski, A., 2009. ToF-SIMS application in the visualization and analysis of fingerprints after contact with amphetamine drugs. Forensic Sci. Int. 184, e24–e26. https://doi.org/10.1016/j.forsciint.2008.11.003

Thiel, V., Blumenberg, M., Kiel, S., Leefmann, T., Liebenau, K., Lindgren, J., Sjovall, P., Treude, T., Zilla, T., 2014. Occurrence and fate of fatty acyl biomarkers in an ancient whale bone (Oligocene, El Cien Formation, Mexico). Org. Geochem. 68, 71–81. https://doi.org/10.1016/j.orggeochem.2013.12.006

Thiel, V., Heim, C., Arp, G., Hahmann, U., Sjovall, P., Lausmaa, J., 2007a. Biomarkers at the microscopic range: ToF-SIMS molecular imaging of Archaea-derived lipids in a microbial mat. Geobiology 5, 413–421. https://doi.org/10.1111/j.1472-4669.2007.00119.x

Thiel, V., Sjövall, P., 2014. Time-of-Flight Secondary Ion Mass Spectrometry (TOF-SIMS): Principles and Practice in the Biogeosciences 122–170. https://doi.org/10.1039/9781782625025-00122

Thiel, V., Sjovall, P., 2011. Using Time-of-Flight Secondary Ion Mass Spectrometry to Study Biomarkers, in: Jeanloz, R., Freeman, K.H. (Eds.), Annual Review of Earth and Planetary Sciences, Vol 39. Annual Reviews, Palo Alto, pp. 125–156.

Thiel, V., Toporski, J., Schumann, G., Sjovall, P., Lausmaa, J., 2007b. Analysis of archaeal core ether lipids using Time of Flight-Secondary Ion Mass Spectrometry (ToF-SIMS): Exploring a new prospect for the study of biomarkers in geobiology. Geobiology 5, 75–83. https://doi.org/10.1111/j.1472-4669.2006.00093.x

Thompson, C.E., Ellis, J., Fletcher, J.S., Goodacre, R., Henderson, A., Lockyer, N.P., Vickerman, J.C., 2006. ToF-SIMS studies of Bacillus using multivariate analysis with possible identification and taxonomic applications. Appl. Surf. Sci. 252, 6719–6722. https://doi.org/10.1016/j.apsusc.2006.02.237

Toporski, J., Steele, A., 2004. Characterization of purified biomarker compounds using time of flight-secondary ion mass spectrometry (ToF-SIMS). Org. Geochem. 35, 793–811. https://doi.org/10.1016/j.orggeochem.2004.03.006

Toporski, J.K.W., Steele, A., Westall, F., Avci, R., Martill, D.M., McKay, D.S., 2002. Morphologic and spectral investigation of exceptionally well-preserved bacterial biofilms from the Oligocene Enspel formation, Germany. Geochim. Cosmochim. Acta 66, 1773–1791. https://doi.org/10.1016/S0016-7037(01)00870-5

Touboul, D., Kollmer, F., Niehuis, E., Brunelle, A., Laprevote, O., 2005. Improvement of biological time-of-flight-secondary ion mass spectrometry imaging with a bismuth cluster ion source. J. Am. Soc. Mass Spectrom. 16, 1608–1618. https://doi.org/10.1016/j.jasms.2005.06.005

Tribovillard, N., Riboulleau, A., Lyons, T., Baudin, F., 2004. Enhanced trapping of molybdenum by sulfurized marine organic matter of marine origin in Mesozoic limestones and shales. Chem. Geol. 213, 385–401. https://doi.org/10.1016/j.chemgeo.2004.08.011

Tribovillard, N., Trentesaux, A., Trichet, J., Défarge, C., 2000. A Jurassic counterpart for modern kopara of the Pacific atolls:: lagoonal, organic matter-rich, laminated carbonate of Orbagnoux (Jura Mountains, France). Palaeogeogr. Palaeoclimatol. Palaeoecol. 156, 277–288.

Tribovillard, N., Trichet, J., Defarge, C., Trentesaux, A., 1999. Jurassic lagoonal environments and quasi-abiotic platy limestone accumulation: microbial interventions. Sedimentology 46, 1183–1197. https://doi.org/10.1046/j.1365-3091.1999.00272.x

Tribovillard, N.-P., Gorin, G.E., Belin, S., Hopfgartner, G., Pichon, R., 1992. Organic-rich biolaminated facies from a Kimmeridgian lagoonal environment in the French Southern Jura mountains—A way of estimating accumulation rate variations. Palaeogeogr. Palaeoclimatol. Palaeoecol. 99, 163–177. https://doi.org/10.1016/0031-0182(92)90013-U

Tuccitto, N., Marletta, G., Carnazza, S., Grasso, L., Caratozzolo, M., Guglielmino, S., Licciardello, A., 2011. ToF-SIMS imaging of surface self-organized fractal patterns of bacteria. Surf. Interface Anal. 43, 370–375. https://doi.org/10.1002/sia.3555

Van Kaam-Peters, H.M.E., Rijpstra, W.I.C., De Leeuw, J.W., Sinninghe Damsté, J.S., 1998. A high resolution biomarker study of different lithofacies of organic sulfur-rich carbonate rocks of a Kimmeridgian lagoon (French southern Jura). Org. Geochem. 28, 151–177. https://doi.org/10.1016/S0146-6380(97)00132-0

Van Kaam-Peters, H.M.E., Sinninghe Damsté, J.S., 1997. Characterisation of an extremely organic sulphur-rich, 150Ma old carbonaceous rock: palaeoenvironmental implications. Org. Geochem. 27, 371–397. https://doi.org/10.1016/S0146-6380(97)00082-X

Van Kranendonk, M.J., Hickman, A.H., Smithies, R.H., Nelson, D.R., Pike, G., 2002. Geology and Tectonic Evolution of the Archean North Pilbara Terrain,Pilbara Craton, Western Australia. Econ. Geol. 97, 695–732. https://doi.org/10.2113/gsecongeo.97.4.695

Vandenbroucke, M., Largeau, C., 2007. Kerogen origin, evolution and structure. Org. Geochem. 38, 719–833. https://doi.org/10.1016/j.orggeochem.2007.01.001

Vasconcelos, C., Warthmann, R., McKenzie, J.A., Visscher, P.T., Bittermann, A.G., van Lith, Y., 2006. Lithifying microbial mats in Lagoa Vermelha, Brazil: Modern Precambrian relics? Sediment. Geol. 185, 175–183. https://doi.org/10.1016/j.sedgeo.2005.12.022

Vickerman, J.C., Briggs, D., 2013. ToF-SIMS: Materials Analysis by Mass Spectrometry. IM Publications.

Vickerman, J.C., Gilmore, I.S., 2011. Surface Analysis: The Principal Techniques. John Wiley & Sons.

Wacey, D., Battison, L., Garwood, R.J., Hickman-Lewis, K., Brasier, M.D., 2016. Advanced analytical techniques for studying the morphology and chemistry of Proterozoic microfossils. Geol. Soc. Lond. Spec. Publ. 448, 81–104. https://doi.org/10.1144/SP448.4

Wacey, D., Gleeson, D., Kilburn, M.R., 2010. Microbialite taphonomy and biogenicity: new insights from NanoSIMS: Microbialite taphonomy and biogenicity. Geobiology 8, 403–416. https://doi.org/10.1111/j.1472-4669.2010.00251.x

Walter, M.R., Buick, R., Dunlop, J.S.R., 1980. Stromatolites 3,400–3,500 Myr old from the North Pole area, Western Australia. Nature 284, 443–445. https://doi.org/10.1038/284443a0

Chapitre III
Analyse à nano-échelle de microfossiles de Draken , Spitsbergen.

Nanoscale analysis of preservation of 700–800 My-old Draken microfossils, Spitsbergen

Alexandre Fadel [1], Kevin Lepot [1], Sylvain Bernard [2], Ahmed Addad [3], Armelle Riboulleau [1], Andrew H. Knoll [4]

[1] Laboratoire d'Océanologie et de Géosciences, Université de Lille, CNRS, Université Littoral Côté d’Opale, UMR8187, Cité Scientifique SN5, 59655 Villeneuve d'Ascq, France.

[2] Institut de Minéralogie, de Physique des Matériaux et de Cosmochimie, CNRS UMR 7590, MNHN, UPMC, 61 rue Buffon, 75005 Paris, France

[3] Unité Matériaux et Transformations, Université de Lille, CNRS UMR 8207, Cité Scientifique C6, 59655 Villeneuve d'Ascq, France

[4] Department of Organismic and Evolutionary Biology, Harvard University, 26 Oxford Street, Cambridge MA 02138, USA

Abstract

The lower flake conglomerates of the Draken Formation, Spitsbergen, contain highly diverse and well-preserved assemblages of Neoproterozoic Bitter Springs-like microfossils. These assemblages are preserved in cherty lenses and are composed principally of filamentous microfossils interpreted as cyanobacterial sheaths forming microbial mats. The silicified mats also contain diverse fossils of benthic and/or allochthonous (possible planktonic) microorganisms. Here, we characterized the ultrastructure of various microfossils with Scanning transmission electron microscopy (STEM) on Focused ion beam (FIB) ultrathin sections, and we documented the composition of the organic matter forming the microfossils with Raman spectroscopy and Scanning transmission X-ray microscopy (STXM). Using these techniques, microfossils could not be distinguished based on molecular structure, which is highly aromatic, likely due to the high maturity of their kerogen. Despite this poor molecular preservation, organic ultrastructures and nano-quartz crystallization patterns from the different types of microfossil help identify sheaths, cells walls, and internal (intracellular ± collapsed membranes) organic material. We show that crystallization of micrometric quartz lead to extensive condensation and displacement of organic matter in the studied microfossils. The nano-scale observation made on well preserved cells of a bacterial filament indicates that even if the cellular wall structure is degraded, the limit of the cell structure can be preserved by nano-quartz crystals forming a ghost structure. The diverse benthic coccoidal microfossils allowed us to derive criteria to constrain the nature of some envelopes. In Chroococcales microfossil, the sheath structure is always preserved as an outer envelope of variable thickness. We also characterized internal nano-organic structures of microbenthic organisms (Gloeodiniopsis), which could not be identified with optical observations. These internal structures probably represent internal membranes (such as thylakoid) and/or cellular membranes that could have thickened through diagenetic polymerization. Moreover, our ultrastructure observations of internal membrane of a Sphaerophycus interpreted as cellular membranes based on optical observation permits to reassign this structure as internal sheath structure. The Synodophycus microfossil appear composed of organic membranes similar to the F-membranes of Pleurocapsalean cyanobacteria. For the first time, the ultrastructure of cyanobacterial Polybessurus microfossil forming large stalk structure (jetted structure) were investigated. These large microfossils have an ultrastructure composed of several sheath layers looking similar to sheaths of Chroococcales microfossils. Nanoanalysis of an unjetted small Polybessurus indicates that inner sheath structure is composed of thinner

layers, which are probably characteristic of earliest stages of the stalk formation. Moreover, this unjetted microfossil contain probable cellular membranes and thylakoid membranes non-observable with optical microscope. We report also an unusual wall ultrastructure forming thick (~1µm) organic pillar structure from simple spheroidal Myxococccoides (possible planktonic microorganisms). If this structure is the original feature of the microfossil, this pillar fabric might be the remain of eukaryote wall structure or cyanobacterial sheath/akinetes membranes. Finnaly, we investigated for the first time the nanostructure of organic matter in vase-shaped microfossils (VSM, eukaryotic microfossil). The wall structure is composed of two layers: an inner thin layer and a thicker organic outer layer forming a reticulated envelope. Our analysis has led to describe new nanostructure which cannot be recognized with optical observations, constrain the nature of several organic ultrastructures of highly mature microfossils. Such studied have permit to defined taxonomic and taphonomic criteria, which can be applied on other unidentified or putative microfossils in paleo-Proterozoic or Archean rocks.

1 Introduction

The first three billion years of the life history on Earth were dominated by prokaryotic life (Brocks et al., 2017; Knoll et al., 2016). In attempt to demonstrate traces of life in Archean rocks many studies have focused on the reference microfossils from the Paleoproterozoic (2.45–1.6 Ga) to define criteria of biogenicity. After the first rise of free oxygen in the atmosphere (the Great Oxygenation Event, 2.45–2.2Ga, Lyons et al., 2014), Gunflint-type assemblages dominate the fossil record between 2.45–1.7 Ga and have been extensively studied to address prokaryotic metabolism/diversity at this time (Barghoorn and Tyler, 1965; Fadel et al., 2017; Guo et al., 2018; Javaux and Lepot, 2018; Knoll et al., 1988; Knoll and Barghoorn, 1976; Lekele Baghekema et al., 2017; Lepot et al., 2017; Wacey et al., 2013). During the mid-Proterozoic, eukaryotes were present but remained at a low diversity (Knoll et al., 2006) and cyanobacteria remained the main primary photosynthetic producers in an ocean characterized by locally euxinic/ferruginous conditions in the water column and weakly oxygenated surface water and atmosphere (Brocks et al., 2017; Lyons et al., 2014). This Mesoproterozoic (1.7-1.0 Ga) statu quo of cyanobacterial domination over phototrophic eukaryote was maintained by chemical conditions such as the low concentration of biologically important trace metals (Anbar and Knoll, 2002), low phosphate fluxes into the ocean (Reinhard et al., 2016). Such low nutrient conditions favored small-sized phototrophic organisms (e.g. cyanobacteria) that have a high surface-to-volume ratio allowing efficient diffusion-controlled uptake of trace nutrients (Irwin et al., 2006). This biogeochemical states were probably maintained by a low primary productive of photosynthetic microorganism and production of oxygen, which reduces the flux of phosphate and maintained the development of deep euxinic water until the end of the Tonian (or the pre-Sturtian) (0.75–0.72 Ga) periods (Anbar and Knoll, 2002; Brocks et al., 2017; Butterfield, 2015; Derry, 2015; Laakso and Schrag, 2014; Reinhard et al., 2016). Although bacteria dominated the pre-Sturtian environment, lot of studies were conducted to document Tonian and younger organic-walled microfossils extracted for palynological studies, which are possibly eukaryotes. The organic-walled microfossils were actively studied to find criteria to constrain the eukaryotic/prokaryotic nature of organic-walled microfossil based on the ultrastructure (Agić et al., 2015; Arouri et al., 1999, 2000; Javaux et al., 2004, 2003; Willman, 2009). Thus, diverse eukaryotic microfossils were reported from Tonian and younger rocks (Battison and Brasier, 2012; Beghin et al., 2017; Butterfield, 2004, 2005a, 2005b; Cohen and Knoll, 2012; Knoll et al., 2006; Lamb et al., 2009; Pang et al., 2013; Porter et al., 2003; Vorob'eva et al., 2015). These include at least a few populations assigned with confidence to extant eukaryotic clades (example of the vase-shaped microfossils: (Porter et al., 2003). The end of the Tonian (and the pre-Sturtian part of the subsequent Cryogenian period) corresponds to the preservation of Bitter Springs-type assemblage, which are dominated by bacterial mats (mainly cyanobacteria) from limited shallow-water/supratidal carbonate environments (Butterfield, 2003). The first well-documented case of this microfossil type assemblage comes from the Bitter Springs formation, central Australia (Barghoorn and Schopf, 1965; Schopf, 1968). This spectacular and well-preserved assemblage of filamentous and spheroidal microfossils occurred in cherts (rocks composed of more than 90% of quartz). Similar assemblages were also found in other Neoproterozoic rocks (Green et al., 1989; Knoll, 1982; Knoll et al., 1991; Schopf, 1968; Schopf and Blacic, 1971; Sergeev and Schopf, 2010). Due to the excellent preservation of these microfossils of these type of assemblage, their biogenicity is well established. Compared to Meso-and Paleoproterozoic microfossils, a smaller number of nanoscale and microscale textural and chemical characterization were performed on this type microfossil assemblages (Foucher and Westall, 2013; Igisu et al., 2009; Lemelle et al., 2008; Oehler, 1976; Oehler, 1977; Oehler et al., 2006; Williford et al., 2013). These studies contributed to define criterion of biogenicity and taxonomic indicators that could be used for older microfossils. Isotope microanalyses could distinguish eukaryotic acritarchs (Leiosphaerida crassa) from colonial cyanobacteria (Myxococcoides sp.) (Williford et al., 2013). The aliphaticity analyzed with infrared spectroscopy has been used to infer the bacterial nature of Bitter Springs Fm microfossils (Igisu et al., 2009). Microscale heterogeneities in N/C in Bitter Springs Fm microfossils suggested that fossil sheath polysaccharide could be distinguished from cell wall peptidoglycan (Oehler et al., 2006). Organic sulfur, possibly derived from proteinaceous material, was detected in Draken Fm microfossils (Lemelle et al., 2008). The ultrastructure of Bitter Springs Fm microfossils has been investigated after palynological extraction and been used to propose distinctions between eukaryotic and prokaryotic cell walls, and to distinguish polysaccharide envelopes and possible intracellular contents (Oehler et al., 1976). Here, we investigate the ultrastructure and molecular structure of various microfossils of the well-preserved Bitter Springs-type assemblage from the Neoproterozoic lower flake conglomerate of the Draken Formation (Knoll et al., 1991). We show that the maturity of organic matter in the Draken microfossils is relatively high, higher than in the Bitter Springs Fm (cf. Schopf et al., 2005) and comparable with the maturity of many Paleoproterozoic and Neoarchean microfossil assemblages. For the first time, we investigate the ultrastructure of a large number (13) of microfossils, spanning 9 morphospecies, at the nanoscale together with their mineral matrices. For the first time, we documented the ultrastructure of Polybessurus and Vase Shaped Microfossils. Moreover, our nanoscale investigations permit to characterize several nanostructures, which are not visible with optical observations. From these microfossils, we also documented the nature of the organic nanostructure based on comparison with modern bacteria. The characterization of the ultrastructure and nano-chemical data obtained from these prokaryotic and eukaryotic (e.g. vase shaped microfossil) microfossils can be useful for assessing microfossil assemblage of Proterozoic/Archean samples.

2 Geological setting

The studied microfossils come from the 700–800 My-old Draken Formation in the eastern part of the Svalbard archipelago. The Draken Formation belongs to the Neoproterozoic succession from the northeast Spitsbergen island that were affected by the Caledonian orogeny (the Silurian-Devonian Ny Friesland orogeny) (Gee and Page, 1994; Halverson et al., 2017, 2007; Harland et al., 1992; Harland and Gayer, 1972; Lyberis and Manby, 1999). In the eastern province of the Svalbard (northeast Spitsbergen and northwestern Nordaustlandet islands), this Neoproterozoic succession is part of the Hecla Hoek Series (Harland and Wilson, 1956) and is exceptionally well preserved compared to the Neoproterozoic rocks in the southwestern province (Bjørnerud, 2010; Halverson et al., 2017; Harland et al., 1992). Moreover, the similarity between the Neoproterozoic stratigraphy of the eastern part of the Svalbard and East Greenland Caledonides is cited as evidence that both were deposited in a contiguous basin forming the East Greenland–East Svalbard platform, which was part of the eastern Laurentia (Halverson et al., 2017; Harland and Gayer, 1972; Hoffman et al., 2012). The Neoproterozoic strata of the northeastern Spitsbergen are subdivided into the Veteranen, Akademikerbreen and Polarisbreen groups.

The Veteranan Group is composed of siliciclastic sediments (mixed of sandstone, siltstone and shale) and minor carbonates deposited predominantly and possibly entirely within a marginal marine environment (Wilson, 1958). The Veteranen Group is constrained to be younger than 940 Ma based on the age of underlying equivalent group in Nordaustlandet (variably the Meyerbukta Formation or the Galtedalen group) and detrital zircon (Johansson et al., 2005, 2000; Sandelin et al., 2001).

The Akademikerbreen Group conformably overlies the Veteranen Group and comprises, in ascending order, the Grusdievbreen, Svanbergfjellet, Draken and Backlundtoppen formations. This group is up to 1900 m thick, 650 km long and contains mostly carbonates rocks with only minor sandstone, siltstone and shale (Knoll and Swett, 1990; Wilson, 1961). The Akademikerbreen limestones and dolomites accumulated in a carbonate ramp in tropical latitudes, during a subsidence phase (Knoll and Swett, 1990; Maloof et al., 2006). The Grusdievbreen formation reaches ~600 m in thickness and is composed of two informal members (upper and lower). The base of this formation is mostly composed of fine dolomitic siltstone settled during the establishment of the storm-dominate carbonate ramp and the upper part of medium-bedded calcilutite to grainstone (Halverson et al., 2007). The overlying Svanbergfjellet formation (~600 m thick) is dominated by limestone ribbon rocks with abundant isolated microbial laminae and stromatolites. This formation is composed of four informal members (Knoll and Swett, 1990; Wilson, 1961). The overlying Draken Formation is 150-250 m thick and composed principally of dolomitic intraformational conglomerates, isolated microbial laminae and grainstones (Knoll et al., 1991). The contact between the Draken Formation and the overlying, ~500 m thick Backlundtoppen Formation is transitional. The latter comprises limestones and dolomites, with oolitic/pisolitic grainstone, dolomite clastic grainstone, stromatolites and several microfossil assemblages (Knoll et al., 1989; Wilson, 1961). Finally the Polarisbreen group overlies the Akademikerbreen Group and is composed a mixed of carbonate-siliclastics rocks with two diamictites units, which probably represents the Sturtian and Marionan glaciations (Halverson et al., 2007, 2004; Hoffman et al., 2012).

The Draken Formation is mainly composed of dolomite (principally intraclastic doloarenite, dolorudite and interbedded dolomicrites). The middle third of the formation comprises frequent oolites and oncolites while the upper part of the formation is composed of stromatolites with tepee structures, which are associated with thin intraclastic dolomites and dolomicrites (Knoll et al., 1991). Microfossils are preserved in several lithologies (carbonates, shale). However, the well preserved Draken microfossils are present in early diagenetic chert forming black (organic-rich) tabular shards. These black chert shards are comprised in an unusual lithology, termed flake conglomerate by Wilson (1961), which is composed of intraclastic dolomicirite round clasts within carbonate rocks. Large dolomite euhedra are also common together with silicified mud clasts. The black chert shards were interpreted as silicified fragment of microbial mats (Fairchild et al., 1991; Knoll, 1982; Knoll et al., 1991). The presence of bends and perturbations of mat laminations in these shards suggest that mats remained flexible during the conglomerate deposition and imply that the silicification occurred rapidly (Knoll, 2003, 1982; Knoll et al., 1991; Wilson, 1961).

The Draken conglomerate were inferred to be deposited in a protected lagoon (Fairchild et al., 1991; Knoll et al., 1991). The microbial mats developed subtidally in a quiet shallow environment. However, storms occasionally breached the barrier, ripping up the mats, the fragments of which deposited with carbonate mud clasts. Organic matter degradation in mat fragments ceased rapidly with the burial caused by storms and early silicification, which resulted in the delicate preservation of microfossils. The alternation of these quiet and turbulent deposition settings lead to the formation of the Draken Conglomerate. Moreover, a series of five subfacies was recognized from the diversity of microfossils permineralized in cherts and were associated with a deposit environment (ranging from subtital to supratidal condition) (see table 1 in Fairchild et al 1991, or Table 9 in Knoll et 1991). The first biofacies is the *Melanocyrillium* biofacies which is named from the vase -shaped microfossils present in this assemblage (Fairchild et al., 1991; Knoll et al., 1991). This assemblage can contain acritarchs, *Myxococcoides* and is characteristic of subtidal, lagoonal environment. The second biofacies is composed of filaments *Siphonophycus (septatum)* mat builders associated with auxiliary *Salome svalbardensis*. This subfacies, characteristic of lower intertidal or transitional lagoon contains also diverse micro-benthic taxa and common allochthonous *Myxococcoides*. (Fairchild et al., 1991; Knoll et al., 1991). The third biofacies is composed of thin-walled *Siphonophycus (inormatum)*, which are the main mat builders and comes from the intertidal zone of the lagoon. Like the second biofacies, the mats builders are associated with diverse micro-benthic taxa and common allochthonous *Myxococcoides spp* (Fairchild et al., 1991; Knoll et al., 1991). The fourth biofacies are composed of thick-walled *Siphonophycus (inormatum)*, characteristic of the upper intertidal zone. This biofacies contains few micro-benthic and allochthonous microfossils (Fairchild et al., 1991; Knoll et al., 1991). The final biofacies is composed of *Siphonophycus (kestron)* filaments and is characteristic of upper intertidal to supratidal zone. Micro-benthic and allochthonous taxa are absent (or rare if present) (Fairchild et al., 1991;

Knoll et al., 1991). Here, all the studied microfossils come from the Lower flake conglomerate assemblage, which contains the best preserved and most diverse fossils from the biofacies 1, 2 and 3, within cherty lenses. Cherty lenses containing the biofacies 4 and 5 are rare. The samples containing microfossils present here come from the Polarisbreen Vettene area, north east part of Spisbergen island (Knoll et al., 1991). The samples studied are labelled P4353-1B, -5A; -6A; -11A (Knoll et al., 1991).

3 Methods

3.1 Semi-thin sections

All observations and analyses were carried out on 400–500 mm thick, polished uncovered semi-thin sections prepared following the procedure described in Fadel et al. (in prep, see chapter 2 of this thesis). The advantage of these semi-thin sections is that their preparation and observation do not require gluing of the section onto a slide with epoxy. In addition, the semi-thin sections were rinsed with organic solvents (acetone, ethanol, followed by HPLC grade dichloromethane and methanol) to remove labile molecules in zones close to the surface that are open to fluids. Therefore, we expect to analyze only insoluble, indigenous organic matter in our preparations.

3.2 Optical microscopy

Optical petrography and microfossils localization were carried out using an Olympus BX60 microscope (LOG, Université de Lille) under bright-field transmitted light and reflected light. Photomicrographs from single focal planes were combined into ‘‘multiplane images” using a weighted average algorithm (CombineZP software by Alan Hadley) in order to fully describe each microfossil and microfossil clusters (Bercovici et al., 2009). Photomicrographs of microfossils are multiplane images, unless otherwise specified. The obtained image were used to locate microfossils at/near the surface of the semi-thin section for further microfossils analysis: Raman spectroscopy, Scanning Electron Microscopy (SEM) and Transmitted Electron Microscopy (TEM) observations on the same microfossils.

3.3 Raman spectroscopy

Raman spectra of microfossils were obtained using a LabRam HR800UV Raman microspectrometer (Horiba Jobin Yvon) (at LOG, Université de Lille). The spectra were acquired with a 532 nm laser focused through an Olympus BX41 microscope with 50× objective (long working distance NA =0.75) during 1–2 min. In order to avoid artifacts, spectra were obtained in focus 1–2 µm below the surface of thin sections and filters were used to limit the laser power to less than 1 mW (point spectra) on the surface of the thin section. The backscattered Raman signal was dispersed by a grating (1800 lines/mm) and analyzed with a front-illuminated CCD detector.

3.4 Scanning electron microscopy and focused ion beam

SEM images were recorded on gold-palladium coated (~20 nm-thick deposit) thin sections using a FEI Quanta 200 (at LOG, Université de Lille) SEM. The secondary electron images (SE) revealed the topographic features that located targets for the preparation of ultrathin sections of microfossils with focused ion beam (FIB). FIB sections were prepared with a FEI strata Dual-Beam 235 FIB (at IEMN, Lille) for Transmitted Electron Microscopy. During the FIB section preparation, the top surface of each region of interest was protected with platinum strip ~25 mm long and ~2 mm thick. Material on each side of the region of interest was removed by a gallium (Ga^+) ion beam (30 kV, 7 nA). Then, FIB sections were lifted out and attached onto a copper TEM grid by depositing platinum at the contact(s) between the section and the grid. The section was thinned to ~150–200 nm using beam with decreasing current (1 nA to 300 pA and 100 pA) grazing on each side of the section. Finally, the plasma-redeposited amorphous material was removed by scanning the section with a 5 kV ion beam at an angle of 4–7° with the section surface.

3.5 Scanning transmitted electron microscopy

STEM analyses were performed on the FIB sections on a FEI TITAN Themis 300 TEM (CCM, Université de Lille) operated at 80 kV. The FIB sections were inserted into the microscope using a cryo-transfer holder (model 914, Gatan) cooled by liquid N_2 (-172°C). Liquid N_2 was added after 3 hours, to allow the recovery of microscope vacuum and avoid formation of frost on the FIB sections. The microscope is equipped with a monochromator and a Cs probe corrector. For high-angle annular dark-field (HAADF) image acquisition, the spot size was #8 (producing a screen current of ~ 50-90 pA) and the camera length was 91 mm. For dark field images, the same parameters were used but the camera length was 285 mm. The contrasts in STEM HAADF images are only influenced by the atomic weight of elements, whereas STEM dark field images are more influenced by diffraction contrasts. Elemental distributions were mapping using a Super-X EDXS (Energy Dispersive X-ray Spectrometry) detector (formed by four SSD detectors integrated to the S-TWIN objective lens), which is sensitive to light-weight elements. This detector allowed us to produce EDXS mappings of the sample in the same horizontal position as that used to record all STEM images.

3.6 XANES –STXM

STXM analyses were performed at the Diamond Light Source beamline I08-SXM and the Canadian Light Source beamline 10ID-1 (SM). The I08-SXM beamline uses radiation ranging from 250 to 4400 eV, generated by an Apple II type ondulator. The X-ray source is optimized to enable studies exploiting linearly or circularly polarized radiation. The intensity of the X-rays transmitted through the sample is directly measured using a photodiode. STXM was used to perform high resolution (~ 30 nm) spectromicroscopy at the carbon K-edge (energy range 275–295 eV) to image the distribution of organic matter and characterize the carbon chemistry in X-ray absorption near-edge spectroscopy (XANES) spectra. We recorded XANES hyperspectral stacks used a spectral resolution of 0.1 eV between 275 and 295 eV and counting times of 3–5 milliseconds per pixel. XANES hyperspectral stacks of nitrogen were also acquired (375–450 eV, 0.5 eV step). XANES stack data were normalized to the absorption of the background. Aromatic carbon maps were obtained by subtraction of X-ray transmission images recorded in mapstacks (using 15 ms/pixel to improve contrasts) at 285.1 eV (aromatics)—280.1 eV (pre-edge absorption 'baseline'). Preliminary analysis was also performed on one microfossil at the Canadian Light Source (CLS) SM beamline 10-ID1 (Kaznatcheev et al., 2007) (chamber back-filled with He instead of vacuum; PMT detector, inferred flux in the 10^6 photons.cm^{-2} order of magnitude, spatial resolution <25 nm, dwell time ≤2 ms). Alignment of images of stacks, extraction of XANES spectra and aromatic carbon maps were obtained using the aXis2000 software available on http://unicorn.mcmaster.ca/aXis2000.html.

4 Results

4.1 Microfossil assemblage

4.1.1 Microfossils assemblage

The microfossil assemblages present here come from the lower flake conglomerate of the Draken formation. (Fig.3.1 and supplementary Fig.3.1)

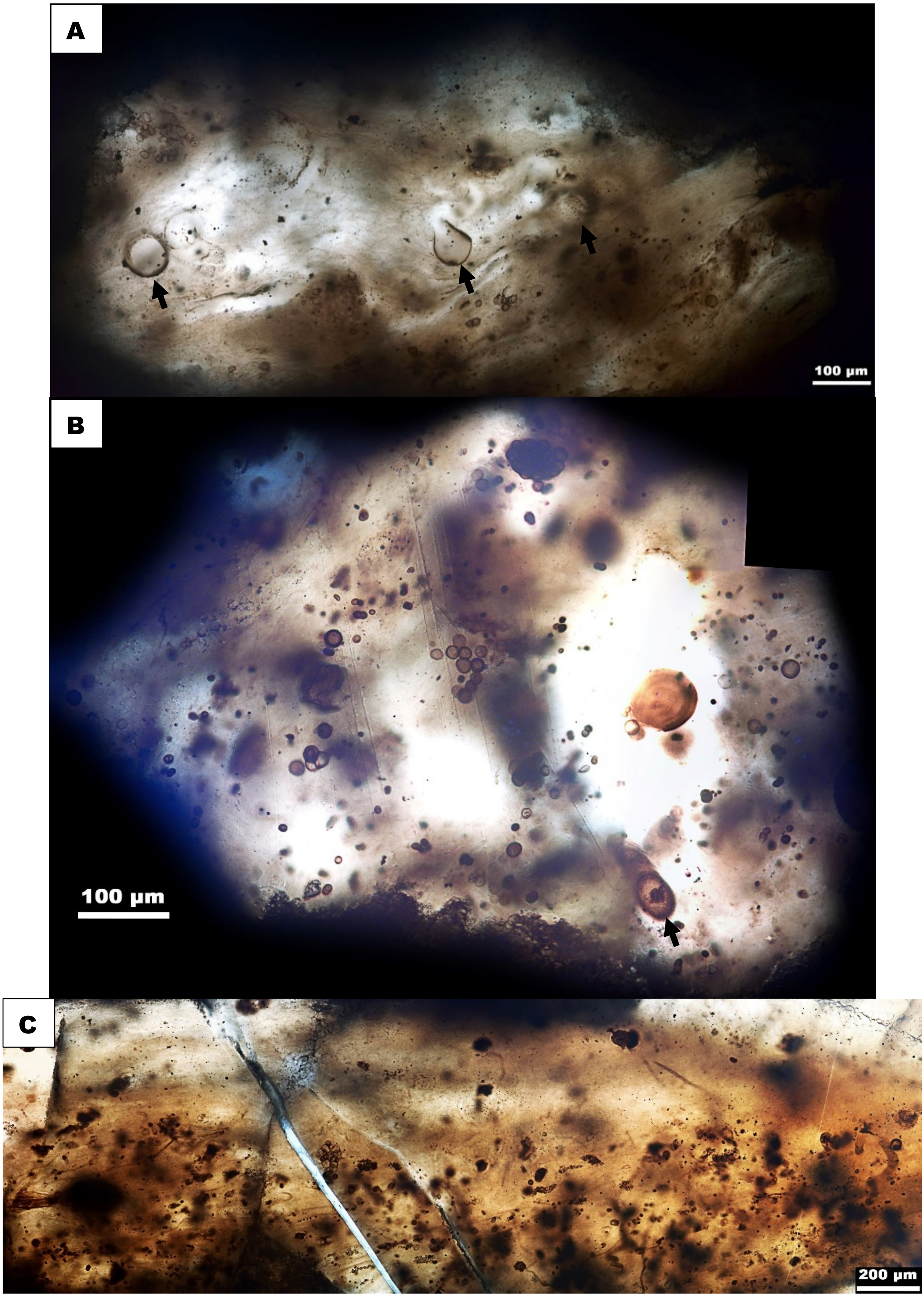
A
100 µm
B
100 µm
C
200 µm

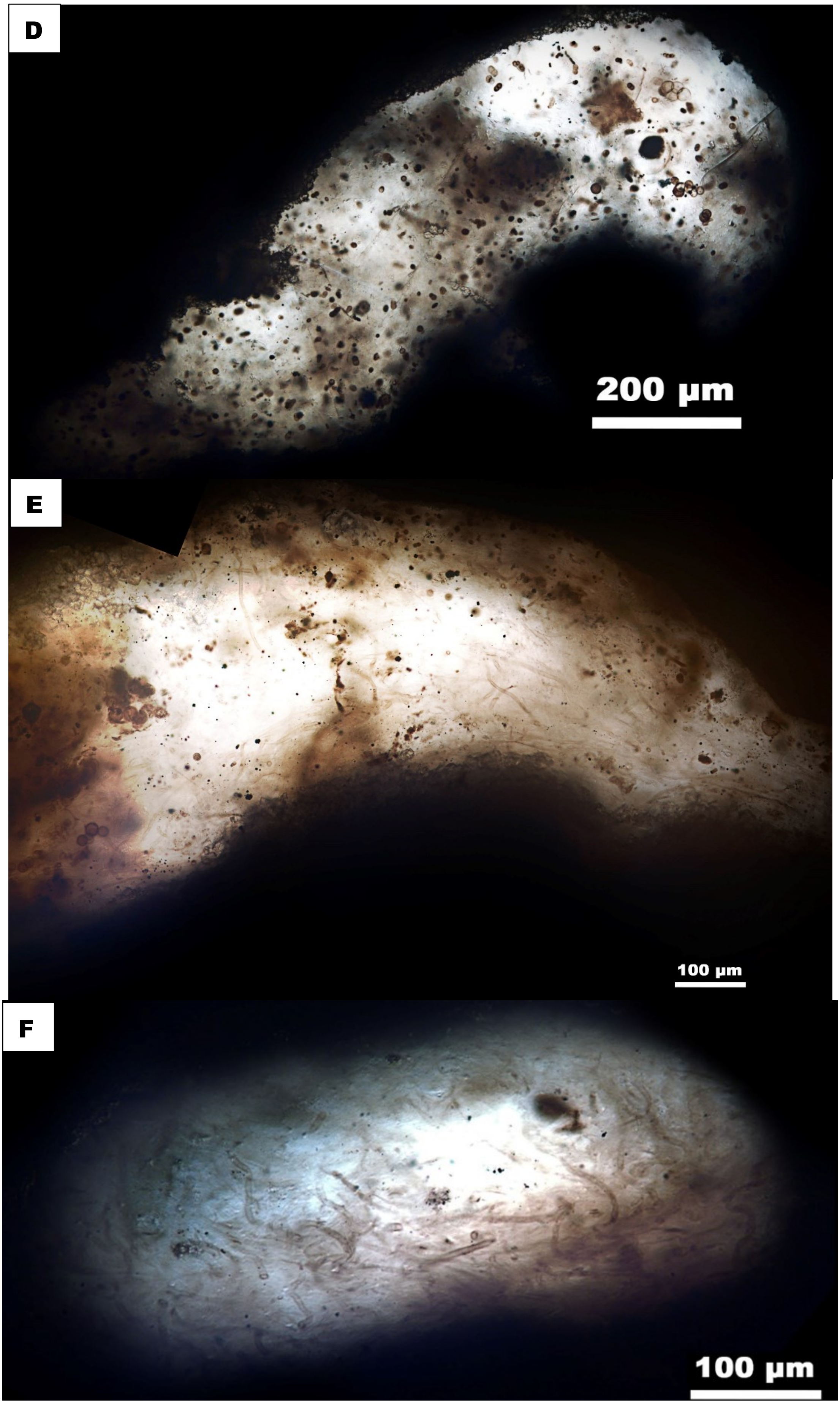
D
200 µm
E
100 µm
F
100 µm

Fig 3.1. General view of cherty lenses containing diverse assmeblage. *A. Assemblage of microfossils with vase-shaped microfossils (arrows) and various Myxococcoides spheroids from lagoonal setting. B. Higly diverse cherty lenses containing various allochthonous and microbenthic microfossils (arrow: Polybessurus). C. Microbial mats composed of Siphonophycus filaments associated with highly diverse micro-benthic microfossils and allochthonous (probably planktonic) microfossils. D. Small fragment of chert shards containing abondant microbenthic and allochtnous microfossils. E. Microbial mat shard of Siphonophycus (inormatum) associated with allochtonous Myxococcoides microfossils. F.Microbial mats only composed of Siphonophicos spetatum. (Samples: A: P4353-1B ;B: P4353-6A ;C: P4353-5A ;D:P4353-11A ;E:P4353-1B ;F: P4353-6A).*

Microfossils in the cherty lenses are highly diverse with 42 microfossil morphospecies, for which the distribution and taxonomy have been characterized by Knoll, 1982 and Knoll et al., 1991. Moreover, the different assemblages present within the cherts comprise mostly different types of filaments (tubular filaments, likely fossil of polysaccharide sheaths, with variable diameter ranging between ~5 and ~15µm) interpreted as mat-forming filamentous cyanobacteria (Figs. 3.1. C,E,F). These microbial mats can be associated with a high variety of well-preserved microfossils, which were interpreted as microbenthic organisms and allochthonous microorganisms (probably planktonic). Interestingly, the diversity of these microbenthic and allochthonous organisms is highly important in cherty lenses with low abundance of filamentous microorganisms (compare cherts in Fig. 3.1A-D vs 3.1F-E). However, the distribution of these microbenthic or allochthonous microfossils is non-homogenous and they can occur as isolated in some cherty lenses. These well preserved microfossil assemblage are also associated with pyrite crystals (also reported by Foucher and Westall, 2013 and Lemelle et al., 2008).

4.1.2 Geothermometry of the carbonaceous material

The excellent morphological preservation of the microfossils as structured carbonaceous remains has been highlighted with Raman mapping by Foucher & Westall (2013). All microfossil displayed similar Raman spectra with five main bands between 1000 and 2000 cm^{-1} that are related to kerogen (Fig. 3.2). This indicated that the different microfossils present in the assemblage are composed of kerogen. Based on peak fitting decomposition the Raman spectra of organic matter, the calculated peak metamorphism temperature of the kerogen is 285°C ± 30°C (Fig. 3.2) [Fitting used: method F of Kouketsu et al. (2014), using equation: $T(°C)= -2.15$ FWHM-D1+478 with a measured full width at half maximum of the D1 band at ca. 1350 cm^{-1} FWHM-D1 of 95 cm^{-1}].

The XANES spectrum obtained at Diamond from organic matter of microfossils appear to be only composed of aromatic molecules (Fig. 3.3E). Moreover, the absence of distinct N K-edge the XANES hyperspectral data obtained show the absence of nitrogen (N) (not show). In contrast, the CLS spectrum obtained from a microfossil indicates a faint signal of C=O bonds (bands at 287.5eV indicative of ketone C=O, and bands at 287.5 eV of carboxylic C=O see supplementary Fig. 3.2). In the CLS spectrum, a weak signal of N at the N K-edge (supplementary Fig. 3.2) was detected not only on the wall structure of the microfossil but everywhere on the FIB section, suggesting that an inorganic N contaminant adsorbed on the thin section. We note that we analysed comparatively volumes of organic carbon at Diamond (e.g. Fig. 3.3D), whereas only nanoparticles were analysed at CLS (Supplementary Fig. 3.2). At such small amounts of carbon, the CLS spectral data are more prone to show the overprint of faint contaminations. The N and C=O bands detected at CLS may thus have come from the fossil or may represent a normalization artefact, or a contaminant on the FIB section. This contaminant, if it exists, was not detected at Diamond, possibly because: i) other FIB sections were not contaminated prior to STXM analysis, ii) better vacuum conditions at Diamond (compared to He-backfilled chamber at CLS) preventing *in situ* beam-deposition of contaminants (e.g. Leontowich and Hitchcock, 2012), iii) radiation damage quickly altered fragile contaminants. Alternatively, these differences in spectral signatures between the Diamond and CLS data could come from intrinsic heterogeneities among Draken microfossils. However, we note that we searched for C K edge XANES heterogeneities among 12 different morphospecies of Draken microfossils using hyperspectral maps of mapstacks: all these analyses (not shown) pointed to a highly aromatic organic matter depleted in oxygen-bearing functional groups. Because the photon dose was higher at Diamond, a small amount of C=O as detected at CLS, may have been obliterated by radiation damage, altough it remains difficult to demonstrate. Irrespective of the possible presence of C=O and N-bearing functional groups, both datasets (Diamond and CLS, Supplementary Fig. 3.2) point to a highly aromatic composition that could have been produced by radiation damage alone.

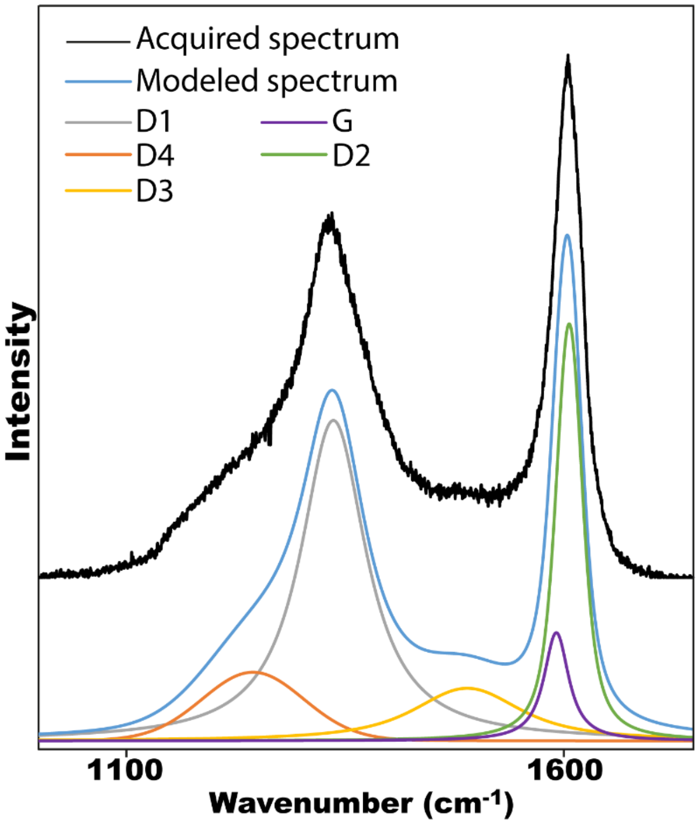

Fig.3.2. *Raman spectra of kerogen obtained from a microfossil and its deconvolution in five bands. The vibrational bands at ~1350cm-1 (D bands) and 1600cm-1 (G bands) established the carbonaceous composition of the microfossil. Centers of the band: D1: 1348cm*$^{-1}$*; D2: 1606cm*$^{-1}$*; D3: 1480 cm*$^{-1}$ *; D4: 1244cm*$^{-1}$ *and G: 1580cm*$^{-1}$*.*

4.1.3 Filamentous microfossils

4.1.3.1 Siphonophycus

The filaments present in the lower flake conglomerate were interpreted as sheath of filamentous cyanobacteria by Knoll 1982 and Knoll et al 1991. These filaments include several species of Siphonophycus filaments based on cross sectional diameter, abundance and distribution within cherty lenses. They form mat assemblages with the other well-preserved microfossils (mat-dwellers or allochthonous microfossils). Here the ultrastructure of a ~5 µm diameter filament (probably S. inornatum) with internal material was investigated (specimen 1). This filament occured in a cherty lens displaying a high diversity of microfossils (mat dwellers and allochthonous material, see Table 5 in Knoll et al. 1991). Interestingly, the content of organic matter within the specimen 1 microfossil (Fig. 3.3A) is high and prominently appears as a thick central organic thread that is absent in other filaments of similar total diameter occurring near this filament (see Supplementary Fig. 3.3). A longitudinal FIB section was prepared for the filament specimen 1 (Fig. 3.2A) and a transversal section on empty sheath filaments (Supplementary Fig. 3.3). The FIB sections reveal that the quartz surrounding the filaments are nanocrystals (~100–200 nm in diameter) (Fig. 3.3B and Supplementary Fig. 3.3). The outer limit of the filament specimen 1 is defined by a thin layer of organic matter (Fig. 3.3A-D). Quartz nanocrystals also found inside and throughout (i.e. impregnating) this thin outer layer. In contrast, larger quartz crystals (up to ~3 µm in diameter) outline the thick central organic thread.

Two Siphonophycus filaments with similar diameters (specimens 2 and 3) display a ~1 µm thick zone interspersed with granular organic material that correspond to the apparently smooth sheath wall seen in optical microscopy (Supplementary Fig. 3.3). Specimen 2 displays a solitary, relatively coarse central organic grain.

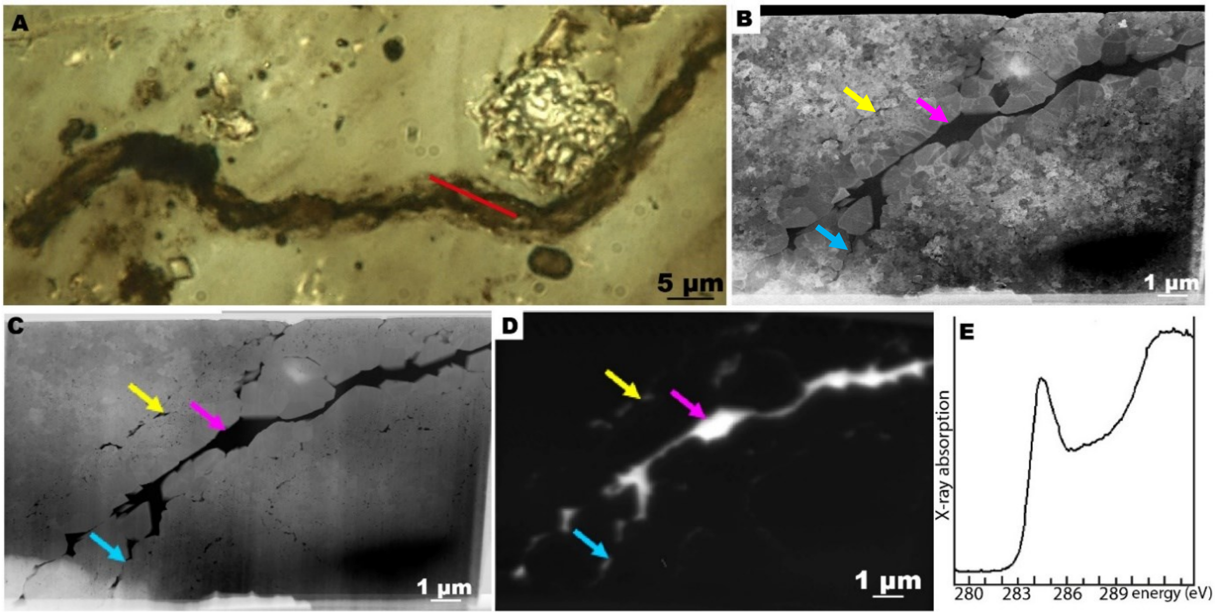

Fig. 3.3. Siphonophycus filaments specimen 1. *A. Photomicrograph in transmitted light (Red line: FIB section position). B. STEM dark field image of the FIB section showing the presence of coarse quartz-crystals within the filaments and surrounding quartz nano-crystals. C. HAADF image of the FIB sections showing the distribution of the organic matter (in dark) and quartz (grey). D. Map aromatic carbon of the FIB section. E. C K edge spectrum obtain form the large central carbon particle of the filaments (Note that the spectrum is slightly shifted by -0.3 eV). Arrows: pink= central thread, yellow= outermost organic layer, blue = migration of the central thread at the interface between micro and nano-quartz. (Sample: P4353-11A)*

4.1.3.2 Salome Svalbardensis

Salome Svalbardensis is a rare type of filament composed of a trichome (chain of disc-shaped cells ~2 µm long and ~6-15 µm wide with a multilayered sheath. The sheath structure includes an inner sheath with a cross section of 8-16µm. This inner sheath is surrounded by up to eight distinct outer sheath layers with cross sections ranging between 23 and 65 µm. However, the partial degradation of trichome or sheath structures makes the identification of this morphospecies difficult in some case such as the microfossil illustrated as *S. Svalbardensis* by Knoll (1982, pl. 3 fig.2) which was reassigned to *Polybessurus bipartitus* after reexamination (Knoll et al., 1991). The combination of multilayered sheath with a partly preserved trichome composed of disc-shaped cells, which is not observed in *Polybessurus* and other filaments with single-layer sheath, is considered diagnostic of *Salome Svalbardensis* (see pl. 3 fig.1 Knoll 1982) Considering other filamentous microfossils, this sheath structure surrounding a trichome was only observed within this morphospecies (references). Based on morphological comparison with modern oscillatorian cyanobacteria (*Lyngbya aestuarii:* Geitler, 1932), this microfossil morphospecies likely is cyanobacterial in origin (Knoll, 1982). One longitudinal FIB section was prepared in such a trichome. In the studied microfossil, the multiple sheath layers are diffuse and difficult to recognize due to low quantity of organic matter (Fig. 3.4A) and due to interspersed nanopyrites (that are also found in the surrounding matrix). Individual disc-shaped cells are heterogeneously preserved along the filament (Fig. 3.4A), and are often replaced by large tubes and clots of organic matter (see left part of the filament in Fig. 3.4A). In this context, it is difficult to determine if the tubular brownish material (arrows in Fig. 3.4A) represents an inner sheath material or degraded cellular material. Although the outer limit of the filaments is not visible within the prepared FIB section, the limit of the disc shaped cells within the sheath structure is distinct (Fig. 3.4D-G). Organic matter within the cells occurs as 200-600 nm large particles that are apparently randomly distributed. Diffuse clouds of organic nanoparticles are present between the well-defined cells. Interestingly, these nanoparticles are less abundant (absent?) in the sheath-region above the cells in Fig. 3.4D-E.

The quartz between the cells and within the sheath structure comprises nanocrystals of ~100–300 µm in diameter. The quartz within the disc-shaped cells are slightly larger (ranging from ~300 nm to 1 µm in diameter). Interestingly, some quartz crystals at the inner border of the cell structures seem to follow (elongate) the shape of the cells and sometimes define the border of the cell structure where carbon is absent (see white arrows in Fig. 3.4E-G).

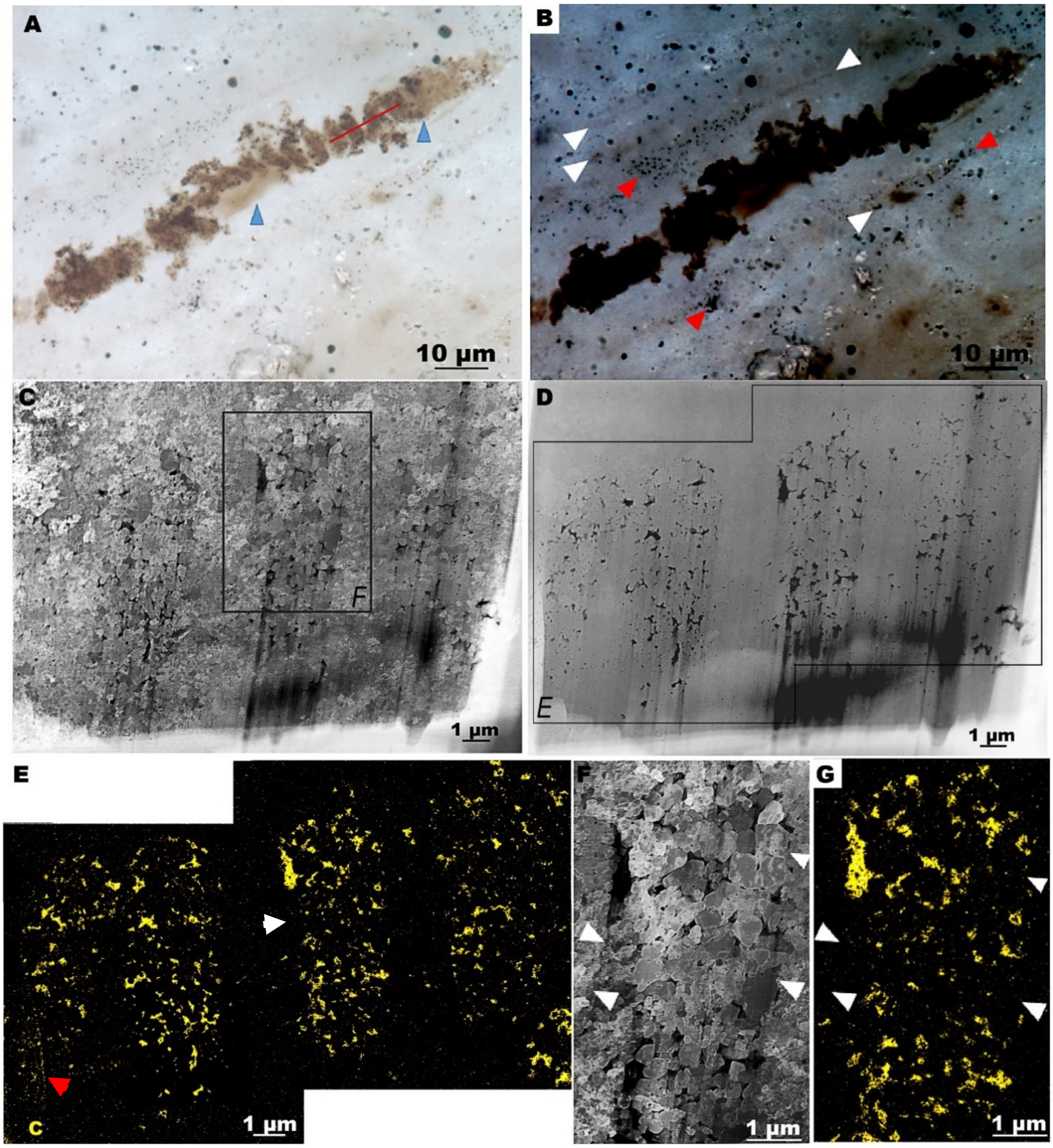

Fig. 3.4. Salome Svalbardensis microfossil. *A. Photomicrograph in transmitted light (Red line: FIB section position; arrows: internal organic material). B. High contrast photomicrograph of the microfossil. Here white arrows outline the multiple organic sheath layers, and red arrows outline locally enrichments in nano-pyrites. C. Dark field STEM image of the FIB section showing the heterogenous distribution of quartz nano-crystals. D. HAADF image of the FIB sections showing the distribution of the organic matter forming disc-shaped cells (in dark) and quartz (grey). E. EDX map of the carbon (C) from the region boxed in D. White arrow: limit of cell devoid of carbon. Note that sub-vertical lines in C-D are an artifact of the FIB preparation process (where preferential FIB etching occurred along vertical lines starting just below organic inclusions). The enrichment in carbon along a vertical line at the left of E (red arrow in the leftmost cell of E) also likely results of a step-in thickness in the FIB section (see corresponding zone in D); this possible analytical artefact needs further verification. F. Zoom*

on the region boxed in C. The white arrows indicate the sharp contact between quartz crystals inside and outside the cell. G. EDX map of the carbon zoom. The white arrows indicate the position of sharp contact between quartz crystals inside and outside the cell and devoid of carbon. (Sample: P4353-1B)

4.1.4 Coccoidal microfossils

Unicellular and colonial coccoids, associated the filaments in microbial mats, are highly diverse (Knoll 1982, Knoll et al., 1991). We have prepared FIB sections of five microfossil morphospecies.

4.1.4.1 Gloeodiniopsis mikros

Gloeodiniopsis genus microfossils were firstly described from the Bitter Springs Formations. The type specie (*G. lamellosa)* consists of large inner wall structures organized in monads, dyad or tetrads (~12.5µm in diameter) surrounded by thick 4-6 concentric outer layers (Schopf 1968). Spheroids with multilamellated walls/envelopes have conventionally been ascribed to *Gloeodiniopsis* (Schopf 1968) but the state of preservation of the inner and outer structures can be variable due to partial degradation (Knoll and Golubic, 1979). The Draken material contain several *Gloeodiniopsis* morphspecies, including *G. Mikros*. The latter is the smallest morphospecies of genus *Gloeodiniopsis* (Knoll, 1982). This microfossil abundant in *S. inormatum* mat shards is composed of spheroidal smooth-walled inner vesicles (~3 µm in diameter) of optically dense organic matter, interpreted as cell remnants, enclosed in an external envelope (~8 µm in diameter) (Fig. 3.5A) interpreted as a polysaccharide capsule (Knoll, 1982, Knoll et al. 1991). External envelop contains only one, two or four vesicles following a simple divisional pattern. The cyanobacterial affinity of *G. mikros* has been inferred by Knoll (1982) based on similarity of size, morphology and division pattern with modern Chroococcaceae, especially the genus *Chroococcus* (i.e. *C. minutus:* Geitler, 1932) and *Gloecapsa.* While the specimens observed are composed of single layered sheath, the assignment of the microfossils present in the Fig. 3.5A and supplementary Fig. 3.4 is based on the size, the wall-texture of inner vesicles and the organization of similar microfossils in dyads/tetrads in the shards where microfossils are hosted. Moreover, the specimens studied have similar size and morphologies with the *G. mikros* population reported in previous studies (see fig.17 2-11 in Knoll et al. 1991). One FIB section was prepared through a cell dyad of *G. mikros* but only one cell structure was thinned to high electron transparency and analyzed (Fig. 3.5B-D). A second FIB section was prepared in a monad of *G. Mikros* (Supplementary Fig. 3.4).

The FIB section shows that the quartz crystals within or outside the microfossil are ~200–500 nm in diameter (Fig. 3.5B). In the dark-field image (Fig. 3.5B), the inner vesicle display appears homogenously darker suggesting that it is populated by coarser, single quartz crystals or similarly-oriented nanocrystals. The envelope comprises a peripheral band of organic matter, ~0.5–1 µm in thickness composed of multiple small (<100 nm in diameter) organic matter grains (Fig. 3.5C-D, red arrows). Contrary to the external envelop, the border of inner vesicle is relatively well defined by a thin layer of organic matter (<100 nm thick). Moreover, the organic matter within the vesicles is not randomly dispersed within the vesicles but formed thin layers (white arrows in Fig. 3.5C–D). The zone between the peripheral band and the inner vesicle is depleted in organic matter (green arrows in Fig. 3.5C-D). A monad (also attributed to *Gloeodiniopsis mikros)* also shows a similar ultrastructure (Supplementary Fig. 3.4). This unicell microfossil is also composed a ~1-µm thick outer envelope of organic nanograins, an intermediate zone depleted in organic matter, and an inner vesicle. The latter displays an outer organic wall (~ 1-nm thick) with thinner (~ 200 nm) internal organic layers.

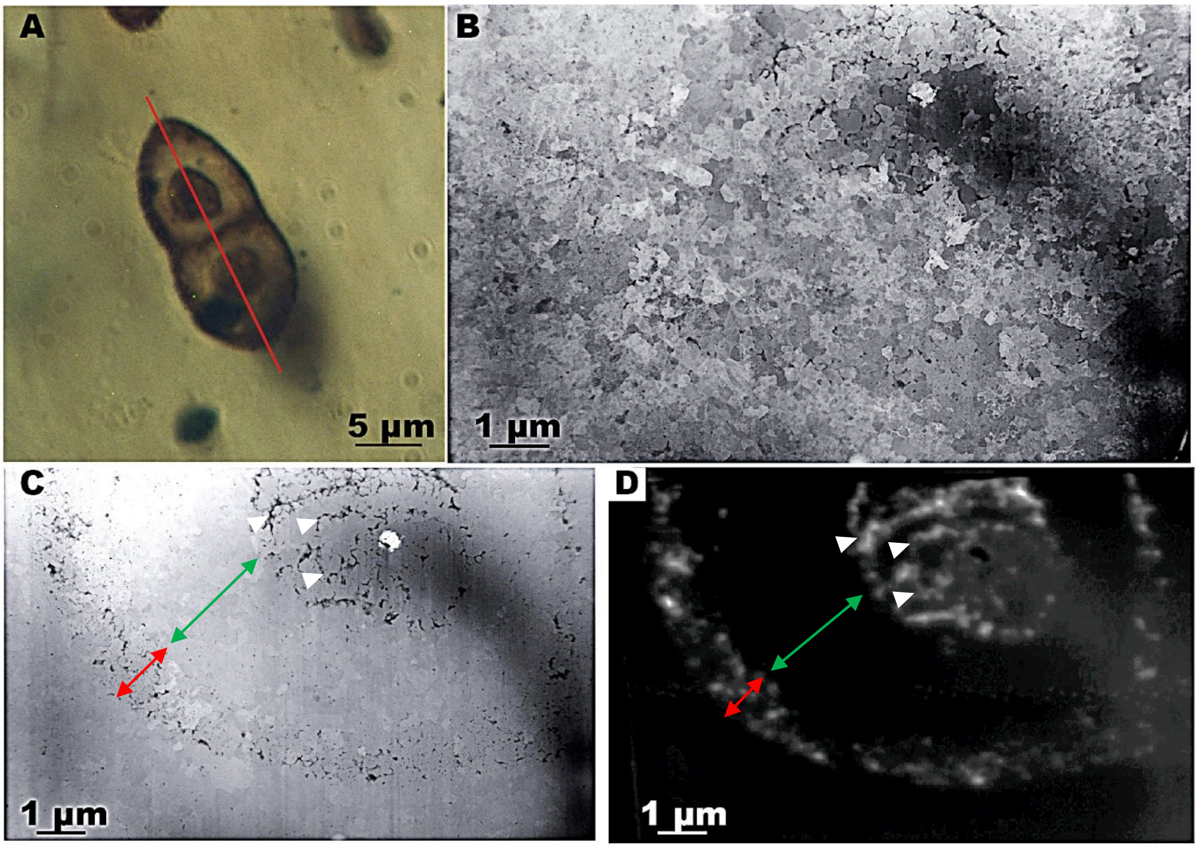

Fig. 3.5. Gloeodiniopsis microfossils. *A. Photomicrograph in transmitted light (Red line: FIB section position). B. STEM dark field image of one cell from the FIB section showing the presence of quartz nano-crystals within and outside the microfossil. C. HAADF image of one from the FIB sections showing the distribution of the organic matter (in dark) and quartz (grey). The white crystal is probably pyrite (need further verification). D. Map aromatic carbon of one*

cell from the FIB section. The white arrows indicate the organic layers in the inner vesicle. The white arrows in C-D indicate the position of thin continuous organic matter layers. The red arrows highlight a ~ 0.5–1 µm large peripheral band of organic matter nanoparticles. The green arrows highlight an intermediate zone depleted in organic matter. (Sample: P4353-11A)

4.1.4.2 Sphaerophycus

A second dyad of coccoidal microfossils was also analyzed. This dyad is composed of inner spheroidal vesicles (~5 µm in diameter) surrounded by a single common envelope. We assigned this microfossil to *Sphaerophycus* (*?) medium* rather than *Gloeodiniopsis mikros* due to the higher relative volume of the inner vesicle compared to the envelope, the granular texture of the inner vesicles (Fig. 3.6A versus 3.5A) and the presence of similar specimens containing more than four inner vesicles in the vicinity of the analyzed microfossils (shard of Fig. 3.1D). The morphological similarity with the extant genus *Aphanocapsa* and the binary division/fission patterns of other *Sphaerophycus* microfossils argue for a cyanobacterial origin (Knoll, 1982). One FIB section was prepared through the two inner vesicles and their enclosing envelope (Fig. 3.6A). Again, the microfossil is associated with quartz nanocrystals (~200–400nm in diameter). Moreover, regions of adjacent quartz nanocrystals display the same darker diffraction contrast suggesting that they have the same orientation at a border of the outer envelope (white arrow in Fig. 3.6B). The dyad is enclosed in an outermost envelope formed by a discontinuous cloud (~1-µm thick) of organic particles smaller than 100 nm (Fig. 3.6C-D). Each vesicle of the dyad is outlined by another similar, more internal, discontinuous envelope (Fig. 3.6C-D), a feature that further distinguishes this microfossil from the *Gloeodiniopsis* dyad (Fig. 3.5). Moreover, the vesicle to the right diplays an innermost layer of organic matter formed by a single layer of organic particles >200 nm in thickness (white arrows in Fig. 3.6C-D). This innermost layer is absent in the left vesicle. In contrast, the latter contains a small patch composed of nanometric organic matter particles (grey arrows in Fig. 3.6C-D).

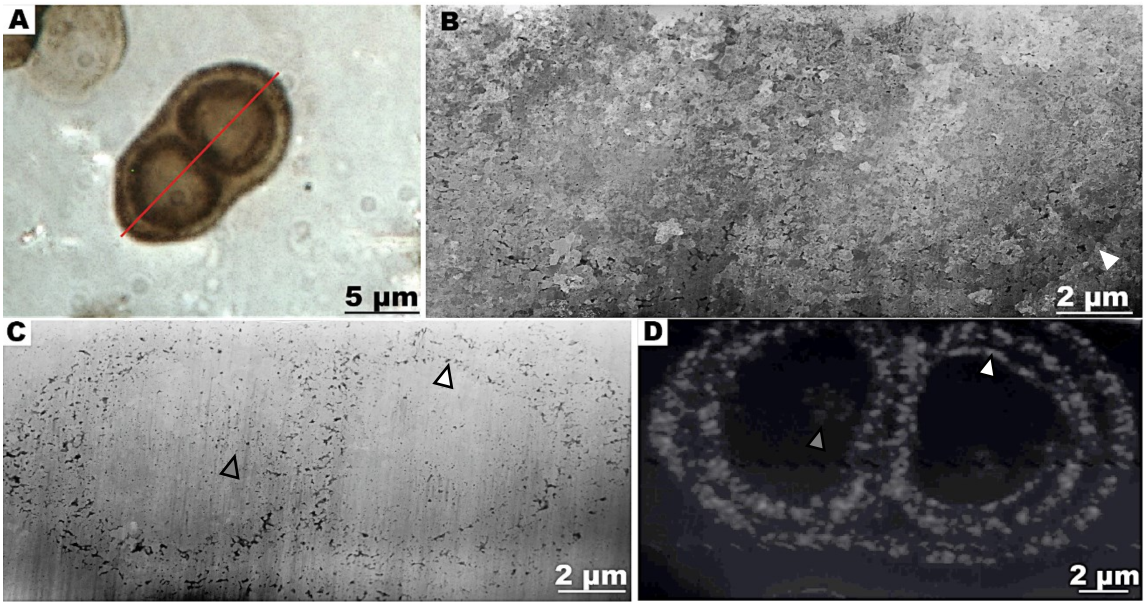

Fig. 3.6. Sphaerophycus dyad. *A. Photomicrograph in transmitted light (Red line: FIB section position). B. STEM dark field image of the FIB section showing the presence of quartz nano-crystals within and outside the microfossil. White arrowhead indicates the position of quartz crystals within the organic layer having the same diffraction contrast. C. HAADF image of one from the FIB sections showing the distribution of the organic matter (in black) and quartz (grey). D. Map aromatic carbon of one cell from the FIB section. The regular oblique white streaks along the red line are an analytical artefact of the synchrotron analysis. In C and D, the white arrowheads indicate the position of an innermost layer in the right part of the dyad and the grey arrowheads show the position of an internal organic patch in the left part of the dyad. (Sample: P4353-11A)*

4.1.4.3 Synodophycus

Synodophycus microfossils were first reported by Knoll (1982). The type species *Synodphycus euthemos* consists of large pluricellular colony composed of 16 to 64 small vesicles (4–7 µm in cross-sectional diameter). The wall structure of the individual vesicles is thin while the envelope of the colony appears dense (Fig. 3.7A). *Synodophycus euthemos* has been interpreted as the fossil of *Pleurocapsalean* cyanobacteria (Waterbury and Stanier, 1978) based on the (uncommon) presence in some vesicles of inner 1–2 µm vesicles interpreted as baeocytes formed by multiple fission in enlarged cells (Knoll et al., 1991). One FIB section was prepared on a *Synodophycus* microfossil. Although the fossil studied here lacks the smaller innermost vesicles diagnostic of baeocytes, the relatively large size of the cells, their small number in the colony, the outer envelope and the presence of this microfossil within a *S. inormatum* mats shard links them best with *Synodophycus euthemos and contrasts with t*rather than the other colonial microfossil common in the Draken Formation that is *Coniunctiophycus* (incertae cedis, Knoll et al., 1991), which aggregate more numerous but smaller cells.

The quartz crystals within and out of the colony are ~200–500 nm in diameter (Fig. 3.7B). The outer layer of the colony is composed of a <1 µm thick discontinuous layer, which contains small organic matter grains (<100 nm in diameter). The structure forming each vesicle in the envelope is also composed of organic matter nanograins forming a thiner (<500 nm) layer (Fig. 3.7C-D). Moreover, the internal and outer layers and envelop layer are for most parts continuous, that is the limit between the internal and outer layers is undefinable. In addition, triple junctions formed by the intersection of two internal layers and the external layer are commonly populated by organic matter forming a local thickening (white arrows in the Fig. 3.7C-D).

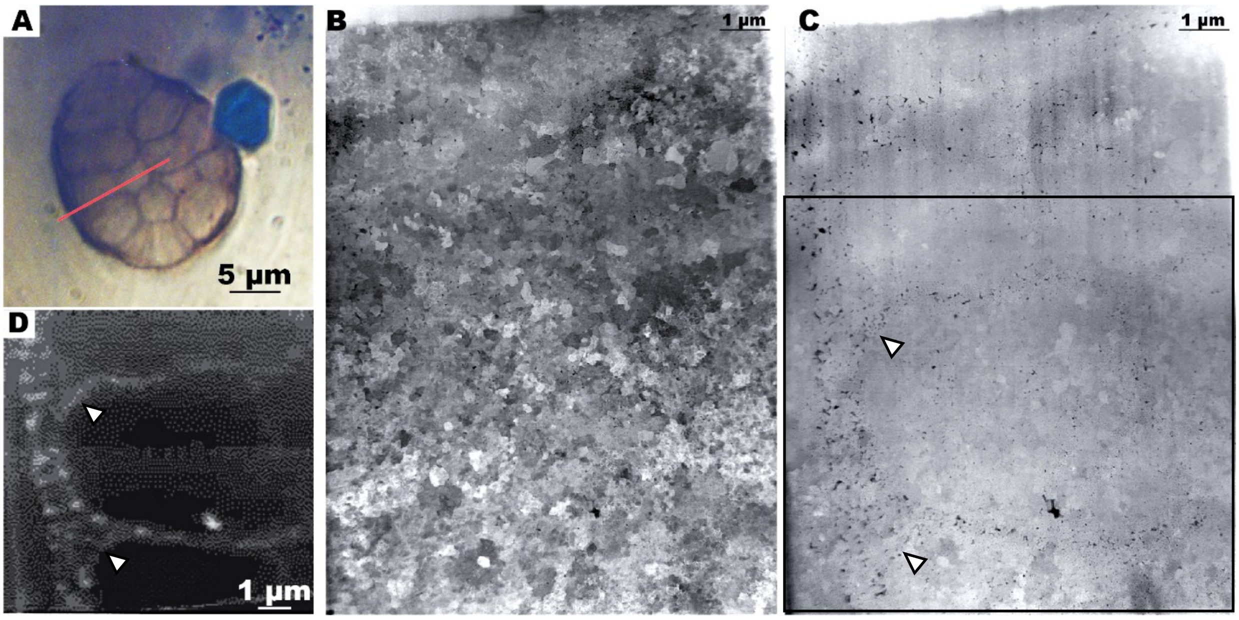

Fig. 3.7. Synodophycus euthemos. *A. Photomicrograph in transmitted light (Red line: FIB section position). B. Dark field STEM image of the FIB section showing the presence of quartz nano-crystals within and outside the microfossil. C. HAADF image of the FIB section showing the distribution of the organic matter (in dark) and quartz (grey). The white arrows indicate the accumulation of kerogen at the junction of the external envelop and internal cell walls. D. Map aromatic carbon of one cell from the region boxed in C. The white arrows indicate the accumulation of kerogen at the junction of the outer envelope and internal cell walls. (Sample: P4353-11A)*

4.1.4.4 Polybessurus

Finally, FIB sections were also prepared on relatively isolated large *Polybessurus* genus microfossils. These microfossils are composed of organic thick-walled, multi laminated stalks with cup-shaped morphology formed by unidirectional (vertical) secretion of polysaccharides (Green et al., 1987). *Polybessurus* have been interpreted as cyanobacteria based on their unequivocal similarity with modern cyanobacteria (*Cyanostylon*) forming crust on tidal flats of the Bahamas (Green et al., 1987; Knoll, 2003; Knoll et al., 1991). Two FIB sections were prepared on *Polybessurus* microfossils. A FIB section made on a smaller unjetted (circular concentric sheath structure) *Polybessurus* microfossil shows that the microfossil is also permineralized in nano-quartz (200-400nm in diameter) (Fig. 3.8A). The microfossil comprises more than seven concentric spherical envelopes. The two-three innermost envelopes display more abundant organic matter nanograins than the following, thinner envelopes (Fig. 3.8C-D). The innermost layers display triple junctions (red arrows in Fig. 3.8) indicating that the 2-3 discontinuous layers observed in the FIB section result from one to two infolded envelopes. The inter-envelope spaces often display small clots of organic matter. A sub-rounded structure, possibly an invagination of the innermost envelope, can also be seen together with small clots at the center of the structure. Another FIB section was prepared on a large thick-walled, multi-laminated vesicle. The ultrastructure of this microfossil shows that the external wall of the vesicle is composed of small granular organic matter and permineralized in nanoquartz (Supplementary Fig. 3.5).

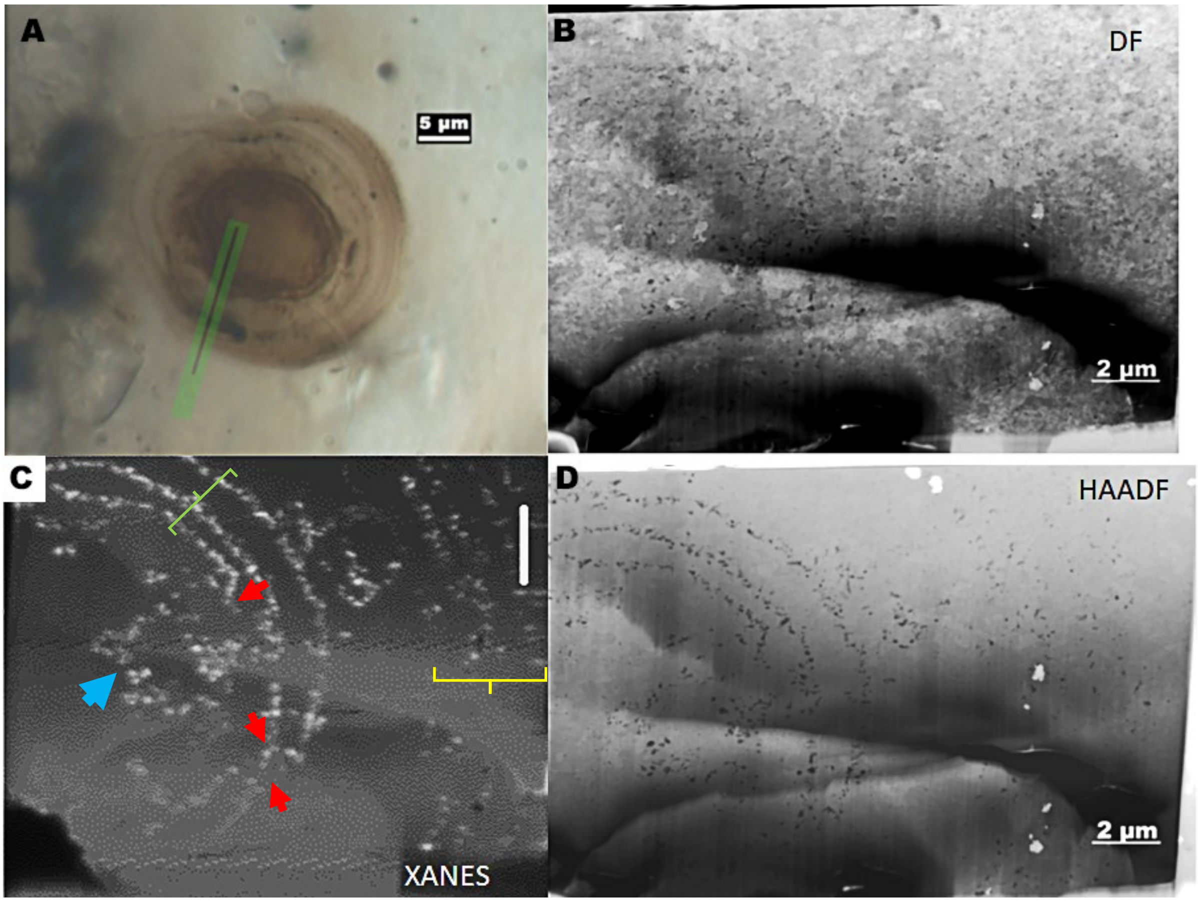

Fig. 3.8. Unjetted Polybessurus specimen 1. *A. Photomicrograph of the microfossil in transmitted light (green line: position of the FIB section through the sheath structure of the stalk and the cell membrane). B. STEM dark field image of the FIB sections showing the distribution of nano-quartz crystals. Note that the large dark zone correspond to holes caused by FIB damage. C. Map aromatic carbon showing the distribution of the internal organic material, the cell membranes and external sheath composing the early stalk. Blue arrow : internal layered organic material ; green bracket : set of thicker internal layers ; red arrows : triple junctions suggesting infolding of the internal layer set ; yellow bracket : set of thinner external layers. D. HAADF image of the of the FIB sections. Carbon appears in dark and quartz in grey. Pyrite appears in bright white. (sample: P4353-6A)*

4.1.4.5 Myxococcoides

The different microfossil assemblages present in the cherty lenses contain remains of various allochthonous microorganisms. The majority of these allochthonous microfossils are spheroidal microorganisms of the genus *Myxococcoides* (Knoll et al., 1991). These spheroidal microfossils (10 to 20 µm in diameter) are randomly dispersed in the different microbial assemblages and occur as isolated or colonies (Fig. 3.9A and Supplementary Fig.3.6). These microfossils are composed of dense thick walls and can contain internal material including pyrite crystals (e.g. Supplementary Fig. 3.6). Two FIB sections were prepared on this type of microfossil (Fig.3.9A; Supplementary Fig. 3.6). The quartz present inside and outside the microfossils are nano-crystals (~100-400nm in diameter) (Fig. 3.9C, Supplementary Fig. 3.6D). The wall structure of these microfossils forms a well-defined ~1-µm thick layer characterized by a series of organic columns oriented in a sub-radial fashion (Figs. 3.9B, E-H). This layer is sometimes surrounded by an additional outer layer of nanograins of organic matter (see white arrows in Fig. 3.9F). The thick wall structure of these microfossil is composed of thick organic grains having columnar shape and forming "bridges" from the inner limit to the outer limit of the wall structure. Fe-rich minerals such as pyrite and probably iron-carbonates with margins enriched in barium occur inside the cells (Fig. 3.9D, Supplementary Fig. 3.6). The internal Fe-minerals are sometimes coated and/or closely associated with organic matter nanograins (Fig. 3.9D-E).

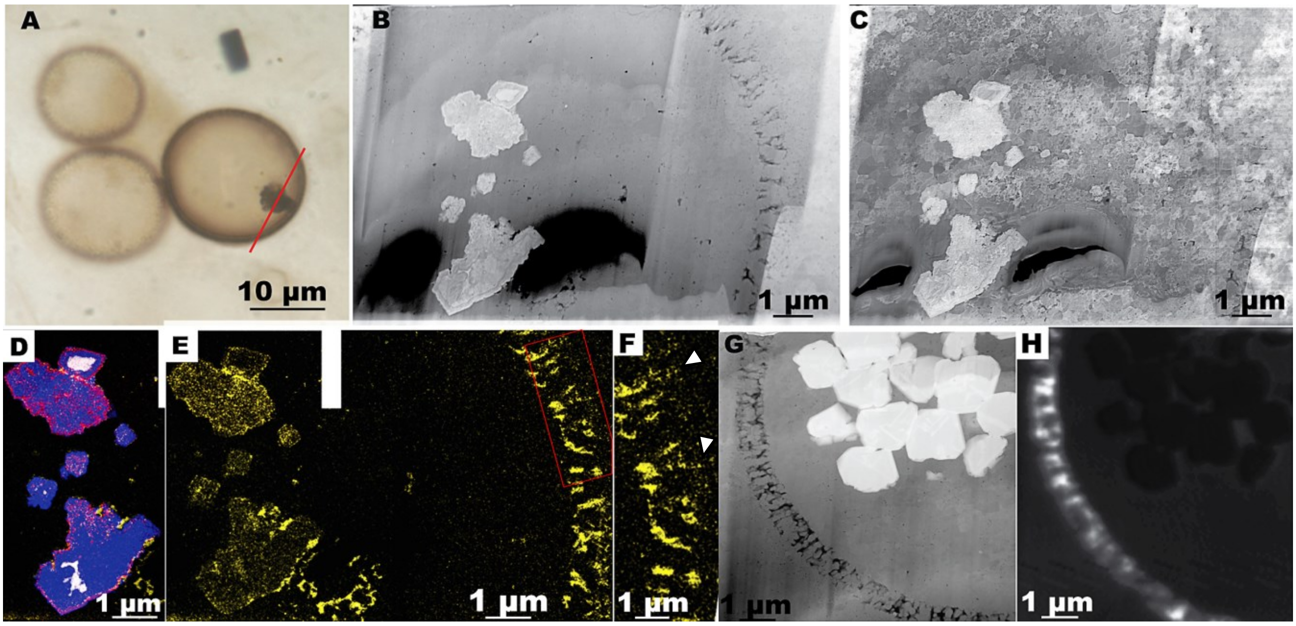

Fig. 3.9. Myxococcoides. *A. Photomicrograph in transmitted light (Red line: FIB section position in specimen 1). B-E. Specimen 1. F-G. Specimen 2 (see supplementary Fig. 3.4). B. HAADF image of the FIB section cut along the line in (A) showing the distribution of organic matter (in dark), quartz (grey) and carbonate/iron sulfide (white). C. Dark field STEM image of the FIB section showing the presence of internal carbonate crystals with an iron sulfide core (white crystals). D. EDX map of the showing the white crystal present within the microfossil. Blue: iron + carbon, magenta: barium + iron + carbon, white: sulfur + iron, yellow: carbon. (see Supplementary Fig. 3.7 for spectra) E. EDX map of the carbon (yellow) present in the FIB section. F. EDX map of the zone boxed in E showing the carbon distribution of the outer wall structure. The white arrows indicate the position of an outer layer of carbon. G. HAADF image of FIB section from specimen 2 (dark: organic matter, grey: quartz). The white cubic crystals present within the cells are iron sulfide (EDX spectrum in Supplementary Fig. 3.4). H. Aomatic carbon map (STXM) of the FIB section from microfossil present in F. (A-F: sample P4353-1B; G-H: sample P4353-11A)*

4.1.5 Vase-shaped microfossils

Rare vase-shaped microfossils (VSM) are also present in some cherty lenses. We have found one cherty lens containing this type of microfossil associated with spheroidal microfossils (mostly *Myxococcoides*) in the semi-thin sections we prepared. These large microfossils (~80–120 µm in diameter) consist of vesicles with well-defined apertures (Fig. 3.10A) and are composed of organic matter, which appears granular under the optical microscope in longitudinal thin section (Fig. 3.10A) or reticulate in a transversal section close to the bottom of the vase shape (Fig. 3.11A). The interior of the microfossils is composed of quartz that is not stained black by organic particles and/or pyrites, in contrast with the quartz embedding the microfossil (Fig. 3.11A). Two FIB sections reveal that the organic walls of two VSM are composed of two layers. One internal layer is composed of small organic matter grains (<300 nm in diameter) (Figs. 3.10C-D, 3.11C-E). This layer is impregnated with nanoquartz (200 to 400 nm in diameter), similar to the internal and external parts of the microfossil. This layer can be associated with rare iron minerals, which are probably iron oxides based on EDXS spectra (not shown) and map (Fig. 3.10E-F). A thicker outer layer of organic matter is irregular and appears to pinch and swell irregularly between micrometric quartz crystals (Figs. 3.10B-D and 3.11B-E). Micrometric quartz crystals also locally extend outside the microfossils (see white arrows in the Figs. 3.10B and 3.11B).

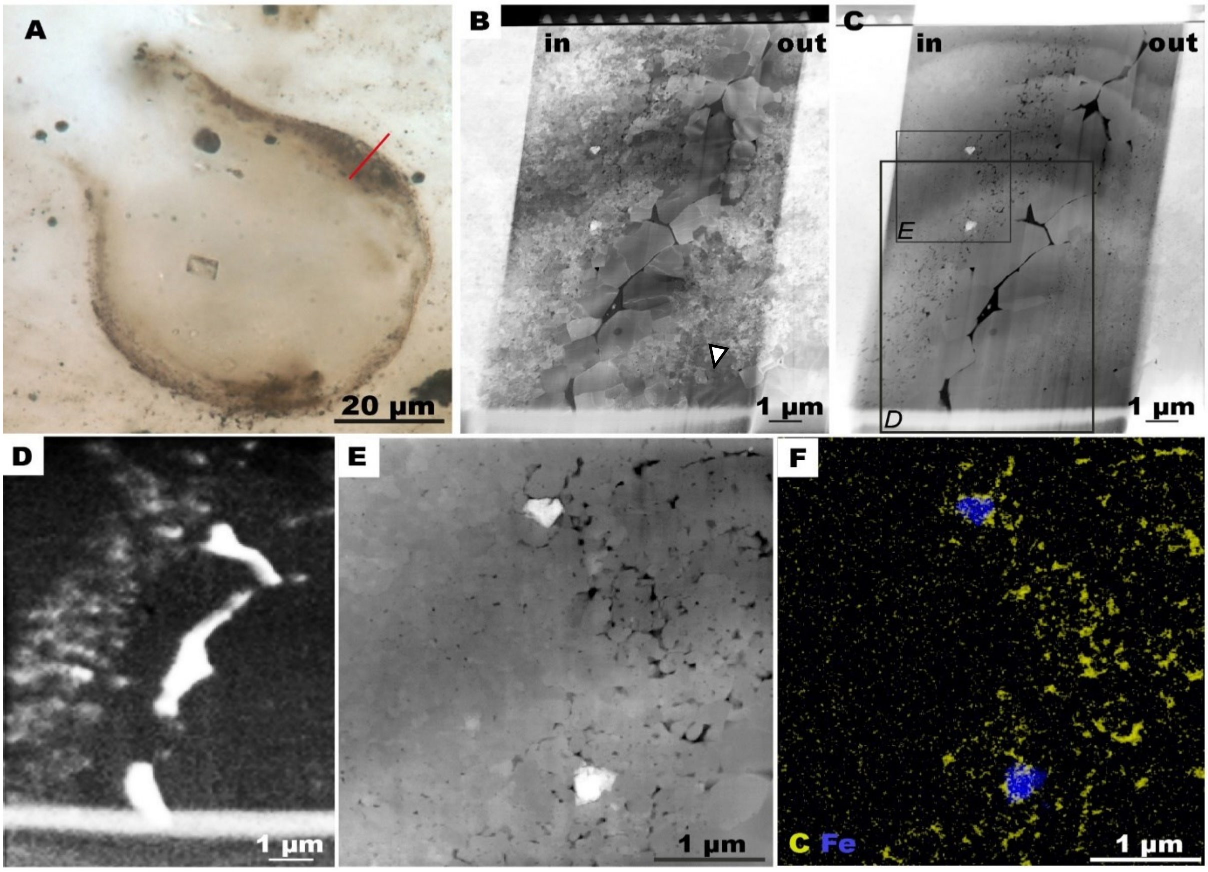

Fig. 3.10. Vase shaped microfossil specimen 1. *A. Single plane photomicrograph in transmitted light 2 µm below the surface (Red line: FIB section position). B. STEM dark field image of the FIB section showing the presence of coarse quartz crystals associated with the wall structure of the microfossil. The white arrow indicate the position of coarse quartz outside of the microfossil wall. C. HAADF image of the FIB sections showing the distribution of the organic matter (in dark) and quartz (grey). D. Map aromatic carbon map of the region in the lower box in C. E. HAADF image of the region in the upper box in C. F. EDX map of F showing the distribution of iron (blue) and carbon (yellow). (Sample: P4353-1B)*

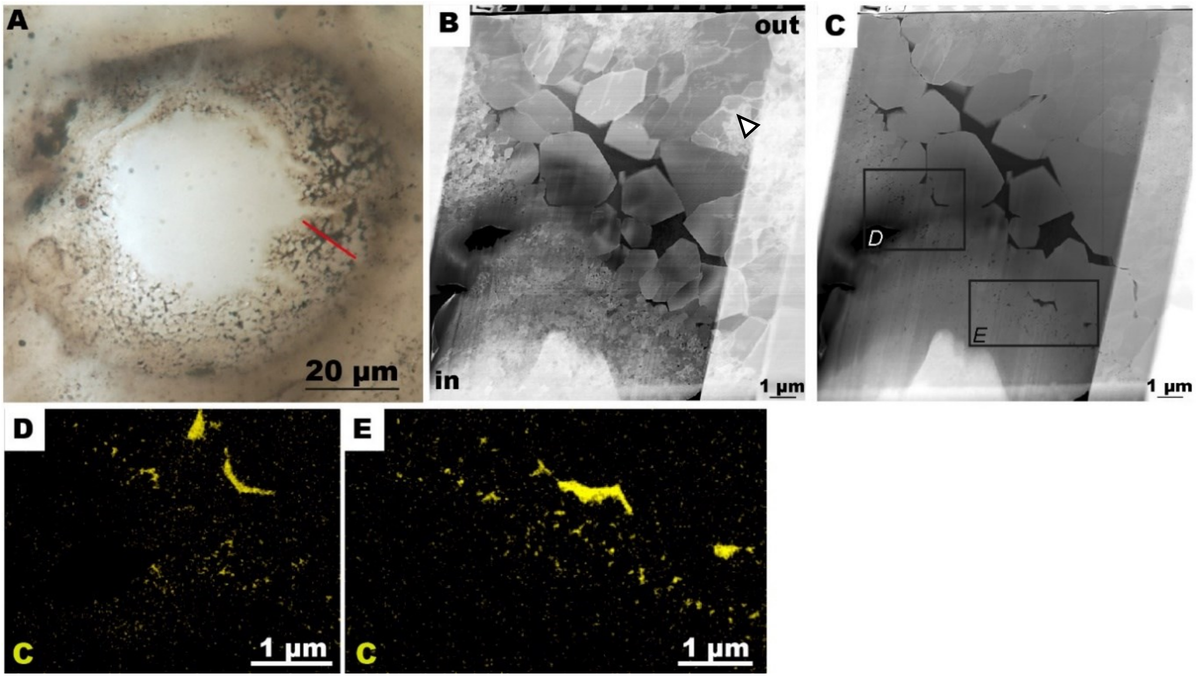

Fig. 3.11. ***Vase shaped microfossil specimen 2.*** *A. Photomicrograph in transmitted light (Red line: FIB section position). The combination of multiple focal planes shows the reticulate texture of the organic wall. B. STEM dark field image of the FIB section showing the presence of coarse quartz crystals associated with the wall structure of the microfossil. The white arrow indicates the position of coarse quartz spreading out of the microfossil wall. C. HAADF image of the FIB section showing the distribution of the organic matter (in dark) and quartz (grey). D-E. EDX maps of carbon (yellow) in the regions in the upper and lower boxes in C, respectively. (Sample: P4353-1B)*

5 Discussion

5.1 Organic matter maturity

The Raman data indicate that the microfossils entered the metamorphism window and are over mature (with a peak metamorphism temperature of 285°C ± 30°C) (Fig. 3.2). While the assemblages from the lower flake conglomerate contains great diversity of well-preserved microorganisms (Fig. 3.1), the microfossil maturity is well above that of the Paleoproterozoic microfossils from the Gunflint Formation (Alleon et al., 2016b), and Mesoproterozoic microfossils from the Gaoyuzhaung Formation (Guo et al., 2018, ~215°C), and us closer to that of the Paleoproterozoic microfossils the Francevillian FC formation (Lekele Baghekema et al., 2017, 296°C) and the Turee Creek Formation (Fadel et al., 2017, 300°C). Based on the Raman Index of Preservation of Schopf et al., (2005) and the smaller D3 and D4 bands of the Draken microfossil Raman spectra, we can also infer that the Draken microfossils are significantly more mature than the Bitter Springs Formation microfossils. The latter are indeed better preserved than the Gunflint Microfossils (Schopf et al., 2005). The Draken microfossils thus display an organic matter maturity that is commonly observed in Paleoproterozoic microfossils as well as in Neoarchean rocks (Lepot et al., 2008). Moreover, the XANES data show the predominance of aromatic moieties, thus confirming the high maturity of the Draken microfossils. However, the XANES spectra obtained at CLS (see supplementary Fig. 3.2) from a microfossil indicate that C=O bonds could be preserved. Irrespective of the small C=O contribution in spectra recorded at CLS, this unexpected result of a mostly aromatic polymer suggests that the molecular maturity of our Draken microfossils is significantly higher than that of the >1 billion year older (but less mature, as indicated by Raman spectroscopy) microfossils of the Gunflint Formation that display more abundant N- and O-bearing functional groups (Alleon et al., 2016b). The homogeneous XANES signature recorded at Diamond could not offer fingerprints to distinguish the precursors of the different microfossil morphospecies, which is likely the result of high molecular maturity.

5.2 Taphonomy and taxonomy of the microfossils

All the microfossils present here are embedded and filled by nanoquartz contrasting with the larger quartz crystals observed in other rocks with better organic Raman index of preservation (Schopf et al, 2005). Indeed, some acritarchs from the ca. 650 million years old Chichkan Formation display micrometric internal crystals (Kempe et al., 2005) not seen here in Draken, and larger submicrometric to micrometric quartz crystals observed in some samples of the Gunflint Iron Formation (Lepot et al., 2017, but see Wacey et al., 2012). Although the Raman and XANES spectroscopy indicate that the microfossils present in the cherty lenses are highly mature in terms of molecular composition, the small size of the quartz crystals allowed for perseveration of a high variety of ultrastructures that could not be resolved solely using optical microscopy.

5.2.1 Filamentous microfossils

5.2.1.1 Siphonophycus

The vast majority of filamentous microfossils present within the different Draken assemblages were interpreted as the remains of cyanobacterial sheath and are classified based on their cross-sectional diameter (Knoll, 1982; Schopf, 1968; Yun, 1981). The *Siphonophycus* filament specimen 1 (Fig. 3.3) shows a higher content of organic matter compared to

Siphonophycus specimen 2 (Supplementary Fig. 3.2). Moreover, the filament specimen 1 shows nanometric and micrometric quartz crystals (Fig. 3.3B) while the quartz present in specimen 2 are only nanograins (Supplementary Fig. 3.3). These differences of quartz mineralogy, organic matter texture, and the close spatial distribution of these microfossils (distance between the different filamentous microfossils is less than 500 µm) indicate that the taphonomy of microfossils can be highly variable at the microscale.

Here the microfossil specimen 1 shows that the quartz in the central part is coarser than the quartz around the microfossil. Such quartz distribution can be explained by the infilling of the microfossil interior after the formation of the surrounding matrix (Campbell et al., 2015; Konhauser et al., 2004; Lynne et al., 2005). The structure of the filament specimen 1 can be explained in (at least) three fashions. First, the outermost thin layer of organic matter could represent the remnant of the sheath, while the dense and irregular inner organic thread could correspond to collapsed cell material. Accordingly, *Siphonophycus* specimens 2 and 3 appear to display better-preserved empty sheaths (under the optical microscope) but display the same nanogranular texture and similar density of organic nanograins as the outermost thin layer in specimen 1. Second, the inner thread could correspond to collapsed cell±sheath material as observed in modern taphonomic experiments (Bartley, 1996). We argue that this central thread is unlikely to have formed by a collapsed *Siphonophycus* sheath material only, as empty sheaths in other specimens (2 and 3, Supplementary Fig. 3.3) do not appear to contain sufficient organic material to account for such a thick thread. The outermost thin layer could represent organic matter that migrated from the central thread (Knoll et al., 1988). Indeed, some organic matter appear to have migrated from the central thread between the micrometric quartz grains to rest at the interface between micro- and nano-quartz (blue arrow in Fig. 3.3). However, the outermost thin layer is fully surrounded by nanoquartz and there is no evidence of organic matter migration in the nanoquartz area between the microquartz and this outer layer (e.g. between the yellow and pink arrows in Fig. 3.3). Third, the central organic thread could represent bitumen that could have migrated in the open porosity left after decay of the cells. However, the absence of bitumen clots elsewhere in the chert flake argues against this process. Altogether, our observations support the interpretation that the central thread represents decayed cell material whereas the thin outer layer represents a remnant of a polysaccharide sheath.

The cellular material were still preserved after peripheral encrustation of the microorganism as observed for modern bacteria, which are first encrusted externally and/or within the polysaccharide sheath by metastable opal before crystallization of quartz(Jones et al., 1998; Konhauser et al., 2004b; Lalonde et al., 2005; Phoenix et al., 2000; Westall et al., 1995). The contacts between the coarser quartz crystals and the central organic thread do not show the “sawtooth-like” pattern described by Wacey et al. (2012) and Lekele Baghekema et al., (2017), which has been interpreted by the latter authors as the effect of recrystallization of microquartz after nanoquartz. Thus, it appears that the morphology of the quartz microcrystals associated with the central thread was not controlled by the texture of the internal organic matter. Rather, the geopolymer forming the central thread likely polymerized and/or migrated locally between the microquartz crystals.

Thus, the living and/or decaying microorganism probably lowered the rate of quartz crystallization as observed in modern fossilization experiment (Alleon et al., 2016a) during the initial encrustation of the inner and outer surfaces of the sheath material. In contrast, late silicification occurred in a local porosity after the cell death and lysis, ultimately leading to the formation of coarser quartz crystal. Moreover, the difference of organic and quartz structures between microfossils present in the same cherty lens (Fig. 3.3 *versus* Supplementary Fig. 3.3) exemplifies the heterogeneity of organic decay and silicification. Such taphonomic difference can be explained by different timing of polymerization and crystallization of the silica. Foucher and Westall (2013) proposed that some microorganisms were encrusted *in situ* in microbial mats by silica while other were free of silica before the transport and deposition of the microbial mat flakes in the peritidal environment. This early silicification may have affected preferentially the decaying microorganisms of the mats. More pervasive silicification carried on after the deposition of the microbial mats within the lagoon (Foucher and Westall, 2013), possibly helped by burial in sediment. This can explain the different state of preservation of the microfossils even within the same cherty lens.

5.2.1.2 Salome Svalbardendis

The *Salome Svalbardendis* microfossil with a distinct trichome structure shows an ultrastructure that differs from *Siphonophycus* (Fig. 3.4D-G). The similarity of quartz grains size from cells and sheath suggests that early silicification was pervasive of all ultrastructures. This might have prevented (in *Salome*) the coarse condensation (in the shape of thick central threads and grains) observed *Siphonophycus* specimens 1 and 3 (Fig. 3.3C and Supplementary Fig. 3.3). However, the coarser (but still sub-micrometric) quartz grains within the cells and the sharp contacts of cells quartz grains with nano-grains from the sheath suggests that two early crystallization episodes have occurred in this *Salome* microfossil (Fig. 3.5 C, F). The sheath was likely silicified first and a second silicification episode permineralized the cells (Fig. 3.5A).

It is well established that polysaccharide sheath and wall ultrastructures are more resistant than cellular bacterial membrane and intracellular contents (Bartley, 1996; Campbell et al., 2015; Chalansonnet et al., 1988; Jones et al., 2001; Lepot et al., 2014). Organic matter within the cells was dispersed randomly as grains (Fig. 3.5D-G). The wall/envelope/membrane of the cells are not preserved. The texture of inner organic grains is similar to that observed in a *Paleolyngbya* (cyanobacterial) microfossil studied by demineralization and TEM (Oehler, 1976). Furthermore, despite the absence of preservation of the cell walls, the nano-quartz crystals present within the cell sometimes form a ghost wall structure, apparently a cast of the wall without preservation of organic matter (Fig. 3.5 E-G, arrows). Thus, the outer cells wall was first encrusted by silica due to the preferential hydrogen bond formation between the hydroxyl groups of silicic acid and cell wall molecules (Orange et al., 2009). After the lysis of the cells, the wall was obliterated and condensation of the cellular organic matter inside the cell structure was likely associated with the second cell-infilling silicification episode. This Salome microfossils indicates that the preservation of the cellular contents of filamentous cyanobacterial organisms is possible during rapid silicification processes. In our case the silicification episodes of the sheaths and cells have probably occurred quite simultaneously and rapidly after the deposition of bacterial mats to prevent the extensive condensation and complete loss of ultrastructures.

5.2.2 Benthic coccoidal microfossils

The microfossils associated with the Draken filaments mats-builders were interpreted as bacterial microfossils (Knoll, 1982; Knoll et al., 1991). These microfossils are composed of various and multiple vesicles and/or envelopes. The nature of this organic layer can be inferred based on the optical observation. However, examination of the ultrastructure of these microfossils provides additional features to identify these ultrastructures and understand the post-mortem and diagenetic processes that occurred during the fossilization of this type of microfossils.

5.2.2.1 Gloeodiniopsis

Gloeodiniopsis microfossils are interpreted as the remain of small spheroid cyanobacteria (from Chroococcales order) based on their size (inner vesicles diameter <5µm), on the simple smooth-walled structure of the internal vesicles observed under optical microscopy, and their organization in monads, dyads and tetrads following binary division patterns within envelops (Knoll et al., 1991; Schopf, 1968). Examination of its ultrastructure indicates that the outer layer present within the *Gloeodiniopsis* microfossils is composed of small organic matter particles (<100 nm) embedded in nanoquartz matrix (Fig. 3.5B-C). This organic matter particles formed broad (up to ~1 µm) homogenously granular layer with a variable thickness (Fig. 3.5C-D). The presence of broad homogenous outer layers composed of small organic grains was also observed in microfossils (*Glenobotrydion* coccoids) of the Bitter Springs Formation by Oehler, (1976), who interpreted these organic matter particles as the remain of mucilaginous envelops (sheath) or extracellular polymeric substances (EPS) produced by the micro-organisms. Thus, in our case the outer layer of the *Gloeodiniopsis* microfossil can be the remain of a sheath encapsulating the cells, an ultrastructure that can be silicified early while the cells are still viable (Oehler, 1976; Phoenix et al., 2000; Westall et al., 1995). The organic internal material present within sheath from the specimen1 (dyad) and 2 (monad) shows a different structure (Fig. 3.5C-D, Supplementary Fig. 3.4). The inner vesicles, which appear composed of only smooth wall structure under light microscopy, have more irregular and complex ultrastructure. In *Gloeodiniopsis* specimen 1, the inner structure is laminated. It could represent a multiple lamination, or an infolded segment of a single layered structure that was cut multiple times in the thickness of the FIB section (*cf.* Oehler 1976). This interpretation is also supported by observation of the specimen 2 (Supplementary Fig. 3.4). In the monad specimen 2, the inner structure displays a relatively thicker layer encompassing a web of thinner layers. Thinner layers are also observed in the most central part of specimen 1 (Fig. 3.5). The ultrastructure of the internal layers is more continuous and distinct of the broad cloud of granular organic matter forming the sheath. As such, they may likely represent the cell walls and/or internal membrane(s) of the bacteria preserved through rapid silicification of the microorganism (Oehler, 1976; Westall et al., 1995). However, the thickness of these internal layers is larger than cell walls or internal membranes observed on modern cyanobacteria (Liberton et al., 2006; van de Meene et al., 2006). In our case, the thicker organic layers may be formed by the condensation of the cellular membranes with various internal organic material adjacent to the plasma membrane in modern cyanobacteria, such as thylakoid membranes (formerly hosts to photosynthetic pigments), glycogen granules, ribosomes, and/or lipid bodies (Frain et al., 2016; Liberton et al., 2006; van de Meene et al., 2006). Similarly, the innermost two sub-spherical objects in specimen 1 and the thinner web-like membranes in specimen 2 may likely represent intracellular membranes, possibly thylakoid membranes condensed with other internal organic materials. Indeed, thylakoid membranes are highly resistant to fast bacterial lysis (Daft and Stewart, 1973) and long term burial diagenesis (Lepot et al., 2014; Pacton et al., 2008) These putative internal membranes could not be distinguished with the optical microscope (Fig. 3.5A). In addition, dark-field STEM imaging (Fig. 3.5B) show that the texture of the internal membranes is not correlated with the texture of the host nanoquartz, supporting that migration at crystal boundaries could not have templated their distribution in the microfossil.

5.2.2.2 Sphaerophycus

The *Sphaerophycus* microfossils are also interpreted as a Chroococcales cyanobacteria based on their size, their simple shape morphology, simple granular-wall structure of the internal vesicles and cellular organization following binary division/fission (Knoll, 1982; Knoll et al., 1991). The microfossils analyzed here shows a different ultrastructure compared to the *Gloeodinospsis* microfossils. The outer layer is also composed of homogenous small organic particles (Fig. 3.6C-D) and probably represent remain of the sheath structure based on observation made on Bitter Spring Formation microfossils by Oehler (1976). The two layers enclosed in this outer envelope show a similar texture (Fig. 3.6C). Based on this similarity, these inner layers delimitating the inner vesicles may also represent a sheath structure. Moreover, the presence of some quartz grains within the sheath that have probably the same orientation suggest that the silicification have been controlled by the presence of the organic matter in the multi-laminar sheath (white arrow in the Fig. 3.6B).

Interestingly, a third, innermost layer occurs within the right cell of the microfossil. This innermost layer is thinner and less granular than the inferred sheath layers, hence it is probably the remains of the cell envelope (wall±membrane) of the microorganism (Oehler 1976). Moreover, the left cell did not preserve an envelope but shows a small internal patch of organic nano-granules (grey arrow in Fig. 3.5C-D), which are not present or not cut by the FIB foil within the right cell. This organic structure might represent the remains of internal organic material of the cell and/or condensed organic membranes (Oehler 1976). The preservation of internal organic material appears surprising in a cell where the cell wall has not been preserved. However, microbial lysis experiments (Daft and Stewart, 1973) and buried sediments (Lepot et al., 2014; Pacton et al., 2008) have shown that some intracellular contents such as cyanobacterial thylakoids may be preserved without preservation of surrounding cell wall and/or cytoplasmic membranes. The distinct ultrastructures observed in two different cells of the *Sphaerophycus* microfossil show the difficulty to constrain the nature of the layers of organic matter present in coccoidal Precambrian microfossils due to the possible condensation of various organic material (membrane, cellular material) from the micro-organism during lysis and silicification. Although multiple layers could be seen with the optical microscope (Fig. 3.6A), the limits in lateral resolution >500 nm and the depth of field >600 nm of X100, NA0.9

optical objectives do not allow to resolve their ultrastructural differences. The distinct textures of the sheath layers and the internal cell wall could be distinguished with STEM.

5.2.2.3 Synodophycus

The *Synodophycus* microfossil analyzed here was identified by a low number (less than 64) of large inner vesicles (~4-7µm) forming an ellipsoidal colony (<40µm in diameter). *Synodophycus* were interpreted as colonies of Pleurocapsalean cyanobacteria (*Xenococcacceae* family) based on the presence of baeocytes formed by cell enlargement and multiple fission from the type specimen identified by Knoll et al. (1991). The discontinuous granular texture of the organic layers is reminiscent of that of the sheaths surrounding the coccoid microfossil discussed above. However, the organic layers observed in *Synodophyus* are relatively poor in organic matter grains and may represent a different type of ultrastructure such as cell walls. Here, we interpret all the organic layers as the remnants of F-layers, that is the fibrillar cell walls of *Pleurocapsan* cyanobacteria. The fused and indistinct contacts between cells and the apparently fused contact between internal and external layers, and the presence of organic matter at triple junction (Fig. 3.7) are all consistent with F-layers of *Pleurocapsan* cyanobacteria (Waterbury and Stanier, 1978). Nevertheless, we note that fused cell walls have also been observed in non-*Pleurocapsalean* Bitter Springs Formation microfossils (Oehler 1976).

5.2.2.4 Polybessurus

Based on comparisons of their size, stalk morphology/formation and environmental occurences, the *Polybessurus* microfossils are similar to the species of the extant genus *Cyanostylon* (Green et al., 1987). The *Polybessurus* are the remains of coccoidal *Chroococcaceaen* cyanobacterial unicells that "jetted" upward from the sediment surface by the highly unidirectional secretion of extracellular polysaccharide stalks (Green et al., 1987). The FIB section *Polybessurus* specimen 2 only intercepted the layered stalk, which displayed one or two thick layer(s) composed of organic matter nanograins and permineralized by nano-quartz grains (Supplementary Fig. 3.5). This carbon distribution is coherent with the sheath structures observed in the other *Chroococcaceaen* microfossils *Gloeodiniopsis* and *Sphaerophycus* (Figs. 3.5-3.6). The FIB section of *Polybessurus* specimen 1 (Fig. 3.8) intercepted both the cell (inferred from optical microscopy) and stalk. In this specimen, all layers are thin compared to the sheaths of *Gloeodiniopsis* and *Sphaerophycus*. The two/three internal layers are well defined, while the outermost set of layers appears less continuous and thinner than the internal layers. Such structure suggests that the internal layers could represent the wall of the cell during its early life cycle (see fig. 21 in Green et al., 1987). This wall appears unfolded and the layers observed in the FIB section may result of 1–2 envelopes at most. Ultrastructural data on the modern *Cyanostylon* is, to our knowledge, lacking to interpret these internal layers. Alternatively, these internal layers may represent sheaths and/or the innermost stalk-forming polysaccharide layers. The outer, thinner layers of organic certainly belong to the laminated polysaccharide structure during the earliest stages stalk formation (i.e. before vertical growth). Moreover, this *Polybessurus* shows organic content attached to (or invaginated from) the most internal organic layer. Such internal organic matter might represent the remains of intracellular material (Oehler, 1976; Oehler, 1977; Westall et al., 1995), possibly remains of thylakoid (photosynthetic) membranes as discussed above for *Gloeodiniopsis* microfossils.

5.2.3 **Myxococcoides *spheroids.***

The fossil genus *Myxococcoides* may comprise algae and/or (cyano)bacteria. Defining *Myxococcoides* microfossils as eukaryote or prokaryote is difficult due to their simple shape (Knoll et al., 1991). The FIB sections of *Myxococcoides* observed here are different from the spheroidal microfossil observed by TEM by Foucher and Westall 2013. The ultrastructure of this previous analyzed *Myxococcoides* is composed of a thin continuous wall structure (<200 nm thick) and an internal organic material which are respectively interpreted as the membrane and the cytoplasm of the microorganism. In all the microfossils, the quartz grains out and within the microfossils are similar indicating that the micro-organisms were rapidly silicified. The relatively thinner wall of this *Myxococcoides* (Foucher and Westall, 2013) could represent a (cyano)bacterial rather than eukaryotic cell wall (Oehler 1976). *Myxococcoides minor* of the Bitter Springs Formation displayed similar thin walls (Oehler, 1976; Schopf, 1970) and were accordingly interpreted as cyanobacteria. Interestingly, microscale C isotopes analyses have distinguished the isotopic composition of *Myxocccoides sp.* ($\delta^{13}C_{org}$ = -22.6 ± 0.5 ‰) and closely associated *Leiosphaerida crassa* ($\delta^{13}C_{org}$ = -28.9 ±1 ‰) in ~775 Ma cherts of the Chichkan Formation (Williford et al., 2013), consistent with the hypotheses that the former were cyanobacteria while the latter were eukaryotes.

However, the ultrastructure of the *Myxococcoides* observed here reveals that the outer layer is much thicker (up to ~1 µm) than the aforementioned occurrences (Figs. 3.9 and Supplementary Fig. 3.6). The radial pillars of organic matter can be envisioned as taphonomic or primary features of the cells.

The organic matter forming this wall structure seems to fill the porosity present between the quartz grains comprising the wall structure. This structure might be caused by a first rapid encrustation by opal of the cell interior and exterior. Then, the space between the different cell membrane became impregnated with silica, giving the outer wall this structure with nanoscale migration of the organic material from the wall. The nano-quartz pillars may have formed between two originally distinct layers of organic matter such the membrane and/or various cell-wall ultrastructures. Development of this columnar fabric might be caused by the capacity of the organic matter to slow the crystallization of quartz (Alleon et al., 2016a), possibly in specific crystallographic directions. Such taphonomic process might be related to that forming the indentation patterns reported by Wacey et al (2012) and Lekele Baghekema et al. (2017). Subsequently, organic matter could have migrated between the quartz pillars, fusing locally these two organic layers. Alternatively, silica may formed nanograins (30-200 nm) on the external surface of an organic layer, as observed on sheath structures of cyanobacteria (Benning et al., 2005; Konhauser et al., 2004; Phoenix et al., 2000).After the death of the microorganisms, the cell interior and exterior rapidly encrusted by amorphous silica, i.e. opal A (Herdianita et al., 2000; Lynne et al., 2005; Preston et al., 2008). Later during diagenesis, the organic matter from outer structures such as sheath/capsule and/or wall may have migrated and filled the spaces between the grains of the crust. Simultaneously, internal cellular material may condensed within the center of the silicified cell as observed in the Fig. 3.9E. However, the fact that most of the quartz pillars cut across the complete organic layer without organic remains at their base similar to the presumably migrated organic remains between the pillars appear difficult to reconcile with these taphonomic models.

Alternatively, the pillared structure may be inherited from an original ultrastructure. In this scenario, the thickness of the microfossil outer wall could represent the original thickness of the micro-organism cell wall. The pillared quartz structure might be inherited from precipitation of silica in a porous ultrastructure such as the outer fibrillary wall layer of algae (Domozych, 2011; Domozych et al., 1992). Radially-developing fibers/pillars have also been observed in the envelope of cyanobacterial akinetes (Clark and Jensen, 1969; Lang, 1968) and in the sheath of filamentous cyanobacteria (Lang 1968). The amorphous organic matrix between fibers in filamentous cyanobacterial sheaths decays preferentially compared to the fibers (Daft and Stewart, 1973), possibly generating radially-oriented pore space favoring silicification in pillars. A very fine layer (~200 nm) of thin fibrils was also observed around unicellular cyanobacteria (Stanier, 1988). Bacteria may also form fibrillary extracellular polysaccharides (Costerton et al., 1981). Altogether, if assuming that the pillared organic structure of the studied *Myxocccoides* is inherited from an original ultrastructure, its thickness and presence in relatively single rounded spheres may correlate best with fibrillary cell walls of eukaryotes. However, the dense internal layers of the cell wall such as the medium and inner layers (respectively 22 and 300 nm thick) reported by Domozych et al., (1992) are absent. They were probably affected by migration and/or lysis. Additional 3D analysis with FIB-SEM tomography (e.g. Wacey et al., 2013) or sequential FIB milling (Schiffbauer and Xiao, 2009) may help resolve the origin of this pillared ultrastructure.

Interestingly, one *Myxococcoides* shows an outer, diffuse layer of small organic grains (< 200 nm) surrounding the pillared layer (Fig. 3.7G). As observed within the mat dwellers microfossils, these small organic grains might represent residue of sheath and/or secreted mucilage. Alternatively, the presence of these organic nanoparticles might be caused by post-mortem outward displacement of organic matter from the wall structure (Knoll et al., 1988). However, should such displacement of organic matter from the wall structure have occurred, these small organic matter particles should also have migrated toward the inside of the cell, which displays the same quartz texture. Thus, the interpretation of these organic particles as remain of mucilage or an additional sheath or wall layer appears more coherent than displacement of organic matter during or after the crystallization of quartz.

The presence of pyrite grains and other possible carbonate grains within the microfossils suggests that additional post mortem processes occurred in addition to lysis and silicification. In a *Myxococcoides* microfossil, internal organic matter patches are associated with probable iron carbonate, which have a core of iron sulfide. The simultaneous presence of organic matter and iron sulfide support the idea of heterotrophic sulfate-reducing bacterial activity. The iron carbonate present within the cells was probably induced by a lower activity of the sulfur reducing bacteria. Thus, the diagenetic iron could have reacted with organic matter to form iron carbonate through microbial or thermal iron reduction (Bernard et al., 2007; Hendry et al., 2000; Koehler et al., 2013; Posth et al., 2013). The peak metamorphism temperature of 285°C obtained from the Raman supports the possibility of thermal iron reduction. This presence of Fe-sulfide and possible Fe-carbonate indicates that anaerobic heterotrophic bacteria were active after the deposition of the mat flakes within the subtidal environment influenced by sea and pore-water. Interestingly, a low quantity of organic matter is preserved within one *Myxococcoides* cell (Fig. 3.9). As observed by Oehler (1976) and in other microfossils (Figs. 3.5-3.6) described above, this organic matter patches may be the residues of internal material and membranes that have condensed after the lysis of the micro-organisms and silicification. Internal organic material may have fueled bacterial sulfate and/or iron reduction in these microfossils.

5.2.4 The organic envelopes of vase-shaped microfossils

The VSM are well known in Neoproterozoic microfossil assemblages (Bosak et al., 2011; Porter et al., 2003; Porter and Knoll, 2000; Strauss et al., 2014). Based on their size, complex morphologies, diversity and ecological distributions, VSM were interpreted as the remain of testate amoeba (unicellular eukaryotes: (Lee et al., 1985)) (Porter et al., 2003; Porter and Knoll, 2000). The modern amoeba are protist predators, hence the VSM are also interpreted to feed on bacteria and single cells eukaryotes present in Neoproterozoic environments. This predatory activity was also confirmed by the presence of perforation (probable trace of predatory and/or scavenging activity) on VSM microfossils (Porter et al., 2003). Here, the organic envelope of the VSM microfossil is preserved and not replaced by minerals (Figs. 3.10D, 3.11C), unlike many other Neoproterozoic occurrences (Porter & Knoll 2000). The preservation of organic content of the VSM suggests that the eukaryote was well preserved due to rapid silicification. The nature of the organic envelope observed here is difficult to interpret in terms of primary ultrastructures of testate amoebae. Porter & Knoll (2000) argued that the walls of testate amoebae are composed of proteinaceous organic matter that is not expected to be preserved. Here, there is no evidence of preservation of agglutinated minerals (e.g. Bosak et al., 2011; Delaine et al., 2017). In case the test was composed of amorphous silica scale (e.g. Porter & Knoll 2000), these would have been recrystallized. Some agglutinating testate amoebae can form tests essentially with quartz (Armynot du Châtelet et al., 2015). However, the coarse quartz crystals associated with the organic envelop cannot be interpreted as agglutinated clastic material as they occur on both internal and external sides of the organic envelop (Figs. 3.10-3.11). Some parts of the VSM display a granular texture, which forms a reticulate structure (Fig. 3.11A). This texture is different from the honeycomb structure described by Porter and Knoll (2000). Indeed, the “honeycomb” VSM are composed of pyrite and the holes structures (imprints of the scales) are larger and more regular (Porter and Knoll, 2000). The reticulate texture observed here may have been formed by hypothetically smaller scales, or by the imprint of the coarse diagenetic quartz crystals that have grown through the envelope. The granular organic matter envelope is composed of dense and large organic matter layer, which seems to fill the space of coarse quartz grains (Figs. 3.10B and 3.11B). Interestingly, the association of a thick organic thread with coarse quartz crystals in the VSM microfossil is reminiscent of that observed in filament specimen 1 (Fig. 3.2B). Such similarity between these different microfossils suggests that the wall structure of the VSM has been affected by similar diagenetic process (Note that the two microfossils are from different samples and microfossil assemblage types). Moreover, the presence of an internal layer of organic matter nanoparticles within the microfossil associated with nanoquartz grains suggest that parts of wall structure were well preserved compared to the outer layer (Figs. 3.10B, 3.11C). However, this internal layer has a variable thickness (Figs. 3.10D-F *versus* 3.11D-E). In specimen 2 (Fig. 3.11), the outer envelope is also thinner than in specimen 1 (Fig. 3.10), which has a thicker outer envelope and a very thin inner layer of organic matter. As discussed for the filament specimen 2, it is unlikely that this innermost layer of nanoparticles embedded in nanoquartz formed through migration from the outer, thicker organic outer envelope, as nanoparticles would be expected in the nanoquartz lying outside the microfossil as well. The fact that the thicker outer envelope displays high amount of organic matter compared to the inner layer argues that the former could not have formed by migration of organic material from the former. Thus, altogether our observations suggest that two distinct envelope ultrastructures have been preserved in the two VSM. Nevertheless, we note that optical images show that the outer reticulated envelopes are highly heterogeneously in thickness and may locally be absent (Figs. 10A, 11A). This may be caused by heterogenous preservation and/or migration of organic matter.

Finally, some iron minerals (possible iron oxides) are associated with the internal layer of the VSM. The presence of such minerals is not surprising as the organic wall of the VSM is generally not preserved and replaced by mineral (pyrite, carbonates, silica, iron oxides…)(Porter and Knoll, 2000). In the studied microfossils, however, it appears that the loss of the organic structures through anaerobic organic matter respiration and/or thermal diagenesis has been largely prevented by early silicification.

Conclusions

The spectroscopic signature of the insoluble organic matter of the Draken microfossils is highly mature, mostly aromatic. In spite of this high maturity, a degree of ultrastructural detail comparable to that observed in the much less mature Bitter Springs Formation microfossils can be observed in FIB sections. In addition, FIB section preparations preserve the petrographic link between organic matter and quartz, allowing us to address taphonomic processes. We describe ultrastructures of microfossils that have been interpreted previously as Chroococcales cyanobacteria (*Gloeodiniopsis mikros, Sphaerophycus*), Pleurocapsalean cyanobacteria (*Synodophycus euthemos),* sheathed filamentous cyanobacteria (*Siphonophycus, Salome svalbardensis*), incertae sedis (*Myxococcoides*), and vase-shaped amoebae. The nanoscale analysis of trichome from *Salome svalbardensis* indicate that the general shape of the cells is conserved within nanoquartz matrix, even as ghost structure, but the cell wall/

envelop/membrane of the cells are not preserved. Our observations also show that the sheath structure of the *Siphonophycus* is always well preserved in nanoquartz matrix even if the filament appear degraded under light microscopy. For the Chroococcales cyanobacteria microfossils, the outer sheath structure identify with optical microscopy is preferentially preserved and have a characteristic ultrastructure. However, nano-scale examination of some internal layers of *Sphaerophycus* and interpreted as cell membrane with light microscopy indicates that these structures are additional sheath structure. This observation made on *Sphaerophycus* shows the importance of nano-scale analysis to assess the nature of organic structure. Moreover, based on comparisons with modern cyanobacteria, we try to constrain the nature of the dense internal vesicles present in *Gloeodiniopsis mikros* which appear hazardous (and probably impossible) with optical observations. The nano-scale analysis indicate that this inner vesicle is encloses internal layered structures. These layers may have formed during the condensation of internal cellular materials (pigments, ribosomes, lipids bodies, carboxysome) onto resistant thylakoid membranes. A thicker organic layer these internal layers and is interpreted as cell wall and/or internal membrane, also possibly affected by condensation of other molecules. The ultrastructural examination of *Synodophycus euthemos* microfossils also indicates that the wall structure, whose the nature is difficult to constrain with optical observations, are probably F-layers typical of Pleurocapsalean cyanobacteria.

For the first time, the ultrastructure of *Polybessurus* microfossils is documented. The ultrastructure of stalk shows similar organic distribution as those observed in sheath structure of the other micro-benthic microfossils. Moreover, we documented the ultrastructure of an unjetted microfossil. Our observations show that the inner sheath structure is composed of thinner layers, which are probably characteristic of earliest stages of the stalk formation. The internal organic material present within the inner vesicle might represent the remain of thylakoid membranes as observed in *Gloeodiniopsis mikros*.

The ultrastructure of *Myxococcoides* observed here reveals that the outer layer of this microfossil is composed of unusual radial pillars of organic matter. This unusual wall structure never observed by previous studies and only observable at the nano-scale, can be interpreted as taphonomic or taxonomic features of the cells. In the second case, it may represent eukaryotic cell-wall and/or structures of cyanobacterial sheaths or cyanobacterial akinetes. Finally, we examined the ultrastructure of vase-shaped microfossils for the first time. These eukaryotic microfossils are composed of two distinct organic layers: an inner layer composed of organic nanoparticles and a thicker organic outer layer forming a reticulated envelope at microscale.

Here the microfossils are all preserved in nano-quartz matrix suggesting that the organic structure are well preserved via rapid silicification processes. However, some ultrastructures of microfossils indicate that coarser quartz crystals are always associated with local displacement of organic matter. Such observations on well preserved microfossils give criteria to discuss the biogenicity, the nature of organic structure and the taphonomy on other unidentified or putative microfossils in paleo-Proterozoic or Archean rocks.

Acknowledgments

David Troadec (IEMN) is highly thanked for the preparation of the FIB section preparation. Sylvie Regnier is thanked for the semi-thin section preparation. Philippe Recourt (LOG) is thanked for help with SEM. We thank the ANR M6fossils (ANR-15-CE31-0003-01) grant to KL for funding the analytical work. FIB work was partly supported by the French RENATECH network. We thank Tohru Araki, Burkhard Kaulich, and Majid Kazemian Abyaneh for help with STXM at the Diamond synchrotron facility. We thank Corentin Le Guillou (UMET) for help with STXM data. We thank the Diamond Light Source for access to beamline I08 (SP14784) and the Canadian Light Source for access to beamline 10ID-1. The TEM facility is supported by the Conseil Regional du Nord-Pas de Calais, and the European Regional Development Fund (ERDF).

References

Agić, H., Moczydłowska, M., Yin, L.-M., 2015. Affinity, life cycle, and intracellular complexity of organic-walled microfossils from the Mesoproterozoic of Shanxi, China. J. Paleontol. 89, 28–50. https://doi.org/10.1017/jpa.2014.4

Alleon, J., Bernard, S., Le Guillou, C., Daval, D., Skouri-Panet, F., Pont, S., Delbes, L., Robert, F., 2016a. Early entombment within silica minimizes the molecular degradation of microorganisms during advanced diagenesis. Chem. Geol. 437, 98–108. https://doi.org/10.1016/j.chemgeo.2016.05.034

Alleon, J., Bernard, S., Le Guillou, C., Marin-Carbonne, J., Pont, S., Beyssac, O., McKeegan, K.D., Robert, F., 2016b. Molecular preservation of 1.88 Ga Gunflint organic microfossils as a function of temperature and mineralogy. Nat. Commun. 7, 11977. https://doi.org/10.1038/ncomms11977

Anbar, A.D., Knoll, A.H., 2002. Proterozoic Ocean Chemistry and Evolution: A Bioinorganic Bridge? Science 297, 1137–1142. https://doi.org/10.1126/science.1069651

Armynot du Châtelet, E., Bernard, N., Delaine, M., Potdevin, J.-L., Gilbert, D., 2015. The mineral composition of the tests of 'testate amoebae' (Amoebozoa, Arcellinida): The relative importance of grain availability and grain selection. Rev. Micropaléontologie 58, 141–154. https://doi.org/10.1016/j.revmic.2015.05.001

Arouri, K., Greenwood, P.F., Walter, M.R., 1999. A possible chlorophycean affinity of some Neoproterozoic acritarchs. Org. Geochem. 30, 1323–1337.

Arouri, K.R., Greenwood, P.F., Walter, M.R., 2000. Biological affnities of Neoproterozoic acritarchs from Australia: microscopic and chemical characterisation. Org. Geochem. 31, 75–89.

Barghoorn, E.S., Schopf, J.W., 1965. Microorganisms from the Late Precambrian of Central Australia. Science 150, 337–339. https://doi.org/10.1126/science.150.3694.337

Barghoorn, E.S., Tyler, S.A., 1965. Microorganisms from the Gunflint chert. Science 147, 563–577. https://doi.org/10.1126/science.147.3658.563

Bartley, J.K., 1996. Actualistic taphonomy of cyanobacteria: Implications for the precambrian fossil record. Palaios 11, 571–586. https://doi.org/10.2307/3515192

Battison, L., Brasier, M.D., 2012. Remarkably preserved prokaryote and eukaryote microfossils within 1Ga-old lake phosphates of the Torridon Group, NW Scotland. Precambrian Res. 196–197, 204–217. https://doi.org/10.1016/j.precamres.2011.12.012

Beghin, J., Storme, J.-Y., Blanpied, C., Gueneli, N., Brocks, J.J., Poulton, S.W., Javaux, E.J., 2017. Microfossils from the late Mesoproterozoic – early Neoproterozoic Atar/El Mreïti Group, Taoudeni Basin, Mauritania, northwestern Africa. Precambrian Res. 291, 63–82. https://doi.org/10.1016/j.precamres.2017.01.009

Benning, L.G., Phoenix, V.R., Mountain, B.W., Lappin-Scott, H., 2005. Biosilicification: the role of cyanobacteria in silica sinter deposition, in: Gadd, G., Semple, K. (Eds.), Micro-Organisms and Earth Systems – Advances in Geomicrobiology. Cambridge University Press, Cambridge, pp. 131–150. https://doi.org/10.1017/CBO9780511754852.008

Bercovici, A., Hadley, A., Villanueva-Amadoz, U., 2009. Improving Depth Of Field Resolution For Palynological Photomicrography. Palaeontol. Electron. 12, 5T.

Bernard, S., Benzerara, K., Beyssac, O., Menguy, N., Guyot, F., Brown, G.E., Goffe, B., 2007. Exceptional preservation of fossil plant spores in high-pressure metamorphic rocks. Earth Planet. Sci. Lett. 262, 257–272. https://doi.org/10.1016/j.epsl.2007.07.041

Bjørnerud, M.G., 2010. Stratigraphic record of Neoproterozoic ice sheet collapse: the Kapp Lyell diamictite sequence, SW Spitsbergen, Svalbard. Geol. Mag. 147, 380–390. https://doi.org/10.1017/S0016756809990690

Bosak, T., Lahr, D.J.G., Pruss, S.B., Macdonald, F.A., Dalton, L., Matys, E., 2011. Agglutinated tests in post-Sturtian cap carbonates of Namibia and Mongolia. Earth Planet. Sci. Lett. 308, 29–40. https://doi.org/10.1016/j.epsl.2011.05.030

Brocks, J.J., Jarrett, A.J.M., Sirantoine, E., Hallmann, C., Hoshino, Y., Liyanage, T., 2017. The rise of algae in Cryogenian oceans and the emergence of animals. Nature 548, 578–581. https://doi.org/10.1038/nature23457

Butterfield, N.J., 2015. Early evolution of the Eukaryota. Palaeontology 58, 5–17. https://doi.org/10.1111/pala.12139

Butterfield, N.J., 2005a. Reconstructing a complex early Neoproterozoic eukaryote, Wynniatt Formation, arctic Canada. Lethaia 38, 155–169. https://doi.org/10.1080/00241160510013231

Butterfield, N.J., 2005b. Probable Proterozoic fungi. Paleobiology 31, 165–182. https://doi.org/10.1666/0094-8373(2005)031<0165:PPF>2.0.CO;2

Butterfield, N.J., 2004. A vaucheriacean alga from the middle Neoproterozoic of Spitsbergen: implications for the evolution of Proterozoic eukaryotes and the Cambrian explosion. Paleobiology 30, 231–252. https://doi.org/10.1666/0094-8373(2004)030<0231:AVAFTM>2.0.CO;2

Butterfield, N.J., 2003. Exceptional Fossil Preservation and the Cambrian Explosion. Integr. Comp. Biol. 43, 166–177. https://doi.org/10.1093/icb/43.1.166

Campbell, K.A., Lynne, B.Y., Handley, K.M., Jordan, S., Farmer, J.D., Guido, D.M., Foucher, F., Turner, S., Perry, R.S., 2015. Tracing Biosignature Preservation of Geothermally Silicified Microbial Textures into the Geological Record. Astrobiology 15, 858–882. https://doi.org/10.1089/ast.2015.1307

Chalansonnet, S., Largeau, C., Casadevall, E., Berkaloff, C., Peniguel, G., Couderc, R., 1988. Cyanobacterial resistant biopolymers. Geochemical implications of the properties of Schizothrix sp. resistant material. Org. Geochem., Proceedings of the 13th International Meeting on Organic Geochemistry 13, 1003–1010. https://doi.org/10.1016/0146-6380(88)90282-3

Clark, R.L., Jensen, T.E., 1969. Ultrastructure of Akinete Development in a Blue-green Alga, Cylindrospermum sp. Cytologia (Tokyo) 34, 439–448. https://doi.org/10.1508/cytologia.34.439

Cohen, P.A., Knoll, A.H., 2012. Scale microfossils from the mid-Neoproterozoic Fifteenmile Group, Yukon Territory. J. Paleontol. 86, 775–800. https://doi.org/10.1666/11-138.1

Costerton, J.W., Irvin, R.T., Cheng, K.J., 1981. The Bacterial Glycocalyx in Nature and Disease. Annu. Rev. Microbiol. 35, 299–324. https://doi.org/10.1146/annurev.mi.35.100181.001503

Daft, M.J., Stewart, W.D.P., 1973. Light and electron microscope observations on algal lysis by bacterium cp-i. New Phytol. 72, 799–808. https://doi.org/10.1111/j.1469-8137.1973.tb02055.x

Delaine, M., Bernard, N., Gilbert, D., Recourt, P., Armynot du Châtelet, E., 2017. Origin and diversity of testate amoebae shell composition: Example of Bullinularia indica living in Sphagnum capillifolium. Eur. J. Protistol. 59, 14–25. https://doi.org/10.1016/j.ejop.2017.03.002

Derry, L.A., 2015. Causes and consequences of mid-Proterozoic anoxia: Causes Of Mid-Proterozoic Anoxia. Geophys. Res. Lett. 42, 8538–8546. https://doi.org/10.1002/2015GL065333

Domozych, D.S., 2011. Algal Cell Walls, in: ELS. American Cancer Society. https://doi.org/10.1002/9780470015902.a0000315.pub3

Domozych, D.S., Wells, B., Shaw, P.J., 1992. The cell wall of the chlamydomonad flagellate,Gloeomonas kupfferi (Volvocales, Chlorophyta). Protoplasma 168, 95–105. https://doi.org/10.1007/BF01666255

Fadel, A., Lepot, K., Busigny, V., Addad, A., Troadec, D., 2017. Iron mineralization and taphonomy of microfossils of the 2.45–2.21 Ga Turee Creek Group, Western Australia. Precambrian Res. 298, 530–551. https://doi.org/10.1016/j.precamres.2017.07.003

Fairchild, I.J., Knoll, A.H., Swett, K., 1991. Coastal lithofacies and biofacies associated with syndepositional dolomitization and silicification (Draken Formation, Upper Riphean, Svalbard). Precambrian Res. 53, 165–197. https://doi.org/10.1016/0301-9268(91)90071-H

Foucher, F., Westall, F., 2013. Raman Imaging of Metastable Opal in Carbonaceous Microfossils of the 700-800Ma Old Draken Formation. Astrobiology 13, 57–67. https://doi.org/10.1089/ast.2012.0889

Frain, K.M., Gangl, D., Jones, A., Zedler, J.A.Z., Robinson, C., 2016. Protein translocation and thylakoid biogenesis in cyanobacteria. Biochim. Biophys. Acta BBA - Bioenerg. 1857, 266–273. https://doi.org/10.1016/j.bbabio.2015.08.010

Gee, D.G., Page, L.M., 1994. Caledonian terrane assembly on Svalbard; new evidence from 40 Ar/ 39 Ar dating in Ny Friesland. Am. J. Sci. 294, 1166–1186. https://doi.org/10.2475/ajs.294.9.1166

Geitler, L., 1932. Cyanophyceae: von Lothar Geitler. Akademische Verlagsgesellschaft m.b.h., Leipzig.

Green, J.W., Knoll, A.H., Golubic, S., Swett, K., 1987. Paleobiology of Distinctive Benthic Microfossils from the Upper Proterozoic Limestone-Dolomite "Series," Central East Greenland. Am. J. Bot. 74, 928. https://doi.org/10.2307/2443874

Green, J.W., Knoll, A.H., Swett, K., 1989. Microfossils from silicified stromatolitic carbonates of the Upper Proterozoic Limestone-Dolomite "Series", central East Greenland. Geol. Mag. 126, 567–585.

Guo, Z., Peng, X., Czaja, A.D., Chen, S., Ta, K., 2018. Cellular taphonomy of well-preserved Gaoyuzhuang microfossils: A window into the preservation of ancient cyanobacteria. Precambrian Res. 304, 88–98. https://doi.org/10.1016/j.precamres.2017.11.007

Halverson, G.P., Kunzmann, M., Strauss, J.V., Maloof, A.C., 2017. The Tonian-Cryogenian transition in Northeastern Svalbard. Precambrian Res. https://doi.org/10.1016/j.precamres.2017.12.010

Halverson, G.P., Maloof, A.C., Hoffman, P.F., 2004. The Marinoan glaciation (Neoproterozoic) in northeast Svalbard. Basin Res. 16, 297–324. https://doi.org/10.1111/j.1365-2117.2004.00234.x

Halverson, G.P., Maloof, A.C., Schrag, D.P., Dudás, F.Ö., Hurtgen, M., 2007. Stratigraphy and geochemistry of a ca 800 Ma negative carbon isotope interval in northeastern Svalbard. Chem. Geol. 237, 5–27. https://doi.org/10.1016/j.chemgeo.2006.06.013

Harland, W.B., Gayer, R.A., 1972. The Arctic Caledonides and earlier Oceans. Geol. Mag. 109, 289–314. https://doi.org/10.1017/S0016756800037717

Harland, W.B., Scott, R.A., Auckland, K.A., Snape, I., 1992. The Ny Friesland Orogen, Spitsbergen. Geol. Mag. 129, 679–707. https://doi.org/10.1017/S0016756800008438

Harland, W.B., Wilson, C.B., 1956. The Hecla Hoek succession in Ny Friesland, Spitsbergen. Geol. Mag. 93, 265–286.

Hendry, J.P., Wilkinson, M., Fallick, A.E., Haszeldine, R.S., 2000. Ankerite cementation in deeply buried Jurassic sandstone reservoirs of the central North Sea. J. Sediment. Res. 70, 227–239. https://doi.org/10.1306/2DC4090D-0E47-11D7-8643000102C1865D

Herdianita, N.R., Browne, P.R.L., Rodgers, K.A., Campbell, K.A., 2000. Mineralogical and textural changes accompanying ageing of silica sinter. Miner. Deposita 35, 48–62. https://doi.org/10.1007/s001260050005

Hoffman, P.F., Halverson, G.P., Domack, E.W., Maloof, A.C., Swanson-Hysell, N.L., Cox, G.M., 2012. Cryogenian glaciations on the southern tropical paleomargin of Laurentia (NE Svalbard and East Greenland), and a primary origin for the upper Russøya (Islay) carbon isotope excursion. Precambrian Res. 206–207, 137–158. https://doi.org/10.1016/j.precamres.2012.02.018

Igisu, M., Ueno, Y., Shimojima, M., Nakashima, S., Awramik, S.M., Ohta, H., Maruyama, S., 2009. Micro-FTIR spectroscopic signatures of Bacterial lipids in Proterozoic microfossils. Precambrian Res. 173, 19–26. https://doi.org/10.1016/j.precamres.2009.03.006

Irwin, A.J., Finkel, Z.V., Schofield, O.M.E., Falkowski, P.G., 2006. Scaling-up from nutrient physiology to the size-structure of phytoplankton communities. J. Plankton Res. 28, 459–471. https://doi.org/10.1093/plankt/fbi148

Javaux, E.J., Knoll, A.H., Walter, M.R., 2004. TEM evidence for eukaryotic diversity in mid-Proterozoic oceans. Geobiology 2, 121–132. https://doi.org/10.1111/j.1472-4677.2004.00027.x

Javaux, E.J., Knoll, A.H., Walter, M.R., 2003. Recognizing and Interpreting the Fossils of Early Eukaryotes. Orig. Life Evol. Biosph. 33, 75–94.

Javaux, E.J., Lepot, K., 2018. The Paleoproterozoic fossil record: Implications for the evolution of the biosphere during Earth's middle-age. Earth-Sci. Rev. 176, 68–86. https://doi.org/10.1016/j.earscirev.2017.10.001

Johansson, A., Gee, D.G., Larionov, A.N., Ohta, Y., Tebenkov, A.M., 2005. Grenvillian and Caledonian evolution of eastern Svalbard - a tale of two orogenies. Terra Nova 17, 317–325. https://doi.org/10.1111/j.1365-3121.2005.00616.x

Johansson, Å., Larionov, A.N., Tebenkov, A.M., Gee, D.G., Whitehouse, M.J., Vestin, J., 2000. Grenvillian magmatism of western and central Nordaustlandet, northeastern Svalbard. Earth Environ. Sci. Trans. R. Soc. Edinb. 90, 221–254. https://doi.org/10.1017/S0263593300002583

Jones, B., Renaut, R.W., Rosen, M.R., 2001. Taphonomy of silicified filamentous microbes in modern geothermal sinters - Implications for identification. Palaios 16, 580–592. https://doi.org/10.2307/3515630

Jones, B., Renaut, R.W., Rosen, M.R., 1998. Microbial biofacies in hot-spring sinters: A model based on Ohaaki Pool, North Island, New Zealand. J. Sediment. Res. 68, 413–434.

Kaznatcheev, K.V., Karunakaran, C., Lanke, U.D., Urquhart, S.G., Obst, M., Hitchcock, A.P., 2007. Soft X-ray spectromicroscopy beamline at the CLS: Commissioning results. Nucl. Instrum. Methods Phys. Res. Sect. Accel. Spectrometers Detect. Assoc. Equip., Proceedings of the 14th National Conference on Synchrotron Radiation Research 582, 96–99. https://doi.org/10.1016/j.nima.2007.08.083

Kempe, A., Wirth, R., Altermann, W., Stark, R.W., Schopf, J.W., Heckl, W.A., 2005. Focussed ion beam preparation and in situ nanoscopic study of Precambrian acritarchs. Precambrian Res. 140, 36–54. https://doi.org/10.1016/j.precamres.2005.07.002

Knoll, A.., Javaux, E.., Hewitt, D., Cohen, P., 2006. Eukaryotic organisms in Proterozoic oceans. Philos. Trans. R. Soc. B Biol. Sci. 361, 1023–1038. https://doi.org/10.1098/rstb.2006.1843

Knoll, A.H., 2003. Life on a Young Planet: The First Three Billion Years of Evolution on Earth. Princeton University Press.

Knoll, A.H., 1982. Microorganisms from the late Precambrian Draken Conglomerate, Ny Friesland, Spitsbergen. J. Paleontol. 56, 755–790.

Knoll, A.H., Barghoorn, E.S., 1976. Gunflint-Type Microbiota from Duck Creek Dolomite, Western-Australia. Orig. Life Evol. Biosph. 7, 417–423. https://doi.org/10.1007/BF00927937

Knoll, A.H., Bergmann, K.D., Strauss, J.V., 2016. Life: the first two billion years. Philos. Trans. R. Soc. B Biol. Sci. 371, 20150493. https://doi.org/10.1098/rstb.2015.0493

Knoll, A.H., Golubic, S., 1979. Anatomy and taphonomy of a precambrian algal stromatolite. Precambrian Res. 10, 115–151. https://doi.org/10.1016/0301-9268(79)90022-6

Knoll, A.H., Strother, P., Rossi, S., 1988. Distribution and diagenesis of microfossils from the lower Proterozoic Duck Creek Dolomite, Western Australia. Precambrian Res. 38, 257–279. https://doi.org/10.1016/0301-9268(88)90005-8

Knoll, A.H., Sweet, K., Mark, J., 1991. Paleobiology of a Neoproterozoic tidal flat/lagoonal complex: the Draken Conglomerate Formation, Spitsbergen. J. Paleontol. 65, 531–570.

Knoll, A.H., Swett, K., 1990. Carbonate deposition during the late Proterozoic Era: an example from Spitsbergen. Am. J. Sci. 290-A, 104–132.

Knoll, A.H., Swett, K., Burkhardt, E., 1989. Paleoenvironmental distribution of microfossils and stromatolites in the Upper Proterozoic Backlundtoppen Formation, Spitsbergen. J. Paleontol. 63, 129–145. https://doi.org/10.1017/S002233600001917X

Koehler, I., Konhauser, K.O., Papineau, D., Bekker, A., Kappler, A., 2013. Biological carbon precursor to diagenetic siderite with spherical structures in iron formations. Nat. Commun. 4, 1741. https://doi.org/10.1038/ncomms2770

Konhauser, K.O., Jones, B., Phoenix, V., Ferris, G., Renaut, R., 2004. The microbial role in hot spring silicification. Ambio 33, 552–558. https://doi.org/10.1639/0044-7447(2004)033[0552:TMRIHS]2.0.CO;2

Kouketsu, Y., Mizukami, T., Mori, H., Endo, S., Aoya, M., Hara, H., Nakamura, D., Wallis, S., 2014. A new approach to develop the Raman carbonaceous material geothermometer for low-grade metamorphism using peak width: Raman CM geothermometer using FWHM. Isl. Arc 23, 33–50. https://doi.org/10.1111/iar.12057

Laakso, T.A., Schrag, D.P., 2014. Regulation of atmospheric oxygen during the Proterozoic. Earth Planet. Sci. Lett. 388, 81–91. https://doi.org/10.1016/j.epsl.2013.11.049

Lalonde, S.V., Konhauser, K.O., Reysenbach, A.-L., Ferris, F.G., 2005. The experimental silicification of Aquificales and their role in hot spring sinter formation. Geobiology 3, 41–52. https://doi.org/10.1111/j.1472-4669.2005.00042.x

Lamb, D.M., Awramik, S.M., Chapman, D.J., Zhu, S., 2009. Evidence for eukaryotic diversification in the ∼1800 million-year-old Changzhougou Formation, North China. Precambrian Res., World Summit on Ancient Microscopic Fossils 173, 93–104. https://doi.org/10.1016/j.precamres.2009.05.005

Lang, N.J., 1968. The Fine Structure of Blue-Green Algae. Annu. Rev. Microbiol. 22, 15–46. https://doi.org/10.1146/annurev.mi.22.100168.000311

Lee, J.J., Hutner, S.H., Bovee, E.C., 1985. An Illustrated guide to the protozoa. Society of Protozoologists.

Lekele Baghekema, S.G., Lepot, K., Riboulleau, A., Fadel, A., Trentesaux, A., El Albani, A., 2017. Nanoscale analysis of preservation of ca. 2.1 Ga old Francevillian microfossils, Gabon. Precambrian Res. 301, 1–18. https://doi.org/10.1016/j.precamres.2017.08.024

Lemelle, L., Labrot, P., Salome, M., Simionovici, A., Viso, M., Westall, F., 2008. In situ imaging of organic sulfur in 700-800 My-old Neoproterozoic microfossils using X-ray spectromicroscopy at the SK-edge. Org. Geochem. 39, 188–202. https://doi.org/10.1016/j.orggeochem.2007.10.008

Leontowich, A.F.G., Hitchcock, A.P., 2012. Secondary electron deposition mechanism of carbon contamination. J. Vac. Sci. Technol. B Nanotechnol. Microelectron. Mater. Process. Meas. Phenom. 30, 030601. https://doi.org/10.1116/1.3698602

Lepot, K., Addad, A., Knoll, A.H., Wang, J., Troadec, D., Beche, A., Javaux, E.J., 2017. Iron minerals within specific microfossil morphospecies of the 1.88 Ga Gunflint Formation. Nat. Commun. 8, 14890. https://doi.org/10.1038/ncomms14890

Lepot, K., Benzerara, K., Brown, G.E., Philippot, P., 2008. Microbially influenced formation of 2,724-million-year-old stromatolites. Nat. Geosci. 1, 118–121. https://doi.org/10.1038/ngeo107

Lepot, K., Compere, P., Gerard, E., Namsaraev, Z., Verleyen, E., Tavernier, I., Hodgson, D.A., Vyverman, W., Gilbert, B., Wilmotte, A., Javaux, E.J., 2014. Organic and mineral imprints in fossil photosynthetic mats of an East Antarctic lake. Geobiology 12, 424–450. https://doi.org/10.1111/gbi.12096

Liberton, M., Howard Berg, R., Heuser, J., Roth, R., Pakrasi, H.B., 2006. Ultrastructure of the membrane systems in the unicellular cyanobacterium Synechocystis sp. strain PCC 6803. Protoplasma 227, 129–138. https://doi.org/10.1007/s00709-006-0145-7

Lyberis, N., Manby, G., 1999. Continental collision and lateral escape deformation in the lower and upper crust: An example from Caledonide Svalbard. Tectonics 18, 40–63. https://doi.org/10.1029/1998TC900013

Lynne, B.Y., Campbell, K.A., Moore, J.N., Browne, P.R.L., 2005. Diagenesis of 1900-year-old siliceous sinter (opal-A to quartz) at Opal Mound, Roosevelt Hot Springs, Utah, USA. Sediment. Geol. 179, 249–278. https://doi.org/10.1016/j.sedgeo.2005.05.012

Lyons, T.W., Reinhard, C.T., Planavsky, N.J., 2014. The rise of oxygen in Earth's early ocean and atmosphere. Nature 506, 307–315. https://doi.org/10.1038/nature13068

Maloof, A.C., Halverson, G.P., Kirschvink, J.L., Schrag, D.P., Weiss, B.P., Hoffman, P.F., 2006. Combined paleomagnetic, isotopic, and stratigraphic evidence for true polar wander from the Neoproterozoic Akademikerbreen Group, Svalbard, Norway. GSA Bull. 118, 1099–1124. https://doi.org/10.1130/B25892.1

Oehler, D.Z., 1977. Pyrenoid-like Structures in Late Precambrian Algae from the Bitter Springs Formation of Australia. J. Paleontol. 51, 885–901.

Oehler, D.Z., 1976. Transmission Electron Microscopy of Organic Microfossils from the Late Precambrian Bitter Springs Formation of Australia: Techniques and Survey of Preserved Ultrastructure. J. Paleontol. 50, 90–106.

Oehler, D.Z., Robert, F., Mostefaoui, S., Meibom, A., Selo, M., McKay, D.S., 2006. Chemical mapping of Proterozoic organic matter at submicron spatial resolution. Astrobiology 6, 838–850.

Oehler, J.H., 1976. Hydrothermal Crystallization of Silica-Gel. Geol. Soc. Am. Bull. 87, 1143–1152. https://doi.org/10.1130/0016-7606(1976)87<1143:HCOSG>2.0.CO;2

Orange, F., Westall, F., Disnar, J.-R., Prieur, D., Bienvenu, N., Leromancer, M., Defarge, C., 2009. Experimental silicification of the extremophilic Archaea Pyrococcus abyssi and Methanocaldococcus jannaschii: applications in the search for evidence of life in early Earth and extraterrestrial rocks. Geobiology 7, 403–418. https://doi.org/10.1111/j.1472-4669.2009.00212.x

Pacton, M., Gorin, G.E., Fiet, N., 2008. Unravelling the Origin of Ultralaminae in Sedimentary Organic Matter: The Contribution of Bacteria and Photosynthetic Organisms. J. Sediment. Res. 78, 654–667. https://doi.org/10.2110/jsr.2008.075

Pang, K., Tang, Q., Schiffbauer, J.D., Yao, J., Yuan, X., Wan, B., Chen, L., Ou, Z., Xiao, S., 2013. The nature and origin of nucleus-like intracellular inclusions in Paleoproterozoic eukaryote microfossils. Geobiology 11, 499–510. https://doi.org/10.1111/gbi.12053

Phoenix, V.R., Adams, D.G., Konhauser, K.O., 2000. Cyanobacterial viability during hydrothermal biomineralisation. Chem. Geol. 169, 329–338. https://doi.org/10.1016/S0009-2541(00)00212-6

Porter, S.M., Knoll, A.H., 2000. Testate amoebae in the Neoproterozoic Era: evidence from vase-shaped microfossils in the Chuar Group, Grand Canyon. Paleobiology 26, 360–385. https://doi.org/10.1666/0094-8373(2000)026<0360:TAITNE>2.0.CO;2

Porter, S.M., Meisterfeld, R., Knoll, A.H., 2003. Vase-Shaped Microfossils From The Neoproterozoic Chuar Group, Grand Canyon: A Classification Guided By Modern Testate Amoebae. J. Paleontol. 77, 21.

Posth, N.R., Koehler, I., Swanner, E.D., Schroeder, C., Wellmann, E., Binder, B., Konhauser, K.O., Neumann, U., Berthold, C., Nowak, M., Kappler, A., 2013. Simulating Precambrian banded iron formation diagenesis. Chem. Geol. 362, 66–73. https://doi.org/10.1016/j.chemgeo.2013.05.031

Preston, L.J., Benedix, G.K., Genge, M.J., Sephton, M.A., 2008. A multidisciplinary study of silica sinter deposits with applications to silica identification and detection of fossil life on Mars. Icarus 198, 331–350. https://doi.org/10.1016/j.icarus.2008.08.006

Reinhard, C.T., Planavsky, N.J., Gill, B.C., Ozaki, K., Robbins, L.J., Lyons, T.W., Fischer, W.W., Wang, C., Cole, D.B., Konhauser, K.O., 2016. Evolution of the global phosphorus cycle. Nature 541, 386–389. https://doi.org/10.1038/nature20772

Sandelin, S., Tebenkov, A.M., Gee, D.G., 2001. The stratigraphy of the lower part of the Neoproterozoic Murchisonfjorden Supergroup in Nordaustlandet, Svalbard. GFF 123, 113–127. https://doi.org/10.1080/11035890101232113

Schiffbauer, J.D., Xiao, S., 2009. Novel application of focused ion beam electron microscopy (FIB-EM) in preparation and analysis of microfossil ultrastructures: A new view of complexity in early Eukaryotic organisms. PALAIOS 24, 616–626. https://doi.org/10.2110/palo.2009.p09-003r

Schopf, J.W., 1970. Electron Microscopy of Organically Preserved Precambrian Microorganisms. J. Paleontol. 44, 1–6.

Schopf, J.W., 1968. Microflora of the Bitter Springs Formation, Late Precambrian, Central Australia. J. Paleontol. 42, 651–688.

Schopf, J.W., Blacic, J.M., 1971. New Microorganisms from the Bitter Springs Formation (Late Precambrian) of the North- Central Amadeus Basin, Australia. J. Paleontol. 45, 925–960.

Schopf, J.W., Kudryavtsev, A.B., Agresti, D.G., Czaja, A.D., Wdowiak, T.J., 2005. Raman imagery: A new approach to assess the geochemical maturity and biogenicity of permineralized Precambrian fossils. Astrobiology 5, 333–371. https://doi.org/10.1089/ast.2005.5.333

Sergeev, V.N., Schopf, J.W., 2010. Taxonomy, Paleoecology and Biostratigraphy of the Late Neoproterozoic Chichkan Microbiota of South Kazakhstan: The Marine Biosphere on the Eve of Metazoan Radiation. J. Paleontol. 84, 363–401. https://doi.org/10.1666/09-133.1

Stanier, G., 1988. [14] Fine structure of cyanobacteria, in: Methods in Enzymology, Cyanobacteria. Academic Press, pp. 157–172. https://doi.org/10.1016/0076-6879(88)67017-0

Strauss, J.V., Rooney, A.D., Macdonald, F.A., Brandon, A.D., Knoll, A.H., 2014. 740 Ma vase-shaped microfossils from Yukon, Canada: Implications for Neoproterozoic chronology and biostratigraphy. Geology 42, 659–662. https://doi.org/10.1130/G35736.1

Van de Meene, A.M.L., Hohmann-Marriott, M.F., Vermaas, W.F.J., Roberson, R.W., 2006. The three-dimensional structure of the cyanobacterium Synechocystis sp. PCC 6803. Arch. Microbiol. 184, 259–270. https://doi.org/10.1007/s00203-005-0027-y

Vorob'eva, N.G., Sergeev, V.N., Petrov, P.Y., 2015. Kotuikan Formation assemblage: A diverse organic-walled microbiota in the Mesoproterozoic Anabar succession, northern Siberia. Precambrian Res. 256, 201–222. https://doi.org/10.1016/j.precamres.2014.11.011

Wacey, D., McLoughlin, N., Kilburn, M.R., Saunders, M., Cliff, J.B., Kong, C., Barley, M.E., Brasier, M.D., 2013. Nanoscale analysis of pyritized microfossils reveals differential heterotrophic consumption in the ~1.9-Ga Gunflint chert. Proc. Natl. Acad. Sci. U. S. A. 110. https://doi.org/10.1073/pnas.1221965110

Wacey, D., Menon, S., Green, L., Gerstmann, D., Kong, C., Mcloughlin, N., Saunders, M., Brasier, M., 2012. Taphonomy of very ancient microfossils from the similar to 3400 Ma Strelley Pool Formation and similar to 1900 Ma Gunflint Formation: New insights using a focused ion beam. Precambrian Res. 220, 234–250. https://doi.org/10.1016/j.precamres.2012.08.005

Waterbury, J.B., Stanier, R.Y., 1978. Patterns of growth and development in pleurocapsalean cyanobacteria. Microbiol. Rev. 42, 2–44.

Westall, F., Boni, L., Guerzoni, E., 1995. The Experimental Silicification of Microorganisms. Palaeontology 38, 495–528.

Williford, K.H., Ushikubo, T., Schopf, J.W., Lepot, K., Kitajima, K., Valley, J.W., 2013. Preservation and detection of microstructural and taxonomic correlations in the carbon isotopic compositions of individual Precambrian microfossils. Geochim. Cosmochim. Acta 104, 165–182. https://doi.org/10.1016/j.gca.2012.11.005

Willman, S., 2009. Morphology and wall ultrastructure of leiosphaeric and acanthomorphic acritarchs from the Ediacaran of Australia. Geobiology 7, 8–20. https://doi.org/10.1111/j.1472-4669.2008.00178.x

Wilson, C.B., 1961. The Upper Middle Hecla Hoek Rocks of Ny Friesland, Spitsbergen. Geol. Mag. 98, 89–116. https://doi.org/10.1017/S0016756800060325

Wilson, C.B., 1958. The Lower Middle Hecla Hoek Rocks of Ny Friesland, Spitsbergen. Geol. Mag. 95, 305–327. https://doi.org/10.1017/S0016756800062865

Yun, Z., 1981. Proterozoic Stromatolite Microfloras of the Gaoyuzhuang Formation (Early Sinian:Riphean), Hebei, China. J. Paleontol. 55, 485–506.

Supplementary figures

Supplementary Fig 3.1. Sample P4353-6A*. The arrows indicate the position of cherty lenses, which appear darker in the dolomitic matrix (grey material).*

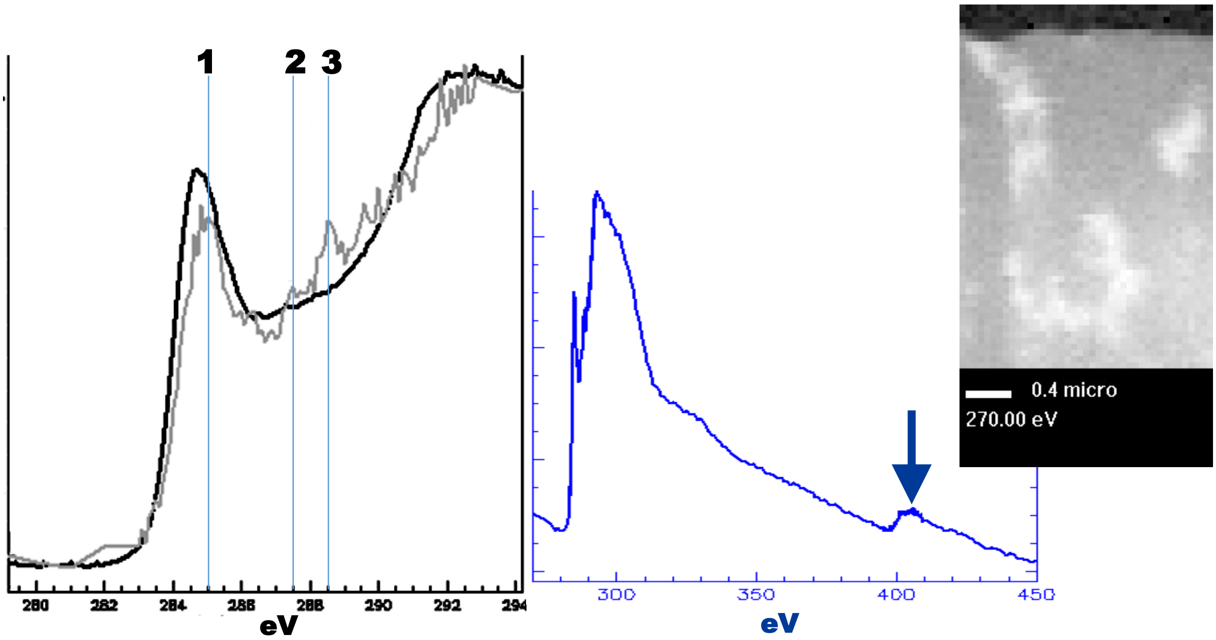

Supplementary Fig 3.2. *Left part: XANES spectra of Draken microfossils recorded at Diamond (black) and CLS (grey) (from different microstructures). Band #1 (285.2 eV) indicates aromatic carbon, band #2 (287.5 eV) indicates ketone C=O and band #3 (288.6 eV) indicates carboxylic C=O. Note that the grey spectrum is slightly shifted by -0.3 eV. Right part: XANES spectra of* *a Draken microfossil recorded at CLS (Arrow: N-K-edge). Image on the rigth: map just below the carbon K-edge (270 eV) showing the location of carbon analyzed at CLS.*

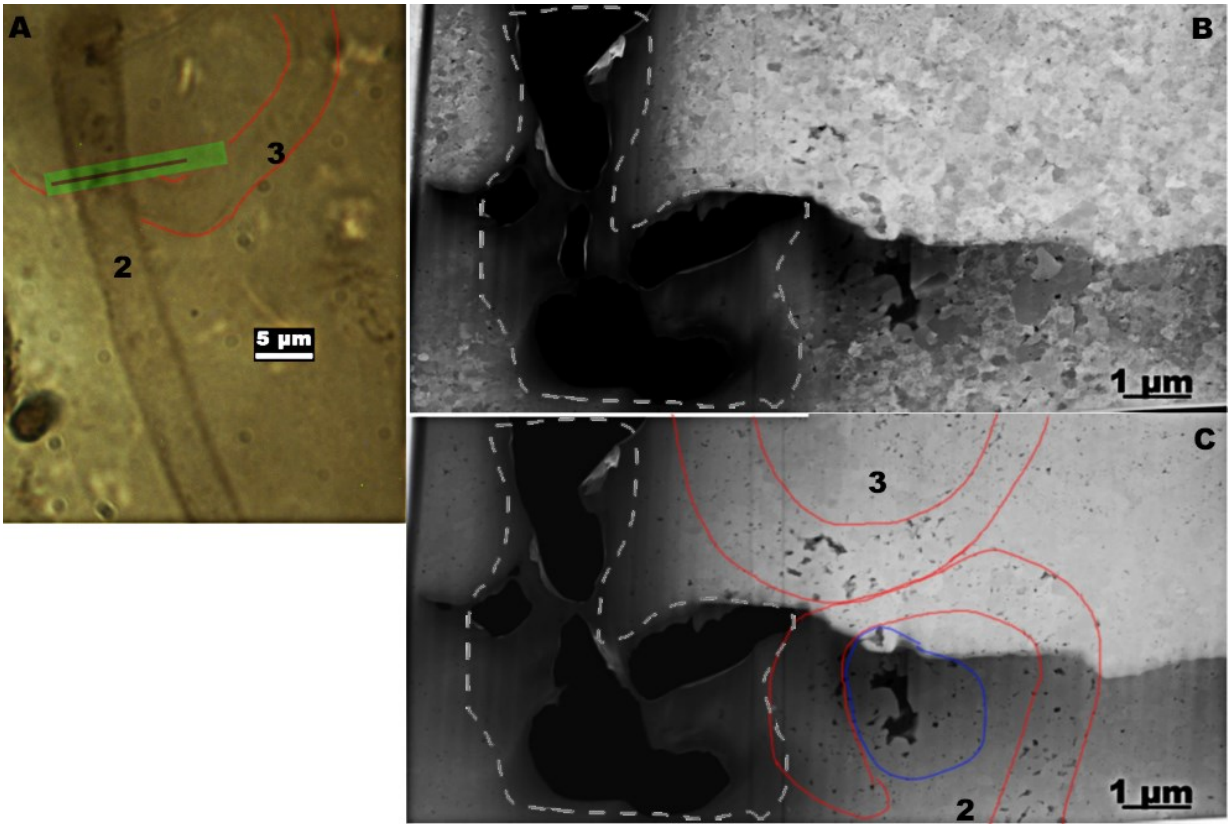

Supplementary Fig. 3.3. Siphonophycus filament specimens 2 and 3. *A. Photomicrograph of the filament in transmitted light (green line: position of the FIB section). B. STEM dark field image of the lateral FIB sections. The microfossils are permineralized by nano-quatrz. C. HAADF image of the FIB section showing the distribution of the carbon (dark) and quartz (grey). Note that the quartz region with a dashed outline is now amorphous or absent due to FIB damage. Outlined in red are the presumed sheath walls defined by a ~1 µm thick zone interspersed with granular organic material. A central zone includes a thick grain of organic matter is outlined in blue. (Sample: P4353-11A)*

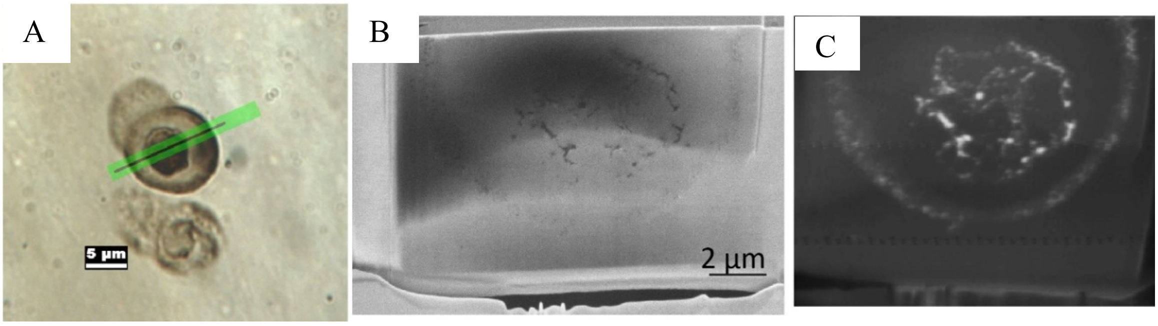

Supplementary Fig. 3.4. Gloeodiniopsis mikros monad. *A. Photomicrograph of the microfossil in transmitted light (green line: position of the FIB section). B. Secondary electron SEM image of the FIB section. C. Map aromatic carbon (STXM) showing the presence of a 0.7-µm thick* *outer layer and an internal organic material. The inner vesicle displays a similar structure as observed in the dyad in Fig. 3.4. (Sample: P4353-11A)*

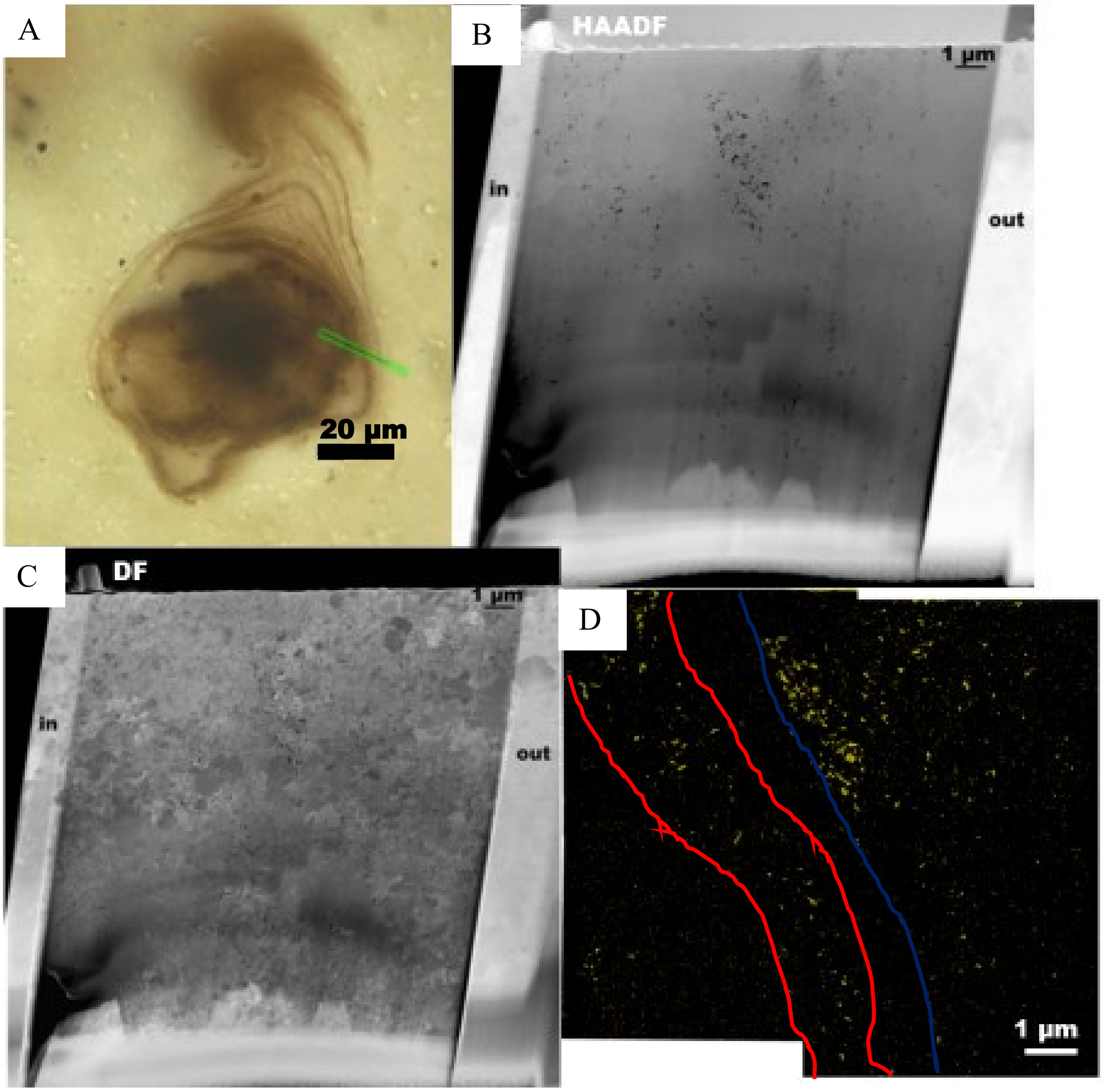

Supplementary Fig. 3.5. Polybessurus specimen 2. *A. Photomicrograph of the microfossil in transmitted light (green line: position of the FIB section). B. HAADF image of the of the FIB sections. Carbon appears in dark and quartz in grey. C. STEM dark field image of the FIB sections showing the distribution of nano-quartz crystals. D. EDX map showing the distribution of carbon in yellow. Red lines: inner sheath structure. Rigth on the blue line: outer sheath structure of the microfossil. (Sample: P4353-A)*

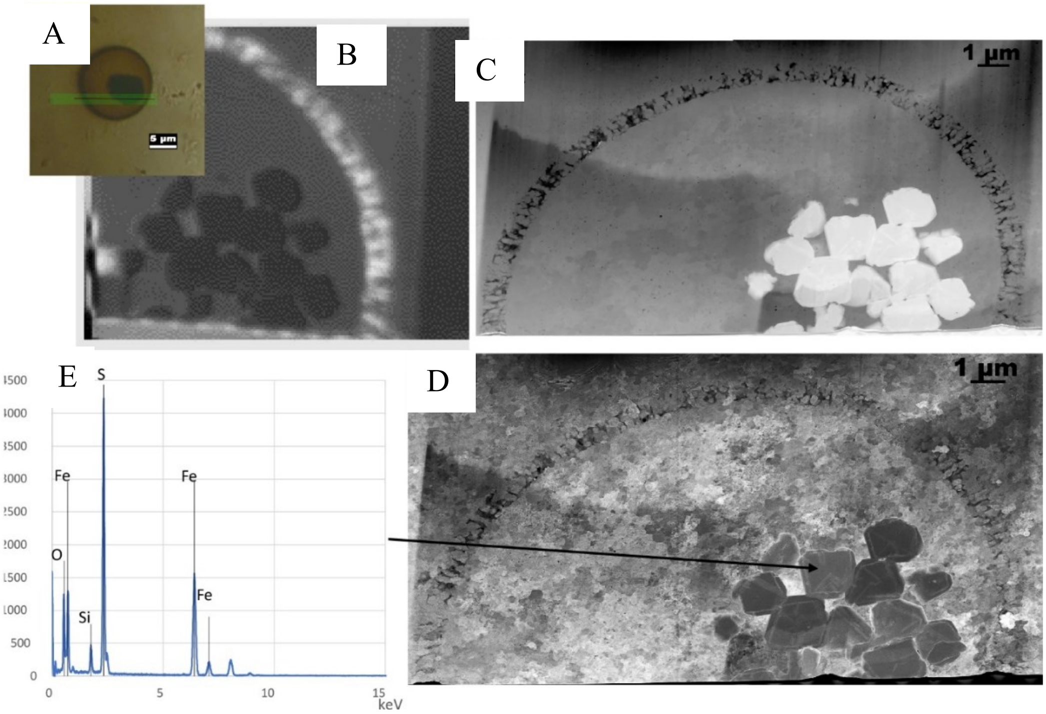

Supplementary Fig. 3.6. Myxococcoides microfossil specimen 2*. A. Photomicrograph of the microfossil in transmitted light (green line: position of the FIB section). B. Map aromatic carbon showing columnar fabric of the cell wall. C. HAADF image of the of the FIB sections. Carbon appear in dark, quartz in grey and pyrite in white. D. STEM dark field image of the FIB sections showing the distribution of nano-quartz crystals. E. EDX spectra obtained from a pyrite grain (point by the arrow). (Sample: P4353-11A)*

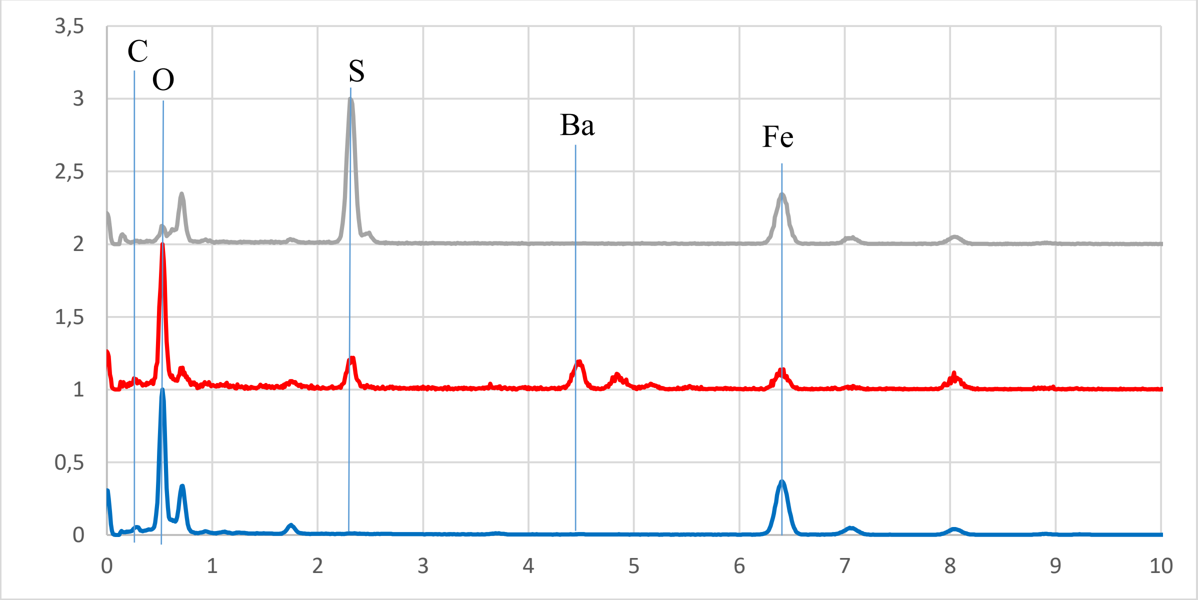

Supplementary Fig. 3.7. EDX spectra from the minerals present in the Myxococcoides microfossil specimen 1. Blue spectrum: carbon+iron. Red spectrum: barium + iron + carbon. Grey spectrum: sulfur+iron

Chapitre IV
Minéralisation de fer et taphonomie des microfossiles de 2,45-2,21 Milliard d'année du Turee Creek Group, Australie occidentale

Présentation

Il y a 2.3 milliards d'années, le Grand Bond d'Oxygénation (aussi appelé Grande Oxygénation) est un événement majeur dans l'histoire de la Terre et l'évolution de la biosphère. En effet avant ce Grand Bond, l'atmosphère de notre planète était bien différente de l'actuelle avec des teneurs en gaz à effet de serre importantes et l'absence de dioxygène. Dans ces conditions à priori hostiles, la vie ne se développe essentiellement sous forme de microorganismes (ex : bactéries) capables de vivre sans dioxygène. Ce serait à partir de ─2,9 milliard d'années que des bactéries particulières, les cyanobactéries commencèrent à fixer le carbone du dioxyde de carbone atmosphérique et rejeter une molécule qui changea le cours de l'évolution : le dioxygène. Cependant, en raison de son aptitude à oxyder de nombreuses espèces chimiques, le dioxygène à peine produit, fut consommé par de nombreux réactifs, dont le fer qui était alors abondant dans les océans. Tout ce fer oxydé précipita sous forme d'oxydes de fer et forma des gisements de fer rubanées (Banded Iron Formation en anglais ou BIF) entre ─3 et ─2,4 milliards d'années. Ce n'est que quand la production d'O_2 a surpassé la quantité de réactifs (dont les ions Fe^{2+}) que la concentration du dioxygène dans l'océan et l'atmosphère augmenta : c'est le Grand Bond d'Oxygénation.

C'est dans ce contexte que se sont déposées les formations sédimentaires du Turee Creek (Australie). Dans ces formations, des microorganismes fossiles (ou microfossiles) associées à des minéraux ferrugineux ont été retrouvés au niveau de formations de fer rubanées. Ce nouvel assemblage a ainsi offert l'opportunité à une équipe de chercheurs de l'Université de Lille-CNRS (Laboratoire d'océanologie et de géosciences ; Unité matériaux et transformation ; Institut d'électronique, de microélectronique et de nanotechnologie) et de l'Institut de Physique du Globe de Paris, d'étudier des microorganismes datant de cette période cruciale de l'évolution de notre planète.

Les observations au microscope optique et Microscope Electronique à Balayage ont montré que ces microorganismes forment un réseau similaire à des toiles d'araignées typique de colonies bactériennes ayant été rapidement fossilisés par de la silice (SiO2). Bien que ces microfossiles bactériens soient de formes assez simples (principalement des filaments sans cellules préservées), nous avons pu mettre en évidence la présence de différentes morpho espèces plus ou moins associées avec des minéraux ferrugineux (voir Fig. 4.1).

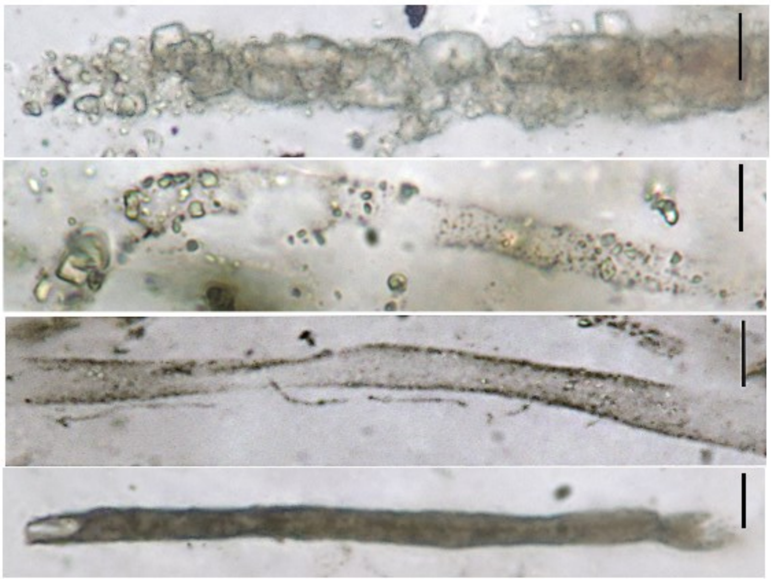

***Fig. 4.1.** Photographie en microscopie optique de différentes morpho-espèces de microfossiles encroutés par des minéraux ferrugineux (avec une augmentation de l'encroutement par les cristaux de gauche vers la droite). Ces microfossiles sont préservés dans un chert (roche siliceuse) de Turee Creek. Barre d'échelle de 5 micromètres (5 millièmes de millimètres).*

Nos nano-analyses effectuées au Microscope Electronique à Transmission (Fig. 4.2) ont montré que la présence des cristaux ferrugineux a eu un impact négatif sur la préservation des parties organiques de certaines morpho espèces de microfossiles. De plus, la signature isotopique du Fer (^{56}Fe/^{54}Fe) des minéraux ferrugineux associés aux microfossiles indique que le fer a pris part à une réaction d'oxydation. Le couplage de ces observations suggère que certains de ces microorganismes étaient des bactéries oxydant du fer dans un environnement relativement profond riche en fer.

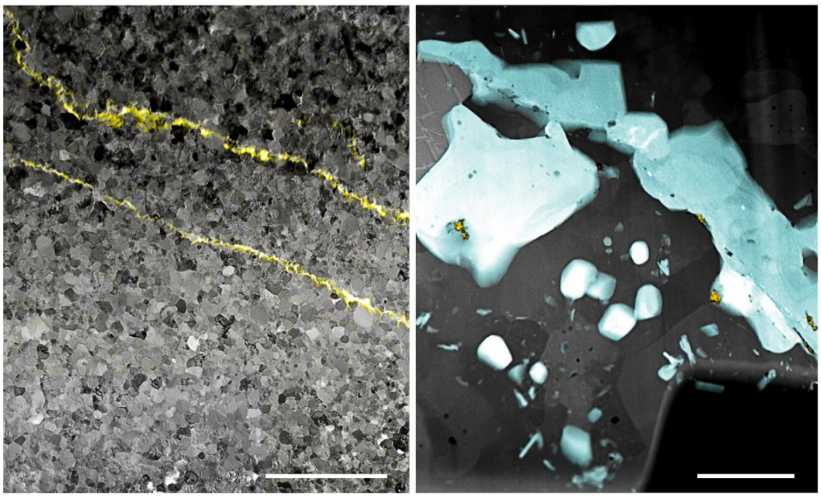

Fig. 4.2. Image en microscopie STEM de deux morpho-espèces de microfossile. A gauche : la matière organique (en jaune) entourée par des cristaux de quartz, forme une fine paroi qui contenait les cellules bactériennes. A droite : autre morpho-espèce de microfossile dont la

matière organique (rares points jaunes) a été remplacée par des minéraux ferrugineux (en bleu et blanc) préservés dans du quartz (gris). Barre d'échelle : 2 micromètres.

Enfin cet assemblage bactérien associé avec des formations de fer présente des similarités avec des microfossiles déjà décrits et issus d'autres strates de la formation de Turee Creek qui avaient été interprétés comme des bactéries métabolisant du soufre plutôt que du fer. Cela suggère que lors d'un changement d'environnement de ferrugineux à sulfuré, caractéristique du Grand Bond d'Oxygénation, les mêmes bactéries auraient pu adapter leur métabolisme, ou être remplacées par d'autres communautés bactériennes d'aspect relativement similaire.

Precambrian Research 298 (2017) 530–551

Contents lists available at ScienceDirect

Precambrian Research

journal homepage: www.elsevier.com/locate/precamres

Iron mineralization and taphonomy of microfossils of the 2.45–2.21 Ga Turee Creek Group, Western Australia

Alexandre Fadel [a], Kevin Lepot [a,*], Vincent Busigny [b], Ahmed Addad [c], David Troadec [d]

[a] Université de Lille, CNRS, Université Littoral Côte d'Opale, Laboratoire d'Océanologie et de Géosciences UMR8187, 59000 Lille, France
[b] Institut de Physique du Globe de Paris, Sorbonne Paris Cité, Université Paris Diderot, UMR 7154 CNRS, 75238 Paris, France
[c] Unité Matériaux et Transformations, Université de Lille, CNRS UMR 8207, 59000 Lille, France
[d] Institut d'Electronique, de Micro-électronique et de Nanotechnologie, CNRS UMR8520, 59655 Villeneuve d'Ascq, France

ARTICLE INFO

Article history:
Received 21 June 2016
Revised 30 June 2017
Accepted 4 July 2017
Available online 5 July 2017

Keywords:
Microfossils
Siderite
Iron oxidation
Chert
Turee Creek Group
Great Oxidation Event

ABSTRACT

We report a new assemblage of carbonaceous microfossils intimately associated with siderite and Fe-silicates, from a black chert nodule included in iron formation of the ca. 2.45–2.21 Ga Turee Creek Group, Western Australia. This chert comprises microbial fabrics dominated by filaments preserved in matrix of nano- to micrometric quartz. Filaments occur in clumps and in a cobweb-like fabric interspersed with coarse crystalline, void filling quartz granules. We studied this chert with optical microscopy combined with Scanning Transmission Electron Microscope observations of Focused Ion Beam sections of microfossils. This distinguished three types of well-preserved fossil interpreted as polysaccharide sheaths that usually do not preserve chains of cells (trichomes): Type 1 comprises narrow filaments with thin continuous kerogen sheaths, Type 2 comprises narrow filaments with thick granular sheaths, and Type 3 comprises broad filaments with thin sheaths. Type 4 filaments are poorly preserved as granular kerogen. Organic ultrastructures of Type 2–4 microfossils are variably replaced by siderite crystals, associated with minor Fe-silicates. Iron isotope analyses on bulk powder and reactive iron fraction show indistinguishable and highly positive δ^{56}Fe values (+1.45‰ relative to the reference IRMM-014), indicating that the bulk of siderite derives from reduction of Fe(III)-oxides. This provides indirect evidence that the microbial community was originally associated with Fe(III)-oxides. Siderite and Fe-silicates are found with Type 2–4 but not Type 1 filaments, suggesting that only the former were encrusted by Fe(III)-oxides, which may have been reduced *in situ*. Siderite and Fe-silicates could result from oxidation of organic matter in filaments coupled with microbial and/or thermal reduction of Fe(III)-bio(?)minerals. The increasing abundance of siderite correlated with decreasing organic matter preservation in filaments supports that this reaction occurred to variable extents, *in situ* on each microfossil. Type 2–4 microfossils may thus represent iron-oxidizing bacteria. These microbial mats display strong similarities with those associated with immediately overlying carbonate rocks of the Turee Creek Group, where filaments were interpreted as sulfur-oxidizing bacteria. Some filamentous bacteria can oxidize both iron and sulfur. Such metabolic versatility could have enabled benthic microbial mats to thrive in the drastically changing chemical conditions of the Great Oxidation Event.

1. Introduction

Although the timing of the first emergence of O_2 producing photosynthesis is unresolved (Lyons et al., 2014; Schopf, 2014), several geochemical tracers recorded the production of free O_2 by photosynthetic cyanobacteria as early as 2.9 Gyrs ago (Anbar et al., 2007; Crowe et al., 2013; Farquhar and Wing, 2003; Frei et al., 2009; Garvin et al., 2009; Kendall et al., 2010; Partin et al., 2013; Planavsky et al., 2014; Reinhard et al., 2013; Thomazo et al., 2011). The disappearance of mass-independent fractionation of sulfur isotopes (MIF-S) indicates the rise of O_2 in the upper layers of the atmosphere at least ca. 2.45 Ga ago (Farquhar and Wing, 2003; Reinhard et al., 2013). This marks the beginning of a substantial rise of free O_2 in the atmosphere named the Great Oxidation Event (GOE, Holland, 2002) and coincides with the end of the Archean eon and a paucity in the deposition of Banded Iron Formations (BIF) (Van Kranendonk, 2010). This GOE was observed for the first time in the Huronian Supergroup, Southern Canada (Hoffman, 2013; Roscoe, 1968). The Huronian Supergroup contains three

---

* Corresponding author.
E-mail address: kevin.lepot@univ-lille1.fr (K. Lepot).

http://dx.doi.org/10.1016/j.precamres.2017.07.003
0301-9268/© 2017 Elsevier B.V. All rights reserved.

formations with diamictites indicating that glacial episodes coincided with the rise of O_2 in the atmosphere during a widespread shutdown of magmatic activity (Condie et al., 2009) associated with a possible drop of biological CH_4 (Konhauser et al., 2009). The development of sulfidic water formed by sulfate reduction also induced a decrease of Fe concentrations (through Fe-sulfide precipitation) in the ocean and likely represent the main cause for the absence of BIF deposits between 1.8 and 0.8 Ga (Anbar and Knoll, 2002; Canfield, 1998; Rasmussen et al., 2012).

The Turee Creek Group (2.45–2.20 Ga) of Western Australia was deposited during the GOE. It conformably overlies BIFs of the Boolgeeda Iron Formation (Van Kranendonk, 2010). The Turee Creek Group contains diamictites recording a glaciation (Martin, 1999; Van Kranendonk, 2010) that could correspond to one of the two lower Huronian glaciations (Hoffman, 2013). In the Turee Creek Group, S isotope compositions of pyrite in shales that directly overly the Boolgeeda BIF show a 90‰ range ($\delta^{34}S$ from −45.5‰ to +46.4‰), suggesting microbial sulfate reduction under non-sulfate limiting conditions (Williford et al., 2011). This result implies significant oxidative weathering of sulfides on the continents, due to atmospheric O_2 accumulation. Small MIF-S are, however, preserved in these shales, suggesting that pO_2 remained low enough to produce MIF-S (Williford et al., 2011), although this may reflect a time lag between atmospheric oxygenation and MIF-S disappearance in the sedimentary record (Reinhard et al., 2013).

Gunflint-type microfossil assemblages dominate the post-GOE fossil record between 2.1 and 1.7 Ga (Barghoorn and Tyler, 1965; Knoll et al., 1988; Knoll and Barghoorn, 1976; Lepot et al., 2017). Gunflint-type microfossil assemblages are dominated by filamentous microfossils (*Gunflintia*) of ca. 1–5 μm in diameter, spherical microfossils (*Huroniospora*) ca. 1.5–12 μm in diameter, and generally comprise uncommon star-shaped microfossils (*Eoastrion*) and scarce umbrella-shaped microfossils (*Kakabekia*). This assemblage has been exemplified by the Gunflint Iron Formation (Canada) occurrence discovered in the 1950 (Barghoorn and Tyler, 1965). The Paleoproterozoic era is dominated by Gunflint-type assemblages (Awramik and Barghoorn, 1977; Barghoorn and Tyler, 1965; Knoll et al., 1978). Moreover, the characterization of nanoscale textures of fossil cell walls or fossil polysaccharide sheaths and the textures of associated entombing quartz provided criteria of biogenicity for the identification of much older microfossils (Moreau and Sharp, 2004; Wacey et al., 2012). The metabolism of filamentous microfossils in the Gunflint-type assemblages is, however, ambiguous (Shapiro and Konhauser, 2015) and could correspond to oxygenic photosynthetic cyanobacteria (Barghoorn and Tyler, 1965) as well as iron-oxidizing bacteria (Cloud, 1965; Planavsky et al., 2009). Microfossil assemblages dominated by filaments have been found in blacks cherts of the Kazput Formation in the upper part of the Turee Creek Group (Schopf et al., 2015; Van Kranendonk et al., 2012). In contrast to many Gunflint-type assemblages that formed stromatolitic mats of microfossils in shallow-water (*e.g.* Barghoorn and Tyler, 1965), the Turee Creek microfossils formed cobweb-like structures in relatively quiet, possibly deeper water similar to the assemblages of the 1.8 Ga Duck Creek Formation (Schopf et al., 2015). Based on environment, isotope ratios of organic carbon and pyritic sulfur, and the morphological similarity between the observed filaments and modern S-oxidizing and/or S-reducing bacteria, it has been proposed that the Duck Creek and Turee Creek microfossil assemblages are dominated by filamentous sulfur-metabolizing organisms of a sulfuretum, a microbial community using sulfur by oxidation and reduction metabolisms in a cyclic fashion (Schopf et al., 2015; Van Kranendonk et al., 2012).

The mineral assemblage associated with microfossils may provide important constraints on the nature of the microfossils and on diagenetic processes. Some Gunflint-type microfossils are intimately associated and/or replaced by hematite (Knoll and Simonson, 1981), which has been used to support iron metabolism (Cloud, 1965; Planavsky et al., 2009). However, association of hematite with microfossil may reflect taphonomic processes rather biomineralization induced by the microorganisms (Shapiro and Konhauser, 2015). Similarly, replacement of organic matter by pyrite in Gunflint-type microfossils is a common taphonomic process (Wacey et al., 2013). In contrast, intra-microfossil Fe-silicates (greenalite) and Fe-carbonates (siderite, $FeCO_3$) were observed in specific morphospecies of the Gunflint Iron Formation (Lepot et al., 2017). The Fe-minerals were interpreted as products of reductive recrystallization of intracellular Fe-biominerals and used to infer that these morphospecies were cyanobacteria performing oxygenic photosynthesis (Lepot et al., 2017).

Here we report Turee Creek Group microfossils that are well preserved to fully replaced by siderite and associated with iron silicates. This study characterized their ultrastructures and the associated mineralizations by nanoscale petrography. Based on textures, mineralogy, elemental composition and bulk-rock isotope ratio of iron ($\delta^{56}Fe$), carbon ($\delta^{13}C$), and oxygen ($\delta^{18}O$), we discuss the metabolism, the environment, the taphonomy and the diagenetic and metamorphic histories of these microfossils.

2. Geological setting

The Turee Creek Group reaches a maximum of 4 km in thickness in the Hardey Syncline (Fig. 1). It comprises, in ascending stratigraphic order: the Kungarra Formation (that contains the Meteorite Bore Member), the Koolbye Formation and the Kazput Formation (Fig. 1D). The Kungarra Formation is composed of approximately 3 km of clastic sediment grading from siltstone, mudstone and shales with minor dolomite that are interpreted as distal turbidites at the base, to grained sandstones with stromatolitic carbonates deposited in shallow water setting (Martindale et al., 2015; Van Kranendonk et al., 2015). The Meteorite Bore Member of the Kungarra Formation consists of 270 m of glaciogenic diamictites and siltstones that have been correlated with the Huronian glaciations (Eriksson and Condie, 2014; Lindsay and Brasier, 2002; Martin, 1999; Martin et al., 2000; Van Kranendonk et al., 2015). The Koolbye Formation that conformably overlies the Kungarra formation, includes 130 m of quartzarenite, siltstone and minor conglomerate deposited in coastal–fluvial setting (Mazumder et al., 2014; Van Kranendonk et al., 2015).

The Kazput Formation, the final stage of the Turee Creek Group displays two mains units (Fig. 1D). The lower unit is mainly composed of dolomite and mudstones, while the upper unit consists mainly of siltstones and fine-grained sandstones (Barlow et al., 2016; Lindsay and Brasier, 2002; Martin et al., 2000; Martindale et al., 2015). Finally, the Lower Wyloo Group succeeds the Turee Creek group above an erosional unconformity and is composed of the Beasley River Quartzite and the Cheela Springs Basalt (Fig. 1D) (Eriksson et al., 1999; Martin, 1999; Martin et al., 2000). The age of the Turee Creek Group is constrained by the underlying Woongarra Rhyolite (2449 ± 3 Ma, (Barley et al., 1997) and the overlying Cheela Springs Basalt (2209 ± 15 Ma, Martin et al., 1998). Detrital zircons in the Meteorite Bore Member indicate a maximum age of deposition of ca. 2420 Ma (Takehara et al., 2010). Hence, the microfossiliferous cherts of the overlying Kazput Formation are 2209 to 2420 Ma old.

The black chert samples studied here were collected within the lower, carbonate-dominated unit of the Kazput formation in the Kazput Syncline locality, at S22 °29.748′, E116 °31.817′ (see Fig. 1C) (Barlow et al., 2016), distinct from the locality of chert reported by Schopf et al. (2015) and Van Kranendonk et al. (2012). There, the sequence consists in shallow-water (domical,

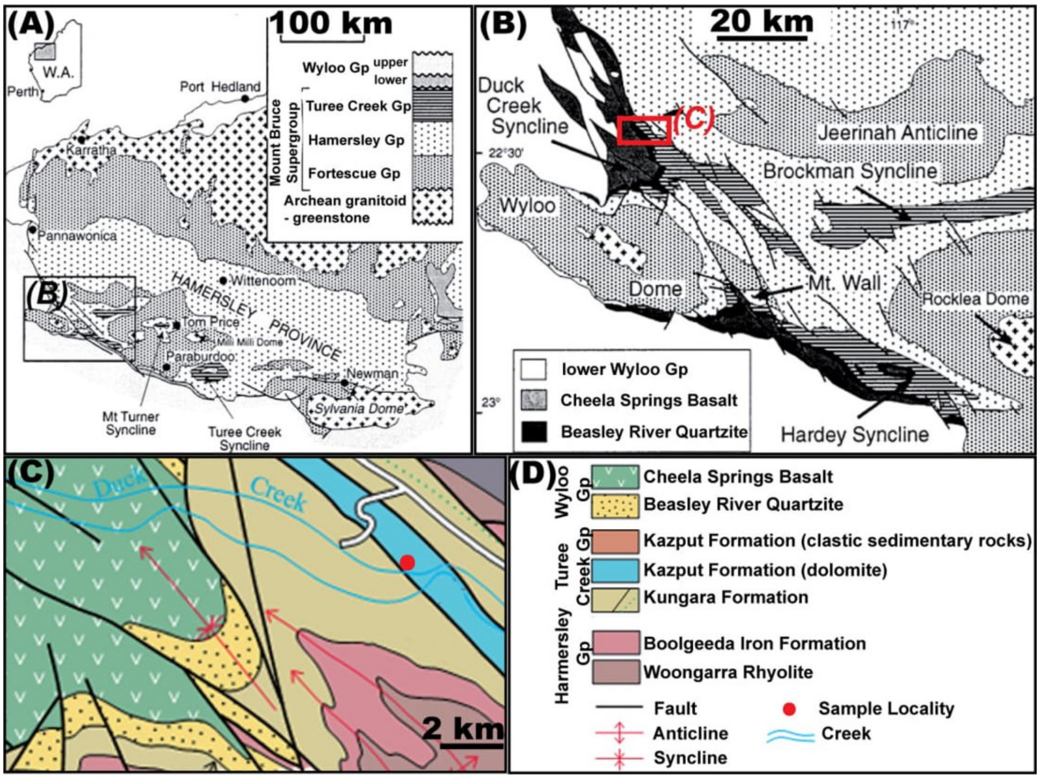

Fig. 1. Geological context. (A) Regional map of the Hamersley province and Pilbara craton with the stratigraphy of the Mount Bruce super group. (B) Regional map showing the principal structures in the western part of Hamersley province. (C)-(D) Localization of the sample localities on a geological map with local stratigraphy (after Martin et al., 2000 and Van Kranendonk, 2010 : A-B reprinted under permission of Elsevier, C-D courtesy of Martin Van Kranendonk).

columnar, club-shaped) stromatolites, overlain by a 20–50 m thick sequence of clotted thrombolite-like carbonates, overlain by an approximately 50 m thick sequence dominated by massive and thin- to very-thinly bedded dolomite that is the Facies Association E of Barlow et al. (2016). In this Facies Association E, the presence of minor shales, turbidites, and banded iron formations, and the absence of breccia, conglomerates, storm deposits or current-reworked facies suggest deposition below storm wave base (Barlow et al., 2016). The chert DCK4_9.3 was sampled in a ca. 2 m large and ca. 10 cm thick black chert lens located at the top of a BIF (or iron formation) deposit at least 50 cm thick occurring in the massive dolomites of Facies Association E (Fig. 2A). K30 and K32 were sampled within the poorly to thinly laminated massive dolomites of Facies Association E (Fig. 2B) several meters above the studied BIF. The BIF is a transient unit between shale and carbonate deposits, and accordingly testify to a change in water depth and may represent a passage through a chemocline in the basin (Barlow et al., 2016). Thus, microfossils present in the black chert DCK4_9.3 are closely associated with iron-shale formations while microfossils reported from previous studies (Schopf et al., 2015; Van Kranendonk et al., 2012) from previous studies from cherts similar to K30 and K32 hosted by the overlying carbonates rock may represent communities that thrived in different environments.

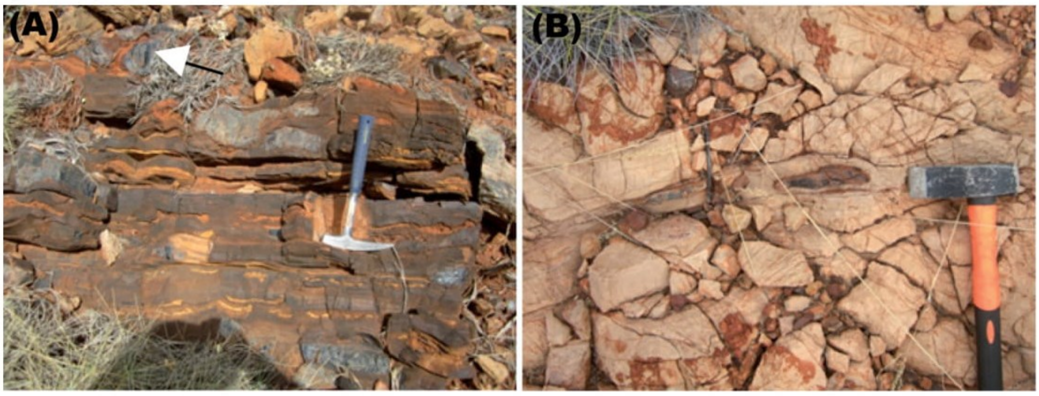

Fig. 2. Locality outcrop. (A) BIF with black cherts nodules. Sample DCK4_9.3 (arrow) occurred at the top of the BIF facies, in contact with carbonate facies. (B) View of the carbonates where the black cherts nodules K30 and K32 were sampled.

3. Methods

3.1. Optical microscopy

Observations were made on 30–40 μm thick, polished uncovered thin sections. Optical petrography and microfossils localization were carried out using an Olympus BX60 microscope (LOG, Université de Lille) under bright-field transmitted light and reflected light. Photomicrographs from single focal planes were combined into "multiplane images" using a weighted average algorithm (CombineZP software by Alan Hadley) in order to fully describe each microfossil and microfossil clusters (Bercovici et al., 2009). Photomicrographs of microfossils are multiplane images, unless otherwise specified. Coordinates of microfossils located at the surface of the thin section were referenced in order to carry out Raman spectroscopy, Scanning Electron Microscopy (SEM) and Transmitted Electron Microscopy (TEM) observations on the same structures.

3.2. Raman spectroscopy

Raman spectra and mappings of microfossils were obtained using a LabRam HR800UV Raman microspectrometer (Horiba Jobin Yvon) (at LOG, Université de Lille) and a LabRam HR (at LASIR, Université de Lille) with 532 nm laser focused through an Olympus BX41 microscope with a $100\times$ objective. In order to avoid artifacts, spectra and mappings were obtained in focus 1–2 μm below the surface of thin sections and filters were used to limit the laser power to less than 7 mW (maps) and 1 mW (point spectra) on the surface of the thin section. The backscattered Raman signal was dispersed by a grating (1800 lines/mm) and analyzed with a front-illuminated CCD detector. Raman mappings were performed on regions of interest with a point by point raster scanning using a XY-motorized stage (precision <1μm) for map that have dimensions exceeding $15\,\mu m \times 15\,\mu m$. For maps smaller than $10\,\mu m \times 10\,\mu m$, the sample was raster-scanned by moving the laser beam rather than the sample stage. The backscattered signal was dispersed by a grating (300 or 600 lines/mm for maps) and baseline subtraction was performed with Labspec software.

3.3. Scanning Electron Microscopy (SEM)

SEM images were recorded on gold-palladium coated ($\sim$20 nm thick deposit) thin sections using a FEI Quanta 200 (at LOG, Université de Lille) SEM. The secondary electron images (SE) revealed the topographic features that located targets for Focused Ion Beam (FIB) foils preparation. Mineral identification was performed at 15–20 kV and at a working distance of 10 mm using backscattered electron (BSE) imaging and Energy Dispersive X-ray Spectroscopy (EDXS) maps with a QuanTax QX2 (ROENTEC) detector. After FIB preparation (see below), Au-Pd coating was polished away and Cathodoluminescence (SEM-CL) images were acquired with a Centaurus detector on the same thin section after carbon-coating.

3.4. Focused Ion Beam (FIB)

FIB foils were prepared on microfossils with a FEI strata DualBeam 235 FIB (at IEMN, Lille) for Transmitted Electron Microscopy. The top surface of each region of interest was protected with platinum strip $\sim$25 μm long and $\sim$2 μm thick. Material on each side of the region of interest was removed by a gallium (Ga) ion beam (30 kV, 7 nA). Then, FIB sections were lifted out and attached onto a copper TEM grid by depositing platinum at the contact(s) between the foil and the grid. The section was thinned to $\sim$150 nm using low beam current (1 nA to 300 pA and 100 pA) grazing on each side of the section. SE images were taken to control the thinning process. Finally, the plasma-redeposited amorphous material was removed by scanning the foil with a 5 kV ion beam at an angle of 4–7° with the foil surface.

3.5. Transmitted Electron Microscopy (TEM) and Scanning-TEM (STEM)

TEM analyses were performed on the FIB foils on a FEI Tecnai G2-20 and a Philips CM30 (CCM, Université de Lille) operated at 200 kV and 300 kV, respectively. Both instruments are equipped with EDXS (Energy Dispersive X-ray Spectrometry) detectors sensitive to light weight elements. Axial and annular detectors and scanning devices allowed operation of the microscopes in STEM mode to collect bright and dark-field images. The contrasts in STEM bright field and, in particular, dark field images are more influenced by the atomic weight of elements, whereas TEM images are more influenced by diffraction contrasts. Elemental distributions were mapping using EDXS (STEM mode of the Philips CM30). Selected Area Electron Diffraction patterns were also acquired for identification of nanoscale Fe-silicates.

3.6. Bulk-rock geochemistry

Major, minor and trace elements were measured using Inductively-Coupled Plasma-Mass Spectrometry (ICP-MS) at Service d'Analyse des Roches et des Minéraux (SARM-CNRS, Nancy) after melting of the sample in LiBO$_2$, and dissolution in acid. Fe (II) concentrations were measured by titration after acid leaching. Sulfur concentrations were measured using an Elemental Analyzer.

Bulk rock isotope analyses were performed on a homogenous powder of the black chert DCK4_9.3 at Institut de Physique du Globe de Paris. For organic carbon isotope analyses ($\delta^{13}C_{org}$), powdered samples were decarbonated in 6 N HCl for one night at 25 °C followed by 2 h at 80 °C. The residue was rinsed in milliQ water several times until it reached neutral pH, and was centrifuged and dried for 2 days at 50 °C. Three aliquots of dried decarbonated samples (101.67 to 146.23 mg) were then loaded into quartz tubes together with CuO wires, sealed under vacuum and combusted at 950 °C for 6 h. The produced CO$_2$ was purified on a vacuum line and quantified manometrically to evaluate Total Organic Carbon (TOC) concentrations. Carbon isotope composition of the purified CO$_2$ was then measured on a DeltaplusXP mass-spectrometer with a precision better than ±0.1‰ (2SD). For C and O isotopes analysis of carbonates, 56.95 to 80.03 mg of rock powder was loaded in a vacutainer tube. The tube was then flushed with helium. Rock powder was treated with 100% phosphoric acid at 130 °C for 2 h to dissolve all carbonates, including siderite (Busigny et al., 2013; Lebeau et al., 2014). The C and O isotope compositions of CO$_2$ were measured using a continuous-flow mass-spectrometer (AP-2003) operated with helium as a carrier gas. Carbonate content in samples was estimated from the ion intensity of the CO$_2$ peak in the mass-spectrometer with a precision better than ±10% (2σ). Organic matter can potentially contribute to the CO$_2$ produced by heating the sample at 130 °C with phosphoric acid, and thus impact C and O isotope compositions measured for carbonates. Accordingly we removed organic matter from the sample, prior to carbonate analysis, by low T oxygen-plasma ashing system (Lebeau et al., 2014). Three replicate measurements of C and O isotopes in carbonates were performed for the plasma-treated sample and three replicates were measured for the pristine powder. Results for $\delta^{13}C_{org}$, $\delta^{13}C_{carb}$, and $\delta^{18}O_{carb}$ are reported using permil deviation relative to the V-PDB standard, and only average values and standard deviations of replicate analyses are reported. For Fe isotope analyses, two different extraction protocols were used (Busigny et al., 2014). First, reactive Fe [including carbonate and poorly crystallized oxides and clay minerals, but not minerals such as pyrite and hematite (Busigny et al., 2014; Raiswell et al., 1994; Severmann et al., 2006)] was "sequentially" dissolved in cold 0.5 N HCl for 4 days. Second, bulk Fe was extracted using acid digestion (multiple heating and evaporation steps) by mixtures of HF + HNO_3 and HCl + HNO_3 in clean Teflon beakers. For both extraction methods, Fe was then separated by exchange chromatography in HCl medium. Iron concentrations and isotopic compositions were measured using a Neptune ThermoFischer MC-ICP-MS (Multiple Collector Inductively Coupled Plasma Mass Spectrometer) at IPGP. Analytical blanks associated with Fe extraction and purification were always lower than 30 ng Fe, a negligible amount compare to the samples (~300 µg Fe). Results are reported as δ^{56}Fe (^{56}Fe/^{54}Fe) and δ^{57}Fe (^{57}Fe/^{54}Fe) using permil deviation relative to the IRMM-014 geostandard (metal Fe from Institute for Reference Materials and Measurements). Only average values and standard deviations of replicate analyses are reported.

4. Result

4.1. Mineralogy of the chert nodules and surrounding carbonates

The chert nodule K30 is composed of quartz with dolomite rhombohedra ~20 to several hundred-micrometer wide (Fig. 3A). The carbonates surrounding the nodule (in the same thin section) are dolomite with cross-cutting veins composed of calcite with quartz and probably late iron/manganese oxides (Fig. 3A). The chert nodule K32 displays 10 to 100 µm large pyrite and ~100 µm rhombohedra of dolomite with ankerite (Fe-Mg-Ca carbonate) overgrowth (Fig. 3B-C). The carbonate sediments that surround this nodule are dolomite with small amounts of iron. K30 and K32 do not contain microfossils.

The black chert DCK4_9.3 is interspersed with large (up to 1 mm) rhombohedra of ankerite and siderite (Fig. 3E-F; H spectra 2 and 3). Unlike other nodules surrounded by dolomitic rocks, the DCK4_9.3 chert occurring in contact with BIF deposits contains swarms of small (mostly <10 µm) rhombohedral to anhedral siderite crystals (Fig. 3D) that only show small amounts of magnesium (Fig. 3G spectrum 1). Some large siderite and ankerite rhombs have been partly replaced by secondary hematite (Fig. 3E-F), but this is not the case for the small (<10 µm) siderite crystals (Fig. 3D). The presence and distribution of siderite is also constrained by Raman spectra with peaks at 190 cm^{-1}, 295 cm^{-1} and 1088 cm^{-1} (Boulard et al., 2012). Pyrite is absent in this sample. DCK4_9.3 is composed of micrometric quartz grains with zones containing coarse quartz crystals grouped as sub-rounded granules (Fig. 4A-D).

4.2. Microfossil assemblage

4.2.1. Correlation with chert textures

The black chert DCK4_9.3 contain microfossils that either occur in tangled clumps (Fig. 4B-F) or display a cobweb-like fabric around coarse quartz granules (Fig. 4B-D, G-K). In clumps, filaments are organized as very dense populations of tangled filaments and form dark zones in both plain and cross polarized light (Fig. 4B, C, E-F). Loosely clustered filaments defining the cobweb-like fabric appear as dark lines in cross polarized light (Fig. 4J-K). Coarse-crystalline quartz fills the granule-shaped voids between the cobweb-like fabric with filaments. The micro-quartz grains at the interface between microfossils and coarse-crystalline granules are fibrous (Fig. 4G-K).

The combination of polarized light (Fig. 4C, H) and cathodoluminescence (SEM-CL, Fig. 4D, I) images of the black cherts DCK4_9.3 distinguishes coarse quartz granules (dark in SEM-CL images), and zones of fine (nanoscale or fibrous) quartz crystals (light grey in SEM-CL images). These images show that all filaments are encased in the finer quartz grains. SEM-CL revealed that the scarce isolated filaments occurring within granules of coarse quartz are in fact also filled and covered by fine quartz, which forms tubular coatings on the filaments (Fig. 4D, I). These tubular coatings of isolated filaments often form columnar fabrics of fine quartz grains that are included in the coarse quartz granules (Fig. 4C-D, H-I). Importantly, the contrast in SEM-CL images was

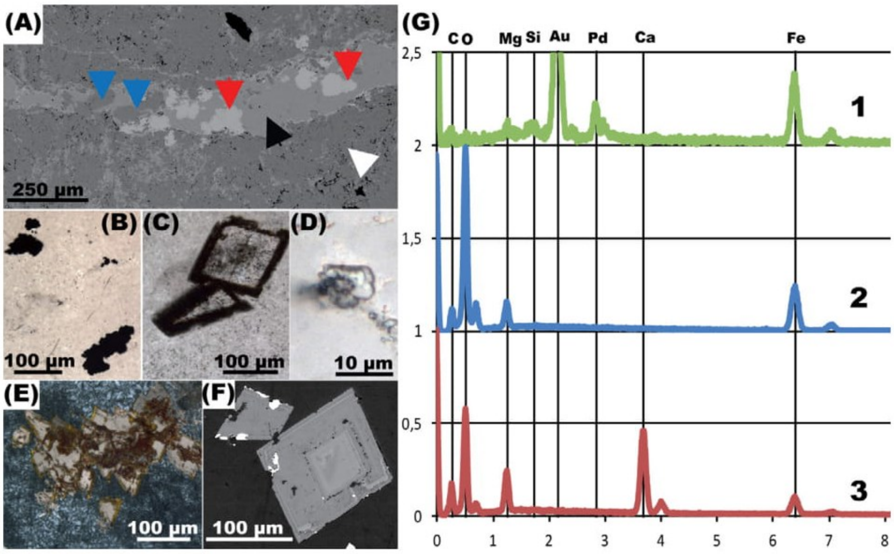

Fig. 3. Petrography of the chert nodules and surrounding carbonates. (A). Sample K30. BSE image of the mostly dolomitic (white arrow: dolomite) sediment surrounding the nodule K30. The cross-cutting vein comprises quartz (blue arrows), calcite (black arrows), and iron/manganese oxide (red arrows). (B)-(C) Sample K32. (B) Photomicrograph of pyrite or pyrrhotite in the black chert K32, transmitted light. (C) Photomicrograph of zoned carbonates in the chert K32. (D)-(F). Sample DCK4_9.3. (D) Photomicrograph of small siderite grain in transmitted light. (E) Zoned siderite (pale brown) in the chert (grey) nodule, under crossed polars. Siderite shows secondary oxidation in hematite (red). Hematite confirmed with Raman spectrometry (not shown). (F) BSE image of zoned ankerite. White zones are relics of a previous gold coating. (H) EDXS spectra of carbonates in the chert nodule DCK4_9.3: (1) siderite in (D), (2) siderite in (E), (3) Ankerite in (F). Au and Pd come from the coating. (For interpretation of the references to colour in this figure legend, the reader is referred to the web version of this article.)

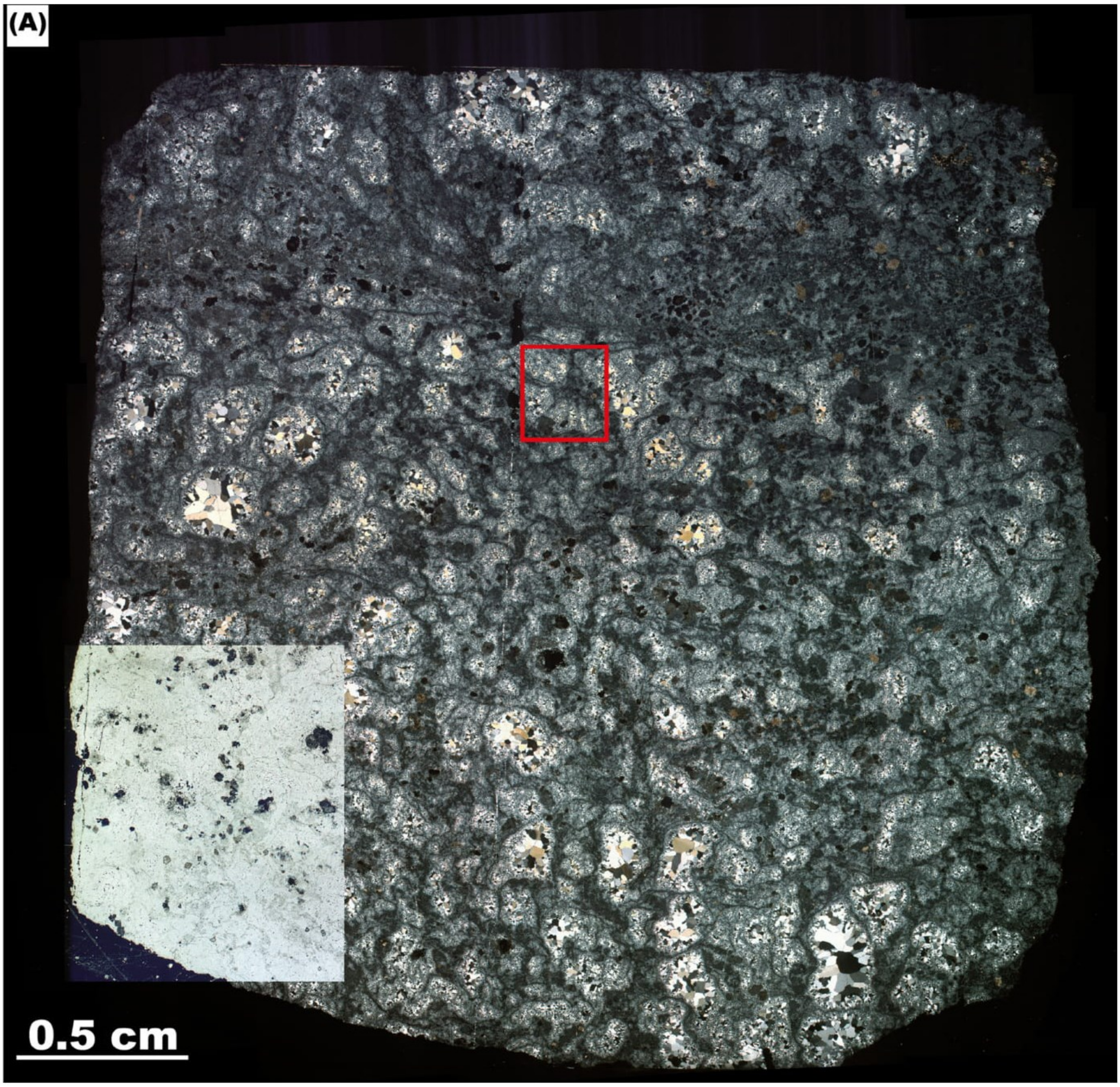

Fig. 4. Quartz textures in the DCK4_9.3 chert. (A) Photomicrograph in transmitted light with crossed polars (the lower left corner is shown in plain polarized light). (B) Photomicrograph (plain polarized light) of the boxed region in (A). Dark regions are composed of microfossils (black arrows indicate clumps of filaments). (C) Same as previous with crossed polars showing fine-grained quartz in/on filaments and coarse-crystalline mosaic-forming quartz forming granules between filaments. (D) SEM-CL image of the area in (B)-(C). Fine-grained quartz appears in mottled grey, coarse-grained quartz in black. Filaments, as seen in (B), are surrounded by fine-grained quartz. (E)-(F) Magnified photomicrograph of a clump boxed in (B). (E) Plain polarized light, (F) crossed polars. (G)-(K) Magnified view of the top left quarter of (B). (G) Plain polarized light, (H) crossed polars, (I) SEM-CL image. Filaments are encapsulated in fine-grained quartz, as highlighted with the arrowhead in (G)-(I). Coarse quartz with mosaic-forming texture fills the space between filaments, forming granules. (J)-(K) Magnified view of clustered filaments boxed in (G) displaying cobweb-like fabric. Fibrous quartz marks the transition between nano-quartz in/on filaments and coarse-grained quartz granules. White arrow indicates the position of filaments present in fine-grained quartz. (J) Plain polarized light, (K) crossed polars.

similar to the contrast observed in secondary electron images, and the SEM-CL signal was very weak. Therefore, the signal in SEM-CL image may not result of cathodoluminescence but might be the result of the size difference between the two types of silica owing to charge effects, as suggested by the bright lines appearing between the two types of silica in Fig. 4D. Therefore, the contrast between coarse and fine grained quartz may not be caused by different trace element concentrations and only the texture can be used to distinguish the two generations of quartz. However, the sub-horizontal quartz veinlets cutting across both coarse and fine quartz matrices show a bright SEM-CL signal (Fig. 4D), indicating formation by a late fluid of distinct composition.

4.2.2. Microfossil population

The microfossil assemblage in DCK4_9.3 is almost entirely composed of filaments. Spherical microfossil (*Huraniospora e.g.* Barghoorn and Tyler, 1965; Cloud, 1965), star-shaped dubiofossils (resembling *Eoastrion e.g.* Barghoorn and Tyler, 1965) and shapeless kerogen are extremely scarce in this sample. They are composed of kerogen as indicated by Raman spectra (Fig. 5). Based

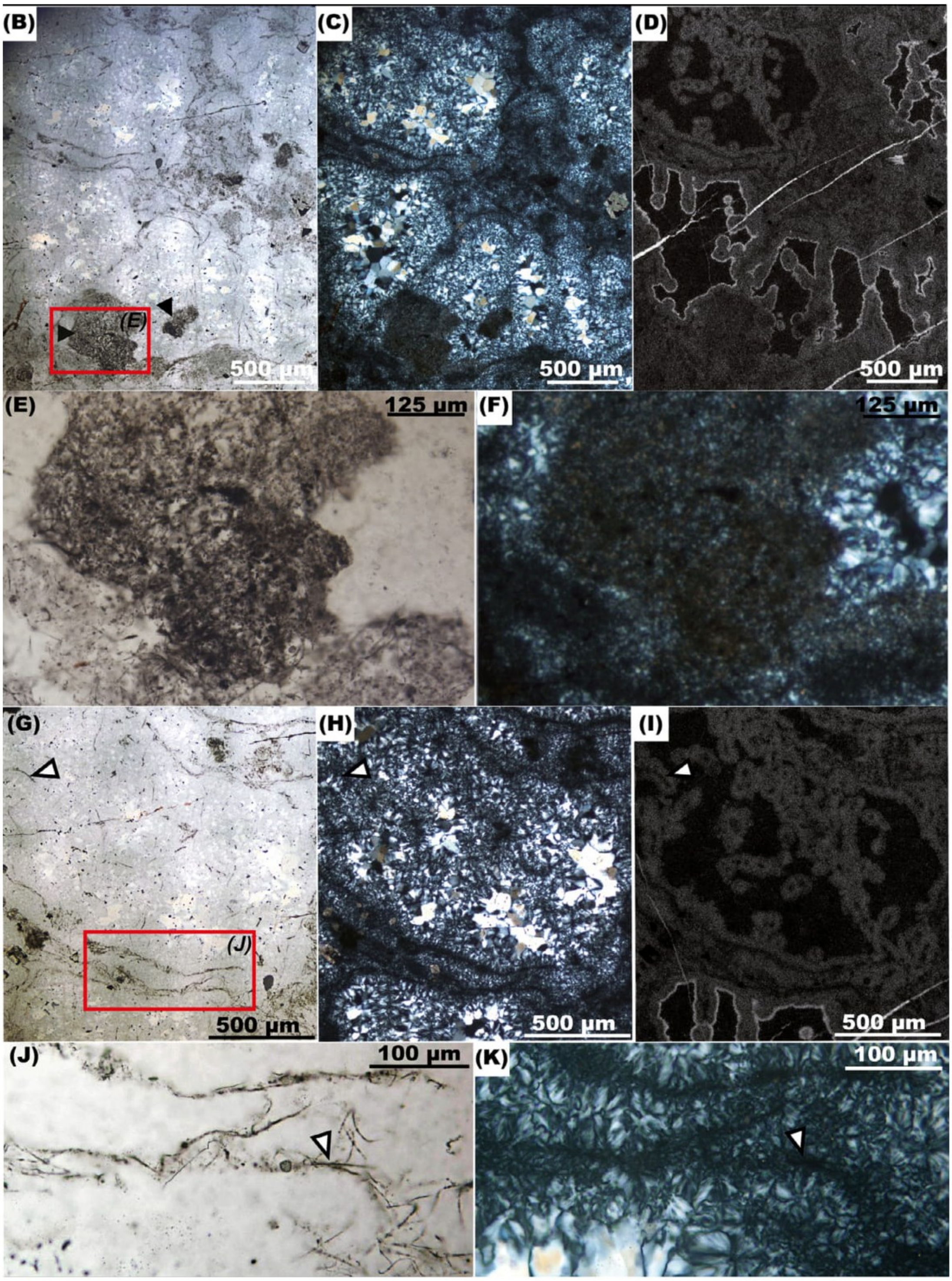

Fig. 4 (*continued*)

on peak-fitting decomposition of Raman spectra of organic matter (Kouketsu et al., 2014), the calculated peak metamorphism temperature of the kerogen is ~280 ± 30 °C (Fig. 5) [Fitting used: F method of Kouketsu et al. (2014), FWHM-D1 = 91.64, using equation: T(°C) = −2.15 FWHM-D1 + 478]. The maturity parameters derived from fitting of the five bands with Lorentz functions [area ratios RA1 = (D1 + D4)/(D1 + D2 + D3 + D4 + G) = 0.62 and RA2 = (D1 + D4)/(D2 + D3 + G) = 1.65] using the method of Lahfid et al. (2010) yield similar temperatures of ca. 300 °C (we used 532 nm incident laser instead of 514 nm, but little change in Raman spectra are expected as shown by Kouketsu et al. (2014)).

The assemblage displays four main types of filamentous microfossils. Type 1 comprises narrow (2–3 µm) filaments preserving a thin sheath (50–100 nm thick) (Fig. 6A-B). Type 2 filaments have a total diameter of 5–7.5 µm bounded by a thick sheath (3.5–5 µm thick) enclosing a narrow central tube (1–1.5 µm across)

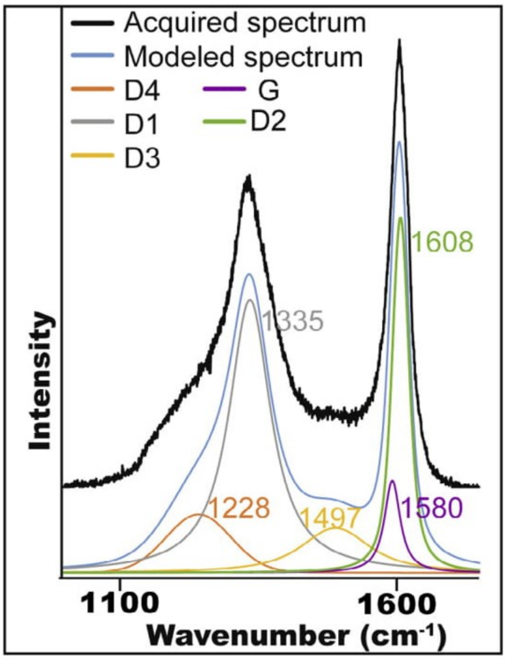

Fig. 5. Raman spectrum of kerogen from the microfossil Type–1 Specimen–1 and its deconvolution in five bands. The vibrational bands as ~1350 cm^{-1} (D band) and 1600 cm^{-1} (G band) establish the carbonaceous composition of the microfossil.

(Fig. 6C-H). Type 3 comprises broad (total diameter >3 μm) filaments with thin sheaths (50–100 nm thick) (Fig. 6I-L). Type 4 comprises highly degraded filaments that could belong to Type 1–3 but cannot be distinguished (Fig. 6M-P). In addition, the assemblage displays very scarce, long thread-like filaments ≤1 μm in diameter (not shown, similar to Fig. 3 of Schopf et al., 2015).

4.2.2.1. Type 1 filaments. Type 1 filaments form a well-defined, brown (organic-rich), non-septate (absence of cross walls structures separating filaments in segments), narrow tubular structure 2–3 μm in diameter and 30–100 μm in length (Figs. 6A-B, 7A-C). These narrow filaments are rare and occur in areas where filaments are scarce. One longitudinal FIB foil was prepared for one of these microfossils (Fig. 7A) and revealed that the quartz grains (Fig. 8 spectrum2), surrounding or within the microfossil, are nanocrystals ~100–200 nm in diameter (Fig. 7D). Moreover, the kerogen forms a thin (50–300 nm) continuous tube devoid of organic sulfur (Figs. 7E, 8 spectrum1) that most likely represents the thin sheath of a narrow filament. EDXS and Raman mapping did not detect minerals other than quartz in association with this type of fossils.

4.2.2.2. Type 2 filaments. Type 2 microfossils are rare filaments showing narrow central tubes (1–1.5 μm wide) surrounded by thick well-defined sheaths (3.5–5 μm wide) containing kerogen (Figs. 6C-G, 9, 10). Type 2 filaments occur isolated or with loosely clustered filaments forming the cobweb fabric. A longitudinal FIB foil from microfossil Type–2 Specimen–1 (Fig. 9A-C) and a transversal FIB foil from microfossil Type–2 Specimen–2 (Fig. 9D-I) reveal that these narrow filaments with thick sheaths are filled by quartz nanocrystals (~100–200 nm in diameter). The longitudinal FIB foil (Type–2 Specimen–1) also reveals the outer limit of the thick sheath (Fig. 9C) and indicates that quartz grains surrounding the microfossil (outside the red box in Fig. 9B) have similar size (~100–200 nm) as those inside the microfossil (in the red box in Fig. 9B). Kerogen occurs as nanograins within the thick sheaths ca.~5 μm in diameter whereas narrow central tubes (~1.4 μm in diameter) appear free of kerogen (Fig. 9). This indicates that the kerogen in the surrounding thick sheath cannot result of migration of carbon away from a sheath-less (or thin-sheated) filamentous microfossil, since no such migration of organic matter is observed in the central tube in spite of the similar quartz matrix structure.

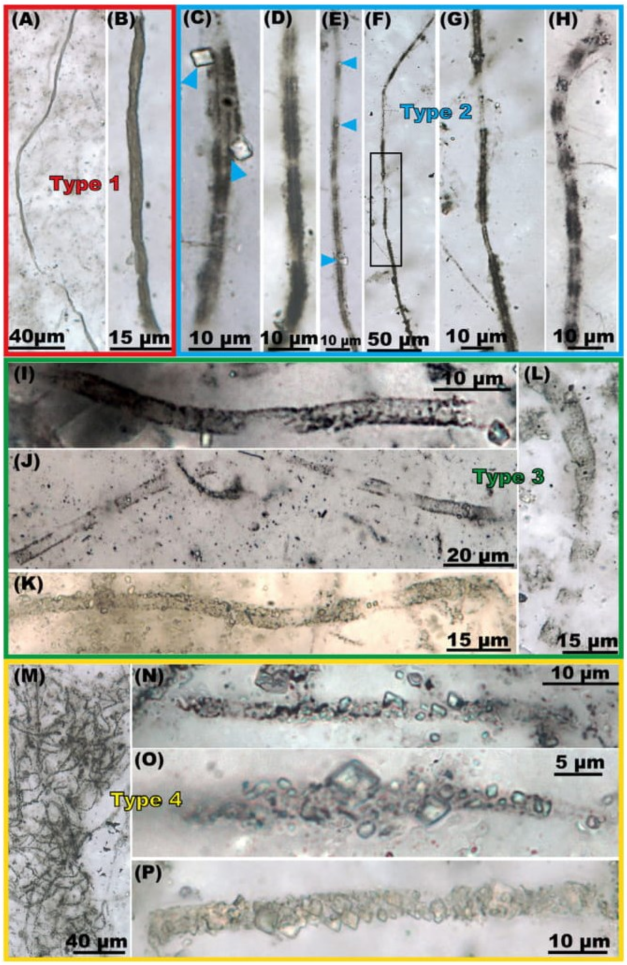

Fig. 6. Various filaments that dominate the microfossil assemblage in DCK4_9.3. Photomicrographs in plain polarized transmitted light. (A)-(B) Type 1 non-septate narrow filaments. (C)-(H) Type 2 filaments displaying a narrow central tube (1–1.5 μm in diameter) enclosed in a thick sheath (3.5–5 μm in diameter) with dark and White segmentation. Blue arrows: siderite grains embedded in sheaths. (G) Zoom of the box in (F). (I)-(L) Type 3 filaments: broad sheaths. (I) Broad (5 μm) delicate filament with a torn thin wall at the center of the photo. (J) Broad (4 μm), fragmented filament with thin wall of kerogen. (K) Broad (4 μm) delicate filament with micrometric or sub-micrometric siderite grains. (L) Broad (9 μm) fragmented filament with small siderite grains embedded in the thin sheath. (M)-(P) Type 4 filaments. (M) Clump of granular filaments. (N)-(P) Granular siderite-rich filaments present at the edge of a clump. Note that in (N) through (P), the abundance of dark carbonaceous grains is decreasing, while the density of carbonate grains is increasing. (For interpretation of the references to colour in this figure legend, the reader is referred to the web version of this article.)

Furthermore, sheaths of some Type 2 microfossils display a white and black striation motif (Fig. 6C-E, H) caused by longitudinal variation of the kerogen nanograin density (Fig. 9). In rare cases portions of filaments are partly unsheathed (Fig. 6F-G).

One narrow filament with a thick kerogen-poor sheath (microfossil Type–2- Specimen–3, Fig. 10) revealed some sections where a 100–500 nm thick, discontinuous kerogen wall outlines the narrow (~2.5 μm) central tube. In longitudinal section, one kerogen wall segments the tube perpendicular to its length (Fig. 10F-G). In Type–2 Specimen–3, the narrow central tube contains granular kerogen. Using TEM EDXS, kerogen could not be detected in the

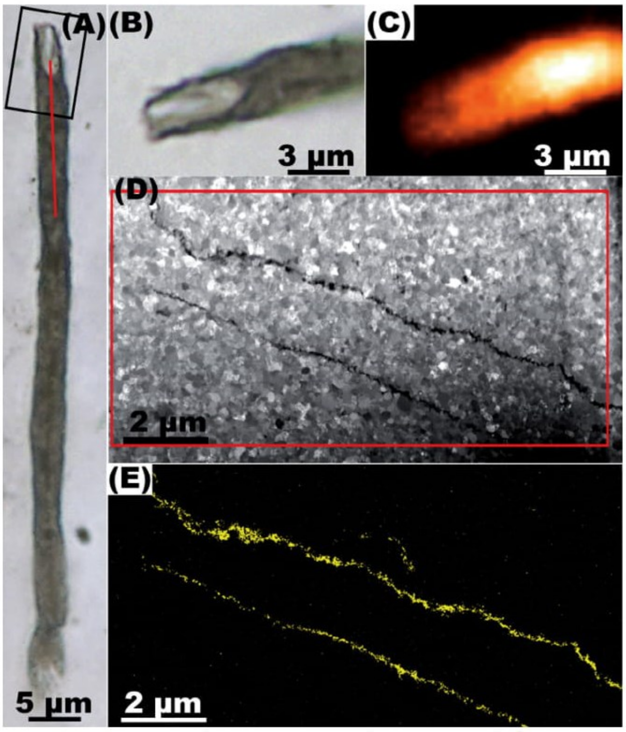

Fig. 7. Type–1 Specimen–1 filament - ultrastructure of microfossil. (A) Photomicrograph in transmitted light (red line: FIB foil position). (B) Detail of the filament (box in a). (C) Raman map of kerogen in (B). (D) STEM dark field image of the FIB foil showing homogeneous distribution of quartz nano-crystals (grey to white), and thin kerogenous sheath (black). (E) Carbon EDXS map of the zone in the red box in (D). (For interpretation of the references to colour in this figure legend, the reader is referred to the web version of this article.)

thick sheath around the narrow internal tube (Fig. 10G), consistent with the very faint contrast of the thick sheath in optical images indicating very low carbon (Fig. 10A). This kerogen distribution contrasts with microfossils Type–2 Specimen–1 and Specimen–2 where kerogen is only located in the surrounding sheath and not in the central tube (Fig. 10).

The narrow central tube of Type–2 Specimen–2 and Specimen–3 contain quartz crystals of variable sizes (~0.3–2 µm in diameter) that are larger than those in the sheath (<200 nm in diameter) (Figs. 9H, 10B, F). In Type–2 Specimen–2, a coarser quartz grain appears to tear the narrow internal tube and kerogen grains are absent near this grain (Fig. 9H-I). Interestingly, one quartz grain inside the narrow internal tube of Type–2 Specimen–3 is ovoid, cell-sized, of similar diameter than the tube, and occurs adjacent to the perpendicular kerogen wall segmenting the tube (Fig. 10H-I). The ovoid grain and several other quartz grains adjacent with the kerogen wall of the narrow central tube show irregular contacts with the surrounding kerogen (Fig. 10H).

Optical observation indicates that Type 2 filaments contain a small number of carbonate grains (Fig. 6C-H). STEM revealed 1–2 µm large siderite crystals, sometimes intergrown with calcite (Fig. 8 spectrum 3, 9, 10G). In addition, nanoscale siderite rhombohedra are included in the ovoid quartz crystal in the central tube of Type–2 Specimen–3 (Fig. 10I). Moreover, in Type–2 Specimen–3, C-free Fe-minerals (likely Fe-silicates) are present near the kerogen wall of the narrow central tube (Fig. 8 spectrum 7, 10D-E). Platy K-aluminosilicates occur near or attached to siderite crystals in sheaths (Fig. 8 spectrum 5, 9 C, 9I) and/or in the central tube (Fig. 10E, G).

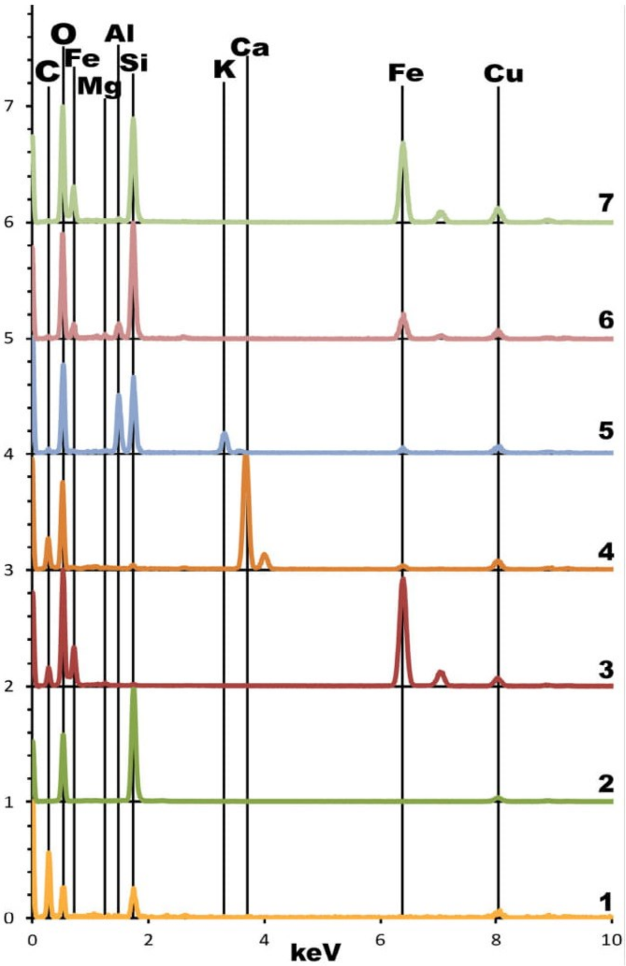

Fig.8. Representative EDXS spectra measured in the Scanning Transmission Electron Microscope. (1) Kerogen in quartz (from microfossil Type–1 Specimen–1). (2) Quartz (from Type–1 Specimen–1). (3) Siderite (from Type–2 Specimen–1). (4) Calcite (from Type–2 Specimen–3). (5) Putative muscovite (from Type–2 Specimen–1). (6) Putative chlorite (from Type–4 Specimen–1). (7) Fe–silicates in quartz (from Type–4 Specimen–1).

4.2.2.3. Type 3 filaments. Type 3 filaments are broad (3–10 µm wide), non-septate, and display a delicate thin sheath of kerogen (Figs. 6I-L, 11A). These microfossils occur in the cobweb-like fabric and near tangled clumps of filaments. Rarely, these filaments have zones where the wall is partially decomposed or obliterated by cross-cutting quartz (Figs. 6I, 11A-C) and often are fragmented, thus preventing assessment of their maximal length (Fig. 6J, L).

A well-preserved part of filament Type–3 Specimen–1 is formed of a discontinuous kerogen sheath (50–100 nm thick) with an ovoid cross section (Fig. 11). Inside the microfossil, quartz crystals are >500 nm, whereas they are smaller (~200 nm in diameter) outside (Fig. 11D). The FIB foil revealed a siderite grain (700 nm in length) in or on the thin sheath (Fig. 11E). Other Fe-rich nanograins (<50 nm in diameter) are observed within the thin kerogen wall, but we could not distinguish siderite from other Fe-minerals due to their small size and close association to kerogen carbon (Fig. 11E).

Type 3 filaments display highly variable carbonate content. Some filaments only show few siderite grains (Type–3 Specimen–1, Fig. 11), whereas others show low to locally complete replacement by siderite (Type–3 Specimen–2, Fig. 12A-G). A longitudinal FIB foil documents the structure of the passage from

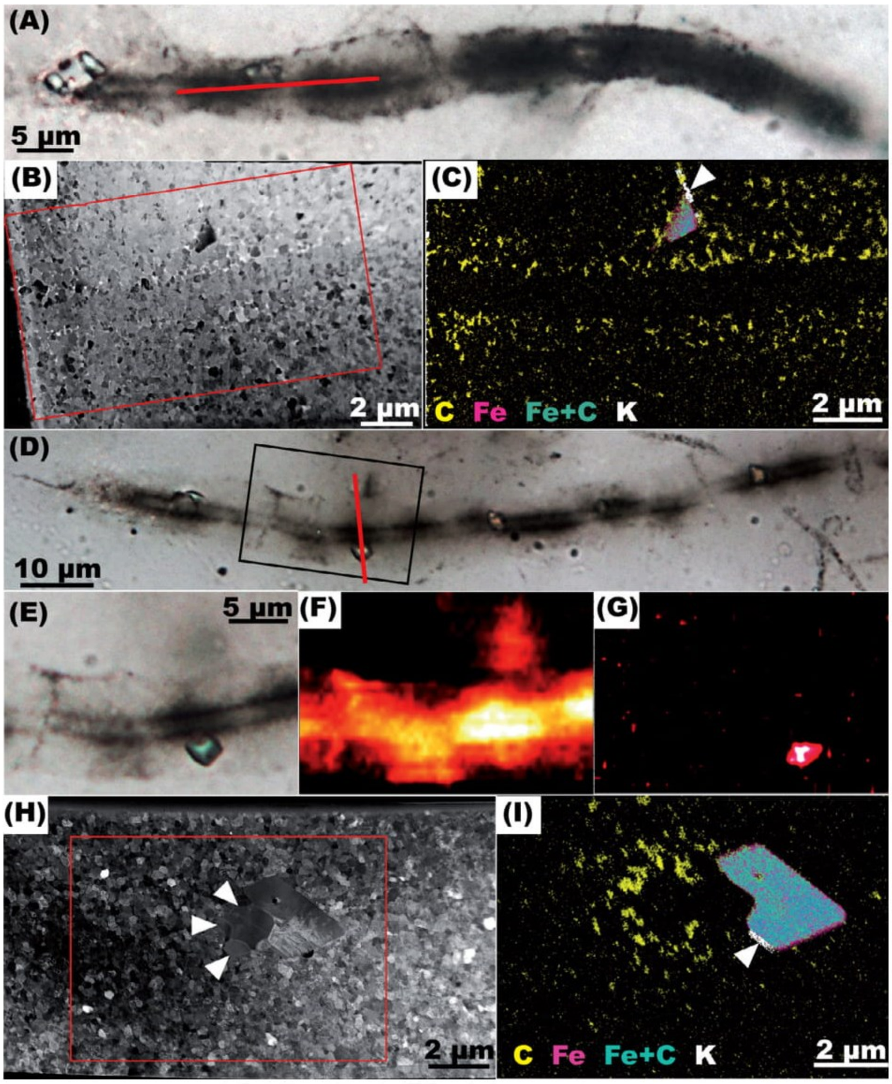

Fig. 9. Type 2 filaments – ultrastructures and compositions. Type–2 Specimen–1 (A)-(C) and Specimen–2 (D)-(I). (A) Photomicrograph of Type–2 Specimen–1 filament (red line: FIB foil position) displaying a central tube surrounded by a thick sheath-like structure. (B) STEM bright field image of the FIB foil. Note the homogenous size of quartz (grey to white) grains inside and outside the microfossil. (C) EDXS map of the zone boxed in red in (B) (Fe + C represents siderite), white arrow indicates a platy K-bearing alumino-silicate grain. Note the absence of kerogen in the central tube and outside the microfossil, and the variations in kerogen content in the sheath along the horizontal axis corresponding to dark/white striae in (A). (D) Type–2 Specimen–2 filament, transmitted light (red line: FIB foil position). (E) Detail of the filament in the boxed area of (D), single plane photomicrograph. (F)-(G) Raman maps of kerogen (F) and siderite (G) distributions in the region shown in (E). Kerogen-rich regions correspond to the dark striae seen in (E). (H) STEM dark field image of the FIB foil along the line in (D). White arrows indicate quartz crystals (ca. 1 µm) inside the microfossil that are larger than those of the nanocrystalline matrix. (I) EDXS map of the region boxed in red in (H) Fe + C represent siderite, the white arrow indicates a K-bearing alumino-silicate. (For interpretation of the references to colour in this figure legend, the reader is referred to the web version of this article.)

siderite-poor to siderite-rich part (left of Fig. 12A, and Fig. 12F-G). First, the siderite-poor part of the filament (bottom left of Fig. 12H-I) contains small size quartz crystals (<1 µm in diameter) compared to the larger ones (1–3 µm large) present in siderite-rich part (top left of Fig. 12H-I). The surrounding matrix is made of quartz crystals 2–5 µm large (right of Fig. 12H-I). In the siderite-poor part (Fig. 12J-K), kerogen nanograins form a discontinuous line between the fine-grained filament infill and the surrounding coarser matrix. Because the broad filament was cropping out at the surface of the thin section before FIB sectioning, this discontinuous line is expected to represent the thin boundary of the sheath that was located at depth in the thin section. Nanoscale platy C-free Fe-mineral (Fe-silicates) are aligned along the thin kerogenous boundary and extend further as inclusions in coarser quartz crystals inside and outside the microfossil (Fig. 12I-K). Second, in the part of filament Type–3 Specimen–2 with coarser quartz (upper half in Fig. 12H-I), abundant siderite formed rhombohedral crystals several micrometers large. Interestingly, the apparently Fe-rich rim (pink) seen in the large EDXS map (Fig. 12I) along the margins of the siderite grains (blue) is not observed on the same crystal in a map at higher spatial resolution (Fig. 12K). This apparently Fe-rich rim in Fig. 12I is an analytical artifact (likely caused by differential C-Kα X-ray absorption) rather than a nanoscale surface oxidation (*e.g.* Bernard et al., 2010) of siderite grains, since the siderite grains do not show rims with diffraction contrast in TEM images. Finally, in this coarse crystalline and sideritic area of Type–3 Specimen–2, kerogen occurs as nanograins close to siderite grains, and Fe-silicates are present in the surrounding quartz with a maximum concentration (Fig. 12L-M) close to the inferred edge of the microfossil (white line in Fig. 12I).

4.2.2.4. Type 4 filaments. Type 4 granular filaments are the most common type of filaments. They occur in the clumps, where other types of filament are absent (Fig. 6M), but also in the cobweb-like

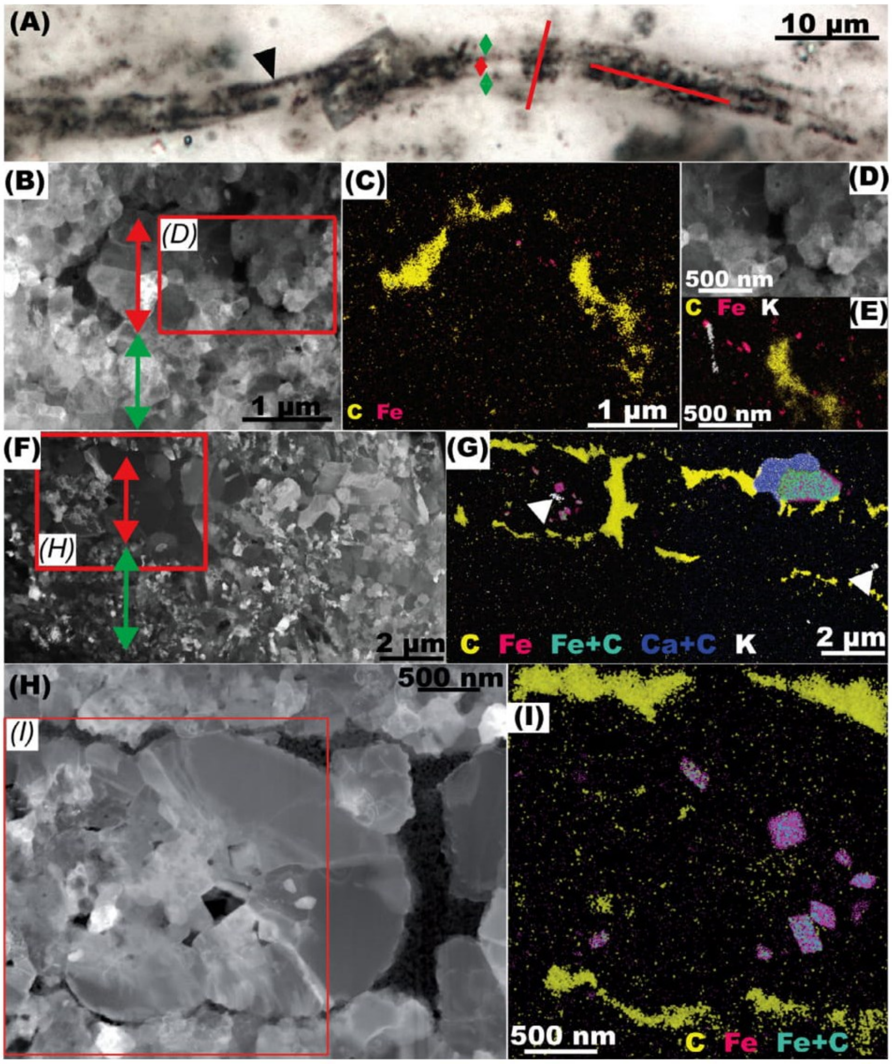

Fig. 10. Type 2 filaments – ultrastructure and composition of Type–2 Specimen–3. (A) Transmitted light photomicrograph. The filament comprises a central tube (red arrow) surrounded by a thick sheath (green arrows). A large siderite rhomb cuts across the filament at the center of the image. Parts of the microfossil are granular (black arrow). The red lines indicate the location of the transversal (left) and longitudinal (right) FIB foils. (B) STEM dark field image of the transversal FIB foil (black: kerogen, shades of grey: quartz). Quartz nanocrystals are coarser in the central tube (red arrow), than in the sheath (green arrow). (C) EDXS map of the region imaged in (B) showing the distributions of carbon (yellow) and iron (magenta) (D) Detail of the red box in (B). (E) EDXS map of the region shown in (D) showing the distributions of carbon (yellow), potassium (white) and iron (magenta). Fe-minerals are carbon-free (verified with EDXS spectra) and are included in quartz in zones where carbon is absent. (F) STEM dark field image of the longitudinal FIB foil. Coarser (0.3–2 µm) quartz grains occur in the central tube (red arrow) of the microfossil, nanograins occur in the sheath (green arrow). The size of the filament exceeds the FIB foil size, which prevented observation of the surrounding matrix. (G) EDXS map of the region shown in (F) showing the distribution of carbon (yellow), iron (magenta), iron + carbon (green: siderite), calcium + carbon (blue: calcite) and potassium (white, white arrows: K-bearing alumino-silicate). (H) STEM dark field image of the region boxed in (F) showing coarser quartz (shades of grey) grains, some sub-rounded, inside the central tube that is outlined by kerogen (black). (I) EDXS map of the region boxed in (H). The carbonaceous wall of the central tube appears in yellow, and siderite inclusions (Fe + C confirmed with EDXS) appear in mottled green/magenta. (For interpretation of the references to colour in this figure legend, the reader is referred to the web version of this article.)

fabric where they loosely cluster with other filaments. These filaments have a tubular shape where kerogen granules are heterogeneously spread (Fig. 6N-P). Compared to Type 3 filaments, kerogenous sheaths are not observed in type 4 filaments. Similar to Type 3, Type 4 microfossils are often associated with pervasive replacement and/or encrustation by siderite grains (Figs. 6N-P, 13). One FIB foils was prepared for the siderite-poor granular microfossil Type–4 Specimen–1 occurring in a clump (Fig. 13A-F). Another foil was prepared for siderite-rich filament Type–4 Specimen–2 occurring at the edge of a clump with high siderite content (Fig. 13G-M). Quartz crystals inside and outside both microfossils are large (1–3 µm in diameter) but small areas display smaller quartz crystals (0.5–1 µm) (Fig. 13B, D, H). In Type–4 Specimen–1, quartz crystals are generally coarser inside the microfossil in association with kerogen (Fig. 13B-C). The kerogen forms nanoscale to 1 µm-large grains (Fig. 13) but these grains do not form a tubular structure (Fig. 13B-E) as in Type 1–3 microfossils. Siderite crystals (~1 to several µm large) occur within the microfossils (Fig. 13C). Some kerogen grains occur at the surface of (Fig. 13C) or inside (Fig. 13J) siderite crystals. The microfossil contains platy crystals of (Fe,Mg)-alumino silicates (Fig. 13 and Fig. 8 spectrum 6) as well as Fe-silicates with low Al (<1 w%) for which diffractions indicate stilpnomelane, serpentine or chlorite and rule out Fe-oxides (Fig. 13N-O). In summary, Type 4 filaments (Fig. 13) are similar to the least preserved parts of Type 3 filaments (Fig. 12H-I), as they display micrometric quartz matrices, locally high replacement and/or encrustation by Fe-minerals, and scarce granular kerogen.

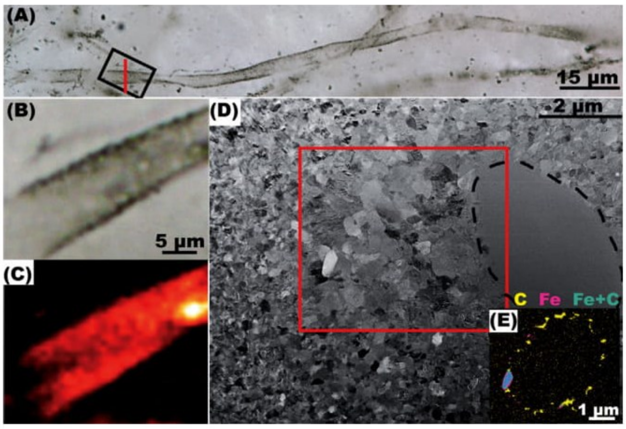

Fig. 11. Type 3 filaments – ultrastructure and composition of Type–3 Specimen–1. (A) Transmitted light photomicrograph (red line: FIB foil position) showing thin, empty sheath structure. (B) Detail of the filament (box in A), single focal depth. (C) Raman map of kerogen in (B). (D) STEM bright field image of the FIB foil. Note the coarser quartz grain size inside the microfossil (boxed region). The quartz region with a dashed outline is now amorphous due to FIB damage. (E) EDXS map of the box in (D) showing a siderite (Fe + C, cyan) crystal in/on the carbonaceous (yellow) wall of the microfossil. (For interpretation of the references to colour in this figure legend, the reader is referred to the web version of this article.)

4.3. Geochemistry

Bulk-rock analyses show a very low carbonate content in DCK4_9.3, with only 0.09 wt% inorganic carbon (Table 1). Carbonates in DCK4_9.3 are dominated by iron (0.59 wt% $FeCO_3$), magnesium (0.12 wt% $MgCO_3$) and calcium (0.10 wt% $CaCO_3$) (Table 1). These include siderite, calcite and (Ca, Mg, Fe)CO_3 solid solutions such as dolomite and ankerite. The Fe(II)/Fe(II + III) ratio of 66% indicates that the majority of iron is reduced. This value is similar to the proportion of Fe present in carbonates (~70%, determined by combining quantification of carbonate C by H_3PO_3 extraction and of Ca-Mg-Fe by ICP-MS; Table 1), indicating that Fe(II) is essentially present as Fe-carbonates. The average chemical composition of ankerite established from EDXS analyses is $(Ca_{1.04}Mg_{0.40}Fe_{0.56})(CO_3)_2$ (n = 7 analyses). Assuming that all Ca measured by ICP-MS is carried by ankerite, we can deduce that at most 7% of Fe occurs in ankerite and at least 63% in siderite (the presence of calcite/dolomite would increase this minimal estimate). Thus, >90% of carbonate-associated Fe occurs in siderite and <10% in ankerite. The dominance of siderite in the Fe(II) pool is also consistent with the observed scarcity of Fe-silicates (occurring as nanocrystals in some microfossils and undetected with optical microscopy, SEM and XRD) and the absence of pyrite in petrographic and ICP-MS (S < 0.01 wt%) analyses. The detection of ~30% Fe(III) is in line with the observation of secondary hematite replacing Fe-carbonates (Fig. 3E). Moreover, Rare Earth Elements (REE) shale-normalized concentrations indicate that the cerium ratio (Ce/Ce*) is 0.97 and praseodymium ratio (Pr/Pr*) is 1.10 (McLennan, 1989). A plot of (Ce/Ce*) vs (Pr/Pr*) graph (not shown) indicates an absence of cerium, lanthanum anomalies and a positive praseodymium anomaly (Bau and Dulski, 1996; Planavsky et al., 2009). The $\delta^{13}C_{carb}$ and $\delta^{18}O_{carb}$ values obtained for the sample DCK4_9.3 are −2.04 ± 0.03‰ and −13.41 ± 0.15‰ (n = 6) respectively. The Total Organic Carbon (TOC) content is 0.01 wt% (Table 1) and associated $\delta^{13}C_{org}$ is −21.85 ± 0.2‰ (n = 3). Bulk rock iron concentration is 0.41 wt% Fe (ICPMS, Table 1), with δ^{56}Fe and δ^{57}Fe values of 1.43 ± 0.03 and 2.14 ± 0.08‰ (2SD, n = 2) respectively. The Fe isotope composition obtained after sequential Fe extraction by cold HCl leaching (δ^{56}Fe = 1.45 ± 0.01‰ and δ^{57}Fe = 2.18 ± 0.05‰, 2SD, n = 2) are similar to the bulk values. The fraction of Fe extracted in the HCl leachate represents ~66% of the Fe measured in the bulk rock.

In carbonate rock embedding the chert K30, cumulated $CaCO_3$ and $MgCO_3$ concentrations (as dolomite) represent ~92.11 wt% of the bulk rock, while Fe-carbonates are absent (Table 1). This samples contains 0.13 wt% of Fe(II), 1.70 wt% of Fe(III), and less than 0.01 wt% S (Table 1), which is consistent with the observation of late iron/manganese oxides in quartz veins (Fig. 3A). Finally, this sample does not show any Ce or La anomaly, as illustrated by Ce/Ce* and Pr/Pr* ratios of 0.89 and 1.03 respectively.

5. Discussion

5.1. Development of chert fabrics

Four main mechanisms have been proposed to explain the formation of Precambrian cherts: (1) seafloor silica precipitation, (2) sedimentation of silica grains precipitated in the water column (Rasmussen et al., 2013; Stefurak et al., 2014), (3) segregation of silica succeeding concomitant, homogenous depositions of iron and silica, forming BIF (Fischer and Knoll, 2009), and (4) diagenetic or metasomatic replacement by quartz of a protolith such as carbonates (Hesse, 1989; Knoll et al., 1988). Hence, in sample DCK4_9.3, the quartz granules could represent primary sedimented silica grains, which may have been wrapped by filaments during or after deposition. The coarse quartz granules could also represent other clasts replaced by silicification. However, when seen in SEM-CL (Fig. 4D, I), the coarse quartz granules do not show clastic shapes or resemble the compacted rounded granules reported in some Archean cherts (Stefurak et al., 2014). Rather, SEM-CL images indicate that coarse quartz granules integrate parts of the columnar, fine grained structures embedding microfossils (Fig. 4D, I). Such columnar structures embedding filaments are observed in modern geothermal siliceous sinters where microbial filaments are present (Berelson et al., 2011; Campbell et al., 2015; Jones et al., 2001; Konhauser et al., 2004; Pepe-Ranney et al., 2012). In these environments, microbial filaments are rapidly silicified and result in the development of rigid and highly porous fabrics (Konhauser et al., 2004). Moreover, in geothermal environments, silica initially formed onto/into microorganisms amorphous opal (opal-A silica) can changes gradually into crystalline opal (opal-CT and/or -C), and finally into microcrystalline quartz (Herdianita et al., 2000; Lynne et al., 2005; Preston et al., 2008) with preservation of large open pores (Campbell et al., 2015). Thus, in our case, it is possible that filaments first formed cobweb fabrics of amorphous or micro to nanocrystalline silica with large pores similar to those observed in recent siliceous sinters (Campbell et al., 2015). Then, the microfossil-free porosity could have been filled by amorphous silica cement (Konhauser et al., 2004) that changed into coarse quartz during later hydrothermal/diagenetic stages (Campbell et al., 2015; Lynne et al., 2005). It is possible that the organic matter of the microfossils slowed the crystallization/-growth of quartz crystals in the cobweb fabric, whereas crystallization of amorphous silica in pores was favored. Indeed, advanced fossilization experiments showed that some microorganisms can slow the crystallization of amorphous silica into quartz compared to inorganic conditions (Alleon et al., 2016a).

Moreover, the microfossils can be organized as i) siderite-rich, very dense clumps of poorly preserved granular Type 4 filaments, or ii) in a cobweb-like mat-forming fabric where filaments are isolated to loosely clustered and display all the types of microfossils. A similar distribution has been observed by Knoll et al. (1988) for filaments of the Gunflint-type assemblage of the ca. 1.8 Ga Duck Creek Formation. They interpreted the filaments present in the clumps as a dense population that initially would have flourished in carbonates mud, and then during diagenesis the carbonates would have been brecciated. Then a second generation of isolated

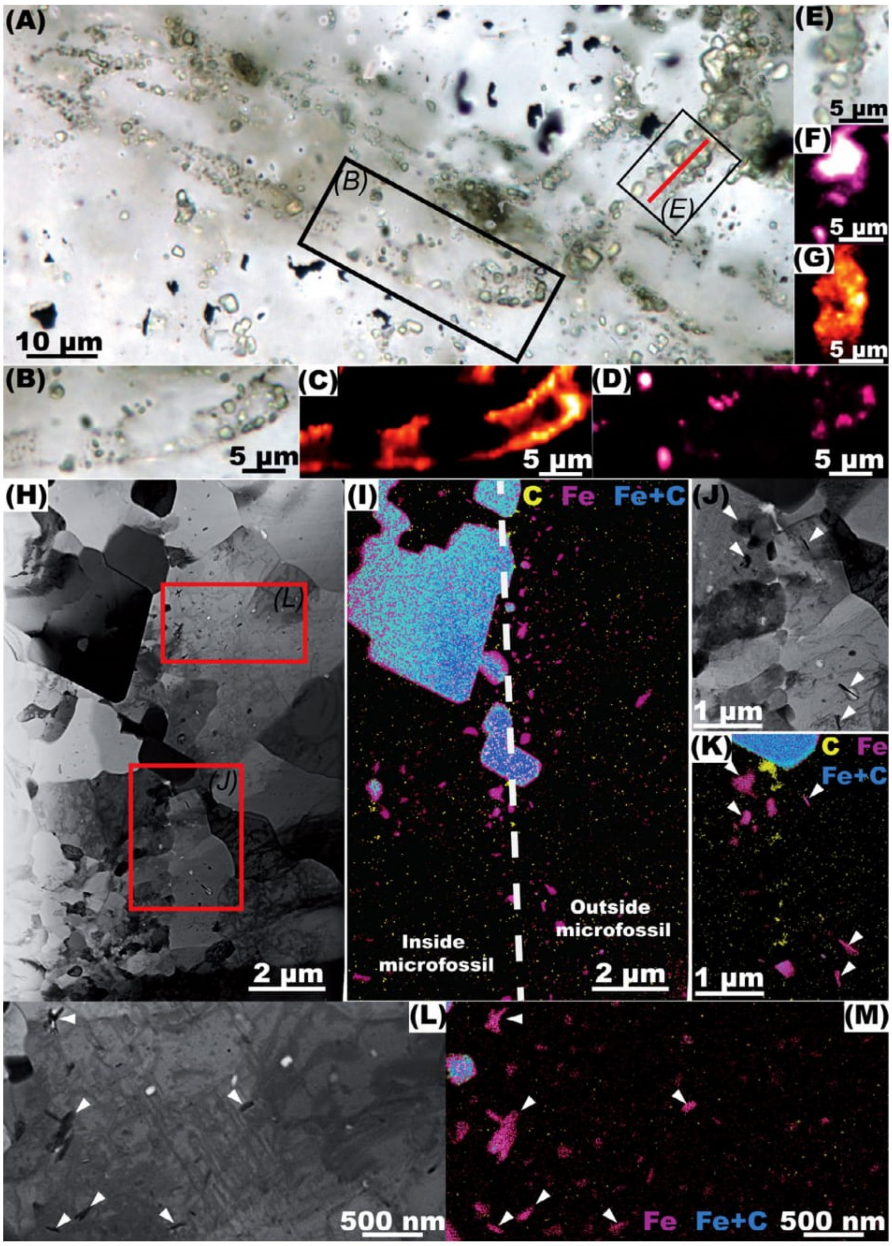

Fig. 12. Type 3 filaments – ultrastructure and composition of Type-3 Specimen-2. (A) Transmitted light photomicrograph (red line: FIB foil position). (B) Magnified view of the filament (lower box in A), single focal depth. (C)-(D) Raman maps of kerogen (C) and siderite (D) in the region shown in (B). (E)-(G). Magnified view of the filament (right box in A), single focal depth photomicrograph (E) with the associated Raman maps of kerogen (F) and siderite (G). (H) STEM bright-field image of the FIB foil. Siderite and Fe-silicates appear in black. Most quartz (shades of grey) crystals are >1 µm in and around this microfossil, and are submicrometric in the siderite-poor region (lower-left corner) of the microfossil. (I) EDXS map of the region in (H). The white line indicates the inferred boundary of the microfossil, which correlates with the limit between the area containing submicrometric quartz (left) and the surrounding microquartz (right). (J)-(K) Magnified STEM bright-field image (J) and EDXS map (K) of the region highlighted by the lower red box in (H) showing Fe-silicates (white arrows) and showing organic carbon at the inferred boundary of the microfossil. (L)-(M) Magnified STEM bright-field image (L) and EDXS map (M) of the region highlighted by the upper red box in (H) (white arrows: Fe-silicates). EDXS maps (I), (K), (M) show carbonaceous matter (C in yellow), non-siderite Fe-minerals (Fe, in magenta), and siderite (Fe + C, in blue). Note that the Fe-rich rim around siderite grains is an analytical artefact (see text). (For interpretation of the references to colour in this figure legend, the reader is referred to the web version of this article.)

to loosely clustered filaments colonized the fractures of the breccia, wrapping around the brecciated clumps and forming the cobweb-like fabric. Silicification would have followed and replaced the carbonates that contained the first generation of microfossils and have fossilized the second generation of isolated or loosely clustered filaments around the brecciated clumps. In our DCK4_9.3 chert nodule, SEM-CL does not show differences between the fine quartz matrix of clumps and the fine quartz matrix of the surrounding cobweb fabric, which contains loosely clustered or isolated filaments (Fig. 4B-D). Interestingly, carbonates found in the black chert nodule DCK4_9.3 are Fe-rich (ankerite, siderite), whereas the carbonates forming the carbonate rocks around the chert nodules are mainly dolomitic. The carbonates (including siderite) found in the chert nodule are thus not relics of dolomite that survived replacement through silicification. Moreover, clumps are relatively scarce in DCK4_9.3 compared to the main cobweb fabric with pores filled by granular quartz (Fig. 4A). This argues that silicification of a primary brecciated carbonate

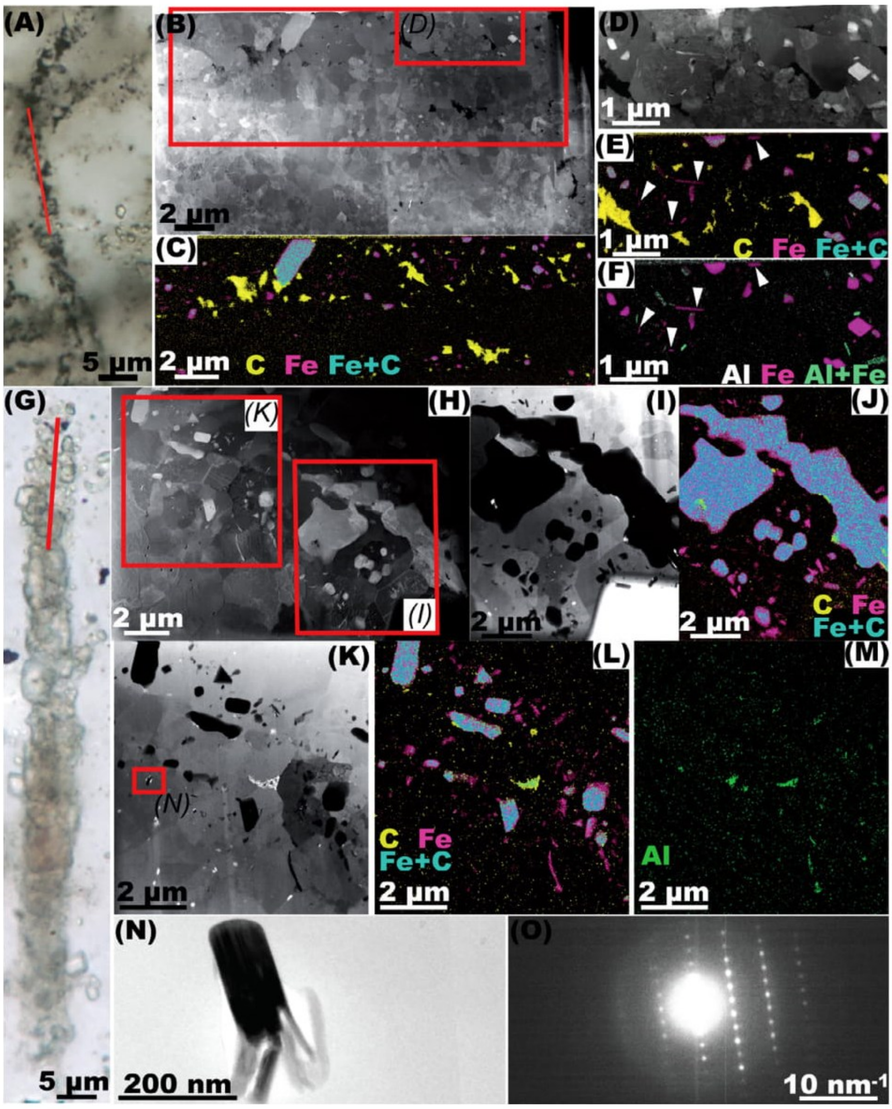

Fig. 13. Type 4 filaments – ultrastructure and composition of microfossils Type–4 Specimen–1 (A-F) and Specimen–2 (G-M). (A) Transmitted light photomicrograph showing the granular texture of Type–4 Specimen–1 (red line: position of the FIB foil). (B) STEM bright field image of the FIB foil showing kerogen granules (black) with coarse (>1 µm) quartz crystals and siderite (white to grey). (C) EDXS map of the larger box in (B). (D)-(F) STEM bright field image (D) and EDXS maps (E)-(F) of the smaller box in (B). (E) Shows kerogen (C yellow) and siderite (Fe + C in blue) and non-siderite Fe (pink, white arrows). (F) Shows Fe-silicates (Fe without C and low Al in magenta, white arrows) and Fe-bearing aluminosilicate (Fe + Al in green). (G) Transmitted light photomicrograph of Type–4 Specimen–2 (red line: position of the FIB foil). (H). STEM dark field image of the FIB foil. Fe-carbonates and Fe-silicates appear in light grey, and quartz in dark shades of grey. (I)-(J). STEM bright field image (I) and EDXS map (J) of the region highlighted by the left box in (H). Organic carbon appears in green inside and on siderite crystals, which appear in blue. Fe-silicates appear in pink (Fe). (K)-(M). STEM bright field image (K), and EDXS maps (L)-(M) of the region highlighted by the right box in (H). (L) Shows C in yellow, Fe in pink, and Fe + C in green. (M) Shows Al of Fe-aluminosilicates in green. (N)-(O) TEM image of the Fe-silicate boxed in (K) with the selected area electron diffraction pattern indicating Fe-serpentine ([−1,1,0] zone axis of cronstedtite) or stilpnomelane ([10,15,3] zone axis) in (O). (For interpretation of the references to colour in this figure legend, the reader is referred to the web version of this article.)

rock was likely not the main process driving the formation of this chert nodule. Rather, a silicified primary microbial mat texture with a cobweb fabric has been preserved in this sample. Filaments in clumps and cobweb-clustered filaments may nevertheless correspond to two generations of microbial colonization, as proposed by Knoll et al. (1988).

5.2. Taphonomy and taxonomy of the microfossils

Raman spectra indicate that organic matter in the microfossils entered the metamorphism window and is over-mature. Filaments in sample DCK4_9.3 have different taphonomic (*post-mortem* alteration) grades, but nevertheless preserve a range of sizes and shapes that may represent a primary taxonomic signal, which we discuss below.

5.2.1. Thin sheaths of Type 1 microfossils

Types 1, narrow filaments with thin sheaths appear very well preserved (Fig. 6A-B). Although their sheaths are very thin (50–300 nm), they are preserved as a continuous and only slightly disrupted kerogen tube in a matrix of nanoquartz (Fig. 7), which highlights their excellent preservation. We interpreted this kerogen tube as the remnant of a thin polysaccharide sheath, which encapsulated narrow cells of ca. 2–3 µm in diameter that formed trichomes (chains of cells) (Fig. 14A-B). The absence of remains of the trichome in the internal tube is probably due to the preferential degradation of cell material, while the sheath is more resistant to

Table 1
Concentrations and calculations of chemical elements in Turee Creek samples.

sample	lithology	Organic C, wt%	wt% inorganic C		composition of bulk carbonates[†]			SiO_2 wt%	Al_2O_3 wt%	S wt%	Fe wt%	Fe in carbonates (%)[¤]	Fe in ankerite [#]	Fe in siderite [#]	Fe(II)/Fe (II + III) (%)
			mass spectrom.	loss on ignition[*]	$CaCO_3$ wt%	$MgCO_3$ wt%	max $FeCO_3$ wt%								
DCK4_9.3	chert	0.01	0.09	0.14	0.10	0.12	*0.59*[‡]	99.34	0.14	B.L.	0.41	*70%*	*7%*	*63%*	66%
AG12_K30	carbonate	n/a	n/a	11.90	54.21	37.90	*0.00*[¥]	2.79	0.49	B.L.	1.83	*0%*	0	0	7%

BL: Below Detection limit of 0.01 wt%.

[†] Values calculated using the assumption (based on petrographic observations) that Ca and Mg are only found in carbonates. We assumed that the wt% organic carbon is negligible compared to the wt% C in carbonates.

[‡] Estimation of the maximum concentration of $FeCO_3$ derived from the wt% C in carbonates that is not associated with Ca and Mg. We used the precise mass spectrometry data for the wt% C in carbonates, which does not include organic carbon.

[¥] Estimation of the maximum concentration of $FeCO_3$ derived from the wt% C in carbonates that is not associated with Ca and Mg. When mass spectrometry data was not available for the wt% C in carbonates, we used loss on ignition data. The latter, however, leads to an overestimation of wt% inorganic C, as a fraction of the loss on ignition comprises water and organic carbon.

[¤] Estimation of iron in the carbonates is based on the estimation of maximum concentration of $FeCO_3$.

[#] Based on SEM-EDXS quantification (average; n = 7) of the composition of ankerites $Ca_{1.04}Mg_{0.40}Fe_{0.56}(CO_3)_2$, we can derive the % of Fe in both Fe-carbonates (ankerite and siderite).

[*] Loss on ignition data were corrected when sulfur was detected.

degradation and silicification (Bartley, 1996; Campbell et al., 2015; Jones et al., 2001; Lepot et al., 2014).

5.2.2. Thick sheaths of Type 2 microfossils

Type 2 filaments are also composed of narrow internal tubes but these are surrounded by thicker sheaths than Type 1 filaments. Here, STEM observations of Type 2 filaments indicate that the narrow central tubes of these filaments are generally kerogen-free, with the exception of microfossil Type–2 Specimen–3 with organic matter inside the sheath (Fig. 10). The narrow central tubes thus represent the ghosts of cell trichomes, defined by the inner boundary of the kerogen in the sheath (*e.g.* Figs. 9C, 14 C) and the coarser quartz grain size in some microfossils (Figs. 9H, 10).

The presence of black and white striations in Type 2 sheaths is problematic. Kerogen in Type–2 Specimen–1 and Specimen–2 (Fig. 9) occurs as nanograins within the thick sheaths and the quartz matrix is composed of nanocrystals (~200 nm in diameter). The dark parts of the thick sheaths likely represent locally enhanced preservation, possibly favored by bands concentrating pigments that might have increased polymerization into kerogen (Bartley, 1996). Alternatively, these white and dark striations could be the result of the fragmentation of the trichome inside the thick sheath as observed during degradation of cyanobacteria (Bartley, 1996). This fragmentation could be followed by lateral mobilization of the cellular organic material within the thick sheaths but it is unknown if cellular material may migrate in the sheaths to form dark, kerogen-rich bands. The absence of organic material in the narrow central tube near dark bands in the thick sheath argues against this process.

Alternatively, Knoll et al. (1988) proposed that taphonomic sheath broadening could result in kerogen displacement outside the microfossils, and that discontinuous displacement along boundaries of fibrous quartz crystals could form striation. The displaced sheath boundary would be delimited by a change in quartz microstructures, *e.g.* the passage from nano-quartz crystals to fibrous quartz (Knoll et al., 1988). However, throughout the striated sheaths, the quartz crystals have the exact same nanostructure as quartz crystals outside the microfossil (Fig. 9B-C). Thus, the outer boundary of the sheath does not correspond to the limit of the matrix embedding the filament and coarser fibrous quartz. Moreover, organic matter is absent beyond the outer boundary of the sheath in spite of similar nanoquartz matrix, and is also usually absent in the central tubes. Hence, we can rule out migration of organic matter away from a thin (<300 nm) continuous sheath (*e.g.* of Type 1, Fig. 7) or from decaying trichomes, as the origin of Type 2 diffuse sheaths several micrometer-thick composed of kerogen nanograins (Type–2 Specimen–1 and Specimen–2, Fig. 6C-H). Nanoquartz in/on the sheath could represent early diagenetic, possibly *in vivo* impregnation/encrustation of the thick sheath (Campbell et al., 2015; Jones et al., 1998; Konhauser et al., 2004). Silica recrystallization and organic matter alteration/condensation in Type 2 sheaths likely resulted in granular organic networks impregnated with nanocrystalline quartz. In the absence of evidence of migrations from within or from outside the tubular sheath, we infer that the thickness of sheaths of Type 2 filaments is a primary, not a taphonomic feature and these microfossils represent a species or morphotype different from the thin-sheathed Type 1 filaments (Fig. 14C-F).

Furthermore, the siderite crystal within the thick sheath of Type–2 Specimen–2 appears in a kerogen-free zone (Fig. 9I), suggesting a replacement of kerogen by siderite.

5.2.3. Remains of trichomes in some Type 2 filaments

While most Type 2 filaments do not contain kerogen in their narrow central tubes, filament Type–2 Specimen–3 does (Fig. 10C, G). Its narrow central tube is outlined by kerogen, contains nanograins of kerogen, and is filled by larger quartz grains than the sheath. The irregular surface of the quartz crystals in contact with kerogen in the central tube (Fig. 10G-H) can be caused by local dissolution of quartz grain by adjacent kerogen (Lepot et al., 2009) or, more likely a special pattern of crystallization of silica in contact with organic structures during the silicification of the microorganism (Wacey et al., 2012). Moreover, as an analogy with the late void-filling quartz granules, the larger quartz crystals in the narrow central tube could correspond to a late silicification step that occurred after lysis of the cells in a filament (that was initially silicified only on the outside), as observed in recent silicified cyanobacteria (Campbell et al., 2015). During the second silicification step, the organic material contained in the cells may have condensed to form the organic material lining and filling the narrow central tube (Fig. 10). Interestingly, the rounded shape and size of one quartz grain (Fig. 10H) filling the entire section of the kerogenous tube evoke the ghost of a single ovoid cell. This ovoid crystal is almost entirely surrounded by kerogen and includes kerogen nanograins (Fig. 10F-I), further suggesting the fossilization of an individual cell. Chains of rod-shaped quartz crystals have

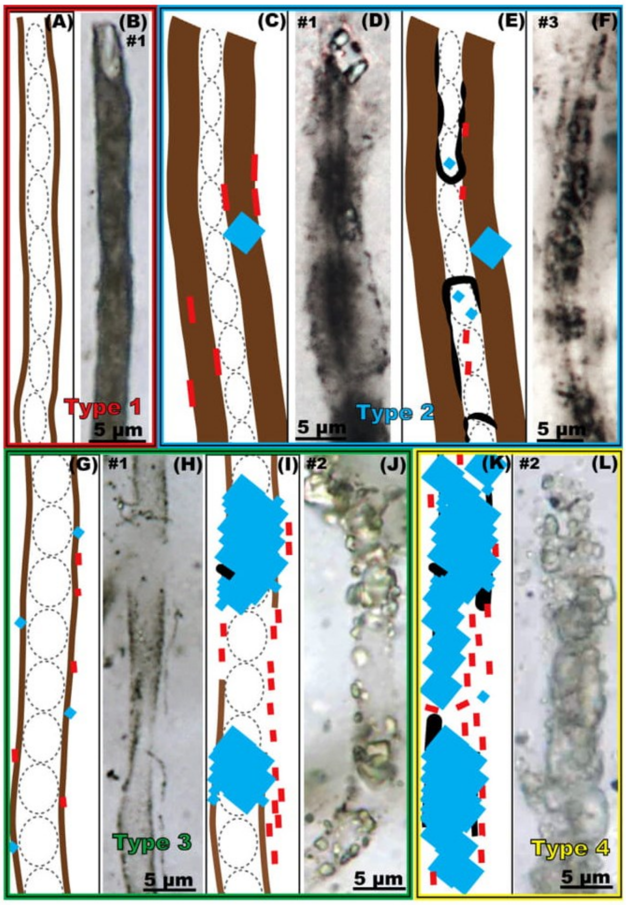

Fig. 14. Inferred reconstructions of Type 1–4 filaments. In hypothetic schematic reconstructions, dashed ovals represent now missing cells forming trichomes, brown lines represent sheaths, granular kerogen (remains of sheaths and/or cells) appears in black, red lines represent Fe-silicates and blue squares represent siderite. The photomicrographs of associated microfossils are shown on the right of each reconstruction. (A)-(B) Type 1 filaments with narrow thin sheath. Now missing cells formed a trichome ca. 3 μm in diameter surrounded by a thin sheath. (C)-(F) Type 2 filaments with thick sheath and narrow central tube. Filaments comprised a (now missing) trichome of ca. 3 μm in diameter inside a narrow central tube, and are associated with Fe-silicates and siderite. Microfossil Type–2 Specimen–3 (E)-(F) displays accumulation of granular kerogen in the central tube that may represent remains of the cells. (G)-(J) Type 3 broad filaments with thin sheath. A thin sheath surrounds a now missing trichome of cells that were ca. 5 μm in diameter. Fe-silicates and siderite occur in/on the sheath. The preservation of the sheath is only partial in filament Type–3 Specimen–2 (J). (K)-(L) Type 4 highly degraded filaments. Filaments with high concentrations of siderites and Fe-silicates. Sheath structures are absent and only granular kerogen is observed. (For interpretation of the references to colour in this figure legend, the reader is referred to the web version of this article.)

been observed in better preserved *Gunflintia* filaments of the Gunflint Iron Formation; their kerogenous outlines and their consistent lengths and widths argued for the preservation of trichomes of rod-shaped cells (Lepot et al., 2017). The central tube of Type–2 Specimen–3 may thus host highly degraded remains of cells ca. 3 μm in diameter (Fig. 14C-F).

5.2.4. Broad sheaths of Type 3 filaments

The broad Type 3 filaments with thin sheaths are different from Type 1–2 filaments. These broad filaments are fragmented but the delicate (*e.g.* twisted) structures suggest that fragments of these sheaths are well preserved. Again, the coarser size of internal quartz crystals suggests that the filaments have been filled with silica after the precipitation of the surrounding matrix (Campbell et al., 2015; Konhauser et al., 2004; Lynne et al., 2005). This quartz crystal size distribution may be the result of filaments that still preserved cellular material (Figs. 1–2 in Phoenix et al., 2000) when they were already completely encrusted by silica (Jones et al., 1998; Konhauser et al., 2004). Soon after complete encrustation, cell death and lysis of the intracellular material could have formed a local porosity, which was filled by late, coarser silica. Thus, the central tube of these broad, thin-sheathed filaments represents the ghost of broad trichomes 4 to 6 μm in diameter (Fig. 14G-H). Cell size and/or sheath thickness distinguish Type 3 of Type 1 and 2 filaments (Fig. 14).

Moreover, the siderite content of these broad filaments is variable: Type–3 Specimen–1 displays one small siderite grain, while other broad filaments show longitudinal variations from low to high siderite concentration. For instance, the longitudinal FIB foil prepared in Type–3 Specimen–2 shows the transition from siderite-poor to siderite-rich parts of the microfossil (Fig. 12A-I). Along the siderite-poor part, the kerogen forms a thin sheath (Fig. 12J), while the highly sideritic part shows only few grains of kerogen. This is consistent with local mineralization of organic matter into carbonate. Moreover, the siderite-poor part displays quartz nanocrystals similar in size to those observed in the siderite-poor microfossil Type–3 Specimen–1. In contrast, the siderite-rich part and the matrix surrounding Type–3 Specimen–2 are composed of micrometer-sized quartz crystals (Fig. 12H, J). The coarser quartz crystals may also be responsible for the localized loss of kerogen. Fe-silicates are concentrated along remnants of the thin sheath (vertical line in Fig. 12I), suggesting Fe-precipitation associated with the sheath structure. Indeed bacterial cell walls and polysaccharide sheaths can immobilize substantial amounts of iron during early silicification (Konhauser et al., 2004; Lalonde et al., 2007; Little et al., 2004; Phoenix et al., 2000). These broad filaments show that different taphonomic processes may locally have affected microfossils, such as the replacement of organic matter by siderite and/or growth of microscale quartz crystals (Fig. 14I-J).

5.2.5. Degraded Type 4 filaments

Filaments of Type 4 (Figs. 6M-P and 13), composed of heterogeneously distributed kerogen granules, could represent different types of microfossils. Sheathed and unsheathed trichomes could converge morphologically toward such granular microfossils with increasing degradation (Hofmann and Schopf, 1983; Knoll et al., 1988). Their anatomic features (tubular ghost trichome, thin or thick sheath) could have been lost because of migration, condensation and granularization of kerogen along the boundaries of the observed coarse quartz crystal.

Similar to some parts of Type 2–3 filaments, the concentration of siderite in Type 4 microfossils is inversely proportional to kerogen abundance (Fig. 6N-P). Microfossil Type–4 Specimen–1 is relatively poor in siderite and preserves abundant, large kerogen granules (Fig. 13A-F), whereas microfossil Type–4 Specimen–2 is siderite-rich and only shows scarce nanoscale kerogen grains (Fig. 13H-M). This supports that siderite formed after *in situ* mineralization of kerogen.

5.3. Origin of Fe minerals associated with microfossils

5.3.1. Fe-rich sediment associated with microfossils

In DCK4_9.3, siderite is mostly found as nanometer- to micrometer-sized crystals associated with microfossils (Figs. 9–13). The formation of siderite is generally limited to sedimentary environment where Fe^{2+} concentrations exceed dissolved hydrogen sulfide (H2S) produced by the sulfate-reduction (Konhauser, 1998). Indeed, Fe^{2+} reacts preferentially with H$_2$S compared to carbonate (CO$_3^{2-}$), and preferentially forms pyrite (FeS$_2$) when the former is present. The presence of siderite and the absence of pyrite or sulfur in the BIF-associated nodule DCK4_9.3 (Table 1) suggest that bacterial sulfate-reduction did not act during deposition and diagenesis. Chert nodules in carbonate facies remote from BIF (K30-K32) do not show siderite but displayed pyrite and dolomite (Table 1, Fig. 3). The siderite-bearing nodule DCK4_9.3 is thus associated with Fe-rich, S-poor sediments, whereas other nodules formed pyrite under S-rich conditions.

5.3.2. Formation of iron carbonates

Siderite is common in BIFs where it is associated with Fe-oxides (magnetite and hematite) and Fe-silicates (Klein, 2005). Similar to the studied chert, the underlying BIF displays abundant siderite and hematite (Barlow et al., 2016). Early studies proposed a biological origin for siderite in BIFs, based on rounded shape (Laberge, 1967, 1973), although the rounded granule morphology has recently been reproduced abiotically (Koehler et al., 2013).

5.3.2.1. Evidence for Fe reduction. Iron isotope analyses obtained on bulk rock and HCl leachate can provide constraints on the origin of Fe-carbonates in DCK4_9.3, when coupled with petrological and geochemical data. First, petrological observation shows that Fe is essentially contained in siderite and hematite, with only minor/accessory Fe-silicate and no detectable pyrite and amorphous Fe-(oxy)hydroxides. Second, assuming that Fe is only carried by siderite and hematite, the proportion of Fe in the two phases can be assessed from two independent methods. Fe contained in carbonate represents ~ 70% of the total Fe (Table 1). Another estimation of carbonate Fe can be derived from Fe(II)/Fe_{tot} ratio (Table 1) since Fe carbonates contain exclusively Fe(II) and hematite only Fe(III), which implies that carbonate Fe (i.e. Fe(II)) represents ~ 66% of the total Fe. Both estimations are in good agreement, suggesting that 66–70% of the Fe is in carbonate, while hematite (and possibly a small fraction of Fe-silicates) represent the remaining ~30%. Considering the respective solubility of carbonate, hematite and Fe-silicates as well as the arguments presented above, we can reasonably assume that the cold-HCl extraction leach corresponds to Fe derived from carbonates, while the bulk Fe extraction includes Fe carbonates, hematite and Fe-silicates. This assumption is strongly supported by the perfect matching between the concentration of Fe extracted by HCl leaching relative to the bulk Fe concentration ($Fe_{HCl}/Fe_{tot} = 66\%$) and the proportion of carbonate Fe determined above (66–70%). Moreover, crystalline Fe-silicates as observed in Fig. 13 (diffraction SAED) are not leached efficiently with cold-HCl (Raiswell et al., 1994) and thus should not contribute significantly to the cold-HCl leachate. The isotope composition of the cold-HCl leachate (δ^{56}Fe of +1.45‰) is thus representative of the isotope composition of Fe-carbonates. Furthermore, the similar isotope compositions between HCl-extraction and bulk analyses (δ^{56}Fe + 1.43‰) indicate that Fe carbonate and the remaining pool formed by hematite and Fe-silicates have indistinguishable Fe isotope compositions within error. This suggests that hematite, which is largely dominant relative to Fe-silicates, derives from total oxidation of initial Fe-carbonates, a conclusion also supported by petrographic observation (Fig. 3E). Indeed, oxidative replacement of Fe-carbonates by secondary Fe-oxides would not modify the bulk-rock isotopic composition because Fe(III) would readily recrystallize *in situ* (*e.g.* Fig. 3E) and would not escape from the rock system (Markl et al., 2006). Although various Fe-bearing minerals occur in sample DCK4_9.3, we thus argue that sequential leachate provides a robust estimate of the isotope composition of bulk Fe carbonates, with an extreme δ^{56}Fe value of ca.+1.45‰. This extremely positive δ^{56}Fe value likely reflects the isotope composition of siderite, which represents ~90% of the bulk carbonate, and should not be significantly affected by ~10% of ankerite. Petrological observation demonstrates that siderite in DCK4_9.3 comprises two different populations, with (1) scarce but very coarse rhombs and (2) very abundant micro- to nano-siderites associated with microfossils. Unfortunately, bulk Fe isotope analyses cannot distinguish between these two populations. Fe-isotope microanalyses could distinguish these populations, but this has, to our knowledge, not yet been achieved on <2 μm to sub-micrometric siderites such as those associated with microfossils.

The highly positive δ^{56}Fe value (1.45‰) observed in DCK4_9.3 is unusual for siderite (*e.g.* Johnson et al., 2013). Abiotic siderite precipitated from hydrothermally-derived Fe(II), with $\delta^{56}Fe_{Fe(II)} \sim 0‰$, should be slightly depleted in heavy isotope and show $\delta^{56}Fe_{sid}$ between −0.5 and 0‰ (Wiesli et al., 2004), which is inconsistent with the isotopic composition measured in DCK4_9.3. Positive δ^{56}Fe values, as observed in DCK4_9.3 carbonates are usually found in Fe(III)-oxides and result from partial Fe oxidation in a Fe(II)-rich water followed by Fe(III) precipitation (Johnson et al., 2008; Czaja et al., 2013; Li et al., 2013). Hence, this value requires that a pool of dissolved Fe(II) has been partially oxidized and precipitated into Fe (III) before being reduced into siderite. Irrespective of the original Fe(III) precipitation mechanism, preservation of the strongly positive δ^{56}Fe values of primary Fe oxides within Fe carbonate of DCK4_9.3 requires near-quantitative reduction of precursor Fe (III)-minerals to siderite. This finding is consistent with the absence of primary Fe-oxides in our sample.

5.3.2.2. Microbial versus thermal Fe reduction. In sample DCK4_9.3, siderite was presumably formed by reduction of primary Fe-(oxy) hydroxides during diagenetic and/or metamorphic reactions. More specifically, siderite may have been formed by two main processes, either through microbially-mediated dissimilatory iron reduction (DIR), and/or abiotically by thermal reduction associated to sediment burial and geological history. In any of these two cases, reducing chemical agent available in the Kazput vicinity were likely organic matter and/or reduced sulfur species. The vast dominance of Fe carbonates over sulfur-bearing compounds, in particular in DCK4_9.3 sample (where no pyritic or organic S was detected) and the underlying BIF (Barlow et al., 2016) suggests sulfur limitation in the system. Hence organic matter is the most likely candidate for Fe reduction.

Siderite may have been formed by bacterial dissimilatory iron reduction (DIR) (Dong et al., 2000; Konhauser, 1998; Roh et al., 2003). The siderite grains formed by DIR can have similar grain size and rhombohedral shape as the grains associated with DCK4_9.3 filaments (Roh et al., 2003). Fe-silicates, such as those observed in DCK4_9.3 microfossils, can also form during DIR (Percak-Dennett et al., 2011). DIR can form Fe(II)-minerals, such as siderite or pyrite, with negative δ^{56}Fe values down to −3‰ (Crosby et al., 2005; Johnson et al., 2008). In Archean sediments, negative δ^{56}Fe values in BIF and pyrites have been interpreted as evidence for DIR as early as 2.7–2.5 Ga (Archer and Vance, 2006; Czaja et al., 2013; Heimann et al., 2010). However, Fe-isotope fractionation by DIR is not expressed in DCK4_9.3 because of near-quantitative reduction of Fe(III).

Alternatively, siderite can form through abiotic reduction of Fe (III)-oxides in presence of organic matter at ca. 170 °C (Koehler et al., 2013; Posth et al., 2013), a process supported by observation of Fe-carbonates replacing organic matter at low diagenetic/metamorphic temperature in the geological record (Bernard et al., 2007; Hendry et al., 2000). The organic matter geothermometry based on Raman spectra of our sample (Fig. 5) indicates that sufficient temperature (~280 °C) was reached for this reaction. This may explain local replacement of organic matter by siderite in association with local coarsening of quartz during deep burial of DCK4_9.3 microfossils.

Oxygen and carbon isotopes can also provide constraints on the history of carbonates. Carbon isotope exchanges between carbonates and organic matter or graphite begin at temperature higher than 300 °C, and are characterized by incomplete exchanges below 500–600 °C (Valley, 2001). Hence, the low metamorphic temperature experienced by our samples (~280 °C) implies that exchange of the C isotopes composition of siderite/ankerite with those of organic matter should have been very limited. $\delta^{13}C_{org}$ could only have been increased by at most 3‰ through cracking reactions (Des Marais, 2001), but not isotope exchange with carbonates. In this context, the absence of a strongly negative δ^{13} C_{carb} signature (here −2.04‰) is unusual assuming formation of carbonate through oxidation of ^{13}C-depleted organic matter by DIR activity (Heimann et al., 2010; Johnson et al., 2013) and/or abiotic thermal reactions. This value suggests a low contribution of the CO_2 produced by organic matter oxidation to the dissolved inorganic carbon budget (*e.g.* Hendry et al., 2000), or a modification of the primary C-isotope composition of carbonate by late interaction with diagenetic/metamorphic fluids during carbonate recrystallization. At the studied Kazput locality, the $\delta^{13}C_{carb}$ of dolomitic facies varies between −0.2 and 1.4‰, which is positively correlated with increasing $\delta^{18}O_{carb}$ (−14.8 to −9.7‰) suggesting alteration of carbonates associated with Paleoproterozoic metamorphism (Barlow et al., 2016; Rasmussen et al., 2005). The DCK4_9.3 $\delta^{13}C_{carb}$ signature of −2.04‰, lower than that of all dolomitic carbonates at the same locality, may thus preserve a weak (though non-diagnostic) signal of organic matter mineralization associated with overprint of diagenetic and/or metamorphic fluids

5.3.2.3. Fe(III) precursors to siderite. The iron oxide precursors to siderite could have precipitated after Fe oxidation by several biogeochemical pathways: 1) direct oxidation using O_2 produced by oxygenic photosynthetic organisms, 2) microaerophilic Fe-oxidizing bacterial metabolism (Emerson and Moyer, 2002; Fleming et al., 2013), 3) nitrate-reducing anaerobic Fe-oxidizing bacteria (Miot et al., 2009), or 4) Fe-oxidizing anoxygenic phototrophs (Ehrenreich and Widdel, 1994; Widdel et al., 1993). The absence of La-Ce anomalies and positive Pr anomaly in our samples suggests a suboxic or anoxic environment (Bau and Dulski, 1996; Planavsky et al., 2009), although REE compositions may have been affected by diagenesis of carbonates (Pattan et al., 2005; Petrash et al., 2016), as suggested by correlated O-C isotopes at the studied locality. Anoxic conditions are also supported by the extremely positive δ^{56}Fe value of +1.43‰ since only a limited fraction of the dissolved Fe(II) source should have been oxidized and precipitated to Fe(III) mineral (Thomazo et al., 2009), which was then reduced into siderite. In contrast, a sharp redox boundary associated with oxygenic photosynthesis and abundant O_2 is expected to produce near-quantitative Fe oxidation without significant Fe isotope fractionation (*e.g.* Czaja et al., 2013).

Fe(III) precursors to siderite may have formed directly in/on DCK4_9.3 microorganisms *in vivo* through any of the above pathways. The anoxic deep-water conditions implied above required a mediator for Fe-oxidation, which could have been DCK4_9.3 microorganisms. Intra-microfossil concentrations of siderite and Fe-silicates in specific morphospecies of the Gunflint Iron Formation were interpreted as products of *in situ* recrystallization of intracellular Fe-biominerals (Lepot et al., 2017). The morphospecies specificity of the Fe-mineral distribution of the Gunflint microfossils (Lepot et al., 2017) is also observed here in DCK4_9.3 with an intimate association of Fe-minerals with specific microfossil Types 2–4, but not Type 1. However, the apparent replacement relationship between siderite and organic matter and the correlation of siderite with microfossil organic structures in DCK4_9.3 contrast with the intra-microfossil, cell-wall independent distribution of Gunflint microfossil Fe-minerals. This replacement relationship is consistent with *post-mortem* formation of Fe-carbonates (*e.g.* Bernard et al., 2007) and Fe-silicates (Wacey et al., 2014). Precursor Fe(III) minerals could have encrusted Type 2–4 microfossils and reduced *in situ* into siderite and Fe-silicates as proposed for Gunflint microfossils (Lepot et al., 2017). Alternatively, Fe(II) could have migrated on these microfossils *post-mortem*. Shapiro and Konhauser (2015) argued that hematite ($Fe^{III}_2O_3$) replaced some of the Gunflint microfossils *post-mortem*. They suggested that groundwater Fe(II) could locally have adsorbed onto organic matter of the microfossils and/or formed siderite. Subsequent percolation by oxygenated groundwater could have oxidized both organic matter and adsorbed/siderite Fe(II). This could explain the contrast between microfossils preserved as kerogen in non-altered sections and those replaced by hematite in oxidized rocks of the Gunflint Iron Formation. Such diagenetic Fe migration could potentially explain the association of Fe-minerals with microfossils of DCK4_9.3. However, petrographic evidence for Fe-migration have not been observed in DCK4_9.3. Fe-bearing veins are absent in this chert. The concentration of iron associated with studied microfossils is highly variable at millimeter and micrometer scales and does not depend on the localization of the microfossils. Moreover, the high δ^{56}Fe value of +1.43‰ is difficult to reconcile with a diagenetic origin of the Fe source since the δ^{56}Fe values of sedimentary porewater fluids released during diagenesis generally range from −3 to +0.5‰ (Severmann et al., 2006). Petrographic and Fe-isotope data are thus best explained by *in situ* precipitation of Fe(III) precursors to siderite in the microbial fabric, possibly as biominerals.

5.3.3. Turee Creek Group microfossils: BIF versus carbonate facies

Microfossils forming cobweb fabrics in black chert nodules of dolomitic carbonate rocks of the Kazput Formation were interpreted as sulfur oxidizing organisms of a sulfuretum thriving below storm wave-base by Schopf et al. (2015) and Van Kranendonk et al. (2012) . This assemblage presented by Schopf et al. (2015) and Van Kranendonk et al. (2012) contains filamentous microfossils similar to those observed in the nodule DCK4_9.3 hosted at the transition between an iron formation, and dolomites. Schopf et al. (2015) reported medium filaments (~2 μm wide) similar to DCK4_9.3′s narrow filaments with thin sheaths (i.e. Type 1 microfossils), and broad septate filaments (~5 μm-wide) having similar diameter to DCK4_9.3's broad Type 3 filaments with thin sheaths. These broad septate filaments often exhibited inferred cellular structures. The length of cells within filaments is compatible with sulfur-oxidizing bacteria (Schopf et al., 2015). In the absence of morphological cellular remnants in DCK4_9.3, similar inferences are not possible, and Type 2–3 microfossil may represent different microorganisms. The long thread-like filaments ≤1 μm in diameter present in the sample DCK4_9.3 were also observed by Schopf et al. (2015) and Van Kranendonk et al. (2012). However, the assemblage described by these studies did not include Type 2 narrow filaments with thick sheaths. Finding molecular signatures preserved within microfossils at submicrometer scale could also support morphological similarities between assemblages from the different chert nodules (Alleon et al., 2016b).

Moreover, sample DCK4_9.3, yielded a bulk-rock $\delta^{13}C_{org}$ value of −21.85‰. This value is considered representative of the whole microfossil assemblage as in this sample, organic matter is essentially in the form of microfossils and amorphous kerogen is extremely scarce. This value is significantly higher than the $\delta^{13}C_{org}$ values of −36 to −25‰ measured in the Turee Creek Group, including dolomitic facies (Ader et al., 2015). This difference cannot be inherited from diagenetic modification since δ^{13}C of organic matter should only shifted by ±2‰ relative to initial organic material (*e.g.* Busigny et al., 2013; Lehmann et al., 2002; Yamaguchi et al., 2010). Two other processes can be invoked to explain the $\delta^{13}C_{org}$ difference in BIF-associated DCK4_9.3 compared to dolomite-associated Turee Creek Group samples. First, the same microorganisms may have fed on different carbon substrates, assuming they were heterotrophs or mixotrophs. Second, the microorganisms may have had distinct metabolisms, *e.g.* iron oxidation, sulfur oxidation or photosynthesis (Pearson, 2010; Van der Meer et al., 2000; Williford et al., 2013). The difference between $\delta^{13}C_{carb}$ and $\delta^{13}C_{org}$ (i.e. $\Delta^{13}C_{carb-org} = \delta^{13}C_{carb} - \delta^{13}C_{org}$) recorded in DCK4_9.3 is 19.8‰. Assuming the carbonates formed from dissolved CO_2 in seawater and using a fractionation value of 10.17‰ between aqueous CO_2 and precipitated carbonate at 20 °C (Emrich et al., 1970), the $\Delta^{13}C_{carb-org}$ can be used to determine a metabolic fractionation ε of 9.6‰ between parent CO_2 and organic matter. Interestingly, this value significantly differs from those of microfossils of the 1.9 Ga Gunflint Iron Formation ($\delta^{13}C_{org} \sim -31.4$‰, $\Delta^{13}C_{carb-org} \sim 28.5$‰, inferred ε ~ 19‰), which were interpreted as photosynthetic cyanobacteria (Williford et al., 2013). A value of 9.6‰ inferred for ε in sample DCK4_9.3 would be consistent with metabolism based on reductive tri-carboxylic acid (TCA) or 3-hydroxypropionate cycles (House et al., 2003), which are used by anoxygenic Fe- and/or S-oxidizing photoautotrophic bacteria. However, the influence of organic matter remineralization on $\delta^{13}C_{carb}$, suggested by the replacement of organic matter by siderite, remains unknown and true ε could be higher than above estimates. Nevertheless, the high absolute value of $\delta^{13}C_{org}$ recorded in DCK4_9.3 contrasts with dolomitic facies of the Turee Creek group and other Paleoproterozoic microfossil assemblages, and could represent a contribution of photoautotrophic and/or lithoautotrophic Fe-oxidizing bacteria (Kennedy et al., 2010). In addition, the intimate association of Fe-minerals with specific microfossil Types 2–4, but not Type 1, and Fe-isotope ratio suggest Fe-oxidation by the DCK4_9.3 microbiota.

5.3.4. Deposition and diagenesis model

Based on these interpretations, we propose scenarios to explain the presence of siderite and Fe-silicates associated with microfossils lying at the interface between BIF and deep-water carbonates of the Kazput Formation (DCK4_9.3). We infer that this specific microbial fabric records iron-oxidizing bacteria, or bacteria inducing iron oxides precipitation, which may have been encrusted by Fe (III)-oxides as proposed for filaments of Gunflint-type microfossil assemblages in the Gunflint Iron Formation and Duck Creek Formation (Planavsky et al., 2009; Wilson et al., 2010). Gunflint's microfossils were observed in sulfate-limited environments, as indicated by S-isotopes (Wacey et al., 2013). Similarly, DCK4_9.3 is devoid of pyrite, organic sulfur, and bulk-rock chemistry indicates a S-poor environment (Table 1). In contrast, filaments reported by Van Kranendonk et al. (2012), permineralized in pyrite rich nodules associated with carbonate (dolomitic) rocks of the Kazput Formation were interpreted as sulfur-oxidizing bacteria (Schopf et al., 2015; Van Kranendonk et al., 2012). The interpretation of some of the DCK4_9.3 microfossils as iron oxidizers is not incompatible with sulfur-oxidizing bacteria since some bacteria can perform both Fe and S oxidation (Hedrich et al., 2011). *Sphaerotilus Natans* and *Leptothrix* species form long, sheathed filaments encrusted by Fe-oxides in Fe-rich microaerophilic environments (Konhauser, 1998; Stokes, 1954) and were considered as possible modern counterparts for filaments of the 1.88 Ga Gunflint Formation (Cloud, 1965). *Sphaerotilus Natans* can also oxidize H_2S (Skerman et al., 1957). Moreover, the detection of functional genes of sulfur metabolism from a subspecies of *Sphaerotilus natans* and phylogenetic analyses of DNA sequences indicate that ancestors of *Sphaerotilus–Leptothrix* were able to oxidize sulfur compounds but some *Sphaerotilus* strains lost this function (Belousova et al., 2013). These modern bacteria exemplify that some filamentous bacteria can oxidize ferrous iron as well as sulfur compounds in different settings, while phylogenetic data suggest that this versatility could have been more common in their ancestors (Belousova et al., 2013; Lane et al., 1992). Some microfossils (Types 1, 3, 4) reported here atop BIF in DCK4_9.3 bear similarities with those in cherts of overlying carbonate rocks (Schopf et al., 2015; Van Kranendonk et al., 2012) and form the same cobweb-like fabrics. Such morphological similarities and metabolic versatility suggest that some benthic filamentous communities could have been selected and could have thrived during drastically changing environmental conditions at the final stage of BIF deposition, including transitions of sulfidic to ferruginous conditions.

Later, heterotrophic bacteria such as iron reducing bacteria and/or other heterotrophs could have oxidized the organic matter of the filaments and reduced almost all the Fe(III) mineral into siderite grains. This scenario can explain the concentration of the most degraded Type 4 filaments in siderite-rich clumps, whereas other, better preserved filaments are generally siderite-poor. Moreover, organic matter in the cell trichomes has been preferentially biodegraded compared to polysaccharide sheaths (Bartley, 1996; Lepot et al., 2014). Interestingly, the organic matter in DCK4_9.3 appears almost completely composed of fossil sheaths and does not show amorphous kerogen forming clots or films, (*e.g.* Lepot et al., 2013). The organic matter that is preserved in this black chert is thus the most resilient part of the biomass that could not be used by heterotrophs such as iron reducers. Otherwise, more labile organic material originating from proteins would have polymerized into amorphous kerogen (Vandenbroucke and Largeau, 2007). Thus, it suggests that the iron-carbon system [using organic C to reduce Fe(III) during DIR] was carbon-limited, which allows the precipitation of Fe-silicates as observed in DCK4_9.3.

Alternatively, in DCK4_9.3, the kerogen and the Fe(III)-encrustation of microfossils could have reacted together during thermal diagenesis to form siderite (Koehler et al., 2013; Posth et al., 2013) as well as Fe-silicates (Planavsky et al., 2012). Fe-oxide precursors encrusting sheaths can explain the distribution of Fe-silicates in or aligned with the sheaths. Thermal reduction could explain the very low TOC of DCK4_9.3 (0.01 wt% C) compared to the concentration of sideritic carbon (0.09 wt% of the bulk rock is inorganic C) as well as the localized replacements of kerogen by siderite.

5.4. Summary

Ultrastructural observations of filamentous microfossils in DCK4_9.3 allowed the distinction of three main types of well-preserved filaments permineralized in nanocrystalline quartz: narrow filaments with thin (Type 1) or thick (Type 2) sheaths, and broad filaments with thin sheaths (Type 3). Rarely, the trichome is partly preserved but is affected by granularization and migration of the organic material associated with the growth of micrometer-sized quartz crystals. Type 4 filaments are granular filaments and too poorly preserved to be affiliated to other types. Types 2–4 filaments display variable and heterogenous replacement of kerogen by siderite. Platy Fe-nanocrystals (silicates) outline microfossil ultrastructures. The geological context, ultrastructures of these filaments and $\delta^{56}Fe$, $\delta^{18}O_{carb}$, $\delta^{13}C_{carb}$ values support that iron precipitated first as Fe(III)-oxides in cobwebs of filamentous bacteria growing in ferruginous conditions. Siderite and ankerite formed through bacterial and/or thermal Fe(III) reduction. Microfossils forming similar cobweb fabrics in overlying iron-poor carbonate have been interpreted as sulfur-oxidizing bacteria (Schopf et al., 2015; Van Kranendonk et al., 2012). Distinct microorganisms may have formed the same benthic cobweb fabrics in ferruginous and sulfur-rich conditions. Alternatively, the existence of modern bacteria able to oxidize both sulfur and iron suggests that benthic Kazput Formation filamentous communities with such metabolic versatility, have been selected through a transition from iron- to sulfur-rich environment during the Great Oxidation Event.

Acknowledgements

Martin Van Kranendonk is thanked for leading us to the field and to sample the outcrops. We thank the Agouron Institute – United States for funding the field mission to Australia. KL thanks other members of the Agouron 2012 team (John Abelson, David Flannery, Kate French, John Grotzinger, Jena Johnson, Andrew Knoll, Rowan Martindale, Rajat Mazumder, Melissa Rice, Erik Sperling, Justin Strauss, Roger Summons, Malcolm Walter) for field work performance and organization. Philippe Recourt and Sandra Ventalon (LOG) are thanked for help with cathololuminescence. Myriam Moreau (LASIR) is thanked for help with Raman. Sylvie Regnier is thanked for thin section preparation. The Service d'Analyse des Roches et des Minéraux (SARM) from the Centre de Recherches Pétrographiques et Géochimiques (CRPG) is thanked for ICPMS analysis. We thank CNRS-INSU SYSTER and ANR M6fossils (ANR-15-CE31-0003-01) grants to KL for funding the analytical work. VB's work was financially supported by the UnivEarths Labex programme at Sorbonne Paris Cité (ANR-10-LABX-0023 and ANR-11-IDEX-0005-02). Parts of this work were also supported by IPGP multidisciplinary program PARI, and by Region île-de-France SESAME (Grant No. 12015908). The TEM national facility in Lille was supported by Conseil Régional des Hauts-de-France, European Regional Development Fund, and CNRS-INSU. FIB work was partly supported by the French RENATECH network. We thank Pr. G. Zhao (editor) and three anonymous reviewers for constructive comments.

References

Ader, M., Thomazo, C., Baton, F., Muller, E., Chaduteau, C., Cartigny, P., Vennin, E., Buoncristiani, J.F., Van Kranendonk, M., Philippot, P., 2015. Paired Carbon Isotope From Three Key Intervals of the Turee Creek Group. Pilbara Craton, Australia.

Alleon, J., Bernard, S., Le Guillou, C., Daval, D., Skouri-Panet, F., Pont, S., Delbes, L., Robert, F., 2016a. Early entombment within silica minimizes the molecular degradation of microorganisms during advanced diagenesis. Chem. Geol. 437, 98–108. http://dx.doi.org/10.1016/j.chemgeo.2016.05.034.

Alleon, J., Bernard, S., Le Guillou, C., Marin-Carbonne, J., Pont, S., Beyssac, O., McKeegan, K.D., Robert, F., 2016b. Molecular preservation of 1.88 Ga Gunflint organic microfossils as a function of temperature and mineralogy. Nat. Commun. 7, 11977. http://dx.doi.org/10.1038/ncomms11977.

Anbar, A.D., Duan, Y., Lyons, T.W., Arnold, G.L., Kendall, B., Creaser, R.A., Kaufman, A. J., Gordon, G.W., Scott, C., Garvin, J., Buick, R., 2007. A whiff of oxygen before the Great Oxidation Event? Science 317, 1903–1906. http://dx.doi.org/10.1126/science.1140325.

Anbar, A.D., Knoll, A.H., 2002. Proterozoic ocean chemistry and evolution: a bioinorganic bridge? Science 297, 1137–1142. http://dx.doi.org/10.1126/science.1069651.

Archer, C., Vance, D., 2006. Coupled Fe and S isotope evidence for Archean microbial Fe(III) and sulfate reduction. Geology 34, 153–156. http://dx.doi.org/10.1130/G22067.1.

Awramik, S.M., Barghoorn, E.S., 1977. Gunflint microbotia. Precambr. Res. 5, 121–142. http://dx.doi.org/10.1016/0301-9268(77)90025-0.

Barghoorn, E.S., Tyler, S.A., 1965. Microorganisms from the Gunflint chert. Science 147, 563. http://dx.doi.org/10.1126/science.147.3658.563.

Barley, M.E., Pickard, A.L., Sylvester, P.J., 1997. Emplacement of a large igneous province as a possible cause of banded iron formation 2.45 billion years ago. Nature 385, 55–58. http://dx.doi.org/10.1038/385055a0.

Barlow, E., Van Kranendonk, M.J., Yamaguchi, K.E., Ikehara, M., Lepland, A., 2016. Lithostratigraphic analysis of a new stromatolite-thrombolite reef from across the rise of atmospheric oxygen in the Paleoproterozoic Turee Creek Group, Western Australia. Geobiology 14, 317–343. http://dx.doi.org/10.1111/gbi.12175.

Bartley, J.K., 1996. Actualistic taphonomy of cyanobacteria: implications for the precambrian fossil record. Palaios 11, 571–586. http://dx.doi.org/10.2307/3515192.

Bau, M., Dulski, P., 1996. Distribution of yttrium and rare-earth elements in the Penge and Kuruman iron-formations, Transvaal Supergroup, South Africa. Precambr. Res. 79, 37–55.

Belousova, E.V., Chernousova, E.Y., Dubinina, G.A., Tourova, T.P., Grabovich, M.Y., 2013. Detection and analysis of sulfur metabolism genes in Sphaerotilus natans subsp sulfidivorans representatives. Microbiology 82, 586–593. http://dx.doi.org/10.1134/S0026261713050020.

Bercovici, A., Hadley, A., Villanueva-Amadoz, U., 2009. Improving depth of field resolution for palynological photomicrography. Palaeontol. Electron. 12, 5T.

Berelson, W.M., Corsetti, F.A., Pepe-Ranney, C., Hammond, D.E., Beaumont, W., Spear, J.R., 2011. Hot spring siliceous stromatolites from Yellowstone National Park: assessing growth rate and laminae formation. Geobiology 9, 411–424. http://dx.doi.org/10.1111/j.1472-4669.2011.00288.x.

Bernard, S., Benzerara, K., Beyssac, O., Brown, G.E., 2010. Multiscale characterization of pyritized plant tissues in blueschist facies metamorphic rocks. Geochim. Cosmochim. Acta 74, 5054–5068. http://dx.doi.org/10.1016/j.gca.2010.06.011.

Bernard, S., Benzerara, K., Beyssac, O., Menguy, N., Guyot, F., Brown, G.E., Goffe, B., 2007. Exceptional preservation of fossil plant spores in high-pressure metamorphic rocks. Earth Planet. Sci. Lett. 262, 257–272. http://dx.doi.org/10.1016/j.epsl.2007.07.041.

Boulard, E., Guyot, F., Fiquet, G., 2012. The influence on Fe content on Raman spectra and unit cell parameters of magnesite-siderite solid solutions. Phys. Chem. Miner. 39, 239–246. http://dx.doi.org/10.1007/s00269-011-0479-3.

Busigny, V., Lebeau, O., Ader, M., Krapez, B., Bekker, A., 2013. Nitrogen cycle in the Late Archean ferruginous ocean. Chem. Geol. 362, 115–130. http://dx.doi.org/10.1016/j.chemgeo.2013.06.023.

Busigny, V., Planavsky, N.J., Jezequel, D., Crowe, S., Louvat, P., Moureau, J., Viollier, E., Lyons, T.W., 2014. Iron isotopes in an Archean ocean analogue. Geochim. Cosmochim. Acta 133, 443–462. http://dx.doi.org/10.1016/j.gca.2014.03.004.

Campbell, K.A., Lynne, B.Y., Handley, K.M., Jordan, S., Farmer, J.D., Guido, D.M., Foucher, F., Turner, S., Perry, R.S., 2015. Tracing biosignature preservation of geothermally silicified microbial textures into the geological record. Astrobiology 15, 858–882. http://dx.doi.org/10.1089/ast.2015.1307.

Canfield, D.E., 1998. A new model for Proterozoic ocean chemistry. Nature 396, 450–453. http://dx.doi.org/10.1038/24839.

Cloud, P., 1965. Significance of Gunflint (Precambrian) Microflora – photosynthetic oxygen may have had Important Local Effects before becoming a major atmospheric gas. Science 148, 27. http://dx.doi.org/10.1126/science.148.3666.27.

Condie, K.C., O'Neill, C., Aster, R.C., 2009. Evidence and implications for a widespread magmatic shutdown for 250 My on Earth. Earth Planet. Sci. Lett. 282, 294–298. http://dx.doi.org/10.1016/j.epsl.2009.03.033.

Crosby, H.A., Johnson, C.M., Roden, E.E., Beard, B.L., 2005. Coupled Fe(II)-Fe(III) electron and atom exchange as a mechanism for Fe isotope fractionation during dissimilatory iron oxide reduction. Environ. Sci. Technol. 39, 6698–6704. http://dx.doi.org/10.1021/es0505346.

Crowe, S.A., Dossing, L.N., Beukes, N.J., Bau, M., Kruger, S.J., Frei, R., Canfield, D.E., 2013. Atmospheric oxygenation three billion years ago. Nature 501. http://dx.doi.org/10.1038/nature12426. 535–+.

Czaja, A.D., Johnson, C.M., Beard, B.L., Roden, E.E., Li, W., Moorbath, S., 2013. Biological Fe oxidation controlled deposition of banded iron formation in the ca. 3770 Ma Isua Supracrustal Belt (West Greenland). Earth Planet. Sci. Lett. 363, 192–203. http://dx.doi.org/10.1016/j.epsl.2012.12.025.

Des Marais, D.J., 2001. Isotopic evolution of the biogeochemical carbon cycle during the Precambrian. In: Valley, J.W., Cole, D.R. (Eds.), Stable Isotope Geochemistry. Mineralogical Soc Amer, Chantilly, pp. 555–578.

Dong, H.L., Fredrickson, J.K., Kennedy, D.W., Zachara, J.M., Kukkadapu, R.K., Onstott, T.C., 2000. Mineral transformation associated with the microbial reduction of magnetite. Chem. Geol. 169, 299–318. http://dx.doi.org/10.1016/S0009-2541(00)00210-2.

Ehrenreich, A., Widdel, F., 1994. Anaerobic oxidation of ferrous iron by purple bacteria, a new-type of phototrophic metabolism. Appl. Environ. Microbiol. 60, 4517–4526.

Emerson, D., Moyer, C.L., 2002. Neutrophilic Fe-Oxidizing bacteria are abundant at the Loihi Seamount hydrothermal vents and play a major role in Fe oxide deposition. Appl. Environ. Microbiol. 68, 3085–3093. http://dx.doi.org/10.1128/AEM.68.6.3085-3093.2002.

Emrich, K., Ehhalt, D.H., Vogel, J.C., 1970. Carbon isotope fractionation during the precipitation of calcium carbonate. Earth Planet. Sci. Lett., 363–371

Eriksson, P.G., Condie, K.C., 2014. Cratonic sedimentation regimes in the ca. 2450–2000 Ma period: relationship to a possible widespread magmatic slowdown on Earth? Gondwana Res. 25, 30–47. http://dx.doi.org/10.1016/j.gr.2012.08.005.

Eriksson, P.G., Mazumder, R., Sarkar, S., Bose, P.K., Altermann, W., van der Merwe, R., 1999. The 2.7-2.0 Ga volcano-sedimentary record of Africa, India and Australia: evidence for global and local changes in sea level and continental freeboard. Precambr. Res. 97, 269–302. http://dx.doi.org/10.1016/S0301-9268(99)00035-2.

Farquhar, J., Wing, B.A., 2003. Multiple sulfur isotopes and the evolution of the atmosphere. Earth Planet. Sci. Lett. 213, 1–13. http://dx.doi.org/10.1016/S0012-821X(03)00296-6.

Fischer, W.W., Knoll, A.H., 2009. An iron shuttle for deepwater silica in Late Archean and early Paleoproterozoic iron formation. Geol. Soc. Am. Bull. 121, 222–235. http://dx.doi.org/10.1130/B26328.1.

Fleming, E.J., Davis, R.E., McAllister, S.M., Chan, C.S., Moyer, C.L., Tebo, B.M., Emerson, D., 2013. Hidden in plain sight: discovery of sheath-forming, iron-oxidizing Zetaproteobacteria at Loihi Seamount, Hawaii, USA. FEMS Microbiol. Ecol. 85, 116–127. http://dx.doi.org/10.1111/1574-6941.12104.

Frei, R., Gaucher, C., Poulton, S.W., Canfield, D.E., 2009. Fluctuations in Precambrian atmospheric oxygenation recorded by chromium isotopes. Nature 461. http://dx.doi.org/10.1038/nature08266. 250-U125.

Garvin, J., Buick, R., Anbar, A.D., Arnold, G.L., Kaufman, A.J., 2009. Isotopic evidence for an aerobic nitrogen cycle in the latest Archean. Science 323, 1045–1048. http://dx.doi.org/10.1126/science.1165675.

Hedrich, S., Schloemann, M., Johnson, D.B., 2011. The iron-oxidizing proteobacteria. Microbiol.-Sgm 157, 1551–1564. http://dx.doi.org/10.1099/mic.0.045344-0.

Heimann, A., Johnson, C.M., Beard, B.L., Valley, J.W., Roden, E.E., Spicuzza, M.J., Beukes, N.J., 2010. Fe, C, and O isotope compositions of banded iron formation carbonates demonstrate a major role for dissimilatory iron reduction in similar to 2.5 Ga marine environments. Earth Planet. Sci. Lett. 294, 8–18. http://dx.doi.org/10.1016/j.epsl.2010.02.015.

Hendry, J.P., Wilkinson, M., Fallick, A.E., Haszeldine, R.S., 2000. Ankerite cementation in deeply buried Jurassic sandstone reservoirs of the central North Sea. J. Sediment. Res. 70, 227–239. http://dx.doi.org/10.1306/2DC4090D-0E47-11D7-8643000102C1865D.

Herdianita, N.R., Browne, P.R.L., Rodgers, K.A., Campbell, K.A., 2000. Mineralogical and textural changes accompanying ageing of silica sinter. Miner. Deposita 35, 48–62. http://dx.doi.org/10.1007/s001260050005.

Hesse, R., 1989. Silica diagenesis – origin of inorganic and replacement cherts. Earth-Sci. Rev. 26, 253–284. http://dx.doi.org/10.1016/0012-8252(89)90024-X.

Hoffman, P.F., 2013. The great oxidation and a Siderian snowball Earth: MIF-S based correlation of Paleoproterozoic glacial epochs. Chem. Geol. 362, 143–156. http://dx.doi.org/10.1016/j.chemgeo.2013.04.018.

Hofmann, H.J., Schopf, J.W., 1983. Early Proterozoic Microfossils, in: Earth's Earliest Biosphere: Its Origin and Evolution. J.W. Schopf, New Jersey, pp. 321–360.

Holland, H.D., 2002. Volcanic gases, black smokers, and the Great Oxidation Event. Geochim. Cosmochim. Acta 66, 3811–3826. http://dx.doi.org/10.1016/S0016-7037(02)00950-X.

House, C.H., Schopf, J.W., Stetter, K.O., 2003. Carbon isotopic fractionation by Archaeans and other thermophilic prokaryotes. Org. Geochem. 34, 345–356. http://dx.doi.org/10.1016/S0146-6380(02)00237-1.

Johnson, C.M., Beard, B.L., Roden, E.E., 2008. The iron isotope fingerprints of redox and biogeochemical cycling in the modern and ancient Earth. Annu. Rev. Earth Planet. Sci. 36, 457–493. http://dx.doi.org/10.1146/annurev.earth.36.031207.124139.

Johnson, C.M., Ludois, J.M., Beard, B.L., Beukes, N.J., Heimann, A., 2013. Iron formation carbonates: Paleoceanographic proxy or recorder of microbial diagenesis? Geology 41, 1147–1150. http://dx.doi.org/10.1130/G34698.1.

Jones, B., Renaut, R.W., Rosen, M.R., 2001. Taphonomy of silicified filamentous microbes in modern geothermal sinters – implications for identification. Palaios 16, 580–592. http://dx.doi.org/10.2307/3515630.

Jones, B., Renaut, R.W., Rosen, M.R., 1998. Microbial biofacies in hot-spring sinters: a model based on Ohaaki Pool, North Island, New Zealand. J. Sediment. Res. 68, 413–434.

Kendall, B., Reinhard, C.T., Lyons, T., Kaufman, A.J., Poulton, S.W., Anbar, A.D., 2010. Pervasive oxygenation along late Archaean ocean margins. Nat. Geosci. 3, 647–652. http://dx.doi.org/10.1038/NGEO942.

Kennedy, C.B., Gault, A.G., Fortin, D., Clark, I.D., Pedersen, K., Scott, S.D., Ferris, F.G., 2010. Carbon isotope fractionation by circumneutral iron-oxidizing bacteria. Geology 38, 1087–1090. http://dx.doi.org/10.1130/G30986.1.

Klein, C., 2005. Some Precambrian banded iron-formations (BIFs) from around the world: Their age, geologic setting, mineralogy, metamorphism, geochemistry, and origin. Am. Mineral. 90, 1473–1499. http://dx.doi.org/10.2138/am.2005.1871.

Knoll, A.H., Barghoorn, E.S., 1976. Gunflint-type microbiota from Duck Creek Dolomite, Western-Australia. Orig. Life Evol. Biosphere. 7, 417–423. http://dx.doi.org/10.1007/BF00927937.

Knoll, A.H., Barghoorn, E.S., Awramik, S.M., 1978. New microorganisms from Aphebian Gunflint iron formation, Ontario. J. Paleontol. 52, 976–992.

Knoll, A.H., Strother, P., Rossi, S., 1988. Distribution and diagenesis of microfossils from the lower Proterozoic Duck Creek Dolomite, Western Australia. Precambr. Res. 38, 257–279. http://dx.doi.org/10.1016/0301-9268(88)90005-8.

Knoll, A.K., Simonson, B., 1981. Early Proterozoic Micro-Fossils and Penecontemporaneous Quartz Cementation in The Sokoman Iron Formation, Canada. Science 211, 478–480. http://dx.doi.org/10.1126/science.211.4481.478.

Koehler, I., Konhauser, K.O., Papineau, D., Bekker, A., Kappler, A., 2013. Biological carbon precursor to diagenetic siderite with spherical structures in iron formations. Nat. Commun. 4, 1741. http://dx.doi.org/10.1038/ncomms2770.

Konhauser, K.O., 1998. Diversity of bacterial iron mineralization. Earth-Sci. Rev. 43, 91–121. http://dx.doi.org/10.1016/S0012-8252(97)00036-6.

Konhauser, K.O., Jones, B., Phoenix, V., Ferris, G., Renaut, R., 2004. The microbial role in hot spring silicification. Ambio 33, 552–558. http://dx.doi.org/10.1639/0044-7447(2004) 033[0552:TMRIHS]2.0.CO;2.

Konhauser, K.O., Pecoits, E., Lalonde, S.V., Papineau, D., Nisbet, E.G., Barley, M.E., Arndt, N.T., Zahnle, K., Kamber, B.S., 2009. Oceanic nickel depletion and a methanogen famine before the Great Oxidation Event. Nature 458. http://dx.doi.org/10.1038/nature07858. 750-U85.

Kouketsu, Y., Mizukami, T., Mori, H., Endo, S., Aoya, M., Hara, H., Nakamura, D., Wallis, S., 2014. A new approach to develop the Raman carbonaceous material geothermometer for low-grade metamorphism using peak width. Isl. Arc 23, 33–50.

Laberge, G., 1973. Possible biological origin of Precambrian iron-formations. Econ. Geol. 68, 1098–1109.

Laberge, G., 1967. Microfossils and Precambrian iron-formations. Geol. Soc. Am. Bull. 78, 331. http://dx.doi.org/10.1130/0016-7606(1967) 78[331:MAPI]2.0.CO;2.

Lahfid, A., Beyssac, O., Deville, E., Negro, F., Chopin, C., Goffe, B., 2010. Evolution of the Raman spectrum of carbonaceous material in low-grade metasediments of the Glarus Alps (Switzerland). Terra Nova 22, 354–360. http://dx.doi.org/10.1111/j.1365-3121.2010.00956.x.

Lalonde, S.V., Amskold, L.A., Warren, L.A., Konhauser, K.O., 2007. Surface chemical reactivity and metal adsorptive properties of natural cyanobacterial mats from an alkaline hydrothermal spring, Yellowstone National Park. Chem. Geol. 243, 36–52. http://dx.doi.org/10.1016/j.chemgeo.2007.05.016.

Lane, D., Harrison, A., Stahl, D., Pace, B., Giovannoni, S., Olsen, G., Pace, N., 1992. Evolutionary relationships among sulfur- and iron-oxidizing eubacteria. J. Bacteriol. 174, 269–278.

Lebeau, O., Busigny, V., Chaduteau, C., Ader, M., 2014. Organic matter removal for the analysis of carbon and oxygen isotope compositions of siderite. Chem. Geol. 372, 54–61. http://dx.doi.org/10.1016/j.chemgeo.2014.02.020.

Lehmann, M.F., Bernasconi, S.M., Barbieri, A., McKenzie, J.A., 2002. Preservation of organic matter and alteration of its carbon and nitrogen isotope composition during simulated and in situ early sedimentary diagenesis. Geochim. Cosmochim. Acta 66, 3573–3584. http://dx.doi.org/10.1016/S0016-7037(02)00968-7.

Lepot, K., Addad, A., Knoll, A.H., Wang, J., Troadec, D., Beche, A., Javaux, E.J., 2017. Iron minerals within specific microfossil morphospecies of the 1.88 Ga Gunflint Formation. Nat. Commun. 8, 14890. http://dx.doi.org/10.1038/ncomms14890.

Lepot, K., Compere, P., Gerard, E., Namsaraev, Z., Verleyen, E., Tavernier, I., Hodgson, D.A., Vyverman, W., Gilbert, B., Wilmotte, A., Javaux, E.J., 2014. Organic and mineral imprints in fossil photosynthetic mats of an East Antarctic lake. Geobiology 12, 424–450. http://dx.doi.org/10.1111/gbi.12096.

Lepot, K., Philippot, P., Benzerara, K., Wang, G.-Y., 2009. Garnet-filled trails associated with carbonaceous matter mimicking microbial filaments in Archean basalt. Geobiology 7, 393–402. http://dx.doi.org/10.1111/j.1472-4669.2009.00208.x.

Lepot, K., Williford, K.H., Ushikubo, T., Sugitani, K., Mimura, K., Spicuzza, M.J., Valley, J.W., 2013. Texture-specific isotopic compositions in 3.4 Gyr old organic matter support selective preservation in cell-like structures. Geochim. Cosmochim. Acta 112, 66–86. http://dx.doi.org/10.1016/j.gca.2013.03.004.

Li, Y.-L., Konhauser, K.O., Kappler, A., Hao, X.-L., 2013. Experimental low-grade alteration of biogenic magnetite indicates microbial involvement in generation of banded iron formations. Earth Planet. Sci. Lett. 361, 229–237. http://dx.doi.org/10.1016/j.epsl.2012.10.025.

Lindsay, J.F., Brasier, M.D., 2002. Did global tectonics drive early biosphere evolution? Carbon isotope record from 2.6 to 1.9 Ga carbonates of Western Australian basins. Precambr. Res. 114, 1–34. http://dx.doi.org/10.1016/S0301-9268(01)00219-4.

Little, C.T.S., Glynn, S.E.J., Mills, R.A., 2004. Four-hundred-and-ninety-million-year record of bacteriogenic iron oxide precipitation at sea-floor hydrothermal vents. Geomicrobiol J. 21, 415–429. http://dx.doi.org/10.1080/01490450490485845.

Lynne, B.Y., Campbell, K.A., Moore, J.N., Browne, P.R.L., 2005. Diagenesis of 1900-year-old siliceous sinter (opal-A to quartz) at Opal Mound, Roosevelt Hot Springs, Utah, USA. Sediment. Geol. 179, 249–278. http://dx.doi.org/10.1016/j.sedgeo.2005.05.012.

Lyons, T.W., Reinhard, C.T., Planavsky, N.J., 2014. The rise of oxygen in Earth's early ocean and atmosphere. Nature 506, 307–315. http://dx.doi.org/10.1038/nature13068.

Markl, G., von Blanckenburg, F., Wagner, T., 2006. Iron isotope fractionation during hydrothermal ore deposition and alteration. Geochim. Cosmochim. Acta 70, 3011–3030. http://dx.doi.org/10.1016/j.gca.2006.02.028.

Martin, D.M., 1999. Depositional setting and implications of Paleoproterozoic glaciomarine sedimentation in the Hamersley Province, Western Australia. Geol. Soc. Am. Bull. 111, 189–203. http://dx.doi.org/10.1130/0016-7606(1999)111<0189:DSAIOP>2.3.CO;2.

Martin, D.M., Li, Z.X., Nemchin, A.A., Powell, C.M., 1998. A pre-2.2 Ga age for giant hematite ores of the Hamersley province, Australia? Econ. Geol. Bull. Soc. Econ. Geol. 93, 1084–1090.

Martin, D.M., Powell, C.M., George, A.D., 2000. Stratigraphic architecture and evolution of the early Paleoproterozoic McGrath Trough, Western Australia. Precambr. Res. 99, 33–64. http://dx.doi.org/10.1016/S0301-9268(99)00053-4.

Martindale, R.C., Strauss, J.V., Sperling, E.A., Johnson, J.E., Van Kranendonk, M.J., Flannery, D., French, K., Lepot, K., Mazumder, R., Rice, M.S., Schrag, D.P., Summons, R., Walter, M., Abelson, J., Knoll, A.H., 2015. Sedimentology, chemostratigraphy, and stromatolites of lower Paleoproterozoic carbonates, Turee Creek Group, Western Australia. Precambr. Res. 266, 194–211. http://dx.doi.org/10.1016/j.precamres.2015.05.021.

Mazumder, R., Van Kranendonk, M.J., Altermann, W., 2014. A marine to fluvial transition in the Paleoproterozoic Koolbye Formation, Turee Creek Group, Western Australia. Precambr. Res. 258, 161–170. http://dx.doi.org/10.1016/j.precamres.2014.12.005.

McLennan, S.M., 1989. Rare earth elements in sedimentary rocks; influence of provenance and sedimentary processes. Rev. Mineral. Geochem. 21, 169–200.

Miot, J., Benzerara, K., Morin, G., Kappler, A., Obst, M., Brown, G.E., Guyot, F., 2009. Iron biomineralization by anaerobic neutrophilic iron-oxidizing bacteria. Geochim. Cosmochim. Acta 73, 696–711.

Moreau, J.W., Sharp, T.G., 2004. A transmission electron microscopy study of silica and kerogen biosignatures in-1.9 Ga gunflint microfossils. Astrobiology 4, 196–210. http://dx.doi.org/10.1089/153110704323175142.

Partin, C.A., Lalonde, S.V., Planavsky, N.J., Bekker, A., Rouxel, O.J., Lyons, T.W., Konhauser, K.O., 2013. Uranium in iron formations and the rise of atmospheric oxygen. Chem. Geol. 362, 82–90. http://dx.doi.org/10.1016/j.chemgeo.2013.09.005.

Pattan, J.N., Pearce, N.J.G., Mislankar, P.G., 2005. Constraints in using Cerium-anomaly of bulk sediments as an indicator of paleo bottom water redox environment: a case study from the Central Indian Ocean Basin. Chem. Geol. 221, 260–278. http://dx.doi.org/10.1016/j.chemgeo.2005.06.009.

Pearson, A., 2010. Pathways of carbon assimilation and their impact on organic matter values 13C., in: Handbook of Hydrocarbon and Lipid Microbiology. Timmis KN, Berlin Heidelberg, pp. 143–156.

Pepe-Ranney, C., Berelson, W.M., Corsetti, F.A., Treants, M., Spear, J.R., 2012. Cyanobacterial construction of hot spring siliceous stromatolites in Yellowstone National Park. Environ. Microbiol. 14, 1182–1197. http://dx.doi.org/10.1111/j.1462-2920.2012.02698.x.

Percak-Dennett, E.M., Beard, B.L., Xu, H., Konishi, H., Johnson, C.M., Roden, E.E., 2011. Iron isotope fractionation during microbial dissimilatory iron oxide reduction in simulated Archaean seawater. Geobiology 9, 205–220. http://dx.doi.org/10.1111/j.1472-4669.2011.00277.x.

Petrash, D.A., Robbins, L.J., Shapiro, R.S., Mojzsis, S.J., Konhauser, K.O., 2016. Chemical and textural overprinting of ancient stromatolites: timing, processes, and implications for their use as paleoenvironmental proxies. Precambr. Res. 278, 145–160. http://dx.doi.org/10.1016/j.precamres.2016.03.010.

Phoenix, V.R., Adams, D.G., Konhauser, K.O., 2000. Cyanobacterial viability during hydrothermal biomineralisation. Chem. Geol. 169, 329–338. http://dx.doi.org/10.1016/S0009-2541(00)00212-6.

Planavsky, N., Rouxel, O., Bekker, A., Shapiro, R., Fralick, P., Knudsen, A., 2009. Iron-oxidizing microbial ecosystems thrived in late Paleoproterozoic redox-stratified oceans. Earth Planet. Sci. Lett. 286, 230–242. http://dx.doi.org/10.1016/j.epsl.2009.06.033.

Planavsky, N., Rouxel, O.J., Bekker, A., Hofmann, A., Little, C.T.S., Lyons, T.W., 2012. Iron isotope composition of some Archean and Proterozoic iron formations. Geochim. Cosmochim. Acta 80, 158–169. http://dx.doi.org/10.1016/j.gca.2011.12.001.

Planavsky, N.J., Asael, D., Hofmann, A., Reinhard, C.T., Lalonde, S.V., Knudsen, A., Wang, X., Ossa, F.O., Pecoits, E., Smith, A.J.B., Beukes, N.J., Bekker, A., Johnson, T. M., Konhauser, K.O., Lyons, T.W., Rouxel, O.J., 2014. Evidence for oxygenic photosynthesis half a billion years before the Great Oxidation Event. Nat. Geosci. 7, 283–286. http://dx.doi.org/10.1038/ngeo2122.

Posth, N.R., Koehler, I., Swanner, E.D., Schroeder, C., Wellmann, E., Binder, B., Konhauser, K.O., Neumann, U., Berthold, C., Nowak, M., Kappler, A., 2013. Simulating Precambrian banded iron formation diagenesis. Chem. Geol. 362, 66–73. http://dx.doi.org/10.1016/j.chemgeo.2013.05.031.

Preston, L.J., Benedix, G.K., Genge, M.J., Sephton, M.A., 2008. A multidisciplinary study of silica sinter deposits with applications to silica identification and detection of fossil life on Mars. Icarus 198, 331–350. http://dx.doi.org/10.1016/j.icarus.2008.08.006.

Raiswell, R., Canfield, D.E., Berner, R., 1994. A comparison of iron extraction methods for the determination of degree of pyritisation and the recognition of iron-limited pyrite formation. Chem. Geol. 111, 101–110. http://dx.doi.org/10.1016/0009-2541(94)90084-1.

Rasmussen, B., Fletcher, I.R., Bekker, A., Muhling, J.R., Gregory, C.J., Thorne, A.M., 2012. Deposition of 1.88-billion-year-old iron formations as a consequence of rapid crustal growth. Nature 484, 498–501. http://dx.doi.org/10.1038/nature11021.

Rasmussen, B., Fletcher, I.R., Sheppard, S., 2005. Isotopic dating of the migration of a low-grade metamorphic front during orogenesis. Geology 33, 773–776. http://dx.doi.org/10.1130/G21666.1.

Rasmussen, B., Meier, D.B., Krapez, B., Muhling, J.R., 2013. Iron silicate microgranules as precursor sediments to 2.5-billion-year-old banded iron formations. Geology 41, 435–438. http://dx.doi.org/10.1130/G33828.1.

Reinhard, C.T., Planavsky, N.J., Lyons, T.W., 2013. Long-term sedimentary recycling of rare sulphur isotope anomalies. Nature 497. http://dx.doi.org/10.1038/nature12021.

Roh, Y., Zhang, C.L., Vali, H., Lauf, R.J., Zhou, J., Phelps, T.J., 2003. Biogeochemical and environmental factors in Fe biomineralization: magnetite and siderite formation. Clays Clay Miner. 51, 83–95. http://dx.doi.org/10.1346/CCMN.2003.510110.

Roscoe, S.M., 1968. Huronian rocks and uraniferous conglomerates in the Canadian Shield. Geol. Surv. Can. Pap. 68–40, 1–205.

Schopf, J.W., 2014. Geological evidence of oxygenic photosynthesis and the biotic response to the 2400–2200 Ma "Great Oxidation Event". Biochem. Mosc. 79, 165–177. http://dx.doi.org/10.1134/S0006297914030018.

Schopf, J.W., Kudryavtsev, A.B., Walter, M.R., Van Kranendonk, M.J., Williford, K.H., Kozdon, R., Valley, J.W., Gallardo, V.A., Espinoza, C., Flannery, D.T., 2015. Sulfur-cycling fossil bacteria from the 1.8-Ga Duck Creek Formation provide promising evidence of evolution's null hypothesis. Proc. Natl. Acad. Sci. U.S.A. 112, 2087–2092. http://dx.doi.org/10.1073/pnas.1419241112.

Severmann, S., Johnson, C.M., Beard, B.L., McManus, J., 2006. The effect of early diagenesis on the Fe isotope compositions of porewaters and authigenic minerals in continental margin sediments. Geochim. Cosmochim. Acta 70, 2006–2022. http://dx.doi.org/10.1016/j.gca.2006.01.007.

Shapiro, R.S., Konhauser, K.O., 2015. Hematite-coated microfossils: primary ecological fingerprint or taphonomic oddity of the Paleoproterozoic? Geobiology 1–16. http://dx.doi.org/10.1111/gbi.12127.

Skerman, V., Dementjeva, G., Carey, B., 1957. Intracellular deposition of sulfur by Sphaerotilus-Natans. J. Bacteriol. 73, 504–512.

Stefurak, E.J.T., Lowe, D.R., Zentner, D., Fischer, W.W., 2014. Primary silica granules-A new mode of Paleoarchean sedimentation. Geology 42, 283–286. http://dx.doi.org/10.1130/G35187.1.

Stokes, J., 1954. Studies on the filamentous sheathed iron bacterium Sphaerotilus-Natans. J. Bacteriol. 67, 278–291.

Takehara, M., Komure, M., Kiyokawa, M., Horie, K., Yokoyama, K., 2010. Detrital zircon SHRIMP U-Pb age of the 23 Ga diamictites of the Meteorite Bore Member in the south Pilbara, Western Australia, in: Geological Survey of Western Australia, Record 2010/18,. pp. 223–224

Thomazo, C., Ader, M., Philippot, P., 2011. Extreme 15N-enrichments in 2.73 Gyr ago sediments: evidence for a turning point in the nitrogen cycle. Geobiology 9, 107–120.

Thomazo, C., Pinti, D.L., Busigny, V., Ader, M., Hashizume, K., Philippot, P., 2009. Biological activity and the Earth's surface evolution: insights from carbon, sulfur, nitrogen and iron stable isotopes in the rock record. C.R. Palevol 8, 665–678. http://dx.doi.org/10.1016/j.crpv.2009.02.003.

Valley, J.W., 2001. Stable isotope thermometry at high temperatures. In: Valley, J. W., Cole, D.R. (Eds.), Stable Isotope Geochemistry. Mineralogical Soc Amer, Chantilly, pp. 365–413.

Van der Meer, M.T.J., Schouten, S., de Leeuw, J.W., Ward, D.M., 2000. Autotrophy of green non-sulphur bacteria in hot spring microbial mats: biological explanations for isotopically heavy organic carbon in the geological record. Environ. Microbiol. 2, 428–435. http://dx.doi.org/10.1046/j.1462-2920.2000.00124.x.

Van Kranendonk, M.J., Schopf JW, Grice K, Walter M, Pages A, Kudryavtsev AB, Gallardo VA, Espinoza C, Melendez I, Lepland A (2012) A 2.3 Ga sulfuretum at the GOE: microfossil and organic geochemistry evidence from the Turee Creek Group, Western Australia. AbSciCon conference, Atlanta, http://absicon2012.arc.nasa.gov/abstracts/.

Van Kranendonk, M.J., 2010. Three and a half billion years of life on Earth: a transect back into deep time: Geological Survey of Western Australia, Record 2010/21.

Van Kranendonk, M.J., Mazumder, R., Yamaguchi, K.E., Yamada, K., Ikehara, M., 2015. Sedimentology of the Paleoproterozoic Kungarra Formation, Turee Creek Group, Western Australia: a conformable record of the transition from early to modern Earth. Precambr. Res. 256, 314–343. http://dx.doi.org/10.1016/j.precamres.2014.09.015.

Vandenbroucke, M., Largeau, C., 2007. Kerogen origin, evolution and structure. Org. Geochem. 38, 719–833. http://dx.doi.org/10.1016/j.orggeochem.2007.01.001.

Wacey, D., McLoughlin, N., Kilburn, M.R., Saunders, M., Cliff, J.B., Kong, C., Barley, M. E., Brasier, M.D., 2013. Nanoscale analysis of pyritized microfossils reveals differential heterotrophic consumption in the $\sim$1.9-Ga Gunflint chert. Proc. Natl. Acad. Sci. U.S.A. 110. http://dx.doi.org/10.1073/pnas.1221965110.

Wacey, D., Menon, S., Green, L., Gerstmann, D., Kong, C., Mcloughlin, N., Saunders, M., Brasier, M., 2012. Taphonomy of very ancient microfossils from the similar to 3400 Ma Strelley Pool Formation and similar to 1900 Ma Gunflint Formation: new insights using a focused ion beam. Precambr. Res. 220, 234–250. http://dx.doi.org/10.1016/j.precamres.2012.08.005.

Wacey, D., Saunders, M., Roberts, M., Menon, S., Green, L., Kong, C., Culwick, T., Strother, P., Brasier, M.D., 2014. Enhanced cellular preservation by clay minerals in 1 billion-year-old lakes. Sci. Rep. 4, 5841. http://dx.doi.org/10.1038/srep05841.

Widdel, F., Schnell, S., Heising, S., Ehrenreich, A., Assmus, B., Schink, B., 1993. Ferrous iron oxidation by anoxygenic phototrophic bacteria. Nature 362, 834–836. http://dx.doi.org/10.1038/362834a0.

Wiesli, R.A., Beard, B.L., Johnson, C.M., 2004. Experimental determination of Fe isotope fractionation between aqueous Fe(II), siderite and "green rust" in abiotic systems. Chem. Geol. 211, 343–362. http://dx.doi.org/10.1016/j.chemgeo.2004.07.002.

Williford, K.H., Ushikubo, T., Schopf, J.W., Lepot, K., Kitajima, K., Valley, J.W., 2013. Preservation and detection of microstructural and taxonomic correlations in the carbon isotopic compositions of individual Precambrian microfossils. Geochim. Cosmochim. Acta 104, 165–182. http://dx.doi.org/10.1016/j.gca.2012.11.005.

Williford, K.H., Van Kranendonk, M.J., Ushikubo, T., Kozdon, R., Valley, J.W., 2011. Constraining atmospheric oxygen and seawater sulfate concentrations during Paleoproterozoic glaciation: in situ sulfur three-isotope microanalysis of pyrite from the Turee Creek Group, Western Australia. Geochim. Cosmochim. Acta 75, 5686–5705. http://dx.doi.org/10.1016/j.gca.2011.07.010.

Wilson, J.P., Fischer, W.W., Johnston, D.T., Knoll, A.H., Grotzinger, J.P., Walter, M.R., McNaughton, N.J., Simon, M., Abelson, J., Schrag, D.P., Summons, R., Allwood, A., Andres, M., Gammon, C., Garvin, J., Rashby, S., Schweizer, M., Watters, W.A., 2010. Geobiology of the late Paleoproterozoic Duck Creek Formation, Western Australia. Precambr. Res. 179, 135–149. http://dx.doi.org/10.1016/j.precamres.2010.02.019.

Yamaguchi, K.E., Oguri, K., Ogawa, N.O., Sakai, S., Hirano, S., Kitazato, H., Ohkouchi, N., 2010. Geochemistry of modern carbonaceous sediments overlain by a water mass showing photic zone anoxia in the saline meromictic Lake Kai-ike, southwest Japan: I. Early diagenesis of organic carbon, nitrogen, and phosphorus. Palaeogeogr. Palaeoclimatol. Palaeoecol. 294, 72–82. http://dx.doi.org/10.1016/j.palaeo.2009.10.024.

Conclusion générale et perspectives

Les microstructures organiques (microfossiles, tapis bactériens fossiles) représentent une part importante du registre fossile précambrien. Les études de ces microstructures ont apporté de nombreuses informations pour comprendre comment la vie microbienne a évolué au cours du précambrien. L'utilisation de nombreuses techniques d'analyse à micro- et nano-échelles est nécessaire pour confirmer la nature biologique des microstructures organiques préservées dans les roches précambriennes. De même, ces diverses études ont aussi comme objectif de contraindre la nature et les métabolismes des micro-organismes préservés dans ces roches. Cependant, les propriétés moléculaires de ces microstructures organiques sont difficilement accessibles et nécessitent une quantité importante de matière organique. Ainsi la spectroscopie ionique secondaire à temps de vol (ToF SIMS), technique d'analyse d'extrême surface offre la possibilité d'obtenir de telles informations avec de faibles quantités de matière organique et sans détruire des échantillons précieux.

L'un des premiers objectifs de cette thèse était de mettre au point un nouveau protocole de préparation d'échantillon permettant d'observer des microstructures organiques sensibles aux contaminations. La préparation de ces tranches épaisses sans résine permet d'observer des microstructures organiques préservées dans des roches siliceuses (cherts) en microscopie transmise optique. De plus l'absence de résine offre la possibilité de réaliser de nombreux nettoyages avec divers solvants organiques. Après ablation ionique à l'argon monoatomique permettant de retirer la nano-couche de contamination aérienne, les analyses ToF-SIMS ont montré la possibilité d'effectuer des analyses moléculaires sur des structures organiques préparées avec notre nouveau protocole.

Ensuite, la caractérisation moléculaire et à micro-échelle du kérogène (partie insoluble de la matière organique) provenant de tapis microbiens fossiles phanérozoïques sulfurisés d'Orbagnoux et archéens de Strelley Pool a été effectuée à la ToF-SIMS. L'analyse de références purs de molécules aromatiques et aliphatiques était nécessaire afin de documenter les différents profils de fragmentations moléculaires et d'effectuer des semi-quantifications. En analysant les profils de fragmentations et divers rapports de fragments organiques, nous avons renseigné le caractère aliphatique et aromatiques de ces différents tapis microbiens fossiles. Grâce à cette méthodologie des micro-hétérogénéités présentes dans des veines ont été détectées dans les échantillons d'Orbagnoux et identifiés comme étant probablement la partie soluble, bitumineuse de la matière organique préservée dans ces tapis microbiens. Ces analyses et semi-quantifications ont aussi mis en évidence le caractère plus aromatique de la matière organique présente dans les roches archéennes de Strelley Pool par rapport à celle préservée dans les tapis microbiens d'Orbagnoux plus récents.

Au cours de cette thèse, l'étude de la matière carbonée constituant des microfossiles de type Bitter Springs provenant de la formation de Draken, d'âge néoprotérozoïque et préservés dans des cherts a été menée à micro- et nano-échelle. Cet assemblage fossilifère est composé de nombreuses morpho-espèces de cyanobactéries et de probables eucaryotes dont la morphologie est exceptionnellement bien préservée. Cependant, la spectroscopie Raman indique que la matière organique composant ces microfossiles est très mature. Cette maturité a été confirmée par les analyses spectroscopiques effectuées à nano-échelles au synchrotron indiquant que les groupements aromatiques dominent. Malgré l'absence de signatures moléculaires diagnostiques et d'hétérogénéités moléculaires en spectroscopies Raman et XANES, les analyses ultrastructurales effectuées sur une grande variété de microfossiles ont apportés des informations sur la taxonomie et la taphonomie des microstructures préservées dans cet assemblage. Ainsi pour la première fois grâce ces observations à nano-échelle, les structures internes (membranes cellulaires internes présumées, probablement des thylakoïdes) de cyanobactéries fossiles de type chroococcales ont pu être observées et identifiées. L'ultrastructure des gaines formant les microfossiles cyanobactériens du genre Polybessurus a aussi été caractérisée pour la première fois. Les analyses à nano-échelles des parois de microfossiles sphéroïdes du genre Myxococcoides ont mis en évidence la présence d'une structure en piliers organiques jamais observés dans le registre fossile précambrien pouvant être d'origine eucaryote ou cyanobactérienne. Enfin, les observations à nano-échelle des microfossiles d'eucaryotes (amibes à thèques en forme de vase) ont montré que leurs parois sont formées de deux structures organiques distinctes : une paroi interne d'épaisseur variable difficilement observable en microscopie optique et une paroi dense formant une structure réticulée externe. De tels résultats et observations sont importants pour les futures investigations qui seront menées sur des microfossiles plus anciens datant de l'Archéen ou du Paléoprotérozoïque.

Enfin, des microfossiles de type Gunflint provenant d'Australie (Turee Creek Group, 2.3Ga) ont aussi été caractérisés à l'aide de nombreuses techniques. Cet assemblage de microfossiles est principalement composé de différentes morpho-espèces de filaments qui sont plus ou moins associées à des carbonates de fer. Les analyses à micro et nano-échelles ont mis en évidence l'impact de la formation des carbonates de fer sur la préservation des structures organiques composant ces microfossiles. La combinaison de ces observations avec les résultats obtenus sur les isotopes du fer suggère que ces microfossiles étaient des bactéries qui ont oxydées le fer au cours du grand bond d'oxydation.

Les travaux de caractérisation à micro et nano échelles effectués pendant cette thèse ont apporté de nombreuses informations sur les structures organiques préservées dans les différentes roches étudiées. En complément des différents rapports introduits sur les données obtenues à la ToF SIMS, des analyses statistiques (Analyses en Composantes Principales ou ACP) représentent le premier axe de travail à mener afin de trouver des facteurs de corrélation sur l'ensemble des données obtenues. Cependant, la caractérisation moléculaire des microfossiles précambriens à l'aide de la ToF SIMS n'a pas été menée à terme du fait de l'extrêmement faible intensité du signal du spectre de masse obtenu. Ces difficultés d'analyse inhérentes à la taille des microfossiles observés (aux parois souvent composées de nanograins de matière organique) pourront être franchies pour des fossiles aux structures organiques plus épaisses (exemples : certains palynomorphes, principalement eucaryotes). Ces analyses pourront être combinées à l'utilisation de clusters d'ions (Ar_{2500}^+, $(H_2O)_n^+$, $(CH_4)_n^+$…) pour nettoyer la surface des échantillons sans perte de signal importante. Ceci représente une des perspectives les plus importantes de ces travaux de thèse. La recherche au synchrotron d'hétérogénéités préservées au sein des structures de microfossiles issues d'assemblages précambriens similaires semble aussi être une perspective intéressante pour contraindre la nature des ultrastructures observées ici. Ces analyses à micro- et nano-échelles pourront être complétés par l'étude de la composition isotopique ($\delta^{13}C$) de la matière organique composant les microfossiles par microsonde ionique afin d'identifier les différents métabolismes présents dans ces assemblages précambriens. Enfin, l'analyse 3D par microscopie confocale à laser ou l'imagerie 3D par microscopie électronique à balayage à faisceau d'ions focalisé (MEB-FIB) des microfossiles présents dans les formations de Draken, pourront compléter les observations effectuées sur les structures à nano échelle.

Annexes

Nanonascale analysis of preservation of ca. 2.1 Ga old Francevillian microfossils, Gabon

Precambrian Research 301 (2017) 1–18

Contents lists available at ScienceDirect

Precambrian Research

journal homepage: www.elsevier.com/locate/precamres

Nanoscale analysis of preservation of ca. 2.1 Ga old Francevillian microfossils, Gabon

Stellina G. Lekele Baghekema[a,b], Kevin Lepot[a,*], Armelle Riboulleau[a], Alexandre Fadel[a], Alain Trentesaux[a], Abderrazak El Albani[b,*]

[a] Université de Lille, CNRS, Université Littoral Côte d'Opale, UMR 8187, LOG, Laboratoire d'Océanologie et de Géosciences, 59000 Lille, France
[b] Université de Poitiers , Institut de Chimie des Milieux et Matériaux de Poitiers, CNRS UMR 7285, 86073 Poitiers, France

ARTICLE INFO

Keywords:
Microfossils
Proterozoic
Gunflint type
Francevillian
Gabon
Eoastrion

ABSTRACT

The FC Formation of the Francevillian of Gabon displays the oldest Gunflint-type assemblage of microfossils that is hosted in shallow-water stromatolites. The FC Formation was deposited between 2.14 and 2.08 billion years ago (Ga), after the Great Oxygenation Event (~2.4–2.3 Ga) and near the end of the Lomagundi event (~2.3–2.06 Ga). Although they have been used as a benchmark for the search for older microfossils, the nature of Gunflint-type microfossils has remained elusive due to their simple shapes, their small sizes, and their alteration. Here, we report the first nanoscale study of Francevillian Gunflint-type microfossils. We used a combination of Raman spectroscopy, palynology, *in situ* focused ion beam sectioning, and analytical electron microscopy. In spite of the relatively high thermal maturity of organic matter (inferred peak burial temperature ~296 ± 30 °C), spherical cell walls (*Huroniospora*) and filamentous sheaths (*Gunflintia minuta*: ≤3 μm in diameter, and broader filaments) are preserved. Organic matter in/on cell walls and sheaths, is associated with nanocrystalline quartz, whereas coarser quartz crystals fill and surround the microfossils. This pattern, likely inherited from recrystallization of texturally heterogenous opal generations, could have allowed the observed preservation of organic structures and limited migrations of organic matter. Moreover, we demonstrate the preservation of thick-sheathed broad (> 3 μm) filaments for the first time in a stromatolitic Gunflint-type assemblage; such thick sheaths are common in cyanobacteria, but not in other filamentous bacteria. We distinguished two types of star-shaped organic microstructures (*Eoastrion*) but found no diagnostic evidence for/against a microfossil nature at the nanoscale. Furthermore, we show that titanium is commonly associated with organic structures of microfossils, likely as a result of diagenetic mineralization. In contrast, iron-rich nanocrystals associated with microfossils occur in quartz, not in organic matter, and could possibly represent recrystallized biominerals.

1. Introduction

The Paleoproterozoic era (2.45–1.6 Ga, billion years) was the scene of some of the most dramatic environmental changes undergone by Earth. This era includes the Great Oxygenation Event (the first significant increase in pO_2 in the atmosphere ca. 2.4–2.3 Ga), followed by the Lomagundi event (~2.3–2.06 Ga), a period of intense O_2 release by increased primary production, that was in turn likely followed by a decline in pO_2 (Canfield et al., 2013; Lyons et al., 2014). The Paleoproterozoic era was characterized by stratified seawater that locally and/temporally fluctuated between anoxic ferruginous, euxinic and oxygenated (Lyons et al., 2014). These environmental changes have likely been driven by a strong coupling between geodynamics (Condie et al., 2009; Rasmussen et al., 2012) and biological evolution (Knoll, 2003). Fossil eukaryotes and macroalgae can be found in rocks 1.87–1.6 Ga (Han and Runnegar, 1992; Knoll et al., 2006; Lamb et al., 2009; Schneider et al., 2002) and possible macrofossils are described in ~2.1 Ga rocks (El Albani et al., 2014, 2010). In contrast, before ~1.8 Ga, the fossil record is dominated by Gunflint-type microfossil assemblages, which are commonly found in stromatolitic cherts (Barghoorn and Tyler, 1965; Schopf and Klein, 1992). The finding of microfossils in the 1.88 Ga Gunflint Iron Formation of Ontario in the 1950's (Tyler and Barghoorn, 1954) stirred the search for the earliest traces of life (Schopf and Klein, 1992). Gunflint-type assemblages host enigmatic microfossils, among which the dominant morphospecies have been variously interpreted as possible cyanobacteria (Awramik and Barghoorn, 1977; Barghoorn and Tyler, 1965; Knoll et al., 1978; Lepot et al., 2017), chemotrophic Fe-oxidizing bacteria (Cloud, 1965;

---

[*] Corresponding authors.
E-mail addresses: kevin.lepot@univ-lille1.fr (K. Lepot), abder.albani@univ-poitiers.fr (A. El Albani).

http://dx.doi.org/10.1016/j.precamres.2017.08.024
Received 6 May 2017; Received in revised form 1 August 2017; Accepted 28 August 2017

Planavsky et al., 2009), and/or heterotrophs (Strother and Tobin, 1987). They also include more enigmatic forms (Barghoorn and Tyler, 1965; Cloud, 1965) as well as evidence of heterotrophic bacterial sulfate reduction (Wacey et al., 2013).

Paleoproterozoic Gunflint-type microfossils have been used as a benchmark for the search and identification of Archean microfossils. Paleoarchean cherts bearing putative microfossils usually have suffered higher metamorphic grades than Proterozoic cherts and often have been subjected to hydrothermal alteration, including hydrothermal transport of organic matter in fractures (Buick, 1990). This, together with the possibility of accreting/displacing organic matter onto cell-mimicking mineral microstructures fueled controversy (Brasier et al., 2005; Buick, 1990; García Ruiz et al., 2002) over the authenticity of the oldest putative fossils (Brasier et al., 2002; Schopf, 1993). Even the biogenicity of the dominant microfossils of Gunflint-type assemblages (*Gunflintia*: filaments), *Huroniospora* (spheres) and *Eoastrion* (star-shaped) has been recently questioned as possible abiotic shapes formed by templating of organic matter onto fossil-mimicking minerals (Cosmidis and Templeton, 2016; García Ruiz et al., 2002). Chain-of-beads and spherical structures similar to *Gunflintia* and *Huroniospora*, respectively, may form during abiotic, mineral-free auto-assembly of organic molecules (Fox and Yuyama, 1963). However, the biogenicity of *Gunflintia* and *Huroniospora* morphospecies is supported by their distribution in stromatolites with respect to clastic fragments and laminae (Knoll et al., 1988; Lanier, 1986) that is often similar to the distribution of microorganisms in modern stromatolites (Reid et al., 2000). However, other possible microfossils such as *Eoastrion* remain highly problematic.

The main problem of early- to mid-Paleoproterozoic microfossils is their simple shapes (e.g. spheres, filaments, stars) that provide little taxonomic information. Small size and post-mortem (taphonomic) alteration of the microfossils blur the information that can be derived using conventional microscopy. Transmission electron microscopy (TEM) has recently been used to investigate the biogenicity of Proterozoic microfossils (Kempe et al., 2005; Moreau and Sharp, 2004; Wacey et al., 2012). This provided important constraints in deciphering the evolution of the organic matter and silicification processes and observations that are consistent with silicification and diagenesis of cellular structures, including in microfossils of the Gunflint Iron Formation. The latter has the lowest organic matter maturity (Alleon et al., 2016; Schopf et al., 2005) and, hence, displays the best preserved Gunflint-type microfossils (Barghoorn and Tyler, 1965). Investigation of more altered Gunflint-type assemblages could provide a better understanding of diagenetic and metamorphic transformations, hence providing a closer connection with the even more mature putative microfossils of the Archean.

Microfossils in the Paleoproterozoic Franceville basin (2.2–2.0 Ga) were first described by Bertrand-Sarfati and Potin (1994). They occur in stromatolitic cherts of the siliceous FC Formation (Amard and Bertrand-Sarfati, 1997; Bertrand-Sarfati and Potin, 1994). They comprise microfossils that define Gunflint-type assemblages, with filamentous *Gunflintia*, coccoid *Huroniospora*, star-shaped *Eoastrion*, as well as the tubular-budding *Archeorestis*. These microfossils (2.14–2.08 Ga) therefore represent the oldest stromatolitic assemblage of the Gunflint type (Amard and Bertrand-Sarfati, 1997; Cloud and Morrison, 1980; Knoll and Simonson, 1981; Oehler, 1977; Schopf and Prasad, 1978; Walter et al., 1976; Yun, 1984). In addition, the FC stromatolites are the only Gunflint-type assemblage hosting *Archaeoellipsoides* microfossils that might represent cyanobacterial akinetes (Amard and Bertrand-Sarfati, 1997). The latter suggests that heterocystous cyanobacteria with the ability to fix N_2 in substantially oxygenated conditions existed by this time (Tomitani et al., 2006). Previous studies (Amard and Bertrand-Sarfati, 1997; Bertrand-Sarfati and Potin, 1994) on these Francevillian microfossils were based on optical microscopy of petrographic thin sections on outcrop and drill core samples.

This study presents contributions to the understanding of the morphology, texture and preservation of these key Paleoproterozoic microfossils in the stromatolitic cherts of the FC Formation using integrated, state-of-the-art analytical techniques. The morphology and ultrastructure of these microfossils were determined by petrographic observations at the micrometric and nanometric scales by coupling confocal laser scanning microscopy (CLSM) (Schopf and Kudryavtsev, 2009), Raman micro-spectroscopy, scanning electron microscopy (SEM) on palynological extracts, and scanning transmission electron microscopy (STEM) on focused ion beam (FIB) sections (Moreau and Sharp, 2004; Wacey et al., 2012). Thus we document the mineralogical textures, the behavior of kerogen and the mineralizations associated with microfossils in order to better constrain the preservation, biogenicity, and affinity of these diverse microfossils.

2. Geological setting

Located in South East part of Gabon, the Francevillian Series is a low deformation Palaeoproterozoic sedimentary succession that was deposited between 2.2 and 2.0 Ga (Préat et al., 2011). The Francevillian deposits are located in four sub-basins (Booué, Lastourville, Franceville and Okandja) formed by a series of normal faults and delimited by Ondili and Amiéni horsts (Gauthier-Lafaye, 1986; Préat et al., 2011). The Franceville sub-basin covers an approximate area of 35,000 km^2 (Fig. 1), and is the basin where the stratigraphic column for the Franceville Series was established (Weber, 1969). Four different lithostratigraphic formations (FA, FB, FC, and FD) have been recognized in the Franceville basin.

The evolution of the Franceville basin has been linked with the rupturing of the Archean blocks of the West Central African (WCA) Belt during the Eburnean orogeny (Feybesse et al., 1998; Préat et al., 2011). The Archean basement is composed of granitoids and gneisses that were emplaced between 3.0 and 2.5 Ga (Gauthier-Lafaye, 2006; Gauthier-Lafaye and Weber, 1989; Préat et al., 2011; Thiéblemont et al., 2009). The first phase of basin opening was characterized by the breaking of the Archean continental blocks, which was accompanied by the development of NW-SE and N-S trending faults, subsidence and deposition of the continental and shallow marine FA Formation sediments. Rapid subsidence along the NW-SE and N-S grabens led to the deposition of fine-grained clastic and chemical sedimentary rocks of the FB and FC formations, respectively. Further expansion of the basin due to tectonic instability resulted in the deposition of volcano-sedimentary rocks of FD Formation (Gauthier-Lafaye, 1986; Gauthier-Lafaye and Weber, 1989, 2003). The FA Formation represents the basal rock units of the Francevillian Series and unconformably rests on the Archean crystalline basement rocks (Bouton et al., 2009; Gauthier-Lafaye, 1986). It comprises mainly fluvial sandstones, followed by fluvio-deltaic sediments and marine sediments towards the top. It contains all the uranium deposits in the basin and also hosts the famous natural nuclear reactors at Oklo (Gauthier-Lafaye and Weber, 1989, 2003).

The FB Formation displays a variable thickness from 300 to 1000 m and has the characteristics of marine sedimentation. It is divided into two major groups: FB1 and FB2 (Azziley Azzibrouck, 1986; Pambo, 2004). The FB1 is composed mainly of black shales and silts containing varying amounts of dolomite and kerogen. Manganese deposits locally occur in the upper part of FB1. FB2 consists of fine-grained sandstones overlain by laminated black shales and siltstones where macrofossils were found (El Albani et al., 2010, 2014).

The FC Formation has a thickness varying between 10 m and 50 m and a wide geographical extension; it constitutes a marker level in the Francevillien. Deposits of the FC Formation often present an angular discordance with the underlying layers and seal the tectono-sedimentary activity of Francevillien B (Bouton et al., 2009; Thiéblemont et al., 2009). According to Bouton et al. (2009) the limits of the FC Formation are not clear because the silicification which allows identifying the formation on the outcrop extends to underlying layers of FB. Similarly, for Gauthier-Lafaye and Weber (2003) the FC Formation is not

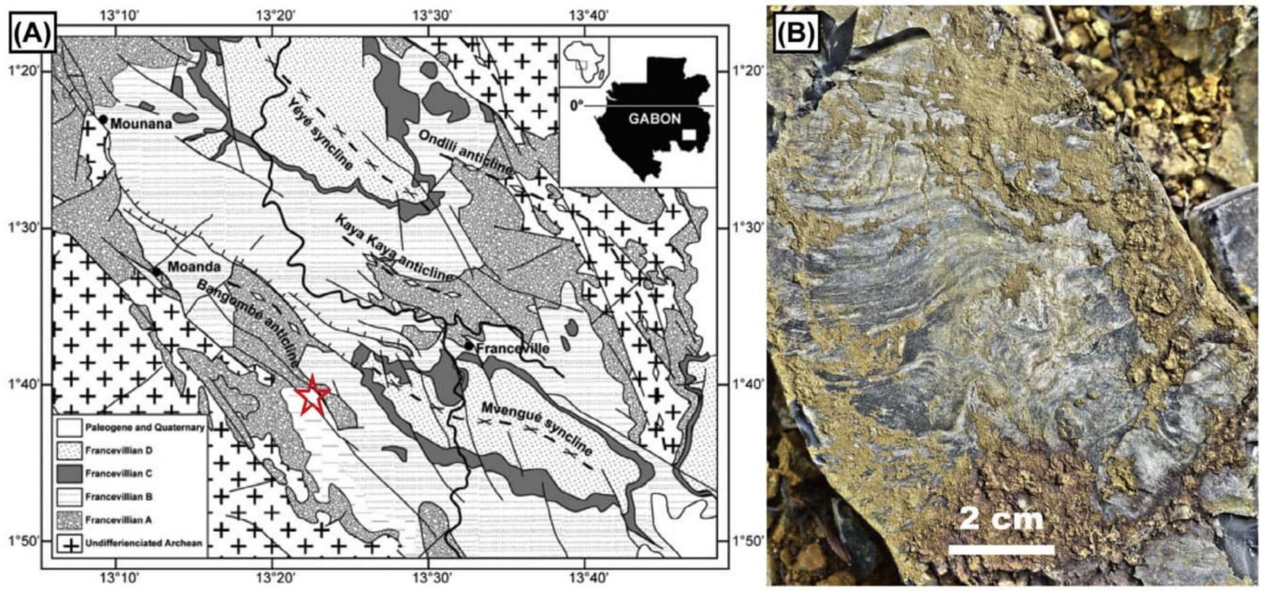

Fig. 1. Geological Context. (A) Structural geological map of the Francevillian basin, adapted from Bouton et al. (2009). Location of the SUCAF outcrop with studied microfossils is indicated by the star. (B) Outcrop picture of a stromatolite at the SUCAF locality.

synchronous: it covers the FB Formation in the central parts of the basin, while in the heights separating the Franceville and Okandja basins, a condensed series that appears equivalent to the FB and FC set rests on the FA sandstone and on the Archean basement (Weber et al., 2016). The FC Formation is composed of massive evaporitic dolomite, thick bands of cherts and stromatolitic cherts interstratified with black shales (Bertrand-Sarfati and Potin, 1994; Bouton et al., 2009; Gauthier-Lafaye and Weber, 1989, 2003; Thiéblemont et al., 2009; Weber et al., 2016; Weber and Gauthier-Lafaye, 2013). Its monotonous appearance due to silicification masks facies heterogeneity. The structures necessary for the reconstruction of the sedimentary environments of the FC Formation are thus difficult to find. However, new data reveal abundance and omnipresence of stromatolites, thus evoking shallow, intertidal to supratidal environments. Column-shaped stromatolites are associated to oncoids and oolithes. Between the most important stromatolitic buildings are placed oncoid rudstones and stromatolite debris indicating periodically agitated media. Microbial veils are also present at the limits of laminations with regular centimetric rounds of stromatolites (Bouton et al., 2009; Thiéblemont et al., 2009). Laterally, the formation passes to evaporatic sabkhas (base of FC at Djibalonga) and to anoxic lagoons, where shales rich in organic matter and sometimes containing gypsum were deposited. The presence of these stromatolites evidence a very low bathymetry. On the outcrop, the stromatolites occur in close contact and show nipple, dome and cauliflower shapes. They present laminae in plane section and concentric structures on the surface (Bouton et al., 2009; Ngombi-Pemba et al., 2014). The silica forming cherts could be of volcanic origin, as suggested by the presence of acidic volcanic ashes interlayered between the cherts (Weber, 1969).

The FD Formation consists of black shales, silicified rhyolitic tuffs, and epiclastic sandstones interbedded with shales in the upper part (Gauthier-Lafaye and Weber, 2003; Thiéblemont et al., 2009).

Welded tuffs near the top of the FD unit yield a U-Pb age of 2083 ± 6 Ma (Canfield et al., 2013). Intrusive volcanics in the lower part of the Francevillian series yielded imprecise ages, with a Rb/Sr age of 2143 ± 140 Ma (Bonhomme et al., 1982) and an U/Pb age of 2027 ± 55 Ma (Moussavou and Edou-Minko, 2006). Diagenetic illites of the FB (top of the FB1b subunit) yielded a Sm-Nd age of 2099 ± 115 Ma (Bros et al., 1992). Altogether, these radiometric data indicate that the studied FC stromatolites deposited during the Lomagundi event ~2.2–2.08 Ga ago, likely near the end of this event.

3. Samples and methods

3.1. Samples

The studied samples (SUC-R-5, SUC-R-5-LE3 and SUC-R-4) are from a surface outcrop close to sugarcane cultures of the SUCAF group, south of Bangombé anticline (S01°40.522′; E13°22.386′) at the edge of the Franceville basin and within the FB Formation [Fig. 1A; (Bouton et al., 2009)]. The collected cherts for this study are a few centimeters thick, and show small domes and concentric structures on the surface of the rock with visible laminae along cutting planes (Fig. 1B). The samples are mostly black and contain well preserved silicified stromatolites. These samples were studied in the form of uncovered thin section (SUC-R-5), thick section (SUC-R-5-LE3), and palynological extract (SUC-R-4).

3.2. Methods

3.2.1. Optical microscopy

A polished thin section ca. 50 µm-thick, a polished section ~ 400 µm thick and a palynological extract were prepared for observation of samples SUC-R-5, SUC-R-5-LE3 and SUC-R-4, respectively. These samples were observed in transmitted, plain and polarized light and reflected light using an Olympus BX60 microscope equipped with a 16 Mpixel SPOT Flex camera at Laboratoire d'Océanologie et de Géosciences, Université de Lille. General pictures of large areas and of the whole sections were acquired as mosaics and stitched with Microsoft Image Composite Editor. Multiplan images were assembled using Combine ZP (software by Alan Hadley) from stacks of photomicrographs taken at focal depth intervals of 1.5 µm (1.5 µm corresponds to one graduation on the micrometer screw), starting from the surface of the section. The obtained images were used as support for further microfossil analyses using SEM, and preparation of FIB sections for STEM.

3.2.2. Raman spectroscopy

The Raman spectra of the microfossils were obtained using a Horiba Jobin Yvon LabRam HR800UV Raman micro-spectrometer at Laboratoire d'Océanologie et de Géosciences, Université de Lille. The spectra were acquired with a 532 nm laser focused through an Olympus BX41 microscope with ×50 (long working distance NA = 0.75) and ×100 (NA = 0.9) objectives for a duration varying between 3 and

5 min. In order to avoid heating damage to organic matter, filters were used to limit incident laser power to ~0.5 mW, and targets were in focus several micrometers below the polished surface. The Raman spectra show five bands/shoulders G, D1, D2, D3, and D4, which are diagnostic of medium-grade carbonaceous material (Kouketsu et al., 2014). These spectral features were fitted using a mixture of Gaussian, Lorentzian and pseudo-Voigt mathematical functions in the software PeakFit. We used the fitting method F of Kouketsu et al. (2014), which is best suited to observed spectral characteristics (a 1600 cm^{-1}/1350 cm^{-1} intensity ratio lower than 1.5 and the presence of D4). For the calculation of the geo-temperatures we used Equation 1 of Kouketsu et al. (2014): T (°C) = −2.15(FWHM-D1) + 478. FWHM represent the full width at half maximum.

3.2.3. *Confocal laser scanning microscopy (CLSM)*

The microfossils in petrographic thin section were analyzed with a Zeiss LSM 780 (Carl Zeiss) confocal head connected to a Z1 Zeiss observer microscope at BiCeL laboratory, Université de Lille. The images are acquired through a ×60 (numerical aperture 1.45) oil immersion objective using 488 nm laser excitation and collecting the reflectance + fluorescence signals over the entire visible spectrum, thus enabling kerogen imaging. Data acquisition was performed using the software ZEN 2012. Images were processed using the software Fiji to extract single confocal slices that were combined as multiplane images using CombineZP. To prevent contamination by immersion oil, CLSM was performed after extraction of focused ion beam sections as described below.

3.2.4. *Scanning electron microscopy (SEM)*

The thin section was covered with an Au-Pd film and observed with a FEI Quanta 200 SEM equipment coupled with X Flash Bruker 3001 energy dispersive spectroscopy (EDS) detector at Laboratoire d'Océanologie et de Géosciences, Université de Lille. Mineral observations and chemical analyses were obtained in secondary electron (SE) and backscattered electron (BSE) modes operated at 15–20 kV and working distance of 10 mm. SEM images were combined with transmitted/reflected optical photomicrographs to precisely locate microfossils for FIB.

3.2.5. *Focused ion beam (FIB) preparation of TEM samples*

Ultrathin sections of microfossils in their quartz matrix were cut using a Dual Beam Strata 235 FEI FIB at Institut d'Électronique, de Microélectronique et de Nanotechnologie, Université de Lille. For each target, a zone of interest 10–20 µm long is covered with a micrometer-thick platinum layer to protect the surface of the material during thinning. The area of interest is thinned with a gallium ion beam that operates with a voltage of 30 kV and a current of 23 nA. Differently from the method of Wacey et al., (2012) and Schiffbauer and Xiao, (2011) thinning is done at an angle of 40° to obtain a tapered section containing the area of interest at the center. The resulting section ca. 2 µm thick was cut out and, using a micromanipulator, was fixed on a copper TEM grid by depositing platinum at contacts between the section and the grid. The micromanipulator is detached and the section is thinned to ~100 nm or ~300 nm thick with decreasing currents. Superficial amorphous nano-layer is removed using an ion beam of 5 kV at a 50° angle.

3.2.6. *Transmission electron microscopy (TEM and STEM)*

TEM analysis was performed on a Philips CM30 equipped with a LaB6 filament operating at 300 kV at Centre Commun de Microscopie, Université de Lille. It is equipped with a XFlash 6 Ti60 Bruker EDS (energy dispersive X-ray spectrometer) detector and operated with Quantax 4000 software for chemical mapping. STEM images were obtained in "bright field" and "dark field". They exhibit a contrast dependent on the chemical composition as well as crystal orientation (diffraction contrast, more important in bright-field images), and highlight grain boundaries. The beam was focused on analysis spots at an inclination of 20°, 13 nm spot size, and a transmission beam current of 4 nA. The time of acquisition of chemical maps depends on the resolution and size of analyzed area, ranging from 10 to 25 min. Bright-field transmission electron microscopy (TEM) images and selected area electron diffraction (SAED) patterns were collected using an Aurius CCD camera and the software Digital Micrograph and indexed using JEMS (software by P. Stadlemann). We used a cryo-trap (cooled with liquid N_2) to limit electron beam deposition of volatile contaminants.

3.2.7. *Palynology*

Sample SUC-R-4 was prepared according to a modified version of the procedure established by Grey (1999). About 50 g of the sample was washed and crushed into pieces of about 2 mm. The extraction was carried out according to the following steps: (1) decarbonation in boiling 10% chloridic acid (HCl) until the end of the reaction; (2) removal of silicates with 200 ml of 70% cold fluorodric acid until the end of the reaction; (3) removal of neoformed minerals such as fluorides in HCl (10%); (4) oxidation with 200 ml of nitric acid until brown fumes disappeared; (5) separation in three fractions using filters (> 27 µm, 27–11 µm and < 11 µm); (6) removal of water and storage in ultrapure ethanol, (7) deposition onto a glass slide for optical microscopy. The extract was observed with aforementioned optical microscope, Raman and SEM (with Au-Pd coating) protocols.

4. Results

4.1. *Mineralogy of the cherts*

The analyzed sample (SUC-R-5) is composed mainly of quartz. Stratification is defined by the distribution of zoned rhombohedral carbonates and laminae rich in kerogen (Fig. 2A). These laminae contain abundant microfossils as described below (Fig. 2C–E). Quartz crystals are almost essentially sub-micrometric to micrometric (~90%), while small amounts of fibrous- and coarse (> 20 µm) quartz are also present. Fibrous quartz forms radial structures. Megaquartz occurs as clusters of coarse crystals. Carbonates occur dispersed in the quartz matrix and concentrate in specific laminae (Fig. 2B). The carbonates are Fe-rich dolomites, and calcite. Some carbonates have regular contours while others appear altered and zoned. The SEM-EDS spectra (not shown) indicate that the zoned carbonates are composed of dolomite in the center and are enriched in iron in the outer zone. Cubic pyrites are rarely observed in the cherts, usually near carbonates. Fluoroapatite, iron and manganese oxides occur as microscopic grains. Mn-and Fe-oxides sometimes substitute for carbonates. Clays (probably chlorites) occur as streaks. SUC-R-5-LE3 and SUC-R-4 have the same characteristics as SUC-R-5 described above.

4.2. *Nature and geothermometry of carbonaceous material*

Raman spectra were acquired on the dark brown carbonaceous materials that form walls and sheaths of microfossils. The same Raman spectrum as displayed in Fig. 3 characterized all types of microfossils (filament, sphere, star-like) as well as shapeless kerogen, whatever the context (*in situ* in the chert and after palynological preparation). These Raman spectra reveal five main bands between 1000 and 2000 cm^{-1} that are related to kerogen (Fig. 3). The microfossils studied are therefore essentially composed of kerogen. Peak metamorphism temperatures calculated from the Raman spectra of the carbonaceous material of the Francevillian microfossils give values of 296 ± 30 °C, corresponding to medium grade carbonaceous matter that has not undergone graphitization (Kouketsu et al., 2014).

4.3. *Microfossil morphotypes*

The microfossils in SUC-R-5 are densely populated, and mainly

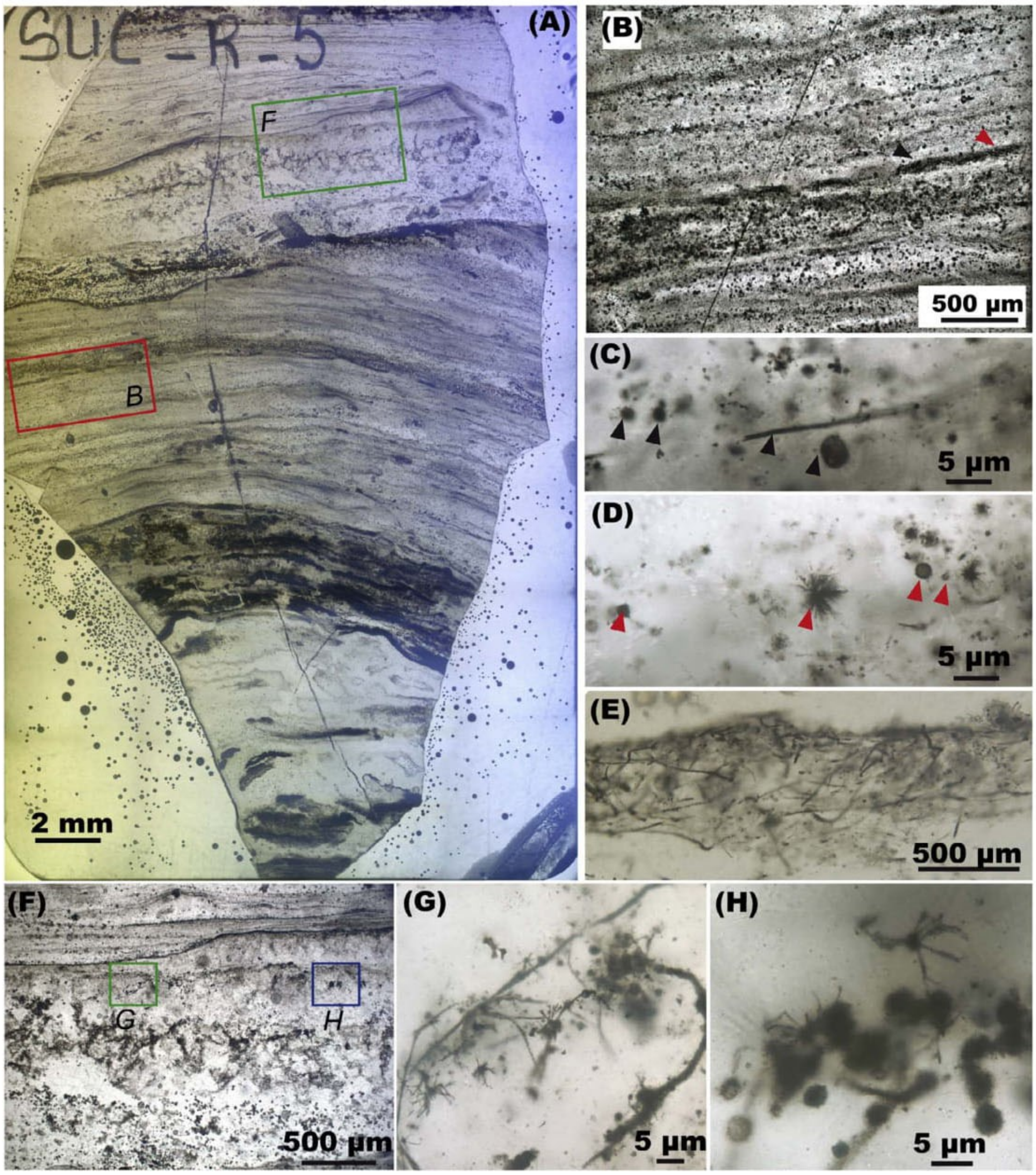

Fig. 2. Plain polarized light photomicrograph of sample SUC-R-5. (A) General view. (B) Close up of the red box in (A) showing laminae rich in organic matter and microfossils (undistinguishable at this scale) and carbonate rhombohedra (small black dots). (C, D) Microfossils (filament, sphere, star-like) in laminae located respectively at the red and black arrowheads in (B). (E) Lamina formed by horizontal and sub-horizontal microfossils. (F) Close up of the green box in (A) showing microfossil clusters in a millimetre-thick lamina below thin, overlapping lamina. (G, H) Close up on microfossil clusters in (F) showing the close association of the three forms of microfossils described in the text. (For interpretation of the references to colour in this figure legend, the reader is referred to the web version of this article.)

observed within laminae (Fig. 2C and E); some occur on the edge of the laminae, while others are dispersed in kerogen-poor laminae (Fig. 2F and H). Two types of filamentous microfossils were identified by morphometric analysis: *Gunflintia minuta* (diameter ≤3 µm, Fig. 4A, 5A), and broad filaments (diameter > 3 µm, Fig. 4B). Filaments are preserved as brown and dark brown tubes, with variations of color possibly reflecting variations of organic matter thickness difficult to distinguish under the optical microscope. Most filaments are oriented parallel to subparallel to the laminae of the stromatolites (Fig. 2E), some are occasionally oriented perpendicular to the laminae and others are randomly oriented. They appear straight, curved, and often coiled (Fig. 4A and B). Their maximum lengths usually reach several hundred micrometers. Spheres 2–11 µm in diameter are dominated by thick-walled *Huroniospora* (Figs. 4C and D, 5B). *Huroniospora* are light- to dark-brown, again likely reflecting variations in organic wall thickness (Fig. 4C and D). Finally, two types of star-shaped microstructures (possible microfossils, see below for discussion) with radially-distributed spines were assigned as *Eoastrion* (Fig. 4E and F). Type 1 *Eoastrion* display 3.5 µm–6 µm long, straight spines that are very thin (needle-like) (Figs. 4E, 5C). In contrast, Type 2 *Eoastrion* display comparatively bent and thicker spines up to 12 µm long. The spines of Type 2 *Eoastrion* often bifurcate, and are attached to a well-defined spherical central body ∼5 µm in diameter (Figs. 4F, 5C). Organic matter is dark brown in all *Eoastrion*. The three types of microfossils are present in unequal proportions. The filaments are the most abundant. *Huroniospora* are much less abundant than the filaments, and *Eoastrion* even less numerous. Some laminae display dispersed (Fig. 2C and D) or clusters of (Fig. 2F–H) individuals of all microfossil morphotypes, whereas other laminae comprise exclusively filaments (Fig. 2E). A selection of these microfossils spanning the different forms and types were sectioned by FIB and characterized at the nanoscale using STEM and at the sub-micrometer scale using CLSM as well as palynological

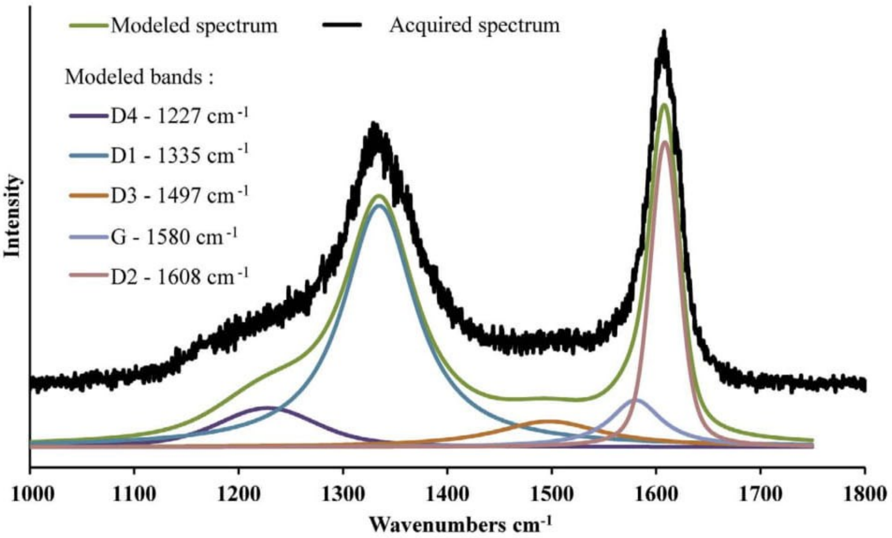

Fig. 3. Raman spectrum of a filamentous microfossil of sample SUC-R-5 and its deconvolution in five bands (goodness of fit criterion R^2 of 0.989, see method section).

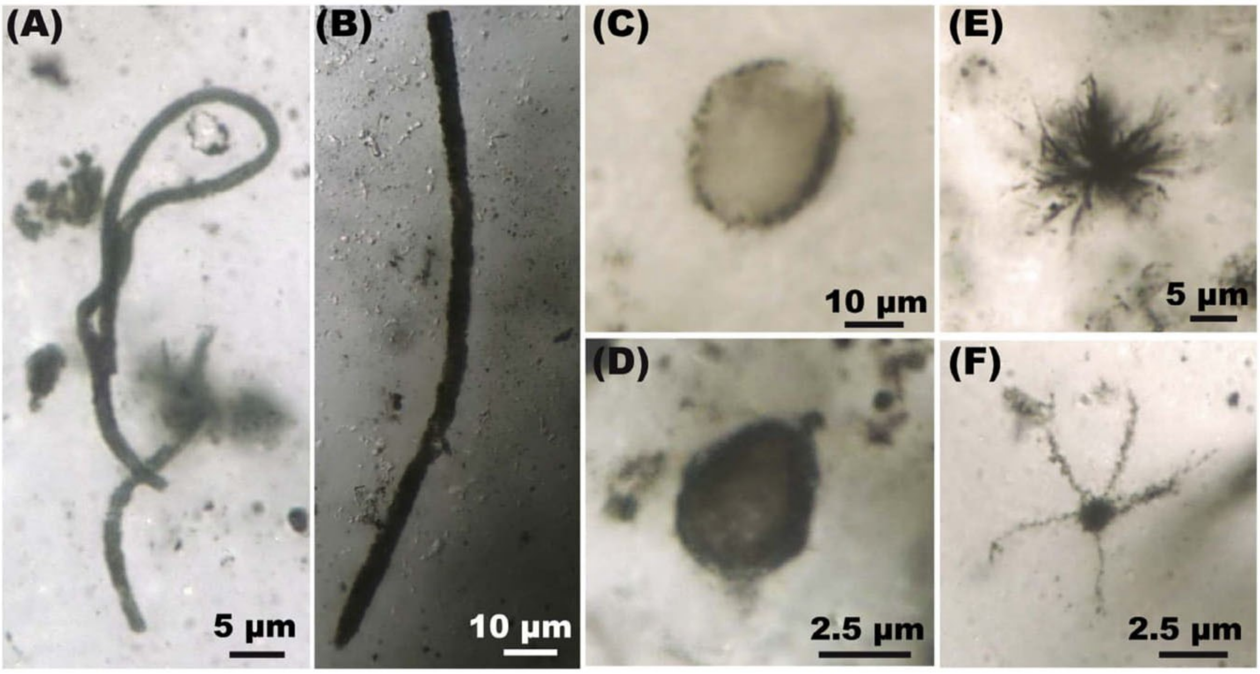

Fig. 4. Photomicrographs in plain polarized light of the different microfossil morphologies that dominates the microfossil assemblage in SUC-R-5. (A) Filaments (1.5 μm in diameter) composed of a narrow central quartz-filled tube wrapped in an organic sheath. (B) Broad filament wrapped in an organic sheath (4.5 μm in diameter). Absence of septa in the sheaths indicate Type 1 *Gunflintia* morphospecies of Lepot et al. (2017). Filaments are straight to coiled. (C) thick-walled *Huroniospora*, brown sphere of 11 μm of diameter; the thickness of the wall was not confirmed with FIB-STEM. (D) thick-walled *Huroniospora* dark brown sphere of 9 μm of diameter. (E, F) *Eoastrion*: star-shaped possible microfossils. (E) Type 1 *Eoastrion* (here, 13 μm in total diameter) showing very thin needle-like spines that are non-segmented, sometimes sinuous, and generally non-bifurcating. Spines radiate irregularly and are attached to an ill-defined central structure. (F) Type 2 *Eoastrion* (here, 22 μm in total diameter) display a spherical central body and relatively bended spines connected to the central body.

extraction and SEM.

4.4. Nanoscale analyses of microfossils

4.4.1. Gunflintia minuta

Lepot et al. (2017) distinguished two morphotypes among *Gunflintia minuta* filaments of the Gunflint Iron Formation: Type 1 comprises cell-free filamentous sheaths, whereas Type 2 comprises chains of cells. Here, STEM analyses of Francevillian *Gunflintia minuta* revealed narrow, non-septate tubes formed by a Type 1 sheath of organic matter free of cell remnants (Fig. 6). The sheaths usually are 1.2 μm–2.2 μm in diameter and about 180–250 nm thick (Fig. 6). STEM and EDS mappings show that kerogen forms almost continuous sheaths (Fig. 6D, H), sometimes interspersed with Ti ± O nanocrystals that likely are TiO_2 (Fig. 6D). The inner surface of the sheath is almost regular. In contrast, the kerogen on the external surface is highly irregular (Fig. 6C, F, and G). Inside of the filaments, quartz crystals range between 0.5 and 1 μm in diameter (Fig. 6B and F). Some nano-crystals of quartz are also present in the wall (Fig. 6C). Outside of *Gunflintia minuta*, quartz crystal range between 0.5 and 3.5 μm and are dominated by crystals coarser than 1 μm (Fig. 6B, F). In one filament, quartz crystals 100–500 nm large are observed against the wall (Fig. 6C) and make a transition with coarser quartz crystals outside the microfossil (Fig. 6B). Kerogen occurs between the sub-micrometric quartz grains on

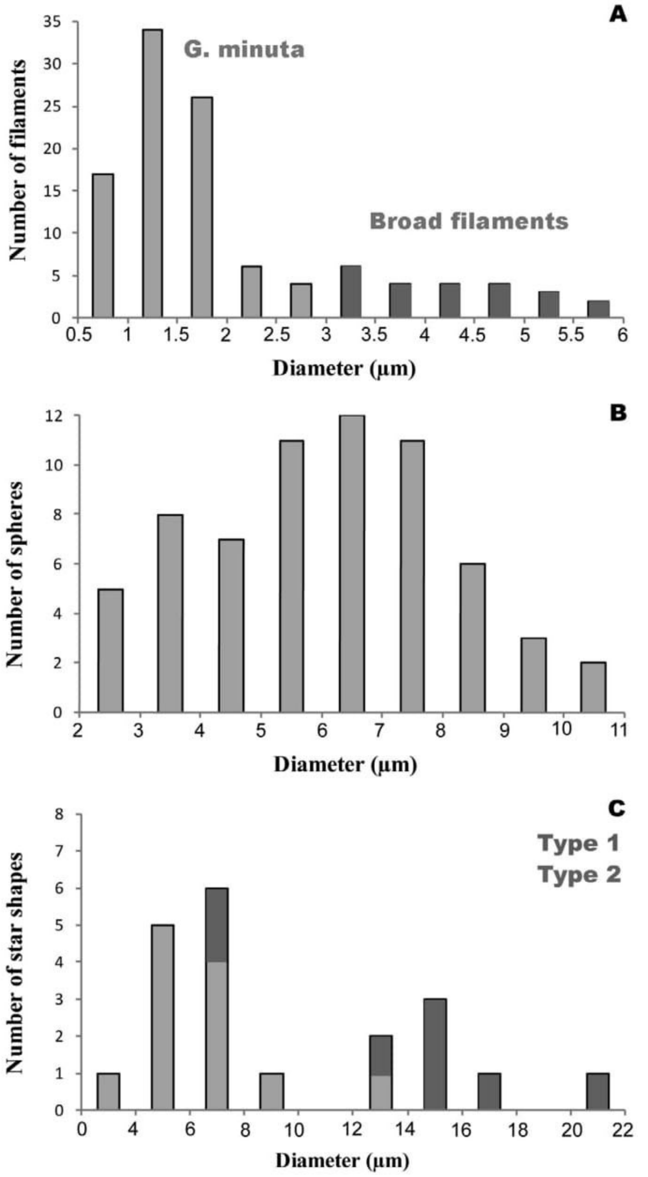

Fig. 5. Histograms showing the diameter distribution of filaments, *Huronisopora* and *Eoastrion* in the Francevillian cherts. A. filaments. *Gunflintia minuta* in blue and broad filament in red. B. *Huroniospora*. C. *Eoastrion* type 1 in blue and type 2 in red. (For interpretation of the references to colour in this figure legend, the reader is referred to the web version of this article.)

the outer surface of this filament, forming the irregular surface texture (green arrows, Fig. 6D and H). In the second filament (Fig. 6E), coarser quartz crystals are directly in contact with the organic sheath. The micrometric crystals arranged along the outer edge of the sheath have indentations filled with kerogen (green arrows in Fig. 6G and H).

Palynological extracts from the SUC-R-4 sample confirm that even the best preserved filaments display a relatively irregular outer surface (Fig. 7B). Some of the *Gunflintia minuta* with locally transpierced/torn sheaths (Fig. 7C) reveal the absence of internal segmentation and confirm the very regular shape of the inner surface. The microstructure of the best-preserved filamentous palynomorphs in Fig. 7A and B is consistent with that of FIB-sectioned *Gunflintia* in Fig. 6. A gradient of increasing degradation is observed in filaments shown in Fig. 7A–E, with an increase in roughness. In the most altered filaments, the tubular structure has completely been obliterated; the possibility that these (Fig. 7D and E) represent altered sheaths rather than sheath-less trichomes is suggested by the locally pierced and crumpled shape of moderately altered sheaths (Fig. 7B and C).

4.4.2. *Broad filaments*

Tubular sheath structure is usually not distinct under the optical microscope in broad filaments, which usually appear as dark, granular tubes (Fig. 2G and H). In one FIB section of a broad filament, an organic-poor region defining a central canal about 1 µm in diameter runs through a sheath-like structure about 4.75 µm in total diameter (Fig. 8A). The sheath is interspersed by quartz nanograins, whereas the central canal comprises slightly coarser sub-micrometric quartz. Only micrometric quartz is observed outside of the sheath. TiO_2 nanocrystals are abundant in organic matter of the sheath structures. Unidentified Fe-rich nanocrystals also occur in this microfossil.

4.4.3. *Huroniospora*

FIB sections of three thick-walled *Huroniospora* spheres 5.5–10 µm in diameter revealed cell walls 120–500 nm in thickness that are variably preserved (Figs. 9 and 10). The global aspect of organic walls ranges from relatively continuous to locally pierced (Fig. 9) to hemispherical only (Fig. 10). Quartz nano-crystals occur inside the walls (Figs. 9C, 10B). Quartz nano-crystals also occur against the walls, dominantly on the outside of microfossils. Quartz micro-crystals dominate away from kerogenous walls inside and outside the microfossils. Preserved parts of two *Huroniospora* walls displayed (Figs. 9C, 10B) textures similar to sheaths of *Gunflintia minuta* with a smooth inner boundary and irregular outer surface, i.e. kerogen pinches and swells preferentially toward the outside of *Huroniospora*. On the inner surface, kerogen is mostly in contact with microcrystalline quartz with small kerogen-filled indentations. In contrast, kerogen on the outer surface is in contact with nanocrystals between which organic matter migrated. In one *Huroniospora* (Fig. 9E and F), the wall is composed of a micrometer-thick band of quartz nanograins interspersed with a discontinuous network of organic nanoparticles; this wall is filled and surrounded by microcrystalline quartz.

Rod-shaped titanium oxide nanocrystals are associated with kerogen in the fossil cell walls of one of the studied *Huroniospora* (Fig. 10). Iron-rich nanocrystals are present in quartz microcrystals inside these thick-walled *Huroniospora* (Fig. 10E and F); these could be Fe-(oxyhydr)oxides or Fe-silicates (which cannot be distinguished due to small size and SiO_2 matrix interference), Fe-carbonate (size too small to detect C efficiently with EDS), but not Fe-sulfides (S not detected).

Spheres resembling *Huroniospora*, of 5–6.8 µm in diameter were observed in palynological residues. They display a granular outer surface (Fig. 7F).

4.4.4. *Type 1 Eoastrion*

Types 1 *Eoastrion* are preserved upon palynological extraction. In 3D, their spines appear as wire to blade shaped (Fig. 7G). A relatively large one (15 µm wide, Fig. 11A) and two smaller Type 1 *Eoastrion* (6 µm and 8 µm wide, Figs. 11B and 12A) were cut with FIB and displayed similar characteristics under STEM. Kerogen spines forming the star-shaped microstructures are relatively continuous and 90 nm–250 nm in diameter. Quartz nano-crystals are found along and inside organic spines. Quartz microcrystals dominate away from organic spines. Similar to filamentous and spherical microfossil morphotypes, organic spines pinch and swell in contact with quartz nanograins. While optical microscopy could not distinguish a central body inside the needle-shaped spines, FIB sectioning shows a micrometric pure kerogen zone in the central part. Spines are thicker at their roots, i.e. at their point of connection with the central part (Figs. 11 and 12). In one Type 1 *Eoastrion* (Fig. 12), two organic spines pass through single chlorite (Fe-Mg aluminosilicate) crystals that occur close to the central body. Pyrite and TiO_2 are also associated with organic matter in the spines of the same *Eoastrion* (Fig. 12).

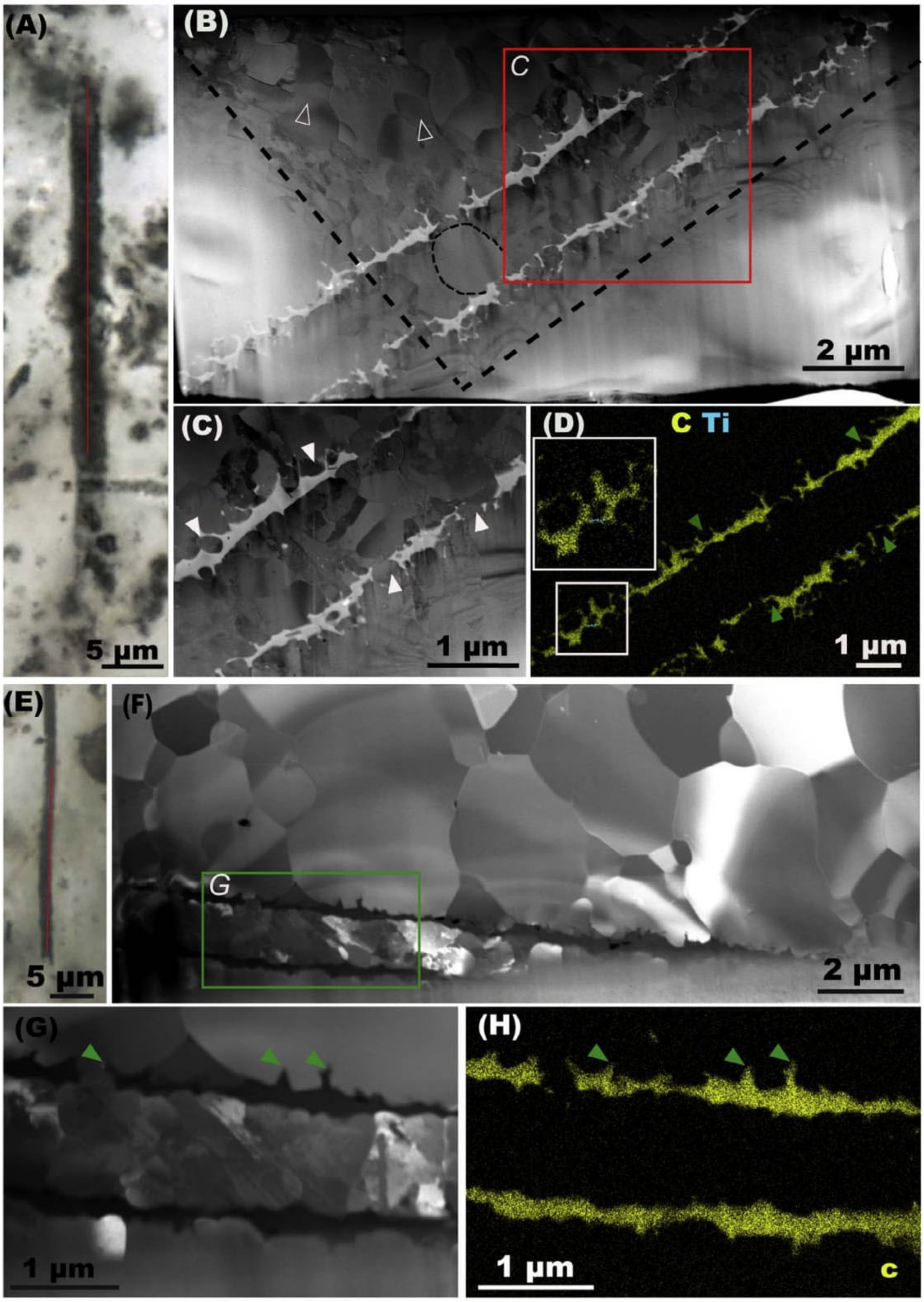

Fig. 6. STEM analysis of a Type 1 *Gunflintia minuta* microfossil. (A) Transmitted light photomicrograph of filament (red line corresponds to the location of FIB section). (B) Bright field STEM image of the FIB section showing heterogeneous distribution of quartz (shades of grey) grain sizes with submicrometric quartz dominating inside the microfossil and quartz micro-crystals (arrowheads) dominating outside microfossil. Thin organic sheath appears in white and displays a regular texture on the internal boundary of the sheath, and an irregular, diffuse texture on the outer boundary of the sheath. Bright (i.e. thinner) regions below the discontinuous lines and within the central circle were made amorphous by FIB damage. (C) Bright field STEM image (of the red box in B) showing quartz nano-crystals in organic matter (white arrowheads). (D) EDS mapping of carbon (yellow) demonstrating the quartz nano-crystals in organic matter (green arrow); the inset at the top left shows a close up of the boxed zone in the lower left part of the map to reveal a Ti-bearing (cyan) nanocrystal in organic matter. (E) Thin section photograph in transmitted light (red line locates the FIB section). (F, G) Dark field STEM images of the FIB section cut along the red line in (E). (G) Shows a zoom on the boxed zone in (F). Quartz nano-crystals appear in grey to white and the thin organic sheath in black. Quartz displays heterogenous grain size, with sub-micrometric quartz inside the microfossil and micrometric quartz outside. (H) EDS mapping of carbon in (G). The thin organic sheath displays a regular texture on the internal boundary of the sheath, and an irregular, diffuse texture on the outer boundary of the sheath. Green arrows in (G, H) show that organic matter occurs in indentations in the quartz micro-crystals of the outer boundary of the microfossil wall. (For interpretation of the references to colour in this figure legend, the reader is referred to the web version of this article.)

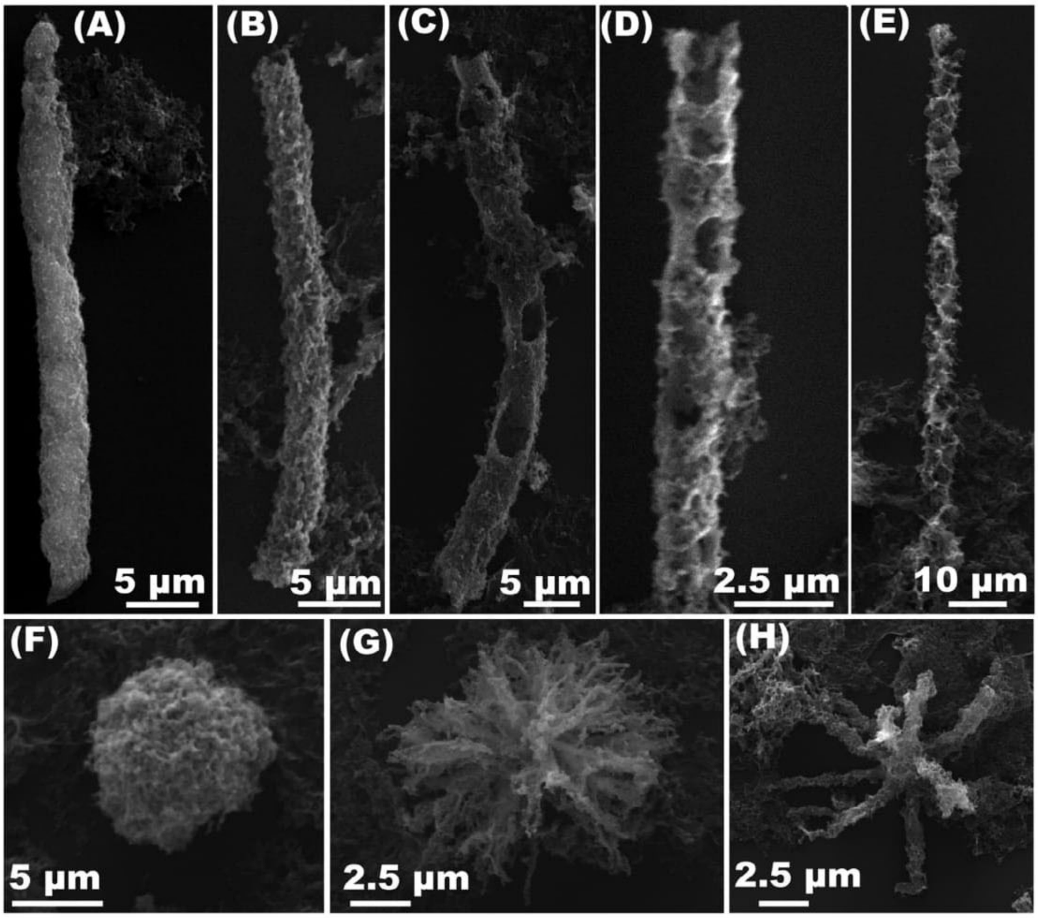

Fig. 7. Secondary electron images of palynomorphs. (A–E) Narrow *Gunflintia minuta*. The images show different preservation status of *Gunflintia minuta*. (A, B) Best preserved (most continuous) sheaths. (C, D) Holes appear where quartz locally replaced or pierced organic matter. (C) The sheath is destroyed in some places and allows the smooth inner surface of the tube to be seen. (E) Highly degraded *G. minuta*. (F) *Huroniospora*-sized sphere. (G) Type 1 *Eoastrion*. (H) Type 2 *Eoastrion*. The carbonaceous nature of these structures was verified using Raman microanalyses and EDS mapping (not shown).

4.4.5. Type 2 *Eoastrion*

Type 2 *Eoastrion* contrast with Type 1 based on the structure of their spines and central body. Type 2 *Eoastrion* display a well-defined subspherical central body under the optical microscope (Fig. 13A–C). Sometimes, the central body appears hollow under the optical microscope and CLSM (Fig. 13A and B). Spines in Type 2 *Eoastrion* are discontinuous and form relatively broad (0.9–2 µm) tubes made of a network of kerogen interspersed with quartz nanocrystals. Quartz crystals outside of the spines are dominantly micrometric (Fig. 3D and E). STEM (Fig. 13D) and CLSM (Fig. 13B) revealed sub-micrometric to micrometric quartz crystals inside the central body. Titanium-rich nanocrystals are associated with kerogen (Fig. 13E). Type 2 *Eoastrion* are also preserved upon palynological extraction. In comparison with Type 1 *Eoastrion*, their spines appear as stiffer blade to rod shapes (Fig. 7H), consistent with FIB observation.

5. Discussion

The assemblage studied here comprises thin- and thick-walled *Huroniospora* microfossils, *G. minuta* microfossils, as well as *Eoastrion* microstructures. These are the main components the stromatolitic Gunflint-type assemblages that dominate the fossil record between 2.4 and 1.7 Ga (Awramik and Barghoorn, 1977; Barghoorn and Tyler, 1965; Bertrand-Sarfati and Potin, 1994; Cloud, 1965). The studied microfossils represent the oldest (~2.14–2.08 Ga) stromatolitic Gunflint-type assemblage, but also are among the most thermally mature Gunflint-type occurrences. In a context where organic matter migration was possible in association with catagenesis and/or quartz (re)crystallization, we discuss morphological preservation and taphonomic processes based on nanoscale observations. We demonstrate a new, originally thick-sheathed filamentous morphospecies. We discuss the biogenicity of *Eoastrion* microstructures, questioned by Krumbein (2010). Finally, we discuss the *in vivo* and/or taphonomic origin of Fe and Ti associated with microfossils.

5.1. Maturity of the kerogen

The Raman spectra of the kerogen of the studied microfossils reveal their carbonaceous nature, consistent with a biochemical origin (Schopf, 2006). They also confirm that the extracted palynomophs had a kerogen composition similar to their counterparts observed in thin sections. Raman spectroscopy moreover provided a geothermometer of peak metamorphic conditions (Beyssac et al., 2002; Kouketsu et al., 2014). According to Kouketsu et al., (2014), the measured 296 ± 30 °C peak temperature corresponds to medium grade (280–400°C) carbonaceous material. At this temperature, organic matter of FC has only initiated the amorphous carbon to graphite transition. This result is consistent with previous studies documenting an anthracite to meta-anthracite stage of thermal maturity for organic matter dispersed in the fine grained deposits of the FC Formation in the near-by M'Vengue syncline (Cortial, 1985). The absolute peak temperature provided by this geothermometer is, however, difficult to reconcile with the presence of early diagenetic minerals in organic matter-rich shales from the underlying FB Formation (Ngombi-Pemba

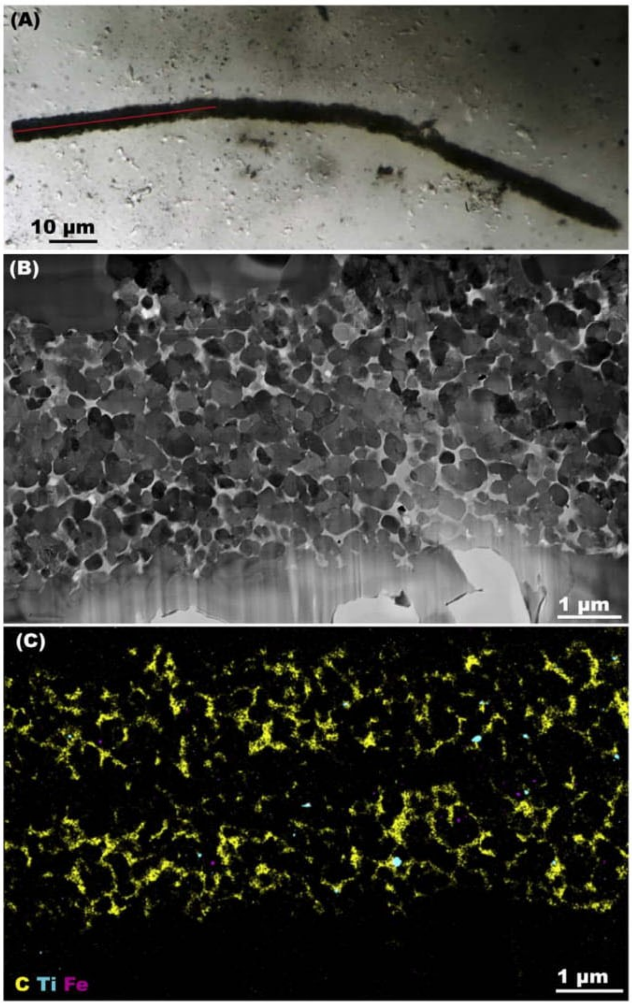

Fig. 8. STEM analysis of a broad filament microfossil. (A) Transmitted light photomicrograph of filament (red line corresponds to the location of FIB section). (B) STEM image field of the FIB section showing a difference in the quartz (gray shade) grain size inside and outside the filament. Not having a differentiated wall, the microfossil is completely filled with nanocrystals of quartz whose sizes are larger at the center of the filament. The quartz outside the microfossil appears coarser showing micrometric-sized crystals. Bright (i.e., thinner) regions at the bottom of the image were rendered amorphous by FIB damage. (C) STEM-EDS map of C (yellow), Ti (cyan) and Fe (magenta) in (B). (For interpretation of the references to colour in this figure legend, the reader is referred to the web version of this article.)

et al., 2014; Ossa Ossa et al., 2013). The maturity of organic matter indicated by Raman spectroscopy could be linked with the duration of the peak thermal event as observed during laboratory experiments (Schiffbauer et al., 2012) in addition to the peak temperature itself. The discrepancy between mineral and organic geothermometers in the Francevillian formations could therefore relate to a long burial time. Regardless of the real burial temperature suffered by these microfossils, the Raman geothermometer provides an estimate of the relative maturity of the organic matter. The FC microfossil maturity is well above that of Gunflint Iron Formation microfossils that range between 160 and 250°C depending on sampled locality (Alleon et al., 2016). Accordingly, the morphology of the microfossils as observed under the optical microscope appears much less distinct, with spheres and filaments for which neither cellular or sheath structures can be distinguished (e.g. Fig. 2H), and with increased granular aspect of the organic microstructures. The maturity of the FC microfossils is similar to that of the Turee Creek microfossils studied by Fadel et al. (2017), although morphological comparison with the latter is difficult, as these have been largely affected by siderite replacement. The maturity is, however, lower than that of the Duck Creek Formation microfossils, whose Raman spectrum displays smaller D3 and D4 bands (Beyssac et al., 2002; Kouketsu et al., 2014; Schopf et al., 2005). Below, we address the nanoscale morphological preservation of kerogen in palynological extracts and in FIB sections of a selection of the microfossils that appeared best preserved under the optical microscope.

5.2. Preservation of *G. minuta* and *Huroniospora*

The *Gunflintia minuta* (Fig. 4A) show a tubular organic sheath totally devoid of trichomes of cells. They are similar to the non-septate Type 1 *Gunflintia minuta* of the Gunflint Iron Formation stromatolites and contrast with the septate Type 2 *Gunflintia minuta* (Awramik and Barghoorn, 1977; Barghoorn and Tyler, 1965; Knoll et al., 1988; Lepot et al., 2017). Trichomes likely have undergone a rapid, early degradation which led to their disappearance. They are more sensitive to degradation and silicification than sheaths (Bartley, 1996; Horodyski and Bloeser, 1977; Jones et al., 2001; Lepot et al., 2014). Alternatively, trichomes of cells may have escaped sheaths before death, as is commonly observed in filaments of the chemotrophic Fe-oxidizing bacteria *Leptothrix* (Emerson et al., 2010), or in cyanobacteria submitted to chemical stress (Lepot et al., 2014). The *Huroniospora* display a size and sub-spherical structure similar to those observed in other Gunflint-type assemblages. *Thin-walled* and *thick-walled Huroniospora* (Cloud, 1965; Lepot et al., 2017) could be distinguished, although we could only analyze the latter, more abundant, with STEM.

Observations of the microfossils under the cross-polarized light microscope show that the microfossils are essentially embedded in microquartz. These observations are in agreement with nanoscale imaging which shows these microfossils embedded in and filled with quartz microcrystals. However, a common feature of *G. minuta* and thick-walled *Huroniospora* of the FC is the occurrence of nano-crystals of quartz inside and against the outer side of the organic wall, a situation similar to what has been observed in Gunflint Iron Formation microfossils (Moreau and Sharp, 2004; Wacey et al., 2012). In contrast, the inner sides of the microfossil organic walls are in contact with coarser, often micrometric crystals of quartz. This textural heterogeneity of quartz crystals in/near microfossils can result of i) the initially heterogenous texture of amorphous silica (opal) precursors, possibly related with taphonomic sequence, and ii) control of organic matter on the recrystallization of opal precursors into quartz.

Cell walls are preferential sites of silica nucleations during the life of microorganisms as hydrogen bonds form between the hydroxyl groups of silicic acid and those of cell wall molecules (Orange et al., 2009, 2011). Bacteria can survive encapsulation in amorphous silica (Nassif et al., 2002; Phoenix et al., 2000) through slow metabolic activity and sleep (Orange et al., 2009). In these conditions, a first, microscopic layer of amorphous and/or nanocrystalline opal may form on cells or sheaths (Campbell et al., 2015) while cellular contents are still preserved in the cell and/or while bacteria are still alive (Phoenix et al., 2000). Second, formation of a dense matrix, mm- to cm-scale deposit of silica encapsulates the fossils, which may still preserve cell contents at this stage (Campbell et al., 2015; Orange et al., 2009). Third, grainy silica may infill the cells in association with (auto)lysis, desiccation and condensation of cytoplasmic content (Campbell et al., 2015). The distinct textures of these three generations of silica may be carried through recrystallization into quartz, as suggested by the nanocrystals in/on FC microfossil walls, coarser quartz crystals inside microfossils, and even coarser quartz crystals outside microfossils (e.g. Fig. 6B).

Quartz nanocrystals concentrate in the walls and on their outer surface, but are scarce on the inner surface of microfossil walls, which are in direct contact with coarser quartz grains. This can be explained by a higher porosity of the outer parts of the wall compared to the inner part of the wall, e.g. during initial precipitation of silica nanograins (Wacey et al., 2012). This is consistent with observation of amorphous

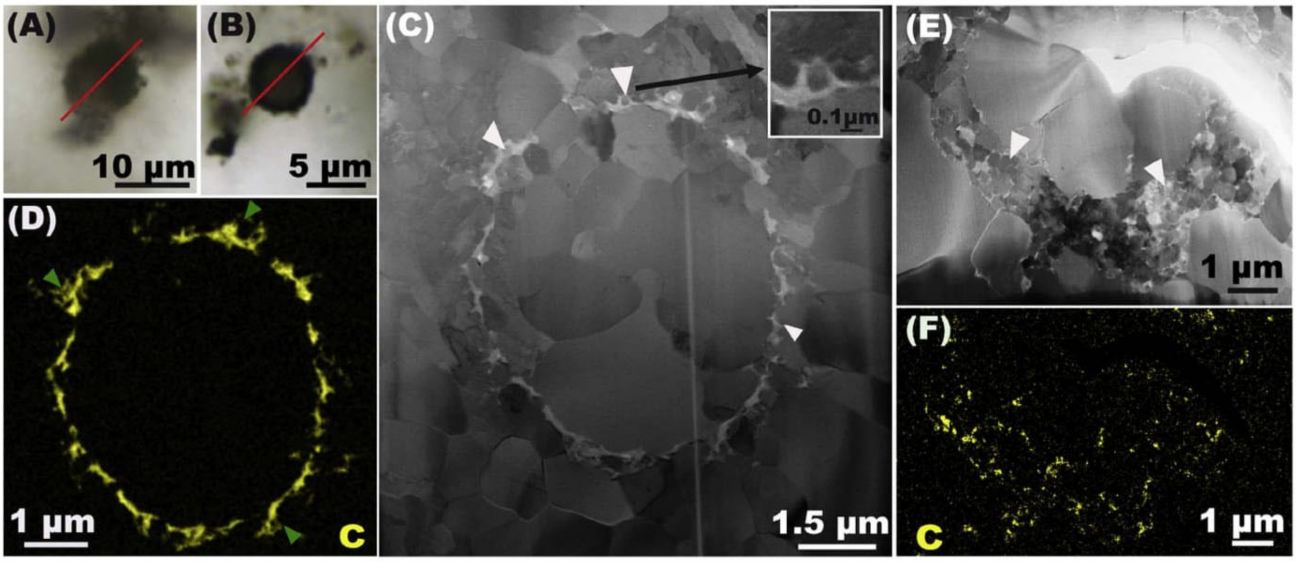

Fig. 9. STEM of thick-walled *Huroniospora* microfossils. (A, B) Photomicrographs (red line locate the FIB sections). (C), (E) bright field STEM images of the FIB section cut along the lines in A and B, respectively. (D), (F) EDS mappings of C (yellow) in C and E, respectively. Quartz occurs as micro-crystals inside and outside the two microfossils and as nano-crystals (white arrowheads in C and E) in the organic walls. In C-D, the organic wall internal boundary displays a regular texture whereas the outer boundary is diffuse (green arrowheads, D). (For interpretation of the references to colour in this figure legend, the reader is referred to the web version of this article.)

opal nanospheres embedded in the outer part of the sheath of silicifying, internally intact cyanobacteria (Campbell et al., 2015). Silica nanograins located only in/on the surface of microfossils may have migrated into organic wall during/after their recrystallization into nanoquartz, possibly in association with sub-micrometric organic matter migration. The proximity of organic molecules in the cell wall may also have templated the recrystallization of amorphous silica into nanoquartz; however, the scarcity of quartz nanograins on the inner side of the organic wall suggests that organic matter could not, alone determine the texture of quartz crystals during diagenesis. Rather, the presence of coarser quartz crystals on the inner side of the organic wall suggests that the primary silica precursor was texturally distinct inside and outside the organic wall, consistent with the distinct patterns of opal in/on recently silicified cells (Campbell et al., 2015).

The indented outer margin of the type 1 *Gunflintia minuta* (Fig. 6) and of thick-walled *Huroniospora* resemble those observed in the filamentous cyanophytes preserved in Proterozoic cherts (Starmach, 1963) and in microfossils of the Gunflint Iron Formation (Cloud, 1965; Wacey et al., 2012). These indentations have been interpreted as the result of the growth of quartz grains during the diagenesis of cherts (Lepot et al., 2017; Moreau and Sharp, 2004; Oehler, 1976; Wacey et al., 2012). This interpretation is consistent with the observation of nanoquartz grains that seem to “push” into organic matter in one *G. minuta* sheath (Fig. 6A–D). In another *G. minuta* sheath, microquartz outlines the outer margin rather than nanoquartz, but series of dents occur along the faces of single quartz microcrystals (Fig. 6E–H), either because i) microquartz recrystallized after nanograins (e.g. Wacey et al., 2012), or ii) organic matter migrated later through local etching of microquartz (e.g. Lepot et al., 2009). The former hypothesis is favored because of the similarity of the indented organic textures in the *G. minuta* sheaths outlined with either nano- or micro-quartz (Fig. 6B vs F). This shows that even through diagenetic coarsening of quartz into crystals several micrometer large (Fig. 6F), the original texture of organic matter defined by initial encapsulation in nanograins can be preserved.

The inner boundary of type 1 *G. minuta* and thick-walled *Huroniospora* appears more smooth and regular than the outer boundary. Intra-microfossil quartz crystals can be sub-micrometric (Figs. 6, 9, 10) but in some case have grown into interlocked masses of pluri-micrometric crystals (Fig. 9C). Nevertheless, the pluri-micrometric quartz crystals display a hemispheric contour following the shape of the organic wall, indicating that they crystallized, or recrystallized (likely after amorphous/nanocrystalline SiO_2), without disrupting organic matter. We suggest that the cell-filling precursor to quartz had less open porosity than the external nanograins that formed earlier on the wall of the still living cell. This could have limited organic matter displacement and compressive imprints of quartz nanograins to the outer margin of the filaments. This is consistent with the observation of coarser silica inside recently fossilized cyanobacteria (Campbell et al., 2015) and should be verified with nanoscale and crystallographic characterization of the internal structures of recently silicified cell interiors.

Altogether, these observations support that the textures of soft organic parts of FC microfossils and associated quartz crystals have strongly been influenced by the original organic biopolymers and the taphonomic sequence associated with cellular decay. Such observations can provide criteria to distinguish putative Archean microfossils (Sugitani et al., 2015; Wacey et al., 2012) against bitumen accreted onto abiotic filamentous/sub-spherical siliceous microstructures. Moreover, these observations confirm that the indented texture observed on the surface of *Huroniospora* and *G. minuta* are taphonomic in origin rather than anatomic features such as wall reticulation in agreement with Wacey et al. (2012).

Experimental taphonomy shows that sheaths may contract/shrink after decay of the trichome (Bartley, 1996; Jones et al., 2001). Outward displacement of organic matter in silica may increase the apparent diameter (or sheath thickness) of microfossils (Knoll et al., 1988). Shrinkage preceding silicification is usually irregular along the length of filaments and associated with folding (Bartley, 1996). The smooth, regular internal boundary of the best preserved *Gunflintia* observed here in FIB sections (Fig. 6) and palynological extract (Fig. 7A and B) is not consistent with sheath shrinkage before silicification. The absence of organic matter displacement toward the inside of the studied *G. minuta* argues that sheath shrinkage has not occurred after silicification either. This migration is observed only on the outer layer of the wall. In the case of a contraction of the diameter, the internal and external textures of the organic wall would both appear irregular. Similarly, in the case of a widening of the diameter, the internal and external layers of the organic wall would both be irregular in appearance due to constraints applied to the wall. Our observations indicate that the inner layer of the tube wall is well preserved and that the inner diameter of *G. minuta*

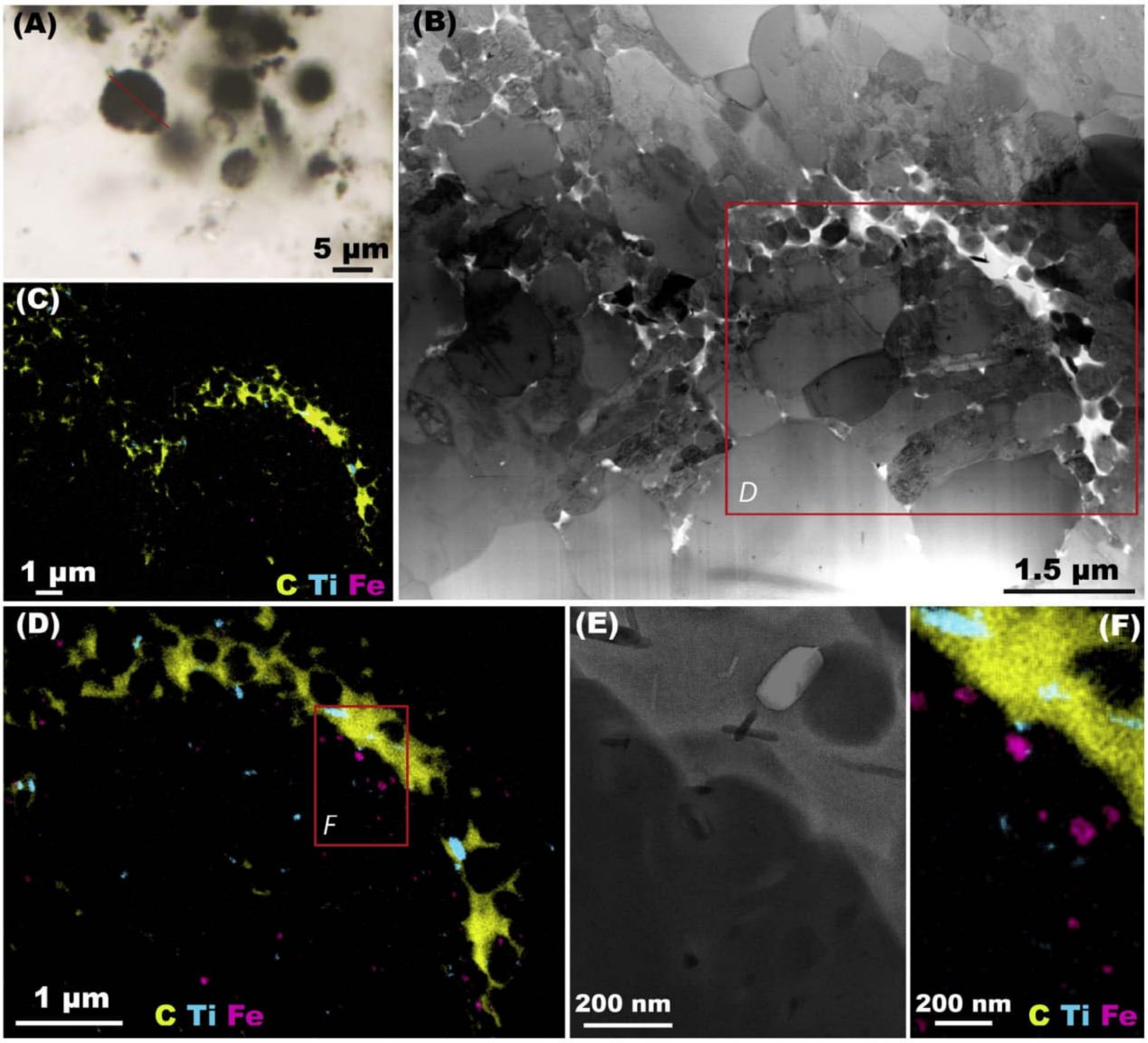

Fig. 10. STEM and TEM of a thick-walled *Huroniospora* microfossil. (A) Photomicrograph of a cluster of *Huroniospora* (the red line locates the FIB section). (B) Bright field STEM image of the FIB section showing nano-crystals along the wall and in the wall. Micro-crystals dominate inside and outside the microfossil. (C) EDS mapping of carbon (yellow), titanium (cyan), and iron (pink) of B. (D) EDS mapping of the red box in B. (E) Bright-field TEM of the area boxed in red in (D) showing organic matter (light grey), holes (white), quartz (medium grey), and Fe- or Ti-bearing nanocrystals (black). (F) EDS map of (E). The sample is parallel to the camera for TEM images, whereas STEM and EDS were recorded at a 20° tilt, resulting in images compressed in the horizontal direction (in F) compared to TEM (in E). Nanocrystals occurring in organic matter are composed of titanium, whereas nanocrystals within quartz are composed of iron. (For interpretation of the references to colour in this figure legend, the reader is referred to the web version of this article.)

reflects that of the unpreserved cells in the trichome. Similarly, the continuous wall structure and regular inner diameter of the best preserved *Huroniospora* (Fig. 9C) indicate that the original cell diameter is preserved.

5.3. Broad filaments

In the best preserved of the broad filaments, the central organic-poor canal demonstrates the preservation of a sheath ultrastructure. Growth of nanocrystals inside the organic matter in the sheath could have been favored by impregnation of porous polysaccharides with silica as well as volume loss of organic matter during desiccation, condensation and/or cracking. Migration of organic matter may, however, have occurred between nanocrystals inside the microfossil. However, migration was not observed in broad filaments of the Turee Creek Group (Fadel et al., 2017), where similar nanoquartz occurred in the canal, the sheath and outside the filament irrespective of the distribution of organic matter. Moreover, the relatively regular diameter of the central canal observed here suggests that it could reflect the diameter of the cells in the obliterated trichome. The absence of segmentation and the sheath thickness contrast with other broad filaments of Gunflint-type assemblages such as *Animikiea* and *Gunflintia grandis* (Lepot et al., 2017; Barghoorn and Tyler, 1965). Broad filaments with thick sheaths have, to our knowledge not yet been reported in shallow-water Gunflint-type assemblages. Such thick-sheathed filaments have been reported as a minor fraction of cobweb-forming assemblages in nodular cherts of the 2.45–2.21 Ga Turee Creek Group, Western Australia (Fadel et al., 2017). The thick-sheath ultrastructure is well known among filamentous cyanobacteria [e.g. *Calothrix* (Lepot et al., 2014); *Petalonema* (Mares et al., 2015)] and uncommon in other filamentous bacteria; to our knowledge, it is unknown in Fe-oxidizing bacteria such as *Leptothrix* (Emerson et al., 2010), anoxygenic photosynthesizers (Hanada, 2003), methane oxidizers such as *Crenothrix* (Stoecker et al., 2006), *Sphaerotilus* [heterotrophs, (Van Veen et al., 1978)], or filamentous sulfur oxidizing bacteria (Larkin and Strohl, 1983).

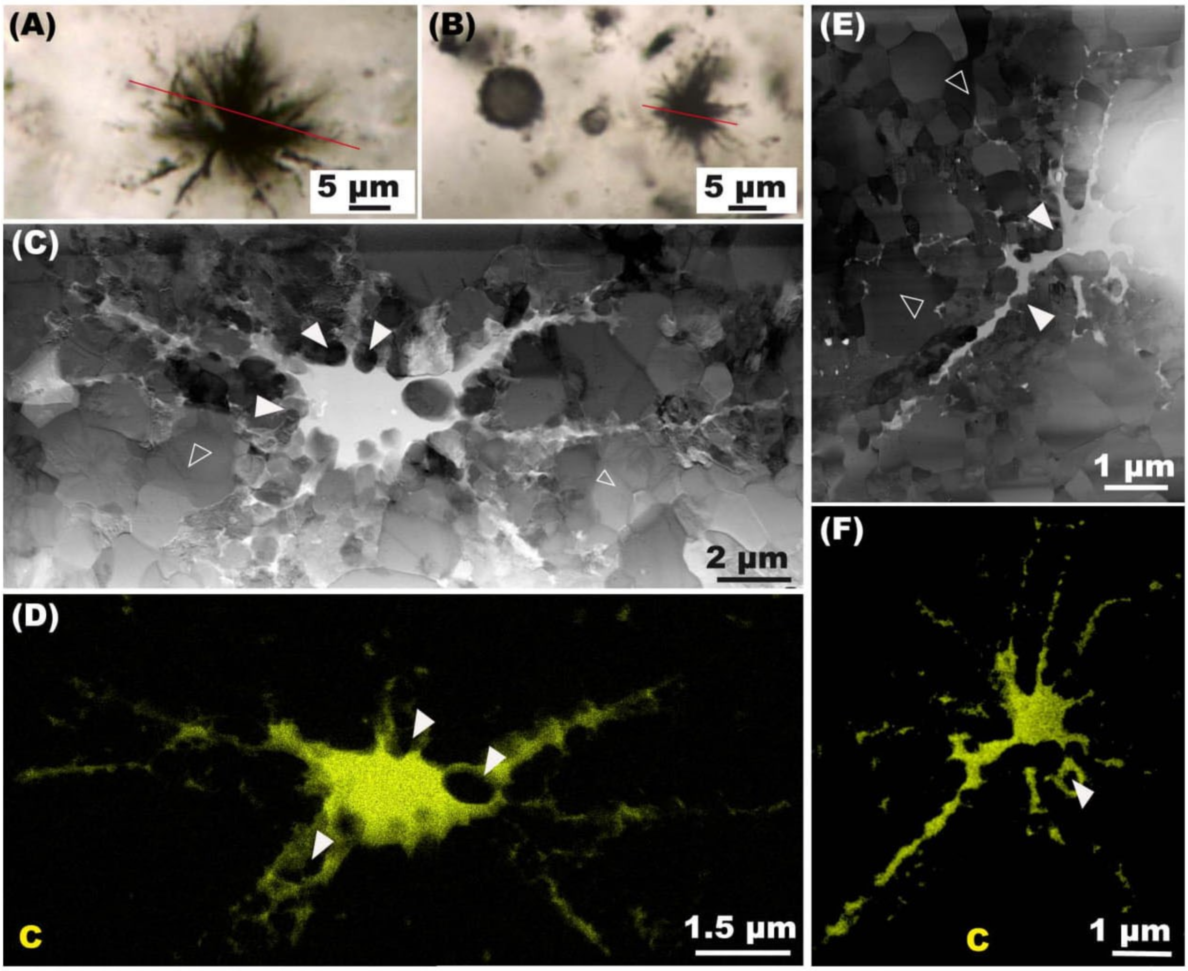

Fig. 11. Ultrastructure of Type 1 *Eoastrion*. (A and B) Photomicrograph of the star-shaped microstructures with straight needle-like spines. The red line indicates the location of the FIB section. (C) Bright field STEM image of the FIB section cut in the microstructure shown in (A). Quartz nano-crystals occur along and inside organic structures (e.g. at the solid arrowheads), whereas the surrounding matrix is microcrystalline (e.g. empty arrowheads). (D) EDS mapping of carbon showing the concentration of organic matter in the central part but also in spines connected to the central part. (E) Bright field STEM image of the FIB section cut in the microstructure shown in (B) showing quartz (shades of grey) nano-crystals (solid arrowheads) along and inside organic structures (in white), and microcrystalline quartz (empty arrowheads) matrix away from the organic structures. (F) EDS mapping of carbon showing the concentrated organic matter in the central part but also in the spines connected to the central part; arrowhead highlights a quartz nanocrystal embedded in an organic spine. (For interpretation of the references to colour in this figure legend, the reader is referred to the web version of this article.)

5.4. Biogenicity of *Eoastrion*

The star-shape microstructures resemble the *Eoastrion* described in the Gunflint Iron Formation, which have been compared to the Fe and Mn oxidizing bacteria *Metallogenium* (Cloud, 1965). The shape and variety of shapes of *Eoastrion* suggest that they could have formed after radial migration of organic matter. Indeed, “filaments“ of organic matter have been observed to radiate away from clots of organic matter in hydrothermal silicification experiments (Fig. 5J in Oehler, 1976). The star-shape may also represent the taphonomic alteration of other type of microorganisms, including fungi (Krumbein, 2010). Nevertheless, *Metallogenium* display a variety of star-shapes (Dubinina, 1970) that are consistent with a biological interpretation for the morphologies observed here and in other Gunflint-type assemblages.

Two morphologically distinct types of *Eoastrion* have been extracted from palynological maceration of FC stromatolites. This indicates that both types are self-supported, cohesive organic microstructures rather than aggregates of organic nano-particles formed through displacement of droplets at the grain boundaries of quartz. This feature is consistent with of a microfossil nature, though not diagnostic alone. In one FIB section (Fig. 12), two spines of *Eoastrion* pass through a single crystal of chlorite. This petrographic relationship can be interpreted either as the result of migration of organic matter dissolving its way through chlorite, or as the result of chlorite embedding organic spines during its growth.

The two types of *Eoastrion* we studied in the FC display quartz textures similar to those associated with *Gunflintia* and *Huroniospora*. Quartz nanocrystals are observed along the spines and the central kerogen grain, whereas quartz microcrystals occur on the outside in the matrix. The process of preservation of these *Eoastrion* could be compared to that of the *Gunflintia* and the *Huroniospora*. However, no differentiated organic wall or sheath structures are found in the spines. Spines of living *Metallogenium* are appendages that sprout from a coccoidal microorganism (Zavarzin, 1981) and that, unlike sheaths of filamentous microorganisms, may not form tubular structures. Moreover, the central part usually forms a dense central mass (Figs. 11–13), and only rarely display a central quartz crystal suggestive of central cell (Fig. 13A and B). *Metallogenium* is a polymorph microorganism that does not possess a resilient cell wall and that is only bound by a cytoplasmic membrane (Zavarzin, 1981), hence limiting the possibility for preservation of cell shape. Altogether, the ultrastructure of FC's *Eoastrion* is compatible with hypothetic degradation pattern of *Metallogenium*. Taphonomic ultrastructural studies on *Metallogenium* and other star-shaped microorganisms (Krumbein, 2010) should be performed to

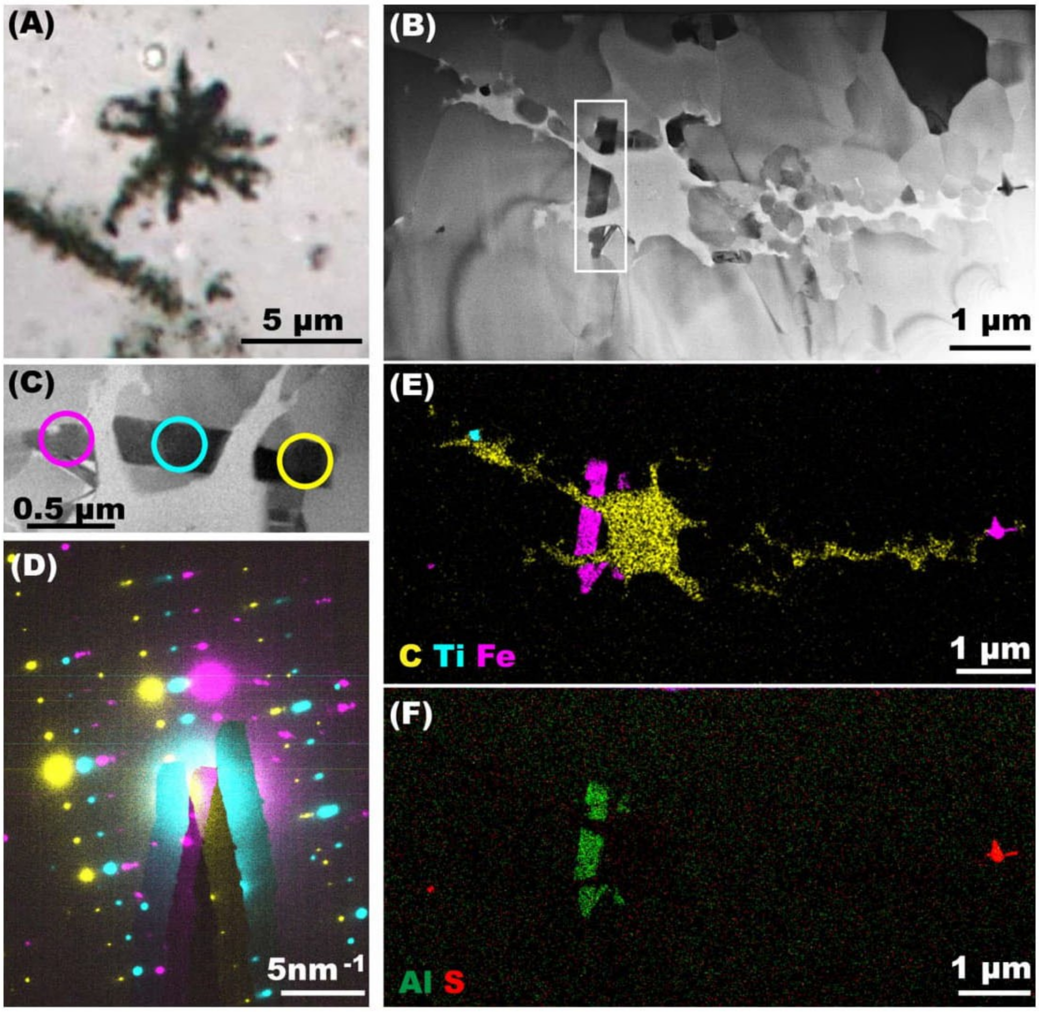

Fig. 12. Ultrastructure of a Type 1 *Eoastrion*. (A) Photomicrograph showing a star-shaped microstructure with straight needle-like spines. (B) Bright field STEM image of the FIB section of the microstructure shown in (A). The image shows the quartz microcrystals (shades of gray) outside the microstructure. The interior is essentially composed of organic matter. Two of the spines of the microstructure pass through a chlorite crystal (boxed). (C) Zoom on the chlorite crystals boxed in (B). The similar contrast in STEM bright-field image suggests that the three circled parts belong to a single crystal, consistent with similar height of the crystal in the yellow and cyan circles. (D) Overlay of three Selected area electron diffractions [recorded on the three circled zones in (C) with a sample tilt less than 1°] showing a similar diffraction pattern, confirming that the three circled parts belong to a single crystal. This diffraction pattern identified chlorite diffracting along the [−7, 0, −3] zone axis. (E and F) EDS carbon maps showing the concentration of organic matter (yellow, carbon) in the central part of the microstructure, but also in the spines connected to the central part. It also shows the chlorite (Al and Fe) crossed by the organic spines, and the presence of pyrite (Fe + S) and titanium in the organic matter. (For interpretation of the references to colour in this figure legend, the reader is referred to the web version of this article.)

better support this hypothesis. We cannot completely rule out that the observed microstructures may have formed through radial displacement of organic matter during diagenesis.

5.5. Titanium in microfossils

This is to our knowledge the first observation of titanium oxide (likely anatase) in the organic matter of Gunflint-type microfossils (here *Huroniospora* and *Eoastrion*). Titanium mineralization of organic matter is uncommon (Parnell, 2004; Pe-Piper and Murphy, 1992). Anatase has also for example been reported in bitumen nodules (Parnell, 2004), in plant fossils in blueschist facies (Galvez et al., 2012), in organic matter associated with Neoarchean mafic volcanic tuffs (Lepot et al., 2011), and in organic matter associated with putative Paleoarchean carbonaceous filamentous microfossils (Ueno et al., 2004). The mobility and dissolution of titanium-rich minerals has been demonstrated. A low temperature (< 140 °C) hydrothermal origin was attributed to Ti concentrations in bitumen (Parnell, 2004). Evidence of hydrothermalism was found in the FA formation. Fluid circulations (meteoric water, hydrocarbon fluid, mineralizing fluid, hot fluid) were found in the FA Formation of the Franceville basin (Cuney and Mathieu, 2000; Mathieu et al., 2000). The Francevillian succession, however, went into the oil window; in particular, shales of the FB Formation generated abundant hydrocarbons that migrated into the FA sandstones (Mossman et al., 2005). In the FB numerous sediment dykes crossing the black-shales and sandstone layers have been observed recently, most of them consist of fluid sands (Ndongo et al., 2016). The existence of a hydrothermal activity in the FC Formation that has been little studied is not excluded. Abundant Ti-oxides observed in plant fossils were interpreted as resulting from diagenetic mobilization of Ti of the protolith under acidic and reducing conditions, possibly associated with aqueous fluids rich in organic ligands (Galvez et al., 2012). Following this model, alteration of (volcano)clastic material associated with oil generation may have permitted transport and deposition of Ti in organic matter of the stromatolites we studied. Ti may also be mobilized and recrystallized through weathering in the presence of living cyanobacteria (Bower et al., 2015), although it is not known whether this could impregnate microfossils with TiO_2 as observed in burial diagenetic processes.

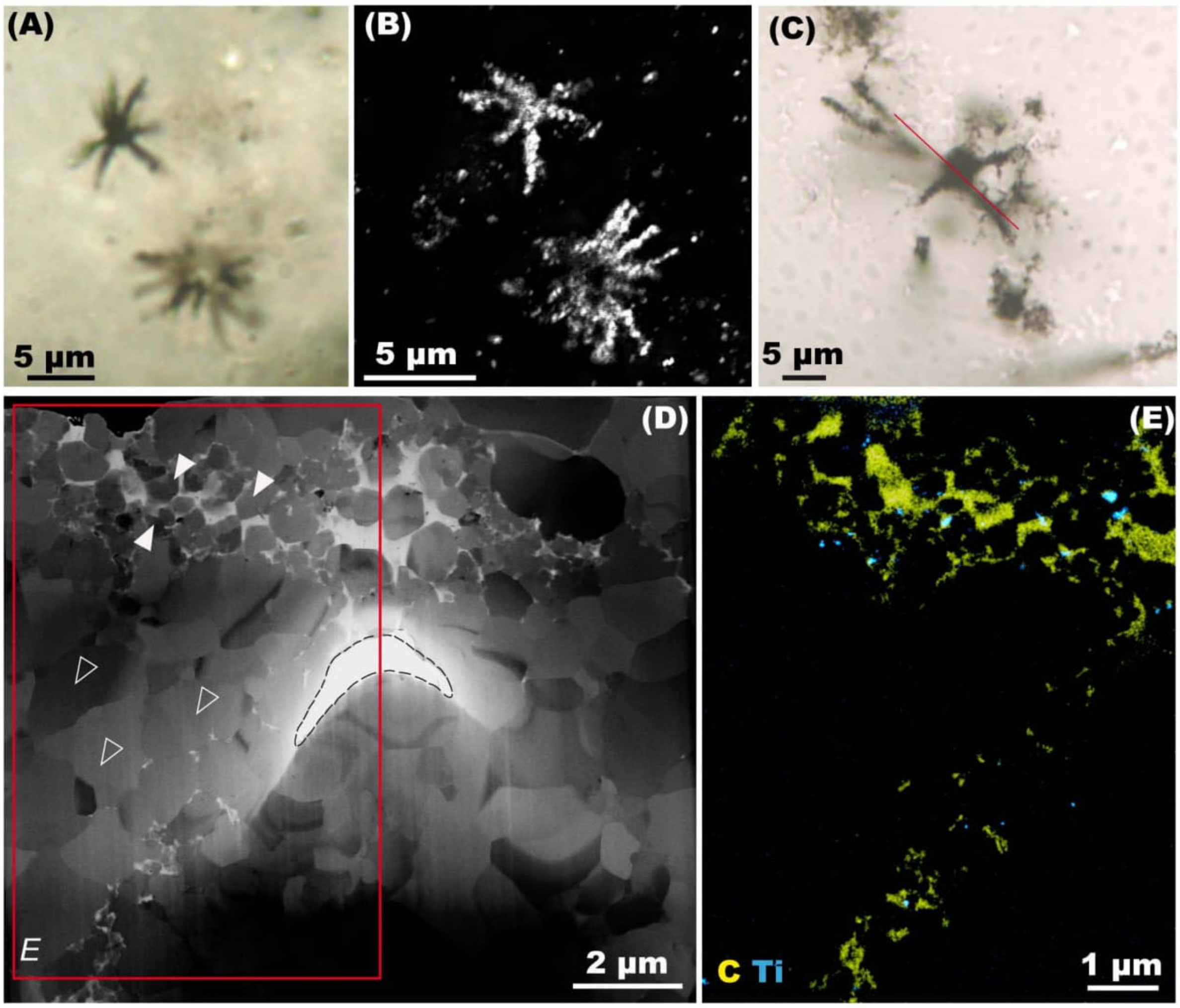

Fig. 13. Ultrastructure of Type 2 *Eoastrion*. (A) Photomicrograph, and (B) CLSM (B) of Type 2 *Eoastrion*. (B) Shows kerogen and residues of gold coating in white and quartz in black. The image was formed by the superposition of several confocal slices recorded at a depth interval of ~2 µm. The lower *Eoastrion* displays a large micrometric central structure devoid of organic matter and likely filled with quartz. (C) Photomicrograph of another *Eoastrion*. (D) STEM image of the FIB section cut along the red line in C. The central white zone outlined with a stippled line is a FIB-generated hole. Organic (in white) spines and central body of the microstructure are thoroughly impregnated with nanocrystals (solid arrowheads) of quartz (shades of grey). The quartz crystals surrounding the microstructure are micrometric (empty arrowheads). (E) EDS mapping of the boxed zone in (D) showing TiO_2 nanocrystals (blue) intimately associated with organic matter (yellow: carbon). (For interpretation of the references to colour in this figure legend, the reader is referred to the web version of this article.)

5.6. Iron in microfossils

The observation of hematite (Fe_2O_3) in association with several assemblages of Gunflint-type microfossils (Barghoorn and Tyler, 1965; Cloud and Licari, 1968; Knoll and Simonson, 1981; Walter et al., 1976) has been proposed as the result of Fe^{3+}-biomineralization by chemotrophic iron-oxidation metabolism. Indeed the morphologies of *G. minuta* and at least some *Eoastrion* are consistent with the Fe-oxidizing *Leptothrix* and *Metallogenium* bacteria, respectively. However, in those assemblages, hematite appears to replace organic matter in all microfossil morphotypes, which suggested that hematite could be the result of *post mortem* diagenetic alteration by oxidizing fluids (Shapiro and Konhauser, 2015). A possible precursor for this hematite could be diagenetic Fe^{2+}-minerals, e.g. pyrite (Wacey et al., 2013) or siderite (Fadel et al., 2017) that pseudomorph/replace microfossils through organic-matter oxidation coupled to S and/or Fe-reduction. Oxidation of pyritized Gunflint-type microfossils into hematite has indeed been observed by Cloud and Morrison (1980).

We observed abundant iron-bearing nanocrystals in one *Huroniospora* (Fig. 10) and a smaller amount in one broad filament (Fig. 8). In both microfossils, the iron-bearing nanocrystals are included in quartz grains and not in organic matter, a situation distinct to that of Ti-minerals. The mineralogy of these nanocrystals could not be addressed due to their small size. Diagenetic Fe^{2+}-minerals were otherwise preserved in this sample as disseminated ankerite, pyrite and chlorite. These Fe-nanocrystals could have formed *in vivo* or during degradation of the microfossils. Concentrations of the Fe^{2+}-minerals greenalite and siderite were observed only inside thick-walled *Huroniospora* and Type 2 *Gunflintia*, but not in thin-walled *Huroniospora*, Type 1 *Gunflintia* or *Animikiea* of the Gunflint Iron Formation (Lepot et al., 2017). These concentrations were interpreted as intracellular Fe-biominerals that recrystallized through *in situ* reduction in the presence of organic matter. The morphospecies-specific distribution and the absence of mineralization of the cell walls argued against *post-mortem* Fe-mineralization associated with diagenetic transport of external Fe into the microfossils (Lepot et al., 2017). Here, in the Francevillian *Huroniospora*, Fe-minerals are not directly associated with organic matter of the microfossil: they are only observed as inclusions in quartz crystals on each side of the organic wall. This distribution is thus reminiscent of that observed in Gunflint Iron Formation microfossils (Lepot et al., 2017). In the latter, the combination of microfossil morphology and intra-microfossil Fe-mineralization has been used to support a cyanobacterial origin and argue against chemotrophic or anoxygenic photosynthetic microorganisms that are smaller and do not mineralize iron intracellularly.

6. Conclusions

In spite of the poor preservation of the molecular structure of organic matter suggested by Raman spectroscopy, the studied ~2.1 Ga microfossils of the FC display similar patterns of preservation as the much less mature microfossils of 1.88 Ga Gunflint Iron Formation. The preservation of organic structures is allowed by local preservation of nanocrystalline quartz in a matrix where quartz is otherwise coarser, that is microcrystalline. The distribution of quartz nanocrystals in/on FC microfossil walls, coarser quartz crystals inside microfossils, and even coarser quartz crystals outside microfossils suggests that the distinct textures of three generations of opal that progressively impregnated and encapsulated the microfossils may have been carried through recrystallization into quartz. This supports that the textures of soft organic parts of FC microfossils and associated quartz crystals have strongly been influenced by the original organic biopolymers and the taphonomic sequence associated with cellular decay. Indentations created by the imprint of quartz nanocrystals at the surface of microfossils can be preserved during recrystallization into coarser quartz microcrystals. Such observations can provide criteria to distinguish putative Archean microfossils (Sugitani et al., 2015; Wacey et al., 2012) against bitumen accreted onto abiotic filamentous/sub-spherical siliceous microstructures.

In *Eoastrion*, similar association of quartz nanocrystals with spines suggests a preservation process similar to those of spherical and filamentous microfossils. The ultrastructures only rarely show a possible cell lumen. For the first time, we could extract *Eoastrion* through palynology, which is consistent though not diagnostic of microfossils in the absence of diagnostic ultrastructure. Observations of *Eoastrion* spines cross-cutting a late diagenetic chlorite crystal is consistent with formation of spines through migration, although it could also form as microfossil-embedding crystal.

Moreover, in the best preserved of the broad filaments, the central organic-poor canal and absence of organic matter migration toward the inside and outside of the sheath demonstrates the preservation of a thick sheath ultrastructure. This is the first report of such microfossils in shallow water Gunflint-type assemblages. The thick-sheath ultrastructure is well known among filamentous cyanobacteria and uncommon in other filamentous bacteria.

Finally, abundant nanocrystals of titanium oxides are embedded in organic matter, likely as the result of diagenetic mobilization of Ti and sequestration in fossil organic matter. In contrast, Fe-rich nanocrystals are located in quartz crystals rather than in organic matter, and may result of diagenetic transformation of intracellular/extracellular Fe-biominerals. The latter were used to support a cyanobacterial affinity for *Huroniospora* and Type 2 *Gunflintia* in the Gunflint Iron Formation (Lepot et al., 2017).

Acknowledgements

We thank for collaboration and support: the Ministry of Education, Research and Culture; Centre National Pour la Recherche Scientifique et Technique du Gabon (CENAREST); Ministry of Mines, Oil, Energy and Hydraulic Resources; General Direction of Mines and Geology of Gabon; Sylvia Bongo Foundation; Agence Nationale des Parcs Nationaux of Gabon; University of Masuku; COMILOG-Company, SOCOBA-Company; French Embassy at Libreville; and Institut Français du Gabon, French Ministry for Foreign Affairs. Permit was provided by CENAREST and National Parc Agency. For information and scientific discussion, we thank, P. Mouguiama, F.D. Idiata, L. White, J.C. Baloche, R. Oslisly, F. Gauthier Lafaye, F. Weber, F. Pambo, C. Laforest and J.L. Albert. Philippe Recourt and Sandra Ventalon are thanked for help with SEM and microscopy. Sylvie Regnier is thanked for thin section preparation. Laurence Debeauvais is thanked for palynological extraction. Ahmed Addad is thanked for help with STEM and SAED. David Troadec is thanked for FIB preparation. Christian Slomianny and the BiCeL laboratory are thanked for CLSM imaging. The TEM national facility in Lille (CCM) was supported by Région Hauts-de-France, European Regional Development Fund, and CNRS-INSU. A.E.A. was funded by the French CNRS-INSU, European financial support (FEDER) and the Région Nouvelle Aquitaine. FIB work was partly supported by the French RENATECH network. Analytical work was funded by Région Hauts-de-France project Vision-AIRR iM4 and ANR M6fossils ANR-15-CE31-0003-01. We thank Guochun Zhao (editor), James D. Schiffbauer, and David Wacey for constructive comments.

Appendix A. Supplementary data

Supplementary data associated with this article can be found, in the online version, at http://dx.doi.org/10.1016/j.precamres.2017.08.024.

References

Alleon, J., Bernard, S., Guillou, C.L., Marin-Carbonne, J., Pont, S., Beyssac, O., McKeegan, K.D., Robert, F., 2016. Molecular preservation of 1.88 Ga Gunflint organic microfossils as a function of temperature and mineralogy. Nat. Commun. 7, 11977. http://dx.doi.org/10.1038/ncomms11977.

Amard, B., Bertrand-Sarfati, J., 1997. Microfossils in 2000 Ma old cherty stromatolites of the Franceville Group, Gabon. Precambrian Res. 81, 197–221. http://dx.doi.org/10.1016/S0301-9268(96)00035-6.

Awramik, S.M., Barghoorn, E.S., 1977. The Gunflint microbiota. Precambrian Res. 5, 121–142. http://dx.doi.org/10.1016/0301-9268(77)90025-0.

Azziley Azzibrouck, G., 1986. Sédimentologie et géochimie du Francevillien B (Proterozoique inferieur). Metallogenie des gisements de manganese de Moanda, Gabon (Ph.D. thesis). Université Louis Pasteur, Strasbourg, France.

Barghoorn, E.S., Tyler, S.A., 1965. Microorganisms from the Gunflint Chert. Science 147, 563–575. http://dx.doi.org/10.1126/science.147.3658.563.

Bartley, J.K., 1996. Actualistic taphonomy of cyanobacteria: implications for the Precambrian fossil record. Palaios 11, 571–586. http://dx.doi.org/10.2307/3515192.

Bertrand-Sarfati, J., Potin, B., 1994. Microfossiliferous cherty stromatolites in the 2000 Ma Franceville Group, Gabon. Precambrian Res. 65, 341–356. http://dx.doi.org/10.1016/0301-9268(94)90112-0.

Beyssac, O., Goffé, B., Chopin, C., Rouzaud, J.N., 2002. Raman spectra of carbonaceous material in metasediments: a new geothermometer. J. Metamorph. Geol. 20, 859–871. http://dx.doi.org/10.1046/j.1525-1314.2002.00408.x.

Bonhomme, M.G., Gauthier-Lafaye, F., Weber, F., 1982. An example of lower proterozoic sediments: the Francevillian in Gabon. Precambrian Res. 18, 87–102. http://dx.doi.org/10.1016/0301-9268(82)90038-9.

Bouton, P., Thiéblemont, D., Gouin, J., Cocherie, A., Guerrot, C., Tegyey, M., Préat, A., Simo Ndounze, S., Kassadou, A., Boulingui, B., Ekhogha, H., Moussavou, M., 2009. Notice explicative de la carte géologique de la république du Gabon à 1/200 000, feuille Franceville – Boumango. Editions DGMG – Ministères des Mines, du Pétrole, des Hydrocarbures. Libreville. 79.

Bower, D.M., Hummer, D.R., Steele, A., Kyono, A., 2015. The Co-evolution of Fe-oxides, Ti-oxides, and other microbially induced mineral precipitates in sandy sediments: understanding the role of cyanobacteria in weathering and early diagenesis. J. Sediment. Res. 85, 1213–1227. http://dx.doi.org/10.2110/jsr.2015.76.

Brasier, M.D., Green, O.R., Jephcoat, A.P., Kleppe, A.K., Van Kranendonk, M.J., Lindsay, J.F., Steele, A., Grassineau, N.V., 2002. Questioning the evidence for Earth's oldest fossils. Nature 416, 76–81. http://dx.doi.org/10.1038/416076a.

Brasier, M.D., Green, O.R., Lindsay, J.F., McLoughlin, N., Steele, A., Stoakes, C., 2005. Critical testing of Earth's oldest putative fossil assemblage from the ~3.5 Ga Apex chert, Chinaman Creek, Western Australia. Precambrian Res. 140, 55–102. http://dx.doi.org/10.1016/j.precamres.2005.06.008.

Bros, R., Stille, P., Gauthier-Lafaye, F., Weber, F., Clauer, N., 1992. Sm-Nd isotopic dating of Proterozoic clay material: an example from the Francevillian sedimentary series, Gabon. Earth Planet. Sci. Lett. 113, 207–218. http://dx.doi.org/10.1016/0012-821X(92)90220-P.

Buick, R., 1990. Microfossil recognition in Archean rocks; an appraisal of spheroids and filaments from a 3500 m.y. old chert-barite unit at North Pole, Western Australia. Palaios 5, 441–459. http://dx.doi.org/10.2307/3514837.

Campbell, K.A., Lynne, B.Y., Handley, K.M., Jordan, S., Farmer, J.D., Guido, D.M., Foucher, F., Turner, S., Perry, R.S., 2015. Tracing biosignature preservation of geothermally silicified microbial textures into the geological record. Astrobiology 15, 858–882. http://dx.doi.org/10.1089/ast.2015.1307.

Canfield, D.E., Ngombi-Pemba, L., Hammarlund, E.U., Bengtson, S., Chaussidon, M., Gauthier-Lafaye, F., Meunier, A., Riboulleau, A., Rollion-Bard, C., Rouxel, O., Asael, D., Pierson-Wickmann, A.-C., Albani, A.E., 2013. Oxygen dynamics in the aftermath of the Great Oxidation of Earth's atmosphere. Proc. Natl. Acad. Sci. U.S.A. 110, 16736–16741. http://dx.doi.org/10.1073/pnas.1315570110.

Cloud, P.E., 1965. Significance of the Gunflint (Precambrian) Microflora. Science 148, 27–35. http://dx.doi.org/10.1126/science.148.3666.27.

Cloud, P.E., Licari, G.R., 1968. Microbiotas of the banded iron formations. Proc. Natl. Acad. Sci. U.S.A. 61, 779–786.

Cloud, P., Morrison, K., 1980. New microbial fossils from 2 Gyr old rocks in Northern Michigan. Geomicrobiol. J. 2, 161–178. http://dx.doi.org/10.1080/01490458009377759.

Condie, K.C., O'Neill, C., Aster, R.C., 2009. Evidence and implications for a widespread magmatic shutdown for 250 My on Earth. Earth Planet. Sci. Lett. 282, 294–298. http://dx.doi.org/10.1016/j.epsl.2009.03.033.

Cortial, F., 1985. Les bitumes du francevillien (protérozoïque inférieur du Gabon, 2000 Ma) et leurs kérogènes. Relations avec les minéralisations uranifères (PhD thesis). Université of Strasbourg, France 217 pp.

Cosmidis, J., Templeton, A.S., 2016. Self-assembly of biomorphic carbon/sulfur microstructures in sulfidic environments. Nat. Commun. 7, 12812. http://dx.doi.org/10.1038/ncomms12812.

Cuney, M., Mathieu, R., 2000. Extreme light rare earth element mobilization by diagenetic fluids in the geological environment of the Oklo natural reactor zones, Franceville basin, Gabon. Geology 28, 743–746. http://dx.doi.org/10.1130/0091-7613(2000) 28**743:ELREEM***2.0.CO;2.

Dubinina, G.A., 1970. Untersuchungen über die Morphologie von Metallogenium und die Beziehungen zu Mycoplasma. Z. Für Allg. Mikrobiol. 10, 309–320. http://dx.doi.org/10.1002/jobm.19700100502.

El Albani, A.E., Bengtson, S., Canfield, D.E., Bekker, A., Macchiarelli, R., Mazurier, A., Hammarlund, E.U., Boulvais, P., Dupuy, J.-J., Fontaine, C., Fürsich, F.T., Gauthier-Lafaye, F., Janvier, P., Javaux, E., Ossa, F.O., Pierson-Wickmann, A.-C., Riboulleau, A., Sardini, P., Vachard, D., Whitehouse, M., Meunier, A., 2010. Large colonial organisms with coordinated growth in oxygenated environments 2.1 Gyr ago. Nature 466, 100–104. http://dx.doi.org/10.1038/nature09166.

El Albani, A., Bengtson, S., Canfield, D.E., Riboulleau, A., Bard, C.R., Macchiarelli, R., Pemba, L.N., Hammarlund, E., Meunier, A., Mouele, I.M., Benzerara, K., Bernard, S., Boulvais, P., Chaussidon, M., Cesari, C., Fontaine, C., Chi-Fru, E., Ruiz, J.M.G., Gauthier-Lafaye, F., Mazurier, A., Pierson-Wickmann, A.C., Rouxel, O., Trentesaux, A., Vecoli, M., Versteegh, G.J.M., White, L., Whitehouse, M., Bekker, A., 2014. The 2.1 Ga old Francevillian biota: biogenicity, taphonomy and biodiversity. PLoS One 9, e99438. http://dx.doi.org/10.1371/journal.pone.0099438.

Emerson, D., Fleming, E.J., McBeth, J.M., 2010. Iron-oxidizing bacteria: an environmental and genomic perspective. Annu. Rev. Microbiol. 64, 561–583. http://dx.doi.org/10.1146/annurev.micro.112408.134208.

Fadel, A., Lepot, K., Busigny, V., Addad, A., Troadec, D., 2017. Iron mineralization and taphonomy of microfossils of the 2.45–2.21Ga Turee Creek Group, Western Australia. Precambrian Res. 298, 530–551. http://dx.doi.org/10.1016/j.precamres.2017.07.003.

Feybesse, J.L., Johan, V., Triboulet, C., Guerrot, C., Mayaga-Mikolo, F., Bouchot, V., Eko N'dong, J., 1998. The West Central African belt: a model of 2.5–2.0 Ga accretion and two-phase orogenic evolution. Precambrian Res. 87, 161–216. http://dx.doi.org/10.1016/S0301-9268(97)00053-3.

Fox, S.W., Yuyama, S., 1963. Abiotic production of primitive protein and formed microparticles. Ann. N. Y. Acad. Sci. 108, 487–494. http://dx.doi.org/10.1111/j.1749-6632.1963.tb13404.x.

Galvez, M.E., Beyssac, O., Benzerara, K., Menguy, N., Bernard, S., Cox, S.C., 2012. Micro- and nano-textural evidence of Ti(–Ca–Fe) mobility during fluid–rock interactions in carbonaceous lawsonite-bearing rocks from New Zealand. Contrib. Mineral. Petrol. 164, 895–914. http://dx.doi.org/10.1007/s00410-012-0780-2.

García Ruiz, J.M., Carnerup, A., Christy, A.G., Welham, N.J., Hyde, S.T., 2002. Morphology: an ambiguous indicator of biogenicity. Astrobiology 2, 353–369. http://dx.doi.org/10.1089/153110702762027925.

Gauthier-Lafaye, F., 1986. Les Gisements d'uranium du Gabon et les réacteurs d'Oklo [WWW Document]. URL: < http://www.idref.fr/028804147 > (accessed 02.01.2017).

Gauthier-Lafaye, F., 2006. Time constraint for the occurrence of uranium deposits and natural nuclear fission reactors in the Paleoproterozoic Franceville Basin (Gabon). Geol. Soc. Am. Mem. 198, 157–167. http://dx.doi.org/10.1130/2006.1198(09).

Gauthier-Lafaye, F., Weber, F., 1989. The Francevillian (Lower Proterozoic) uranium ore deposits of Gabon. Econ. Geol. 84, 2267–2285. http://dx.doi.org/10.2113/gsecongeo.84.8.2267.

Gauthier-Lafaye, F., Weber, F., 2003. Natural nuclear fission reactors: time constraints for occurrence, and their relation to uranium and manganese deposits and to the evolution of the atmosphere. Precambrian Res. 120, 81–100. http://dx.doi.org/10.1016/S0301-9268(02)00163-8.

Grey, K., 1999. A modified palynological preparation technique for the extraction of large Neoproterozoic acanthomorph acritarchs and other acid-insoluble microfossils, Western Australia Geological Survey, Record 1999/10, 23 pp.

Han, T.M., Runnegar, B., 1992. Megascopic eukaryotic algae from the 2.1-billion-year-old negaunee iron-formation, Michigan. Science 257, 232–235. http://dx.doi.org/10.1126/science.1631544.

Hanada, S., 2003. Filamentous Anoxygenic Phototrophs in Hot Springs. Microbes Environ. 18, 51–61. http://dx.doi.org/10.1264/jsme2.18.51.

Horodyski, R.J., Bloeser, B., 1977. Laminated algal mats from a coastal lagoon, Laguna Mormona, Baja California, Mexico. J. Sediment. Res. 47, 680–696. http://dx.doi.org/10.1306/212F7220-2B24-11D7-8648000102C1865D.

Jones, B., Renaut, R.W., Rosen, M.R., 2001. Taphonomy of silicified filamentous microbes in modern geothermal sinters—implications for identification. Palaios 16, 580–592. http://dx.doi.org/10.1669/0883-1351(2001) 016**0580:TOSFMI***2.0.CO;2.

Kempe, A., Wirth, R., Altermann, W., Stark, R.W., Schopf, J.W., Heckl, W.M., 2005. Focussed ion beam preparation and in situ nanoscopic study of Precambrian acritarchs. Precambrian Res. 140, 36–54. http://dx.doi.org/10.1016/j.precamres.2005.07.002.

Knoll, A.H., 2003. The geological consequences of evolution. Geobiology 1, 3–14. http://dx.doi.org/10.1046/j.1472-4669.2003.00002.x.

Knoll, A.H., Simonson, B., 1981. Early proterozoic microfossils and penecontemporaneous quartz cementation in the Sokoman Iron Formation, Canada. Science 211, 478–480. http://dx.doi.org/10.1126/science.211.4481.478.

Knoll, A.H., Barghoorn, E.S., Awramik, S.M., 1978. New microorganisms from the Aphebian gunflint iron formation, Ontario. J. Paleontol. 52, 976–992.

Knoll, A.H., Strother, P.K., Rossi, S., 1988. Distribution and diagenesis of microfossils from the lower Proterozoic Duck Creek Dolomite, Western Australia. Precambrian Res. 38, 257–279. http://dx.doi.org/10.1016/0301-9268(88)90005-8.

Knoll, A.H., Javaux, E.J., Hewitt, D., Cohen, P., 2006. Eukaryotic organisms in proterozoic oceans. Philos. Trans. R. Soc. Lond. B Biol. Sci. 361, 1023–1038. http://dx.doi.org/10.1098/rstb.2006.1843.

Kouketsu, Y., Mizukami, T., Mori, H., Endo, S., Aoya, M., Hara, H., Nakamura, D., Wallis, S., 2014. A new approach to develop the Raman carbonaceous material geothermometer for low-grade metamorphism using peak width. Isl. Arc 23, 33–50. http://dx.doi.org/10.1111/iar.12057.

Krumbein, W.E., 2010. Gunflint Chert Microbiota Revisited - Neither Stromatolites, Nor Cyanobacteria. In: Microbial Mats, Cellular Origin, Life in Extreme Habitats and Astrobiology. Springer, Dordrecht, pp. 53–70. http://dx.doi.org/10.1007/978-90-481-3799-2_4.

Lamb, D.M., Awramik, S.M., Chapman, D.J., Zhu, S., 2009. Evidence for eukaryotic diversification in the ~1800 million-year-old Changzhougou Formation, North China. Precambrian Res. 173, 93–104. http://dx.doi.org/10.1016/j.precamres.2009.05.005.

Lanier, W.P., 1986. Approximate growth rates of early Proterozoic microstromatolites as deduced by biomass productivity. Palaois 1, 525–542. http://dx.doi.org/10.2307/3514705.

Larkin, J.M., Strohl, W.R., 1983. Beggiatoa, thiothrix, and thioploca. Annu. Rev. Microbiol. 37, 341–367. http://dx.doi.org/10.1146/annurev.mi.37.100183.002013.

Lepot, K., Philippot, P., Benzerara, K., Wang, G.-Y., 2009. Garnet-filled trails associated with carbonaceous matter mimicking microbial filaments in Archean basalt. Geobiology 7, 393–402. http://dx.doi.org/10.1111/j.1472-4669.2009.00208.x.

Lepot, K., Benzerara, K., Philippot, P., 2011. Biogenic versus metamorphic origins of diverse microtubes in 2.7 Gyr old volcanic ashes: multi-scale investigations. Earth Planet. Sci. Lett. 312, 37–47. http://dx.doi.org/10.1016/j.epsl.2011.10.016.

Lepot, K., Compère, P., Gérard, E., Namsaraev, Z., Verleyen, E., Tavernier, I., Hodgson, D.A., Vyverman, W., Gilbert, B., Wilmotte, A., Javaux, E.J., 2014. Organic and mineral imprints in fossil photosynthetic mats of an East Antarctic lake. Geobiology 12, 424–450. http://dx.doi.org/10.1111/gbi.12096.

Lepot, K., Addad, A., Knoll, A.H., Wang, J., Troadec, D., Béché, A., Javaux, E.J., 2017. Iron minerals within specific microfossil morphospecies of the 1.88 Ga Gunflint Formation. Nat. Commun. 8, 14890. http://dx.doi.org/10.1038/ncomms14890.

Lyons, T.W., Reinhard, C.T., Planavsky, N.J., 2014. The rise of oxygen in Earth's early ocean and atmosphere. Nature 506, 307–315. http://dx.doi.org/10.1038/nature13068.

Mares, J., Lara, Y., Dadakova, I., Hauer, T., Uher, B., Wilmotte, A., Kastovsky, J., 2015. Phylogenetic analysis of cultivation-resistant terrestrial cyanobacteria with massive sheaths (*Stigonema Spp*. and *Petalonema Alatum*, Nostocales, Cyanobacteria) using single-cell and filament sequencing of environmental samples. J. Phycol. 51, 288–297. http://dx.doi.org/10.1111/jpy.12273.

Mathieu, R., Cuney, M., Cathelineau, M., 2000. Geochemistry of palaeofluids circulation in the Franceville basin and around Oklo natural nuclear reaction zones (Gabon). J. Geochem. Explor. 69–70, 245–249. http://dx.doi.org/10.1016/S0375-6742(00)00054-6.

Moreau, J.W., Sharp, T.G., 2004. A transmission electron microscopy study of silica and kerogen biosignatures in approximately 1.9 Ga gunflint microfossils. Astrobiology 4, 196–210. http://dx.doi.org/10.1089/153110704323175142.

Mossman, D.J., Gauthier-Lafaye, F., Jackson, S.E., 2005. Black shales, organic matter, ore genesis and hydrocarbon generation in the Paleoproterozoic Franceville Series, Gabon. Precambrian Res. 137, 253–272. http://dx.doi.org/10.1016/j.precamres.2005.03.005.

Moussavou, M., Edou-Minko, A., 2006. Contribution à l'histoire thermo-tectonique précambrienne du complexe annulaire de Ngoutou par la géochimie et la géochronologie U/Pb sur minéraux accessoires (Bassin Francevillien d'Okondja, Gabon). Afr. Geosci. Rev. 13, 53–61.

Nassif, N., Bouvet, O., Noelle Rager, M., Roux, C., Coradin, T., Livage, J., 2002. Living bacteria in silica gels. Nat. Mater. 1, 42–44. http://dx.doi.org/10.1038/nmat709.

Ndongo, A., Guiraud, M., Vennin, E., Mbina, M., Buoncristiani, J.-F., Thomazo, C., Flotté, N., 2016. Control of fluid-pressure on early deformation structures in the Paleoproterozoic extensional Franceville Basin (SE Gabon). Precambrian Res. 277, 1–25. http://dx.doi.org/10.1016/j.precamres.2016.02.003.

Ngombi-Pemba, L., Albani, A.E., Meunier, A., Grauby, O., Gauthier-Lafaye, F., 2014. From detrital heritage to diagenetic transformations, the message of clay minerals contained within shales of the Palaeoproterozoic Francevillian basin (Gabon). Precambrian Res. Part 1, 63–76. http://dx.doi.org/10.1016/j.precamres.2014.09.016.

Oehler, J.H., 1976. Experimental studies in Precambrian paleontology: structural and chemical changes in blue-green algae during simulated fossilization in synthetic chert. Geol. Soc. Am. Bull. 87, 117–129. http://dx.doi.org/10.1130/0016-7606(1976) 87**117:ESIPPS***2.0.CO;2.

Oehler, J.H., 1977. Microflora of the H.Y.C. Pyritic Shale Member of the Barney Creek Formation (McArthur Group), middle Proterozoic of northern Australia, Alcheringa Australas. J. Palaeontol. 1, 315–349. http://dx.doi.org/10.1080/03115517708527768.

Orange, F., Westall, F., Disnar, J.-R., Prieur, D., Bienvenu, N., Romancer, M.L., Défarge, C., 2009. Experimental silicification of the extremophilic Archaea *Pyrococcus abyssi* and *Methanocaldococcus jannaschii*: applications in the search for evidence of life in early Earth and extraterrestrial rocks. Geobiology 7, 403–418. http://dx.doi.org/10.1111/j.1472-4669.2009.00212.x.

Orange, F., Chabin, A., Gorlas, A., Lucas-Staat, S., Geslin, C., Le Romancer, M., Prangishvili, D., Forterre, P., Westall, F., 2011. Experimental fossilisation of viruses from extremophilic Archaea. Biogeosciences 8, 1465–1475. http://dx.doi.org/10.5194/bg-8-1465-2011.

Ossa Ossa, F., El Albani, A., Hofmann, A., Bekker, A., Gauthier-Lafaye, F., Pambo, F., Meunier, A., Fontaine, C., Boulvais, P., Pierson-Wickmann, A.-C., Cavalazzi, B., Macchiarelli, R., 2013. Exceptional preservation of expandable clay minerals in the ca. 2.1 Ga black shales of the Francevillian basin, Gabon and its implication for atmospheric oxygen accumulation. Chem. Geol. 362, 181–192. http://dx.doi.org/10.1016/j.chemgeo.2013.08.011.

Pambo, F., 2004. Conditions de formation des carbonates de manganèse protézoïques et analyse minéralogique et géochimique des minerais à bioxydes de manganèse associés dans le gisement de Moanda (Sud-Est, Gabon) (Ph.D. thesis). Université de Bourgogne, Dijon.

Parnell, J., 2004. Titanium mobilization by hydrocarbon fluids related to sill intrusion in a sedimentary sequence, Scotland. Ore Geol. Rev. 24, 155–167. http://dx.doi.org/10.1016/j.oregeorev.2003.08.010.

Pe-Piper, G., Murphy, J.B., 1992. Late Proterozoic high-titanium basalts in the Avalon Zone of Nova Scotia. Can. Mineral. 30, 1167–1176.

Phoenix, V.R., Adams, D.G., Konhauser, K.O., 2000. Cyanobacterial viability during hydrothermal biomineralisation. Chem. Geol. 169, 329–338. http://dx.doi.org/10.1016/S0009-2541(00)00212-6.

Planavsky, N., Rouxel, O., Bekker, A., Shapiro, R., Fralick, P., Knudsen, A., 2009. Iron-oxidizing microbial ecosystems thrived in late Paleoproterozoic redox-stratified oceans. Earth Planet. Sci. Lett. 286, 230–242. http://dx.doi.org/10.1016/j.epsl.2009.06.033.

Préat, A., Bouton, P., Thiéblemont, D., Prian, J.-P., Ndounze, S.S., Delpomdor, F., 2011. Paleoproterozoic high $\delta^{13}C$ dolomites from the Lastoursville and Franceville basins (SE Gabon): stratigraphic and synsedimentary subsidence implications. Precambrian Res. 189, 212–228. http://dx.doi.org/10.1016/j.precamres.2011.05.013.

Rasmussen, B., Fletcher, I.R., Bekker, A., Muhling, J.R., Gregory, C.J., Thorne, A.M., 2012. Deposition of 1.88-billion-year-old iron formations as a consequence of rapid crustal growth. J. Geol. Soc. India 80http://dx.doi.org/10.1007/s12594-012-0112-1. 147–147.

Reid, R.P., Visscher, P.T., Decho, A.W., Stolz, J.F., Bebout, B.M., Dupraz, C., Macintyre, I.G., Paerl, H.W., Pinckney, J.L., Prufert-Bebout, L., Steppe, T.F., Des Marais, D.J., 2000. The role of microbes in accretion, lamination and early lithification of modern marine stromatolites. Nature 406, 989–992.

Schiffbauer, J.D., Xiao, S., 2011. Paleobiological Applications of focused ion beam electron microscopy (FIB-EM): an ultrastructural approach to the (micro)fossil record. In: Quantifying the Evolution of Early Life, Topics in Geobiology. Springer, Dordrecht, pp. 321–354. http://dx.doi.org/10.1007/978-94-007-0680-4_13.

Schiffbauer, J.D., Wallace, A.F., Hunter, J.L., Kowalewski, M., Bodnar, R.J., Xiao, S., 2012. Thermally-induced structural and chemical alteration of organic-walled microfossils: an experimental approach to understanding fossil preservation in metasediments. Geobiology 10, 402–423. http://dx.doi.org/10.1111/j.1472-4669.2012.00332.x.

Schneider, D.A., Bickford, M.E., Cannon, W.F., Schulz, K.J., Hamilton, M.A., 2002. Age of volcanic rocks and syndepositional iron formations, Marquette Range Supergroup: implications for the tectonic setting of Paleoproterozoic iron formations of the Lake Superior region. Can. J. Earth Sci. 39, 999–1012. http://dx.doi.org/10.1139/e02-016.

Schopf, J.W., 1993. Microfossils of the early Archean apex chert: new evidence of the antiquity of life. Science 260, 640–646. http://dx.doi.org/10.1126/science.260.5108.640.

Schopf, J.W., 2006. Fossil evidence of Archaean life. Philos. Trans. R. Soc. Lond. B Biol. Sci. 361, 869–885. http://dx.doi.org/10.1098/rstb.2006.1834.

Schopf, J.W., Klein, C., 1992. The Proterozoic Biosphere: A Multidisciplinary Study. Cambridge University Press.

Schopf, J.W., Kudryavtsev, A.B., 2009. Confocal laser scanning microscopy and Raman imagery of ancient microscopic fossils. Precambrian Res. 173, 39–49. http://dx.doi.org/10.1016/j.precamres.2009.02.007.

Schopf, J.W., Prasad, K.N., 1978. Microfossils in Collenia-like stromatolites from the proterozoic Vempalle formation of the Cuddapah Basin, India. Precambrian Res. 6, 347–366. http://dx.doi.org/10.1016/0301-9268(78)90022-0.

Schopf, J.W., Kudryavtsev, A.B., Agresti, D.G., Czaja, A.D., Wdowiak, T.J., 2005. Raman imagery: a new approach to assess the geochemical maturity and biogenicity of permineralized precambrian fossils. Astrobiology 5, 333–371. http://dx.doi.org/10.1089/ast.2005.5.333.

Shapiro, R.S., Konhauser, K.O., 2015. Hematite-coated microfossils: primary ecological fingerprint or taphonomic oddity of the Paleoproterozoic? Geobiology 13, 209–224. http://dx.doi.org/10.1111/gbi.12127.

Starmach, K., 1963. *Plectonema tatricum Starmach*, a new species of blue-green algae from the Tatra Mountains. Acta Hydrobiol. 10 (4), 427–434.

Stoecker, K., Bendinger, B., Schöning, B., Nielsen, P.H., Nielsen, J.L., Baranyi, C., Toenshoff, E.R., Daims, H., Wagner, M., 2006. Cohn's Crenothrix is a filamentous methane oxidizer with an unusual methane monooxygenase. Proc. Natl. Acad. Sci. U.S.A. 103, 2363–2367. http://dx.doi.org/10.1073/pnas.0506361103.

Strother, P.K., Tobin, K., 1987. Observations on the genus *huroniospora barghoorn*: implications for paleoecology of the gunflint microbiota. Precambrian Res. 36, 323–333. http://dx.doi.org/10.1016/0301- 9268(87)90029-5.

Sugitani, K., Mimura, K., Takeuchi, M., Lepot, K., Ito, S., Javaux, E.J., 2015. Early evolution of large micro-organisms with cytological complexity revealed by microanalyses of 3.4 Ga organic-walled microfossils. Geobiology 13, 507–521. http://dx.doi.org/10.1111/gbi.12148.

Thiéblemont, D., Castaing, C., Billa, M., Bouton, P., Préat, A., 2009. Notice explicative de la Carte géologique et des Ressources minérales de la République gabonaise à 1/1 000 000. Editions DGMG, Ministère des Mines, du Pétrole, des Hydrocarbures. Libreville. 384p.

Tomitani, A., Knoll, A.H., Cavanaugh, C.M., Ohno, T., 2006. The evolutionary diversification of cyanobacteria: molecular–phylogenetic and paleontological perspectives. Proc. Natl. Acad. Sci. 103, 5442–5447. http://dx.doi.org/10.1073/pnas.0600999103.

Tyler, S.A., Barghoorn, E.S., 1954. Occurrence of structurally preserved plants in pre-Cambrian rocks of the Canadian Shield. Science 119, 606–608. http://dx.doi.org/10.1126/science.119.3096.606.

Ueno, Y., Yoshioka, H., Maruyama, S., Isozaki, Y., 2004. Carbon isotopes and petrography of kerogens in ~3.5-Ga hydrothermal silica dikes in the North Pole area, Western Australia1. Geochim. Cosmochim. Acta 68, 573–589. http://dx.doi.org/10.1016/S0016-7037(03)00462-9.

Van Veen, W.L., Mulder, E.G., Deinema, M.H., 1978. The *Sphaerotilus-Leptothrix* group of bacteria. Microbiol. Rev. 42, 329–356.

Wacey, D., Menon, S., Green, L., Gerstmann, D., Kong, C., Mcloughlin, N., Saunders, M., Brasier, M., 2012. Taphonomy of very ancient microfossils from the ~3400 Ma Strelley Pool Formation and ~1900 Ma Gunflint Formation: New insights using a focused ion beam. Precambrian Res. 220–221, 234–250. http://dx.doi.org/10.1016/j.precamres.2012.08.005.

Wacey, D., McLoughlin, N., Kilburn, M.R., Saunders, M., Cliff, J.B., Kong, C., Barley, M.E., Brasier, M.D., 2013. Nanoscale analysis of pyritized microfossils reveals differential heterotrophic consumption in the ~1.9-Ga Gunflint chert. Proc. Natl. Acad. Sci. 110, 8020–8024. http://dx.doi.org/10.1073/pnas.1221965110.

Walter, M.R., Goode, A.D.T., Hall, W.D.M., 1976. Microfossils from a newly discovered Precambrian stromatolitic iron formation in Western Australia. Nature 261, 221–223. http://dx.doi.org/10.1038/261221a0.

Weber, F., 1969. Une série précambrienne du Gabon: le Francevillien. Sédimentologie, géochimie, relations avec les gîtes minéraux associés (PhD thesis). Université Louis Pasteur and Memoire Service Cartes Géologique Alsace-Lorraine, Strasbourg, France 328 pp.

Weber, F., Gauthier-Lafaye, F., 2013. No proof from carbon isotopes in the Francevillian (Gabon) and Onega (Fennoscandian shield) basins of a global oxidation event at 1980–2090 Ma following the Great Oxidation Event (GOE). C. R. Geosci. 345, 28–35. http://dx.doi.org/10.1016/j.crte.2012.12.003.

Weber, F., Gauthier-Lafaye, F., Whitechurch, H., Ulrich, M., El Albani, A., 2016. The 2-Ga Eburnean Orogeny in Gabon and the opening of the Francevillian intracratonic basins: a review. C. R. Geosci. 348, 572–586. http://dx.doi.org/10.1016/j.crte.2016.07.003.

Yun, Z., 1984. A Gunflint type of microfossil assemblage from early Proterozoic stromatolitic cherts in China. Nature 309, 547–549. http://dx.doi.org/10.1038/309547a0.

Zavarzin, G.A., 1981. The Genus Metallogenium. In: Starr, M.P., Stolp, H., Trüper, H.G., Balows, A., Schlegel, H.G. (Eds.), The Prokaryotes. Springer, Berlin Heidelberg, pp. 524–528. http://dx.doi.org/10.1007/978-3-662-13187-9_43.

ToF-SIMS Tables

Nonadecanone ($C_{19}H_{38}O$) positif ions

Proposed formula	Meas. m/z	Calc. m/z	δ (Da)	Int.	Rel. Int. (%)
H^+	1.0098	1.0078	0.0020	28	0,028%
C^+	11.9991	12.0000	-0.0009	2	0,002%
CH^+	13.0078	13.0078	-0.0000	5	0,005%
CH_2^+	14.0156	14.0157	-0.0001	11	0,011%
CH_3^+	15.0242	15.0235	0.0008	53	0,054%
$C_2H_2^+$	26.0146	26.0157	-0.0011	19	0,019%
$C_2H_3^+$	27.0234	27.0235	-0.0000	486	0,494%
$C_2H_4^+$	28.0313	28.0313	-0.0000	57	0,058%
$C_2H_5^+$	29.0399	29.0391	0.0008	719	0,731%
$C_2H_6^+$	30.0438	30.0469	-0.0032	22	0,022%
CH_3O^+	31.0186	31.0184	0.0002	22	0,022%
C_3H^+	37.0058	37.0078	-0.0021	2	0,002%
$C_3H_2^+$	38.0137	38.0157	-0.0020	9	0,009%
$C_3H_3^+$	39.0219	39.0235	-0.0015	354	0,360%
$C_3H_4^+$	40.0282	40.0313	-0.0031	44	0,045%
C_2HO^+	41.0078	41.0027	0.0050	57	0,058%
$C_3H_5^+$	41.0385	41.0391	-0.0006	1062	1,080%
$C_3H_6^+$	42.0443	42.0470	-0.0027	153	0,156%
$C_2H_3O^+$	43.0194	43.0184	0.0010	1226	1,247%
$C_3H_7^+$	43.0544	43.0548	-0.0004	282	0,287%
$C_2H_4O^+$	44.0228	44.0262	-0.0035	46	0,047%
$C_3H_8^+$	44.0583	44.0626	-0.0043	60	0,061%
$C_2H_5O^+$	45.0355	45.0340	0.0014	179	0,182%
$C_4H_2^+$	50.0116	50.0157	-0.0041	18	0,018%
$C_4H_3^+$	51.0211	51.0235	-0.0023	70	0,071%
$C_4H_4^+$	52.0290	52.0313	-0.0023	39	0,040%
C_3HO^+	53.0050	53.0027	0.0023	12	0,012%
$C_4H_5^+$	53.0366	53.0391	-0.0025	246	0,250%
$C_4H_6^+$	54.0470	54.0470	0.0000	149	0,152%
$C_3H_3O^+$	55.0179	55.0184	-0.0005	111	0,113%
$C_4H_7^+$	55.0548	55.0548	0.0000	861	0,876%
$C_3H_4O^+$	56.0218	56.0262	-0.0044	13	0,013%
$C_4H_8^+$	56.0593	56.0626	-0.0033	145	0,147%
$C_3H_5O^+$	57.0335	57.0340	-0.0005	62	0,063%
$C_4H_9^+$	57.0717	57.0704	0.0013	490	0,498%
$C_3H_6O^+$	58.0436	58.0419	0.0018	314	0,319%
$C_4H_{10}^+$	58.0729	58.0782	-0.0054	54	0,055%
$C_3H_7O^+$	59.0515	59.0497	0.0018	133	0,135%
$C_5H_3^+$	63.0185	63.0235	-0.0050	26	0,026%
$C_5H_5^+$	65.0353	65.0391	-0.0038	95	0,097%
$C_5H_6^+$	66.0437	66.0469	-0.0032	46	0,047%
$C_5H_7^+$	67.0540	67.0548	-0.0008	343	0,349%

$C_4H_4O^+$	68.0301	68.0262	0.0039	15	0,015%
$C_5H_8{}^+$	68.0617	68.0626	-0.0009	111	0,113%
$C_4H_5O^+$	69.0373	69.0340	0.0033	35	0,036%
$C_5H_9{}^+$	69.0718	69.0704	0.0014	390	0,397%
$C_4H_6O^+$	70.0404	70.0419	-0.0015	20	0,020%
$C_5H_{10}{}^+$	70.0766	70.0782	-0.0017	56	0,057%
$C_4H_7O^+$	71.0510	71.0497	0.0013	625	0,636%
$C_5H_{11}{}^+$	71.0864	71.0861	0.0004	108	0,110%
$C_4H_8O^+$	72.0563	72.0575	-0.0013	52	0,053%
$C_6H_5{}^+$	77.0334	77.0391	-0.0057	91	0,093%
$C_6H_6{}^+$	78.0405	78.0469	-0.0064	37	0,038%
$C_6H_7{}^+$	79.0500	79.0548	-0.0048	132	0,134%
$C_6H_8{}^+$	80.0562	80.0626	-0.0064	36	0,037%
$C_6H_9{}^+$	81.0697	81.0704	-0.0007	214	0,218%
$C_6H_{10}{}^+$	82.0838	82.0782	0.0056	56	0,057%
$C_5H_7O^+$	83.0495	83.0497	-0.0002	53	0,054%
$C_6H_{11}{}^+$	83.0899	83.0861	0.0038	168	0,171%
$C_5H_8O^+$	84.0583	84.0575	0.0007	43	0,044%
$C_6H_{12}{}^+$	84.0874	84.0939	-0.0065	21	0,021%
$C_5H_9O^+$	85.0658	85.0653	0.0005	75	0,076%
$C_6H_{13}{}^+$	85.1125	85.1017	0.0108	68	0,069%
$C_5H_{10}O^+$	86.0660	86.0732	-0.0071	14	0,014%
$C_7H_7{}^+$	91.0483	91.0548	-0.0064	95	0,097%
$C_7H_9{}^+$	93.0725	93.0704	0.0020	51	0,052%
$C_7H_{10}{}^+$	94.0833	94.0782	0.0051	19	0,019%
$C_7H_{11}{}^+$	95.0878	95.0861	0.0017	120	0,122%
$C_7H_{12}{}^+$	96.0982	96.0939	0.0043	34	0,035%
$C_6H_9O^+$	97.0660	97.0653	0.0007	52	0,053%
$C_7H_{13}{}^+$	97.1088	97.1017	0.0071	79	0,080%
$C_6H_{10}O^+$	98.0716	98.0732	-0.0015	39	0,040%
$C_6H_{11}O^+$	99.0791	99.0810	-0.0019	30	0,031%
$C_8H_9{}^+$	105.0643	105.0704	-0.0062	32	0,033%
$C_8H_{11}{}^+$	107.0846	107.0861	-0.0014	16	0,016%
$C_8H_{13}{}^+$	109.1082	109.1017	0.0065	49	0,050%
$C_8H_{14}{}^+$	110.1066	110.1095	-0.0029	14	0,014%
$C_7H_{11}O^+$	111.0772	111.0810	-0.0038	28	0,028%
$C_7H_{12}O^+$	112.0933	112.0888	0.0045	18	0,018%
$C_7H_{13}O^+$	113.0966	113.0966	-0.0000	32	0,033%
$C_9H_8{}^+$	116.0602	116.0626	-0.0024	13	0,013%
$C_9H_9{}^+$	117.0662	117.0704	-0.0042	16	0,016%
$C_9H_{15}{}^+$	123.1170	123.1174	-0.0004	11	0,011%
$C_9H_{16}{}^+$	124.1235	124.1252	-0.0017	6	0,006%
$C_9H_{17}{}^+$	125.1280	125.1330	-0.0051	9	0,009%
$C_8H_{15}O^+$	127.1101	127.1123	-0.0022	16	0,016%
$C_{10}H_8{}^+$	128.0530	128.0626	-0.0096	15	0,015%
$C_{17}H_{35}O^+$	255.2584	255.2688	-0.0104	25	0,025%

$C_{18}H_{35}O^+$	267.2565	267.2688	-0.0123	33	0,034%
$C_{18}H_{37}O^+$	269.2690	269.2844	-0.0155	22	0,022%
$C_{19}H_{35}O^+$	279.2654	279.2688	-0.0034	13	0,013%
$C_{19}H_{37}O^+$	281.2863	281.2844	0.0018	91	0,093%
$C_{19}H_{38}O^+$	282.2930	282.2923	0.0007	45	0,046%
$C_{19}H_{39}O^+$	283.2994	283.3001	-0.0007	406	0,413%
$C_{19}H_{40}O^+$	284.2992	284.3079	-0.0087	126	0,128%
$C_{19}H_{41}O^+$	285.3017	285.3157	-0.0140	19	0,019%
$C_{20}H_{41}O^+$	297.3040	297.3157	-0.0117	27	0,027%
$C_{21}H_{43}O^+$	311.3388	311.3314	0.0075	13	0,013%
$C_{22}H_{43}O^+$	323.3038	323.3314	-0.0276	14	0,014%
$C_{22}H_{45}O^+$	325.3057	325.3470	-0.0413	14	0,014%
$C_{23}H_{47}O^+$	339.3235	339.3627	-0.0392	14	0,014%
$C_{38}H_{73}O_2{}^+$	561.5497	561.5611	-0.0114	13	0,013%
$C_{38}H_{75}O_2{}^+$	563.5970	563.5767	0.0203	49	0,050%
$C_{38}H_{76}O_2{}^+$	564.5844	564.5845	-0.0001	34	0,035%
$C_{38}H_{77}O_3{}^+$	565.5917	565.5924	-0.0007	93	0,095%
$C_{38}H_{78}O_2{}^+$	566.6075	566.6002	0.0073	38	0,039%
$C_{38}H_{79}O_2{}^+$	567.6240	567.6080	0.0160	13	0,013%
Na^+	22.9921	22.9898	0.0024	180	0,183%
K^+	38.9668	38.9637	0.0031	32	0,033%

Nonadecanone ($C_{19}H_{38}O$) negative ions					
Proposed formula	Meas. m/z	Calc. m/z	δ (Da)	Int.	Rel. Int. (%)
H^-	1.0080	1.0078	0.0002	3940	13,744%
C^-	12.0002	12.0000	0.0002	83	0,290%
CH^-	13.0079	13.0078	0.0001	267	0,931%
$CH_2{}^-$	14.0158	14.0157	0.0002	61	0,213%
$CH_3{}^-$	15.0239	15.0235	0.0005	7	0,024%
O^-	15.9946	15.9949	-0.0004	50	0,174%
HO^-	17.0022	17.0027	-0.0005	59	0,206%
$C_2{}^-$	24.0000	24.0000	-0.0000	99	0,345%
C_2H^-	25.0091	25.0078	0.0013	645	2,250%
$C_2H_2{}^-$	26.0121	26.0157	-0.0036	21	0,073%
$C_2H_3{}^-$	27.0269	27.0235	0.0034	12	0,042%
$C_3{}^-$	36.0013	36.0000	0.0013	35	0,122%
C_3H^-	37.0101	37.0078	0.0022	42	0,147%
$C_3H_2{}^-$	38.0169	38.0157	0.0012	53	0,185%
$C_3H_3{}^-$	39.0242	39.0235	0.0007	15	0,052%
C_2O^-	39.9955	39.9949	0.0006	11	0,038%
C_2HO^-	41.0059	41.0027	0.0031	145	0,506%
$C_2H_3O^-$	43.0180	43.0184	-0.0004	20	0,070%
$C_4{}^-$	48.0008	48.0000	0.0008	43	0,150%

C_4H^-	49.0100	49.0078	0.0022	223	0,778%
$C_4H_2^-$	50.0143	50.0157	-0.0014	21	0,073%
$C_4H_3^-$	51.0246	51.0235	0.0011	32	0,112%
$C_3H_3O^-$	55.0191	55.0184	0.0008	7	0,024%
$C_3H_4O^-$	56.0319	56.0262	0.0057	11	0,038%
$C_3H_5O^-$	57.0395	57.0340	0.0055	53	0,185%
$C_2H_2O_2^-$	58.0107	58.0055	0.0053	16	0,056%
$C_2H_3O_2^-$	59.0140	59.0133	0.0007	28	0,098%
C_5^-	60.0018	60.0000	0.0018	29	0,101%
C_5H^-	61.0113	61.0078	0.0035	17	0,059%
$C_5H_2^-$	62.0183	62.0157	0.0026	27	0,094%
$C_5H_3^-$	63.0233	63.0235	-0.0002	20	0,070%
$C_5H_4^-$	64.0300	64.0313	-0.0013	8	0,028%
C_4HO^-	65.0094	65.0027	0.0066	12	0,042%
$C_4H_3O^-$	67.0202	67.0184	0.0018	12	0,042%
$C_4H_5O^-$	69.0399	69.0340	0.0059	20	0,070%
C_6^-	72.0002	72.0000	0.0002	25	0,087%
C_6H^-	73.0099	73.0078	0.0021	108	0,377%
$C_6H_2^-$	74.0144	74.0156	-0.0013	9	0,031%
C_7^-	84.0047	84.0000	0.0047	17	0,059%
C_7H^-	85.0107	85.0078	0.0029	10	0,035%
$C_7H_2^-$	86.0213	86.0156	0.0056	16	0,056%
C_8^-	96.0004	96.0000	0.0004	13	0,045%
C_8H^-	97.0088	97.0078	0.0009	36	0,126%
C_9^-	107.9979	108.0000	-0.0021	8	0,028%
C_9H^-	109.0026	109.0078	-0.0052	9	0,031%
$C_9H_2^-$	110.0143	110.0156	-0.0014	9	0,031%
$C_{10}H^-$	121.0045	128.0626	-7.0581	20	0,070%
$C_{11}H^-$	133.0107	133.0078	0.0029	7	0,024%
$C_{12}H^-$	145.0064	152.0626	-7.0562	6	0,021%
$C_{17}H_{33}O^-$	253.2611	253.2531	0.0080	10	0,035%
$C_{17}H_{35}O^-$	255.2196	255.2688	-0.0492	17	0,059%
$C_{18}H_{33}O^-$	265.2540	265.2531	0.0009	6	0,021%
$C_{18}H_{35}O^-$	267.2742	267.2688	0.0054	8	0,028%
$C_{18}H_{37}O^-$	269.2645	269.2844	-0.0199	12	0,042%
$C_{19}H_{35}O^-$	279.2808	279.2688	0.0120	13	0,045%
$C_{19}H_{37}O^-$	281.2868	281.2844	0.0024	148	0,516%
$C_{19}H_{38}O^-$	282.2899	282.2923	-0.0024	30	0,105%
$C_{19}H_{39}O^-$	283.2759	283.3001	-0.0242	83	0,290%
$C_{19}H_{40}O^-$	284.2767	284.3079	-0.0313	21	0,073%
$C_{20}H_{39}O^-$	295.2916	295.3001	-0.0085	6	0,021%
$C_{20}H_{41}O^-$	297.2718	297.3157	-0.0439	7	0,024%

Phenanthrene ($C_{14}H_{10}$) positive ions

Proposed formula	Meas. m/z	Calc. m/z	δ (Da)	Int.	Rel. Int. (%)
H^+	1.0077	1.0078	-0.0001	1116	0,315%
C^+	11.9999	12.0000	-0.0001	247	0,070%
CH^+	13.0079	13.0078	0.0000	211	0,060%
CH_2^+	14.0156	14.0157	-0.0000	174	0,049%
CH_3^+	15.0237	15.0235	0.0002	195	0,055%
O^+	15.9953	15.9949	0.0004	43	0,012%
C_2^+	23.9982	24.0000	-0.0018	31	0,009%
C_2H^+	25.0073	25.0078	-0.0006	74	0,021%
$C_2H_2^+$	26.0152	26.0157	-0.0005	407	0,115%
$C_2H_3^+$	27.0236	27.0235	0.0001	633	0,179%
$C_2H_4^+$	28.0307	28.0313	-0.0006	35	0,010%
CHO^+	29.0025	29.0027	-0.0002	164	0,046%
$C_2H_5^+$	29.0391	29.0391	-0.0000	193	0,054%
CH_3O^+	31.0194	31.0184	0.0010	23	0,006%
C_3H^+	37.0076	37.0078	-0.0002	177	0,050%
C_3H^+	37.0076	37.0078	-0.0002	177	0,050%
$C_3H_2^+$	38.0160	38.0157	0.0003	319	0,090%
$C_3H_2^+$	38.0160	38.0157	0.0003	319	0,090%
$C_3H_3^+$	39.0240	39.0235	0.0005	276	0,078%
$C_3H_4^+$	40.0302	40.0313	-0.0011	52	0,015%
$C_3H_5^+$	41.0393	41.0391	0.0002	309	0,087%
$C_3H_6^+$	42.0430	42.0470	-0.0039	28	0,008%
$C_3H_7^+$	43.0552	43.0548	0.0004	108	0,030%
C_4H^+	49.0073	49.0078	-0.0005	54	0,015%
$C_4H_2^+$	50.0159	50.0157	0.0003	509	0,144%
$C_4H_3^+$	51.0248	51.0235	0.0013	700	0,198%
$C_4H_4^+$	52.0314	52.0313	0.0001	128	0,036%
$C_4H_5^+$	53.0401	53.0391	0.0010	118	0,033%
$C_4H_6^+$	54.0453	54.0470	-0.0016	16	0,005%
$C_4H_7^+$	55.0557	55.0548	0.0010	100	0,028%
$C_4H_9^+$	57.0694	57.0704	-0.0011	30	0,008%
C_5H^+	61.0085	61.0078	0.0007	94	0,027%
$C_5H_2^+$	62.0167	62.0157	0.0011	376	0,106%
$C_5H_3^+$	63.0253	63.0235	0.0018	667	0,188%
$C_5H_4^+$	64.0311	64.0313	-0.0002	78	0,022%
$C_5H_5^+$	65.0415	65.0391	0.0024	92	0,026%
$C_5H_7^+$	67.0548	67.0548	0.0000	33	0,009%
$C_5H_8^+$	68.0601	68.0626	-0.0025	5	0,001%
$C_5H_9^+$	69.0762	69.0704	0.0058	17	0,005%
C_6H^+	73.0083	73.0078	0.0005	28	0,008%
$C_6H_2^+$	74.0169	74.0156	0.0013	378	0,107%
$C_6H_3^+$	75.0243	75.0235	0.0009	373	0,105%
$C_6H_4^+$	76.0323	76.0313	0.0010	110	0,031%

$C_6H_5^+$	77.0404	77.0391	0.0013	168	0,047%
$C_6H_6^+$	78.0471	78.0469	0.0001	49	0,014%
$C_6H_8^+$	80.0618	80.0626	-0.0008	6	0,002%
$C_6H_9^+$	81.0755	81.0704	0.0051	13	0,004%
C_7H^+	85.0100	85.0078	0.0022	38	0,011%
$C_7H_2^+$	86.0170	86.0156	0.0014	188	0,053%
$C_7H_3^+$	87.0248	87.0235	0.0013	279	0,079%
$C_7H_4^+$	88.0313	88.0313	0.0000	54	0,015%
$C_7H_5^+$	89.0401	89.0391	0.0009	95	0,027%
$C_7H_7^+$	91.0554	91.0548	0.0006	47	0,013%
$C_8H_2^+$	98.0160	98.0156	0.0003	144	0,041%
$C_8H_3^+$	99.0251	99.0235	0.0016	106	0,030%
$C_8H_4^+$	100.0361	100.0313	0.0048	26	0,007%
$C_8H_5^+$	101.0409	101.0391	0.0018	44	0,012%
$C_8H_6^+$	102.0464	102.0469	-0.0005	83	0,023%
$C_8H_7^+$	103.0528	103.0548	-0.0020	24	0,007%
$C_9H_2^+$	110.0149	110.0156	-0.0007	62	0,018%
$C_9H_3^+$	111.0236	111.0235	0.0002	55	0,016%
$C_9H_4^+$	112.0307	112.0313	-0.0006	11	0,003%
$C_9H_5^+$	113.0400	113.0391	0.0009	58	0,016%
$C_9H_6^+$	114.0479	114.0469	0.0010	26	0,007%
$C_9H_7^+$	115.0572	115.0548	0.0024	140	0,040%
$C_9H_8^+$	116.0575	116.0626	-0.0051	16	0,005%
$C_9H_9^+$	117.0702	117.0704	-0.0002	4	0,001%
$C_9H_{11}^+$	119.0893	119.0861	0.0032	2	0,001%
$C_{10}H_2^+$	122.0143	122.0156	-0.0013	34	0,010%
$C_{10}H_3^+$	123.0268	123.0235	0.0033	28	0,008%
$C_{10}H_6^+$	126.0468	126.0469	-0.0001	132	0,037%
$C_{10}H_7^+$	127.0555	127.0548	0.0007	73	0,021%
$C_{10}H_8^+$	128.0637	128.0626	0.0011	76	0,021%
$C_{11}H_5^+$	137.0386	137.0391	-0.0005	35	0,010%
$C_{11}H_6^+$	138.0478	138.0470	0.0008	28	0,008%
$C_{11}H_7^+$	139.0553	139.0548	0.0005	215	0,061%
$C_{11}H_8^+$	140.0599	140.0626	-0.0027	31	0,009%
$C_{11}H_9^+$	141.0709	141.0704	0.0005	48	0,014%
$C_{12}H_6^+$	150.0468	150.0470	-0.0001	104	0,029%
$C_{12}H_7^+$	151.0530	151.0548	-0.0018	155	0,044%
$C_{12}H_8^+$	152.0624	152.0626	-0.0002	208	0,059%
$C_{12}H_9^+$	153.0675	153.0704	-0.0029	42	0,012%
$C_{13}H_7^+$	163.0541	163.0548	-0.0007	178	0,050%
$C_{13}H_9^+$	165.0712	165.0704	0.0007	295	0,083%
$C_{13}H_{10}^+$	166.0757	166.0782	-0.0026	56	0,016%
$C_{14}H_8^+$	176.0645	176.0626	0.0019	347	0,098%
$C_{14}H_9^+$	177.0617	177.0704	-0.0087	145	0,041%
$C_{14}H_{10}^+$	178.0782	178.0782	-0.0000	1165	0,329%
$C_{14}H_{11}^+$	179.0872	179.0861	0.0012	718	0,203%

$C_{14}H_{12}^+$	180.0943	180.0939	0.0004	104	0,029%
$C_{14}H_{13}^+$	181.1058	181.1017	0.0040	30	0,008%
$C_{15}H_9^+$	189.0691	189.0704	-0.0013	117	0,033%
$C_{15}H_{10}^+$	190.0750	190.0782	-0.0032	29	0,008%
$C_{15}H_{11}^+$	191.0888	191.0861	0.0027	53	0,015%
$C_{16}H_{10}^+$	202.0780	202.0782	-0.0002	58	0,016%
Na^+	22.9897	22.9898	-0.0001	23710	6,694%
Mg^+	23.9845	23.9850	-0.0006	457	0,129%
$^{25}Mg^+$	24.9856	24.9858	-0.0002	49	0,014%
$^{26}Mg^+$	25.9822	25.9826	-0.0004	59	0,017%
Al^+	26.9815	26.9815	-0.0000	2786	0,787%
Si^+	27.9769	27.9769	-0.0001	13935	3,934%
$^{29}Si^+$	28.9763	28.9765	-0.0002	848	0,239%
SiH^+	28.9843	28.9848	-0.0004	3535	0,998%
$^{30}Si^+$	29.9736	29.9738	-0.0001	535	0,151%
K^+	38.9639	38.9637	0.0002	21271	6,005%
Ca^+	39.9624	39.9626	-0.0002	5634	1,591%
$^{41}K^+$	40.9617	40.9618	-0.0002	2546	0,719%
$^{42}Ca^+$	41.9583	41.9586	-0.0003	37	0,010%
$^{44}Ca^+$	43.9558	43.9555	0.0003	98	0,028%
$SiOH^+$	44.9799	44.9797	0.0002	4232	1,195%
$SiOH_2^+$	45.9791	45.9875	-0.0084	261	0,074%

Phenanthrene ($C_{14}H_{10}$) negative ions

Proposed formula	Meas. m/z	Calc. m/z	δ (Da)	Int.	Rel. Int. (%)
H^-	1.0088	1.0078	0.0009	18473	5,251%
C^-	12.0009	12.0000	0.0009	2088	0,593%
CH^-	13.0084	13.0078	0.0006	3341	0,950%
CH_3^-	14.0164	14.0157	0.0007	178	0,051%
O^-	15.9951	15.9949	0.0002	34833	9,901%
OH^-	17.0031	17.0027	0.0004	17084	4,856%
C_2^-	24.0005	24.0000	0.0005	5036	1,431%
C_2H^-	25.0086	25.0078	0.0008	9203	2,616%
CN^-	26.0039	26.0031	0.0008	661	0,188%
S^-	31.9717	31.9721	-0.0003	212	0,060%
O_2^-	31.9892	31.9898	-0.0006	816	0,232%
HS^-	32.9806	32.9799	0.0007	43	0,012%
HO_2^-	32.9975	32.9977	-0.0001	154	0,044%
C_3^-	36.0008	36.0000	0.0008	819	0,233%
C_3H^-	37.0087	37.0078	0.0009	371	0,105%
$C_3H_2^-$	38.0170	38.0157	0.0014	113	0,032%
C_2HO^-	41.0043	41.0027	0.0016	773	0,220%
C_4^-	48.0005	48.0000	0.0005	889	0,253%
C_4H^-	49.0089	49.0078	0.0011	1385	0,394%
$C_4H_2^-$	50.0124	50.0157	-0.0033	72	0,020%

C_5^-	60.0019	60.0000	0.0019	194	0,055%
C_5H^-	61.0091	61.0078	0.0013	128	0,036%
$C_5H_2^-$	62.0171	62.0157	0.0015	77	0,022%
C_6^-	72.0012	72.0000	0.0012	254	0,072%
C_6H^-	73.0093	73.0078	0.0014	408	0,116%
$C_6H_2^-$	74.0132	74.0156	-0.0024	37	0,011%
C_7^-	84.0008	84.0000	0.0008	93	0,026%
C_7H^-	85.0083	85.0078	0.0004	53	0,015%
$C_7H_2^-$	86.0173	86.0156	0.0017	37	0,011%
C_8^-	96.0009	96.0000	0.0009	91	0,026%
C_8H^-	97.0092	97.0078	0.0014	130	0,037%
C_9^-	107.9999	108.0000	-0.0001	31	0,009%
C_9H^-	109.0047	109.0078	-0.0031	23	0,007%
C_{10}^-	119.9999	120.0000	-0.0001	15	0,004%
$C_{10}H^-$	121.0067	121.0078	-0.0011	42	0,012%
$C_{12}H^-$	145.0085	145.0078	0.0007	16	0,005%
Si^-	27.9765	27.9769	-0.0005	856	0,243%
$^{29}Si^-$	28.9764	28.9765	-0.0001	43	0,012%
SiH^-	28.9844	28.9848	-0.0004	616	0,175%
SiH_2^-	29.9920	29.9926	-0.0006	85	0,024%
Cl^-	34.9691	34.9689	0.0002	286	0,081%
SiO_2^-	59.9668	59.9668	0.0000	8439	2,399%
SiO_2H^-	60.9749	60.9746	0.0003	4135	1,175%
SiO_3^-	75.9614	75.9617	-0.0003	4957	1,409%
SiO_3H^-	76.9699	76.9695	0.0004	5745	1,633%
$SiO_3H_2^-$	77.9676	77.9773	-0.0097	391	0,111%
$Si_3O_2H_3^-$	118.9370	118.9441	-0.0071	207	0,059%
$Si_2O_4^-$	119.9334	119.9335	-0.0001	310	0,088%
$Si_2O_4H^-$	120.9412	120.9413	-0.0001	363	0,103%
$Si_2O_4H_2^-$	121.9380	121.9492	-0.0111	61	0,017%
$Si_2O_5^-$	135.9273	135.9284	-0.0011	478	0,136%
$Si_2O_5H^-$	136.9360	136.9363	-0.0002	1231	0,350%
$Si_2O_5H_2^-$	137.9342	137.9441	-0.0098	156	0,044%
$Si_2O_5H_3^-$	138.9335	138.9519	-0.0184	108	0,031%
$Si_4O_4H_3^-$	178.9046	178.9108	-0.0062	149	0,042%
$Si_3O_3^-$	179.9003	179.9003	0.0000	67	0,019%
$Si_3O_3H^-$	180.9082	180.9081	0.0001	81	0,023%
$Si_3O_7^-$	195.8895	195.8952	-0.0056	103	0,029%
$Si_3O_7H^-$	196.9023	196.9030	-0.0007	360	0,102%
$Si_4O_9H^-$	256.8683	256.8698	-0.0015	75	0,021%

Anthracène D_{10} ($C_{14}D_{10}$) negative ions

Proposed formula	Meas. m/z	Calc. m/z	δ (Da)	Int.	Rel. Int. (%)
H^-	1.0077	1.0078	-0.0002	6655	11,681%
D^-	2.0142	2.0141	0.0001	1216	2,134%
C^-	12.0004	12.0000	0.0004	1108	1,945%
CH^-	13.0081	13.0078	0.0003	1275	2,238%
CD^-	14.0145	14.0141	0.0004	560	0,983%
C_2^-	23.9999	24.0000	-0.0001	3091	5,425%
C_2H^-	25.0085	25.0078	0.0006	2856	5,013%
C_2D^-	26.0145	26.0141	0.0004	1769	3,105%
C_3^-	35.9997	36.0000	-0.0003	422	0,741%
C_3H^-	37.0068	37.0078	-0.0010	59	0,104%
C_3D^-	38.0146	38.0141	0.0005	69	0,121%
C_4^-	47.9994	48.0000	-0.0006	571	1,002%
C_4H^-	49.0081	49.0078	0.0003	228	0,400%
C_4D^-	50.0144	50.0141	0.0003	283	0,497%
C_5^-	60.0005	60.0000	0.0005	154	0,270%
C_5H^-	61.0081	61.0078	0.0003	18	0,032%
C_5D^-	62.0137	62.0141	-0.0004	20	0,035%
C_6^-	72.0009	72.0000	0.0009	195	0,342%
C_6H^-	73.0085	73.0078	0.0007	85	0,149%
C_6D^-	74.0146	74.0141	0.0005	73	0,128%
C_7^-	83.9992	84.0000	-0.0008	79	0,139%
C_7H^-	85.0066	85.0078	-0.0012	6	0,011%
C_7D^-	86.0174	86.0141	0.0033	11	0,019%
C_8^-	96.0001	96.0000	0.0001	102	0,179%
C_8H^-	97.0066	97.0078	-0.0013	47	0,082%
C_8D^-	98.0152	98.0141	0.0011	44	0,077%
C_9^-	108.0010	108.0000	0.0010	37	0,065%
C_9H^-	109.0067	109.0078	-0.0011	15	0,026%
C_9D^-	110.0099	110.0156	-0.0058	9	0,016%
C_{10}^-	119.9998	120.0000	-0.0002	25	0,044%
$C_{10}H^-$	121.0138	121.0078	0.0060	15	0,026%
$C_{10}D^-$	122.0157	122.0141	0.0016	13	0,023%
C_{11}^-	132.0026	132.0000	0.0026	17	0,030%
C_{12}^-	144.0055	144.0000	0.0055	11	0,019%
$C_{12}H^-$	145.0107	145.0078	0.0028	10	0,018%
$C_{12}D^-$	146.0245	146.0141	0.0104	10	0,018%

Orbagnoux (orba) lamine positive ions

Proposed formula	Meas. m/z	Calc. m/z	δ (Da)	Int.	Rel. Int. (%)
H^+	1.0075	1.0078	-0.0003	11790	0,212%
C^+	11.9980	12.0000	-0.0020	4182	0,075%
CH^+	13.0066	13.0078	-0.0012	1789	0,032%
CH_2^+	14.0137	14.0157	-0.0019	3024	0,054%
CH_3^+	15.0227	15.0235	-0.0007	5524	0,099%
C_2H^+	25.0046	25.0078	-0.0032	787	0,014%
$C_2H_2^+$	26.0138	26.0157	-0.0019	3475	0,062%
$C_2H_3^+$	27.0230	27.0235	-0.0005	15150	0,272%
$C_2H_4^+$	28.0300	28.0313	-0.0013	2646	0,048%
$C_2H_5^+$	29.0379	29.0391	-0.0013	15082	0,271%
$C_2H_6^+$	30.0353	30.0469	-0.0116	977	0,018%
C_3H^+	37.0060	37.0078	-0.0018	1648	0,030%
$C_3H_2^+$	38.0132	38.0157	-0.0024	4110	0,074%
$C_3H_3^+$	39.0216	39.0235	-0.0019	22894	0,411%
$C_3H_4^+$	40.0291	40.0313	-0.0022	2808	0,050%
$C_3H_5^+$	41.0389	41.0391	-0.0002	32205	0,579%
$C_3H_6^+$	42.0431	42.0470	-0.0038	2506	0,045%
$C_3H_7^+$	43.0542	43.0548	-0.0006	12644	0,227%
$C_4H_2^+$	50.0138	50.0157	-0.0018	3581	0,064%
$C_4H_3^+$	51.0224	51.0235	-0.0011	9642	0,173%
$C_4H_4^+$	52.0299	52.0313	-0.0014	3025	0,054%
$C_4H_5^+$	53.0386	53.0391	-0.0005	10507	0,189%
$C_4H_6^+$	54.0435	54.0470	-0.0035	1520	0,027%
$C_4H_7^+$	55.0542	55.0548	-0.0006	10128	0,182%
$C_4H_8^+$	56.0576	56.0626	-0.0050	951	0,017%
$C_4H_9^+$	57.0706	57.0704	0.0002	3340	0,060%
C_5H^+	61.0053	61.0078	-0.0025	1522	0,027%
$C_5H_2^+$	62.0142	62.0157	-0.0015	2717	0,049%
$C_5H_3^+$	63.0220	63.0235	-0.0015	8280	0,149%
$C_5H_4^+$	64.0290	64.0313	-0.0023	1180	0,021%
$C_5H_5^+$	65.0393	65.0391	0.0001	5546	0,100%
$C_5H_6^+$	66.0457	66.0469	-0.0013	1354	0,024%
$C_5H_7^+$	67.0540	67.0548	-0.0008	3752	0,067%
$C_5H_8^+$	68.0598	68.0626	-0.0028	503	0,009%
$C_5H_9^+$	69.0704	69.0704	0.0000	2202	0,040%
$C_5H_{10}^+$	70.0711	70.0782	-0.0072	304	0,005%
$C_6H_2^+$	74.0136	74.0156	-0.0021	2567	0,046%
$C_6H_3^+$	75.0218	75.0235	-0.0017	3165	0,057%
$C_6H_4^+$	76.0293	76.0313	-0.0020	1134	0,020%
$C_6H_5^+$	77.0379	77.0391	-0.0012	7839	0,141%
$C_6H_6^+$	78.0444	78.0469	-0.0026	2169	0,039%
$C_6H_7^+$	79.0536	79.0548	-0.0012	2337	0,042%
$C_6H_8^+$	80.0588	80.0626	-0.0038	461	0,008%

$C_6H_9^+$	81.0703	81.0704	-0.0001	1560	0,028%
$C_6H_{10}^+$	82.0716	82.0782	-0.0066	180	0,003%
$C_6H_{11}^+$	83.0881	83.0861	0.0020	547	0,010%
$C_6H_{12}^+$	84.0890	84.0939	-0.0049	77	0,001%
C_7H^+	85.0076	85.0078	-0.0002	1295	0,023%
$C_6H_{13}^+$	85.1040	85.1017	0.0023	166	0,003%
$C_7H_2^+$	86.0132	86.0156	-0.0024	1946	0,035%
$C_7H_3^+$	87.0221	87.0235	-0.0014	2640	0,047%
$C_7H_4^+$	88.0293	88.0313	-0.0020	576	0,010%
$C_7H_5^+$	89.0375	89.0391	-0.0017	1347	0,024%
$C_7H_6^+$	90.0429	90.0469	-0.0041	390	0,007%
$C_7H_7^+$	91.0531	91.0548	-0.0017	4590	0,082%
$C_7H_8^+$	92.0554	92.0626	-0.0072	638	0,011%
$C_7H_9^+$	93.0693	93.0704	-0.0011	684	0,012%
$C_7H_{10}^+$	94.0655	94.0782	-0.0128	192	0,003%
$C_7H_{11}^+$	95.0846	95.0861	-0.0015	653	0,012%
$C_7H_{12}^+$	96.0868	96.0939	-0.0071	83	0,001%
C_8H^+	97.0074	97.0078	-0.0004	1427	0,026%
$C_7H_{13}^+$	97.1024	97.1017	0.0007	140	0,003%
$C_8H_2^+$	98.0122	98.0156	-0.0035	1580	0,028%
$C_8H_3^+$	99.0220	99.0235	-0.0015	1299	0,023%
$C_8H_4^+$	100.0238	100.0313	-0.0075	266	0,005%
$C_8H_5^+$	101.0363	101.0391	-0.0028	531	0,010%
$C_8H_6^+$	102.0451	102.0469	-0.0019	1123	0,020%
$C_8H_7^+$	103.0516	103.0548	-0.0031	1095	0,020%
$C_8H_8^+$	104.0555	104.0626	-0.0071	386	0,007%
$C_8H_9^+$	105.0680	105.0704	-0.0025	1151	0,021%
$C_8H_{10}^+$	106.0700	106.0782	-0.0083	199	0,004%
$C_8H_{11}^+$	107.0820	107.0861	-0.0041	232	0,004%
$C_8H_{12}^+$	108.0871	108.0939	-0.0068	90	0,002%
$C_8H_{13}^+$	109.1014	109.1017	-0.0003	169	0,003%
$C_9H_2^+$	110.0132	110.0156	-0.0025	1018	0,018%
$C_8H_{14}^+$	110.0977	110.1095	-0.0118	35	0,001%
$C_9H_3^+$	111.0218	111.0235	-0.0016	1109	0,020%
$C_9H_4^+$	112.0277	112.0313	-0.0036	185	0,003%
$C_9H_5^+$	113.0375	113.0391	-0.0016	518	0,009%
$C_9H_6^+$	114.0455	114.0469	-0.0015	323	0,006%
$C_9H_7^+$	115.0523	115.0548	-0.0025	3312	0,060%
$C_9H_8^+$	116.0574	116.0626	-0.0052	672	0,012%
$C_9H_9^+$	117.0694	117.0704	-0.0010	566	0,010%
$C_9H_{10}^+$	118.0726	118.0782	-0.0057	195	0,004%
$C_9H_{11}^+$	119.0822	119.0861	-0.0039	408	0,007%
$C_9H_{12}^+$	120.0860	120.0939	-0.0079	115	0,002%
$C_9H_{13}^+$	121.0974	121.1017	-0.0044	107	0,002%
$C_{10}H_2^+$	122.0116	122.0156	-0.0040	750	0,013%
$C_9H_{14}^+$	122.1113	122.1095	0.0018	20	0,000%

$C_{10}H_3^+$	123.0221	123.0235	-0.0013	773	0,014%
$C_9H_{15}^+$	123.1150	123.1174	-0.0023	67	0,001%
$C_9H_{16}^+$	124.1275	124.1252	0.0023	3	0,000%
$C_9H_{17}^+$	125.1388	125.1330	0.0058	9	0,000%
$C_{10}H_6^+$	126.0437	126.0469	-0.0033	753	0,014%
$C_{10}H_7^+$	127.0509	127.0548	-0.0038	936	0,017%
$C_{10}H_8^+$	128.0581	128.0626	-0.0045	1943	0,035%
$C_{10}H_9^+$	129.0651	129.0704	-0.0053	694	0,012%
Cs^+	132.9011	132.9054	-0.0043	572379	10,287%
$C_{13}H_9^+$	165.0640	165.0704	-0.0064	1460	0,026%
$C_{14}H_{10}^+$	178.0646	178.0782	-0.0136	724	0,013%
$C_{15}H_9^+$	189.0614	189.0704	-0.0091	998	0,018%
$C_{15}H_{11}^+$	191.0669	191.0861	-0.0191	361	0,006%
$C_{16}H_{10}^+$	202.0663	202.0782	-0.0120	749	0,013%
Na^+	22.9885	22.9898	-0.0013	124116	2,231%
Al^+	26.9801	26.9815	-0.0014	662079	11,900%
Si^+	27.9738	27.9769	-0.0031	9503	0,171%
K^+	38.9625	38.9637	-0.0012	105458	1,895%
Ca^+	39.9593	39.9626	-0.0033	156827	2,819%

Orbagnoux (orba) lamine negative ions

Proposed formula	Meas. m/z	Calc. m/z	δ (Da)	Int.	Rel. Int. (%)
H^-	1.0089	1.0078	0.0010	125749	6,309%
C^-	12.0000	12.0000	0.0000	32730	1,642%
CH^-	13.0086	13.0078	0.0008	31851	1,598%
CH_2^-	14.0160	14.0157	0.0003	2301	0,115%
CH_3^-	15.0247	15.0235	0.0013	367	0,018%
O^-	15.9956	15.9949	0.0007	58079	2,914%
OH^-	17.0030	17.0027	0.0003	56236	2,821%
C_2^-	23.9996	24.0000	-0.0004	67204	3,372%
C_2H^-	25.0078	25.0078	-0.0000	83303	4,179%
CN^-	26.0035	26.0031	0.0004	30117	1,511%
S^-	31.9715	31.9721	-0.0006	45742	2,295%
HS^-	32.9798	32.9799	-0.0001	13191	0,662%
$_{34}S^-$	33.9659	33.9679	-0.0020	1779	0,089%
C_3^-	35.9998	36.0000	-0.0002	10905	0,547%
C_3H^-	37.0068	37.0078	-0.0011	2970	0,149%
$C_3H_2^-$	38.0155	38.0157	-0.0001	1175	0,059%
$C_3H_3^-$	39.0233	39.0235	-0.0002	494	0,025%
C_2O^-	39.9940	39.9949	-0.0009	1626	0,082%
C_2HO^-	41.0032	41.0027	0.0004	3264	0,164%
CNO^-	41.9998	41.9980	0.0018	3117	0,156%
CHO_2^-	44.9967	44.9977	-0.0010	2820	0,141%
C_4^-	47.9989	48.0000	-0.0011	21497	1,078%
C_4H^-	49.0087	49.0078	0.0008	20649	1,036%

C_3N^-	50.0062	50.0031	0.0031	2412	0,121%
$C_4H_2^-$	50.0062	50.0157	-0.0095	2412	0,121%
$C_4H_3^-$	51.0234	51.0235	-0.0001	568	0,028%
C_2S^-	55.9711	55.9721	-0.0010	4702	0,236%
C_2SH^-	56.9804	56.9799	0.0005	5398	0,271%
CNS^-	57.9759	57.9751	0.0008	1254	0,063%
AlO_2^-	58.9724	58.9714	0.0010	12540	0,629%
SiO_2^-	59.9661	59.9668	-0.0006	2441	0,122%
C_5^-	60.0009	60.0000	0.0009	8727	0,438%
C_5H^-	61.0083	61.0078	0.0005	2376	0,119%
$C_5H_2^-$	62.0169	62.0157	0.0012	1269	0,064%
$C_5H_3^-$	63.0245	63.0235	0.0010	355	0,018%
S_2^-	63.9452	63.9441	0.0010	1106	0,055%
O_2S^-	63.9619	63.9619	-0.0000	1704	0,085%
HS_2^-	64.9515	64.9520	-0.0004	118	0,006%
C_4HO^-	65.0041	65.0027	0.0013	432	0,022%
C_3S^-	67.9715	67.9721	-0.0006	1095	0,055%
C_3HS^-	68.9810	68.9799	0.0011	648	0,033%
$C_3H_2S^-$	69.9877	69.9877	-0.0000	174	0,009%
$C_3H_3O_2^-$	71.0137	71.0133	0.0004	191	0,010%
C_6^-	71.9992	72.0000	-0.0008	10141	0,509%
C_6H^-	73.0085	73.0078	0.0007	9678	0,486%
$C_6H_2^-$	74.0111	74.0156	-0.0046	1200	0,060%
$C_6H_3^-$	75.0242	75.0235	0.0007	442	0,022%
C_4S^-	79.9715	79.9721	-0.0006	2261	0,113%
C_4SH^-	80.9815	80.9799	0.0016	3004	0,151%
C_7^-	84.0006	84.0000	0.0006	4497	0,226%
C_7H^-	85.0073	85.0078	-0.0006	1442	0,072%
$C_7H_2^-$	86.0164	86.0156	0.0007	875	0,044%
$C_7H_3^-$	87.0218	87.0235	-0.0017	234	0,012%
C_5S^-	91.9728	91.9721	0.0007	746	0,037%
C_5HS^-	92.9793	92.9799	-0.0006	460	0,023%
$C_5H_2S^-$	93.9865	93.9877	-0.0012	225	0,011%
C_8^-	95.9989	96.0000	-0.0011	4536	0,228%
C_8H^-	97.0085	97.0078	0.0007	4971	0,249%
$C_8H_2^-$	98.0100	98.0156	-0.0056	634	0,032%
$C_8H_3^-$	99.0245	99.0235	0.0010	189	0,009%
$C_3S_2^-$	99.9423	99.9441	-0.0019	173	0,009%
$C_3S_2H^-$	100.9534	100.9520	0.0015	235	0,012%
C_6S^-	103.9729	103.9721	0.0009	1099	0,055%
C_6SH^-	104.9811	104.9799	0.0012	1721	0,086%
$C_6H_2S^-$	105.9809	105.9877	-0.0068	264	0,013%
$C_6H_3S^-$	106.9944	106.9955	-0.0012	196	0,010%
C_9^-	107.9995	108.0000	-0.0005	1879	0,094%
C_9H^-	109.0069	109.0078	-0.0009	1049	0,053%
$C_9H_2^-$	110.0159	110.0156	0.0002	424	0,021%

$C_9H_3^-$	111.0214	111.0235	-0.0021	141	0,007%
$C_4S_2^-$	111.9441	111.9441	-0.0001	340	0,017%
C_7S^-	115.9721	115.9721	-0.0000	452	0,023%
C_7HS^-	116.9814	116.9799	0.0015	239	0,012%
$C_7H_2S^-$	117.9887	117.9877	0.0010	168	0,008%
C_{10}^-	119.9990	120.0000	-0.0010	1031	0,052%
$C_{10}H^-$	121.0083	121.0078	0.0005	2459	0,123%
$C_{10}H_2^-$	122.0097	122.0156	-0.0059	380	0,019%
C_{11}^-	131.9990	132.0000	-0.0010	655	0,033%
$C_{11}H^-$	133.0071	133.0078	-0.0007	682	0,034%
$C_{11}H_2^-$	134.0152	134.0156	-0.0004	310	0,016%
C_9S^-	139.9727	139.9721	0.0006	193	0,010%
C_9HS^-	140.9815	140.9799	0.0016	112	0,006%
$C_9H_2S^-$	141.9864	141.9877	-0.0013	112	0,006%
C_{12}^-	143.9977	144.0000	-0.0023	644	0,032%
$C_{12}H^-$	145.0072	145.0078	-0.0006	1215	0,061%
$C_{12}H_2^-$	146.0109	146.0156	-0.0047	187	0,009%
$C_{10}S^-$	151.9720	151.9721	-0.0001	175	0,009%
$C_{10}SH^-$	152.9787	152.9799	-0.0012	325	0,016%
C_{13}^-	155.9984	156.0000	-0.0016	300	0,015%
$C_{13}H^-$	157.0066	157.0078	-0.0012	335	0,017%
C_{14}^-	167.9922	168.0000	-0.0078	134	0,007%
$C_{14}H^-$	169.0065	169.0078	-0.0013	512	0,026%
C_{15}^-	179.9939	180.0000	-0.0061	100	0,005%
$C_{15}H^-$	181.0063	181.0078	-0.0015	134	0,007%
Cl^-	34.9684	34.9689	-0.0004	30852	1,548%
$^{37}Cl^-$	36.9661	36.9659	0.0002	9280	0,466%
AlO^-	42.9756	42.9765	-0.0008	5722	0,287%
SiO^-	43.9699	43.9718	-0.0019	382	0,019%
SiO_2H^-	60.9739	60.9746	-0.0007	1177	0,059%
SiO_3^-	75.9631	75.9617	0.0015	1677	0,084%
$SiHO_3^-$	76.9700	76.9695	0.0005	2464	0,124%
Si_3O^-	99.9264	99.9257	0.0007	224	0,011%
$Si_3OH_2^-$	101.9467	101.9413	0.0053	659	0,033%
$Si_3OH_3^-$	102.9486	102.9492	-0.0006	405	0,020%
$Si_2O_2H_2^-$	117.9417	117.9363	0.0054	355	0,018%
$Si_3O_2H_3^-$	118.9426	118.9441	-0.0015	1726	0,087%
I^-	126.8993	126.9045	-0.0052	4333	0,217%
$Si_2O_5^-$	135.9435	135.9284	0.0151	221	0,011%
$Si_2O_5H^-$	136.9333	136.9363	-0.0030	350	0,018%
$Al_3O_4^-$	144.9239	144.9243	-0.0004	259	0,013%
$Al_3O_5^-$	160.9162	160.9192	-0.0030	317	0,016%
$Si_4O_4H_3^-$	178.9116	178.9108	0.0008	395	0,020%
Au^-	196.9551	196.9666	-0.0114	18668	0,937%
AuO^-	212.9486	212.9615	-0.0129	131	0,007%
$AuOH^-$	213.9562	213.9693	-0.0131	221	0,011%

AuH_2O^-	214.9672	214.9771	-0.0099	135	0,007%
C_2Au^-	220.9539	220.9666	-0.0127	888	0,045%
C_2HAu^-	221.9635	221.9744	-0.0108	568	0,028%
$CAuN^-$	222.9715	222.9696	0.0019	969	0,049%
$C_2H_3Au^-$	223.9715	223.9900	-0.0185	474	0,024%
AuS^-	228.9267	228.9386	-0.0120	3733	0,187%
AuO_2^-	228.9267	228.9564	-0.0297	3733	0,187%
$HAuO_2^-$	229.9373	229.9642	-0.0269	1073	0,054%
$HAuS^-$	229.9373	229.9464	-0.0092	1073	0,054%
H_2AuS^-	230.9477	230.9543	-0.0065	818	0,041%
$AuO_2H_2^-$	230.9477	230.9720	-0.0243	818	0,041%
$AuCl^-$	231.9241	231.9354	-0.0113	322	0,016%
C_3Au^-	232.9452	232.9666	-0.0213	362	0,018%
C_4Au^-	244.9563	244.9666	-0.0103	364	0,018%
AuO_3^-	244.9563	244.9513	0.0050	364	0,018%
C_4HAu^-	245.9641	245.9744	-0.0103	322	0,016%
$C_4H_2Au^-$	246.9774	246.9822	-0.0048	1017	0,051%
$C_4H_3Au^-$	247.9766	247.9900	-0.0134	665	0,033%
C_2AuS^-	252.9310	252.9386	-0.0076	282	0,014%
C_2HAuS^-	253.9395	253.9464	-0.0070	951	0,048%
$C_2H_2AuS^-$	254.9474	254.9543	-0.0068	1426	0,072%
$AuAlO_2^-$	255.9455	255.9379	0.0076	835	0,042%
$C_2H_3AuS^-$	255.9455	255.9621	-0.0166	835	0,042%
$AuSiO_2^-$	256.9376	256.9333	0.0043	394	0,020%
$AuAlO_2H^-$	256.9376	256.9457	-0.0082	394	0,020%
C_5Au^-	256.9376	256.9666	-0.0290	394	0,020%
$AuSiO_2H^-$	257.9537	257.9411	0.0126	233	0,012%
$AuAlO_2H_2^-$	257.9537	257.9536	0.0002	233	0,012%
C_5HAu^-	257.9537	257.9744	-0.0207	233	0,012%
$C_5H_2Au^-$	258.9702	258.9822	-0.0120	173	0,009%
$AuAlO_2H_3^-$	258.9702	258.9614	0.0088	173	0,009%
$C_5H_3Au^-$	259.9814	259.9900	-0.0086	141	0,007%
C_6Au^-	268.9604	268.9666	-0.0062	172	0,009%
C_6HAu^-	269.9576	269.9744	-0.0168	190	0,010%
$C_6H_2Au^-$	270.9753	270.9822	-0.0069	770	0,039%
Au_2^-	393.9053	393.9331	-0.0278	3243	0,163%
$C_2HAu_2^-$	418.9274	418.9409	-0.0136	1193	0,060%
Au_2S^-	425.8772	425.9052	-0.0279	1968	0,099%
Au_2SH^-	426.8982	426.9130	-0.0148	1667	0,084%
Au_3^-	590.8590	590.8997	-0.0407	5877	0,295%
$C_2Au_3^-$	614.8614	614.8997	-0.0382	178	0,009%
Au_3S^-	622.8307	622.8717	-0.0410	1468	0,074%
Au_4^-	787.7964	787.8662	-0.0698	774	0,039%

Orbagnoux (orba) veine positive ions

Proposed formula	Meas. m/z	Calc. m/z	δ (Da)	Int.	Rel. Int. (%)
H^+	1.0070	1.0078	-0.0008	3153	0,203%
C^+	11.9993	12.0000	-0.0007	366	0,024%
CH^+	13.0064	13.0078	-0.0014	265	0,017%
CH_2^+	14.0151	14.0157	-0.0006	447	0,029%
CH_3^+	15.0229	15.0235	-0.0006	902	0,058%
C_2H^+	25.0054	25.0078	-0.0024	85	0,005%
$C_2H_2^+$	26.0146	26.0157	-0.0011	559	0,036%
$C_2H_3^+$	27.0235	27.0235	0.0000	4235	0,272%
$C_2H_4^+$	28.0306	28.0313	-0.0007	640	0,041%
CHO^+	29.0016	29.0027	-0.0011	298	0,019%
$C_2H_5^+$	29.0398	29.0391	0.0007	5391	0,347%
$C_2H_6^+$	30.0420	30.0469	-0.0049	172	0,011%
CH_4N^+	30.0420	30.0344	0.0077	172	0,011%
$C_2H_6^+$	30.0420	30.0469	-0.0049	172	0,011%
C_3H^+	37.0071	37.0078	-0.0007	171	0,011%
$C_3H_2^+$	38.0152	38.0157	-0.0005	534	0,034%
$C_3H_3^+$	39.0240	39.0235	0.0005	4563	0,293%
$C_3H_4^+$	40.0305	40.0313	-0.0008	366	0,024%
$C_3H_5^+$	41.0404	41.0391	0.0013	10511	0,676%
$C_3H_6^+$	42.0457	42.0470	-0.0012	812	0,052%
$C_2H_3O^+$	43.0201	43.0184	0.0018	704	0,045%
$C_3H_7^+$	43.0566	43.0548	0.0018	6055	0,389%
$C_3H_8^+$	44.0594	44.0626	-0.0032	228	0,015%
$C_4H_2^+$	50.0164	50.0157	0.0007	673	0,043%
$C_4H_3^+$	51.0246	51.0235	0.0011	1921	0,124%
$C_4H_4^+$	52.0316	52.0313	0.0003	621	0,040%
$C_4H_5^+$	53.0407	53.0391	0.0016	2350	0,151%
$C_4H_6^+$	54.0472	54.0470	0.0003	447	0,029%
$C_4H_7^+$	55.0571	55.0548	0.0023	5602	0,360%
$C_4H_8^+$	56.0620	56.0626	-0.0006	468	0,030%
$C_4H_9^+$	57.0739	57.0704	0.0035	1334	0,086%
$C_5H_2^+$	62.0171	62.0157	0.0014	446	0,029%
$C_5H_3^+$	63.0255	63.0235	0.0021	1131	0,073%
$C_5H_4^+$	64.0315	64.0313	0.0002	203	0,013%
$C_5H_5^+$	65.0420	65.0391	0.0029	1057	0,068%
$C_5H_6^+$	66.0485	66.0469	0.0015	279	0,018%
$C_5H_7^+$	67.0576	67.0548	0.0029	1239	0,080%
$C_5H_8^+$	68.0637	68.0626	0.0011	179	0,012%
$C_5H_9^+$	69.0743	69.0704	0.0039	1722	0,111%
$C_5H_{10}^+$	70.0793	70.0782	0.0011	143	0,009%
$C_5H_{11}^+$	71.0924	71.0861	0.0064	415	0,027%
$C_6H_2^+$	74.0164	74.0156	0.0007	389	0,025%

$C_6H_3^+$	75.0265	75.0235	0.0030	505	0,032%
$C_6H_4^+$	76.0331	76.0313	0.0018	211	0,014%
$C_6H_5^+$	77.0414	77.0391	0.0023	1520	0,098%
$C_6H_6^+$	78.0483	78.0469	0.0013	430	0,028%
$C_6H_7^+$	79.0570	79.0548	0.0022	614	0,039%
$C_6H_8^+$	80.0633	80.0626	0.0007	138	0,009%
$C_6H_9^+$	81.0739	81.0704	0.0035	766	0,049%
$C_6H_{10}^+$	82.0759	82.0782	-0.0023	89	0,006%
$C_6H_{11}^+$	83.0926	83.0861	0.0065	361	0,023%
$C_6H_{12}^+$	84.0947	84.0939	0.0008	47	0,003%
$C_6H_{13}^+$	85.1094	85.1017	0.0077	149	0,010%
$C_7H_2^+$	86.0176	86.0156	0.0019	212	0,014%
$C_7H_3^+$	87.0262	87.0235	0.0027	334	0,021%
$C_7H_4^+$	88.0381	88.0313	0.0068	94	0,006%
$C_7H_5^+$	89.0410	89.0391	0.0019	279	0,018%
$C_7H_6^+$	90.0426	90.0469	-0.0044	70	0,005%
$C_4H_{11}S^+$	91.0578	91.0581	-0.0003	1259	0,081%
$C_7H_7^+$	91.0578	91.0548	0.0030	1259	0,081%
$C_4H_{12}S^+$	92.0623	92.0660	-0.0037	184	0,012%
$C_7H_8^+$	92.0623	92.0626	-0.0003	184	0,012%
$C_7H_9^+$	93.0725	93.0704	0.0020	228	0,015%
$C_4H_{13}S^+$	93.0725	93.0738	-0.0013	228	0,015%
$C_7H_{10}^+$	94.0830	94.0782	0.0047	42	0,003%
$C_7H_{11}^+$	95.0907	95.0861	0.0046	368	0,024%
$C_7H_{12}^+$	96.1007	96.0939	0.0068	39	0,003%
C_8H^+	97.0070	97.0078	-0.0008	192	0,012%
$C_7H_{13}^+$	97.1086	97.1017	0.0069	169	0,011%
$C_8H_2^+$	98.0180	98.0156	0.0024	187	0,012%
$C_8H_3^+$	99.0290	99.0235	0.0056	159	0,010%
$C_8H_4^+$	100.0301	100.0313	-0.0012	35	0,002%
$C_8H_5^+$	101.0426	101.0391	0.0035	73	0,005%
$C_8H_6^+$	102.0490	102.0469	0.0021	193	0,012%
$C_8H_7^+$	103.0569	103.0548	0.0021	214	0,014%
$C_8H_8^+$	104.0606	104.0626	-0.0020	102	0,007%
$C_8H_9^+$	105.0742	105.0704	0.0037	447	0,029%
$C_8H_{10}^+$	106.0756	106.0782	-0.0026	70	0,005%
$C_8H_{11}^+$	107.0889	107.0861	0.0028	77	0,005%
$C_8H_{12}^+$	108.0958	108.0939	0.0019	20	0,001%
$C_8H_{13}^+$	109.1059	109.1017	0.0042	120	0,008%
$C_9H_2^+$	110.0194	110.0156	0.0038	143	0,009%
$C_8H_{14}^+$	110.1059	110.1095	-0.0036	17	0,001%
$C_9H_3^+$	111.0260	111.0235	0.0026	146	0,009%
$C_9H_4^+$	112.0327	112.0313	0.0014	34	0,002%
$C_9H_5^+$	113.0423	113.0391	0.0032	64	0,004%
$C_9H_6^+$	114.0543	114.0469	0.0073	53	0,003%
$C_9H_7^+$	115.0568	115.0548	0.0021	729	0,047%

$C_9H_8^+$	116.0642	116.0626	0.0016	134	0,009%
$C_9H_9^+$	117.0711	117.0704	0.0007	172	0,011%
$C_9H_{10}^+$	118.0809	118.0782	0.0027	56	0,004%
$C_9H_{11}^+$	119.0896	119.0861	0.0036	240	0,015%
$C_9H_{12}^+$	120.0900	120.0939	-0.0039	48	0,003%
$C_9H_{13}^+$	121.1137	121.1017	0.0120	34	0,002%
$C_9H_{14}^+$	122.1195	122.1095	0.0099	5	0,000%
$C_9H_{15}^+$	123.1178	123.1174	0.0004	45	0,003%
$C_9H_{16}^+$	124.1232	124.1252	-0.0020	7	0,000%
$C_9H_{17}^+$	125.1386	125.1330	0.0056	6	0,000%
$C_{10}H_7^+$	127.0543	127.0548	-0.0005	217	0,014%
$C_{10}H_8^+$	128.0632	128.0626	0.0006	472	0,030%
$C_{10}H_9^+$	129.0710	129.0704	0.0006	222	0,014%
$C_{11}H_7^+$	139.0556	139.0548	0.0008	272	0,017%
$C_{11}H_9^+$	141.0693	141.0704	-0.0011	229	0,015%
$C_{12}H_8^+$	152.0616	152.0626	-0.0010	318	0,020%
$C_{13}H_9^+$	165.0716	165.0704	0.0011	424	0,027%
$C_{13}H_{13}^+$	169.0997	169.1017	-0.0020	209	0,013%
$C_{14}H_{10}^+$	178.0772	178.0782	-0.0010	222	0,014%
$C_{14}H_{11}^+$	179.0848	179.0861	-0.0013	174	0,011%
$C_{15}H_9^+$	189.0705	189.0704	0.0000	257	0,017%
$C_{15}H_{11}^+$	191.0784	191.0861	-0.0076	153	0,010%
$C_{15}H_{14}^+$	194.1011	194.1096	-0.0084	211	0,014%
$C_{15}H_{16}^+$	196.1182	196.1252	-0.0070	203	0,013%
$C_{16}H_{10}^+$	202.0835	202.0782	0.0052	206	0,013%
$C_{16}H_{14}^+$	206.1111	206.1096	0.0016	207	0,013%
$C_{17}H_{16}^+$	220.1270	220.1252	0.0018	204	0,013%
Na^+	22.9892	22.9898	-0.0006	38143	2,453%
Mg^+	23.9840	23.9850	-0.0011	3750	0,241%
$^{25}Mg^+$	24.9862	24.9858	0.0004	512	0,033%
$^{26}Mg^+$	25.9814	25.9826	-0.0012	535	0,034%
Al^+	26.9811	26.9815	-0.0004	46038	2,961%
Si^+	27.9756	27.9769	-0.0013	681	0,044%
AlH^+	27.9880	27.9894	-0.0014	557	0,036%
K^+	38.9642	38.9637	0.0005	13198	0,849%
Ca^+	39.9607	39.9626	-0.0019	107303	6,901%
CaH^+	40.9691	40.9704	-0.0013	10438	0,671%
$^{42}Ca^+$	41.9567	41.9586	-0.0019	755	0,049%
$^{43}Ca^+$	42.9582	42.9588	-0.0005	180	0,012%
AlO^+	42.9745	42.9765	-0.0019	200	0,013%
$^{44}Ca^+$	43.9542	43.9555	-0.0013	2878	0,185%
$AlOH^+$	43.9834	43.9843	-0.0009	922	0,059%
$SiOH^+$	44.9813	44.9797	0.0016	1073	0,069%
Ti^+	47.9517	47.9479	0.0038	189	0,012%
Cr^+	51.9406	51.9405	0.0001	1284	0,083%

$^{53}Cr^+$	52.9410	52.9406	0.0003	165	0,011%
CaO^+	55.9561	55.9575	-0.0014	10567	0,680%
$CaOH^+$	56.9644	56.9653	-0.0009	51629	3,320%
Ca_2O^+	95.9188	95.9201	-0.0013	6760	0,435%
$Ca_2O_2^+$	111.9139	111.9150	-0.0011	6967	0,448%
$Ca_2O_2H^+$	112.9227	112.9228	-0.0001	19080	1,227%
Cs^+	132.9092	132.9054	0.0037	79109	5,088%
$Ca_3O_3^+$	167.8712	167.8725	-0.0013	1940	0,125%
$Ca_3O_3H^+$	168.8801	168.8803	-0.0002	6288	0,404%
$Ca_4O_4^+$	223.8280	223.8300	-0.0020	1104	0,071%
$Ca_4O_4^+$	224.8385	224.8378	0.0007	2686	0,173%
$Ca_5O_5^+$	279.7865	279.7875	-0.0010	360	0,023%
$Ca_5O_5H^+$	280.7972	280.7954	0.0019	784	0,050%
$Ca_6O_6^+$	335.7427	335.7450	-0.0023	423	0,027%
$Ca_6O_6H^+$	336.7554	336.7529	0.0026	650	0,042%

Orbagnoux (orba) veine negative ions

Proposed formula	Meas. m/z	Calc. m/z	δ (Da)	Int.	Rel. Int. (%)
C^-	12.0005	12.0000	0.0005	1818	0,540%
CH^-	13.0080	13.0078	0.0002	3472	1,031%
CH_2^-	14.0160	14.0157	0.0004	346	0,103%
O^-	15.9951	15.9949	0.0002	11782	3,497%
OH^-	17.0030	17.0027	0.0002	10576	3,139%
C_2^-	24.0003	24.0000	0.0003	3325	0,987%
C_2H^-	25.0087	25.0078	0.0008	7366	2,186%
CN^-	26.0041	26.0031	0.0010	2092	0,621%
S^-	31.9716	31.9721	-0.0005	1925	0,571%
HS^-	32.9805	32.9799	0.0006	1377	0,409%
Cl^-	34.9691	39.9689	-4.9998	2980	0,885%
C_3^-	36.0007	36.0000	0.0007	641	0,190%
$_{37}Cl^-$	36.9659	36.9659	-0.0000	987	0,293%
C_3H^-	37.0087	37.0078	0.0009	253	0,075%
$C_3H_2^-$	38.0170	38.0157	0.0013	212	0,063%
C_4^-	48.0012	48.0000	0.0012	815	0,242%
C_4H^-	49.0090	49.0078	0.0012	1841	0,546%
C_2S^-	55.9738	55.9721	0.0017	206	0,061%
C_2HS^-	56.9823	56.9799	0.0024	495	0,147%
C_5^-	60.0013	60.0000	0.0013	343	0,102%
C_5H^-	61.0100	61.0078	0.0022	172	0,051%
C_3S^-	67.9745	67.9721	0.0024	68	0,020%
C_3HS^-	68.9836	68.9799	0.0037	47	0,014%
C_6^-	72.0012	72.0000	0.0012	348	0,103%
C_6H^-	73.0107	73.0078	0.0029	706	0,210%
C_4S^-	79.9676	79.9721	-0.0044	113	0,034%
C_4HS^-	80.9830	80.9799	0.0031	225	0,067%

C_7^-	84.0020	84.0000	0.0020	157	0,047%
C_7H^-	85.0107	85.0078	0.0028	99	0,029%
C_5S^-	91.9713	91.9721	-0.0008	51	0,015%
C_5HS^-	92.9728	92.9799	-0.0071	55	0,016%
C_8^-	96.0013	96.0000	0.0013	156	0,046%
C_8H^-	97.0105	97.0078	0.0027	300	0,089%
C_6S^-	103.9730	103.9721	0.0010	44	0,013%
C_6HS^-	104.9823	104.9799	0.0024	102	0,030%
C_9^-	108.0029	108.0000	0.0029	56	0,017%
C_9H^-	109.0109	109.0078	0.0031	62	0,018%
C_7S^-	115.9738	115.9721	0.0017	11	0,003%
C_7HS^-	116.9835	116.9799	0.0037	15	0,004%
C_{10}^-	120.0023	120.0000	0.0023	47	0,014%
$C_{10}H^-$	121.0116	121.0078	0.0038	121	0,036%
C_8S^-	127.9741	127.9721	0.0020	14	0,004%
C_8HS^-	128.9798	128.9799	-0.0000	45	0,013%
C_{11}^-	131.9991	132.0000	-0.0009	20	0,006%
$C_{11}H^-$	133.0071	133.0078	-0.0007	23	0,007%
C_9S^-	139.9691	139.9721	-0.0029	7	0,002%
C_9SH^-	140.9742	140.9799	-0.0057	7	0,002%
C_{12}^-	144.0026	144.0000	0.0026	23	0,007%
$C_{12}H^-$	145.0077	145.0078	-0.0002	49	0,015%
Au^-	196.9641	196.9666	-0.0025	2409	0,715%
Au_2^-	393.9192	393.9331	-0.0139	278	0,083%
Au_3^-	590.8753	590.8997	-0.0243	472	0,140%

Strelley Pool Chert (SPC) positive ions

Proposed formula	Meas. m/z	Calc. m/z	δ (Da)	Int.	Rel. Int. (%)
H^+	1.0075	1.0078	-0.0003	354	0,209%
C^+	12.0006	12.0000	0.0006	26	0,015%
CH^+	14.0166	13.0078	1.0088	71	0,042%
CH_2^+	15.0245	14.0157	1.0088	381	0,225%
$C_2H_2^+$	26.0179	26.0157	0.0022	43	0,025%
$C_2H_3^+$	27.0267	27.0235	0.0033	372	0,220%
$C_2H_4^+$	28.0333	28.0313	0.0020	44	0,026%
CHO^+	29.0058	29.0027	0.0030	200	0,118%
$C_2H_5^+$	29.0412	29.0391	0.0021	288	0,170%
$C_2H_6^+$	30.0387	30.0469	-0.0083	97	0,057%
C_3H^+	37.0116	37.0078	0.0038	31	0,018%
$C_3H_2^+$	38.0181	38.0157	0.0025	53	0,031%
$C_3H_3^+$	39.0264	39.0235	0.0030	423	0,250%
$C_3H_4^+$	40.0342	40.0313	0.0029	47	0,028%
$C_3H_5^+$	41.0435	41.0391	0.0043	557	0,329%
$C_3H_6^+$	42.0392	42.0470	-0.0078	228	0,135%
$C_3H_7^+$	43.0590	43.0548	0.0042	159	0,094%
$C_3H_8^+$	44.0564	44.0626	-0.0062	208	0,123%
$C_4H_2^+$	50.0192	50.0157	0.0036	41	0,024%
$C_4H_3^+$	51.0290	51.0235	0.0055	148	0,087%
$C_4H_4^+$	52.0347	52.0313	0.0034	50	0,030%
$C_4H_5^+$	53.0441	53.0391	0.0050	211	0,125%
$C_4H_6^+$	54.0406	54.0470	-0.0064	36	0,021%
$C_4H_7^+$	55.0611	55.0548	0.0064	228	0,135%
$C_4H_8^+$	56.0566	56.0626	-0.0060	91	0,054%
$C_4H_9^+$	57.0764	57.0704	0.0060	43	0,025%
$C_5H_2^+$	62.0209	62.0157	0.0052	37	0,022%
$C_5H_3^+$	63.0300	63.0235	0.0065	99	0,058%
$C_5H_4^+$	64.0333	64.0313	0.0020	23	0,014%
$C_5H_5^+$	65.0442	65.0391	0.0051	102	0,060%
$C_5H_6^+$	66.0497	66.0469	0.0027	30	0,018%
$C_5H_7^+$	67.0622	67.0548	0.0075	73	0,043%
$C_5H_8^+$	68.0560	68.0626	-0.0066	24	0,014%
$C_5H_9^+$	69.0784	69.0704	0.0079	47	0,028%
$C_6H_2^+$	74.0173	74.0156	0.0017	38	0,022%
$C_6H_3^+$	75.0295	75.0235	0.0061	45	0,027%
$C_6H_4^+$	76.0349	76.0313	0.0036	13	0,008%
$C_6H_5^+$	77.0440	77.0391	0.0049	195	0,115%
$C_6H_6^+$	78.0512	78.0469	0.0043	36	0,021%
$C_6H_7^+$	79.0581	79.0548	0.0034	51	0,030%
$C_6H_8^+$	80.0645	80.0626	0.0019	18	0,011%
$C_6H_9^+$	81.0785	81.0704	0.0081	51	0,030%
$C_6H_{10}^+$	82.0775	82.0782	-0.0007	14	0,008%

$C_6H_{11}^+$	83.0884	83.0861	0.0023	14	0,008%
$C_6H_{12}^+$	84.0994	84.0939	0.0055	6	0,004%
$C_7H_2^+$	86.0187	86.0156	0.0030	23	0,014%
$C_7H_3^+$	87.0287	87.0235	0.0052	29	0,017%
$C_7H_4^+$	88.0303	88.0313	-0.0010	271	0,160%
$C_7H_5^+$	89.0349	89.0391	-0.0043	39	0,023%
$C_7H_7^+$	91.0594	91.0548	0.0047	118	0,070%
$C_7H_8^+$	92.0503	92.0626	-0.0123	17	0,010%
$C_7H_9^+$	93.0625	93.0704	-0.0079	23	0,014%
$C_7H_{10}^+$	94.0821	94.0782	0.0039	14	0,008%
$C_7H_{11}^+$	95.0986	95.0861	0.0125	26	0,015%
$C_7H_{12}^+$	96.0973	96.0939	0.0034	6	0,004%
C_8H^+	97.0093	97.0078	0.0015	15	0,009%
$C_8H_2^+$	98.0251	98.0156	0.0094	10	0,006%
$C_8H_3^+$	99.0264	99.0235	0.0030	16	0,009%
$C_8H_4^+$	100.0293	100.0313	-0.0020	8	0,005%
$C_8H_5^+$	101.0405	101.0391	0.0014	8	0,005%
$C_8H_6^+$	102.0502	102.0469	0.0032	19	0,011%
$C_8H_7^+$	103.0562	103.0548	0.0014	25	0,015%
$C_8H_8^+$	104.0761	104.0626	0.0135	12	0,007%
$C_8H_9^+$	105.0777	105.0704	0.0072	28	0,017%
$C_9H_2^+$	110.0169	110.0156	0.0013	8	0,005%
$C_9H_3^+$	111.0403	111.0235	0.0168	17	0,010%
$C_9H_4^+$	112.0405	112.0313	0.0092	4	0,002%
$C_9H_5^+$	113.0379	113.0391	-0.0013	12	0,007%
$C_9H_6^+$	114.0513	114.0469	0.0044	10	0,006%
$C_9H_7^+$	115.0604	115.0548	0.0056	65	0,038%
$C_9H_8^+$	116.0595	116.0626	-0.0031	19	0,011%
$C_9H_9^+$	117.0623	117.0704	-0.0082	20	0,012%
$C_9H_{10}^+$	118.0802	118.0782	0.0019	9	0,005%
$C_9H_{11}^+$	119.0989	119.0861	0.0128	9	0,005%
$C_9H_{12}^+$	120.0909	120.0939	-0.0030	2	0,001%
$C_9H_{13}^+$	121.1041	121.1017	0.0024	8	0,005%
$C_9H_{14}^+$	122.0948	122.1095	-0.0147	5	0,003%
$C_9H_{15}^+$	123.1092	123.1174	-0.0082	4	0,002%
$C_{10}H_7^+$	127.0636	127.0548	0.0088	28	0,017%
$C_{10}H_8^+$	128.0515	128.0626	-0.0111	40	0,024%
$C_{10}H_9^+$	129.0630	129.0704	-0.0074	27	0,016%
$C_{10}H_{11}^+$	131.0888	131.0861	0.0027	22	0,013%
$C_{11}H_7^+$	139.0614	139.0548	0.0066	24	0,014%
$C_{12}H_7^+$	151.0394	151.0548	-0.0154	22	0,013%
$C_{12}H_8^+$	152.0390	152.0626	-0.0236	29	0,017%
$C_{13}H_9^+$	165.0701	165.0704	-0.0004	24	0,014%
$C_{14}H_{10}^+$	178.0753	178.0782	-0.0030	14	0,008%
$C_{15}H_9^+$	189.0594	189.0704	-0.0110	16	0,009%
$C_{15}H_{11}^+$	191.0725	191.0861	-0.0136	10	0,006%

$C_{16}H_{10}^+$	202.0652	202.0782	-0.0131	10	0,006%
Na^+	22.9910	22.9898	0.0013	7132	4,211%
K^+	38.9672	38.9637	0.0035	21006	12,402%

Strelley Pool Chert (SPC) negative ions

Proposed formula	Meas. m/z	Calc. m/z	δ (Da)	Int.	Rel. Int. (%)
H^-	1.0084	1.0078	0.0006	17054	3,248%
C^-	12.0006	12.0000	0.0006	1536	0,293%
CH^-	13.0083	13.0078	0.0005	1575	0,300%
CH_2^-	14.0165	14.0157	0.0009	126	0,024%
O^-	15.9951	15.9949	0.0002	30376	5,785%
OH^-	17.0032	17.0027	0.0005	8050	1,533%
C_2^-	24.0010	24.0000	0.0010	4572	0,871%
C_2H^-	25.0097	25.0078	0.0018	4701	0,895%
CN^-	26.0050	26.0031	0.0019	15789	3,007%
S^-	31.9724	31.9721	0.0003	2162	0,412%
O_2^-	31.9895	31.9898	-0.0004	653	0,124%
HS^-	32.9807	32.9799	0.0008	410	0,078%
HO_2^-	32.9970	32.9977	-0.0006	143	0,027%
C_3^-	36.0025	36.0000	0.0025	403	0,077%
C_3H^-	37.0087	37.0078	0.0009	97	0,018%
CNO^-	42.0014	41.9980	0.0034	1320	0,251%
C_4^-	48.0035	48.0000	0.0035	661	0,126%
C_4H^-	49.0122	49.0078	0.0044	439	0,084%
$C_4H_2^-$	50.0086	50.0157	-0.0070	267	0,051%
C_2S^-	55.9741	55.9721	0.0020	52	0,010%
C_2HS^-	56.9869	56.9799	0.0070	47	0,009%
C_5^-	60.0052	60.0000	0.0052	193	0,037%
C_5H^-	61.0104	61.0078	0.0025	58	0,011%
C_3S^-	67.9743	67.9721	0.0023	15	0,003%
C_3HS^-	68.9915	68.9799	0.0116	9	0,002%
C_6^-	72.0064	72.0000	0.0064	180	0,034%
C_6H^-	73.0148	73.0078	0.0070	139	0,026%
C_4S^-	79.9727	79.9721	0.0006	95	0,018%
C_4HS^-	80.9729	80.9799	-0.0070	16	0,003%
C_7^-	84.0054	84.0000	0.0054	64	0,012%
C_7H^-	85.0165	85.0078	0.0087	27	0,005%
C_8^-	96.0077	96.0000	0.0077	76	0,014%
C_8H^-	97.0108	97.0078	0.0030	55	0,010%
C_9^-	108.0076	108.0000	0.0076	29	0,006%
C_9H^-	109.0075	109.0078	-0.0003	17	0,003%
C_{10}^-	120.0030	120.0000	0.0030	20	0,004%
$C_{10}H^-$	121.0175	121.0078	0.0097	26	0,005%
F^-	18.9989	18.9984	0.0005	991	0,189%

Si^-	27.9764	27.9769	-0.0005	309	0,059%
Cl^-	34.9700	34.9689	0.0012	7728	1,472%
$^{37}Cl^-$	36.9673	36.9659	0.0014	2400	0,457%
SiO_2^-	59.9687	59.9668	0.0019	2561	0,488%
SiO_2H^-	60.9764	60.9746	0.0018	599	0,114%
SiO_3^-	75.9643	75.9617	0.0026	2151	0,410%
SiO_3H^-	76.9733	76.9695	0.0038	1517	0,289%
$SiO_3H_2^-$	77.9682	77.9773	-0.0091	134	0,026%
$Si_2O_5^-$	135.9319	135.9284	0.0034	197	0,038%
$Si_2O_5H^-$	136.9408	136.9363	0.0045	250	0,048%
$Si_4O_4H_3^-$	178.9189	178.9108	0.0080	198	0,038%
Au^-	196.9658	196.9666	-0.0008	2570	0,489%
Au_2^-	393.9297	393.9331	-0.0034	462	0,088%
$Au_2C_2H_2^-$	419.9452	419.9488	-0.0035	295	0,056%
Au_2CN^-	419.9452	419.9362	0.0090	295	0,056%
Au_3^-	590.8988	590.8997	-0.0009	1060	0,202%
Au_4^-	787.8632	787.8662	-0.0030	141	0,027%